Fakultät für Naturwissenschaften

Novel Approaches for Tuning Iron Photosensitizers: Exploring the Reservoir Effect and One-Component Systems

Dissertation zur Erlangung des akademischen Grades

DOKTOR DER NATURWISSENSCHAFTEN

Vorgelegt von

LENNART SCHMITZ

Paderborn 2026

Promotionskommission

Prof Dr. Nieves López Salas	Kommissionsvorsitzende
Prof. Dr. Matthias Bauer	Erstgutachter
Prof. Dr. Felix Richard Fischer	Zweitgutachter
Prof. Dr. Torsten Gutmann	Drittprüfer

Eingereicht: 30.03.2026

Disputation: 26.05.2026

Eidesstattliche Erklärung

Hiermit versichere ich, dass ich die vorliegende Arbeit selbstständig verfasst habe und keine anderen als die von mir angegebenen Hilfsmittel verwendet habe. Ich versichere, dass ich keine anderen als die angegebenen Quellen benutzt und alle wörtlich oder sinngemäß aus anderen Werken übernommenen Aussagen als solche gekennzeichnet habe. Genehmigungen zur Veröffentlichung der urheberrechtlich geschützten Publikationen wurden eingeholt.

Paderborn, den 30.03.2026,

It is good to have an end to journey toward,

but it is the journey that matters in the end.

- ***Ernest Hemingway***

Danksagungen

Zuerst möchte ich Matthias Bauer danken, in dessen Arbeitskreis ich für 9 Jahre während meines Studiums und meiner Promotion forschen und arbeiten durfte. Die Unterstützung hat mir immer Sicherheit gegeben und mich die Zeit genießen lassen. Auch meinem Zweitgutachter Hans Egold, der nicht nur ein großartiger Dozent war, sondern mich auch bei meiner Forschung immer unterstützt hat möchte ich hier danken. Mein Drittprüfer Felix Fischer ist erst zum Ende meiner Promotion zu dieser Gruppe gestoßen, doch war von Anfang eine willkommene Ergänzung, und ich möchte auch ihm für seine Unterstützung danken.

Auch bei den anderen Personen, die mich bei meiner Arbeit unterstützt haben, möchte ich mich bedanken. Das gesamte Team von der zentralen Analytik für ihre Hilfe bei meiner Arbeit. Britta für den administrativen Support. Und auch Roland nicht nur für seine Forschungsunterstützung, sondern auch als heimlicher Vizechef der sich um so viele Kleinigkeiten in der Gruppe kümmert.

Auch unter meinen Kollegen habe ich viele Freunde gefunden. Wenn man so lange in einem Arbeitskreis bleibt, ist das wohl selbstverständlich. Auch wenn sie die letzten Jahre meiner Promotion nicht mehr im Arbeitskreis war, ist die K4.09 Crew noch immer das erste, woran ich denke, wenn ich an meine Zeit hier denke. Insbesondere bei Marina, die mich unter ihre Fittiche genommen und in den Arbeitskreis integriert hat, möchte ich mich bedanken. Ich hoffe ich habe ihr das Leben nicht zu schwer gemacht. Aber auch die vielen anderen netten Kollegen, die ich teilweise meine Freunde nennen darf, waren ein wichtiger Teil des Arbeitskreises für mich.

Als Nächstes möchte ich allen Freunden außerhalb des Arbeitskreises danken die während Studien- und Promotionszeit an meiner Seite waren. Meine Jungs aus der Schulzeit, welch in alle Himmelsrichtungen verstreut sind, aber zu welchen ich zum Glück immer den Kontakt erhalten konnte. Unsere „Lerngruppe“, die auch jetzt, lange nach unserer Studienzeit, immer noch zusammenhält. Und natürlich die vielen verstreuten Freunde die ich entlang des Weges aufgesammelt habe.

Der größte Danke gilt aber auf der einen Seite meinen Eltern und auf der anderen Seite meiner Frau Nicole (Während ich das schreibe, sind wir zwar noch verlobt, aber wenn diese Arbeit veröffentlicht wird, hat sich das geändert). Meine Eltern haben mich zu dem Menschen gemacht der ich bin und mir durch ihre Unterstützung ermöglicht den Weg zu gehen den ich gegangen bin. Und bis heute kann ich immer darauf zählen, dass ihr mich bei allem unterstützt. Dafür bin ich euch auf ewig dankbar und ich hätte mir nichts Besseres wünschen können.

Nicole, du bist der Dreh- und Angelpunkt meines Lebens geworden, und egal was gerade so los ist in meinem Leben, sobald ich durch die Haustür komme, ist das alles halb so wichtig, weil ich weiß, dass du immer für mich da bist. Du unterstützt mich bei meiner Arbeit, du unterstützt mich, wenn ich schwere Zeiten habe, und teilst die guten Zeiten mit mir. Dafür werde ich dir immer dankbar sein.

Contents

Abstract

Given the growing global demand for energy, the development of sustainable methods for chemical synthesis is essential. Homogeneous transition metal systems capable of utilising sunlight directly for chemical reactions represent a promising approach.

To develop economically viable systems based on more abundant alternatives to late transition metals, this work focuses on iron-based photosensitizers. These are characterised by good redox stability and high extinction coefficients. Two fundamental methods are investigated to address the reduced lifetimes compared to analogous late transition metal systems. Both approaches are applied to the same base complex.

The first approach focuses on the reservoir effect, which is intended to significantly extend the lifetime of excited states through combination with an organic chromophore. The influence of the energy difference between the excited states of both molecular parts and their electronic decoupling is investigated.

In the second approach, the concept of a single-component system is investigated, in which a second catalytic unit is directly bound to the base complex. This reduces the dependence on diffusion-limited processes. To investigate the effects on the base complex, coordination is simulated by methylation.

Kurzzusammenfassung

Angesichts des wachsenden globalen Energiebedarfs ist die Entwicklung nachhaltiger Wege zur chemischen Synthese unerlässlich. Homogene Übergangsmetall-Systeme, die Sonnenlicht direkt für chemische Reaktionen nutzen können sind ein vielversprechender Ansatz.

Um wirtschaftlich tragfähige Systeme zu entwickeln, die auf weniger seltenen Alternativen zu späten Übergangsmetallen basieren, konzentriert sich diese Arbeit auf eisenbasierte Photosensibilisatoren. Diese zeichnen sich durch gute Redoxstabilität und hohe Extinktionskoeffizienten aus. Es werden zwei grundlegende Methoden untersucht, um die im Vergleich zu analogen Systemen mit späten Übergangsmetallen verkürzten Lebensdauern zu beheben. Beide Ansätze werden am selben Basiskomplex angewandt.

Der erste Ansatz konzentriert sich auf den Reservoir-Effekt, der die Lebensdauer angeregter Zustände durch die Kombination mit einem organischen Chromophor erheblich verlängern soll. Der Einfluss der Energiedifferenz der angeregten Zustände beider Molekülteile und ihrer elektronischen Entkopplung wird untersucht.

Beim zweiten Ansatz wird das Konzept des Einkomponentensystem untersucht, bei dem eine zweite katalytische Einheit direkt an den Basiskomplex gebunden ist. Die Abhängigkeit von diffusionsbegrenzten Prozessen wird so verringert. Um die Auswirkungen auf den Basiskomplex zu untersuchen, wird die Koordination durch Methylierung simuliert.

Publications

L. Schmitz, M. A. Argüello Cordero, M. J. Al-Marri, R. Schoch, H. Egold, A. Neuba, J. Steube, B. Bracht, O. S. Bokareva, S. Lochbrunner and M. Bauer, Chromophore Induced Effects in Iron(III) Complexes, *Inorg. Chem.*, **2025**, 64, 14101. - 10.1021/acs.inorgchem.5c00526.

L. Schmitz, S. Dabelstein, M. A. Cordero, L. Fritsch, B. Bracht, R. Schoch, H. Egold, J. Steube, F. Fischer, S. Lochbrunner and M. Bauer, Reservoir Effect in bichromophoric Fe^{III} Complexes with Methylene Bridge, *Dalton Trans.,* **2026** - 10.1039/D5DT02915E.

L. Schmitz, J. L. Pérez Lustres, R. Viel, J. Löseke, L. Fritsch, X. Li, R. Schoch, S. Haacke, K. Heyne, M. Bauer, Pyridine-substituted Fe(III) complexes – On the way to one-component photo-catalytical systems, *Phys. Chem. Chem. Phys.*, **2026**.

M. Huber-Gedert, M. Nowakowsky, A. Kertem, L. Burkhardt, N. Lindner, R. Schoch, R. Herbst-Irmer, A. Neuba, L. Schmitz, T.-K. Choi, J. Kubicki, W. Gawelda and M. Bauer, Fundamental Characterization, Photophysics and Photocatalysis of a Base Metal Iron(II)-Cobalt(III) Dyad, *Chem. Eur. J.*, **2021** - 10.1002/chem.202100766.

J. Steube, L. Fritsch, A. Kruse, O. S. Bokareva, S. Demeshko, H. Elgabarty, R. Schoch, M. Alaraby, H. Egold, B. Bracht, L. Schmitz, S. Hohloch, T. D. Kühne, F. Meyer, O. Kühn, S. Lochbrunner and M. Bauer, Isostructural Series of a Cyclometalated Iron Complex in Three Oxidation States, *Inorg. Chem.*, **2024**, 63, 16964 - 10.1021/acs.inorgchem.4c02576.

Talks

M. A. Argüello Cordero, L. Schmitz, J. Steube, A. Kruse, M. Lang, P. Dierks, O. Bokareva, M. Bauer, O. Kühn and S. Lochbrunner: „Ultrafast Excited-State Dynamics of analogous FeIII-Photosensitizers with Linked Organic Chromophores“ **SPP (2102)-Meeting 2024 Universität Stuttgart 18.03. - 20.03.2024** *(Replacing Jakob Steube in a shared presentation with Miguel A. Argüello Cordero).*

L. Schmitz, M. A. Argüello Cordero, R. Schoch, A. Neuba, J. Steube, B. Bracht, O. Bokareva, S. Lochbrunner, M. Bauer: “Multichromophoric approach for CCC-coordinated iron complexes – Changes in photochemical behaviour” **29th GDCh Lecture Conference on Photochemistry in Mainz 16.09 – 19.09 2024**.

Poster Presentations

L. Schmitz, M. Bauer: “Cyclometalated Fe(III)-complexes linked to organic chromophores as photosensitizers for photocatalytic water splitting (proton reduction)” **SPP-Meeting 2022 Jena May 2022**.

L. Schmitz, O. Bokareva, M. Cordero, M. Lang, R. Schoch , A. Neuba, S. Lochbrunner, O. Kühn, M. Bauer: “Improving a Cyclometalated Fe(III)-complex as photosensitizer by coupling of organic chromophores” **The 31st International Conference on Photochemistry in Sapporo 23.07 – 28.07 2023**.

L. Schmitz, O. Bokareva, M. Cordero, M. Lang, R. Schoch , A. Neuba, S. Lochbrunner, O. Kühn, M. Bauer: “Improving a Cyclometalated Fe(III)-complex as photosensitizer by coupling of organic chromophores” **Central European Conference on Photochemistry 18.02 – 22.02.2024**.

Cooperations and Tools

NMR spectra were analyzed with TopSpin 4.1.3 ©2021 Bruker Biospin GmbH. MestReNova 11.0.4 ©2017 Mestrelab Research S.L. was utilized for NMR visualization and mass spectra analysis. Chemical structures were drawn with ChemDraw 20.1.1 ©1998-2021 PerkinElmer Informatics, Inc. Spectroscopic data was processed and visualized with OriginPro 10.0.0.154 ©1991-2022 OriginLab Corporation. The thesis was written in Microsoft Word Version 2601.

Transient absorption spectroscopy and time resolved emission spectroscopy for the reservoir effect focused projects were done by Dr. Miguel A. Argüello Cordero and Samira Dabelstein in the work group of Prof. Dr. Stefan Lochbrunner at the University of Rostock. For the third project transient absorption spectroscopy was done by Dr. Jose L. Perez Lustres in the work group of Prof. Dr. Karsten Heyne at the Freie Universität Berlin. Time-resolved emission spectroscopy was done by Dr. Ronan Viel in the work group of Prof. Dr. Stefan Haacke at the Strasbourg University. (TD)DFT for the projects were done by Dr. Olga Bokareva at the University of Rostock (Project 1), and by Dr. Lorena Fritsch (Project 2) and Jannik Löseke (Project 3) in our work group. Crystal Structures were analyzed by Dr. Roland Schoch from our work group. Bastian Bracht and Niklas Mergard contributed to this work as student assistants.

List of Abbreviations

CV	Cyclic Voltammetry
GS	Ground State
ISC	Intersystem Crossing
LMCT	Ligand-to-Metal Charge Transfer
MC	Metal-Centred
MLCT	Metal-to-Ligand Charge Transfer
MS	Mass Spectrometry
NHC	N-Heterocyclic Carbene
NMR	Nuclear Magnetic Resonance
PGM	Platinum Group Metals
PS	Photosensitizer
SR	Sacrificial Reagent
TCSPC	Time-Correlated Single Photon Counting
TR	Transfer Reagent

1. Introduction

The current growth of humankinds' energy and resource demand is unsustainable, especially considering CO_2 emissions[1] and the resulting climate change.[2] It is estimated that this will lead to a global income reduction of 19%, far outweighing the costs necessary to mitigate this manmade climate change.[3] Since most nations in the world operate within a free market framework, a reduction of greenhouse gases by reducing economic growth or even shrinking economies is unlikely at best. Therefore, the responsibility lies with the scientific community to uncover new more sustainable ways to generate energy and apply them in the synthesis of all manners of chemical compounds, possibly enabling the hotly debated concept of "green growth".[4]

The most widely and easily available energy source for sustainable processes is undoubtedly solar energy, which is already being used on a large and ever increasing scale for electricity production worldwide.[5] Nevertheless, the direct application of sunlight as an energy source in chemical reactions without the bypass of electric energy would relieve the photovoltaic sector during the transition to sustainable electricity generation necessary to prevent a global climate catastrophe. A look at the total electricity production worldwide shows a promising trend with renewables being close to the biggest electricity source in 2023 at more than 30%.[5,6] However, looking at primary energy sources reveals, that electricity production only accounts for 17% of human energy consumption. And this broader view on the issue shows a much bleaker situation with renewables below 15% of the total energy produced (Figure 1).[6,7] Including nuclear energy as a sustainable energy source, which is stretching the term, still does not push this value above 20%. The direct use of sunlight as a primary energy source for chemical reactions could make renewable energy more readily available outside the electricity sector and is therefore highly desirable.

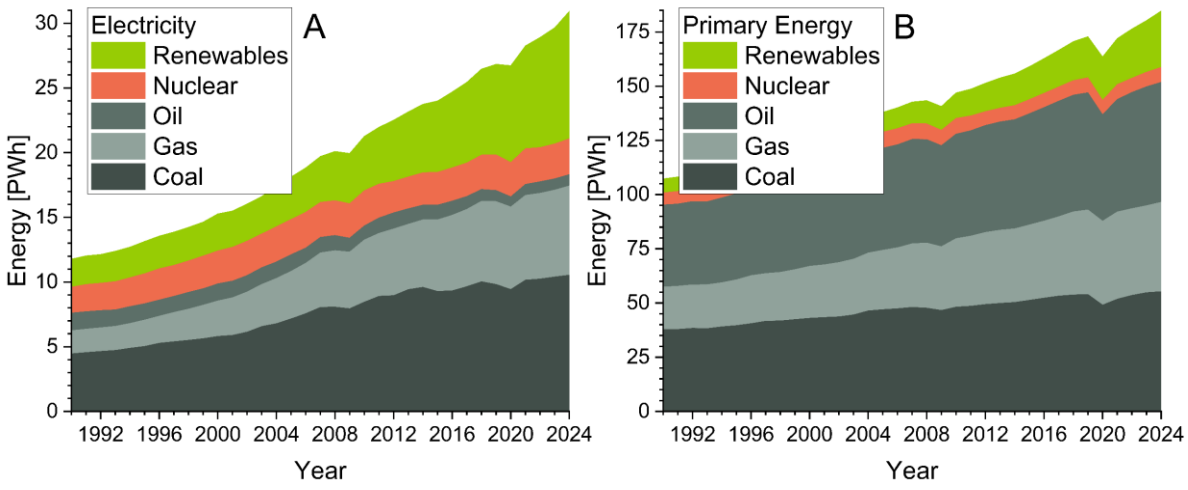

Figure 1: Energy sources used worldwide from 1990 to 2024. ***A:*** *Global electricity production by energy source.*[5,6] ***B:*** *Primary energy consumption by energy source.*[6,7]

To make this omnipresent energy source directly available for the chemical industry the application of organometallic photosensitizers as light harvesters in homogenous photocatalysis is an intriguing approach.[8]

Many capable photosensitizers for this application based on late transition metals are known, mostly utilizing metal-to-ligand-charge-transfer states (MLCT).[9] Their general efficiency in photocatalysis can be summarized by three technical criteria.[10] First, they must absorb in the solar spectrum, which is dominated by the visible spectrum.[11] Second, they must be able to withstand many cycles of oxidation and reduction at sufficiently high potentials for the reaction in question. Both criteria are fulfilled by many published organometallic photosensitizers,[9,12,13] while organic photosensitizers often lack strong absorption bands in the visible range and are less redox stable. The third criterion, a high lifetime of the excited state, necessary for efficient energy/electron transfer from the catalyst to the substrate is fulfilled by organic chromophores and late transition metal complexes. The latter inhibit a quick relaxation of the catalytically active MLCT state into a metal-centred state (MC) due to their high ligand field splitting. However, a fourth criterion not focusing on the catalytic mechanism is necessary to gauge a given system's potential for large-scale industrial processes, such as the production of hydrogen through water splitting: The economic impact. Due to their scarcity, photosensitizers based on late transition metals are not viable in this regard.[12] Additionally they often have high environmental impacts.[14,15] Therefore, organometallic photosensitizers need to be utilizing early transition metals to make photocatalysis feasible on a large scale.[16] Iron, the most abundant transition metal,[17] is obviously the ideal candidate.

The research topic of this dissertation is the design of such iron photosensitizers, considering all four criteria. In three publications, different series of complexes based on the same base structure were synthesized and thoroughly investigated. The main design principles applied were the realization of the reservoir effect as well as the utilization of one-component systems. These results significantly provided to the scientific advance on this topic.

2. Theoretical Background

Photocatalysis

In photocatalysis, the energy necessary for a chemical reaction is provided by irradiation instead of the traditional application of heat. This allows for milder reaction conditions and a more energy efficient catalysis, since the energy is provided right at the involved molecules instead of heating the entire reaction medium.

A vital part of photocatalysis is the photosensitizer (PS), that converts light into chemically accessible energy. This energy can then be transferred (by energy transfer or electron transfer) to a different substrate. In the case of electron transfer, photoredox catalysis is observed: After excitation of the photosensitizer, the changed redox potentials enable a reduction or oxidation reaction exchanging an electron with another substrate (S1). The resulting $PS^{+/-}$ species must then undergo the opposite exchange with a second substrate (S2) to return to its original state closing the catalytic cycle (Scheme 1 A).[9]

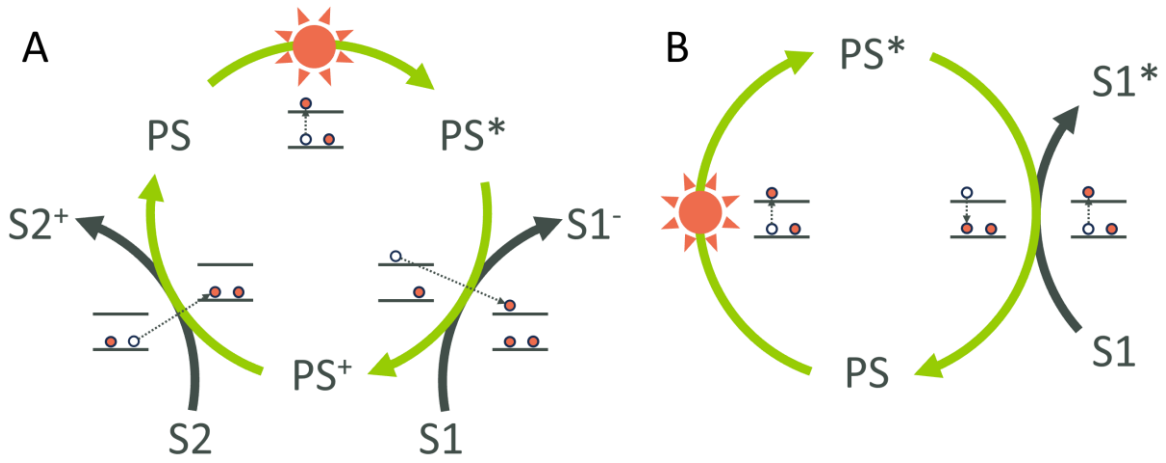

Scheme 1: Schematic depictions of A) a photoredox catalytic cycle. The oxidative quenching mechanism is shown. Inverting oxidation and reduction results in the reductive quenching cycle. B) a photocatalytic energy transfer cycle. The förster energy transfer is shown here, however, a Förster mechanism is also possible.[18] For each transition the change of electronic configuration in the HOMO/LUMO is depicted. S1 and S2 represent different substrates utilized in the catalytic process.

In an ideal system, both the reactions at S1 and at S2 are desired redox mechanisms (e.g. water splitting, where protons are reduced (S1) and oxygen atoms are oxidized (S2) to yield molecular hydrogen and oxygen respectively). In practice, these two reactions are often difficult to realize in the same reaction medium, since they enable reverse reactions between the product substrates S1' and S2'. In addition, both processes might include multistep mechanisms leading to overall complicated processes. Therefore, one of them is often replaced with a sacrificial reagent used to close the catalytic cycle while the other redox reaction yields a desired product.[19]

When the photocatalytic cycle undergoes energy transfer instead of electron transfer, only one substrate is needed, since the ground state is immediately recovered (Scheme 1B). This energy transfer can follow the Dexter energy transfer, where two electrons are transferred between

both moieties leaving the charge unchanged but affecting occupied energy levels. The Förster Resonance transfer mechanism, where the energy is transferred without electron transfer or radiation by dipole-dipole coupling is also possible.[18]

Instead of direct electron transfer to the substrate, it is typical to employ a second catalyst that mediates the desired chemical reaction. While this second catalyst is a vital part of the photocatalytic mechanism,[20] this work focuses on optimizing the light harvesting part of the cycle and therefore on new photosensitizer designs.

Photosensitizers

Photosensitizers are compounds used in heterogeneous or homogeneous systems to harvest light and enable chemical reactions. Heterogeneous PS research mainly focuses on semiconductors and is a promising and active field of research viable for many chemical reactions.[21] This section, however, will only focus on homogeneous systems due to the nature of the systems developed in this work.

In homogeneous photocatalysis, organic photosensitizers are widely used.[22] Eliminating the need for any metal centres is an intriguing path to prevent concerns about price and environmental impact of said metal. However, the increased stability, higher redox potentials and visible light absorption make organometallic compounds the more popular research topic. One of the earliest complexes investigated for their potential as photosensitizers are polypyridyl complexes, especially of ruthenium.[13,23] $[Ru(bpy)_3]^{2+}$ with a lifetime of roughly 1 µs may well be the most thoroughly investigated photoactive complex.[9,24] With visible light absorption, a long-lived ^{3}MLCT excited state and a reversible redox pair, it is an optimal prototype PS. However, this and other well-performing PS are based on Platinum Group Metals (PGM) famous for their scarcity and thus high prices and high environmental impact.[15]

Iron on the other hand is very abundant in earth's crust, in fact is the fourth most abundant element and most abundant transition metal in earth's crust and mantle.[25] It boasts a perfectly reversible redox pair and many reported iron complexes absorb strongly in the solar spectrum.[26] Therefore, an obvious first step was to investigate the analogous iron complexes of typical PGM-PS. Fe(II) and Ru(II) are isoelectronic, leading to the same available electronic ground- and excited states. What varies however is the relative energetic level of these states. The main reason for this is the primogenic effect, that reduces overlap of the d-orbitals with ligand orbitals. This decreased overlap is due to the lack of radial nodes in the wave functions of 3d-orbitals.[27] The bond strength in 3d-metal complexes is therefore generally reduced leading to less stable compounds. Utilization of multidentate ligands mostly solves this issue. However, the reduced ligand field splitting enabling an ultrafast relaxation pathway not present in the heavier homologs is the more pressing issue: The low-lying MC states enable an intersystem crossing (ISC) cascade, quenching the charge separated excited state on the 100 fs time scale.[28] Additionally, the long lifetime of the populated MC states can lead to a light-induced excited spin state trapping scenario (Scheme 2).[29] This leads to a depopulation of the

ground state (GS) making further excitation into the MLC state impossible effectively deactivating the PS.

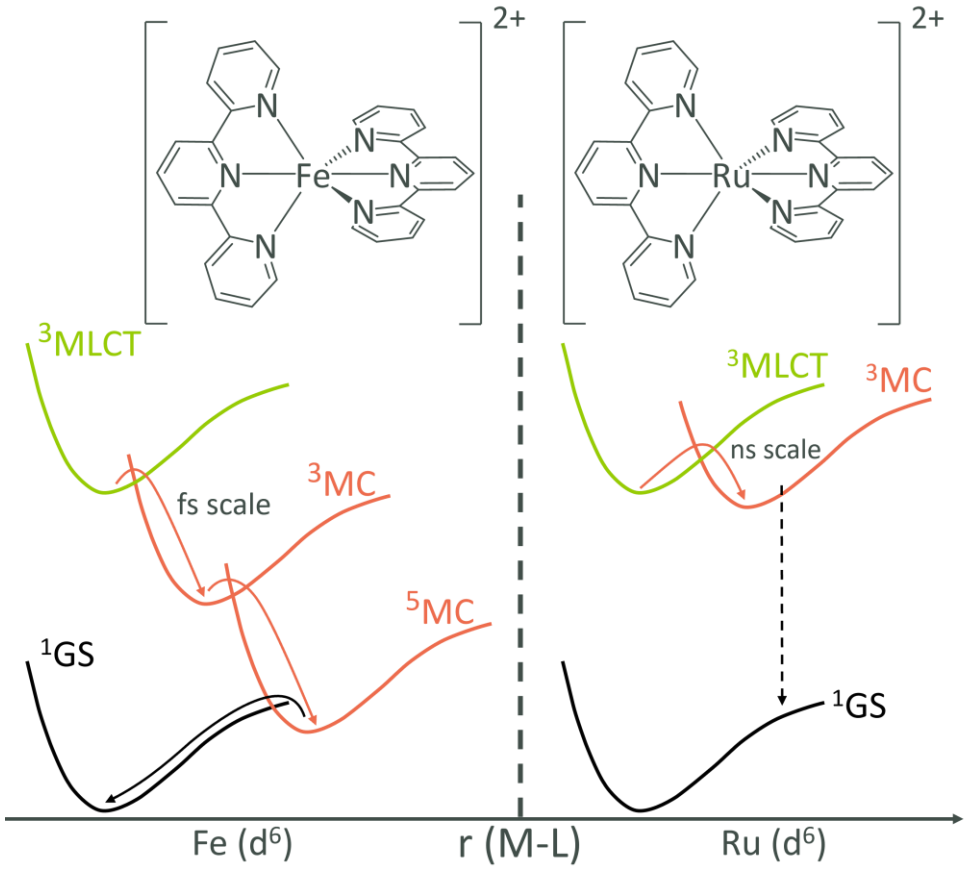

Scheme 2: Schematic depiction of the relaxation cascade after optical excitation in Iron polypyridyl complexes compared to their ruthenium homologs.[28]

Addressing this low lifetime in iron photosensitizers by smart ligand design is the main focus of research on iron photosensitizers.[30,31,32–35] Numerous approaches aiming at increasing the lifetime of the charge separated state are being investigated. Most of these follow one of two targets: Either the MC states are destabilized or the MLCT state is stabilized, to achieve an inversion of these states and inhibiting the relaxation cascade (Scheme 2).[35]

Since weak ligand field splitting is an inherent issue for iron PS's, a strong coordination sphere mitigating this is desirable. For typical Fe(II) d^5 or Fe(III) d^6 systems the octahedral coordination is an optimal case. The splitting between the HOMO and LUMO orbital sets is large compared to other typical coordination geometries.[36] Any distortion from the optimal 90° angle between ligands weakens the ligand metal overlap and therefore ligand field splitting. Nevertheless, most investigated systems are of distorted octahedral geometry due to the limiting bite angle of the applied ligands. This disadvantage is accepted to make ligand design more versatile and prevent a possible disruption of a conjugated π-electron system.

These delocalized electron systems represent another strategy for ligand design, since they stabilize the ligand localized acceptor orbitals in MLCT states slowing down relaxation into the

ground state.[28] A similar effect occurs from introducing electron withdrawing groups. The nature of the ligand can also directly influence the orbital structure at the metal centre.

One major advance with this approach was the introduction of NHC ligands (N-heterocyclic carbenes). These strong σ donors destabilize the e_g^* orbitals of the metal centre, which correspond to the MC states. The increased energy of those states leads to a slower relaxation, increasing the charge separated lifetime.[37] The excited state lifetime of such iron complexes is increased into the ps range (Figure 2).[30,33]

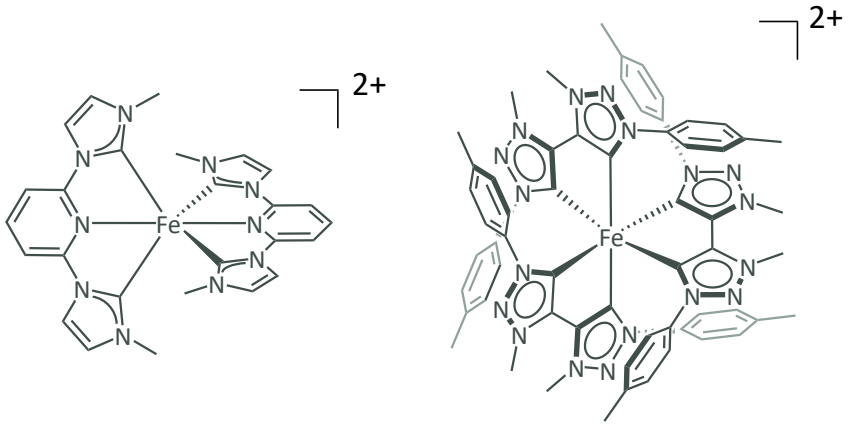

Figure 2: A: Exemplary Fe(II)-NHC complexes with increased MLCT lifetimes.[33] The right complex is not stable in aerated solutions.[30]

Complex A shown in Figure 2 has 4 NHC moieties resulting in a lifetime of 9 ps, which is already an improvement of about two orders of magnitude compared to the corresponding bis-terpyridine complex. By introducing two more NHC moieties complex B in Figure 2 achieves an additional increase in lifetime of two orders of magnitude. These strong σ donors lead to a high electron density at the iron centre and therefore a preferred oxidation state of +III. Accordingly, complex B is not stable in its +II oxidation state under ambient conditions and can only be obtained in deaerated solutions or as a solid, making its application for homogeneous photocatalysis questionable.

Since strong σ donors leading to a +III oxidation is a general issue, the focus of more recent iron photosensitizer research lies on Fe(III) complexes. Due to the d^5 electron configuration in these complexes, a ^{2}LMCT (ligand-to-metal charge-transfer) state is available. Here an electron from the ligand π orbital is transferred to the t_{2g} orbitals. This state is comparably low in energy and has generally longer lifetimes in the middle ps to low ns range due to the increased ligand field splitting.[32,34,38]

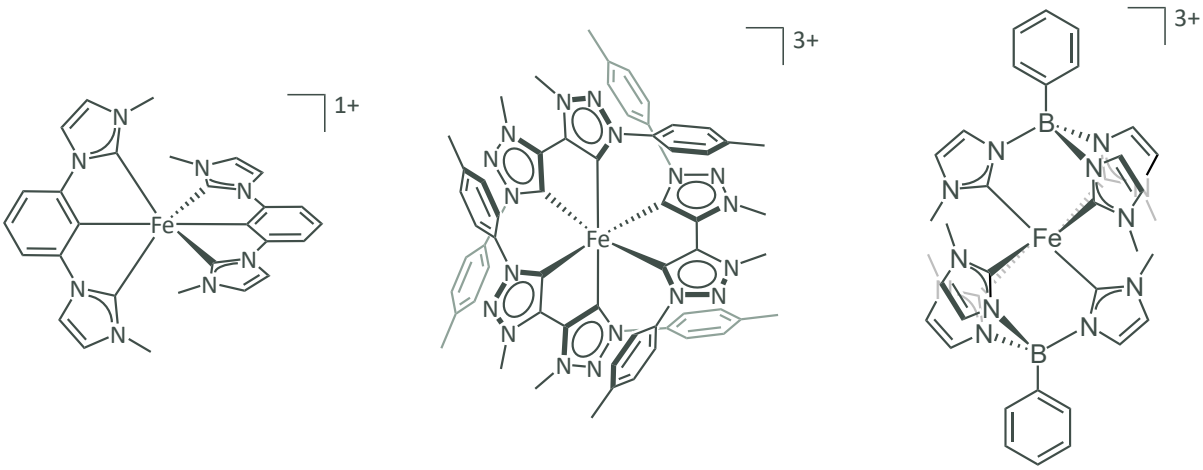

Figure 3: Exemplary Fe(III) complexes and their LMCT lifetimes. C: A bis-tridentate C^C^C complex utilizing two cyclometalated carbons and four NHC units.[34] D: A tris-bidentate applying 6 mesoionic carbene units.[38] E: A bis-tridentate scorpionate complex applying 6 NHC units.[32]

The ligand structures shown in Figure 3 all lead to air stable Fe(III) complexes and present a strong basis for further optimized systems. One of the more recently published complexes based on complex **C** reaches a lifetime of about 100 ns by connecting organic chromophores to the base complex[39] - a lifetime increase of six orders of magnitude compared to the "base" system $[Fe(terpy)_3]^{2+}$.

Reservoir Effect

The vast increase in lifetime in this combination of complex **C** and organic chromophores is due to the application of the reservoir effect. This approach utilizes the advantages of organometallic and organic chromophores by combining both units into one system. Organic chromophores often show large triplet state lifetimes but lack efficient ISC from the optically excited singlet state into this triplet manifold. Additionally, they frequently lack a sufficient absorption cross section in the solar spectrum.[40] Transition metal complexes on the other hand exhibit strong absorption in this range and often undergo ISC with unity.[16] However, especially first-row transition metal complexes suffer from short-lived excited charge transfer states. If the excited states of both units are sufficiently close in energy, an equilibrium between the two can be achieved, utilizing the advantages of both systems (Scheme 3).

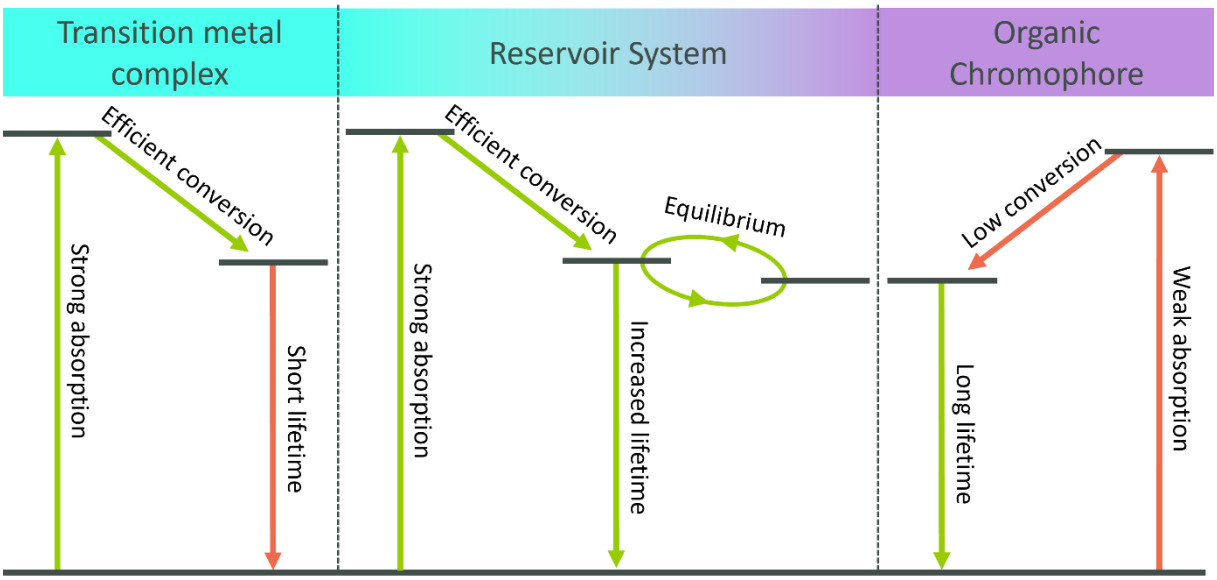

Scheme 3: Schematic depiction of the advantages and disadvantages of transition metal complexes/organic chromophores and the combination of both in a reservoir system.

One of the first deliberate implementations of this mechanism was a Ruthenium pyrene system from the work group Castellano et al. in 1999.[41,42] In this system emission was observed only from the metalorganic moiety, and the lifetime of this emission was improved by about one order of magnitude compared to the base bipyridine system. In addition, an antenna effect [43] was observed in the form of singlet-singlet energy transfer from organic chromophore to metalorganic framework. This enables an efficient improvement of absorption cross section. Although the improved lifetimes are much more relevant for early transitions metals than for their late homologs, it took two decades for this approach to be applied to iron systems.[39,44]

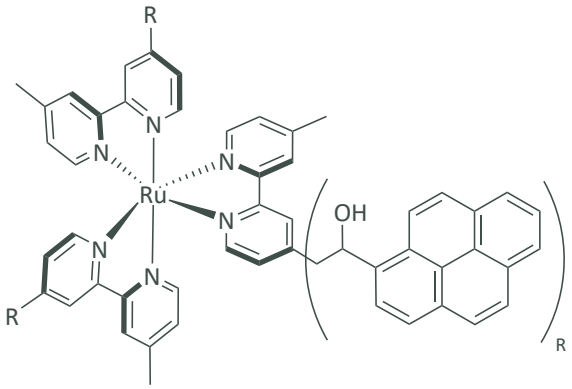

Figure 4: Original Ru(II) reservoir system investigated by Castellano et al.[41]

3. Objectives and Motivation

The worldwide energy demand is rising, significantly contributing to manmade climate change. New ways to utilize the most widely available renewable energy source, solar power, in chemistry need to be developed. The progress in the field of homogeneous iron-based photosensitizers over the recent years makes this an intriguing field to contribute to the scientific advancement. The established Fe(III) photosensitizers utilizing several NHC moieties are a strong basis for this endeavour. While a lot of previous research was focussed on the direct ligand metal interaction, tuning excited state energies to increase charge separated lifetimes, this work will focus on two secondary approaches to improve efficiency without directly addressing the basic relaxation cascade. The reservoir effect detailed above introduces an organic moiety to the system. This second unit should possess an excited state with prolonged lifetimes that is similar in energy to the charge separated state of the metal complex leading to an equilibrium between both states (Scheme 3). Two research projects leading to a lineup of 8 complexes (Figure 5) based on complex **C** focus on this strategy. The first work (Panel A) focuses on the effect of chromophore energy. By applying four different organic chromophores the changes in photochemical properties depending on the triplet state energies can be investigated. The second work focuses on the chromophore with the most fitting triplet state energy compared to the ^{2}LMCT energy of the base complex, anthracene, and a methylene bridging group is introduced to electronically decouple both moieties (Panel B).

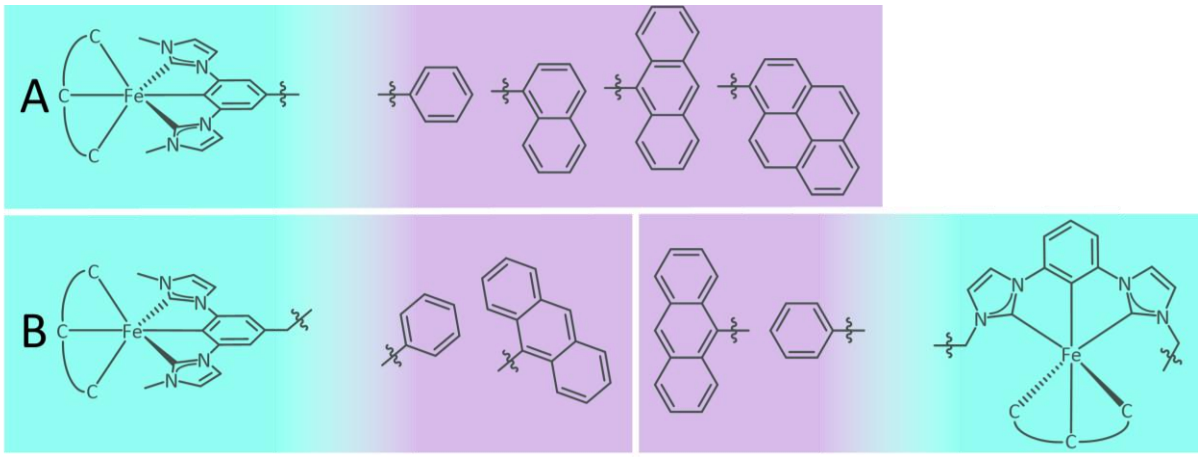

Figure 5: Complexes investigated in the reservoir effect focused papers of this work. A: The 4 directly conjugated Fe(III) chromophore complexes investigated in Chapter 4. B: The 4 methyl-linked Fe(III) chromophore complexes investigated in Chapter 5.

In the third publication in this work the focus is shifted to the one-component system approach. Here, the second catalyst at which the chemical reaction should occur is directly connected to the photosensitizer to eliminate the diffusion limitation of the electron/energy transfer between the two. The complexes investigated are a preliminary work on this topic focusing on the base complex **C**. The coordination of a second metal centre is only simulated by methylation of a pyridine unit in the backbone of the central phenyl ring and compared to the unmethylated system (Figure 6). This approach enables investigation of the effects on the Photosensitizer without the masking effects of the additional transitions introduced by the second metal centre.

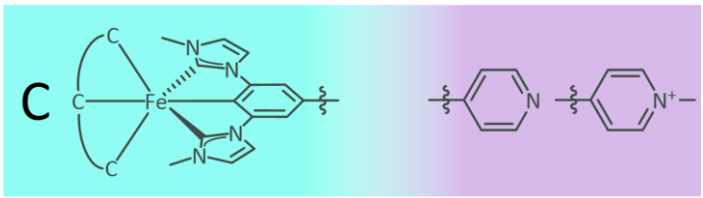

Figure 6: The 2 one-component system precursor complexes investigated in Chapter 6.

4. Chromophore Induced Effects in Iron(III) Complexes

The series of complexes investigated in this project had the goal to apply the reservoir effect expanding on base complex **C**. The four chromophores phenyl, naphthalene, anthracene and pyrene are directly connected to the central phenyl unit of the base complex, forming the simplest possible combination of complex and organic chromophore for this compound class. The dependence of the occurrence of a reservoir effect on the energy difference between the chromophores' triplet states[45] and the excited state at the organometallic moiety was investigated with this series. It was postulated that anthracene exhibits the closest matching energy for the required equilibrium of states, thus enabling a reservoir effect. However, the electronic coupling between the two components was underestimated leading to a planarization of the whole organic structure. The excited state is delocalized both in the transition metal complex and the attached organic chromophore. This “superligand state” exhibits a significantly reduced lifetime (≈20 ps) compared to the LMCT of the base complex (≈250 ps), presumably due to its low excited state energy.

Author Contributions:

Lennart Schmitz: Design and synthesis of investigated complexes, Characterization (NMR, MS, EA), Structural investigation by NMR, CV, Absorption spectroscopy, Room/low temperature emission spectroscopy), Main manuscript author.

Dr. Miguel A. Argüello Cordero: Transient absorption spectroscopy, Manuscript author

Dr. Mohammed J. Al-Marri: (TD)-DFT calculations

Dr. Roland Schoch: Single-crystal X-ray diffraction

Dr. Hans Egold: Characterization (NMR), Structural investigation by NMR

Dr. Adam Neuba: Spectroelectrochemical measurements

Dr. Jakob Steube: Planning of the research

Bastian Bracht: Synthesis of investigated complexes, Structural investigation by NMR

Dr. Olga S. Bokareva: (TD)-DFT calculation, Manuscript author

Prof. Dr. Stefan Lochbrunner: Transient absorption spectroscopy, Conception of the research

Prof. Dr. Matthias Bauer: Conception of the research, Corresponding author

Inorganic Chemistry

pubs.acs.org/IC

Article

Chromophore Induced Effects in Iron(III) Complexes

Lennart Schmitz, Miguel A. Argüello Cordero, Mohammed J. Al-Marri, Roland Schoch, Hans Egold, Adam Neuba, Jakob Steube, Bastian Bracht, Olga S. Bokareva, Stefan Lochbrunner, and Matthias Bauer*

Cite This: *Inorg. Chem.* 2025, 64, 14101−14117

Read Online

ACCESS | Metrics & More | Article Recommendations | Supporting Information

ABSTRACT: In the search for noble metal free photocatalytic systems, iron is the dream candidate. To increase excited state lifetimes of iron complexes, the multichromophoric approach is promising, combining organic chromophores with photoactive iron complexes, potentially enabling a reservoir effect. We present a series of chromophore-functionalized complexes based on the parental Fe^{III} complex $[Fe(ImP)_2][PF_6]$ (HImP = 1,1′-(1,3-phenylene)bis(3-methyl-1-imidazole-2-ylidene)). The four organic chromophores benzene, naphthalene, anthracene, and pyrene are attached to the ImP-ligand in para-position to the coordination site to systematically investigate the influence of the steric demand and electronic properties of the chromophore on charge transfer lifetimes as well as photodynamics. A thorough ground state characterization was conducted in addition to investigations of the excited state dynamics by transient absorption spectroscopy and streak camera emission measurements. The conclusions drawn are supported by extensive DFT calculations. The emission coefficients could be significantly improved by the addition of chromophores. After excitation of the complexes with larger chromophores, coplanarization of the backbone and complex motif occurs to stabilize the formal charge. This results in population of a superligand state that exhibits a much faster radiationless relaxation to the ground state compared to the parent complex, hindering a reservoir effect.

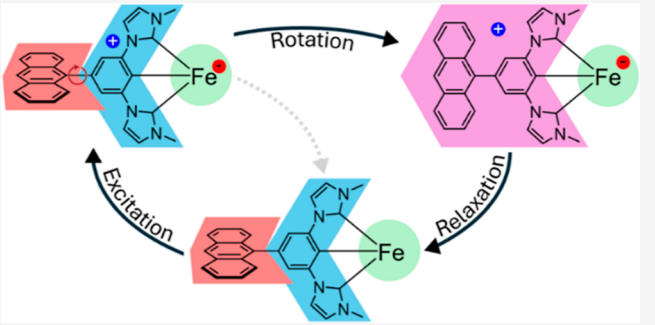

INTRODUCTION

In the face of climate change and its associated challenges, many efforts have been dedicated to developing sustainable chemical processes utilizing green energy sources such as sunlight. In recent years, photocatalysis has emerged as a promising approach to convert light directly into chemical energy.[1,2] Since most substrates and catalysts do not sufficiently absorb light in the visible region, photosensitizers (PS) are usually required to accomplish this task. In order to increase the sustainable character of such reactions, the recent focus is on replacing the current generation of PSs based on platinum group metal (PGM) complexes such as Ru^{II} or Ir^{III} complexes with PSs featuring abundant 3d transition metals.[3−7] Due to their long-lived excited states, PGM complexes enable more efficient electron transfer to catalytic systems. However, PGMs are scarce and therefore less suitable ecologically and economically than 3d transition metals.[6] In particular, there has been a lot of interest in iron as it is the most abundant transition metal.[8] However, the weak ligand field splitting, which leads to low-energy metal-centered (MC) states, is usually disadvantageous for photochemical applications as these states promote fast deactivation from the catalytically active excited states.[9] To resolve this issue, it is necessary to tailor the involved excited states by designing ligands that increase the excited state lifetimes.[6]

Strong σ-donor ligands, particularly carbon-donor ligands such as *N*-heterocyclic carbenes (NHCs), have been shown to prolong the lifetimes of metal-to-ligand charge-transfer (MLCT) states in Fe^{II} complexes from roughly 150 fs in the purely *N*-coordinated iron terpyridine complex to 9 ps with four coordinating NHC moieties in the pyridine-bis-imidazolylidene ligand motif.[10] Despite extensive studies on complexes based on this base ligand motif, only MLCT lifetimes of under 50 ps were achieved with this coordination motif.[7,11−13] Utilizing different ligand motifs leads to much better lifetime results, showing that investigating different ligand design strategies is important.[14−16]

One other approach to increase the excited state lifetime is to introduce an organic chromophore into the backbone of the ligand. The extended π-system stabilizes the π^*-orbitals of the ligand, and thus, the MLCT states relative to the MC states in d^6-systems.[7] Furthermore, the long-lived triplet states of these chromophores (^{3}Chrom) can act as an energy reservoir for charge-transfer excited states, as seen for example in [Ru(phen-

Received: February 5, 2025
Revised: June 11, 2025
Accepted: June 20, 2025
Published: July 8, 2025

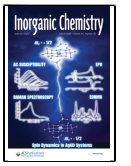

https://doi.org/10.1021/acs.inorgchem.5c00526
Inorg. Chem. 2025, 64, 14101−14117

Scheme 1. Synthetic Route of Complexes (C1) to (C4)

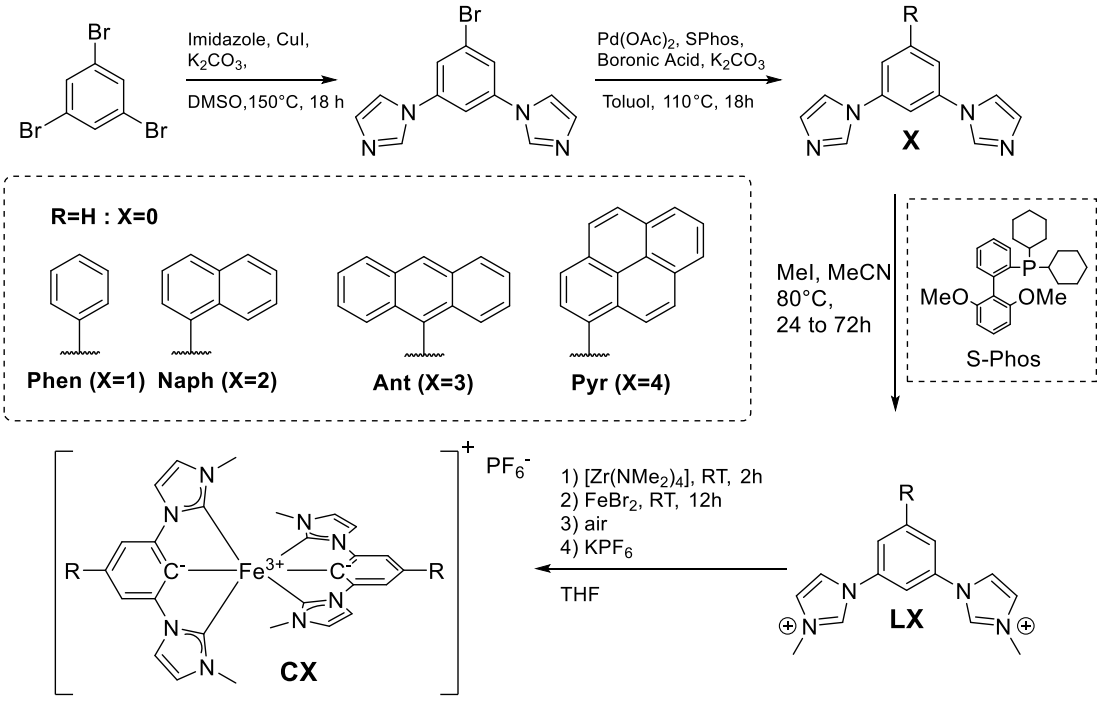

pyr)$_3$]$^{2+}$ (phen-pyr = 5-(pyren-1-yl)-1,10-phenanthroline).[17] The strongest effect is observed for charge-transfer and chromophore states with similar energies. However, chromophores with somewhat lower triplet energies than the CT state were also observed to exhibit an increase in lifetime of the excited CT state as long as the energy barrier between both states is small enough to enable a backtransfer.[18] In addition, the introduced chromophores can act as a light antenna, leading to increased absorption cross sections, since excited states located on the chromophore backbone can cascade into charge-separated MLCT and LMCT states.[19−22] Furthermore, intersystem crossing (ISC) can be induced in the attached chromophore by the heavy atom effect of the metal. In a study on Fe^{II} complexes based on the previously mentioned pyridine-bis-imidazolylidene motif extended with organic chromophores in the backbone, it was demonstrated that the absorption properties can be tuned through the antenna effect and expansion of the π-system.[23] However, no reservoir effect was observed, presumably due to the short-lived ^{3}MLCT state, whose deactivation via MC states is faster than internal conversion (IC) to the local ^{3}Chrom state.

Recent efforts focus on Fe^{III} complexes and the exploration of ligand-to-metal charge-transfer (^{2}LMCT) states in the doublet manifold for photochemical applications. These low-spin Fe^{III} d^5 complexes can show fluorescence from LMCT states. For example [Fe(phtmeimb)$_2$]PF$_6$ (phtmeimb$^-$ = phenyl[tris(3-methylimidazol-1-ylidene)borate]$^-$) is characterized by a ^{2}LMCT lifetime of up to 2 ns and a quantum yield of up to 2%.[24] In addition, cyclometalating functions are investigated, which proved to increase the MLCT lifetime of Fe^{II} complexes.[16,25] In combination with NHCs this leads to the Fe^{III} complex [Fe(ImP)$_2$]$^+$ (HImP = 1,1′-(1,3-phenylene)-bis(3-methyl-1-imidazole-2-ylidene) with a 240 ps ^{2}LMCT lifetime. This complex additionally shows a ^{2}MLCT absorption band reaching into the visible range which is more intense than the ^{2}LMCT absorption.[26] In follow up work, the originally reported MLCT emission was proved to originate from a highly emissive impurity,[27] which could not be further identified yet.[28]

In this work, a potential reservoir effect in Fe^{III} complexes of the [Fe(ImP)$_2$]$^+$ type is explored. For this purpose, the 1,3-phenylene-bis(1*H*-imidazole) ligand in [Fe(ImP)$_2$]$^+$ is functionalized by phenyl, naphthalene, anthracene, or pyrene, respectively. A similar complex with phenyl substitution was published recently.[29] The effect on ground and excited state characteristics, such as absorption, excited state lifetime, and emission properties is studied by various methods, such as cyclic voltammetry, spectroelectrochemistry, UV/vis spectroscopy, ultrafast transient absorption spectroscopy, as well as emission spectroscopy and streak camera measurements. The results from these experimental methods are supported by (TD)DFT calculations to understand the dynamics of the complex upon excitation.

EXPERIMENTAL SECTION

The chemicals for synthesis were commercially obtained and used without further purification. For purification with column chromatography, silica gel columns were used. All chromophore complexes were obtained via the same synthetic route.

The synthesis of the complexes (**C1**) to (**C4**) (the number corresponds to the number of six-membered rings in the attached chromophore, see Scheme 1) is reported below.

The ligands were synthesized starting from 1,3,5-tribromobenzene in a copper-catalyzed *N*-arylation, according to the literature,[30] resulting in 1,1′-(5-bromo-1,3-phenylene)bis(1*H*-imidazole): 1,3,5-tribromobenzene (1 equiv., 70 mmol, 22 g), imidazole (2 equiv., 140 mmol, 9.5 g), K_2CO_3 (4 equiv., 280 mmol, 38.7 g) and CuI (0.2 equiv., 14 mmol, 2.7 g) were suspended in DMSO (100 mL). The suspension was heated to 150 °C for 18 h. Afterward, the suspension was concentrated under reduced pressure until it solidified. The resulting solid was suspended in water and filtered. The residue was repeatedly rinsed with water until no further coloration of the water was visible. The remining residue was suspended in methanol and filtered. The resulting solution was evaporated under reduced pressure

https://doi.org/10.1021/acs.inorgchem.5c00526
Inorg. Chem. 2025, 64, 14101−14117

and the remaining solid was purified via column chromatography (SiO_2; CH_2Cl_2/MeOH 9:1). The product was obtained as a colorless solid (32.9 mmol/9.5 g/47% yield). The singly substituted product was isolated as well (21.0 mmol/6.3 g/30% yield). It was then reacted in the same procedure with halved amounts of imidazole, CuI and K_2CO_3. An additional product fraction was obtained as a colorless solid (13.2 mmol/3.8 g/62% yield), resulting in an overall yield of 66%.

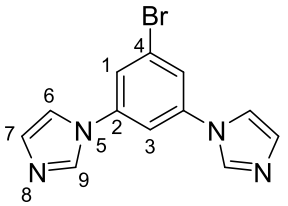

^{1}H NMR (700 MHz, DMSO-d_6, δ): (ppm) = 8.48 (dd, J = 1.4, 0.9 Hz, 2H, H^9), 8.02 (t, J = 2.0 Hz, 1H, H^3), 7.96 (t, J = 1.4 Hz, 2H, H^7), 7.95 (d, J = 2.0 Hz, 2H, H^1), 7.14 (dd, J = 1.4, 0.9 Hz, 2H, H^6). **^{13}C NMR (176 MHz, DMSO-d_6, δ): (ppm)** = 139.0 (C_q, 2C, C^2), 135.9 (CH, 2C, C^9), 130.1 (CH, 2C, C^6), 123.6 (C_q, 1C, C^4), 120.5 (CH, 2C, C^1), 118.1 (CH, 2C, C^7), 110.6 (CH, 1C, C^3). **^{15}N NMR (71 MHz, DMSO-d_6, δ): (ppm)** = 267 (2N, N^8), 183 (2N, N^5). ESI-MS (m/z): $[M + H]^+$ calcd for $C_{12}H_9BrN_4$, 289.0083; found, 289.0092.

Precursors (1) to (4). Subsequently, 1′-(5-bromo-1,3-phenylene)-bis(1*H*-imidazole) was reacted in Suzuki−Miyaura cross coupling reactions with boronic acids (phenyl and naphthalene) or boronic acid pinacol esters (anthracene and pyrene) of the different chromophores to obtain proligand precursors with the four chromophores phenyl (**1**), naphthyl (**2**), anthracenyl (**3**) and pyrenyl (**4**). This synthetic route is based on a similar procedure for the corresponding C^N^C complexes.[23] The reactions were carried out under an argon atmosphere. The solvents were deoxygenated prior to the reaction by sparging them with argon. Palladium(II)acetate ($Pd(OAc)_2$) (0.05 equiv) and 2-dicyclohexylphosphino-2′,6′-dimethoxybiphenyl (S-Phos, 0.11 equiv) were dissolved in toluene (0.1 M). K_2CO_3 (2.4 equiv), dissolved in water (1 M) was added resulting in a toluene water ratio of 5:1. Then, 1,1′-(5-bromo-1,3-phenylene)-bis(1*H*-imidazole) (1 equiv) and the corresponding boronic acid (1.2 equiv) or boronic acid pinacol ester (1.2 equiv) was added. The mixture was heated to reflux and stirred for 18 h. After cooling, the solvents were removed under reduced pressure. The residue was suspended in methanol and filtered. The solvent of the filtrate was evaporated under reduced pressure. The raw product was purified with column chromatography (CH_2Cl_2/MeOH 9:1; 4:1 for **4**).

1,1′-(5-Phenyl-1,3-phenylene)bis(1H-imidazole) (**1**). The product was obtained as a colorless solid (3 mmol batch size; 2.94 mmol/843 mg/98% yield)

^{1}H NMR (700 MHz, DMSO-d_6, δ): (ppm) = 8.53 (t, J = 1.1 Hz, 2H, H^9), 8.03 (t, 2H, J = 1.3 Hz, H^7), 7.96 (t, J = 2.0 Hz, 1H, H^3), 7.94−7.92 (m, 2H, H^{12}), 7.91 (d, J = 2.0 Hz, 2H, H^1), 7.54 (m, 2H, H^{11}), 7.46 (tt, J = 7.3, 1.9 Hz, 1H, H^{13}), 7.16 (t, J = 1.1 Hz, 2H, H^6). **^{13}C NMR (176 MHz, DMSO-d_6, δ): (ppm)** = 143.5 (Cq, 1C, C^{10}), 138.5 (CH, 2C, C^2), 138.4 (CH, 1C, C^4), 136.0 (CH, 2C, C^9), 129.9 (CH, C2, C^6), 128.9 (CH, 2C, C^{11}), 128.5 (CH, 1C, C^{13}), 127.4 (CH, 2C, C^{12}), 118.3 (CH, 2C, C^7), 116.3 (CH, 2C, C^1), 110.8 (CH, 1C, C^3) **^{15}N NMR (71 MHz, DMSO-d_6, δ): (ppm)** = 266 (2N, N^8), 185 (2N, N^5). ESI-MS (m/z): $[M + H]^+$ calcd for $C_{18}H_{14}N_4$, 287.1291; found, 287.1287.

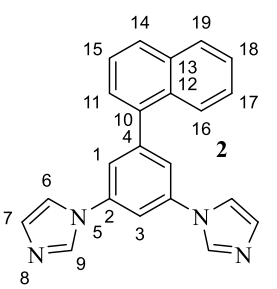

1,1′-(5-(naphtalen-1-yl)-1,3-phenylene)bis(1H-imidazole) (**2**). The product was obtained as a colorless solid (10 mmol batch size; 5.51 mmol/1.85 g/55% yield)

^{1}H NMR (700 MHz, DMSO-d_6, δ): (ppm) = 8.52 (t, J = 1.1 Hz, 2H, H^9), 8.10 (t, J = 2.0 Hz, 1H, H^3), 8.05−8.03 (m, 2H, $H^{14, 19}$), 8.01 (t, J = 1.4 Hz, 2H, H^6), 7.89 (d, J = 8.5 Hz, 1H, H^{16}), 7.79 (d, J = 2.0 Hz, 2H, H^1), 7.66−7.62 (m, 2H, $H^{11, 15}$), 7.59 (ddd, J = 8.1, 6.8, 1.2 Hz, 1H, H^{18}), 7.55 (ddd, J = 8.1, 6.8, 1.4 1H, H^{17}) 7.15 (dd, J = 0.7 Hz, 2H, H^7). **^{13}C NMR (176 MHz, DMSO-d_6, δ): (ppm)** = 143.4 (C_q, 1C, C^{10}), 138.1 (C_q, 2C, C^2), 137.7 (C_q, 1C, C^4), 135.9 (CH, 2C, C^9), 133.4 (C_q, 1C, C^{12}), 130.7 (C_q, 1C, C^{13}), 130.0 (CH, 2C, C^7), 128.41, 128.37 (2 CH, 2 × 1C, $C^{14, 19}$), 127.3 (CH, 1C, C^{15}), 126.9 (CH, 1C, C^{17}), 126.1 (CH, 1C, C^{18}), 125.5 (CH, 1C, C^{11}), 125.2 (CH, 1C, C^{16}), 119.1 (CH, 2C, C^1), 118.2 (CH, 2C, C^6), 110.7 (CH, 1C, C^3) **^{15}N NMR (71 MHz, DMSO-d_6, δ): (ppm)** = 266 (2N, N^8), 185 (2N, N^5). ESI-MS (m/z): $[M + H]^+$ calcd for $C_{22}H_{16}N_4$, 337.1448; found, 337.1435.

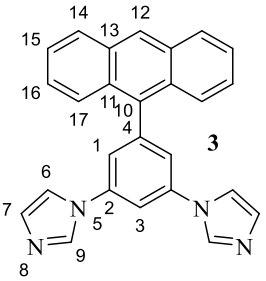

1,1′-(5-(anthracen-9-yl)-1,3-phenylene)bis(1H-imidazole) (**3**). The product was obtained as an off-white solid (4 mmol batch size; 2.93 mmol/1.13 g/73% Yield)

^{1}H NMR (700 MHz, DMSO-d_6, δ): (ppm) = 8.76 (s, 1H, H^{12}), 8.55 (s, 2H, H^9), 8.26 (t, J = 2.0 Hz, 1H, H^3), 8.20 (d, J = 8.5 Hz, 2H, H^{14}) 8.03 (s, 2H, H^6), 7.79 (d, J = 2.0 Hz, 2H, H^1), 7.67 (d, J = 8.8 Hz, 2H, H^{17}), 7.56 (t, J = 7.1 Hz, 2H, H^{16}), 7.48 (ddd, J = 8.7, 6.5, 1.2 Hz, 2H, H^{15}), 7.14 (s, 2H, H^7). **^{13}C NMR (176 MHz, DMSO-d_6, δ): (ppm)** = 141.7 (C_q, 1C, C^{10}), 138.3 (C_q, 2C, C^2), 135.9 (CH, 2C, C^9), 134.4 (C_q, 1C, C^4), 130.9 (C_q, 2C, C^{11}), 130.1 (CH, 2C, C^{17}), 129.4 (C_q, 2C, C^{13}), 128.4 (CH, 2C, C^{14}), 127.1 (CH, 1C, C^{12}), 126.3 (CH, 2C, C^{15}), 126.0 (CH, 2C, C^{17}), 125.5 (CH, 2C, C^{16}), 119.7 (CH, 2C, C^1), 118.0 (CH, 2C, C^6), 110.2 (CH, 1C, C^3) **^{15}N NMR (71 MHz, DMSO-d_6, δ): (ppm)** = 266 (2N, N^8), 184 (2N, N^5). ESI-MS (m/z): $[M + H]^+$ calcd for $C_{26}H_{18}N_4$, 387.1604; found, 0.387.1601.

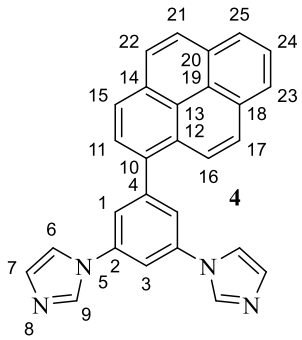

1,1′-(5-(pyren-1-yl)-1,3-phenylene)bis(1H-imidazole) (**4**). The product was obtained as a pale yellow solid (7.4 mmol batch size; 4.43 mmol/1.82 g/60% Yield)

^{1}H NMR (700 MHz, DMSO-d_6, δ): (ppm) = 8.56 (t, J = 1.1 Hz, 2H, H^9), 8.44 (d, J = 7.8 Hz, 1H, H^{16}), 8,37 (dd, J = 7.6, 0.8 Hz, 1H, H^{25}), 8.33 (d, J = 7.1 Hz, 1H, H^{23}), 8.3−8.25 (m, 2H, $H^{21,22}$), 8.25−8.18 (m, 3H, $H^{11,15,17}$), 8.16 (t, J = 7.1 Hz, 1H, H^3), 8.13 (t, J = 7.6 Hz, 1H, H^{24}), 8.05 (t, J = 1.3 Hz, 2H, H^6), 7.94 (d, J = 2.0 Hz, 2H, H^1), 7.17 (t, J = 1.2 Hz, 2H, H^7). **^{13}C NMR (176 MHz, DMSO-d_6, δ): (ppm)** = 143.7 (C_q, 1C, C^{10}), 138.2 (C_q, 2C, C^2), 136.0 (C_H, 2C, C^9), 135.2 (C_q, 1C, C^4), 130.9 (C_q, 1C, C^{20}), 130.7 (C_q, 1C, C^{18}), 130.4 (C_q, 1C, C^{14}), 130.1 (CH, 2C, C^7), 128.3 (CH, 1C, C^{17}), 127.9 (2xCH, 2 × 1C, $C^{11 \text{ or } 15,21}$), 127.3 (CH, 2C, C^{22}), 126.6 (CH, 1C,

https://doi.org/10.1021/acs.inorgchem.5c00526
Inorg. Chem. 2025, 64, 14101−14117

C^{24}), 125.6 (CH, 1C, C^{25}), 125.2 (CH, 1C, C^{23}), 124.8 (CH, 1C, C^{16}), 124.5 (CH, 1C, $C^{11\ or\ 15}$), 124.1 (C_q, 1C, C^{12}), 123.9 (C_q, 1C, C^{19}), 119.7 (CH, 2C, C^1), 118.3 (CH, 2C, C^6), 110.8 (CH, 1C, C^3) A resonance for C^{13} could not be assigned. **^{15}N NMR (71 MHz, DMSO-d_6, δ): (ppm)** = 282 (2N, N^8), 184 (2N, N^5). ESI-MS (m/z): $[M + H]^+$ calcd for $C_{28}H_{18}N_4$, 411.1604; found, 411.1618.

Proligands L0 to L4. The syntheses of the different proligands with the chromophores phenyl (**L1**), naphthyl (**L2**), anthracenyl (**L3**) and pyrenyl (**L4**) were carried out under similar conditions.[31] The corresponding substrate (**1** to **4**) (1 equiv) was suspended in acetonitrile (MeCN, 0.1 M). Methyl iodide (4 equiv) was added, and the suspension was stirred under reflux for 18 h (**L1**, **L2** and **L3**) or for 42 h (**L4**). After cooling, the volatiles were removed in vacuo and the residue was washed with acetone. An anion exchange utilizing KPF_6 was executed to replace the more reactive Iodide. For this the compounds were each dissolved in water. Under stirring a saturated aqueous KPF_6 solution was added resulting in the formation of white (off-white for L4) precipitation. The suspension was filtered, the solid washed with water and dried. These PF_6^- salts of L1 to L4 could then be investigated. For further synthesis, this anion exchange could not be applied, since the coordination of iodide is essential for the complexation reaction.

1,1′-([1,1′-biphenyl]-3,5-diyl)bis(3-methyl-1H-imidazole-3-ium) (L1).

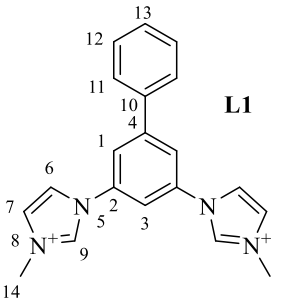

The product was obtained as a colorless solid (0.33 mmol batch size; 0.32 mmol/570 mg/98% yield)

^{1}H NMR (700 MHz, DMSO-d_6, δ): (ppm) = 10.04 (s, 2H, H^9), 8.49 (t, J = 1.9 Hz, 2H, H^6), 8.33 (d, J = 2.0 Hz, 2H, H^1), 8.32 (t, J = 2.0 Hz, 1H, H^3), 8.06 (t, J = 1.7 Hz, 2H, H^7), 7.97 (m, 2H, H^{12}), 7.61 (t, J = 7.6 Hz, 2H, H^{11}), 7.54 (tt, J = 7.4, 1.7, 1H, $H_{backbone}$), 4.02 (s, 6H, H^{14}). **^{13}C NMR (176 MHz, DMSO-d_6, δ): (ppm)** = 143.8 (C_q, 1C, C^{10}), 137.0 (C_q, 1C, C^4), 136.5 (CH, 2C, C^9), 136.2 (C_q, 2C, C^2), 129.3 (CH, 1C, C^{13}), 129.2 (CH, 2C, C^{11}), 127.3 (CH, 2C, C^{12}), 124.7 (CH, 2C, C^7), 121.0 (CH, 2C, C^6), 120.6 (CH, 2C, C^1), 114.0 (CH, 1C, C^3), 36.4 (CH_3, 2C, C^{14}) **^{15}N NMR (71 MHz, DMSO-d_6, δ): (ppm)** = 186 (2N, N^5), 175 (2N, N^8). ESI-MS (m/z): $[M]^{2+}$ calcd for $C_{20}H_{20}N_4$, 158,5839; found, 158.5849.

Elemental analysis calculated for $C_{20}H_{20}N_4P_2F_{12}$: C, 39.62; H, 3.32; N, 9.42. Found: C, 39.73; H, 3.71; N, 9.55.

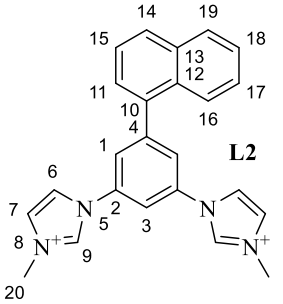

1,1′-(5-(naphthalen-1-yl)-1,3-phenylene)bis(3-methyl-1H-imidazole-3-ium) (**L2**). The product was obtained as colorless solid (3 mmol batch size; 2.98 mmol/1.85 g/99% yield).

^{1}H NMR (700 MHz, DMSO-d_6, δ): (ppm) = 9.97 (s, 2H, H^9), 8.47 (t, J = 1.9 Hz, 2H, H^6), 8.42 (t, J = 2.0 Hz, 1H, H^3), 8.19 (d, J = 2H, H^1), 8.12 (d, 1H, H^{14}), 8.10 (d, 1H, H^{19}), 8.04 (t, 2H, H^7), 7.92 (d, 1H, H^{16}), 7.71 (dd, 1H, H^{15}), 7.66 (dd, 1H, H^{11}), 7.64 (ddd, 1H, H^{18}), 7.58 (ddd, 1H, H^{17}), 3.99 (s, 6H, H^{20}). **^{13}C NMR (176 MHz, DMSO-d_6, δ):(ppm)** = 143.7 (C_q, 1C, C^{10}), 136.5 (C_H, 2C, C^9), 136.2 (C_q, 1C, C^4), 135.8 (C_q, 2C, C^2), 133.4 (C_q, 1C, C^{12}), 130.2 (C_q, 1C, C^{13}), 129.2 (CH, 1C, C^{14}), 128.6 (CH, 1C, C^{19}), 127.7 (CH, 1C, C^{11}), 127.2 (CH, 1C, C^{17}), 126.4 (CH, 1C, C^{18}), 125.5 (CH, 1C, C^{15}), 124.9 (CH, 1C, C^{16}), 124.7 (CH, 2C, C^7), 123.6 (CH, 2C, C^1), 120.9 (CH, 2C, C^6), 114.1 (CH, 1C, C^3), 36.4 (CH_3, 2C, C^{20}) **^{15}N NMR (71 MHz, DMSO-d_6, δ):(ppm)** = 185 (2N, N^5), 176 (2N, N^8).ESI-MS (m/z): $[M]^{2+}$ calcd for $C_{24}H_{22}N_4$, 183,0917; found, 183.0907.

Elemental analysis calculated for $C_{24}H_{22}N_4P_2F_{12}$ + 0.5 H_2O: C, 43.32; H, 3.48; N, 8.42. found: C, 43.34; H, 3.70; N, 8.61.

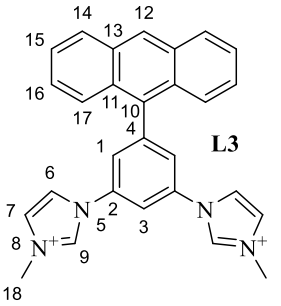

1,1′-(5-(anthracen-9-yl)-1,3-phenylene)bis(3-methyl-1H-imidazole-3-ium) (**L3**). The product was obtained as an off white solid (3 mmol batch size; 2.54 mmol/1.70 g/85% Yield)

^{1}H NMR (700 MHz, DMSO-d_6, δ): (ppm) = 9.97 (s, 2H, H^9), 8.85 (s, 1H, H^{12}), 8.57 (t, J = 2.1 Hz, 1H, H^3), 8.49 (t, J = 2.0 Hz, 2H, H^6), 8.25 (d, J = 8.5 Hz, 2H, H^{14}), 8.16 (d, J = 2.1 Hz, 2H, H^1), 8.03 (t, J = 1.8 Hz, 2H, H^7), 7.63−7.59 (m, 4H, $H^{15,17}$), 7.52 (ddd, J = 8.8, 6.5, 1.3 Hz, 2H, H^{16}), 3.96 (s, 6H, H^{18}). **^{13}C NMR (176 MHz, DMSO-d_6, δ): (ppm)** = 142.1 (C_q, 1C, C^{10}),0.136.6 (CH, 2C, C^9), 136.1 (C_q, 2C, C^2), 132.6 (C_q, 1C, C^4), 130.7 (C_q, 2C, C^{10}), 129.3 (C_q, 2C, C^{15}), 128.6 (CH, 2C, C^{14}), 127.9 (CH, 1C, C^{12}), 126.6 (CH, 2C, C^{16}), 125.62, 125.59 (2 × CH, 2 × 2C, $C^{15,17}$), 124.6 (CH, 2C, C^7), 124.3 (CH, 2C, C^1), 120.7 (CH, 2C, C^6), 113.9 (CH, 1C, C^3), 36.3 (CH_3, 2C, C^{18}) **^{15}N NMR (71 MHz, DMSO-d_6, δ): (ppm)** = 186 (2N, N^5), 176 (2N, N^8). ESI-MS (m/z): $[M]^{2+}$ calcd for $C_{28}H_{24}N_4$ 208.0995, found, 208.1003.

Elemental analysis calculated for $C_{28}H_{24}N_4P_2F_{12}$: C, 47.60; H, 3.42; N, 7.93. found: C, 47.32; H, 3.59; N, 8.15.

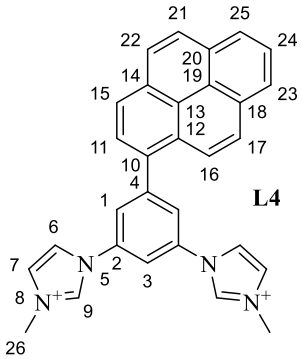

1,1′-(5-(pyren-1-yl)-1,3-phenylene)bis(3-methyl-1H-imidazole-3-ium) (**L4**). The product was obtained as a pale-yellow solid (3.75 mmol batch size; 2.36 mmol/1.64 g/70% Yield)

^{1}H NMR (700 MHz, DMSO-d_6, δ): (ppm) = 10.00 (s, 2H, H^9), 8.52−8.49 (m, 2H, H^6, 1H, H^{16}), 8.47 (t, J = 2.0 Hz, 1H, H^3), 8.41 (dd, J = 7.7, 0.9 Hz, 1H, H^{25}), 8.39 (m, 1H, H^{23}) 8.33 (d, J = 8.33 Hz, 2H, H^1), 8.32 (m, 2H, $H^{21,22}$), 8.30−8.20 (m, 3H, $H^{11,15,17}$), 8.16 (t, J = 7.6 Hz, 1H, H^{24}), 8.06 (t, J = 8.06 Hz, 2H, H^7), 4.01 (s, 6H, H^{26}). **^{13}C NMR (176 MHz, DMSO-d_6, δ): (ppm)** = 144.0 (C_q, 1C, C^{10}), 136.6 (CH, 2C, C^9), 135.9 (C_q, 2C, C^2), 133.5 (C_q, 1C, C^4), 131.1 (C_q, 1C, C^{14}), 130.9 (C_q, 1C, C^{20}), 130.3 (C_q, 1C, C^{18}), 128.7 (CH, 1C, C^{17}), 128.3 (CH, 1C, C^{21}), 127.9 (CH, 1C, $C^{11,15}$), 127.7 (C_q, 1C, C^{13}), 127.3 (CH, 1C, C^{22}), 126.8 (CH, 1C, C^{24}), 126.0 (CH, 1C, C^{25}), 125.5 (CH, 1C, C^{23}), 125.0 (CH, 1C, C^{16}), 124.7 (CH, 2C, C^7),

https://doi.org/10.1021/acs.inorgchem.5c00526
Inorg. Chem. 2025, 64, 14101−14117

124.1 (CH, 1C, C^{1}), 124.0 (CH, 1C, $C^{11,15}$), 123.8 (C_q, 1C, C^{19}), 121.0 (CH, 1C, C^{6}), 114.2 (CH, 1C, C^{3}), 36.4 (CH_3, 2C, C^{26}). A resonance for C^{12} could not be assigned. **^{15}N NMR (71 MHz, DMSO-d_6, δ): (ppm)** = 187 (2N, $N_{imidazole}$), 176 (2N, $N_{imidazole}$). ESI-MS (m/z): $[M]^{2+}$ for $C_{30}H_{24}N_4$, 220.0995; found, 220.0993.

Elemental analysis calculated for $C_{30}H_{24}N_4P_2F_{12}$ + 0.5 H_2O: C, 48.73; H, 3.41; N, 7.58. found: C, 48.80; H, 3.39; N, 7.84.

Complexes C0 to C4. Complex **C0** was synthesized according to the literature.[26] An impurity leading to apparent dual emission that occurred in this procedure was not reproduced and pure compound was obtained. The reactions for the chromophore-appended complexes **C1** (phenyl), **C2** (naphthyl), **C3** (anthracenyl) and **C4** (pyrenyl) were carried out in dry solvents inside a glovebox with an argon atmosphere following the same procedure based on a modified previously published method.[32,33] The proligand (2 equiv) was suspended in THF (0.1 M) and $Zr(NMe_2)_4$ (2.1 equiv) was added. The suspension was stirred for 2 h, before $FeBr_2$ (1 equiv) was added. The resulting suspension was stirred for 18 h. The reaction was quenched under ambient conditions by adding methanol. The resulting suspension was filtered, and the solvent of the filtrate was removed under reduced pressure. The resulting solid was dissolved in CH_2Cl_2, filtered, concentrated, and subsequently passed over a silica gel column (First CH_2Cl_2, then MeCN). An anion exchange by dissolving the respective complexes in MeCN and subsequent dropwise addition into an aqueous solution of KPF_6, yielded the desired products. Diffusion of *n*-pentane into CH_2Cl_2 solutions of the complexes yielded green crystals suitable for X-ray diffraction analysis.

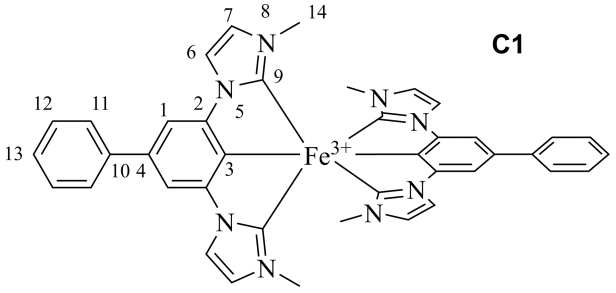

$[Fe(L1)_2][PF_6]$ **(C1).** The product was obtained as dark green crystals (0.3 mmol batch size; 0.1 mmol/80 mg/32% yield).

^{1}H NMR (700 MHz, CD_3CN, δ): (ppm) = 26.91 (s, 4H, H^{1}), 12.32 (t, J = 7.0 Hz, 4H, H^{12}), 10.00 (s, 12H, H^{14}), 3.00 (s, 4H, H^{7}), 1.69 (d, J = 6.5 Hz, 4H, H^{11}), 0.56 (t, J = 7.4 Hz, 2H, H^{13}), −2.7 (s, 4H, H^{6}). **^{13}C NMR (176 MHz, CD_3CN, δ): (ppm)** = 530.8 (C_q, 4C, C^{2}), 522.8 (C_q, 2C, C^{4}), 231.0 (CH, 4C, C^{11}), 175.6 (CH, 2C, C^{13}), 98.4 (CH, 4C, C^{12}), 91.2 (CH, 4C, C^{6}), 78.5 (CH, 4C, C^{7}), −11.3 (Cq, 2C, C^{10}), −212.4 (CH, 4C, C^{1}). ESI-MS (m/z): $[M]^+$ calcd for $C_{40}H_{34}FeN_8$, 682.2251; found, 682.2243.

Elemental analysis calculated for $C_{40}H_{34}FeN_8PF_6$ + 0.5 H_2O: C, 57.43; H, 4.22; N, 13.39. found: C, 57.50; H, 4.59; N, 13.65.

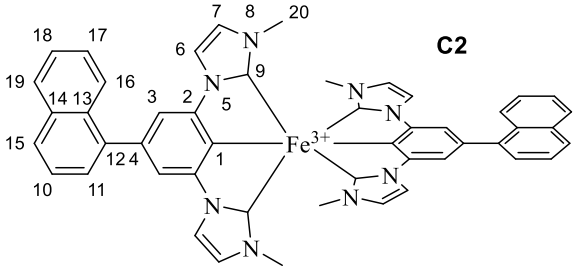

$[Fe(L2)_2][PF_6]$ **(C2).** The product was obtained as dark green crystals (0.3 mmol batch size; 0.1 mmol/114 mg/31% yield).

^{1}H NMR (700 MHz, CD_3CN, δ): (ppm) = 25.61 (s, 4H, H^{3}), 12.43 (t, J = 8.2 Hz, 2H, H^{16}), 11.84 (dd, J = 8.1, 5.7 Hz, 2H, H^{10}), 9.41 (s, 6H, H^{20}), 8.94 (t, J = 8.4, 5.6 Hz, 2H, H^{18}), 8.55 (t, J = 8.5 Hz, 2H, H^{19}), 8.05 (t, J = 7.5, 6.1 Hz, 2H, H^{17}), 5.78 (t, J = 8.3 Hz, 2H, H^{15}) 5.46 (d, J = 5.4 Hz, 2H, H^{11}), 2.80 (d, 4H, H^{7}), −1.83 (s, 4H, H^{6}). **^{13}C NMR (176 MHz, CD_3CN, δ): (ppm)** = 517.0 (Cq, 2C, C^{12}), 512.4 (Cq, 4C, C^{2}), 280.6 (CH, 2C, C^{11}), 237.3 (Cq, 2C, C^{13}), 154.2 (CH, 2C, C^{15}), 138.1 (CH, 2C, C^{19}), 133.1 (CH, 2C, C^{17}), 128.2 (Cq, 2C, C^{14}), 125.7 (CH, 2C, C^{10}), 124.1 (CH, 2C, C^{18}), 90.1 (CH, 2C, C^{6}), 75.7 (CH, 2C, C^{7}) ESI-MS (m/z): $[M]^+$ calcd for $C_{48}H_{38}FeN_8$, 782.2563; found, 782.2537.

Elemental analysis calculated for $C_{48}H_{38}FeN_8PF_6$ + 2.2 H_2O: C, 59.60; H, 4.42; N, 11.58. found: C, 59.76; H, 4.56; N, 11.40 $[Fe(L3)_2][PF_6]$**(C3).**

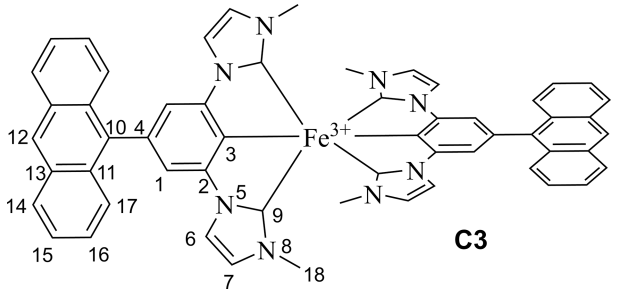

The product was obtained as dark green crystals (0.5 mmol batch size; 0.134 mmol/138 mg/27% yield).

^{1}H NMR (700 MHz, CD_3CN, δ): (ppm) = 25.42 (s, 4H, H^{1}), 12.80 (d, J = 8.8 Hz, 4H, H^{17}), 10.36 (s, 12H, H^{18}), 8.97 (d, J = 9.0 Hz, 4H, H^{14}), 8.73 (dd, J = 8.6, 5.3 Hz, 4H, H^{15}), 8.24 (dd, 4H, H^{16}), 7.76 (s, 2H, H^{12}), 2.88 (s, 4H, H^{7}), −2.75 (s, 4H, H^{6}). **^{13}C NMR (176 MHz, CD_3CN, δ): (ppm)** = 520.2 (Cq, 2C, C^{4}), 517.2 (Cq, 4C, C^{2}), 261.0 (Cq, 4C, C^{11}), 138.8 (CH, 4C, C^{17}), 138.5 (CH, 2C, C^{12}), 138.4 (CH, 4C, C^{14}), 134.5 (Cq, 4C, C^{13}), 133.0 (CH, 4C, C^{16}), 127.1 (CH, 4C, C^{15}), 89.3 (CH, 4C, C^{6}), 78.5 (CH, 4C, C^{7}), 12.7 (Cq, 2C, C^{10}), 3.1 (CH_3, 4C, C^{18}). ESI-MS (m/z): $[M]^+$ calcd for $C_{56}H_{42}FeN_8$, 882.2876; found, 882.2890.

Elemental analysis calculated for $C_{56}H_{42}FeN_8PF_6$ + 2 H_2O: C, 63.22; H, 4.36; N, 10.53. found: C, 62.95; H, 4.36; N, 10.21.

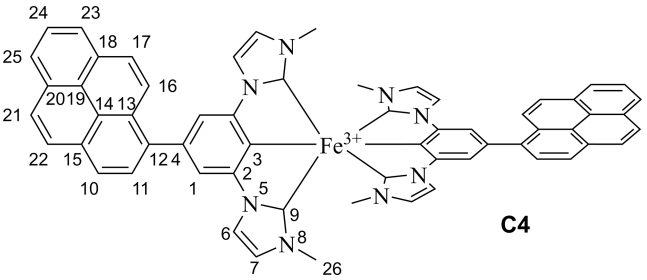

$[Fe(L4)_2][PF_6]$ **(C4).** The product was obtained as dark green crystals (0.9 mmol batch size; 0.018 mmol/19 mg/5% yield).

^{1}H NMR (700 MHz, CD_3CN, δ): (ppm) = 25.94 (s, 4H, H^{1}), 13.18 (d, J = 6.2 Hz, 2H, H^{10}), 12.91 (d, J = 9.1 Hz, 2H, H^{16}), 10.27 (s, 12H, H^{26}), 10.08 (d, J = 9.0 Hz, 2H, H^{22}), 9.09 (dd, J = 7.8, 6.6 Hz, 2H, H^{24}), 7.68 (d, J = 9.1 Hz, 2H, H^{17}), 7.39 (d, J = 7.9 Hz, 2H, H^{25}), 7.26 (d, J = 6.5 Hz, 2H, H^{23}), 6.58 (d, J = 8.9 Hz, 2H, H^{21}), 6.51 (d, J = 6.5 Hz, 2H, H^{11}), 2.98 (s, 4H, H^{7}), −2.69 (s, 4H, H^{6}). **^{13}C NMR (176 MHz, CD_3CN, δ): (ppm)** = 523.0 (Cq, 4C, C^{2}), 517.1 (C_q, 2C, C^{4}), 278.6 (CH, 2C, C^{11}), 238.0 (C_q, 2C, C^{13}), 153.2 (C_q, 2C, C^{15}) 139.8 (CH, 2C, C^{17}), 142.2 (CH, 2C, C^{21}), 135.9 (C_q, 2C, C^{19}), 135.8 (CH, 2C, C^{25}), 135.5 (CH, 2C, C^{23}), 125.6 (C_q, 2C, C^{18}), 124.5 (CH, 2C, C^{10}), 123.8 (C_q, 2C, C^{20}), 120.5 (CH, 2C, C^{24}) 119.7 (CH, 2C, C^{16}), 115.3 (CH, 2C, C^{22}), 114.7 (C_q, 2C, C^{14}) 90.3 (CH, 4C, C^{6}), 78.4 (CH, 4C, C^{7}), 1.7 (C_q, 2C, C^{12}) −211.5 (CH, 4C, C^{1}). ESI-MS (m/z): $[M]^+$ for $C_{48}H_{38}FeN_8$, 930.2871; found, 930.2890.

Elemental analysis calculated for $C_{48}H_{38}FeN_8PF_6$ + 2.25 H_2O: C, 64.55; H, 4.20; N, 10.21 found: C, 64.29; H, 4.23; N, 10.38.

Cyclic Voltammetry. Potentiostatic measurements were performed at room temperature in dry and degassed 0.1 M $[n\text{-}Bu_4N][PF_6]$ MeCN solution with an analyte concentration of 10^{-3} M using a PGSTAT 101 potentiostat from Metrohm. A platinum working electrode (1 mm diameter), an $Ag/AgNO_3$ reference electrode, and a platinum pin electrode were utilized in a three-electrode configuration. After the measurements ferrocene was added as an internal standard to reference against the $FcH^{0/+}$ redox couple.

https://doi.org/10.1021/acs.inorgchem.5c00526
Inorg. Chem. 2025, 64, 14101−14117

The resulting voltammograms were analyzed using the NOVA 2.1.3 software. The reversibility of redox couples was investigated with the criteria proposed by Nicholson and Shain, and the Randles−Sevcik equation.[34]

UV/Vis Spectroscopy. Absorption spectra were recorded at concentrations of 10^{-5} M in 99.9% pure acetonitrile with a PerkinElmer Lambda465 single-beam spectrophotometer. Spectroscopic-grade solvents from VWR in quartz cuvettes by Hellma with an optical path length of 10 mm were used.

Luminescence Measurements. The emission and excitation spectra were recorded with an Edinburgh Instruments FLS1000 spectrometer with single monochromators and a red-extended PMT-980 detector. The same solutions in quartz cuvettes as for UV/vis spectroscopy were used. For low-temperature emission measurements an Oxford Instruments Optistat DN-X cryostat was used. The samples were dissolved in butyronitrile and filled into quartz tubes. The samples were measured at 77 K and 277 K.

Spectroelectrochemistry. Spectroelectrochemical measurements were performed in dry and degassed MeCN/0.1 M $[n\text{-}Bu_4N][PF_6]$ solutions at room temperature in an optically transparent cell (d = 4 mm) with a platinum wire mesh working electrode. The spectral changes during oxidations/reductions were recorded on a Varian Cary 50 spectrophotometer.

Time-Resolved Emission Measurements. Time-resolved emission measurements were carried out by means of a streak camera system (Streakscope C10627, Hamamatsu Photonics) applying ultrashort excitation pulses at 350 nm. The latter were generated by frequency doubling the output of a noncollinear optical parametric amplifier (NOPA) tuned to a center wavelength of 700 nm. The NOPA is pumped by a regenerative Ti/sapphire amplifier system (CPA 2001, CLARK MXR, INC.) operating at a center wavelength of 775 nm and a repetition rate of 1 kHz. MeCN solutions of the compounds were prepared under argon and measured in 1 cm thick fused silica cuvettes. All samples were prepared with an optical density of about 0.1 at the excitation wavelength to avoid signal distortions due to self-absorption. To determine the emission lifetime, the time and wavelength resolved emission was integrated over its spectrum and the resulting decay curve fitted by a monoexponential decay function.

Transient Absorption Spectroscopy. Transient absorption (TA) spectra were recorded with a time resolution of about 100 fs employing a pump−probe setup in which a white light continuum is used for probing and a NOPA for the generation of the excitation pulses.[35] Both, the NOPA and the white light stage are pumped by a regenerative Ti/sapphire laser system (CPA 2001, CLARK MXR, INC.) operating at a center wavelength of 775 nm and a repetition rate of 1 kHz. The white light continuum is generated by focusing a small fraction of the near-infrared pump light into a moving CaF_2 crystal. To excite the compounds at their lowest absorption band, the NOPA was tuned to a center wavelength of 650 nm. The dispersion of the NOPA output was minimized by a compressor based on fused silica prisms resulting in excitation pulses with a length of about 50 fs. To address the more intense absorption bands in the near-ultraviolet (UV), the NOPA was tuned to 700 nm and its output frequency doubled by a 0.7 mm thick β-barium borate crystal. Excitation and probe beam were focused onto the sample to overlapping spots with diameters of approximately 200 and 140 μm, respectively. Behind the sample, the probe was dispersed by a prism and transient absorption changes were spectrally resolved and recorded by a photodiode array detector. The chirp of the white light probe was corrected in the evaluated TA spectra. To exclude effects caused by orientational relaxation, the polarizations of the pump and probe pulses were set to magic angle with respect to each other. For compound **C4** also measurements with parallel and perpendicular polarizations were performed, but no significant differences to the measurements with magic angle configuration were found. The compounds were dissolved in MeCN, and the sample solutions filled into fused silica cuvettes. For measurements with excitation at the rather weak, lowest absorption bands, cuvettes with a thickness of 2 mm were used while in the case of excitation in the near UV 1 mm thick cuvettes were employed. The optical density at the excitation wavelength was about 0.3 in the former and 0.4 in the latter case.

Time-Correlated Single Photon Counting. Time-Correlated Single Photon Counting (TCSPC) was done using a Ultima 01-DD TCSPC system (HORIBA Jobin Yvon). The degassed sample solution was excited at 374 nm with a HORIBA DD375L laser diode with a maximum repetition rate of 100 MHz. The emission was recorded with an emission monochromator which was set to 415 nm. A histogram of photons was recorded as a function of 16,383 channels on a time range of 100 ns (0.012 ns per channel) until one channel reached 10,000 counts. In addition, a scattering solution was measured to characterize the prompt response.

Quantum-Chemical Calculations migrationsamt@rostock.de. Geometry optimization was done based on the respective experimental geometry as a starting point using the optimally tuned LC-BLYP functional together with the ZORA-def2-SVP/ZORA-def-TZVP[36] (C, N, H/Fe) basis sets and D4 dispersion correction.[37] The two range−separation parameters were taken from our previous studies, as it was shown that for metal−organic complexes with additional chromophores, those parameters only slightly depended on the precise chemical structure. Solvent effects (MeCN) were modeled by the polarizable continuum model (PCM).[38] Absorption spectra were calculated using the linear-response time-dependent density functional theory (TDDFT). The broadening of the resulting absorption stick spectra was done using Gaussians of fwhm 0.20 eV. All calculations were performed with the ORCA4.1.2[39] and Gaussian16 suites of programs.[40] Excited-state analysis was carried out using the TheoDORE package,[41] which enables automatic quantitative wave function analysis and localization of excitations at predefined molecular moieties. The excitation-based fragmentation analysis (hierarchical clustering) was done following the strategy suggested in ref 42 Pre- and postprocessing was performed using Python and Bash scripts for text-based data handling and visualization.

Single Crystal X-ray Analysis. The presented X-ray single crystal data were measured on a Bruker Venture D8 three-cycle diffractometer equipped with a Mo K_α μ-source (λ = 0.71073 Å), an *Incoatec* multilayer monochromator and a Photon III detector cooled down to 120 K. The data were integrated with SAINT and afterward a multiscan absorption correction was applied using SADABS.[43] Structure solution was achieved by direct methods in SHELXT and structure refinement was conducted using full-matrix least-squares refinement based on F^2.[44]

NMR-Spectroscopy. NMR spectra were recorded on a Bruker Ascent 700 spectrometer. Chemical shifts are expressed in parts per million (ppm, δ) downfield from tetramethyl silane (TMS). The spectra were referenced to the residual proton signals of the respective deuterated solvent or the solvent carbons respectively. The ^{15}N-HMBC spectra were referenced externally against liquid ammonia. The spectra were analyzed according to first order. Exact assignment of signals was done under consideration of ^{1}H−^{1}H−COSY, ^{1}H−^{13}C-HMQC, ^{1}H^{13}C- HMBC, ^{1}H−^{15}N-HMBC, ^{1}H−^{1}H-NOESY and DEPT135 spectra. For the paramagnetic ^{13}C NMR spectra no proton decoupling was applied leading to multiplets in ^{13}C NMR spectra.

RESULTS AND DISCUSSION

Synthesis. Complex **C0** was synthesized according to the literature.[26] The synthesis of complexes **C1**−**C4** was carried out via the general route shown in Scheme 1.

For all complexes, 1,3,5-tribromobenzene was used as starting material. It was coupled in an Ullmann-type reaction with imidazole to yield 1,1′-(5-bromo-1,3-phenylene)bis(1*H*-imidazole) with 47% yield.[30] The singly and triply coupled compounds were obtained as byproducts. While the fully substituted byproduct had to be discarded, the singly substituted one could be reacted again with modified quantities of imidazole, CuI, and K_2CO_3 to obtain the desired product, effectively increasing the overall yield to 66%. This bromo-functionalized compound was reacted with boronic

https://doi.org/10.1021/acs.inorgchem.5c00526
Inorg. Chem. 2025, 64, 14101−14117

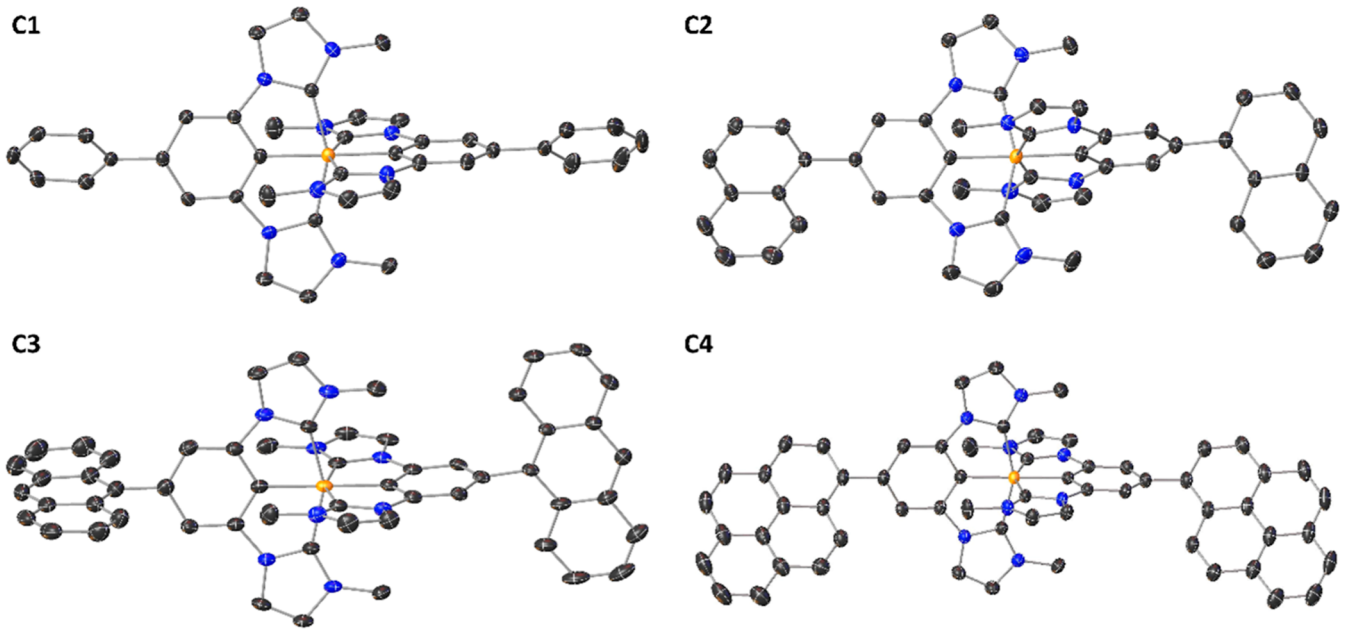

Figure 1. Crystal structures of the chromophore complexes **C1** to **C4.**

acids of the different chromophores in a Suzuki−Miyaura coupling. With increasing chromophore size, protodeboronation of the used boronic acids became a major side reaction. Therefore, the pinacolone-esters of the anthracene and pyrene boronic acids had to be used, resulting in yields of 55 to 98%.[23] The proligands (**L1**) to (**L4**) were obtained in good yields (70 to 99%) by a subsequent methylation with iodomethane.[23] For the complex syntheses, a modified route based on previously published procedures[32,33] was applied that was reported also for the base complex **C0**.[26] The proligands were suspended in dry and degassed THF in a glovebox. $[Zr(NMe_2)_4]$ was added to obtain the intermediate Zr-complexes, which transmetalated the ligand onto iron after addition of $FeBr_2$.[33] After workup under ambient conditions, all complexes were obtained as Fe^{III} single crystals suitable for X-ray diffraction analysis by diffusing *n*-pentane into a solution of the respective purified complex in CH_2Cl_2. The identity and purity of the obtained compounds was investigated by NMR, mass spectrometry, elemental analysis, and X-ray diffraction. For complexes **C1** to **C4**, the coordinating carbon atoms could not be identified in NMR spectroscopy due to strong paramagnetic effects.

Ground State Characterization. The crystal structures of all complexes were determined via single crystal X-ray diffraction measurements (Figure 1). They are discussed in direct comparison with the calculated structures in MeCN and the NMR spectroscopy results. In the $Fe(ImP)_2$-moieties of **C1**−**C4**, no significant differences in geometry were observed, nor any significant difference to **C0**.

Only the dihedral angles between the ImP fragment and the chromophore (see Table 1) show structural differences between the 4 complexes. Since this angle is significant for the electronic coupling between both fragments, elucidating the dihedral angle in solution is of critical interest. Since this angle cannot be measured directly, different approaches have been used in this work to estimate it. Although the values in crystallography can be affected by packing effects, a clear trend is still apparent: **C1**, with the smallest chromophore shows the smallest average dihedral angle with 39.4°. **C2** and **C4**, with an additional phenyl ring in direct proximity to the ImP ligand,

Table 1. Selected Angles of Measured and Calculated Structures[a]

	dihedral angle (X-ray structure)	dihedral angle (geo. optimization)
C1	39.4	29.5
C2	60.4	50.1
C3	86.2	68.7
C4	45.6	48.7

[a]All angles are averaged over all occurrences of that angle.

exhibit larger angles at 60.4° and 45.6°, respectively. In **C4**, smaller angles are observed although the steric effects should be similar. A possible explanation is that the overlap of the p-orbitals in the conjugated π-system has a more significant impact on the molecule's energy for the bigger pyrene moiety, favoring a more planar structure in **C4** over **C2**. In **C3**, with two additional phenyl rings in proximity to ImP, the chromophores are nearly perpendicular to the coordinating phenylene. In the ideal planarized structure both the protons of the central phenyl and the peripheral anthracene rings would experience significant steric repulsion with each other, while this would only be the case for one ring in **C2** and **C4**, respectively. This steric effect on the dihedral angle is schematically shown in Figure 2.

The theoretical calculations, which are discussed in detail below, yield optimized structures which reflect the behavior observed by single crystal diffraction. While the calculated angles are generally smaller than those obtained from diffraction, the trend pointed out above still holds true (see Table 1). These results hint at two main influences on complex geometry. On the one hand, steric hindrance favors larger interplanar angles, as shown in Figure 2; on the other hand, electronic effects, favor small angles to maintain a high orbital overlap between backbone and central phenyl. While the latter increases with growing chromophore size, the former depends on the number of rings in close proximity to the central phenyl of the ImP moiety.

The calculated geometries and crystal structures form the basis for further investigations. As the exact structure in

https://doi.org/10.1021/acs.inorgchem.5c00526
Inorg. Chem. 2025, 64, 14101−14117

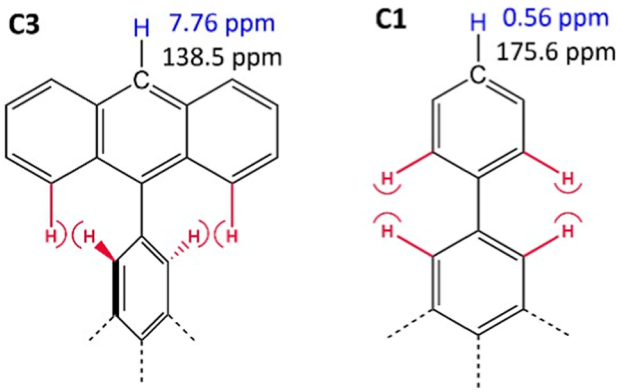

Figure 2. Schematic depiction of steric repulsion between protons of the backbone chromophore and the central phenyl unit. **C1** and **C3** are compared. Additionally, the chemical shifts obtained by NMR spectroscopy of the proton (blue) and carbon (black) in the chromophore backbones are depicted.

solution is hardly accessible, NMR-spectroscopy is employed, to utilize the paramagnetic properties of the complexes for this purpose. For conjugated aromatic systems, the unpaired electron of the Fe^{III} metal center leads to an alternating polarization and, therefore, spin density throughout the aromatic system.[45] The protons and carbon atoms show the corresponding alternating highfield and lowfield shifts. As seen in Figure 2, the chemical shifts of the para-carbon and para-hydrogen atoms of the phenyl substituent in **C1** show significant deviation from the typical aromatic region with 175.6 and 0.56 ppm respectively. This finding is attributed to a strong electronic interaction of the phenyl substituent with the coordinating phenyl ring and the Fe^{III} center, which is only possible for a small dihedral angle in solution. The analogous carbon and hydrogen atoms of the anthracene in **C3**, however, show the typical shifts for aromatic compounds. Thus, little to no electronic interaction with the central phenyl ring and the Fe^{III} center is present, confirming a large dihedral angle. The corresponding NMR shifts of **C2**, at 5.78 and 152.2 ppm respectively, lie between those of **C1** and **C3**, as expected from the dihedral angles. The additional rings in **C4** make a similar analysis for that system not feasible. These findings correlate well with the insights from the crystal structures and calculations.

The electronic ground state structure of the complexes was further investigated via cyclic voltammetry. All complexes show reversible $Fe^{III/IV}$ and $Fe^{II/III}$ redox processes (Figure 3). The redox potentials and corresponding electrochemical energy gaps are listed in Table 2.

The differences in iron oxidation/reduction potentials observed for the different chromophores are very small, as shown in Table 2 and Figure 3. Also, the unfunctionalized complex **C0** fits in the same potential range as **C1** to **C4**. Therefore, no significant influence of the chromophore on the energies of the metal d-orbitals is found. Ligand oxidation could be observed for all complexes in the potential window of 0.9−1.3 V. The lowest oxidation potential decreases with increasing chromophore size, while the current and number of oxidation processes increase. For **C1**, reversible ligand oxidation is observed, while the larger chromophores exhibit irreversible oxidation events. No ligand reductions were observed in the solvent window. Therefore, no electrochemical band gap for ligand reduction/metal oxidation could be

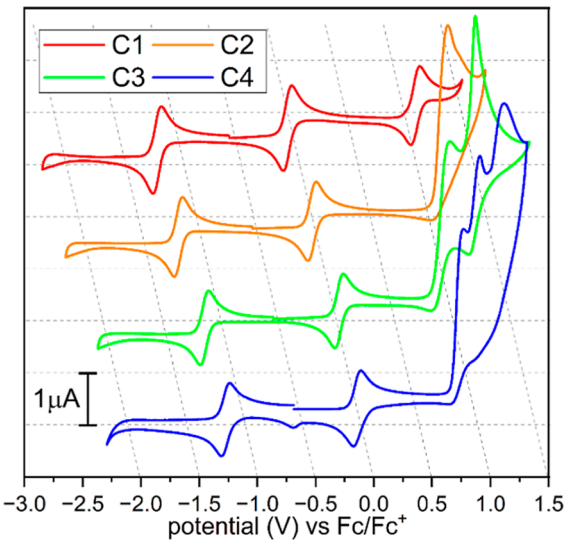

Figure 3. Cyclic voltammograms measured in MeCN at 1 mmol/L. NBu_4PF_6 was added as conducting salt at 10 mmol/L. The voltammograms show reversible $Fe^{II/III}$ and $Fe^{III/IV}$ redox processes in all complexes. The X- scale is shifted for each subsequent voltammogram as can be seen by the tilted gridlines to decrease overlap. Ligand oxidations are decreasingly reversible with growing chromophore size. Ligand reductions are not seen in the solvent window. For readability the voltammograms are offset by 1 μA to each other.

Table 2. Redox Properties of C0 to C4 Derived from Cyclic Voltammetry[a]

	E_{Red} $Fe^{II/III}$ [V]	E_{Ox} $Fe^{III/IV}$ [V]	E_{Ox}[b] Lig. [V]	ΔE_p[c] [V]
C0[26]	−1.16	0.08	1.31	2.47
C1	−1.11	0.01	1.11	2.22
C2	−1.11	0.02	1.19	2.30
C3	−1.20	0.11	1.001.22	2.20
C4	−1.20	0.06	0.921.061.26	2.12

[a]Oxidation and reduction potentials of each complex and its ligand moieties are listed. The electrochemical energy gaps for ligand-to-metal charge transfer are calculated. [b]For **C3** and **C4** multiple electrochemical ligand oxidations occurred and are listed. [c]ΔE_p is the electrochemical energy gap for ligand oxidation and iron reduction. For **C3** and **C4** the lowest ligand oxidation energies are used.

defined. In the next step, the frontier orbitals and the HOMO−LUMO regions for **C1**−**C4** were computed and compared to those of the parent complex **C0** and the corresponding chromophores. In the parent compound, both HOMO and LUMO orbitals are of dominantly d(Fe) character with some delocalization toward the ImP-ligands. The SOMO in **C0**, corresponding to the singly occupied t_2g orbital, is energetically clearly separated from the manifolds of the occupied and the virtual LUMO + n ($n \geq 1$) orbitals. The same frontier orbitals picture is observed for all derivatives (**C1** to **C4**) (see Figure S1). In agreement with cyclic voltammetry, the chromophore exhibits only minor influence on the shape and energetic position of the SOMO. Upon modification with chromophores, the α-LUMO becomes clearly localized on the chromophores, with the exception of **C1**, where the chromophore-localized LUMO is energetically higher than the d(Fe) orbital. The corresponding α-HOMO is partially delocalized over the whole superligand for the two largest compounds, **C3** and **C4**, while for **C1** and **C2**, it is only located

https://doi.org/10.1021/acs.inorgchem.5c00526
Inorg. Chem. 2025, 64, 14101−14117

on the ImP-part. Importantly, in complexes **C1**−**C4**, many molecular orbitals have a very delocalized character, ranging from the whole ImP-chromophore ligand to mixed metal/ligand character, which is reflected in the presence of delocalized electronic excitations in the absorption spectra.

The absorption spectra of all complexes are shown in Figure 4. The corresponding proligand absorption is depicted in Figure S18. Overall, the complex spectra can be separated into three distinct regions with different transition types. Intense bands at wavelengths smaller than 300 nm correspond to $\pi-\pi^*$ transitions in the ImP and phenyl moieties in **C0** and are assigned in the same manner for **C1** to **C4**.[26] Therefore, these bands are visible in all complexes, as well as in their corresponding proligands. In the region between 300 and 500 nm, two additional transitions are observed. First, local ^{2}Chrom excitations of the larger backbone chromophores are visible. Here, the given multiplicity refers to the total spin of 1/2 of the entire complex, while for the chromophore itself the state corresponds to the singlet S_1 state. In the proligands, these bands are the only transitions in the 300−500 nm range, and their absorption maxima correspond to those of the isolated chromophores.[46] In the complexes **C1** to **C4**, additional MLCT transitions are found in this range, assigned by comparison to similar complexes exhibiting features in the same region as the present complexes.[23,26] For **C1** and **C2**, the chromophore based absorption maxima are below or at 300 nm, making a clear identification of the MLCT bands possible.

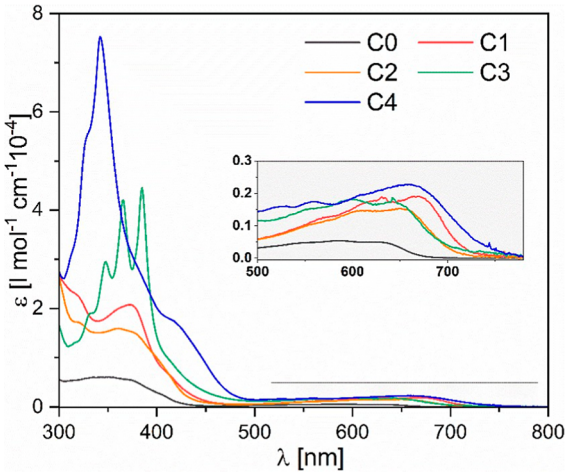

Figure 4. UV−vis absorption spectra of **C1** to **C4** ($c = 1 \times 10^{-5}$ mol/L in MeCN) compared to the absorption spectrum of **C0**.

However, in contrast to **C0**, both **C1** and **C2** exhibit two absorption bands in this range that do not occur for **L1** or **L2**. A possible explanation is the mixing of ligand and chromophore orbitals in the ligand HOMO, leading to different ligand centered (LC), ligand-to-ligand charge transfer (LLCT), or MLCT transitions. For **C3** and **C4**, the chromophore-based LC transitions, and the ^{2}MLCT absorption bands overlap, making a clear assignment of the bands difficult. For **C3**, the characteristic three absorption bands of anthracene at 347, 365, and 385 nm are markedly visible in both the complex and proligand spectra and are only slightly shifted compared to free anthracene (see Figure S69). For **C4**, the chromophore absorption band at 342 nm shows a shoulder at 415 nm that is not present in the corresponding proligand **L4**. This observation suggests that the shoulder originates from ^{2}MLCT absorption, which is red-shifted compared to base complex **C0** due to energetically lower π^*-orbitals. However, other contributions from interligand (IL) and LC transitions cannot be excluded. The ^{2}MLCT absorptions of **C1** and **C2** occur at similar energies, although a shift to higher wavelengths for **C2** was expected due to the increasing π-electron system. Typical for these complexes are ^{2}LMCT absorption bands occurring at wavelengths above 500 nm.[26,47] While they are red-shifted compared to **C0**, no clear trend related to the chromophore energy is apparent.

All complexes show a larger integrated absorption cross section than **C0**. However, no clear correlation with increasing chromophore size can be established, presumably because the dihedral angle between ImP-backbone and chromophore plays a crucial role here. **C4** shows the largest absorptivity in the MLCT/LC as well as the LMCT absorption region, as is expected for the largest chromophore. However, **C3** shows an absorptivity comparable to **C1** and **C2**. This finding is attributed to the large dihedral angle as detected by paramagnetic NMR spectroscopy (see above). The same trend in absorptivity from pyrene to anthracene is apparent in the MLCT transition bands of the related C^N^C complexes.[23] Accordingly, the absorptivity of **C2** is somewhat smaller than that of **C1**, which shows the smallest dihedral angle for the ImP-chromophore torsion.

In agreement with the electrochemical bandgaps given above, the chromophores show little to no effect on the corresponding LMCT optical bandgaps listed in Table 3. Due to the two MLCT bands in **C1** and **C2**, two optical bandgaps are assigned, which are also almost identical in energy when compared between both complexes. A clear assignment of optical bandgaps for MLCT transitions in **C3** and **C4** is

Table 3. Absorption Wavelengths and Extinction Coefficients of C0 to C4[a]

	λ_{MLCT}[b] [nm]	ε_{MLCT} [l × mol^{-1} × cm^{-1}]	$\Delta E_{O,\,MLCT}$[c] [eV]	λ_{LMCT}[d] [nm]	ε_{LMCT} [l × mol^{-1} × cm^{-1}]	$\Delta E_{O,LMCT}$[c] [eV]	ΔE_P [eV]
C0[26]	343	6.0×10^3	3.61	500−700 (585)	0.5×10^3	1.77−2.48 (2.31)	2.47
C1	320	2.2×10^4	3.87	500−750 (669)	1.9×10^3	1.65−2.48 (1.85)	2.22
	372	2.1×10^4	3.33				
C2	320	1.7×10^4	3.87	500−750 (649)	1.5×10^3	1.65−2.48 (1.91)	2.30
	361	1.6×10^4	3.43				
C3	320−400		3.01−3.87	500−750 (642)	1.9×10^3	1.65−2.48 (1.93)	2.20
C4	300−450		2.76−4.13	500−750 (656)	2.3×10^3	1.65−2.48 (1.89)	2.12

[a]From these bands, the energy gaps for MLCT and LMCT transitions are estimated. The electrochemical band gaps described above are listed for comparison. [b]Two MLCT bands are apparent for **C1** and **C2**. For **C3** and **C4**, no clear MLCT band can be assigned due to the overlap with the chromophore absorption. [c]ΔE_O are the optical energy gaps for MLCT and LMCT, respectively. [d]Since the LMCT absorption bands are relatively broad, a range is shown. The value in brackets is the maximum.

https://doi.org/10.1021/acs.inorgchem.5c00526
Inorg. Chem. 2025, 64, 14101−14117

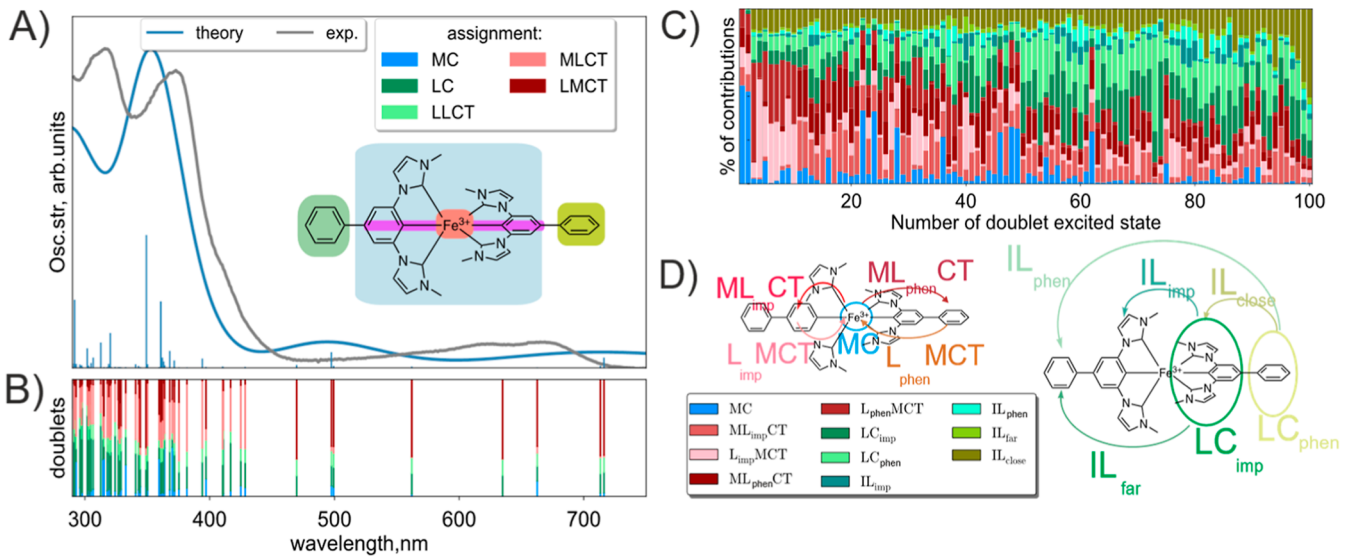

Figure 5. Simulated absorption spectrum of **C1** compared to the experimental data (A); the results of the clustering analysis (see text) are shown as inset. In (B), the transitional density-matrix analysis of TDDFT transitions is shown versus the relative energetic position. Part (D) presents the partitioning of the supermolecule into 5 fragments for the TDDFT analysis shown in panel (C).

impossible due to the strong overlap with the corresponding chromophore absorption. The LMCT bandgaps of the four complexes are similar in energy and close to that of **C0**.

The challenge of accurately modeling charge−transfer properties with (TD)DFT due to erroneous self-interaction is well-known.[48,49] To address this, an optimally tuned range-separated functional was employed, which ensures that Koopmans' theorem is fulfilled for both ionization potential (IP) and electron affinity (EA). This approach significantly improves the description of all properties related to fundamental and optical energy gaps.[50−52] However, since the tuning primarily adjusts the HOMO and LUMO positions, excitations involving deeper-lying or higher-lying orbitals may still retain some functional-dependent inaccuracies. Nevertheless, such transitions are often improved as well as a consequence of the tuning process.[53,54]

The absorption spectra calculated by TDDFT are in moderate agreement with the experimental results (Figures 5 and S2 for Fe^{III} and Figures S3 and S4 for spectra of reduced and oxidized species, respectively). Note that the calculated spectra contain only doublet−doublet or singlet−singlet transitions, while multiple formally forbidden transitions are only shown as sticks of zero intensity to mark their positions. However, for iron complexes, the influence of spin−orbit coupling on the UV−vis spectra is expected to be only minor, which has been shown for other iron complexes of similar size.[55] The shift of the positions of some absorption bands might also be, in general, the result of the approximate nature of TDDFT calculations.

An example of the transition assignment is shown in Figure 5 for **C1** (results for the other compounds are shown in Figure S2). To understand the influence of the organic chromophore moieties on the spectral properties, each complex was partitioned into the metal center, two ImP ligands, and two organic chromophore groups. Figure 5D shows the notation of different types of transitions and their corresponding assignments. For all compounds, the mixing between MLCT and LMCT transitions with local LC/MC states is notable. The calculations were performed at the frozen ground-state geometry, without considering ligand coplanarization. Some transitions are dominantly localized on either the ImP or the organic chromophore part, while other transitions exhibit significant mixing even in the nonplanar geometry. Both MLCT and LMCT transitions involve the superligands composed of ImP and the chromophore, with the degree of charge transfer mixing varying across different states. This indicates the principal possibility of long-range charge transfer in such systems, though fully capturing the transition between different LMCT states during structural relaxation would require excited-state geometry optimizations and explicit solvent modeling for reliable backbone angle predictions.

Further, the hole and electron correlations in the manifold of computed excitations were analyzed following the hierarchical clustering approach to rationalize the role of the organic chromophores in the excited state evolution.[26] All computed excited states are analyzed in terms of the localization of excitations, which results in partitioning of the molecule based solely on the correlations between the excitations. The resulting partitioning is presented in Figure 5A for **C1** (see Figure S2 for partitioning of the other complexes **C2**−**C4**, and Figures S3 and S4 for partitioning of reduced and oxidized species). The most important finding in this fragmentation analysis is a clear separation of the organic chromophore units regardless of the chromophore size, considered excitations, or oxidation state of the compounds. This result justifies the employment of such organic chromophores as possible tuning tools to modify the photoexcited properties, as they influence the latter by their individual properties.

All complexes were also investigated by fluorescence spectroscopy, and the results are shown in Figure 7. For **C1** and **C2,** an emission originating from the ^{2}LMCT state occurs between 650 and 900 nm, similar to the emission of **C0**.[26] **C4** exhibits a weaker emission located above 700 nm. For **C3**, no emission from this ^{2}LMCT state was initially resolved. However, by increasing the concentration by a factor of 10, a weak emission in the range above 700 nm was observed. Therefore, a different photodynamic relaxation behavior in **C3** and **C4** can be assumed due to the low-lying excited triplet

https://doi.org/10.1021/acs.inorgchem.5c00526
Inorg. Chem. 2025, 64, 14101−14117

states and oxidation potentials of the chromophores. The excited triplet state energy of anthracene in **C3** is slightly lower than that of pyrene in **C4.**[56] This difference can explain the more intense emission of **C4** in the LMCT range. **C3** samples exhibit an additional emission around 400 nm caused by fluorescence from a singlet anthracene state. This emission may result from minor anthracene impurities, that are undetectable with other methods but still visible here due to anthracenés high quantum yield of 0.36.[57] The relative emission of pure anthracene compared to the **C3** sample is 3 orders of magnitude higher (see Figure S69). Therefore, the concentration of anthracene is much lower than **C3** and it should not influence any other measurements. Using time-correlated single photon counting (TCSPC) spectroscopy, the lifetime of this emission was determined to be 6.8 ns (see Figure S71), similar to the singlet emission lifetime of anthracene in other solvents which supports the conclusion that the emission results from a small anthracene impurity.[58]

The maxima of the observed LMCT emissions shift to longer wavelengths with decreasing chromophore energy due to decreasing energy of the involved LMCT state. For **C1**, the emission maximum is at 731 nm and shifts to 742 nm for **C2** and to 845 nm for **C4**, which is at the edge of the spectroscopic range of the used spectrometer. The weak LMCT emission of **C3** also shows a maximum at 845 nm, but at a high noise level. Therefore, this band needs to be interpreted with caution. From the intersection of the absorption and corresponding emission bands, the E_{00} energies can be estimated. The ^{2}LMCT energies of complexes **C0** to **C2** are similar and are in the range of 1.80 (**C1**/**C2**) to 1.90 (**C0**) eV. These values are compared in Scheme 2 to the spectroscopically determined ^{3}Chrom transition energies[56] of the organic chromophores. The small energy difference between anthracene and pyrene triplet states, and the ^{2}LMCT state could lead to a nonradiative relaxation pathway from the ^{2}LMCT to the ground state via chromophore triplet states, explaining the weak emission of **C4** and **C3**. However, if this was the case, the long lifetimes of the respective triplet states of these chromophores should be apparent in the TA spectra below. Since this is not the case, a simple relaxation cascade of LMCT to the chromophore to GS cannot explain these observations.

Scheme 2. Triplet State Energies of the Different Chromophores and the LMCT Energy of the Unfunctionalized Complex C0[26,56]

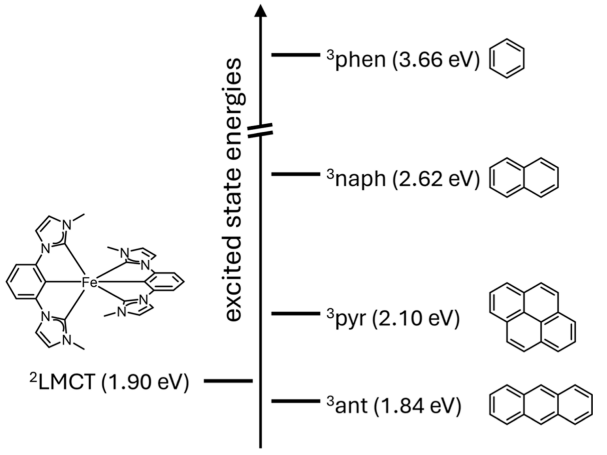

Excited State Dynamics. To obtain a first impression of the excited state dynamics, the time evolution of the emission of the complexes was studied by time-resolved measurements with a streak camera. The compounds were dissolved in MeCN and optically excited by ultrashort laser pulses with a center wavelength of 350 nm. For complexes **C1** and **C2**, it was found that the LMCT emissions, known from stationary fluorescence spectroscopy, decay monoexponentially with time constants of 237 and 223 ps, respectively. These coincide with the decay time of 240 ps for the LMCT emission of **C0** within the experimental accuracy.[26] In the case of **C3** and **C4** no significant signal was detected by the streak camera as expected from the very weak LMCT emission bands reported in Figure 6. This observation points to lifetimes for these emissions well below the time resolution of the streak camera of about 90 ps.

For deeper insights into the light-induced dynamics of the complexes, ultrafast transient absorption (TA) studies were performed, applying a white light continuum for probing and tunable pulses from a NOPA with pulse lengths of about 50 fs for pumping.[35] As samples served MeCN solutions of the compounds with an optical density of about 0.3 to 0.4 at the excitation wavelength. The complexes were excited in the LMCT absorption band at 650 nm. Since this band is quite weak (ε < 2500), rather high concentrations had to be used. This resulted in strong absorption below 430 nm, which limits the probed spectral range to longer wavelengths. TA spectra at various time delays between pump and probe pulses are shown in Figure 7 for complexes **C1** and **C3**. Corresponding data for **C2** and **C4** are presented in Figure S63 of the Supporting Information. To analyze the dynamics, a global fit of a sum of exponential decay components was applied, giving both a time constant and a decay associated amplitude spectrum (DAS) for each component as results of the fits. The obtained DAS, labeled with the corresponding time constants, are shown in the lower panels of Figure 7 for **C1** and **C3**, and in Figure S63 of the Supporting Information for **C2** and **C4**. The TA spectra of **C1** exhibit an ESA band in the blue spectral region and a broad and rather structureless ESA extending into the red. Both components decay simultaneously and monoexponentially with a time constant of 270 ps. This behavior is nearly identical to **C0**.[26] In the case of **C3**, significant deviations from this behavior are found. The TA spectra show again an ESA band in the blue and a broad ESA covering the whole visible spectral range. However, in addition a second ESA band at 615 nm appears during the first picoseconds. Furthermore, the TA signal decays completely within a few tens of picoseconds. The global fit reveals that the ESA band at 615 nm rises with a time constant of 2.6 ps, as is evident from the associated DAS, mirroring the band and its spectral environment at wavelengths above 575 nm. The overall signal then decays with a lifetime of 18 ps. Interestingly, the ESA bands observed for **C1** and **C3** fit rather well to the absorption spectra of the corresponding Fe^{II} species (Figure S67 in the Supporting Information). The ESA band of **C1** seems to resemble the absorption band of reduced **C1** besides a blue shift of about 20 nm. In the case of **C3**, the ESA rising below 450 nm seems to reflect the band at 411 nm of the reduced form, and the ESA band in the red seems to be related to the band at 627 nm. However, as spectra of the ligand-oxidized species are not obtainable, this factor can influence the absorption in the red as well. Nevertheless, these results indicate that the excited state population resides in the lowest LMCT state. In **C1** this state is directly populated and lives for 270 ps.

https://doi.org/10.1021/acs.inorgchem.5c00526
Inorg. Chem. 2025, 64, 14101−14117

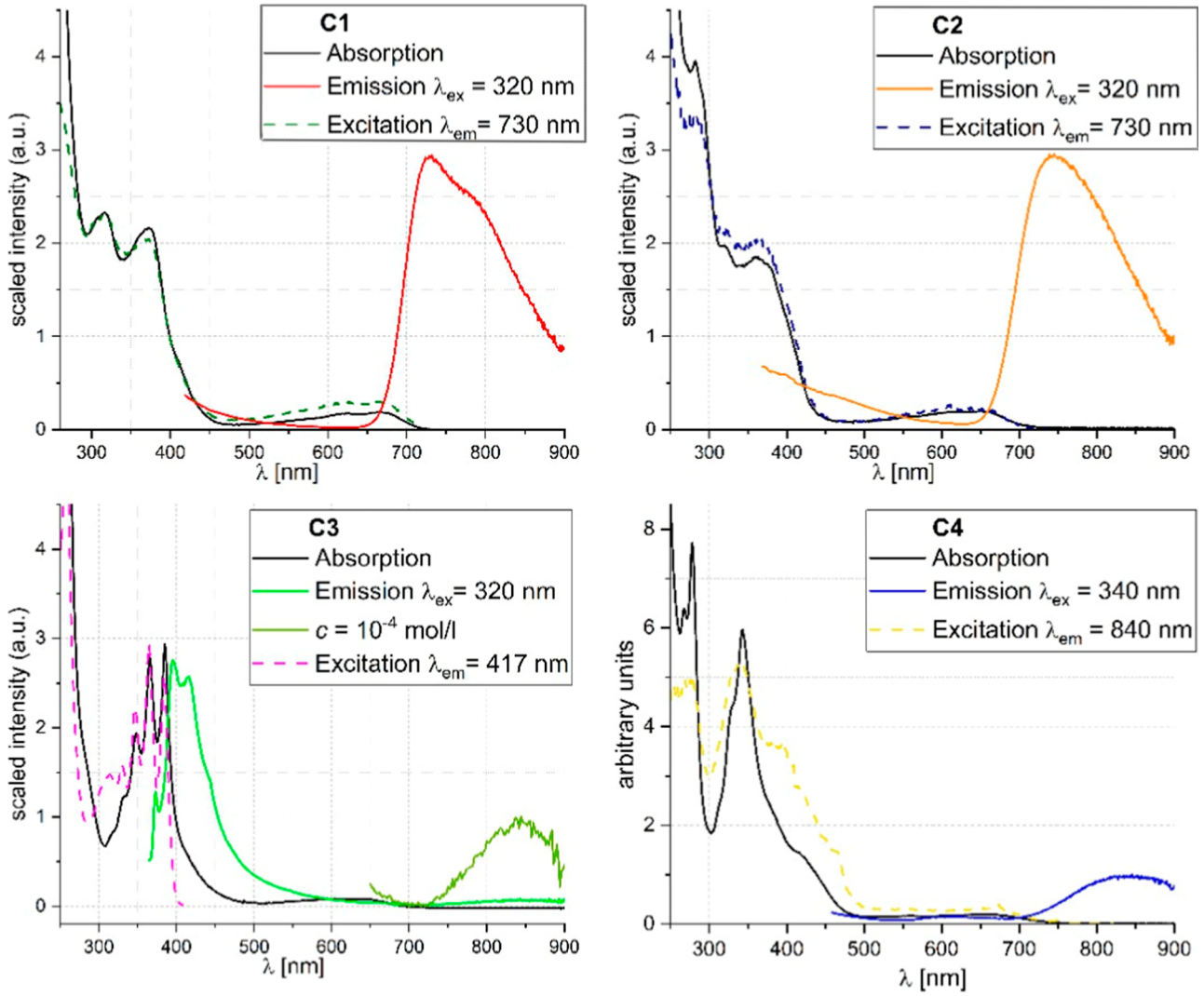

Figure 6. Emission spectra of **C1** to **C4**. The absorption spectra and emission spectra are scaled for better comparability. All spectra are measured in MeCN (10^{-5} mol/L). For **C3** an additional spectrum at 10^{-4} mol/L was recorded.

In contrast, after optical excitation of **C3**, only a first relaxation step seems to lead to the lowest lying LMCT state. This step might be related to a planarization of the chromophore which is perpendicularly oriented to the ImP-backbone in the ground state. At the same time, the step presumably reflects a stronger delocalization of the π-electrons in the electronically excited state and a population transfer to an LMCT state with the whole superligand as donor. This notion is supported by the rise of the ESA feature around 614 nm which might be related to absorption features involving the anthracenyl-cation. The isolated anthracene cation exhibits absorption bands in the visible at 438 and 726 nm.[59] Since the expanded π-system of the ligand motif compared to the isolated chromophore can lead to a pronounced spectral shift of electronic transitions, we assume that the ESA feature at 614 nm is a reminiscence of one these bands. Thus, internal conversion to the lowest LMCT state from somewhat higher lying LMCT states is a possible explanation for the initial ESA changes. The ab initio calculations suggest that such states exist and can be populated by the excitation pulses. This charge-separated state involving the whole superligand as donor would be significantly lower in energy and is quickly populated from the optically excited LMCT state involving a twist motion of the anthracene moiety. It seems to open a new relaxation channel and enables a fast radiationless decay into the ground state explaining the 18 ps lifetime and the almost fully quenched emission of **C3** The small difference in energy between the local triplet state of the anthracene chromophore and the LMCT state of **C3** indicates that strong mixing of the corresponding orbitals and the formation of the superligand charge transfer state are feasible, see Scheme 2.

As shown in the SI, TA spectroscopy on **C2** reveals a LMCT lifetime of 238 ps, which is in excellent agreement with the streak camera measurements. In addition, indications for a fast initial relaxation step with a time constant of 1.6 ps are found which leads to the lowest LMCT state similar as in **C3**. **C4**, whose chromophore pyrene has a triplet energy close to the energy of the lowest LMCT state, exhibits a light-induced dynamic comparable to that of **C3**, see Figure S63. The LMCT lifetime is only 20 ps and the lowest LMCT state is also populated by a relaxation step on the picosecond time scale. The DAS of this step might reflect contributions of the pyrene cation at 580 nm which would correspond to a redshift of about 130 nm of the dominant absorption band of the isolated pyrene cation.[59] This observation suggests a delocalization of the hole over the entire π-system of the superligand similar to

https://doi.org/10.1021/acs.inorgchem.5c00526
Inorg. Chem. 2025, 64, 14101−14117

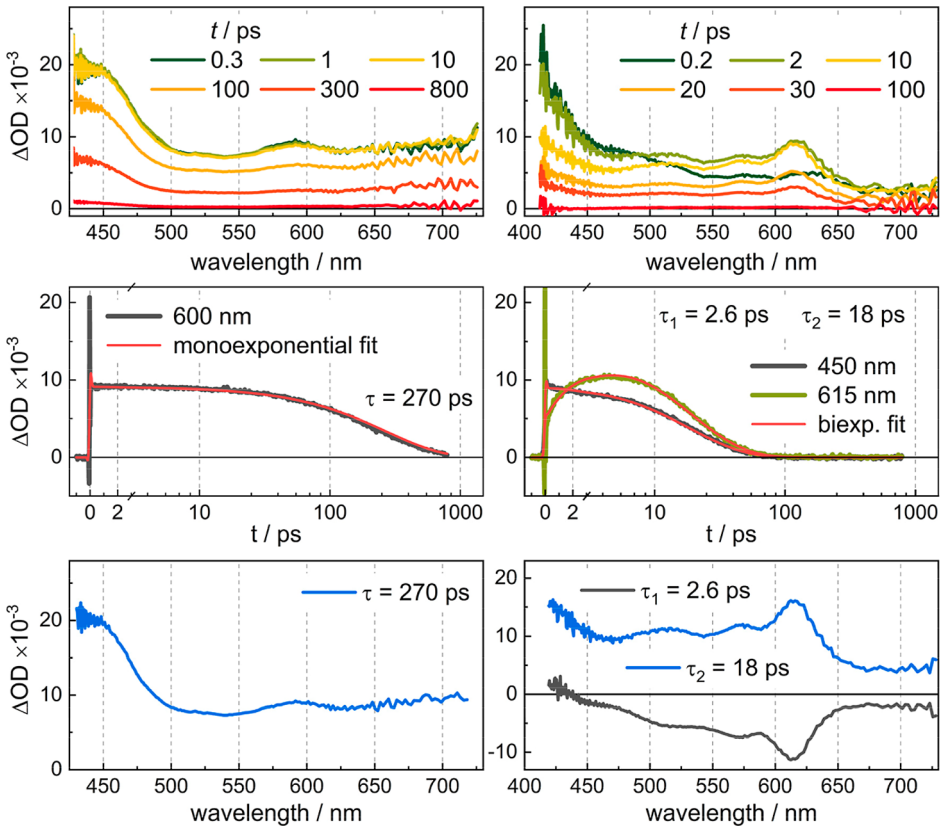

Figure 7. Ultrafast TA-spectra at the given delay-times (top), time-traces of selected wavelengths with the corresponding fits along their results (middle) and DAS (bottom) of **C1** (left) and **C3** (right). The complexes are dissolved in MeCN and optically excited at 650 nm. The polarizations of the pump and probe pulses are set to magic angle.

the case of **C3**. The DAS assigned to the lowest LMCT state fits again to the absorption spectra of the reduced complexes for both **C2** and **C4** as seen in Figure S63 in comparison with Figure S67 As pointed out above, we expected different dynamics for the larger chromophores due to their low lying triplet states, which can couple to the LMCT state and thereby increase the degree of delocalization of this state. Also, the low lying oxidation potentials of anthracene and pyrene, which are with 1.0 and 1.1 V closer to those of the complexes than benzene and naphthalene,[60] indicate that in the case of the larger chromophores an extended delocalization of the hole across the entire ligand is conceivable. In summary, the TA measurements indicate that in the case of anthracene and pyrene as substituted chromophores a fast relaxation step to a lowered LMCT state occurs after optical excitation and this state is associated with a delocalization over the entire superligand.

In a second set of TA measurements the MLCT transitions were optically excited by pump pulses with a center wavelength of 350 nm. The corresponding TA data is shown in Figure S64. For **C3** and **C4**, a simultaneous excitation of the ^{1}Chrom state could not be prevented due to the overlap of the individual absorption bands. Since these transitions are quite intense, a low sample concentration could be used and, in contrast to the TA experiments described above, the probe light is not blocked in the blue and near UV. Accordingly, TA spectra covering the spectral range down to 350 nm could be recorded. They clearly show that in the near UV, the bleach of the chromophores and MLCT transitions shape the absorption changes and lead to a strong decrease of the TA signal below 400 nm. For all complexes, a rise of the ESA band, associated with the population of the energetically lowest LMCT state, is observed. While this population takes 0.6 to 0.8 ps for **C1**, **C2** and **C4**, in the case of **C3** a somewhat longer value of 4.4 ps is obtained. This finding suggests a relationship to the 90° dihedral angle between the anthracene chromophore and the ImP-backbone of **C3**, which requires a more pronounced rotation for planarization. The relaxation from the optically excited chromophore and MLCT states to the LMCT states seems to be contained in the picosecond component, where no distinct signature of an MLCT state is observed. In the case of **C1** and **C4**, an additional weak component is observed with a time constant in the order of 5 ps, which seems to represent a slight red shift of the ESA bands and is tentatively assigned to cooling processes. For the lowest LMCT state, lifetimes of 246 and 224 ps in **C1** and **C2** and of 20 and 18 ps in **C3** and **C4** are found, in good agreement with TA data obtained with an excitation wavelength of 650 nm and the streak camera measurements. All determined lifetimes are listed in Table 4.

Table 4. Excited State Lifetimes from Transient Absorption Spectroscopy

excitation wavelength	350 nm (330 nm for C0)	650 nm
C0[26]	0.5 ps, 6.0 ps, 235 ps	
C1	0.6 ps, 4.8 ps, 246 ps	270 ps
C2	0.6 ps, 224 ps	1.6 ps, 238 ps
C3	4.4 ps, 20 ps	2.6 ps, 18 ps
C4	0.8 ps, 6.1 ps, 18 ps	0.3 ps, 2.2 ps, 20 ps

https://doi.org/10.1021/acs.inorgchem.5c00526
Inorg. Chem. 2025, 64, 14101−14117

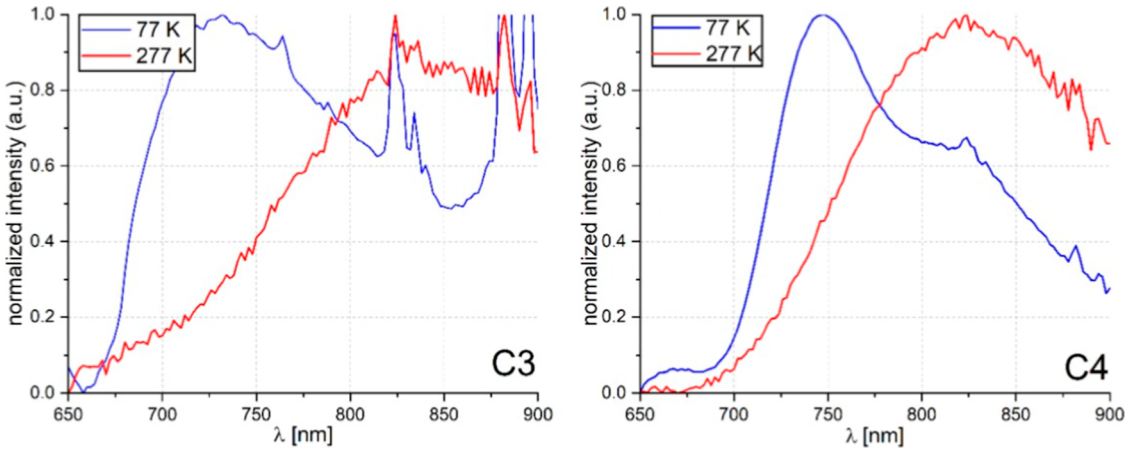

Figure 8. Comparison of emission spectra in butyronitrile for **C3** (10^{-4} mol/L) and **C4** (10^{-5} mol/L) at 77 and 277 K. Solvent emission spectra were measured at both temperatures and subtracted from the corresponding emission spectra.

The key finding of the TA experiments is that the photo dynamics of **C1** and **C2** are very similar to that of **C0**, while **C3** and **C4** exhibit a strongly reduced LMCT lifetime of only about 20 ps. A likely explanation is that after a relaxation step from an ImP-centered ^{2}LMCT to a superligand-centered ^{2}LMCT state, a relaxation channel to the ground state is established.

Low Temperature Emission Spectroscopy. To confirm the postulated rotation of the chromophore backbone after excitation, which results in a superligand state and the emission above 800 nm for **C3** and **C4**, low temperature emission spectroscopy was performed to freeze the complex geometry. The emission spectra at 277 and 77 K are shown in Figure 8 for both complexes. An emission above 750 nm is present for both **C3** and **C4** at 277 K. However, an emission band below 750 nm for both complexes is observed at 77 K. This band closely resembles the characteristic LMCT emission for complexes **C0** to **C2**. For **C3**, this band is significantly weaker than for **C4**. In fact, it was only resolved at a concentration of 10^{-4} mol/L, ten times the concentration of **C4**. Based on these results, we postulate that the frozen complex geometry prevents the formation of a superligand state by hindering rotation. Instead, the chromophore and complex fragments remain decoupled even after excitation. Under these conditions, the LMCT state of **C3** is probably almost fully depopulated by the lower lying nonemissive triplet state of the anthracene moiety, leading to significantly weakened residual LMCT emission. In this case, the excited state population would actually live longer than in **C0**−**C2**; however, it would reside in the nonemissive local triplet state of the chromophore. Since the triplet state of pyrene is higher in energy than the ^{2}LMCT state, **C4** is not quenched in the same way, resulting in an emission with an intensity comparable to complexes **C0** to **C2**. These postulated photodynamics are depicted in Scheme 3.

Scheme 3. Postulated Photodynamic Processes for C3 (Green) and C4 (Blue) at 77 K after Freezing the Dihedral Angle between Base Complex Fragment and Backbone Leading to Decoupled States

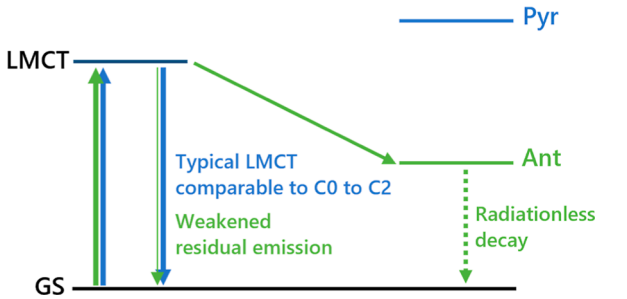

CONCLUSION

A new series of multichromophoric Fe^{III} complexes (**C1** to **C4**) based on the previously published complex Fe^{III}-complex $[Fe(ImP)_2][PF_6]$, utilizing benzene, naphthalene, anthracene and pyrene in the backbone of the C^C^C ligand at the Fe^{III} center is presented. The complexes were investigated to understand the effects of chromophore substitution on their ground- and excited-state properties with a focus on the application as photosensitizers, utilizing the reservoir effect. The extinction coefficients of the base complex were successfully increased more than 2-fold, while the absorption energies of both MLCT and LMCT states remained practically unchanged. This reveals that no strong coupling between the chromophore and the central ligand motif occurs. This is indeed a prerequisite for the reservoir effect, which relies on the long lifetime of a more or less undisturbed local triplet state ^{3}Chrom of the chromophore. However, the desired increase of excited state lifetime could not be realized. Instead, for the chromophores with triplet states close to the energy of the LMCT state, i.e. anthracenyl and pyrenyl, quenching of the excited state emission was observed at room temperature. The experimentally obtained crystal structures, as well as the calculated structures and qualitative NMR studies confirm a large dihedral angle between the C^C^C ligand scaffold and these large chromophore units. This finding suggests electronic decoupling between the chromophore and metal complex, which is required to realize a reservoir effect. However, coplanarization of the chromophore with the C^C^C scaffold after excitation leads to a pronounced coupling of the electronically excited states, apparent from a characteristic absorption arising in the TA spectra. This planarization leads to delocalization of the excited state over the whole superligand and subsequent relaxation into the ground state within 20 ps, which is significantly faster than in the corresponding base complex. The complete excited state landscape at room temperature for the example of **C3** is

https://doi.org/10.1021/acs.inorgchem.5c00526
Inorg. Chem. 2025, 64, 14101−14117

Scheme 4. Schematic Representation of the Excited State Dynamics for C3[a]

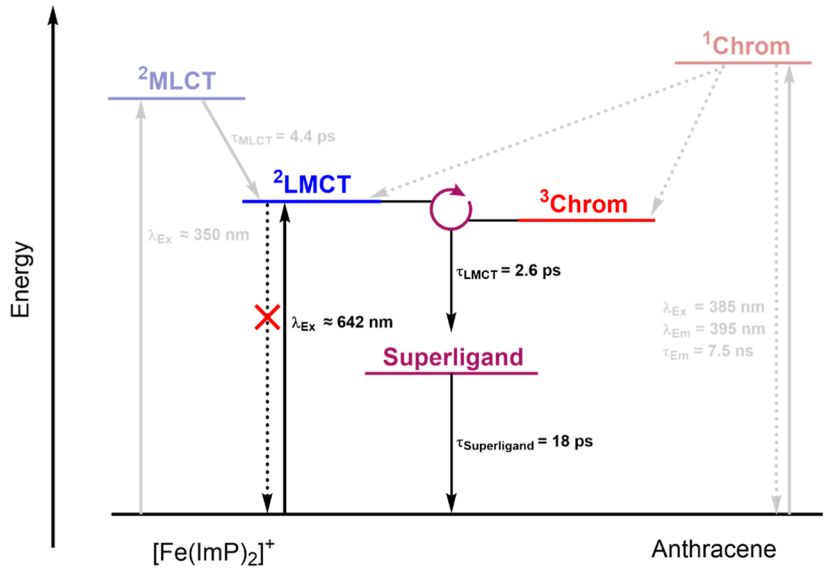

[a]The ^{1}Chrom emission lifetime is derived from TCSPC. All other lifetimes are derived from TA.

depicted in Scheme 4. On the chromophore side, the singlet emission is presumably completely quenched. The possible quenching pathways could be decay processes into the ^{2}LMCT or ^{3}Chrom states. The ^{2}LMCT state is either populated directly or after excitation into the MLCT manifold. Instead of exhibiting the desired reservoir effect and boosting the LMCT lifetime, a superligand state, consisting of the coplanarized C^C^C and anthracene group is populated to stabilize the formal positive charge. This superligand state is populated within 2.6 ps and is lower in energy than the previously decoupled ^{2}LMCT and ^{3}Chrom states. This enables a fast mostly radiationless relaxation into the ground state within 18 ps. For **C4**, similar dynamics are postulated, although a slightly stronger ^{2}LMCT emission was observed. **C1** and **C2** show dynamics comparable to the previously published **C0** and are not depicted here.[26] While coplanarization may also occur for these complexes, the smaller chromophores have a much weaker effect on excited state lifetime and emission energy.

For future designs of functioning reservoir complexes, the decoupling of the two functional units - metal complex and chromophore reservoir - needs to be enforced even after excitation, e.g. through the implementation of spacer groups or steric hindrance.

■ ASSOCIATED CONTENT

Supporting Information

The Supporting Information is available free of charge at https://pubs.acs.org/doi/10.1021/acs.inorgchem.5c00526.

NMR spectra, MS data, additional computational studies, electrochemistry, spectroelectrochemistry, additional spectra regarding an anthracene impurity, additional transient absorption data (PDF)

Accession Codes

Deposition Numbers 2402183−2402186 contain the supplementary crystallographic data for this paper. These data can be obtained free of charge via the joint Cambridge Crystallographic Data Centre (CCDC) and Fachinformationszentrum Karlsruhe Access Structures service.

■ AUTHOR INFORMATION

Corresponding Author

Matthias Bauer − *Faculty of Science, Chemistry Department and Center for Sustainable Systems Design, Paderborn University, Paderborn 33098, Germany;* orcid.org/0000-0002-9294-6076; Email: Matthias.Bauer@uni-paderborn.de

Authors

Lennart Schmitz − *Faculty of Science, Chemistry Department and Center for Sustainable Systems Design, Paderborn University, Paderborn 33098, Germany*

Miguel A. Argüello Cordero − *Institute of Physics and Department of Life, Light and Matter, University of Rostock, Rostock 18051, Germany*

Mohammed J. Al-Marri − *Department of Chemical Engineering, Qatar University, Doha 2713, Qatar;* orcid.org/0000-0002-9223-487X

Roland Schoch − *Faculty of Science, Chemistry Department and Center for Sustainable Systems Design, Paderborn University, Paderborn 33098, Germany*

Hans Egold − *Faculty of Science, Chemistry Department and Center for Sustainable Systems Design, Paderborn University, Paderborn 33098, Germany*

Adam Neuba − *Faculty of Science, Chemistry Department and Center for Sustainable Systems Design, Paderborn University, Paderborn 33098, Germany*

Jakob Steube − *Faculty of Science, Chemistry Department and Center for Sustainable Systems Design, Paderborn University, Paderborn 33098, Germany;* orcid.org/0000-0003-3178-4429

Bastian Bracht − *Faculty of Science, Chemistry Department and Center for Sustainable Systems Design, Paderborn University, Paderborn 33098, Germany*

Olga S. Bokareva − *Institute of Physics and Department of Life, Light and Matter, University of Rostock, Rostock 18051, Germany; Institute of Chemistry, University of Rostock and Leibniz Institute for Catalysis, Rostock 18057, Germany;* orcid.org/0000-0002-2313-7996

https://doi.org/10.1021/acs.inorgchem.5c00526
Inorg. Chem. 2025, 64, 14101−14117

Stefan Lochbrunner − *Institute of Physics and Department of Life, Light and Matter, University of Rostock, Rostock 18051, Germany;* orcid.org/0000-0001-9729-8277

Complete contact information is available at: https://pubs.acs.org/10.1021/acs.inorgchem.5c00526

Notes

The authors declare no competing financial interest.

■ ACKNOWLEDGMENTS

L.S. thanks the Fonds der Chemischen Industrie for a Kekulé grant. The authors thank Lorena Fritsch (Univeristy of Paderborn) for supporting theoretical calculations. M.B. gratefully achnowledges financial support through the priority program SPP 2102 from the German Science Foundation DFG (BA 4467/7-2) and in frame of project BA 4467/10-1. S.L. and O.S.B. gratefully acknowledge financial support through SPP 2102 (LO 714/11-2, KU 952/12-2), project no. 404479188, and GRK 2943 'Spectroscopic Tools for Challenging Reduction Reactions: Catalytic Coupling of CO_2', project no. 507189291. S.L. further acknowledges funding from SFB 1477 'Light−Matter Interactions at Interfaces', project no. 441234705. O.S.B. also acknowledges support from the Leibniz Association through the Leibniz Competition, project no. J.S.113/2021.

■ REFERENCES

(1) Crisenza, G. E. M.; Melchiorre, P. Chemistry glows green with photoredox catalysis. *Nat. Commun.* **2020**, *11* (1), 803.
(2) Beil, S. B.; Bonnet, S.; Casadevall, C.; Detz, R. J.; Eisenreich, F.; Glover, S. D.; Kerzig, C.; Næsborg, L.; Pullen, S.; Storch, G.; Wei, N.; Zeymer, C. Challenges and Future Perspectives in Photocatalysis: Conclusions from an Interdisciplinary Workshop. *JACS Au* **2024**, *4* (8), 2746−2766.
(3) Sinha, N.; Wegeberg, C.; Häussinger, D.; Prescimone, A.; Wenger, O. S. Photoredox-active Cr(0) luminophores featuring photophysical properties competitive with Ru(II) and Os(II) complexes. *Nat. Chem.* **2023**, *14*, 1730−1736.
(4) Förster, C.; Heinze, K. Photophysics and photochemistry with Earth-abundant metals - fundamentals and concepts. *Chem. Soc. Rev.* **2020**, *49* (4), 1057−1070.
(5) Chábera, P.; Lindh, L.; Rosemann, N. W.; Prakash, O.; Uhlig, J.; Yartsev, A.; Wärnmark, K.; Sundström, V.; Persson, P. Photofunctionality of iron(III) N-heterocyclic carbenes and related d transition metal complexes. *Coord. Chem. Rev.* **2021**, *426*, 213517.
(6) Dierks, P.; Vukadinovic, Y.; Bauer, M. Photoactive iron complexes: more sustainable, but still a challenge. *Inorg. Chem. Front.* **2022**, *9* (2), 206−220.
(7) Liu, Y.; Persson, P.; Sundström, V.; Wärnmark, K. Fe N-Heterocyclic Carbene Complexes as Promising Photosensitizers. *Acc. Chem. Res.* **2016**, *49* (8), 1477−1485.
(8) Wenger, O. S. Is Iron the New Ruthenium? *Chem.—Eur. J.* **2019**, *25* (24), 6043−6052.
(9) McCusker, J. K. Electronic structure in the transition metal block and its implications for light harvesting. *Science* **2019**, *363* (6426), 484−488.
(10) Liu, Y.; Harlang, T.; Canton, S. E.; Chábera, P.; Suárez-Alcántara, K.; Fleckhaus, A.; Vithanage, D. A.; Göransson, E.; Corani, A.; Lomoth, R.; Sundström, V.; Wärnmark, K. Towards longer-lived metal-to-ligand charge transfer states of iron(II) complexes: an N-heterocyclic carbene approach. *Chem. Commun.* **2013**, *49* (57), 6412.
(11) Dierks, P.; Kruse, A.; Bokareva, O. S.; Al-Marri, M. J.; Kalmbach, J.; Baltrun, M.; Neuba, A.; Schoch, R.; Hohloch, S.; Heinze, K.; Seitz, M.; Kühn, O.; Lochbrunner, S.; Bauer, M. Distinct photodynamics of κ-N and κ-C pseudoisomeric iron(II) complexes. *Chem. Commun.* **2021**, *57* (54), 6640−6643.
(12) Zimmer, P.; Müller, P.; Burkhardt, L.; Schepper, R.; Neuba, A.; Steube, J.; Dietrich, F.; Flörke, U.; Mangold, S.; Gerhards, M.; Bauer, M. N-Heterocyclic Carbene Complexes of Iron as Photosensitizers for Light-Induced Water Reduction. *Eur. J. Inorg. Chem.* **2017**, *2017* (11), 1504−1509.
(13) Francés-Monerris, A.; Gros, P. C.; Pastore, M.; Assfeld, X.; Monari, A. Photophysical properties of bichromophoric Fe(II) complexes bearing an aromatic electron acceptor. *Theor. Chem. Acc.* **2019**, *138* (7), 86.
(14) Malme, J. T.; Clendening, R. A.; Ash, R.; Curry, T.; Ren, T.; Vura-Weis, J. Nanosecond Metal-to-Ligand Charge-Transfer State in an Fe(II) Chromophore: Lifetime Enhancement via Nested Potentials. *J. Am. Chem. Soc.* **2023**, *145* (11), 6029−6034.
(15) Chábera, P.; Kjaer, K. S.; Prakash, O.; Honarfar, A.; Liu, Y.; Fredin, L. A.; Harlang, T. C. B.; Lidin, S.; Uhlig, J.; Sundström, V.; Lomoth, R.; Persson, P.; Wärnmark, K. FeII Hexa N-Heterocyclic Carbene Complex with a 528 ps Metal-to-Ligand Charge-Transfer Excited-State Lifetime. *J. Phys. Chem. Lett.* **2018**, *9* (3), 459−463.
(16) Leis, W.; Argüello Cordero, M. A.; Lochbrunner, S.; Schubert, H.; Berkefeld, A. A Photoreactive Iron(II) Complex Luminophore. *J. Am. Chem. Soc.* **2022**, *144* (3), 1169−1173.
(17) Tyson, D. S.; Bialecki, J.; Castellano, F. N. Ruthenium(II) complex with a notably long excited state lifetime. *Chem. Commun.* **2000**, No. 23, 2355−2356.
(18) Morales, A. F.; Accorsi, G.; Armaroli, N.; Barigelletti, F.; Pope, S. J. A.; Ward, M. D. Interplay of light antenna and excitation "energy reservoir" effects in a bichromophoric system based on ruthenium-polypyridine and pyrene units linked by a long and flexible poly(ethylene glycol) chain. *Inorg. Chem.* **2002**, *41* (25), 6711−6719.
(19) Moore, E. G.; Samuel, A. P. S.; Raymond, K. N. From antenna to assay: lessons learned in lanthanide luminescence. *Acc. Chem. Res.* **2009**, *42* (4), 542−552.
(20) Perry, W. S.; Pope, S. J. A.; Allain, C.; Coe, B. J.; Kenwright, A. M.; Faulkner, S. Synthesis and photophysical properties of kinetically stable complexes containing a lanthanide ion and a transition metal antenna group. *Dalton Trans.* **2010**, *39* (45), 10974−10983.
(21) Uh, H.; Petoud, S. Novel antennae for the sensitization of near infrared luminescent lanthanide cations. *C. R. Chim.* **2010**, *13* (6−7), 668−680.
(22) Jiang, T.; Bai, Y.; Zhang, P.; Han, Q.; Mitzi, D. B.; Therien, M. J. Electronic structure and photophysics of a supermolecular iron complex having a long MLCT-state lifetime and panchromatic absorption. *Proc. Natl. Acad. Sci. U.S.A.* **2020**, *117* (34), 20430−20437.
(23) Dierks, P.; Päpcke, A.; Bokareva, O. S.; Altenburger, B.; Reuter, T.; Heinze, K.; Kühn, O.; Lochbrunner, S.; Bauer, M. Ground- and Excited-State Properties of Iron(II) Complexes Linked to Organic Chromophores. *Inorg. Chem.* **2020**, *59* (20), 14746−14761.
(24) Kjær, K. S.; Kaul, N.; Prakash, O.; Chábera, P.; Rosemann, N. W.; Honarfar, A.; Gordivska, O.; Fredin, L. A.; Bergquist, K.-E.; Häggström, L.; Ericsson, T.; Lindh, L.; Yartsev, A.; Styring, S.; Huang, P.; Uhlig, J.; Bendix, J.; Strand, D.; Sundström, V.; Persson, P.; Lomoth, R.; Wärnmark, K. Luminescence and reactivity of a charge-transfer excited iron complex with nanosecond lifetime. *Science* **2019**, *363* (6424), 249−253.
(25) Steube, J.; Burkhardt, L.; Päpcke, A.; Moll, J.; Zimmer, P.; Schoch, R.; Wölper, C.; Heinze, K.; Lochbrunner, S.; Bauer, M. Excited-State Kinetics of an Air-Stable Cyclometalated Iron(II) Complex. *Chem.—Eur. J.* **2019**, *25* (51), 11826−11830.
(26) Steube, J.; Kruse, A.; Bokareva, O. S.; Reuter, T.; Demeshko, S.; Schoch, R.; Argüello Cordero, M. A.; Krishna, A.; Hohloch, S.; Meyer, F.; Heinze, K.; Kühn, O.; Lochbrunner, S.; Bauer, M. Janus-type emission from a cyclometalated iron(III) complex. *Nat. Chem.* **2023**, *15*, 468−474.
(27) Johnson, C. E.; Schwarz, J.; Deegbey, M.; Prakash, O.; Sharma, K.; Huang, P.; Ericsson, T.; Häggström, L.; Bendix, J.; Gupta, A. K.; Jakubikova, E.; Wärnmark, K.; Lomoth, R. Ferrous and ferric complexes with cyclometalating N-heterocyclic carbene ligands: a

case of dual emission revisited. *Chem. Sci.* **2023**, *14* (37), 10129−10139.
(28) Steube, J.; Fritsch, L.; Kruse, A.; Bokareva, O. S.; Demeshko, S.; Elgabarty, H.; Schoch, R.; Alaraby, M.; Egold, H.; Bracht, B.; Schmitz, L.; Hohloch, S.; Kühne, T. D.; Meyer, F.; Kühn, O.; Lochbrunner, S.; Bauer, M. Isostructural Series of a Cyclometalated Iron Complex in Three Oxidation States. *Inorg. Chem.* **2024**, *63* (37), 16964−16980.
(29) Wellauer, J.; Ziereisen, F.; Sinha, N.; Prescimone, A.; Velić, A.; Meyer, F.; Wenger, O. S. Iron(III) Carbene Complexes with Tunable Excited State Energies for Photoredox and Upconversion. *J. Am. Chem. Soc.* **2024**, *146* (16), 11299−11318.
(30) Li, C.; Gao, C.; Lan, J.; You, J.; Gao, G. An AIE active Y-shaped diimidazolylbenzene: aggregation and disaggregation for Cd(2+) and Fe(3+) sensing in aqueous solution. *Org. Biomol. Chem.* **2014**, *12* (47), 9524−9527.
(31) Rubio, R. J.; Andavan, G. T. S.; Bauer, E. B.; Hollis, T. K.; Cho, J.; Tham, F. S.; Donnadieu, B. Toward a general method for CCC N-heterocyclic carbene pincer synthesis: Metallation and transmetallation strategies for concurrent activation of three C−H bonds. *J. Organomet. Chem.* **2005**, *690* (23), 5353−5364.
(32) Hollis, T. K.; Webster, C. E. Unsymmetric CCC - NHC pincer metal complexes and methods of use thereof. U.S. Patent 1,092,7099 B2, 2021.
(33) Reilly, S. W.; Webster, C. E.; Hollis, T. K.; Valle, H. U. Transmetallation from CCC-NHC pincer Zr complexes in the synthesis of air-stable CCC-NHC pincer Co(III) complexes and initial hydroboration trials. *Dalton Trans.* **2016**, *45* (7), 2823−2828.
(34) Randles, J. E. B. A cathode ray polarograph. Part II.—The current-voltage curves. *Trans. Faraday Soc.* **1948**, *44* (0), 327−338.
(35) Päpcke, A.; Friedrich, A.; Lochbrunner, S. Revealing the initial steps in homogeneous photocatalysis by time-resolved spectroscopy. *J. Condens. Matter Phys.* **2020**, *32* (15), 153001.
(36) Weigend, F.; Ahlrichs, R. Balanced basis sets of split valence, triple zeta valence and quadruple zeta valence quality for H to Rn: Design and assessment of accuracy. *Phys. Chem. Chem. Phys.* **2005**, *7* (18), 3297−3305.
(37) Caldeweyher, E.; Bannwarth, C.; Grimme, S. Extension of the D3 dispersion coefficient model. *J. Chem. Phys.* **2017**, *147* (3), 34112.
(38) Tomasi, J.; Mennucci, B.; Cammi, R. Quantum mechanical continuum solvation models. *Chem. Rev.* **2005**, *105* (8), 2999−3093.
(39) Neese, F. The ORCA program system. *Wiley Interdiscip. Rev.: Comput. Mol. Sci.* **2012**, *2* (1), 73−78.
(40) Frisch, M. J.; Trucks, G. W.; Schlegel, H. B.; Scuseria, G. E.; Robb, M. A.; Cheeseman, J. R.; Scalmani, G.; Barone, V.; Petersson, G. A.; Nakatsuji, H.; Li, X.; Caricato, M.; Marenich, A. V.; Bloino, J.; Janesko, B. G.; Gomperts, R.; Mennucci, B.; Hratchian, H. P.; Ortiz, J. V.; Izmaylov, A. F.; Sonnenberg, J. L.; Williams-Young, D.; Ding, F.; Lipparini, F.; Egidi, F.; Goings, J.; Peng, B.; Petrone, A.; Henderson, T.; Ranasinghe, D.; Zakrzewski, V. G.; Gao, J.; Rega, N.; Zheng, G.; Liang, W.; Hada, M.; Ehara, M.; Toyota, K.; Fukuda, R.; Hasegawa, J.; Ishida, M.; Nakajima, T.; Honda, Y.; Kitao, O.; Nakai, H.; Vreven, T.; Throssell, K.; Montgomery, J. A., Jr.; Peralta, J. E.; Ogliaro, F.; Bearpark, M. J.; Heyd, J. J.; Brothers, E. N.; Kudin, K. N.; Staroverov, V. N.; Keith, T. A.; Kobayashi, R.; Normand, J.; Raghavachari, K.; Rendell, A. P.; Burant, J. C.; Iyengar, S. S.; Tomasi, J.; Cossi, M.; Millam, J. M.; Klene, M.; Adamo, C.; Cammi, R.; Ochterski, J. W.; Martin, R. L.; Morokuma, K.; Farkas, O.; Foresman, J. B.; Fox, D. J. *Gaussian 16*, Revision C. 01; Gaussian Inc.: Wallingford, CT, 2016.
(41) Plasser, F. TheoDORE: A toolbox for a detailed and automated analysis of electronic excited state computations. *J. Chem. Phys.* **2020**, *152* (8), 84108.
(42) Mai, S.; Plasser, F.; Dorn, J.; Fumanal, M.; Daniel, C.; González, L. Quantitative wave function analysis for excited states of transition metal complexes. *Coord. Chem. Rev.* **2018**, *361*, 74−97.
(43) Krause, L.; Herbst-Irmer, R.; Sheldrick, G. M.; Stalke, D. Comparison of silver and molybdenum microfocus X-ray sources for single-crystal structure determination. *J. Appl. Crystallogr.* **2015**, *48* (1), 3−10.
(44) Sheldrick, G. M. SHELXT - integrated space-group and crystal-structure determination. *Acta Crystallogr. A* **2015**, *71* (1), 3−8.
(45) Enders, M. Assigning and Understanding NMR Shifts of Paramagnetic Metal Complexes. In *Modeling of Molecular Properties*; Comba, P., Ed.; Wiley, 2011; pp 49−63.
(46) Kumke, M. U.; Löhmannsröben, H. G.; Roch, T. Fluorescence spectroscopy of polynuclear aromatic compounds in environmental monitoring. *J. Fluoresc.* **1995**, *5* (2), 139−152.
(47) Rosemann, N. W.; Lindh, L.; Bolaño Losada, I.; Kaufhold, S.; Prakash, O.; Ilic, A.; Schwarz, J.; Wärnmark, K.; Chábera, P.; Yartsev, A.; Persson, P. Competing Dynamics of Intramolecular Deactivation and Bimolecular Charge Transfer Processes in Luminescent Fe(III) N-Heterocyclic Carbene Complexes. *Chem. Sci.* **2023**, *14*, 3569−3579.
(48) Dreuw, A.; Head-Gordon, M. Single-reference ab initio methods for the calculation of excited states of large molecules. *Chem. Rev.* **2005**, *105* (11), 4009−4037.
(49) Peach, M. J. G.; Benfield, P.; Helgaker, T.; Tozer, D. J. Excitation energies in density functional theory: an evaluation and a diagnostic test. *J. Chem. Phys.* **2008**, *128* (4), 44118.
(50) Autschbach, J.; Srebro, M. Delocalization error and "functional tuning" in Kohn-Sham calculations of molecular properties. *Acc. Chem. Res.* **2014**, *47* (8), 2592−2602.
(51) Refaely-Abramson, S.; Sharifzadeh, S.; Govind, N.; Autschbach, J.; Neaton, J. B.; Baer, R.; Kronik, L. Quasiparticle spectra from a nonempirical optimally tuned range-separated hybrid density functional. *Phys. Rev. Lett.* **2012**, *109* (22), 226405.
(52) Zobel, J. P.; Kruse, A.; Baig, O.; Lochbrunner, S.; Bokarev, S. I.; Kühn, O.; González, L.; Bokareva, O. S. Can range-separated functionals be optimally tuned to predict spectra and excited state dynamics in photoactive iron complexes? *Chem. Sci.* **2023**, *14* (6), 1491−1502.
(53) Bokarev, S. I.; Bokareva, O. S.; Kühn, O. A theoretical perspective on charge transfer in photocatalysis. The example of Ir-based systems. *Coord. Chem. Rev.* **2015**, *304*−*305*, 133−145.
(54) Bokareva, O.; Möhle, T.; Neubauer, A.; Bokarev, S.; Lochbrunner, S.; Kühn, O. Chemical Tuning and Absorption Properties of Iridium Photosensitizers for Photocatalytic Applications. *Inorganics* **2017**, *5* (2), 23.
(55) Johansson, E. M. J.; Odelius, M.; Plogmaker, S.; Gorgoi, M.; Svensson, S.; Siegbahn, H.; Rensmo, H. Spin−Orbit Coupling and Metal−Ligand Interactions in Fe(II), Ru(II), and Os(II) Complexes. *J. Phys. Chem. C* **2010**, *114* (22), 10314−10322.
(56) Murov, S. L., Carmichael, I., Hug, G. L. *Handbook of Photochemistry*, 2nd ed.; Marcel Dekker, 1993.
(57) Berlman, I. B. *Handbook of Fluorescence Spectra of Aromatic Molecules*, 2nd ed.; Academic Press, 1971.
(58) Boens, N.; Qin, W.; Basarić, N.; Hofkens, J.; Ameloot, M.; Pouget, J.; Lefèvre, J.-P.; Valeur, B.; Gratton, E.; vandeVen, M.; Silva, N. D.; Engelborghs, Y.; Willaert, K.; Sillen, A.; Rumbles, G.; Phillips, D.; Visser, A. J. W. G.; van Hoek, A.; Lakowicz, J. R.; Malak, H.; Gryczynski, I.; Szabo, A. G.; Krajcarski, D. T.; Tamai, N.; Miura, A. Fluorescence lifetime standards for time and frequency domain fluorescence spectroscopy. *Anal. Chem.* **2007**, *79* (5), 2137−2149.
(59) Shida, T.; Iwata, S. Electronic spectra of ion radicals and their molecular orbital interpretation. III. Aromatic hydrocarbons. *J. Am. Chem. Soc.* **1973**, *95* (11), 3473−3483.
(60) Peover, M. E.; White, B. S. The electro-oxidation of polycyclic aromatic hydrocarbons in acetonitrile studied by cyclic voltammetry. *J. Electroanal. Chem. Interfacial Electrochem.* **1967**, *13* (1−2), 93−99.

https://doi.org/10.1021/acs.inorgchem.5c00526
Inorg. Chem. 2025, 64, 14101−14117

5. Reservoir Effect in bichromophoric Fe^{III} Complexes with Methylene Bridge

With the insights obtained from the first study, a new series of complexes was designed. To prevent electronic coupling between the chromophore and the base metal complex, a separating methylene linker was introduced (Figure 5 C). The linker bridged chromophores phenyl and anthracene were introduced in the backbone of the central phenyl. The simple addition of this smallest possible linker led to the realization of a reservoir effect, significantly increasing the system's lifetime compared to the base complex **C** from about 250 ps to roughly 5 ns. Additionally, the methyl-bridged chromophores were also introduced at the peripheral imidazole nitrogen atoms. This results in four attached chromophores per iron centre, and a stronger decoupling of both moieties, as is apparent from absorption spectra. However, this did not increase the lifetime further than the backbone chromophore complex. Additionally, this substitution pattern leads to photoinstability for the anthracenyl-complex, releasing a free anthracene species.

Author Contributions:

Lennart Schmitz: Design and synthesis of investigated complexes, Characterization (NMR, MS, EA), CV, Absorption spectroscopy, Room/low temperature emission spectroscopy, TCSPC, Main manuscript author.

Samira Dabelstein: Transient absorption spectroscopy, Streak camera measurements, Manuscript author

Dr. Miguel A. Argüello Cordero: Transient absorption spectroscopy, Streak camera measurements, Manuscript author

Dr. Lorena Fritsch: (TD)-DFT calculations, Manuscript author

Bastian Bracht: Synthesis of investigated complexes, Characterization (NMR)

Dr. Roland Schoch: Single-crystal X-ray diffraction

Dr. Hans Egold: Characterization (NMR)

Dr. Jakob Steube: Planning of the research

Prof. Dr. Felix Fischer: Manuscript Author, Revision supervision

Prof. Dr. Stefan Lochbrunner: Transient absorption spectroscopy, Streak camera measurements

Prof. Dr. Matthias Bauer: Conception of the research, Corresponding author

Dalton Transactions

ROYAL SOCIETY OF CHEMISTRY

PAPER

View Article Online
View Journal

Cite this: DOI: 10.1039/d5dt02915e

Reservoir effect in bichromophoric Fe^{III} complexes with a methylene bridge

Lennart Schmitz,[a] Samira Dabelstein,[b] Miguel A. Argüello Cordero,[b] Lorena Fritsch,[a] Bastian Bracht,[a] Roland Schoch,[a] Hans Egold,[a] Jakob Steube,[a] Felix Fischer,[a] Stefan Lochbrunner[b] and Matthias Bauer *[a]

Received 5th December 2025,
Accepted 16th February 2026

DOI: 10.1039/d5dt02915e

rsc.li/dalton

Replacing noble metals in photocatalytic systems by their abundant counterparts to enhance sustainability aspects is the focus of current research. Iron is still a dream candidate despite the usually short lifetimes of photoactive states. The multichromophoric approach, where an organic chromophore with a long triplet lifetime acts as an excited state reservoir when connected to an iron complex, is a highly promising strategy that has gained attention recently. This effect cannot be realized by direct covalent connection of organic chromophores to the Fe^{III} complex $[Fe(ImPH)_2][PF_6]$ (HImPH = 1,1′-(1,3-phenylene)bis(3-methyl-1-imidazol-2-ylidene)) due to highly delocalized states enabling fast relaxation pathways. In this work, we present the effect of the shortest aliphatic chain bridge, *i.e.*, methylene, on the electronic state decoupling in complexes combining the base complex $[Fe(ImPH)_2][PF_6]$ with both phenyl and anthracenyl moieties as chromophoric entities. Chromophore connection to $[Fe(ImPH)_2][PF_6]$ was realized at the central phenyl ring and on the imidazole sides, resulting in four multichromophoric complexes. A thorough ground and excited state characterization was carried out in addition to extensive DFT calculations. The results clearly show an efficient decoupling utilizing the smallest possible space in a methylene bridge, realizing a reservoir effect for the anthracenyl-substituted complexes leading to excited state lifetimes beyond 5 ns.

Introduction

The replacement of precious metals like ruthenium and iridium with more abundant 3d transition metals in photoactive complexes is a highly active research field.[1–4] Iron is one of the dream candidates due to its abundance, but the realization of active state lifetimes that can potentially be used for photochemical applications requires creative approaches.[5–7]

The application of the reservoir effect, which has been known for around two decades in other transition metal complexes,[3,8,9] opens a new, promising method for tuning the lifetime of iron complexes.[6,7,10] It combines the advantages of organometallic and organic chromophores by integrating both units into one molecule.

Many organic chromophores show triplet excited states with long lifetimes but lack a large absorption cross section in the visible range and efficient intersystem crossing (ISC) from the optically excited singlet state to the triplet manifold.[11] Transition metal complexes, on the other hand, often undergo complete ISC and exhibit strong visible light absorption.[2] However, especially first-row transition metal complexes suffer from short-lived excited charge transfer (CT) states. Therefore, after optical excitation of the CT state on the organometallic part and subsequent ISC, the excited state population can be transferred to the triplet chromophore state ^{3}Chrom. When the excited state energies of the chromophore and the metal complex are similar, a reservoir effect in the form of an equilibrium between both states is possible.[8,12] The consequence is an extended metal-centred charge transfer state lifetime due to the long lifetime of the ^{3}Chrom state.[13]

In a previous study, a series of Fe^{III} complexes with different chromophores directly attached to a C^C^C ligand (**$[Fe(ImPChrom)_2][PF_6]$**, where HImPChrom = 1,1′-(5-(chromophore)-1,3-phenylene)bis(3-methyl-1-imidazol-2-ylidene), chromophore = phenyl, naphthyl, anthracenyl, and pyrenyl) was investigated.[14] While it was possible to tune the absorption cross section of the complex, a reservoir effect was not observed. In contrast to the initial idea, the chromophore significantly quenched the lifetime of the ligand-to-metal charge transfer state (^{2}LMCT). This effect is caused by strong electronic coupling between the organic chromophore and the iron complex in the excited state.

Recently, the importance of electronic decoupling in bichromophoric complexes was demonstrated by Wenger

[a]Faculty of Science, Chemistry Department and Center for Sustainable Systems Design, Paderborn University, 33098 Paderborn, Germany.
E-mail: bauerm@mail.uni-paderborn.de
[b]Institute of Physics and Department of Life, Light and Matter, University of Rostock, 18059 Rostock, Germany

et al.[3] They achieved decoupling by introducing a *meta*-substituted phenylene between the ImP ligand and the anthracenyl group. This led to an excited state lifetime of 1.4 ns for unmodified anthracenyl, which could be boosted to almost 100 ns by the introduction of a second anthracenyl moiety and excited state tuning by replacing anthracenyl with 9-cyanoanthracenylene, proving the viability of utilizing the reservoir effect in iron complexes. The scientific interest in this combination of the Fe photosensitizer (PS) with organic chromophores is underlined by a second recent publication by Troian-Gautier *et al.*, who utilized a different Fe(III) complex substituted with an anthracenyl chromophore.[6] While an equilibrium between the ^{2}LMCT and ^{3}Chrom states was not achieved, they observed mono-directional energy transfer into a dark ^{3}Chrom state with a lifetime of more than 10 μs.

In this work, we explore a novel decoupling approach by application of the smallest possible 'spacer' between the Fe^{III} base complex **C0** ($[Fe(ImP)_2][PF_6]$)[4] and the chromophoric phenyl and anthracenyl fragments in the form of a methylene bridge. This substitution is achieved at two positions of the base complex. By substitution in the backbone of the central phenylene, complexes analogous to the aforementioned $[Fe(ImPChrom)_2]^+$ complexes are obtained, further referred to as $[Fe(Im_2PPh)_2]^+$ and $[Fe(Im_2PAnt)_2]^+$ (see Scheme 2). A second set of complexes was realized by substitution of the *N*-imidazole methyl groups for methylene-chromophore groups, referred to as $[Fe((ImPh)_2P)_2]^+$ and $[Fe((ImAnt)_2P)_2]^+$ (see Scheme 1). As a result, an effective electronic decoupling between the iron complex and the chromophore could be achieved in the excited state and a reservoir effect could be observed *via* these simple methylene bridges.

Results

Synthesis

Four Fe^{III} complexes with methylene bridge connected chromophores were synthesized following two synthetic routes (see Schemes 1 and 2). Anthracenyl and phenyl chromophores were utilized. Anthracene exhibits a triplet energy of 1.84 eV,[15] slightly lower than the LMCT energy of the base complex **C0** (1.90 eV),[4] and should therefore be a suitable candidate to realize a reservoir effect. The phenyl chromophore is used for comparison as the reference chromophore with a non-matching triplet state energy (3.66 eV).[15]

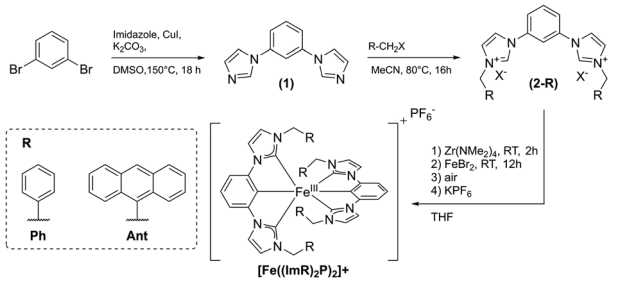

Scheme 1 Synthetic route for the complexes $[Fe((ImR)_2P)_2]^+$ from 1,3-dibromobenzene.

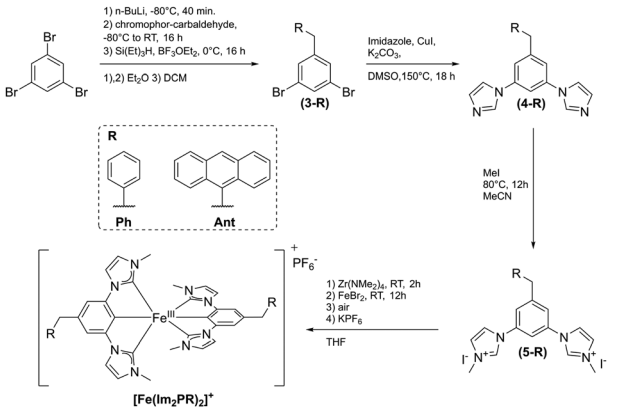

Scheme 2 Synthetic route for the synthesis of the complexes $[Fe(Im_2PR)_2]^+$ from 1,3,5-tribromobenzene.

The two complexes with modified imidazole groups (Scheme 1), with a total of four chromophores each, were obtained by first synthesizing **1** from 1,3-dibromobenzene using imidazole through an Ullmann-style coupling.[16] The imidazole moieties were then reacted with either bromotoluene or 9-(chloromethyl)anthracene to obtain **2-Ph** and **2-Ant**, respectively. By the application of a well-established synthetic route for cyclometalated iron complexes *via* an intermediate Zr-complex,[17] the desired complexes $[Fe((ImPh)_2P)_2]^+$ and $[Fe((ImAnt)_2P)_2]^+$ were obtained. After the synthesis, $[Fe((ImAnt)_2P)_2]^+$ was observed to decompose under irradiation, resulting in a free anthracene species (*cf.* the SI, Fig. S1). While this complicated the characterisation, it was still possible to obtain satisfactory results by utilizing fresh samples for each measurement.

The backbone-substituted complexes, with a total of 2 chromophores in the backbone, were obtained by a different synthetic approach (Scheme 2). The ligand precursors **3-R** were synthesized following a procedure reported by Young *et al.*[18] While this route was published for **3-Ph**, only minor modifications (see the SI) in the procedure were necessary for **3-Ant**.

First, 1,3,5-tribromobenzene was lithiated and subsequently reacted with either phenyl or anthracenyl carboxaldehyde. The resulting intermediate alcohols were reduced with triethylsilane in the presence of BF_3OEt_2 to obtain products **3-R**. These were then converted to the proligands following the previously shown route, where an Ullmann-style coupling was followed by alkylation with methyl iodide instead of the chromophore, methylene halides, to obtain **5-R**. In the final step, the $[Fe(Im2PPh)2]^+$ and $[Fe(Im2PAnt)2]^+$ complexes were obtained *via* the same complexation procedure as shown above.

Ground and excited state characterization

After several crystallization attempts, the obtained single crystals of these complexes were not suitable for the publication of crystallographic data, but we were able to prove connectivity of the backbone-substituted species (*cf.* the SI, Fig. S2). All com-

plexes were instead identified by a combination of HR mass spectroscopy, NMR analysis, and elemental analysis. The electronic ground and excited states were investigated using a wide array of analytical methods and *ab initio* calculations.

The chemical shifts in NMR spectroscopy serve as a first indicator for the success of electronic decoupling of the base complex and chromophore moieties. Since the investigated complexes are paramagnetic, a deviation alternating between negative and positive changes from the typical chemical shift in diamagnetic complexes is expected due to a continued electron polarization starting from the unpaired electron at the Fe^{III} centre.[19] This effect is shown in Fig. 1, which displays the deviation of the ^{13}C-NMR shifts in $[\mathbf{Fe(Im_2PPh)_2}]^+$ from a typical value of 130 ppm for aromatic carbons.[20] The shifts are compared to those observed in the previously published $[\mathbf{Fe(ImP\text{-}Ph)_2}]^+$.[14] The two complexes differ only in the bridging methylene group.

While the carbons located at the central ImP ligand (C1 to C3) show essentially equal shifts in both complexes, this trend clearly subsides after the first carbon of the attached phenylene (C5): C6 to C8 in the "spacerless" complex retain a significant deviation from the typical 130 ppm, showing the coupling of the phenyl group with the paramagnetic complex. In contrast, these carbons show shifts in the expected range for aromatic carbons in $[\mathbf{Fe(Im_2PPh)_2}]^+$, indicating a missing influence of the unpaired electron on the Fe^{III}. Thus, an efficient electronic decoupling of the phenyl moiety from the central complex part is concluded. The strong deviation observed for the shift of C5 can be explained by hyperconjugation through the bridging methylene group. A similar trend is observed for $[\mathbf{Fe((ImPh)_2P)_2}]^+$; however, this trend is less clear, since the paramagnetic effect on NMR resonances is generally lower in the imidazolyl groups (see SI Fig. S3). This electronic decoupling is also apparent for the anthracene-substituted complexes. Since the corresponding anthracene complex with a directly conjugated anthracene moiety in the backbone is already decoupled in the ground state due to a high dihedral angle that only planarizes upon excitation,[14] a similar comparison to that in Fig. 1 for $[\mathbf{Fe(Im_2PAnt)_2}]^+$ is not possible.

To provide deeper insight into the underlying electronic structure of the complexes, DFT-optimized molecular geometries of the four complexes were obtained by predicting a distorted octahedral structure in the electronic ground state (^{2}GS) for all complexes. These calculated structures are in good agreement with the single-crystal XRD results we were able to obtain for $[\mathbf{Fe(Im_2PPh)_2}]^+$ and $[\mathbf{Fe(Im_2PAnt)_2}]^+$ (see Fig. S2). A closer examination of the spin density in the optimized ground state (see Fig. 2) reveals that spin polarization extends across the entire base complex, while the chromophores themselves exhibit almost no spin density. This observation agrees with the results obtained from NMR spectroscopy, which show little influence of the unpaired electron of the Fe^{III} centre on the chromophore. Consequently, the postulated decoupling of the chromophores from the central complex moiety is supported by the calculations, which is an important aspect for the realization of a reservoir effect.

The ground state oxidation and reduction potentials were analysed *via* cyclic voltammetry. The resulting voltammograms are shown in Fig. 3. All complexes show the same three redox processes as the unsubstituted base complex **C0**:[4,21] an $Fe^{III/IV}$ transition around 0 V, an $Fe^{II/III}$ transition below −1 V and a ligand oxidation around 1 V. While the iron redox processes are reversible, the oxidation of ligands exhibits only partial reversibility for the phenyl-substituted complexes and no reversibility for the anthracenyl-substituted complexes as previously observed for the directly substituted complexes.[14] Additionally, the anthracene containing complexes exhibit ligand oxidation at slightly smaller potentials, as is expected for larger

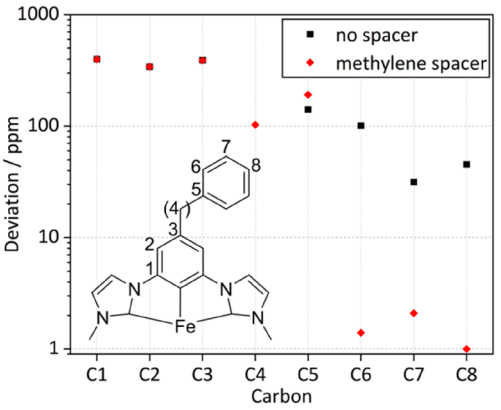

Fig. 1 Absolute deviation from the expected chemical shift in ^{13}C-NMR spectroscopy. The central phenyl carbons C1–C3 and backbone carbons C5–C7 of the two complexes $[\mathbf{Fe(ImP\text{-}Ph)_2}]^+$ and $[\mathbf{Fe(Im_2PPh)_2}]^+$ are referenced against a roughly expected value of 130 ppm. In addition, the bridging carbon C4 only present in $[\mathbf{Fe(Im_2PPh)_2}]^+$ is depicted and referenced against 30 ppm.[20]

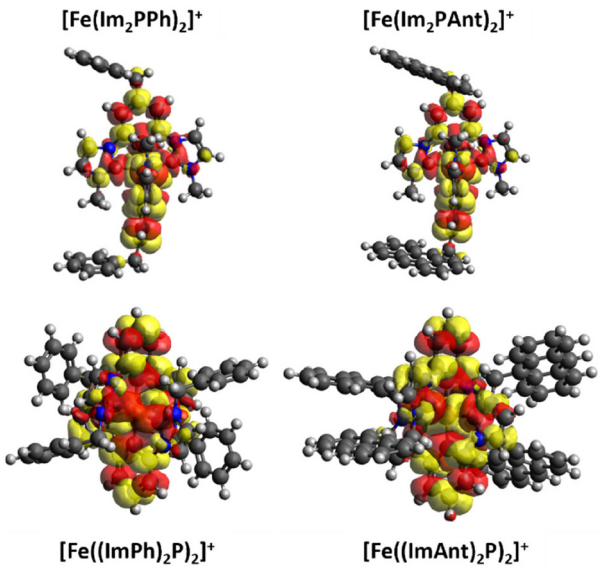

Fig. 2 Spin density plots of $[\mathbf{Fe(Im_2PPh)_2}]^+$, $[\mathbf{Fe(Im_2PAnt)_2}]^+$, $[\mathbf{Fe((ImPh)_2P)_2}]^+$ and $[\mathbf{Fe((ImAnt)_2P)_2}]^+$ (from left to right).

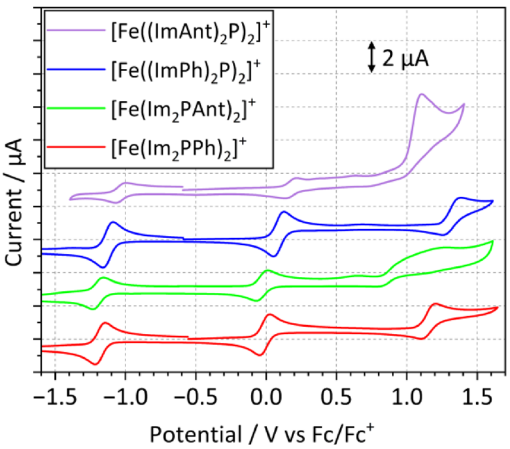

Fig. 3 Cyclic voltammograms of the four investigated complexes in MeCN with 0.1 M [nBu$_4$N][PF$_6$] at a scan rate of 0.1 V s^{-1}. The complexes were measured at a concentration of 1 mmol l^{-1}. The side-substituted anthracene complex was significantly less soluble and was measured at 0.3 mmol l^{-1}. To improve readability, the measured current was scaled by a factor of 1.5.

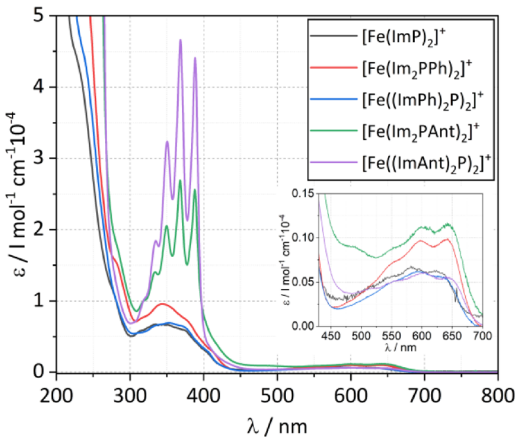

Fig. 4 UV-vis absorption spectra of all complexes and the base complex **C0** (c = 10^{-5} M) in MeCN.

π-systems, which are more suited to stabilizing the introduced positive charge. The oxidation of anthracene occurs at similar oxidation potentials.[22] The corresponding values are listed in Table 1.

The metal redox potentials seem to be primarily influenced by the substitution position. The backbone-substituted complexes show virtually identical oxidation/reduction potentials, whereas those of the side-substituted species are shifted to higher potentials. **[Fe((ImPh)$_2$P)$_2$]$^+$** shows potentials shifted by 0.1 V (Fe$^{III/IV}$) and 0.06 V (Fe$^{II/III}$) compared to **[Fe(Im$_2$PPh)$_2$]$^+$**. This effect is amplified by the anthracene substituent, where **[Fe((ImAnt)$_2$P)$_2$]$^+$** shows potentials shifted by 0.21 V (Fe$^{III/IV}$) and 0.16 V (Fe$^{II/III}$) compared to **[Fe(Im$_2$PAnt)$_2$]$^+$**. The origin of these counterintuitive shifts is not yet clear. However, similar results were found for an analogous Co(III) complex.[23]

Stationary absorption and emission spectra

The electrochemical properties provide insight into the electronic environment of the complexes, which also influences their optical behaviour. To further understand these effects, the electronic transitions were investigated *via* UV/vis and fluorescence spectroscopy. The near UV and visual range, as shown in Fig. 4, can be divided into three distinct absorption ranges, which can be assigned by comparison with similar previously published systems and TD-DFT calculations (*vide infra*).[4]

Below 300 nm, π–π*-transitions lead to strong absorption, especially for the anthracene-substituted complexes. Between 300 and 500 nm, mainly MLCT transitions are located, as was observed for similar complexes.[14] However, for the anthracenyl-substituted complexes, this absorption is masked by a strong characteristic absorption band corresponding to the singlet anthracene absorption.[24] This absorption band is just slightly shifted from the corresponding band in free anthracene since the methylene spacer largely prevents excited states involving both parts of the ligand (anthracenyl and bisimidazole phenylene). This is apparent when combining the base complex spectrum with the free anthracene spectrum multiplied by 2 or 4 depending on the number of chromophores in the complex, as shown in the SI (Fig. S4).

In addition to the literature comparison, vertical transitions of the optimized geometries in the UV/vis range were calculated using the B3LYP functional[25] and compared to the experimental spectra, supporting our band assignments. In Fig. 5, the spectra of the backbone-substituted complexes are shown, while those of the side-substituted complexes are shown in the SI (Fig. S15). Additionally, transition density analysis was performed to identify the involved orbitals in the different transitions. The calculated spectra of the complexes with phenyl substituents are in good agreement with the experimental data, while those of the anthracene-containing complexes are less well reproduced. This discrepancy is mainly attributed to the fact that TD-DFT is not taking vibronic progression into account, which is responsible for the typical absorption structure of anthracene.[26] The band in the range of 300–400 nm exhibits a mixed character. The most intense transition, centred around 340 nm for all complexes, is predominantly MLCT in nature involving acceptor orbitals, which mostly comprise the ImP ligand excluding the chromophores.

Table 1 Redox potentials of the investigated complexes in MeCN

	Fe$^{II/III}$ [V]	Fe$^{III/IV}$ [V]	Lig. oxidation [V]
[Fe(Im$_2$PPh)$_2$]$^+$	−1.18	−0.01	1.15
[Fe((ImPh)$_2$P)$_2$]$^+$	−1.12	0.09	1.32
[Fe(Im$_2$PAnt)$_2$]$^+$	−1.19	−0.04	0.87, 1.20[a]
[Fe((ImAnt)$_2$P)$_2$]$^+$	−1.03	0.17	1.09[b]
C0 (ref. 4)	−1.16	0.08	1.31[b]

[a] For **[Fe(Im$_2$PAnt)$_2$]$^+$**, a rather broad oxidation peak was observed, revealing two separate oxidation states in square wave voltammetry results listed here. [b] For the oxidation of ligands in the anthracene complexes, the anodic potential is listed.

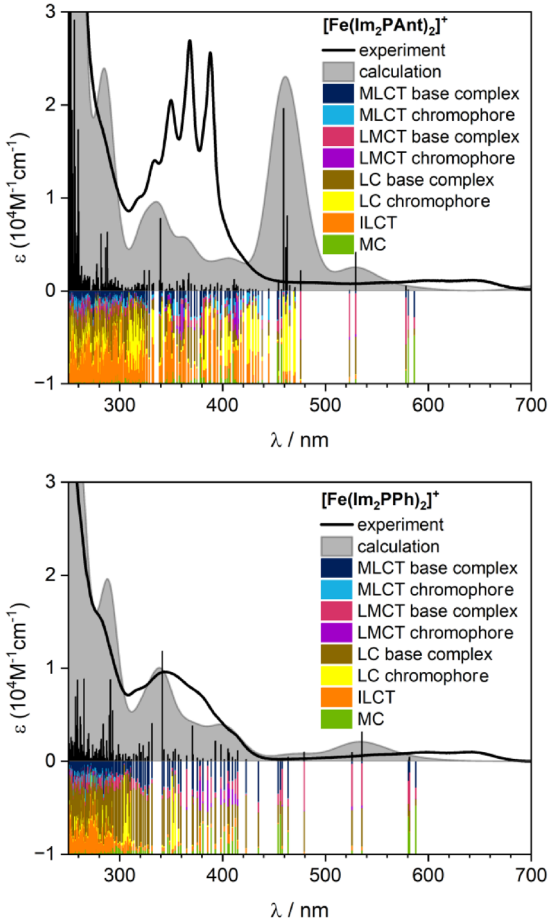

Fig. 5 Experimental and TD-DFT-calculated UV-vis spectra (broadened with a full-width at half maximum (FWHM) of 2000 cm^{-1}) of **[Fe(Im$_2$PPh)$_2$]$^+$** and **[Fe(Im$_2$PAnt)$_2$]$^+$**. LC refers to electronic transitions where the charge remains localized within the same part of the ligand (base complex ligand or chromophore), whereas ILCT (intra ligand charge transfer) describes charge transfer between different regions within the same ligand.

Additionally, ligand-centred (LC) transitions located within the ImP framework contribute to this band. In the anthracenyl-substituted systems, a significant portion of the absorption also arises from purely chromophore-based LC transitions. While these transitions are predicted by the calculations at around 460 nm, they can be associated with the experimentally observed band in the 300–400 nm range, suggesting a slight underestimation of their energy in the computational results.

The low-energy band at around 600–650 nm is identified as a ligand-to-metal charge transfer (LMCT) band in the central complex moiety, consistent with the experimental observations discussed earlier and calculations for similar systems.[4,14] For the anthracene-containing complexes, the calculations predict that this band also exhibits a slight anthracene-based LMCT character. Due to the increased number of chromophores, this character is especially visible in **[Fe((ImAnt)$_2$P)$_2$]$^+$**.

The UV/Vis calculations only account for spin-allowed excitation. However, indirect insights into the energetic alignment can be obtained. For the anthracenyl-containing complexes, chromophore-based transitions appear close in energy to the LMCT band (600–650 nm). This suggests that the corresponding chromophore state is also in this range, facilitating a reservoir effect. In contrast, the phenyl-substituted complexes exhibit chromophore-based transitions at much higher energies, implying that the energy of the triplet states is too high to efficiently interact with the LMCT state. Further support comes here from the calculated ground state orbital energies (Fig. 6), which reveal that the energy gap between the HOMO and the LUMO of the anthracene-based chromophore is comparable to that of the LUMO of the base complex ligand and the HOMO of the metal.

The much stronger experimental absorptivity of **[Fe((ImAnt)$_2$P)$_2$]$^+$** (ε_{368nm} = 4.5 × 10^4 M^{-1} cm^{-1}) compared to **[Fe(Im$_2$PAnt)$_2$]$^+$** (ε_{368nm} = 2.7 × 10^4 M^{-1} cm^{-1}) is due to the increased number of organic chromophores (four instead of two). The characteristic anthracene bands are only slightly shifted compared to free anthracene,[27] indicating an effective electronic decoupling of the chromophore from the complex. The MLCT bands observed in the phenyl-substituted complexes are also not notably shifted, with only a slight enhancement in intensity in the case of **[Fe(Im$_2$PPh)$_2$]$^+$** compared to **C0**. This observation further underlines the limited influence of the methylene-bridged chromophore on MLCT transitions. The bands above 500 nm are dominated by LMCT transitions. Here, the same trends as for the MLCT bands are obvious. While the side-substituted complexes show no changes in extinction coefficients or band positions, the backbone-substituted complexes show virtually no changes in extinction coefficients. This contrasts with the complexes that contain a chromophore directly linked to the iron complex. They show a larger influence of the chromophore backbones on the MLCT and LMCT states.[14] In conclusion, the absorption properties of the decoupled complexes are less favourable when compared to direct connection and conjugation. However, this reduced interaction is an expected side effect of the desired decoupling, considered as a prerequisite for the reservoir effect.

Efficient decoupling of the chromophores from the complexes is also observable in stationary emission spectroscopy. For this, all complexes were excited at 350 nm (MLCT range).

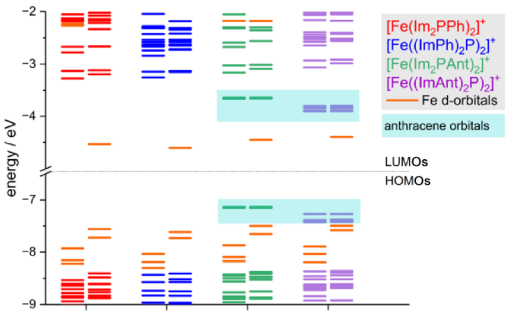

Fig. 6 DFT (B3LYP) calculated ground state orbital energies of all four complexes.

As observed for similar complexes before, this leads to an emission from the LMCT state above 650 nm following Kasha's Rule.[28] This relaxation from ^{2}MLCT to ^{2}LMCT was previously reported and investigated in more depth after an originally reported dual emission was shown to be erroneous. The lifetime of this ^{2}MLCT state for **C0** is smaller than 10 ps and was not investigated for the systems presented here.[29] The high extinction coefficients in this range enable a stronger emission signal. To confirm the nature of the present emission, additional emission spectra after excitation at 600 nm (LMCT range) leading to the same emission bands are presented in the SI (Fig. S5). All complexes show a similar LMCT emission to **C0**, with maxima between 700 and 750 nm, as shown in Fig. 7.

Consequently, even after optical excitation, the electronically excited states remain largely decoupled due to the bridging methylene group. Therefore, energetically low-lying mixed states are prevented, which would result in a fast non-radiative decay, as is the case for the complexes with a directly substituted chromophore.[14] As a reminder, among such complexes with direct connection between the iron complex and chromophores, only those functionalised with phenyl and naphthalene showed a comparable LMCT emission to **C0** due to their high triplet energy. However, pyrene- and anthracene-functionalised complexes resulted in a significantly weakened and redshifted LMCT emission due to the formation of a "superligand" LMCT state, delocalized over the whole complex.

Instead, the emission of the anthracene-substituted complexes in this study is only weakened, as is apparent from the non-normalized emission spectra in the SI (Fig. S5). To a lesser extent, the side-substituted complexes exhibit weaker emission than their backbone-substituted counterparts, leading to the emission intensity order $\mathbf{[Fe(Im_2PPh)_2]^+}$ > $\mathbf{[Fe((ImPh)_2P)_2]^+}$ > $\mathbf{[Fe(Im_2PAnt)_2]^+}$ > $\mathbf{[Fe((ImAnt)_2P)_2]^+}$. Additionally, the side-substituted complexes have slightly redshifted emission maxima, which may relate to the shifted potentials observed in cyclic voltammetry (*vide supra*).

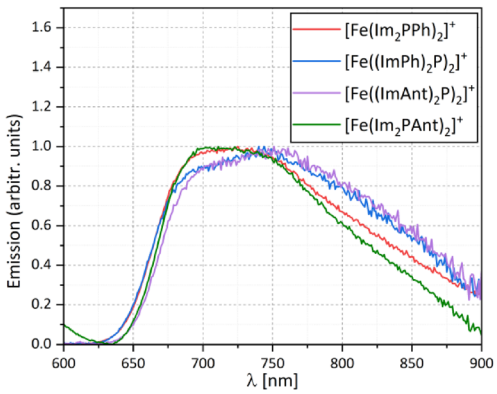

Fig. 7 Emission spectra of all investigated complexes excited at 350 nm. The emission spectra are normalized for improved comparability. All spectra were measured in MeCN (10^{-5} M).

The anthracene-substituted compounds also exhibit singlet anthracene emission, as shown in SI Fig. S5. As stated in a previous publication, a likely explanation for this emission is a minor impurity of free anthracene that leads to a strong effect on the emission spectra due to the high quantum yield of anthracene.[14] Because of its very low concentration and the wavelength of the emission, we do not expect this to interfere with any other measurements done in this study.

Since the emission intensity of the reservoir-enabled complexes relies on thermal energy for a back transfer to the LMCT state, all complexes were investigated in low-temperature emission spectroscopy (see the SI, Fig. S6). Both phenyl complexes exhibit emission significantly increased by a factor of 10 when cooled to 77 K with two maxima at around 675 nm and 740 nm, due to the vibronic fine structure of the LMCT state. While an increase in emission intensity is also apparent for $\mathbf{[Fe(Im_2PAnt)_2]^+}$, the effect is weaker by a factor of 5 compared to room temperature measurements. This weaker emission intensity enhancement is due to the back transfer from the ^{3}Chrom state to the ^{2}LMCT state being inhibited at low temperatures. Since many excited electrons never enter the ^{3}Chrom state and instead relax into the ground state immediately, the emission is still enhanced, albeit to a lesser extent. This increase in emission intensity is even weaker for $\mathbf{[Fe((ImAnt)_2P)_2]^+}$ by a factor of about 2, which is presumably the result of the increased number of anthracene units, accelerating the quenching of the LMCT state. Due to the generally weak emission of these compounds, an increasing baseline with lower temperatures and scattering from the frozen butyronitrile affect these measurements significantly, as can be seen in Fig. S6 in the SI. However, the general trend of an increasing emission intensity is still apparent.

Time-resolved emission measurements

The temporal evolution of the LMCT emission was studied using a streak camera and TCSPC measurements for all four complexes. The results obtained for $\mathbf{[Fe(Im_2PAnt)_2]^+}$ are shown in Fig. 8, and all other data on the emission dynamics are presented in the SI (Fig. S6 and S7). For $\mathbf{[Fe(Im_2PPh)_2]^+}$ and $\mathbf{[Fe((ImPh)_2P)_2]^+}$ excited in the LMCT absorption band at 600 nm, a monoexponential decay of the fluorescence with a time constant of 0.19 and 0.20 ns, respectively, is found. These values are close to the LMCT lifetime of the base complex **C0** (0.24 ns), pointing to a similar relaxation cascade.

Conversely, the anthracene-functionalized complexes show very distinct photodynamics. The emission is weaker (Fig. S7) and exhibits time zero contributions caused by scattering of the excitation light. After a pronounced signal drop within the experimental time resolution, a part of the LMCT emission remains and decays monoexponentially with a time constant of 5.3 ns. These findings are shown in the bottom graph of Fig. 8 by the amplitude spectra of the fast and monoexponentially decaying component, which are obtained by a global lifetime analysis described below. The spectrum of the 5.3 ns component resembles the stationary emission spectrum very well, strongly indicating that it is due to emission from the

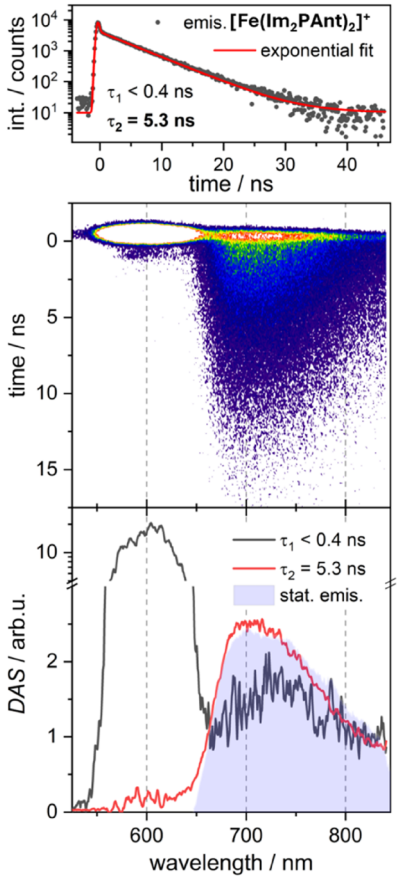

Fig. 8 Time-resolved emission of $[Fe(Im_2PAnt)_2]^+$ dissolved in MeCN after optical excitation at 600 nm. Top: time trace of the spectrally integrated emission intensity (int. in total counts, black dots) together with a double exponential fit. The short time constant of the fit is below the time resolution of the measurement, and the corresponding signal contribution can be regarded as practically instantaneous. Middle: two-dimensional plot of the time-resolved emission intensity. Bottom: decay-associated amplitude spectra (DAS) resulting from a global lifetime analysis of the dataset with two exponential decay components. For comparison, the stationary emission spectrum is shown (grey area). The *y*-axis has a logarithmic scale above a break at 3 arbitrary units (arb. u.) to enable a plot including the high-intensity areas.

LMCT state. If the emission originated from anthracene, the characteristic vibrational structure of the anthracene fluorescence would be expected at shorter wavelengths.[30] Thus, a significant contribution of anthracene fluorescence can be excluded. The fast component is dominated by scattered excitation light around 600 nm.

The results show that the lifetime of the excited state population is extended to several nanoseconds in the anthracenyl-substituted complex $[Fe(Im_2PAnt)_2]^+$. However, most of it does not reside in the LMCT state, since the LMCT emission is not very intense. This observation indicates that another state operates as a reservoir for the excited state population. The local triplet state of the chromophore is a natural candidate, as it has a suitable energy and a very long lifetime. This is further investigated in the transient absorption studies (*vide infra*). Time-resolved emission was measured using time-correlated single photon counting (TCSPC), which exhibits a higher dynamic range, but a reduced spectral resolution compared to streak camera measurements, reproduced the results obtained with the latter, see Fig. S9 in the SI.

The emission of $[Fe((ImAnt)_2P)_2]^+$ shows a very similar behaviour to that of $[Fe(Im_2PAnt)_2]^+$, see Fig. S6 and S7 for the corresponding measurements with the streak camera and their evaluation. Again, the emission at time zero is dominated by scattered excitation light and drops immediately after the optical excitation. Thereafter, weak emission from the LMCT state with a lifetime of 4.4 ns is observed. Interestingly, a similar system with anthracene as the reservoir was recently reported by Wenger *et al.* with a lifetime of 1.4 ns.[7] Instead of a methylene bridge, a *meta*-substituted phenyl spacer was utilized to achieve electronic decoupling. Additionally, chromophores with lower triplet state energies were utilized to match (9-phenyl anthracene at 5.2 ns) or exceed (9-cyano-anthracene at 45 ns for two chromophores and 98 ns for four chromophores) the lifetimes reported here.

Ultrafast transient absorption measurements

To investigate the photo-induced dynamics of the complexes with higher time resolution and to characterize the nature of the reservoir state, ultrafast transient absorption (TA) measurements were conducted. The phenyl-functionalized complexes exhibit similar TA signatures and dynamics to those of the base complex $[Fe(ImP)_2]^+$. Therefore, only the results for $[Fe(Im_2PPh)_2]^+$ are presented here, while those for $[Fe((ImPh)_2P)_2]^+$ are shown in the SI (Fig. S11). The TA spectra, as shown in Fig. 9A, are dominated by an excited state absorption (ESA) signal, representing the absorption of the excited states. Similar to **C0**,[4] the ESA signal builds up with the experimental time resolution and decays within a few hundred picoseconds. Due to the high concentration necessary for excitation in the LMCT band and the resulting strong sample absorption in the near ultraviolet (UV), it was not possible to record TA signals in the UV region. Therefore, only a part of the ESA band in the visible spectra could be studied. The ESA dominates the TA signal and covers the ground state bleach (GSB). In Fig. 9C, the spectral shape and position of the GSB are indicated in violet based on the stationary absorption spectra. The TA data $\Delta OD(\lambda,t)$ were globally analysed by fitting a sum of exponential decay components to the transient spectra following the function in section 7 in the SI.

An overview of the time constants obtained from this global lifetime analysis (GLA) can be found in Table 2, while the DAS are shown in the corresponding figures. For both phenyl-substituted complexes, two time constants were necessary to describe the evolution of the TA spectra, with one time constant being effectively infinite. In both cases, the contributions associated with the infinite time constant were minimal and are assumed to be artifacts of the measurements. The shorter time constants correspond to the LMCT lifetimes and were determined as 190 ps for $[Fe(Im_2PPh)_2]^+$ and 180 ps for $[Fe((ImPh)_2P)_2]^+$. The corresponding decay associated spectra

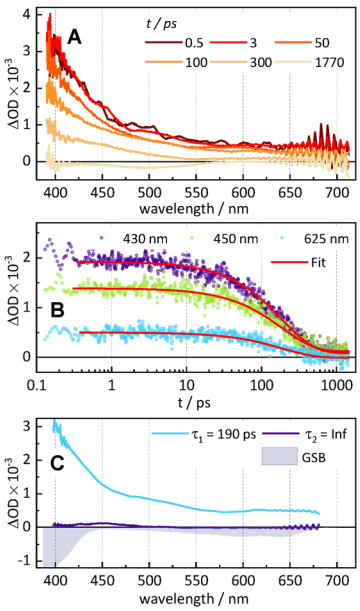

Fig. 9 (A) TA spectra of $[Fe(Im_2PPh)_2]^+$ in MeCN at different times *t* after optical excitation at 600 nm. (B) Time traces (dots) at the specified probe wavelengths together with respective fit curves resulting from the GLA (red solid line). (C) DAS obtained by GLA and labelled with the respective time constants. The dynamics are well described by a mono-exponential decay with a time constant of τ_1 = 190 ps. A further, long-lived component modelled by a decay with an infinite time constant τ_2 = inf was used to account for tiny offsets at long delay times. The component is at all wavelengths practically zero and within the experimental accuracy insignificant.

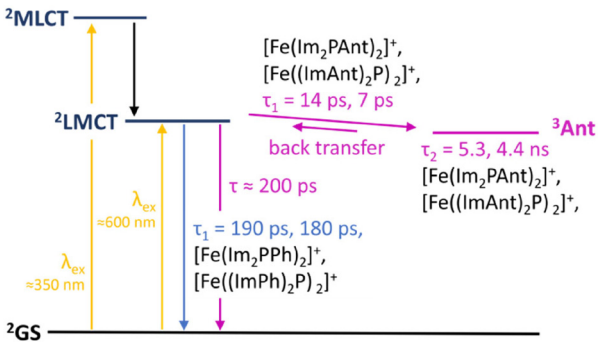

Scheme 3 Jablonski diagram describing the relaxation to the ground state after optical excitation into the ^{2}MLCT or ^{2}LMCT state. Decay steps of $[Fe(Im_2PPh)_2]^+$ and $[Fe((ImPh)_2P)_2]^+$ are shown in blue and decay processes of $[Fe(Im_2PAnt)_2]^+$ and $[Fe((ImAnt)_2P)_2]^+$ are shown in purple. Additional radiationless decay processes were obscured for clarity.

(DAS) are shown in Fig. 9C and Fig. S11C in the SI. The associated Jablonski diagram, see Scheme 3, illustrates that the complexes are excited from the ground state into the ^{2}LMCT state.

Excitation of the ^{2}MLCT band leads to population of the same state through internal conversion, as is evident from the same emission occurring after excitation of either band. The LMCT state decays directly back into the ground state with a lifetime given by the time constant τ_1.

This reduction in lifetime may be due to steric effects induced by different geometries ($[Fe((ImPh)_2P)_2]^+$) or electron pushing effects of the methylene spacer ($[Fe(Im_2PPh)_2]^+$). This difference is apparent, albeit small, when comparing the crystal structures of **C0** with the optimized geometries of these compounds in Table 3.

Next, the TA spectra of the complexes with anthracene as the substituent were analysed. Both complexes, $[Fe(Im_2PAnt)_2]^+$ and $[Fe((ImAnt)_2P)_2]^+$, exhibit similar dynamics, which differ from those of the basic and the phenyl-substituted complexes. As before, only the results for $[Fe(Im_2PAnt)_2]^+$ are presented here, while those for $[Fe((ImAnt)_2P)_2]^+$ are presented in the SI (Fig. S13A). After optical excitation, the TA spectra are dominated by a broad ESA band (Fig. 10A), similar to those of the other complexes, covering the ground state bleach. As before, the spectral shape and position of the GSB is indicated in grey based on the stationary absorption spectrum. However, after a few picoseconds, a new, narrow band with a sharp maximum around 425 nm emerges. This band results from the local $^3\pi\pi^*$ state of anthracene, as evidenced by a comparison with the triplet–triplet absorption of dissolved anthracene,[31] as well as with the transient spectra of an anthracene-functionalized ruthenium complex.[32] At the same time, the initial ESA contributions in the visible range disappear. The remaining ESA signal is highly persistent, with a lifetime exceeding the maximum delay time of 1.8 ns accessible with the present setup. Additionally, the TA spectra of the samples display two isosbestic points. For $[Fe(Im_2PAnt)_2]^+$, the isosbestic points are located at approximately 415 nm and 430 nm, while for $[Fe((ImAnt)_2P)_2]^+$, they are at approximately 415 nm and 435 nm. These isosbestic points suggest a straightforward population transfer without intermediate steps. To exclude other possible processes, we compared our results with the TA signature of singlet anthracene[33] and examined the stationary absorption spectra of the anthracene cation and anion.[34] This analysis allows both the population of the electronically excited singlet state of anthracene and any significant charge transfer to or from anthracene to be ruled out. Thus, the excited state population is at longer delay times in

Table 2 Time constants obtained by GLA of the TA data

	C0 (ref. 4)	$[Fe(Im_2PPh)_2]^+$	$[Fe((ImPh)_2P)_2]^+$	$[Fe(Im_2PAnt)_2]^+$	$[Fe((ImAnt)_2P)_2]^+$
τ_1	240 ps	190 ps	180 ps	14 ps	8 ps
τ_2	—	—	—	5.3[a] ns*	4.4[a] ns

[a] Time constant obtained from streak camera measurements.

Table 3 Relevant structural parameters for **C0** (crystal structure) and the investigated phenyl complexes (calculated structure)

Compound	**C0** (ref. 21)	$[Fe(Im_2PPh)_2]^+$	$[Fe((ImPh)_2P)_2]^+$
Fe–C_{phenyl} mean distance (Å)	1.948(3)	1.94	1.93
Fe–$C_{imidazole}$ mean distance (Å)	1.982(3)	2.01	2.00
Mean bite angle (°)	155.36(15)	156.0	156.5

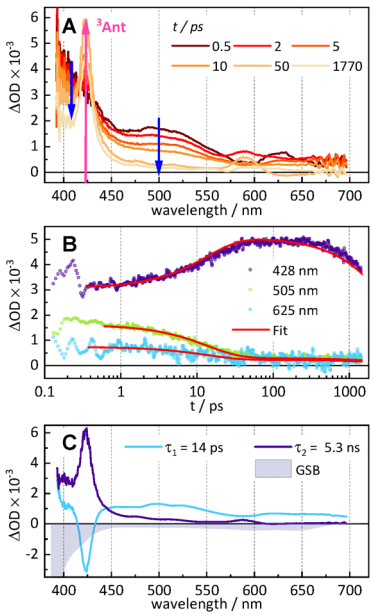

Fig. 10 (A) TA spectra of $[Fe(Im_2PAnt)_2]^+$ dissolved in MeCN at different times after optical excitation at 600 nm. (B) Time traces (dots) at the specified probe wavelengths together with respective fit curves resulting from the GLA (red solid line). (C) DAS obtained by GLA and labelled with the respective time constants. The dynamics is well described by a double exponential decay with time constants τ_1 = 14 ps and τ_2 = 5.3 ns.

the triplet state of the anthracene unit. Furthermore, we compared the TA spectrum of $[Fe(Im_2PAnt)_2]^+$ at 0.5 ps with the TA spectra of the corresponding "spacerless" complex $[Fe(ImP\text{-}Ant)_2]^+$ and the base complex **C0** at the same delay time, see Fig. S14. The data for the corresponding "spacerless" complex and the base complex **C0** were adapted from our previous publication.[14] The early TA signatures of all three complexes are very similar, supporting the conclusion that the LMCT state is initially populated upon photoexcitation of $[Fe(Im_2PAnt)_2]^+$. The TA data of the anthracene complexes were fitted with two exponential decay components, as shown in Fig. 10C. The shorter time constant τ_1 is associated with the rise of the narrow ESA band at 425 nm, which is evident from the fact that the corresponding DAS (blue) contains an inverted image of the narrow ESA band. Consequently, this component describes the population transfer from the ^{2}LMCT state to the local anthracene triplet state ^{3}Ant. In the case of $[Fe(Im_2PAnt)_2]^+$, the shorter time constant τ_1 amounts to 14 ps and for $[Fe((ImAnt)_2P)_2]^+$, it amounts to 8 ps. Therefore, the population transfer occurs twice as fast for the $[Fe((ImAnt)_2P)_2]^+$ complex with four anthracene units compared to the $[Fe(Im_2PAnt)_2]^+$ complex with only two anthracene units. This behaviour suggests that the transfer rate per anthracene unit is similar in both complexes and the faster dynamics of $[Fe((ImAnt)_2P)_2]^+$ are simply a result of the increased number of transfer acceptors and channels. However, this proportional relationship between the number of chromophores and the lifetime is not true for the LMCT emission lifetimes, which are similar for two ($[Fe(Im_2PAnt)_2]^+$) and four ($[Fe((ImAnt)_2P)_2]^+$) chromophore units. The apparent trend may therefore just be a coincidence. The DAS of the time constant τ_2 reflects the decay of the local anthracene triplet state on a timescale in the order of a few nanoseconds. Therefore, the time window of 1.8 ns accessible with the present setup is exceeded. Consequently, the time constant τ_2 cannot be determined accurately from the TA data. However, the time should be equal to the lifetime of the luminescence determined by the time-resolved emission experiments (see above). Indeed, fixing τ_2 to the values of 5.3 ns and 4.4 ns for $[Fe(Im_2PAnt)_2]^+$ and $[Fe((ImAnt)_2P)_2]^+$, respectively, in the GLA leads to excellent agreement between fits and data. Thus, the long-lived TA component is fully consistent with the luminescence behaviour of the complexes.

The light-induced dynamics of the anthracene-functionalized complexes is shown by pink arrows in the Jablonski diagram shown in Scheme 3. The anthracene complexes are excited from the ground into the ^{2}LMCT state, as is the case for the phenyl-substituted complexes. From there, a population transfer occurs with the time constant τ_1 to the local ^{3}Ant state, which then decays back to the ground state with the time constant τ_2. Thus, the excited state population is stored for several nanoseconds in the local triplet state of the anthracene substituents and a reservoir effect is achieved. The triplet lifetime of anthracene in solution is many orders of magnitude larger than τ_2.[35] In the complex, however, the ^{3}Ant state is depopulated by a weak back transfer of the population to the ^{2}LMCT state, which is also responsible for the observed fluorescence. The intrinsic lifetime of the ^{2}LMCT state should be on the order of 200 ps, comparable to those of the base and phenyl-substituted complexes.

Conclusion

In this work, four multichromophoric Fe^{III} complexes based on the previously published base complex **C0** ($[Fe(ImP)_2]^+$) were synthesized and investigated.[4] To potentially enable a reservoir effect, a methylene bridge as the smallest possible decoupling unit was installed between the central iron complex and the

organic chromophore functionalities.[14] The ImP framework was modified both in the backbone of the central phenylene and at the imidazole *N*-alkyl position. Anthracene was chosen as the chromophore with a triplet energy nearly matching that of the LMCT state of **C0**,[24] while the phenyl substituent serves as a reference with a chromophore energy being very different from the LMCT state. The electronic ground states and the excited state dynamics were investigated by experimental methods, supported by (TD-)DFT calculations.

The phenyl-substituted complexes $[Fe(Im_2PPh)_2]^+$ and $[Fe((ImPh)_2P)_2]^+$ show the same photodynamics as those of previously published complexes with emission lifetimes of about 200 ps.[14] In contrast, the anthracenyl-substituted complexes $[Fe(Im_2PAnt)_2]^+$ and $[Fe((ImAnt)_2P)_2]^+$ exhibit lifetimes that extend beyond 5 ns. This lifetime is associated with the population of the ^{3}Chrom state, which was confirmed by transient absorption spectroscopy. However, repopulation of the LMCT state is also necessary for the reservoir effect.[6] This aspect was confirmed by time-resolved emission spectroscopy, which revealed ns lifetimes of the excited state consistent with the TA results. Thus, a reservoir effect could be realized even with the spatially small methylene bridge, which allows an effective electronic decoupling between the iron complex part and the organic chromophore. In turn, this further confirms that both a considerable original CT state lifetime plus an electronic decoupling of the metal complex and the organic chromophore are mandatory to achieve a detectable reservoir effect.

Author contributions

L. S. and B. B. carried out the synthesis of the compounds. L. S., B. B. and H. E. carried out the characterisation of the compounds. L. S carried out the steady-state photophysical measurements, as well as the electrochemical and TCSPC measurements. S. D., M. A. C. and S. L. carried out the time-resolved measurements *via* transient absorption spectroscopy and streak camera measurements and analysed the data. L. F. carried out quantum chemical calculations. R. S. recorded and analysed the single-crystal X-ray diffraction data. L. S. drafted the manuscript together with S. D., M. A. C., L. F. and J. S. All authors read and commented on the manuscript. M. B. carried out conceptualization, supervised the project and contributed to writing the manuscript. F. F. supervised and contributed to the revision process of the manuscript.

Conflicts of interest

There are no conflicts to declare.

Data availability

Data supporting this article have been included in the supplementary information (SI). Supplementary information: detailed synthetic procedures, available single-crystal X-ray diffraction data, NMR spectra and additional paramagnetic NMR investigations, additional steady-state absorption and emission data, additional time-resolved emission data, additional TD-DFT data, and mass spectroscopy data. See DOI: https://doi.org/10.1039/d5dt02915e.

Data used in this publication are available at Zenodot (https://doi.org/10.5281/zenodo.18609881).

Acknowledgements

L. S. and L. F. thank the Fonds der Chemischen Industrie for a Kekulé grant. M. B. gratefully acknowledges financial support through the priority program SPP 2102 from the German Science Foundation DFG (BA 4467/7-2) and within the frame of project BA 4467/10-1. S. L. gratefully acknowledges financial support through SPP 2102 (LO 714/11-2) and GRK 2943 'Spectroscopic Tools for Challenging Reduction Reactions: Catalytic Coupling of CO2', project no. 507189291. S. L. further acknowledges funding from SFB 1477 'Light–Matter Interactions at Interfaces'. The grant of computer time at the Paderborn Center for Parallel Computing PC^2 is acknowledged.

References

1 (*a*) O. S. Wenger, *Chem. – Eur. J.*, 2019, **25**, 6043–6052; (*b*) P. Dierks, Y. Vukadinovic and M. Bauer, *Inorg. Chem. Front.*, 2022, **9**, 206–220; (*c*) A. Ghosh, J. T. Yarranton and J. K. McCusker, *Nat. Chem.*, 2024, **16**, 1665–1672; (*d*) M. Pastore, S. Caramori and P. C. Gros, *Acc. Chem. Res.*, 2024, **57**, 439–449.

2 C. Förster and K. Heinze, *Chem. Soc. Rev.*, 2020, **49**, 1057–1070.

3 C. Wegeberg and O. S. Wenger, *Dalton Trans.*, 2022, **51**, 1297–1302.

4 J. Steube, A. Kruse, O. S. Bokareva, T. Reuter, S. Demeshko, R. Schoch, M. A. Argüello Cordero, A. Krishna, S. Hohloch, F. Meyer, K. Heinze, O. Kühn, S. Lochbrunner and M. Bauer, *Nat. Chem.*, 2023, **15**, 468–474.

5 (*a*) W. Leis, M. A. Argüello Cordero, S. Lochbrunner, H. Schubert and A. Berkefeld, *J. Am. Chem. Soc.*, 2022, **144**, 1169–1173; (*b*) P. Chábera, K. S. Kjaer, O. Prakash, A. Honarfar, Y. Liu, L. A. Fredin, T. C. B. Harlang, S. Lidin, J. Uhlig, V. Sundström, R. Lomoth, P. Persson and K. Wärnmark, *J. Phys. Chem. Lett.*, 2018, **9**, 459–463; (*c*) A. R. Marri, B. Marekha, T. Penfold, S. Haacke and P. C. Gros, *Inorg. Chem. Front.*, 2022, **10**, 118–126.

6 F. Glaser, S. de Kreijger and L. Troian-Gautier, *J. Am. Chem. Soc.*, 2025, **147**, 8559–8567.

7 J. Wellauer, B. Pfund, I. Becker, F. Meyer, A. Prescimone and O. S. Wenger, *J. Am. Chem. Soc.*, 2025, **147**, 8760–8768.

8 D. S. Tyson and F. N. Castellano, *J. Phys. Chem. A*, 1999, **103**, 10955–10960.

9 A. J. Howarth, M. B. Majewski and M. O. Wolf, *Coord. Chem. Rev.*, 2015, **282–283**, 139–149.
10 (*a*) P. Dierks, A. Päpcke, O. S. Bokareva, B. Altenburger, T. Reuter, K. Heinze, O. Kühn, S. Lochbrunner and M. Bauer, *Inorg. Chem.*, 2020, **59**, 14746–14761; (*b*) S. Campagna, S. Genovese, A. Cancelliere, A. Arrigo and F. Puntoriero, *Fe (III) complexes with prolonged luminescence lifetimes and symmetry-breaking charge separation*, Preprint, 2024.
11 B. Valeur and M. N. Berberan-Santos, *Molecular Fluorescence. Principles and Applications*, Wiley-VCH, Weinheim, 2012.
12 A. F. Morales, G. Accorsi, N. Armaroli, F. Barigelletti, S. J. A. Pope and M. D. Ward, *Inorg. Chem.*, 2002, **41**, 6711–6719.
13 D. S. Tyson, J. Bialecki and F. N. Castellano, *Chem. Commun.*, 2000, 2355–2356.
14 L. Schmitz, M. A. Argüello Cordero, M. J. Al-Marri, R. Schoch, H. Egold, A. Neuba, J. Steube, B. Bracht, O. S. Bokareva, S. Lochbrunner and M. Bauer, *Inorg. Chem.*, 2025, **64**, 14101–14117.
15 M. Montalti, J. Michl and V. Balzani, *Handbook of photochemistry*, Taylor & Francis, Boca Raton, 3rd edn, 2006.
16 C. Li, C. Gao, J. Lan, J. You and G. Gao, *Org. Biomol. Chem.*, 2014, **12**, 9524–9527.
17 S. W. Reilly, C. E. Webster, T. K. Hollis and H. U. Valle, *Dalton Trans.*, 2016, **45**, 2823–2828.
18 L. Zhuang, J. S. Wai, M. W. Embrey, T. E. Fisher, M. S. Egbertson, L. S. Payne, J. P. Guare, J. P. Vacca, D. J. Hazuda, P. J. Felock, A. L. Wolfe, K. A. Stillmock, M. V. Witmer, G. Moyer, W. A. Schleif, L. J. Gabryelski, Y. M. Leonard, J. J. Lynch, S. R. Michelson and S. D. Young, *J. Med. Chem.*, 2003, **46**, 453–456.
19 M. Enders, *Assigning and Understanding NMR Shifts of Paramagnetic Metal Complexes*, Wiley-VCH, Weinheim, 1st edn, 2011.
20 H. Günther, *NMR Spectroscopy. Basic Principles, Concepts, and Applications in Chemistry*, Wiley-VCH, Weinheim, 3rd edn, 2013.
21 J. Steube, L. Fritsch, A. Kruse, O. S. Bokareva, S. Demeshko, H. Elgabarty, R. Schoch, M. Alaraby, H. Egold, B. Bracht, L. Schmitz, S. Hohloch, T. D. Kühne, F. Meyer, O. Kühn, S. Lochbrunner and M. Bauer, *Inorg. Chem.*, 2024, **63**, 16964–16980.
22 C. A. Paddon, C. E. Banks, I. G. Davies and R. G. Compton, *Ultrason. Sonochem.*, 2006, **13**, 126–132.
23 A. Krishna, L. Fritsch, J. Steube, M. A. Argüello Cordero, R. Schoch, A. Neuba, S. Lochbrunner and M. Bauer, *Inorg. Chem.*, 2025, **64**, 1401–1409.
24 S. L. Murov, I. Carmichael and G. L. Hug, *Handbook of photochemistry*, Marcel Dekker, New York, 2nd edn, 1993.
25 A. D. Becke, *J. Chem. Phys.*, 1993, **98**, 5648–5652.
26 J. R. Lakowicz, *Principles of fluorescence spectroscopy*, Springer Science+Business Media LLC, Boston, MA, 3rd edn, 2006.
27 I. B. Berlman, *Handbook of fluorescence spectra of aromatic molecules*, Academic Press, New York, 2nd edn, 1971.
28 M. Kasha, *Discuss. Faraday Soc.*, 1950, **9**, 14.
29 (*a*) A. Mishra, K. Sharma, C. E. Johnson, E. A. Fosu, J. Schwarz, O. Prakash, A. K. Gupta, P. Huang, F. Lindgren, L. Häggström, J. Bendix, E. Jakubikova, R. Lomoth and K. Wärnmark, *Chemistry*, 2025, **31**(47), e01985; (*b*) C. E. Johnson, J. Schwarz, M. Deegbey, O. Prakash, K. Sharma, P. Huang, T. Ericsson, L. Häggström, J. Bendix, A. K. Gupta, E. Jakubikova, K. Wärnmark and R. Lomoth, *Chem. Sci.*, 2023, **14**, 10129–10139.
30 W. McCall, T. M. Christy, D. A. Pipp, B. Jaster, J. White, J. Goodrich, J. Fontana and S. Doxtader, *Environ. Earth Sci.*, 2018, **77**, 374.
31 C. B. Roberts, J. F. Brennecke and J. E. Chateauneuf, *J. Chem. Soc., Chem. Commun.*, 1993, 868–869.
32 J. R. Schoonover, D. M. Dattelbaum, A. Malko, V. I. Klimov, T. J. Meyer, D. J. Styers-Barnett, E. Z. Gannon, J. C. Granger, W. S. Aldridge and J. M. Papanikolas, *J. Phys. Chem. A*, 2005, **109**, 2472–2475.
33 B. Lang, S. Mosquera-Vázquez, D. Lovy, P. Sherin, V. Markovic and E. Vauthey, *Rev. Sci. Instrum.*, 2013, **84**, 73107.
34 J. K. S. Wan, *Res. Chem. Intermed.*, 1990, **13**, 193.
35 R. Livingston and D. W. Tanner, *Trans. Faraday Soc.*, 1958, **54**, 765.

6. Pyridine-substituted Fe(III) complexes – On the way to one-component photo-catalytical systems

The third publication changes the general focus from reservoir systems to one-component systems. The previously presented complexes function as photosensitizers but cannot mediate the desired chemical reaction since they do not possess free coordination sites. Therefore, they only fulfil part of a full catalytic system in regards to proton reduction. Generally, a second compound (catalyst) is necessary to realize a working multi-component system (Scheme 4 top). An energy/electron transfer between these two compounds makes the sunlight harvested by the photosensitizer available for the catalyst to undergo desired chemical reactions. Since this energy/electron transfer needs close spatial proximity between both compounds, the process is strongly dependent on diffusion.[46] Addition of a transfer reagent that is present in high concentration can reduce this issue, but still not eliminate it.

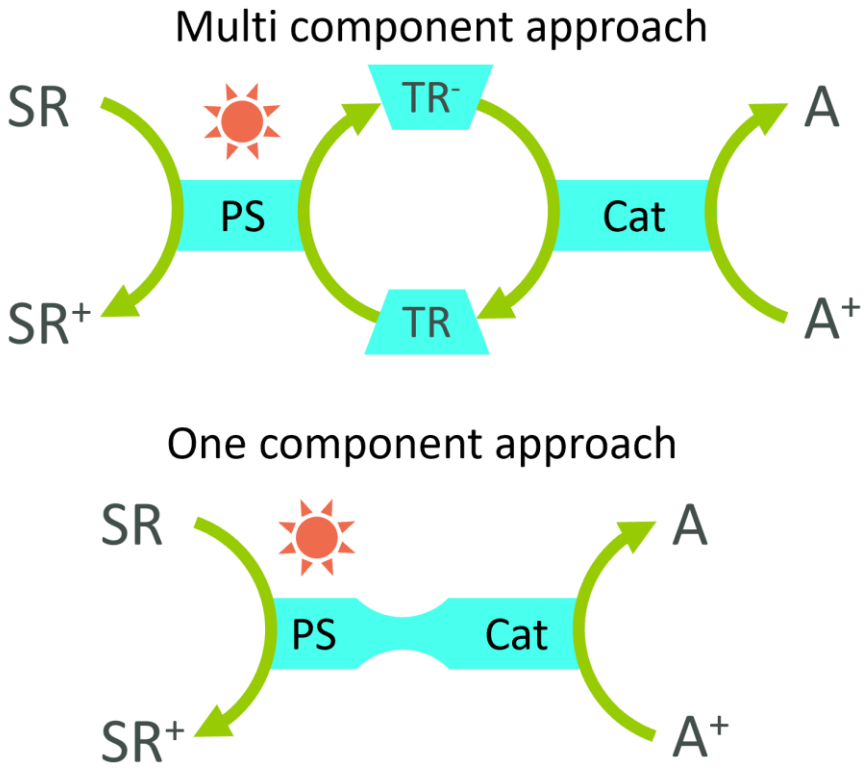

Scheme 4: Schematic comparison of a multi- and a one-component system for the photocatalytic reduction of a generic susbtrate A+ to product A (SR = Sacrifical reagent, TR = Transfer reagent, Cat = Catalyst). The green arrows represent diffusion limited processes.

The application of one-component systems could rather elegantly solve this issue, replacing the intermolecular energy/electron transfer with an intramolecular mechanism by simply connecting both components in the same complex via a linker (Scheme 4 bottom). This approach has been widely studied for systems employing late transition metals in the PS moiety.[47] Base metal one-component systems are however insufficiently researched. Nevertheless, one system based on Fe^{II} was previously shown to exhibit slightly enhanced catalytic activity in proton reduction compared to the analogous multi-component system,

making this a promising approach.[48] Considering the similarity of a reservoir system and a one-component system in the fact that both rely on energy/electron transfer inside a single molecule, the successful application of one (see above) makes the other a reasonable next approach. Therefore, the third project of this thesis again presents a photosensitizer based on the base complex **C**. A pyridine moiety in the backbone enables coordination of a second metal centre, therefore realizing both functions in a single molecule (typically labelled dyads or triads depending on the number of metal centres). This coordination of the second metal centre influences the electronic structure of the photosensitizer.[49] However, these effects may be obscured by the introduction of a new set of possible transitions in the introduced metalorganic moiety or between both components. To simulate the coordination of a second metal centre without introducing these masking effects, the pyridine is simply methylated to investigate the photosensitizer moiety. This modification leads to the lowest energy excited state changing from one with LMCT character to one with MLCT character. Photoreduction catalysis is generally also possible from an LMCT state following a reductive quenching cycle. The intramolecular electron transfer which is often the focus for one-component systems might however be easier in the case of an MLCT, where a high energy state localized on the ligand structure is populated.

Author Contributions:

Lennart Schmitz: Design and synthesis of investigated complexes, Characterization (NMR, MS, EA), CV, Absorption spectroscopy, Steady state emission spectroscopy, TCSPC, Main manuscript author.

Dr. J. Luis Pérez Lustres: Transient absorption spectroscopy, Manuscript Author

Dr. Ronan Viel: Time-resolved fluorescence spectroscopy, Manuscript Author

Jannik Löseke: (TD)-DFT calculations, Manuscript Author

Dr. Lorena Fritsch: (TD)-DFT calculations

Xiao-Hui Li: Transient absorption spectroscopy

Dr. Roland Schoch: Single-crystal X-ray diffraction

Prof. Dr. Stefan Haacke: Conception of the research, Supervision

Prof. Dr. Karsten Heyne: Conception of the research, Supervision

Prof. Dr. Matthias Bauer: Conception of the research, Corresponding author

Pyridine-substituted Fe(III) complexes – On the way to one-component photo-catalytical systems

Lennart Schmitz[a], J. Luis Pérez Lustres[b], Ronan Viel[c], Jannik Löseke[a], Lorena Fritsch[a], Xiao-Hui Li[b], Roland Schoch[a], Stefan Haacke[c], Karsten Heyne[b], Matthias Bauer[a,*]

Submitted on 06.02.2026 to
Physical Chemistry Chemical Physics

Linked photosensitizer-catalyst dyads based on earth-abundant metal complexes are currently potential candidates for sustainable proton reduction systems. Iron(III) carbene complexes showing ligand-to-metal charge transfer (LMCT) states with lifetimes in the 0.2 – 0.3 ns range are promising candidates for the photosensitizer side. In addition, a proton reduction catalyst of usually cationic character – like cobaloxime – is required, that is connected to the photosensitizer. We explore the feasibility of this approach with a model compound mimicking the effect of a positively charged moiety on the electronic state structure of a Fe(III) photosensitizer. The homoleptic pyridine-substituted **[Fe(ImPPy)$_2$]$^+$** (HImPPy = 1,1'-(5-(pyridin-4-yl)-1,3-phenylene)bis(3-methyl-1H-imidazol-3-ium)) complex was modified by attaching a methyl group at the pyridinyl nitrogen. This simulates the main effects of a metal fragment like a Co(III) centre on the Fe(III) photosensitizer, which is expected to reduce the ligand's electron density and thereby stabilize the metal-to-ligand (^{2}MLCT) excited states. TD-DFT calculations support this expectation, which is corroborated experimentally by a combination of cyclic voltammetry and ultrafast spectroscopies. **[Fe(ImPPyMe)$_2$]$^{3+}$** shows a lifetime of 80±10 ps for the ^{2}MLCT state, which constitutes a promising starting point for the use of **[Fe(ImPPy)$_2$]$^+$** as a photosensitizer in bimetallic one-component dyads.

Introduction

Photocatalysis is a growing research field due to the urgent demand for alternative energy sources for synthesis of industrial chemical and energy carriers.[1,2] Especially in the face of climate change, catalysts able to directly utilize sunlight for photochemical conversion and energy storage are of high interest.[3] For this application, homogeneous organometallic catalyst systems are historically based on late transition metals of the platinum group for their long excited-state lifetimes.[1] However, especially in recent years, the focus has been directed towards early transition metals such as iron.[4–7] This is the obvious consequence of significantly lower environmental and economic impact of mining and purification as a result of their abundance in earth's crust.[8,9] Short excited-state lifetimes resulting from a comparatively smaller ligand-field splitting constitute an important drawback for the implementation of early transition metal complexes.[10] The reason is that deactivation to the ground state may occur well before diffusion-limited reactive collisions required for electron transfer reactions in photocatalysis take place. One-component systems, where photosensitizer and catalyst are covalently linked, are a potential way to adress this limitation.[11] In this work, we present a photosensitiser (PS) based on the Fe(III) complex **[Fe(ImP)$_2$]$^+$** (HImP=1,1'-(1,3-phenylene)bis(3-methyl-1-imidazol-2-ylidene)) and specifically designed for application in one-component systems.[12] **[Fe(ImP)$_2$]$^+$** shows impressive photostability, a long lived ^{2}LMCT (ligand to metal charge transfer state), and simple tunability.[13–17] All this makes **[Fe(ImP)$_2$]$^+$** a suitable candidate for one-component photocatalytic dyads based exclusively on earth-abundant metals.

Further derivatization becomes possible by introducing a pyridine moiety in the complex backbone: **[Fe(ImPPy)$_2$]$^+$** (HImPPy = 1,1'-(5-(pyridin-4-yl)-1,3-phenylene)bis(3-methyl-1H-imidazol-3-ium)) (Scheme 1b). The latter can be incorporated into a one component system by coordinating e.g. cobaloxime at the pyridine-nitrogen.[18]

The photoexcited ^{2}LMCT state is generally the excited state of lowest energy in this Fe(III) complex group.[12,16] Therefore, these compounds are in principle best suited for photocatalytic oxidation reactions, which take advantage of the long-living hole generated on the ligand moiety. This contrasts to the more frequently found photoreduction via MLCT (metal-to-ligand charge transfer state) targeted in most Fe(II) complexes.[19] In this study we show, that this behaviour can be easily inverted by a methyl group attached to the pyridyl nitrogen, as quantum chemical calculations suggest (cf. Scheme 1). The methyl group reduces the ligand's electron density, stabilizing MLCT's relative to the LMCT manifold. The former then become available for photoreduction reactions. In the same manner, coordination of a second metal centre at the pyridyl nitrogen is postulated to confer strong MLCT character to the lowest energy excited state of the Fe(III) complex. This would enable efficient electron transfer to the catalytic centre, where the photoreduction finally takes place.

However, some risk exists that additional photochemical and electrochemical transitions arising from the second metal centre obscure the expected inductive effect of the catalytic unit on the photosensitizer.

To test this hypothesis, the N-methylated complex **[Fe(ImPPyMe)$_2$]$^{3+}$** (Scheme 1) was prepared. This should introduce significant changes in photochemical and electrochemical behaviour of the parent **[Fe(ImP)$_2$]$^+$** compound. At the same time, additional electronic states associated to a second metal complex are avoided. These could mask the pure inductive effect on the photochemical properties of the base Fe(III) complex. The postulated switch of MLCT and LMCT states is investigated by quantum chemical calculations. While the

inductive effects of the methyl group may still be significantly different from those of the metal centre, the present multidisciplinary approach of various analytical methods, as well as calculations should help to rationalize the effect of the catalyst on the electronic structure of the functionalized iron complex **[Fe(ImPPyMe)$_2$]$^{3+}$** by comparison to the base complex **[Fe(ImP)$_2$]$^{3+}$** and the previously published complex **[Fe(ImPPh)$_2$]$^+$** (HImPPh = 1,1'-([1,1'-biphenyl]-3,5-diyl) bis(3-methyl-1H-imidazol-3-ium)).[14]

Experimental Section

Synthesis

[Fe(ImPPh)$_2$]$^+$ was synthesized following a previously published route.[14] **[Fe(ImPPyMe)$_2$]$^{3+}$** was obtained by the same route with small adjustments described in the SI. For **[Fe(ImPPy)$_2$]$^+$**, however, this synthetic procedure had to be modified significantly.

All ligands were synthesized from the same starting molecule 1,3,5-tribromobenzene in a copper-catalysed *N*-arylation, according to a procedure previously published by our work group[14] based on a similar synthetic route[20], resulting in 1,1′-(5-bromo-1,3-phenylene)bis(1*H*-imidazole) . After Suzuki-Miyaura cross coupling 4-(3,5-di(1H-imidazol-1-yl)phenyl)pyridine was obtained. While the methylation of this ligand precursor with methyl iodide readily affords HImPPyMe, the high affinity of the pyridine moiety for methylation compared to the imidazole moieties makes it necessary to protect it prior to methylation to obtain HImPPy. This is done via an N-oxide generated by meta-Chloroperoxybenzoic acid. Afterward the methylation with methyl iodide affords the correct methylation pattern. Reduction of the N-oxide is then achieved by application of freshly activated zinc dust. The proligand could then be purified by precipitation as a PF_6^--salt out of water after addition of KPF_6. Since the complexation reaction utilizing [Zr(NMe$_2$)$_4$] depends

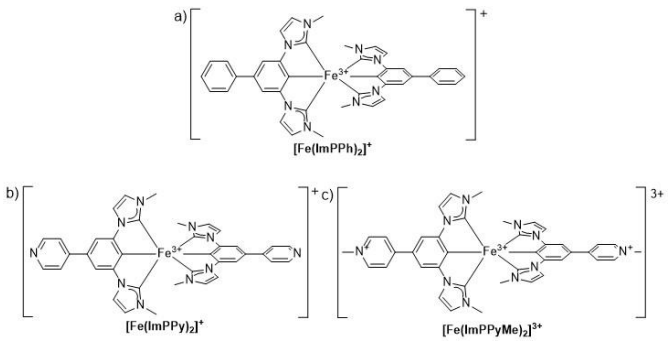

Scheme 1: The previously published complex **[Fe(ImPPh)$_2$]$^+$** (a)[10] and the newly synthesized Fe(III) complexes [**Fe(ImPPy)$_2$]$^+$** (b) and [**Fe(ImPPyMe)$_2$]$^{3+}$** (c). All complexes were obtained and analysed as PF_6^- salts.

on coordinating anions, a route previously published for Fe(II) complexes based on the reactive precursor Fe(N(SiMe$_3$)$_2$)$_2$ was utilized for **[Fe(ImPPy)$_2$]$^+$**, while **[Fe(ImPPyMe)$_2$]$^{3+}$** was obtained by the former approach via [Zr(NMe$_2$)$_4$]. Complete synthetic procedures are presented in the SI.

Computational Methods

The theoretical investigations are based on quantum chemical calculations performed with the Orca 6.1.0 program package.[21–32] Initially, the structures were optimized in their doublet ground state.[33] Local minima were confirmed by frequency analysis. The vertical excitations of this structure were calculated using time-dependent DFT (TD-DFT). For this purpose, the TPSSh functional,[34] the def2-TZVPP basis set[35] and D4 dispersion correction[36] were employed. Furthermore, the Conductor-like Polarization Continuum Model of acetonitrile was utilized.[37] As is common practice, calculated spectra were broadened and shifted to compare with experimental absorption. A broadening factor σ of 1200 cm^{-1} was employed and red shifts of 2000 cm^{-1} for **[Fe(ImPPh)$_2$]$^+$**, 600 cm^{-1} for **[Fe(ImPPy)$_2$]$^+$** and 250 cm^{-1} both for **[Fe(ImPPyH)$_2$]$^{3+}$** and **[Fe(ImPPyMe)$_2$]$^{3+}$** were applied. Both, **[Fe(ImPPh)$_2$]$^+$** and **[Fe(ImPPy)$_2$]$^+$**, exhibit pronounced charge-transfer character in the relevant excited states. The different energy shifts required to align the TDDFT results to experimental data are most plausibly attributed to the intrinsic sensitivity of conventional TDDFT to such charge-transfer excitations.[38] Further, the utilized implicit solvation model might not capture the different solvation of the phenyl- and pyridine-fragments accurately.[39] The transition density analysis was conducted with the TheoDORE software package.[40] The structure and Kohn-Sham orbital visualizations were produced with IboView[41] and VMD[42,43] while the spectra were generated using custom Python code utilizing Matplotlib[44] and NumPy.[45]

Cyclic Voltammetry

Potentiostatic measurements were performed at room temperature in dry and degassed 0.1 M [*n*-Bu$_4$N][PF_6] MeCN solutions with an analyte concentration of 10^{-3} M using a PGSTAT 101 potentiostat from Metrohm. A platinum working electrode (1 mm diameter), an Ag/$AgNO_3$ reference electrode and a platinum pin electrode were utilized in a three-electrode configuration. After the measurements ferrocene was added as an internal standard to reference against the $FcH^{0/+}$ redox couple by measuring a square wave voltammetry of the resulting solution. The resulting voltammograms were analysed using the *NOVA 2.1.3* software.

Single crystal X-ray Analysis

The presented X-ray single crystal data were measured on a *Bruker* Venture D8 three-cycle diffractometer equipped with a Mo K_α μ-source (λ=0.71073 Å), an *Incoatec* multilayer monochromator and a Photon III detector cooled down to 120 K. The data were integrated with SAINT and afterwards a multi-scan absorption correction was applied using SADABS.[46] Structure solution was achieved by direct methods in SHELXT and structure refinement was conducted using full-matrix least squares refinement based on F^2.[47]

UV/VIS Spectroscopy

Absorption spectra were recorded at concentrations of 10^{-5} M in 99.9% pure acetonitrile with a PerkinElmer Lambda465 single-beam spectrophotometer. Spectroscopic-grade solvents

from VWR in quartz cuvettes by Hellma with an optical path length of 10 mm were used.

Luminescence Measurements

The emission and excitation spectra were recorded with an Edinburgh Instruments FLS1000 spectrometer with single monochromators and a red-extended PMT-980 detector. The same solutions in quartz cuvettes as for UV/Vis spectroscopy were used.

Transient Absorption Spectroscopy

Transient absorption measurements were performed in a home-built setup as described before.[48,49] Basically, fs pulses were obtained from a Clark-MRX-2001 Ti:Sa amplified laser system, which pumps two home-built non-collinear parametric amplifiers (NOPA). The latter were tuned to 530 and 600 nm. Pulses were compressed with fused silica prism pairs and used for continuum generation (30 fs, 6 uJ) on a CaF_2 plate and for optical pumping (30 fs, 0.4 uJ), respectively. Transient spectra were recorded with two independent signal and reference spectrographs at 0.92 kHz repetition rate and 2 nm spectral resolution. Typically, 100 pump events were averaged for each delay time. Final signal is the mean value of eight independent scans. Pump-probe magic angle polarization was used. Samples were dissolved in acetonitrile (Sigma Aldrich, spectroscopic grade) and circulated in a 0.2 mm flowing cell (Starna) to ensure fresh sample conditions after every laser shot. UV/Vis absorption spectra were measured before and after fs measurements. No indication of photodegradation was observed.

Picosecond Luminescence Spectroscopy

A Hamamatsu C10627 streak camera with 10 ps time resolution (fast single sweep unit), in photon counting mode, coupled to a 25-cm focal length Jobin-Yvon spectrograph (spectral resolution 5 nm) was used. Excitation pulses at 630 nm (0.3 ps duration, 100 kHz) were produced by a home-built OPA pumped by a Yb:fiber laser (Tangerine, Amplitude). The excitation density was typically 50 $\mu J/cm^2$. The linear polarisation of the excitation beam is oriented at magic angle with respect to the one of an analyser placed in front of the spectrograph.

Results and Discussion

Ground State Characterization

To gain a good understanding of these complexes in their ground state, a wide array of analytical methods was applied. On the basis of these we can then investigate the excited state dynamics to determine whether a change in lowest energy excited state occurs.

Single crystal X-ray diffraction

For **$[Fe(ImPPy)_2]^+$** single crystals suitable for X-ray diffraction were obtained by gas-phase diffusion of pentane into DCM solution. The obtained geometry will be compared to the previously published structure of **$[Fe(ImPPh)_2]^+$**.[14] After repeated crystallization setups, varying the solvent, antisolvent and crystallization methods (layering and diffusion) no crystals

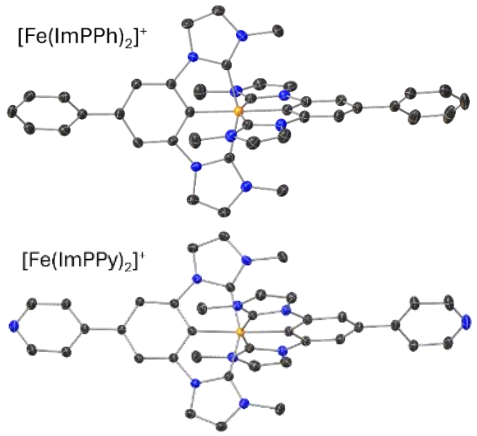

Figure 1: Molecular geometry obtained from single crystal X-ray diffraction.

of **$[Fe(ImPPyMe)_2]^{3+}$** suitable for X-ray diffraction were obtained. Thin needles or plates were formed that were too small for measurement in at least one dimension. The obtained crystal structure and **$[Fe(ImPPh)_2]^+$** are depicted in Figure 1, and selected structural data is listed in Table 1.

Table 1: Selected structural values obtained from single crystal X-Ray diffraction. The bond lengths between the iron centre and the phenyl coordination sites (Ph) or imidazole coordination sites (Im), as well as the bite angles of the tridentate ligand and the angles between the base ligand motif and the attached chromophore (Phenyl/Pyridinyl) are listed where applicable. In every case the values are averaged over all occurrences of the corresponding value.

	$[Fe(ImP)_2]^+$ [12]	*$[Fe(ImPPh)_2]^+$*	*$[Fe(ImPPy)_2]^+$*
C(Ph)-Fe [Å]	1.948 (3)	1.938 (3)	1.942 (2)
C(Im)-Fe [Å]	1.982 (3)	1.980 (3)	1.989 (2)
Bite Angle	155.35 (15)	155.44° (12)	155.04° (6)
Backbone Angle	-	39.3° (5)	19.8° (2)

$[Fe(ImPPy)_2]^+$ shows a distorted octahedral geometry with a bite angle of about 155° imposed by the contracted in-plane distances between the phenylene and imidazolylene moieties of the tridentate ligands. This is expected and comparable to **$[Fe(ImPPh)_2]^+$** and the base complex.[12] The lengths of the iron carbon bonds are also very similar in all three complexes, with **$[Fe(ImPPh)_2]^+$** being slightly shorter and **$[Fe(ImPPy)_2]^+$** being slightly longer than **$[Fe(ImPPh)_2]^+$**. Only the backbone angles (between the base ligand structure and the attached backbone) differ considerably between **$[Fe(ImPPy)_2]^+$** and **$[Fe(ImPPh)_2]^+$**, with around 40° for the phenyl substituted and ca 20° for the pyridine substituted respectively. This difference is also apparent in DFT optimized geometries, albeit weaker at 39° and 31° respectively (see Figure S5). Although a planar structure is preferred electronically, the steric hindrance between both rings leads to this distortion, as is observed for biphenyl species.[50] The smaller angle in **$[Fe(ImPPy)_2]^+$** suggests a stronger influence of the electronic effect, while the steric hindrance is virtually identical. The calculated structure of **$[Fe(ImPPyMe)_2]^{3+}$** reveals an even smaller dihedral angle at 25°, presumably to

stabilize the positive charge at the pyridine moiety by further delocalization.

Electrochemistry

Since the introduced positive charges in **[Fe(ImPPyMe)$_2$]$^{3+}$** should affect the redox behaviour of the complex, the electronic ground state of **[Fe(ImPPy)$_2$]$^{+}$** and **[Fe(ImPPyMe)$_2$]$^{3+}$** was investigated by cyclovoltammetry and compared to the previously published results of **[Fe(ImPPh)$_2$]$^{+}$** (Figure 2).[14]

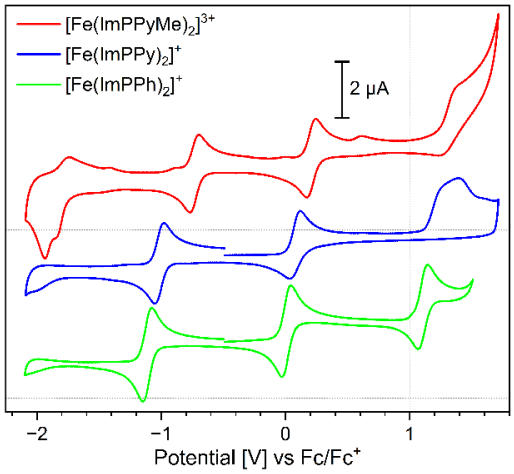

Figure 2: Cyclic voltammograms measured in MeCN at 1 mmol/L. NBu_4PF_6 was added as conducting salt at 10 mmol/L. The voltammogram was referenced against Fc/Fc^+. Reversible Fe II/III and Fe III/IV transitions are apparent in all complexes between 0.5V and -1.5V. Ligand oxidation is seen for all complexes above 0.5 V. Additionally **[Fe(ImpPyMe)$_2$]$^{3+}$** exhibits an additional irreversible reduction below -1.5V.

For **[Fe(ImPPy)$_2$]$^{+}$** a small positive shift of all redox potentials compared to **[Fe(ImPPh)$_2$]$^{+}$** is observed, which can be explained by the electron withdrawing effect of pyridine ring that leads to a stabilization of the electronic levels through reduced electron density. Additionally, ligand oxidation is not reversible for the pyridine complex. This trend is continued for the methylated species, where the positive charge further pushes redox potentials to higher values. This results in an additional observable redox process within the solvent window at -1.9 V as seen in Table 2. This transition is assumed to be a ligand reduction, suggesting lower lying π* orbitals that should allow a lower energy MLCT. Comparing the differences between ligand reduction (resp. oxidation) with complex oxidation (resp. reduction) (to estimate MLCT (resp. LMCT) energy) for **[Fe(ImPPyMe)$_2$]$^{3+}$** results in similar energies for both transitions at 2.05V (MLCT) and 2.13V (LMCT). However, the irreversible ligand transitions only allow an estimate of the redox potentials.

Table 2: Electronic potentials of redox transitions in the investigated compounds. a) Ligand reduction was only visible in **[Fe(ImPPyMe)]$^{3+}$**. Two reduction bands are apparent, and both maxima are listed b) This redox process was irreversible, therefore the maximum of the corresponding peak is listed here.

	E_{Red}[a)] Lig. [V]	E_{Red} $Fe^{II/III}$ [V]	E_{Ox} $Fe^{III/IV}$ [V]	E_{Ox} Lig. [V]
[Fe(ImPPh)$_2$]$^{+}$		-1.11	0.01	1.11
[Fe(ImPPy)$_2$]$^{+}$		-1.01	0.08	1.42[b)]
[Fe(ImPPyMe)$_2$]$^{3+}$	-1.84[b)] -1.94[b)]	-0.73	0.21	1.4[b)]

Optical absorption

The influence of pyridine methylation on the complexes electronic structure visible in cyclovoltammetry also significantly affects UV/Vis absorption as seen in Figure 3, where band positions and intensities are significantly changed.

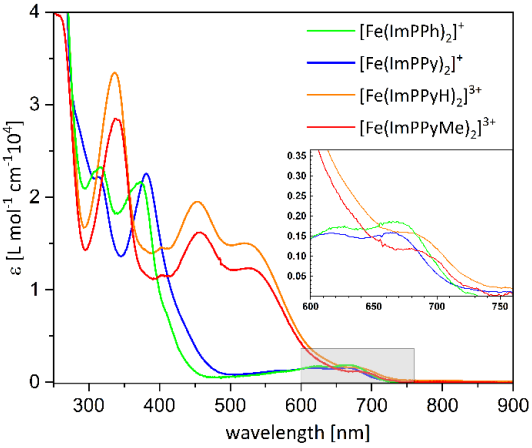

Figure 3: Absorption spectra of the investigated complexes measured in MeCN ($1*10^{-5}$ mmol/L). Additionally, **[Fe(ImPPy)$_2$]$^{+}$** was protonated by addition of a small amount of hydrochloric acid (**[Fe(ImPPyH)$_2$]$^{3+}$**).

Both the phenyl- and the pyridine-substituted complexes, **[Fe(ImPPh)$_2$]$^{+}$** and **[Fe(ImPPy)$_2$]$^{+}$**, however, have almost identical absorption spectra, very much reminiscent of the absorption spectrum of the parent complex **[Fe(ImP)$_2$]$^{+}$**.[12] All three complexes include a weak absorption band at low energies (ε < 3000 $Lmol^{-1}cm^{-1}$, 500 – 700 nm), a significant absorption band at wavelengths slightly shorter than 400 nm and a strong absorption band below 300 nm with a shoulder slightly above 300 nm. As for **[Fe(ImP)$_2$]$^{+}$**, LMCT character can be assigned to the low-energy absorption band for both complexes according to TD-DFT calculations. The vertical transitions, the theoretical spectrum generated from these via gaussian broadening and experimental spectrum for each of the four complexes are displayed in Figure 4. This assignment is in agreement with the results from previous publications.[12,14] The band at 372 nm/381 nm exhibits mixed MLCT-LC character in the TD-DFT calculations showing a clear red shift from **[Fe(ImPPh)$_2$]$^{+}$** to **[Fe(ImPPy)$_2$]$^{+}$** (Figure 4), presumably due to the lower lying π* orbitals in the later, in agreement with the CV results. Lastly, the shoulder at 317 nm/314 nm and the strong absorption at higher energies exhibits primarily ligand centred character.

By addition of small amounts of HCl **[Fe(ImPPy)$_2$]$^+$** can be protonated in situ to give **[Fe(ImPPyH)$_2$]$^{3+}$**. After addition of NaOH this can be reversed proving a simple acid/base interaction. The absorption spectra of this protonated and the methylated variation of **[Fe(ImPPy)$_2$]$^+$**, **[Fe(ImPPyH)$_2$]$^{3+}$** and **[Fe(ImPPyMe)$_2$]$^{3+}$**, differ significantly from the spectra of the singly charged complexes previously discussed above but again share a high degree of similarity with each other also apparent in TD-DFT calculated spectra, suggesting the kind of substituent at the pyridine moiety having little influence on the electronic structure. For both complexes the low energy shoulders above 500 nm are characterized as MLCT dominated transitions by the transition density analysis (Figure 4). The intensity of the band at around 450 nm is significantly underestimated by TD-DFT, which identifies a transition at around 470 nm with primarily intraligand charge transfer (ILCT) character between the central phenyl and the backbone pyridyl unit. All transition orbitals and their corresponding bands are depicted in the SI Tables S1 to S4 The transition strength is highly affected by the dihedral angle between these units, which might lead to the mismatch between measured and calculated intensities. Finally, the small

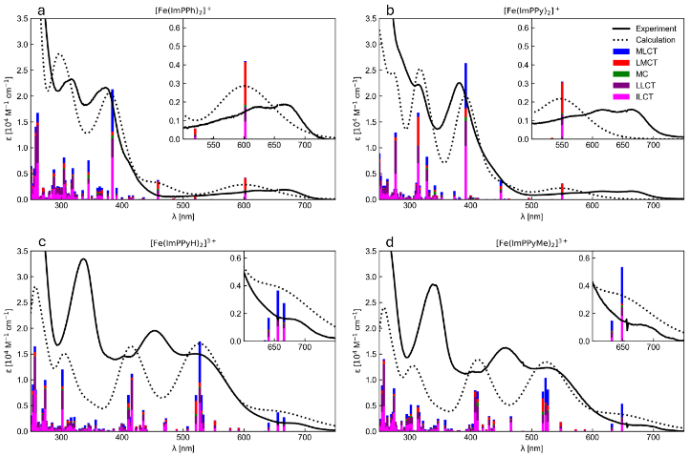

Figure 4: UV-Vis spectra of **[Fe(ImPPh)$_2$]$^+$** (a), **[Fe(ImPPy)$_2$]$^+$** (b), **[Fe(ImPPyH)$_2$]$^{3+}$** (c) and **[Fe(ImPPyMe)$_2$]$^{3+}$** (d) calculated from the TD-DFT vertical transitions. Character of the transitions is marked by colour.

shoulder slightly above 400 nm, the strong band at around 340 nm and the strong absorption below 300 nm are ligand dominated.

Consequently going from the singly positively charged **Fe(ImPPh)$_2$]$^+$** and **[Fe(ImPPy)$_2$]$^+$** to the triply charged **[Fe(ImPPyH)$_2$]$^{3+}$** and **[Fe(ImPPyMe)$_2$]$^{3+}$** changes the character of the low energy absorption band from LMCT to MLCT. When tracking the influence of the positive charge on the change of the Loewdin atomic charges (see Figure S7), a delocalization focused on the pyridine unit is observable. The pyridine nitrogen stands out with a charge increase of over 0.3 e in the protonated complex and almost 0.25 e in the methylated complex, which is expected since it acts as an L-type ligand (donating its free electron pair) in both cases, as it would in one-component systems coordinating a metal centre. In line with this observation, it can be found that the Kohn-Sham orbitals with large contributions of the phenyl-pyridine π-system tend to be more stabilized than the metal or imidazole centred orbitals (see Figure S6). Consequently, the gap between the virtual metal centred LUMO and the phenyl centred LUMO+1/+2 in the beta set is significantly reduced, even resulting in mixing of the metal and phenyl centred virtual orbitals. These stabilized phenyl-pyridine orbitals enable the observed low energy MLCT transitions as can be further verified by the large contribution of the phenyl-pyridine π-system to the acceptor orbitals of the most significant TD-DFT transitions of the MLCT bands (see Table S3 and S4).

Steady state emission

Figure 5 highlights a broad emission band above 650 nm. The mirror image symmetry between the absorption and emission spectra observed for **[Fe(ImPPh)$_2$]$^+$** and **[Fe(ImPPh)$_2$]$^+$** was already pointed out for the base complex.[12] The shape and Stokes shift of the spectra are very similar for the three complexes, indicating that the emission stems from the lowest excited state responsible for the weak absorption tail at 680-700 nm.

The emission intensity decreases slightly from phenyl to pyridinyl substitution and much more for the methylated species, as seen in Figure 5 Panel D. The mirror image symmetry

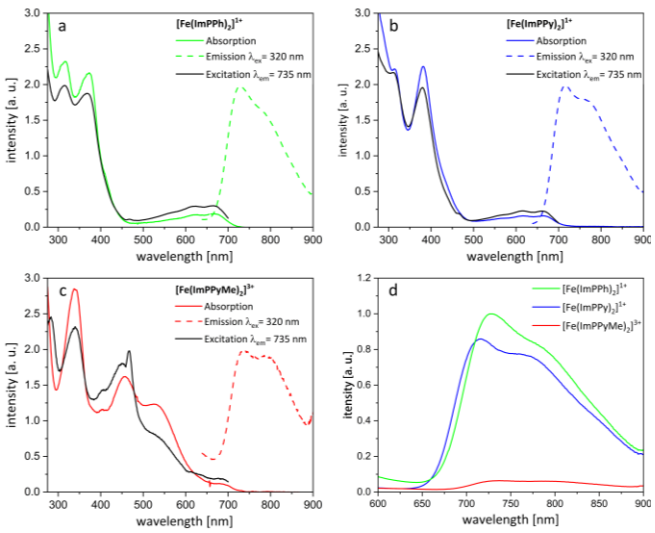

Figure 5: Absorption, emission and excitation spectra of **[Fe(ImPPh)$_2$]$^+$** (a), **[Fe(ImPPy)$_2$]$^+$** (b), and **[Fe(ImPPyMe)$_2$]$^{3+}$** (c), in degassed MeCN at c = 10^{-5} mol/L. The emission spectra are normalized to the same height to highlight band shape and position. The excitation spectra are adjusted by a factor that best aligns them with the absorption spectra. The moderate agreement between excitation and emission spectrum for **[Fe(ImPPyMe)$_2$]$^{3+}$** is likely due to the weak emission of this complex. The emission spectra in Panel d were not scaled and show the different emission intensities. All emission spectra were measured under the same conditions, and excited at similar extinction coefficients to enable comparability.

suggests the emission to originate from the low energy ^{2}LMCT states for **[Fe(ImPPh)$_2$]$^+$** and **[Fe(ImPPy)$_2$]$^+$**, as for the parent compound **[Fe(ImP)$_2$]$^+$**.[12,14] On the other hand, since according to the TD-DFT calculations the low energy transitions (≈670 nm) in **[Fe(ImPPyMe)$_2$]$^{3+}$** are dominated by an MLCT character, one might attribute the decreased emission intensity to a lower radiative rate and/or a shorter excited state lifetime of the ^{2}MLCT transition. This will be addressed in the next section, centred on ultrafast spectroscopy of the complexes.

Excited State Dynamics

To investigate the influence of the predicted changes in the electronic structure on the excited state dynamics, we applied transient absorption- and time-resolved emission spectroscopy, with the base complex **[Fe(ImP)$_2$]$^+$** as reference.

Transient Absorption Spectroscopy

Transient absorption spectroscopy of **[Fe(ImPPy)$_2$]$^+$** and **[Fe(ImPPyMe)$_2$]$^{3+}$** was measured in acetonitrile (ACN) and compared to the phenyl substituted compound **[Fe(ImPPh)$_2$]$^+$**. Figure 6 shows the transient spectra obtained by excitation at 600 nm, corresponding to a transition with LMCT character for **[Fe(ImPPy)$_2$]$^+$** or MLCT character in the case of **[Fe(ImPPyMe)$_2$]$^{3+}$**. The corresponding spectra for **[Fe(ImPPh)$_2$]$^+$** are shown in the SI (Figure S10).

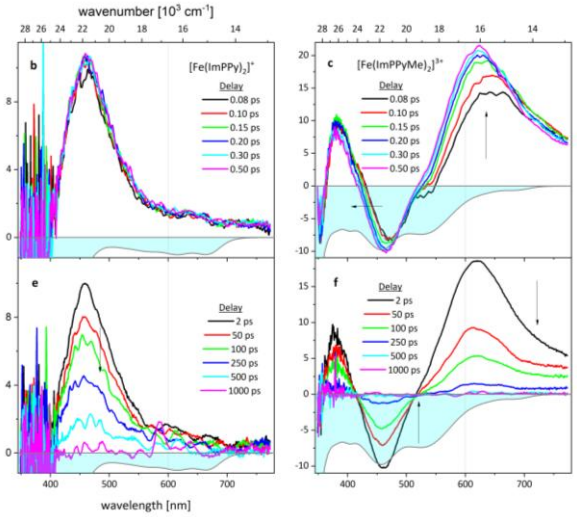

Figure 6: Time evolution of the transient absorption spectra upon 600 nm fs excitation (vertical dotted line). Upper panels focus early spectral redistribution while the lower row shows overall signal decay on the ps timescale for the three compounds, as indicated in the inset. Signal for magic-angle polarization is shown. Pump-probe time delays are quoted in the legend. Arrows indicate the direction of signal evolution towards longer delays. A horizontal black line marks the zero-signal level. Absorption spectra are shown as negative cyan filled curves as a guide to assign bleach contributions.

Transient spectra are characterized by two bands in our spectral window, see Figure 6. The excited-state absorption (ESA) band around 400 nm, here observed at 430 nm and 460 nm for **[Fe(ImPPh)$_2$]$^+$**, and **[Fe(ImPPy)$_2$]$^+$**, respectively, was already assigned by us to the ^{2}LMCT on the basis of its similarity to the difference spectra between the Fe^{II} and Fe^{III} species of the base complex, as observed via spectroelectrochemical measurements.[12] This also aligns well with recently published spectroelectrochemical data for **[Fe(ImPPh)$_2$]$^+$**, exhibiting a strong absorption band at 470 nm after reduction to Fe^{II}.[14] For **[Fe(ImPPyMe)$_2$]$^{3+}$** a similar ESA band is observed at 385 nm, and is assigned likewise to ESA of the ^{2}LMCT. Only for **[Fe(ImPPyMe)$_2$]$^{3+}$** we observe a second broader ESA band at 610 nm that extends from about 500 to 750 nm (Figure 6c and f). We observed distinct sub-picosecond dynamics for the two ESA bands, indicating distinct electronic states. This is supported by our calculated TD-DFT vertical transitions (Figure 4), showing an additional low-energy transition for **[Fe(ImPPyMe)$_2$]$^{3+}$** around 640 nm.

This second band is assigned to the ESA of the ^{2}MLCT state as it resembles the difference spectrum between the Fe(IV) and Fe(III) species of **[Fe(ImPPh)$_2$]$^+$**,[14] as well as the one of the base complex.[12] The exact position and strength of both bands depend on the structure of the compound. Only in the case of **[Fe(ImPPyMe)$_2$]$^{3+}$** a negative bleach contribution becomes obvious. This results from the blue and red shifts of the ESA bands assigned to ^{2}LMCT and ^{2}MLCT, respectively, and a stronger extinction coefficient of the ground state, which opens a window for the negative bleach signal to be observed. For the other two compounds, stronger overlap with the positive ESA bands obscures the weaker bleach contribution. Also remarkable, the LMCT ESA band is stronger for **[Fe(ImPPy)$_2$]$^+$** and **[Fe(ImPPh)$_2$]$^+$**, while in the case of **[Fe(ImPPyMe)$_2$]$^{3+}$** the ^{2}MLCT ESA band is more intense. This is consistent with TD-DFT calculations of the compounds showing high LMCT character for the low energy ground state absorption band in the case of **[Fe(ImPPh)$_2$]$^+$** and **[Fe(ImPPy)$_2$]$^+$**, while in **[Fe(ImPPyMe)$_2$]$^{3+}$** MLCT transitions dominate the low energy part of the absorption spectrum, where the excitation pulse is located. In either case, only the stronger ESA band exhibits some spectral evolution on the sub-picosecond timescale.

The first 2 ps are characterized by spectral reorganization, most prominent on the LMCT ESA band for **[Fe(ImPPh)$_2$]$^+$** (Figure 6a) or on the MLCT ESA band for **[Fe(ImPPyMe)$_2$]$^{3+}$** (Figure 6c). **[Fe(ImPPy)$_2$]$^+$** shows minor changes during this timescale (Figure 6b). Later, on the picosecond timescale (Figure 6d-f), the signal decays and reaches the zero level at about 500 ps, when the excited-state population has returned to the ground electronic state. One observes that, first, the decay of **[Fe(ImPPyMe)$_2$]$^{3+}$** is clearly faster than for the other two compounds. The latter decay with time-constants of about 300 ps. And second, the signal decays along with only subtle spectral changes, more prominent in the case of **[Fe(ImPPyMe)$_2$]$^{3+}$**. Notice that the ESA band at 385 nm and assigned here to the ^{2}LMCT state decays slower than the ESA band at 610 nm and assigned to the ^{2}MLCT state. The sub-nanosecond dynamics of the processes is analysed below in parallel to the time-resolved fluorescence data. Future studies need to clarify the contribution of individual states to the dynamics.

Time-Resolved Emission Spectroscopy

To further analyse the presented complexes, a series of picosecond luminescence experiments was performed with a streak camera. The samples were excited at 630 nm, i.e. in the LMCT absorption band for **[Fe(ImPPh)$_2$]$^+$** and **[Fe(ImPPy)$_2$]$^+$**, and the MLCT band for **[Fe(ImPPyMe)$_2$]$^{3+}$** (see Figure 4). We give in Figure 7 a comparison between **[Fe(ImPPy)$_2$]$^+$** and **[Fe(ImPPyMe)$_2$]$^{3+}$** (see Figures S11 and S12 for **[Fe(ImPPh)$_2$]$^+$**). Note that the shape of the time-dependent spectra is not the same as the ones recorded by a time-integrating fluorimeter (Figure 5), since the streak camera data are not corrected for the spectral response of the camera's photocathode.

From Figure 7 (a) to (d), it is confirmed that **[Fe(ImPPyMe)$_2$]$^{3+}$** has a much shorter excited state lifetime than **[Fe(ImPPy)$_2$]$^+$**,

since the luminescence of the former falls below the noise level by 0.6 ns (Figure 7b and d) while the latter has only decayed by a factor
of ≈10 at the same delay time (Figure 7a and c). The spectra of **[Fe(ImPPy)$_2$]$^+$** and **[Fe(ImPPyMe)$_2$]$^{3+}$** do not present significant spectral changes with time suggesting a global fit approach to provide good fits. As can be observed in Figure 7e and f, two lifetimes were needed to best fit the decays (see Figure 7c and d, and the residuals). Table 3 gives a summary of the lifetimes for all three complexes reported herein, which are compared to global fits of the TA data across the full spectral window. The latter were performed on the sub-ns timescale with 2 ps sampling rate, so that repopulation of the ground state is monitored while fast spectral reorganization is not considered at this stage . These conditions are also very similar to those of the time-resolved fluorescence measurements, so that dynamics from both techniques can be directly compared. The agreement between these results from different laboratories is excellent. For **[Fe(ImPPy)$_2$]$^+$** and **[Fe(ImPPh)$_2$]$^+$** the small amplitude τ_1 component (see Table 3) seems to be too long for invoking a solvent relaxation process in acetonitrile. Intramolecular relaxation is also improbable as the transient fluorescence spectra barely show any dynamic redshift (see Figure 7a and b). It is therefore concluded that the population decays biexponentially to the ground state either via parallel routes of sub-populations of the same electronic state or by reversible dynamics involving some other poorly populated state.[51] The values of the longer τ_2 decay times are in good agreement too with the excited state lifetimes found by global analysis of TA measurements in comparable conditions: 320 ps for (**[Fe(ImPPy)$_2$]$^+$**), and 253 ps for **[Fe(ImPPh)$_2$]$^+$** from transient fluorescence while values of 362 and 286 ps, respectively, are obtained from TA data (see Table 3). From the calculations and as reported for the original complex **[Fe(ImP)$_2$]$^{3+}$**, this emission is assigned to the ^{2}LMCT state, i.e. to a spin-allowed transition.[8] For **[Fe(ImPPyMe)$_2$]$^{3+}$**, the fluorescence decays with two lifetimes with values of τ_1=40 ±6 and τ_2=113 ± 5 ps, which are in very good agreement with the TAS data: 37± 1 and 117 ± 1 ps (see Table 3). Interestingly, fluorescence is largely dominated by the faster τ_1 component. The spectra associated with both decay times are very similar (Figure 7f), which is again compatible with two sub-populations of the same ^{2}MLCT state or with reversible dynamics. Interestingly, TA global analysis shows that spectral shapes for both decay components are quite different, suggesting that they should result from a reversible process. Thus, biexponential repopulation of the ground state is concluded.

Table 3: Summary of the different lifetimes obtained for all three compounds after global fitting of the streak camera 2D maps and TA data obtained in equivalent experimental conditions. The samples were excited by a 630-nm pulsed beam at 100 kHz repetition rate in fluorescence and at 600 nm, 460 Hz in TA. The angle between pump polarization and detected emission was set at magic angle (MA). Likewise, TA was measured with pump-probe polarization set at magic angle. The τ_2 lifetimes are in good agreement with those already reported.[14] All lifetimes are reported in ps.

		[Fe(ImPPh)$_2$]$^+$	*[Fe(ImPPy)$_2$]$^+$*	*[Fe(ImPPyMe)$_2$]$^{3+}$*
Fluo-rescence	τ_1	85 ± 6 (13%)	95 ± 6 (15%)	40 ± 6 (95%)
	τ_2	253 ± 7 (87%)	320 ± 10 (85%)	113 ± 5 (5%)
Transient Absorption	τ_1	129 ± 4	112 ± 2	37 ± 1
	τ_2	286 ± 6	362 ± 4	117 ± 1

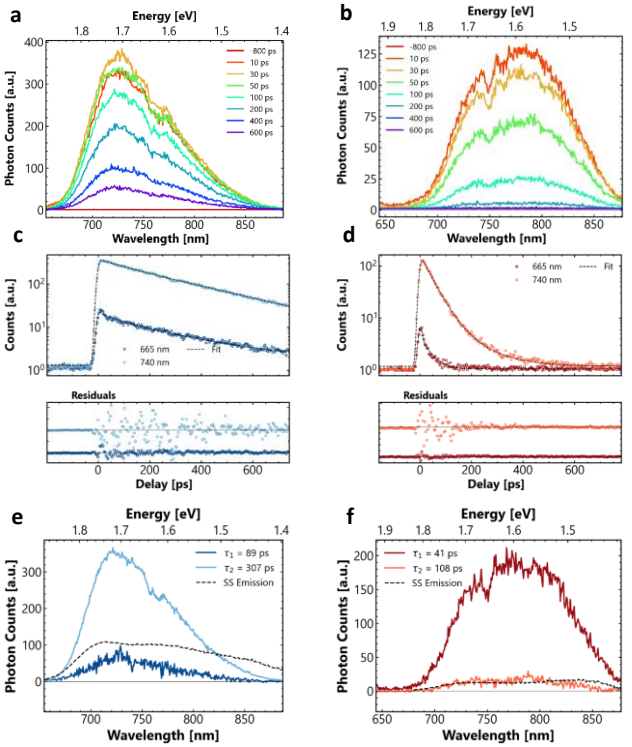

Figure 7: (a) and (b): Photon Counting 2D maps of [Fe(ImPPy)$_2$]$^{3+}$ and [Fe(ImPPyMe)$_2$]$^+$ respectively. (c) and (d): Selection of kinetics of the same complexes with best fitting lines and residuals. (e) and (f): Decay Associated Spectra obtained from a global fitting of the 2D maps with 2 resolved lifetimes (solid lines) and the steady-state emission spectrum (dashed black line).

Conclusion

Two new iron complexes expanding on the base complex **[Fe(ImP)$_2$]$^+$** were investigated to gain insights into their possible role as photosensitizer in one-component systems. The complex **[Fe(ImPPy)$_2$]$^+$** has a pyridine moiety with a free nitrogen in the backbone of the central phenyl making the coordination of a second catalyst possible. Its spectroscopic and excited state properties are affected only slightly when compared to the base complex and especially to the phenylene analogue **[Fe(ImPPh)$_2$]$^+$** with both complexes exhibiting an ^{2}MLCT absorption band at the high energy edge of the visible

spectrum and a ^{2}LMCT absorption band at lower wavelength. A ^{2}LMCT emission above 650 nm is also present for both, with slightly different excited state lifetimes according to TA and time-resolved luminescence (ca. 250 ps for the phenyl and 320 ps for the pyridine species). The methylation of the pyridine as a "coordination simulation" without introduction of a second metal centre leads to fundamental changes in electro- and photochemical behaviour of the resulting complex **[Fe(ImPPyMe)$_2$]$^{3+}$**: According to TD-DFT calculations, the lowest energy absorption band (650 – 700 nm) now has mostly ^{2}MLCT character, while new bands in the visible between 400 and 600 nm have mixed character, albeit with major MLCT character (absorption maximum at ≈530 nm). Corresponding changes are evidenced by femtosecond TAS experiments, which show a second low energy ESA band in addition to the typical LMCT ESA band around 430 nm, as observed for the other complexes. This low energy ESA band is populated within the first picosecond after excitation at 600 nm and then decays in parallel to the LMCT ESA band. These observations are in line with the theoretically predicted ^{2}MLCT character for the lowest excited state in **[Fe(ImPPyMe)$_2$]$^{3+}$**. The significant associated change of the excited state landscape is also apparent in time-resolved emission spectroscopy, where an emission is still visible above 650 nm, but with much weaker intensity compared to **[Fe(ImPPy)$_2$]$^+$**/**[Fe(ImPPh)$_2$]$^+$**. The lower fluorescence yield results from a shorter excited state lifetime in **[Fe(ImPPyMe)$_2$]$^{3+}$**.

With the initial motivation to prepare for the use of **[Fe(ImP)$_2$]$^+$** or **[Fe(ImPPy)$_2$]$^+$** as photosensitisers in bimetallic dyads, the present study shows how a positively charged phenylene-pyridine moiety stabilizes the excited state with a dominant 2MLCT character. As a result, the Fe(III) PS can then potentially photo-reduce an assembled photo-catalyst, provided that the charge transfer is fast enough. Further studies are indeed required to identify the processes that limit the lifetime of the ^{2}MLCT state to tens of ps. Are short-lived MC states quenching the PS excited state, as reported for Fe(II)-NHC complexes ?[4,52,53] This and other questions will be addressed in a follow-up paper reporting on a more detailed investigation of the excited state relaxation processes of these promising Fe(III) complexes.

Author Contributions

L.S. carried out the synthesis of the compounds, and analysis by NMR and Mass spectroscopy. R.S. recorded and analysed the single crystal X-ray diffraction data. L.S. investigated the complexes by steady state absorption and emission spectroscopy, as well as electrochemical investigations. J.L. carried out quantum chemical calculations. R.V. carried out the time-resolved fluorescence experiments. X.H.L. conducted the transient absorption measurements and the corresponding global analysis together with J.L.P.L. L.S. drafted the manuscript with support of J.L., R.V. and J.L.P.L. All authors read and commented on the manuscript. M.B., K.H. and S.H. supervised the project, and contributed to writing the manuscript.

Conflicts of interest

There are no conflicts to declare.

Data availability

A data availability statement (DAS) is required to be submitted alongside all articles. Please read our full guidance on data availability statements for more details and examples of suitable statements you can use.

Acknowledgements

The authors thank the ANR-DFG project "SUNHY" (ANR 21-CE50-0040 & DFG 490942819) for financial support. The Strasbourg team acknowledges funding from the ITI QMAT, through IdEx program (ANR 10 IDEX 0002) of the University of Strasbourg.

References

1. C.K. Prier, D.A. Rankic and D.W.C. MacMillan, *Chem. Rev.*, 2013, **113**(7), 5322.
2. S.B. Beil, S. Bonnet, C. Casadevall, R.J. Detz, F. Eisenreich, S.D. Glover, C. Kerzig, L. Næsborg, S. Pullen, G. Storch, N. Wei and C. Zeymer, *JACS Au*, 2024, **4**(8), 2746.
3. D.G. Nocera, *Acc. Chem. Res.*, 2012, **45**(5), 767.
4. C. Förster and K. Heinze, *Chem. Soc. Rev.*, 2020, **49**(4), 1057.
5. L.N. Satheesh, K. Achilleos, A.M. Abudayyeh and L. Troian-Gautier, *EcoEnergy*, 2025, **3**(3).
6. C. Cebrián, M. Pastore, A. Monari, X. Assfeld, P.C. Gros and S. Haacke, *Chemphyschem*, 2022, **23**(7).
7. F. Ma, Z.-M. Luo, J.-W. Wang, B.M. Aramburu-Trošelj and G. Ouyang, *Coord. Chem. Rev.*, 2024, **500**, 215529.
8. P. Dierks, Y. Vukadinovic and M. Bauer, *Inorg. Chem. Front.*, 2022, **9**(2), 206.
9. G.B. Haxel, J.B. Hedrick and G.J. Orris, *USGS*, 2002, **087-02**.
10. J.K. McCusker, *Science*, 2019, **363**(6426), 484.
11. P. Zimmer, L. Burkhardt, R. Schepper, K. Zheng, D. Gosztola, A. Neuba, U. Flörke, C. Wölper, R. Schoch, W. Gawelda, S.E. Canton and M. Bauer, *Eur. J. Inorg. Chem.*, 2018, **2018**(48), 5203.
12. J. Steube, A. Kruse, O.S. Bokareva, T. Reuter, S. Demeshko, R. Schoch, M.A. Argüello Cordero, A. Krishna, S. Hohloch, F. Meyer, K. Heinze, O. Kühn, S. Lochbrunner and M. Bauer, *Nat. Chem.*, 2023, **15**, 468.
13. J. Wellauer, B. Pfund, I. Becker, F. Meyer, A. Prescimone and O.S. Wenger, *J. Am. Chem. Soc.*, 2025, **147**(10), 8760.
14. L. Schmitz, M.A. Argüello Cordero, M.J. Al-Marri, R. Schoch, H. Egold, A. Neuba, J. Steube, B. Bracht, O.S. Bokareva, S. Lochbrunner and M. Bauer, *Inorg. Chem.*, 2025, **64**(28), 14101.
15. C.E. Johnson, J. Schwarz, M. Deegbey, O. Prakash, K. Sharma, P. Huang, T. Ericsson, L. Häggström, J. Bendix, A.K. Gupta, E. Jakubikova, K. Wärnmark and R. Lomoth, *Chem Sci*, 2023, **14**(37), 10129.

16. J. Wellauer, F. Ziereisen, N. Sinha, A. Prescimone, A. Velić, F. Meyer and O.S. Wenger, *J. Am. Chem. Soc.*, 2024, **146**(16), 11299.
17. B. Dietzek-Ivanšić, K. Heinze, S. Rau, O.S. Wenger and A. Pannwitz, *Coord. Chem. Rev.*, 2025, **526**, 216362.
18. M. Huber-Gedert, M. Nowakowsky, A. Kertem, L. Burkhardt, N. Lindner, R. Schoch, R. Herbst-Irmer, A. Neuba, L. Schmitz, T.-K. Choi, J. Kubicki, W. Gawelda and M. Bauer, *Chemistry*, 2021.
19. O.S. Wenger, *Chemistry*, 2019, **25**(24), 6043.
20. C. Li, C. Gao, J. Lan, J. You and G. Gao, *Org. Biomol. Chem.*, 2014, **12**(47), 9524.
21. F. Neese and G. Olbrich, *Chem.l Phys. Lett.*, 2002, **362**(1-2), 170.
22. F. Neese, *J Comput Chem*, 2003, **24**(14), 1740.
23. F. Neese, F. Wennmohs, A. Hansen and U. Becker, *Chem. Phys.*, 2009, **356**(1-3), 98.
24. D. Bykov, T. Petrenko, R. Izsák, S. Kossmann, U. Becker, E. Valeev and F. Neese, *Mol. Phys.*, 2015, **113**(13-14), 1961.
25. E. Caldeweyher, S. Ehlert, A. Hansen, H. Neugebauer, S. Spicher, C. Bannwarth and S. Grimme, *J Chem Phys*, 2019, **150**(15), 154122.
26. E. Caldeweyher, J.-M. Mewes, S. Ehlert and S. Grimme, *PCCP*, 2020, **22**(16), 8499.
27. M. Garcia-Ratés and F. Neese, *J Comput Chem*, 2019, **40**(20), 1816.
28. M. Garcia-Ratés and F. Neese, *J Comput Chem*, 2020, **41**(9), 922.
29. B. Helmich-Paris, B. de Souza, F. Neese and R. Izsák, *J Chem Phys*, 2021, **155**(10), 104109.
30. F. Neese, *J Comput Chem*, 2023, **44**(3), 381.
31. L. Wittmann, I. Gordiy, M. Friede, B. Helmich-Paris, S. Grimme, A. Hansen and M. Bursch, *PCCP*, 2024, **26**(32), 21379.
32. F. Neese, *WIREs Comput. Mol. Sci.*, 2025, **15**(2).
33. S. Grimme, J.G. Brandenburg, C. Bannwarth and A. Hansen, *Chem. Phys.*, 2015, **143**(5), 54107.
34. V.N. Staroverov, G.E. Scuseria, J. Tao and J.P. Perdew, *J Chem Phys*, 2003, **119**(23), 12129.
35. F. Weigend and R. Ahlrichs, *Phys. Chem. Chem. Phys.*, 2005, **7**(18), 3297.
36. E. Caldeweyher, C. Bannwarth and S. Grimme, *J Chem Phys*, 2017, **147**(3), 34112.
37. V. Barone and M. Cossi, *J. Phys. Chem. A*, 1998, **102**(11), 1995.
38. A. Dreuw and M. Head-Gordon, *J. Am. Chem. Soc.*, 2004, **126**(12), 4007.
39. T.J. Zuehlsdorff, P.D. Haynes, F. Hanke, M.C. Payne and N.D.M. Hine, *J Chem Theory Comput*, 2016, **12**(4), 1853.
40. F. Plasser, *J Chem Phys*, 2020, **152**(8), 84108.
41. G. Knizia and J.E.M.N. Klein, *Angew. Chem. Int. Ed.*, 2015, **54**(18), 5518.
42. W. Humphrey, A. Dalke and K. Schulten, *J. Mol. Graph.*, 1996, **14**, 33.
43. J. Stone, *An Efficient Library for Parallel Ray Tracing and Animation*, 1998.
44. J.D. Hunter, *Comput. Sci. Eng.*, 2007, **9**(3), 90.
45. C.R. Harris, K.J. Millman, S.J. van der Walt, R. Gommers, P. Virtanen, D. Cournapeau, E. Wieser, J. Taylor, S. Berg, N.J. Smith, R. Kern, M. Picus, S. Hoyer, M.H. van Kerkwijk, M. Brett, A. Haldane, J.F. Del Río, M. Wiebe, P. Peterson, P. Gérard-Marchant, K. Sheppard, T. Reddy, W. Weckesser, H. Abbasi, C. Gohlke and T.E. Oliphant, *Nature*, 2020, **585**(7825), 357.
46. L. Krause, R. Herbst-Irmer, G.M. Sheldrick and D. Stalke, *J Appl Crystallogr*, 2015, **48**(Pt 1), 3.
47. G.M. Sheldrick, *Acta Crystallogr. A*, 2015, **71**(Pt 1), 3.
48. S.A. Kovalenko, A.L. Dobryakov, J. Ruthmann and N.P. Ernsting, *Phys. Rev. A*, 1999, **59**(3), 2369.
49. A.L. Dobryakov, S.A. Kovalenko, A. Weigel, J.L. Pérez-Lustres, J. Lange, A. Müller and N.P. Ernsting, *Rev Sci Instrum*, 2010, **81**(11), 113106.
50. M. Kim, C.H. Ryu, D.K. You, J.H. Hong and K.M. Lee, *ACS Omega*, 2022, **7**(27), 24027.
51. R.M. Stratt and M. Maroncelli, *J. Phys. Chem.*, 1996, **100**(31), 12981.
52. L. Lindh, T. Pascher, S. Persson, Y. Goriya, K. Wärnmark, J. Uhlig, P. Chábera, P. Persson and A. Yartsev, *J. Phys. Chem. A*, 2023, **127**(48), 10210.
53. L. Lindh, P. Chábera, N.W. Rosemann, J. Uhlig, K. Wärnmark, A. Yartsev, V. Sundström and P. Persson, *Catalysts*, 2020, **10**(3), 315.

7. Conclusion

Three research projects building upon the same fundamental base complex **C** (Figure 3) were completed during this work. The first two explore the reservoir effect as an approach to enhance excited state lifetimes through the introduction of an organic chromophore, which leads to an excited state equilibrium gaining the advantages of both systems (Scheme 3). There are two major findings resulting from those projects. First, a similar excited state energy for both components is necessary to achieve the desired equilibrium. Secondly, while both components are present in the same molecule, they must be sufficiently electronically decoupled to prevent the formation of highly delocalized states. Otherwise, the low energy of these states enables fast deactivation of the system. A different work on these topics, published during the investigation of the chromophore-decorated systems, leads to similar results, where fine tuning of the excited state energies increases lifetimes even further.[39]

The third research topic applies a different approach to enable economically viable base metal photocatalytic systems. By combining both components of a homogeneous catalytic system the dependence on diffusion limited processes is reduced (Scheme 4). In this work, a preliminary study on one-component system candidates is presented. Here, the second catalytic centre is replaced by a methyl group to simulate a coordination, without obscuring the effect on the PS by introduction of various new transitions involving the second catalytic centre. The excited state landscape of a system based on complex **C** was significantly affected, leading to an inversion of LMCT and MLCT excited states.

The research presented herein shows that the framework of complex **C** can be used to significantly enhance the lifetimes of Fe(III) complexes, and that the excited state landscape can be tuned by different modifications of the backbone. Thus, this work functions as a further stepping stone on the way to sustainable and economically viable base metal photocatalysis. Future works on these topics could even combine both investigated approaches to obtain a one-component system with intermediate rerservoir to store energy obtained from absorption, that can then be provided to the catalyst in intramolecular processes (Scheme 5).

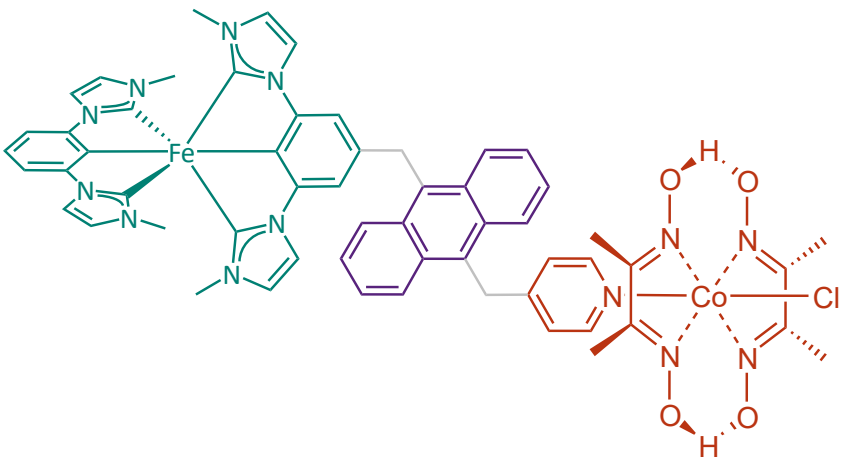

Scheme 5: Possible combination of reservoir effect and one component approach in one homogeneous catalytic system based on iron and cobalt.

8. Appendix

List of Figures and Schemes

Experimental Section

General Synthetic Procedures

All chemicals used in this work, where no synthetic procedure is pointed out, were obtained commercially from different suppliers and used without further purification. Syntheses under inter atmosphere were either carried out in an Argon Glovebox or under Schlenk conditions with Argon and a vacuum provided by a rotary vane pump (roughly 10^{-3} mbar). Utilized solvents were degassed before use, and dry solvents obtained from a MBraun SPS-800 solvent purification system were applied when necessary. For Schlenk syntheses all glassware was preheated to remove humidity. Column chromatography was either undertaken by hand or utilizing a Combiflash RF+UV (Teledyne ISCO).

Preparation of solutions utilized in spectroscopy

For electrochemical investigations, Acetonitrile (HPLC grade) was passed batchwise through a column packed with MP Biomedicals MP Alumina N-Super I that was heated to 150 °C for 2 days. The solvent was degassed by bubbling trough argon and stored under argon. Prepared solutions were degassed again by bubbling argon. For absorption and emission spectroscopy as well as TCSPC, 99.9% pure Acetonitrile (farUV/Gradient grade, ABCR) was utilized to prepare solutions, that were degassed either by bubbling trough Argon or by freeze-pump-thaw cycles right before spectra were measured.

Cyclic voltammetry

Cyclic voltammograms and square wave voltammograms were obtained from 1 mM solution of the corresponding analyte in dry, degassed acetonitrile (see above) with Tetrabutylammonium hexafluorophosphate (0.1M) as supporting electrolyte under Argon atmosphere. A three-elctrode setup consisting of a 1 mm platinum disk working electrode, a platinum wire counter electrode and a Ag/AgCl reference electrode was used in conjunction with a PGSTAT101 potentiostat (Metrohm). Ferrocene was added after each experiment to reference the observed redox processes to the $Fc^{0/+}$ redox couple. Where applicable, reversibility was evaluated using the Randles-Sevcik equation.[50]

Elemental analysis

Elemental analysis was performed on a vario MicroCube (Elementar), determining the amounts of Hydrogen, Carbon, Nitrogen and Sulfur in the sample.

Mass spectrometry

The samples were ionized by electrospray ionisation and mass spectra were recorded on a G2 quadrupole time-of-flight spectrometer (SYNAPT).

NMR spectroscopy

NMR spectroscopy was carried out on either a 500 Avance or a 700 Ascent spectrometer (Bruker). Hydrogen and Carbon spectra were referenced to the carbon or residual proton signals of the deuterated solvents. Nitrogen spectra were externally referenced against liquid ammonia. Next to standard methods, some advanced NMR techniques were applied to obtain spectra of the investigated paramagnetic complexes.[51]

Single-crystal X-ray diffraction

Single-crystal X-ray diffraction data was collected on a SMART CCD area-detector diffractometer (Bruker) with a graphite monochromator. Measurements were performed using Mo Kα radiation (λ = 0.71073 Å) at 120(2) K.

Steady-state emission spectroscopy

Solutions at 10^{-5} mol/L in dry degassed Acetonitrile (see above) were prepared and spectra were obtained on a FLS1000 spectrometer (Edinburgh Instruments). Variable temperature emission spectra were recorded with an Optistat DN cryostat (Edinburgh Instruments).

Time-correlated single-photon counting

Samples for TCSPC were prepared following the same procedure as above. The measurements were performed on a Horiba Ultima-01-DD system (Horiba Jobin Yvon GmbH). Different laser excitation sources from the same company were utilized. Measured time ranges and emission wavelengths were chosen on a case-by-case basis. Data was collected until the most intense channel reached 10000. To obtain the instrument response function, a LUDOX scattering solution in water was measured at the excitation wavelength. Decay curves were fitted using varying multi-exponential model, increasing the component number until χ^2 reached a satisfactory level.

UV-Vis absorption spectroscopy

Absorption spectra were measured on a Cary 50 (Varian) and a Lambda 465 (PerkinElmer) single-beam spectrophotometer utilizing the same sample preparation procedure pointed out above to obtain solutions at 10^{-5} mol/L. Extinction coefficients were obtained via the Beer-Lambert equation.

Transient absorption spectroscopy and time-resolved emission spectroscopy

TA and time-resolved emission spectra were recorded by varying cooperation partners. For their experimental procedures refer to the corresponding publication or its supporting information.

References

The references of the 3 publications are listed at the end of the corresponding chapters.

[1] P. Friedlingstein, R. M. Andrew, J. Rogelj, G. P. Peters, J. G. Canadell, R. Knutti, G. Luderer, M. R. Raupach, M. Schaeffer, D. P. van Vuuren et al., *Nature Geosci* **2014**, *7*, 709.

[2] C. T. A. Berger, *Surv. geophys.* **1992**, *13*, 523.

[3] M. Kotz, A. Levermann, L. Wenz, *Nature* **2024**, *628*, 551.

[4] J. Infante-Amate, E. Travieso, E. Aguilera, *Nat Commun* **2025**, *16*, 3766.

[5] H. Ritchie, P. Rosado, "Electricity Mix. Explore data on where our electricity comes from and how this is changing.", **2024**.

[6] Energy Institute, "Statistical Review of World Energy", can be found under https://www.energyinst.org/statistical-review, **2025**.

[7] H. Ritchie, P. Rosado, "Energy Mix. Explore global data on where our energy comes from, and how this is changing.", **2024**.

[8] D. M. Arias-Rotondo, J. K. McCusker, *Chem. Soc. Rev.* **2016**, *45*, 5803.

[9] C. K. Prier, D. A. Rankic, D. W. C. MacMillan, *Chem. Rev.* **2013**, *113*, 5322.

[10] D. Kim, V. Q. Dang, T. S. Teets, *Chem. Sci.* **2023**, *15*, 77.

[11] G. Thuillier, M. Hersé, D. Labs, T. Foujols, W. Peetermans, D. Gillotay, P.C. Simon & H. Mandel, *Sol. Phys.* **2003**, *214*, 1.

[12] P. Dierks, Y. Vukadinovic, M. Bauer, *Inorg. Chem. Front.* **2022**, *9*, 206.

[13] V. Balzani, S. Campagna (Eds.) *Topics in Current Chemistry*, Springer Berlin Heidelberg, Berlin, Heidelberg, **2007**.

[14] K. Ravindra, L. Bencs, R. van Grieken **2004**, *318*, 1.

[15] T. Bossi, J. Gediga, *Johns. Matthey technol. rev.* **2017**, *61*, 111.

[16] C. Förster, K. Heinze, *Chem. Soc. Rev.* **2020**, *49*, 1057.

[17] G. B. Haxel, J. B. Hedrick, G. J. Orris, *USGS* **2002**, *087-02*.

[18] S. Dutta, J. E. Erchinger, F. Strieth-Kalthoff, R. Kleinmans, F. Glorius, *Chem. Soc. Rev.* **2024**, *53*, 1068.

[19] J. Schneider, D. W. Bahnemann, *J. Phys. Chem. Lett.* **2013**, *4*, 3479.

[20] V. Artero, M. Chavarot-Kerlidou, M. Fontecave, *Angew. Chem. Int. Ed.* **2011**, *50*, 7238.

[21] a) M. Cherevatskaya, M. Neumann, S. Füldner, C. Harlander, S. Kümmel, S. Dankesreiter, A. Pfitzner, K. Zeitler, B. König, *Angew. Chem. Int. Ed.* **2012**, *51*, 4062; b) D. C. Fabry, J. Zoller, M. Rueping, *Org. Chem. Front.* **2019**, *6*, 2635.

[22] N. A. Romero, D. A. Nicewicz, *Chem. Rev.* **2016**, *116*, 10075.

[23] K. Kalyanasundaram, *Coord. Chem. Rev.* **1982**, *46*, 159.

[24] A. Juris, V. Balzani, F. Barigelletti, S. Campagna, P. Belser, A. von Zelewsky, *Coord. Chem. Rev.* **1988**, *84*, 85.

[25] David R. Lide (Ed.), *CRC Handbook of Chemistry and Physics*, **2003-2004**.

[26] F. Lafolet, J. Chauvin, M.-N. Collomb, A. Deronzier, H. Laguitton-Pasquier, J.-C. Leprêtre, J.-C. Vial, B. Brasme, *Phys. Chem. Chem. Phys.* **2003**, *5*, 2520.

[27] a) J. K. McCusker, *Science* **2019**, *363*, 484; b) M. Kaupp, *J. Comput. Chem.* **2007**, *28*, 320.

[28] Y. Liu, P. Persson, V. Sundström, K. Wärnmark, *Acc. Chem. Res.* **2016**, *49*, 1477.

[29] a) W. Zhang, R. Alonso-Mori, U. Bergmann, C. Bressler, M. Chollet, A. Galler, W. Gawelda, R. G. Hadt, R. W. Hartsock, T. Kroll et al., *Nature* **2014**, *509*, 345; b) C. Sousa, C. de Graaf, A. Rudavskyi, R. Broer, J. Tatchen, M. Etinski, C. M. Marian, *Chem. Eur. J.* **2013**, *19*, 17541.

[30] P. Chábera, K. S. Kjaer, O. Prakash, A. Honarfar, Y. Liu, L. A. Fredin, T. C. B. Harlang, S. Lidin, J. Uhlig, V. Sundström et al., *J Phys Chem Lett* **2018**, *9*, 459.

[31] a) P. Dierks, A. Kruse, O. S. Bokareva, M. J. Al-Marri, J. Kalmbach, M. Baltrun, A. Neuba, R. Schoch, S. Hohloch, K. Heinze et al., *Chem. Commun.* **2021**, *57*, 6640; b) T. Jiang, Y. Bai, P. Zhang, Q. Han, D. B. Mitzi, M. J. Therien, *Proc. Natl. Acad. Sci. USA* **2020**, *117*, 20430; c) W. Leis, M. A. Argüello Cordero, S. Lochbrunner, H. Schubert, A. Berkefeld, *J. Am. Chem. Soc.* **2022**, *144*, 1169.

[32] K. S. Kjær, N. Kaul, O. Prakash, P. Chábera, N. W. Rosemann, A. Honarfar, O. Gordivska, L. A. Fredin, K.-E. Bergquist, L. Häggström et al., *Science* **2019**, *363*, 249.

[33] Y. Liu, T. Harlang, S. E. Canton, P. Chábera, K. Suárez-Alcántara, A. Fleckhaus, D. A. Vithanage, E. Göransson, A. Corani, R. Lomoth et al., *Chem. Commun.* **2013**, *49*, 6412.

[34] J. Steube, A. Kruse, O. S. Bokareva, T. Reuter, S. Demeshko, R. Schoch, M. A. Argüello Cordero, A. Krishna, S. Hohloch, F. Meyer et al., *Nat. Chem.* **2023**, *15*, 468.

[35] C. E. Johnson, J. Schwarz, M. Deegbey, O. Prakash, K. Sharma, P. Huang, T. Ericsson, L. Häggström, J. Bendix, A. K. Gupta et al., *Chem. Sci.* **2023**, *14*, 10129.

[36] B. N. Figgis, M. A. Hitchman, *Ligand field theory and its applications*, Wiley-VCH, New York, N.Y., Chichester, **2000**.

[37] N. Sakander, A. Ahmed, B. Rasool, Mukherjee, Debaraj, Takashiro Akitsu, *Electrophile and Lewis Acid*. *An Overview of N-heterocyclic carbene: Properties and Applications*, IntechOpen, Lodon, **2023**.

[38] P. Chábera, Y. Liu, O. Prakash, E. Thyrhaug, A. E. Nahhas, A. Honarfar, S. Essén, L. A. Fredin, T. C. B. Harlang, K. S. Kjær et al., *Nature* **2017**, *543*, 695.

[39] J. Wellauer, B. Pfund, I. Becker, F. Meyer, A. Prescimone, O. S. Wenger, *J. Am. Chem. Soc.* **2025**, *147*, 8760.

[40] Bernard Valeur, Mário Nuno Berberan-Santos, *Molecular Fluorescence*. *Principles and Applications*, Wiley-VCH, Weinheim, **2012**.

[41] D. S. Tyson, F. N. Castellano, *J. Phys. Chem. A* **1999**, *103*, 10955.

[42] D. S. Tyson, J. Bialecki, F. N. Castellano, *Chem. Commun.* **2000**, 2355.

[43] A. F. Morales, G. Accorsi, N. Armaroli, F. Barigelletti, S. J. A. Pope, M. D. Ward, *Inorg. Chem.* **2002**, *41*, 6711.

[44] P. Dierks, A. Päpcke, O. S. Bokareva, B. Altenburger, T. Reuter, K. Heinze, O. Kühn, S. Lochbrunner, M. Bauer, *Inorg. Chem.* **2020**, *59*, 14746.

[45] M. Montalti, J. Michl, V. Balzani, *Handbook of photochemistry*, Taylor & Francis, Boca Raton, **2006**.

[46] J. C. Scaiano, *Chem. Soc. Rev.* **2023**, *52*, 6330.

[47] a) T. Kowacs, Q. Pan, P. Lang, L. O'Reilly, S. Rau, W. R. Browne, M. T. Pryce, A. Huijser, J. G. Vos, *Faraday Discuss.* **2015**, *185*, 143; b) E. Rousset, D. Chartrand, I. Ciofini, V. Marvaud, G. S. Hanan, *Chem. Commun.* **2015**, *51*, 9261.

[48] M. Huber-Gedert, M. Nowakowsky, A. Kertem, L. Burkhardt, N. Lindner, R. Schoch, R. Herbst-Irmer, A. Neuba, L. Schmitz, T.-K. Choi et al., *Chem. Eur. J.* **2021**, *27*, 9905.
[49] P. Zimmer, L. Burkhardt, R. Schepper, K. Zheng, D. Gosztola, A. Neuba, U. Flörke, C. Wölper, R. Schoch, W. Gawelda et al., *Eur. J. Inorg. Chem.* **2018**, *2018*, 5203.
[50] a) J. E. B. Randles, *Trans. Faraday Soc.* **1948**, *44*, 327; b) N. Elgrishi, K. J. Rountree, B. D. McCarthy, E. S. Rountree, T. T. Eisenhart, J. L. Dempsey, *J. Chem. Educ.* **2018**, *95*, 197.
[51] a) M. Enders, *Assigning and Understanding NMR Shifts of Paramagnetic Metal Complexes*, Wiley-VCH, Weinheim, **2011**; b) J. Novotny, S. Komorovsky, R. Marek, *Acc. Chem. Res.* **2024**, *57*, 1467.

Publication Licenses

Licenses for republication of the published works (Chapters 4 and 5) in this thesis were obtained and are shown below

AMERICAN CHEMICAL SOCIETY LICENSE
TERMS AND CONDITIONS

Mar 13, 2026

This Agreement between Lennart Schmitz ("You") and American Chemical Society ("American Chemical Society") consists of your license details and the terms and conditions provided by American Chemical Society and Copyright Clearance Center.

License Number	6226920131932
License date	Mar 13, 2026
Licensed Content Publisher	American Chemical Society
Licensed Content Publication	Inorganic Chemistry
Licensed Content Title	Chromophore Induced Effects in Iron(III) Complexes
Licensed Content Author	Lennart Schmitz, Miguel A. Argüello Cordero, Mohammed J. Al-Marri, et al
Licensed Content Date	Jul 1, 2025
Licensed Content Volume	64
Licensed Content Issue	28
Volume number	64
Issue number	28
Type of Use	Thesis/Dissertation

Requestor type	Author (original work)
Format	Print and Electronic
Portion	Full article
Title of new work	Novel approaches for tuning iron photosensitizers: Exploring the reservoir effect and one component systems
Institution name	University of Paderborn
Expected presentation date	May 2026
The Requesting Person / Organization to Appear on the License	Lennart Schmitz
Requestor Location	Mr. Lennart Schmitz Alte Brauerei 3 Paderborn, 33098 Germany
Payment Type	Invoice
Email Address	lennart.schmitz@medionmail.com
Billing Address	Mr. Lennart Schmitz Alte Brauerei 3 Paderborn, Germany 33098
Total	0.00 USD
Terms and Conditions	

Sales Operations
Thomas Graham House
Science Park, Milton Road
Cambridge CB4 0WF, UK

Tel +44 (0) 1223 420066

Email contracts-copyright@rsc.org

www.rsc.org

Permission Request Form for RSC Material

To request permission to use material from material published by The Royal Society of Chemistry (RSC), please complete and return this form.

From: Name: Lennart Schmitz E-mail: Lennart.Schmitz@UPB.de

Address: Alte Brauerei 3, 33098 Paderborn, Germany

I am preparing the following work for publication:

Article/Chapter Title	Novel approaches for tuning iron photosensitizers:Exploring the reservoir effect and one component systems
Journal/Book Title	Thesis/Dissertation
Editor/Author(s)	Lennart Schmitz
Publisher	University of Paderborn

I would very much appreciate your permission to use the following material:

Journal/Book Title	Reservoir effect in bichromophoric FeIII complexes with a methylene bridge
Article/Chapter Title	
RSC Editor/Author(s)	
DOI	https://doi.org/10.1039/D5DT02915E
Year of Publication	2026
Description of Material	This publication is part of my PhD studies, and i want to publish it in my thesis
Page(s)	Full article

I will acknowledge the original source as specified at the https://rsc.li/permissions.

Signed: Date: 10/03/2026

The Royal Society of Chemistry hereby grants permission for the use of the material specified above in the work described and in all subsequent editions of the work for distribution throughout the world, in all media including electronic and microfilm. You may use the material in conjunction with computer-based electronic and information retrieval systems, grant permissions for photocopying, reproductions and reprints, translate the material and to publish the translation, and authorise document delivery and abstracting and indexing services. Please note that if the material specified above or any part of it appears with credit or acknowledgement to a third party then you must also secure permission from that third party before reproducing that material. The Royal Society of Chemistry is a signatory to the STM Guidelines on Permissions (available on request).

Signed: DocuSigned by: Becky Roberts C0B8BD4FBFD54CA... Date: 11/3/2026

Supplementary Information

The supplementary information for the presented works is provided below. For further data please consult the respective publisher websites.

Supporting Information

Chromophore induced effects in Iron(III) complexes

*Lennart Schmitz[a], Miguel A. Argüello Cordero[b], Mohammed J. Al-Marri[d], Roland Schoch[a], Hans Egold[a], Adam Neuba[a], Jakob Steube[a], Bastian Bracht[a], Olga S. Bokareva[b, c], Stefan Lochbrunner[b] and Matthias Bauer[a]**

[a] Faculty of Science, Chemistry Department and Center for Sustainable Systems Design, Paderborn University, 33098 Paderborn, Germany

[b] Institute of Physics and Department of Life, Light and Matter, University of Rostock, 18051 Rostock, Germany

[c] Institute of Chemistry, University of Rostock, Albert-Einstein-Str. 27, 18057 Rostock, Germany and Leibniz Institute for Catalysis, Albert-Einstein-Str. 29A, 18057 Rostock, Germany

[d] Department of Chemical Engineering, Qatar University, Doha, Qatar

* Matthias.Bauer@uni-paderborn.de

Contents

Calculations

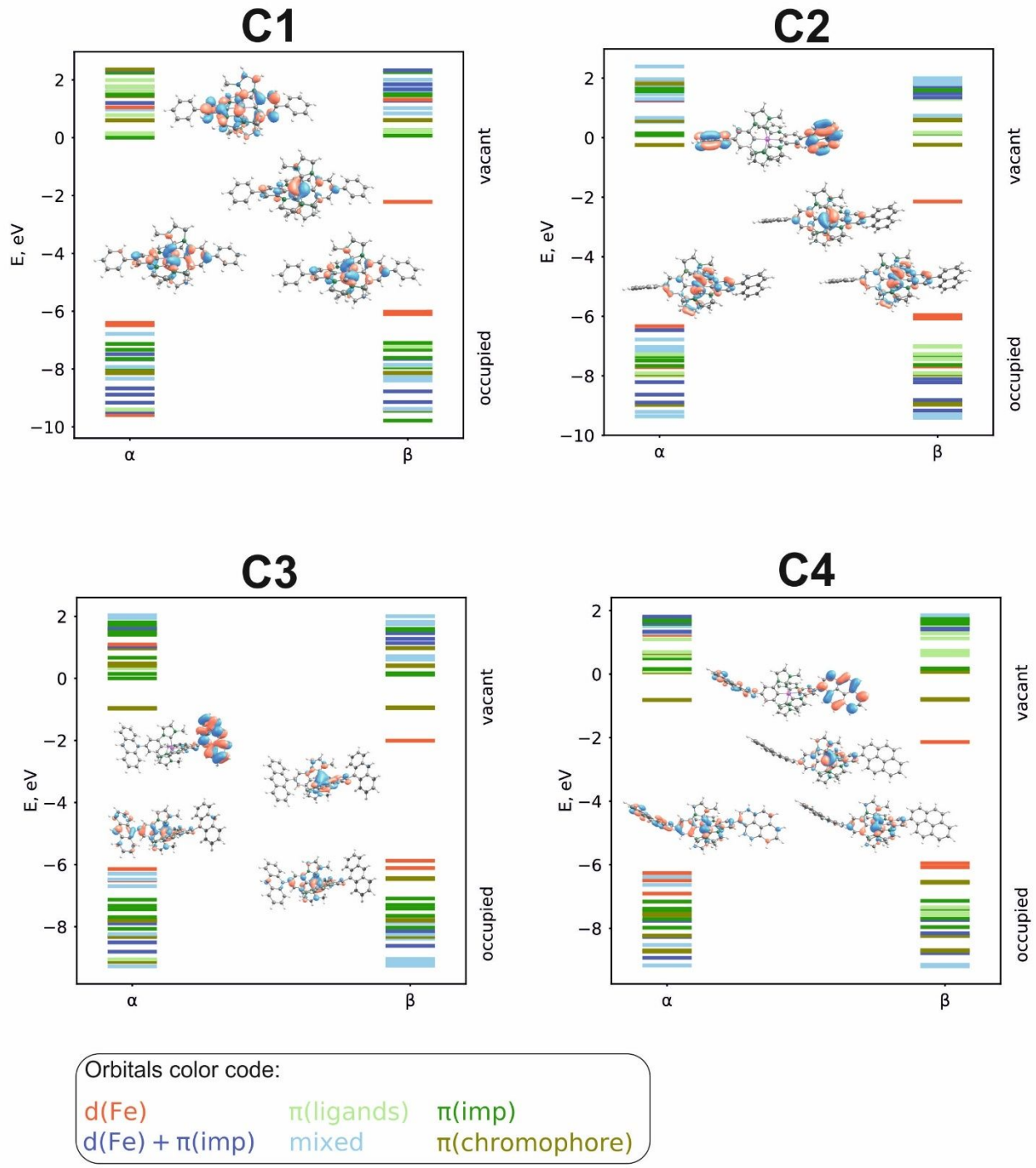

*Figure S1: Molecular orbital Figures of **C1-C4** The localization of orbitals is shown with different color codes. The shapes of all α and β HOMOs and LUMOs are shown as insets.*

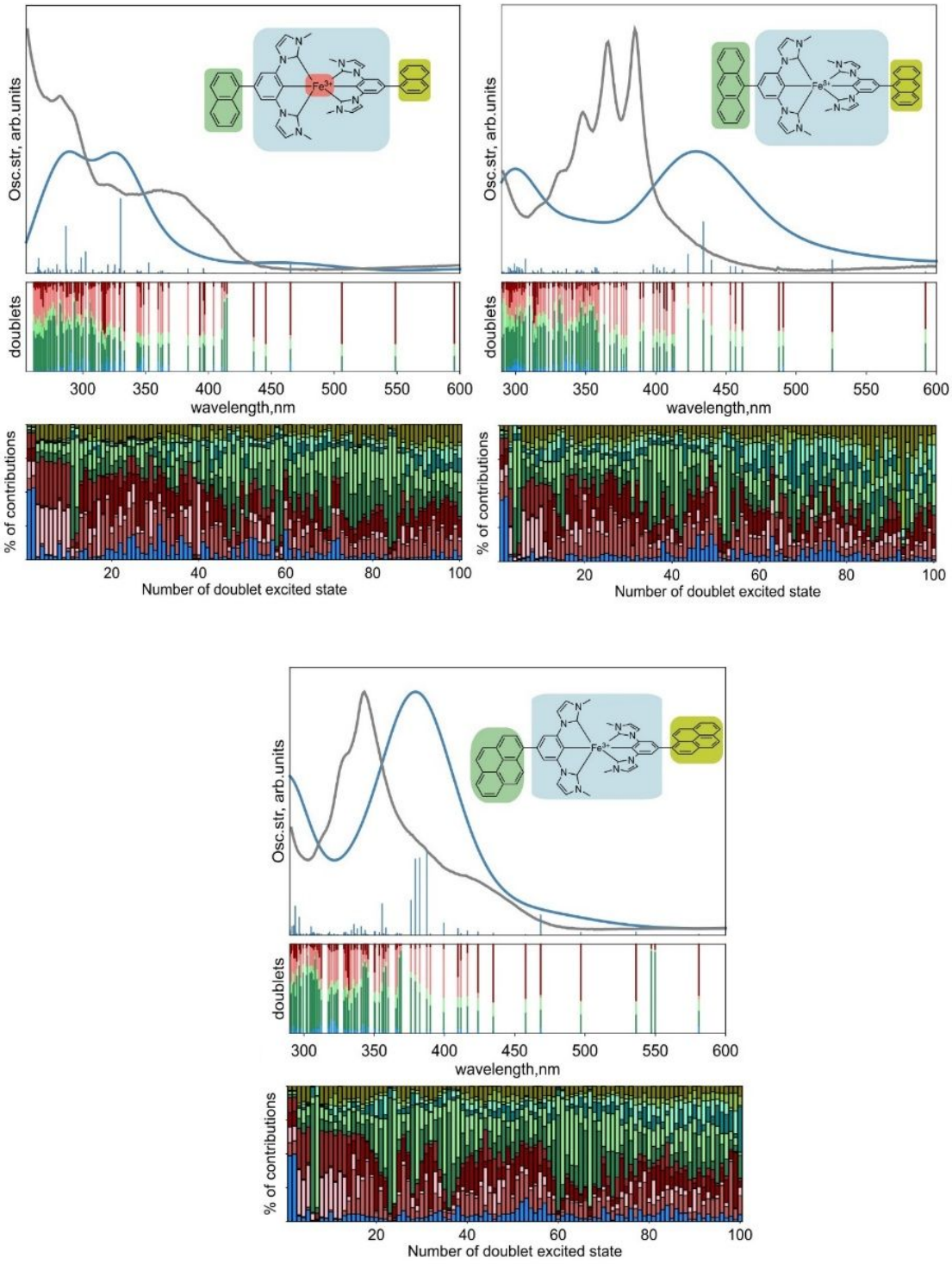

*Figure S2: Computed absorption spectra of **C2-C4** as well as assignment and fragmentation according to the clustering analysis (the color code is the same as in the main text).*

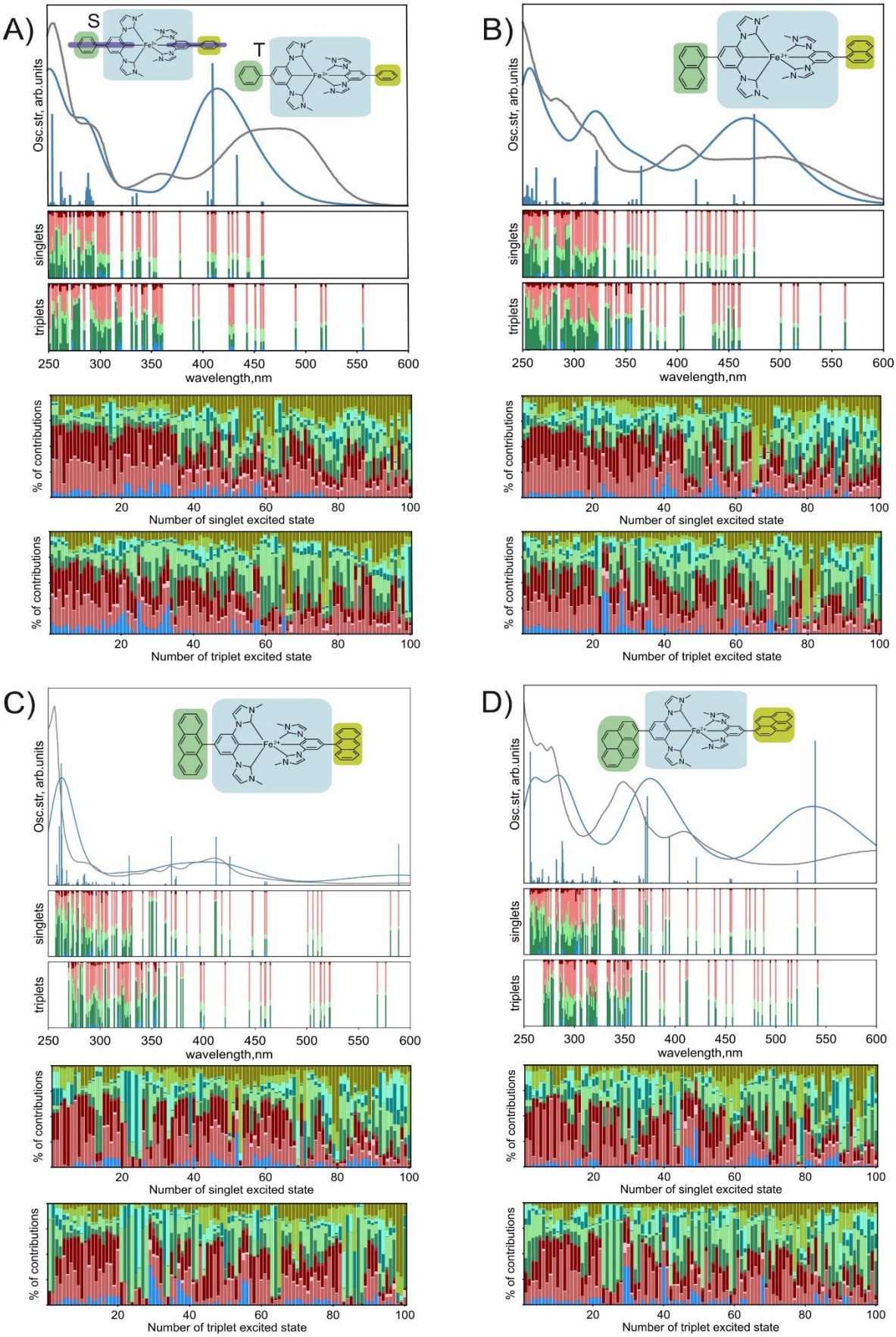

Figure S3: Computed absorption spectra of reduced Fe(II) species ***C2^0-C4^0*** *(Panels A (C1), B (C2), C (C3) and D (C4)) as well as assignment and fragmentation according to the clustering analysis (the color code is the same as in the main text).*

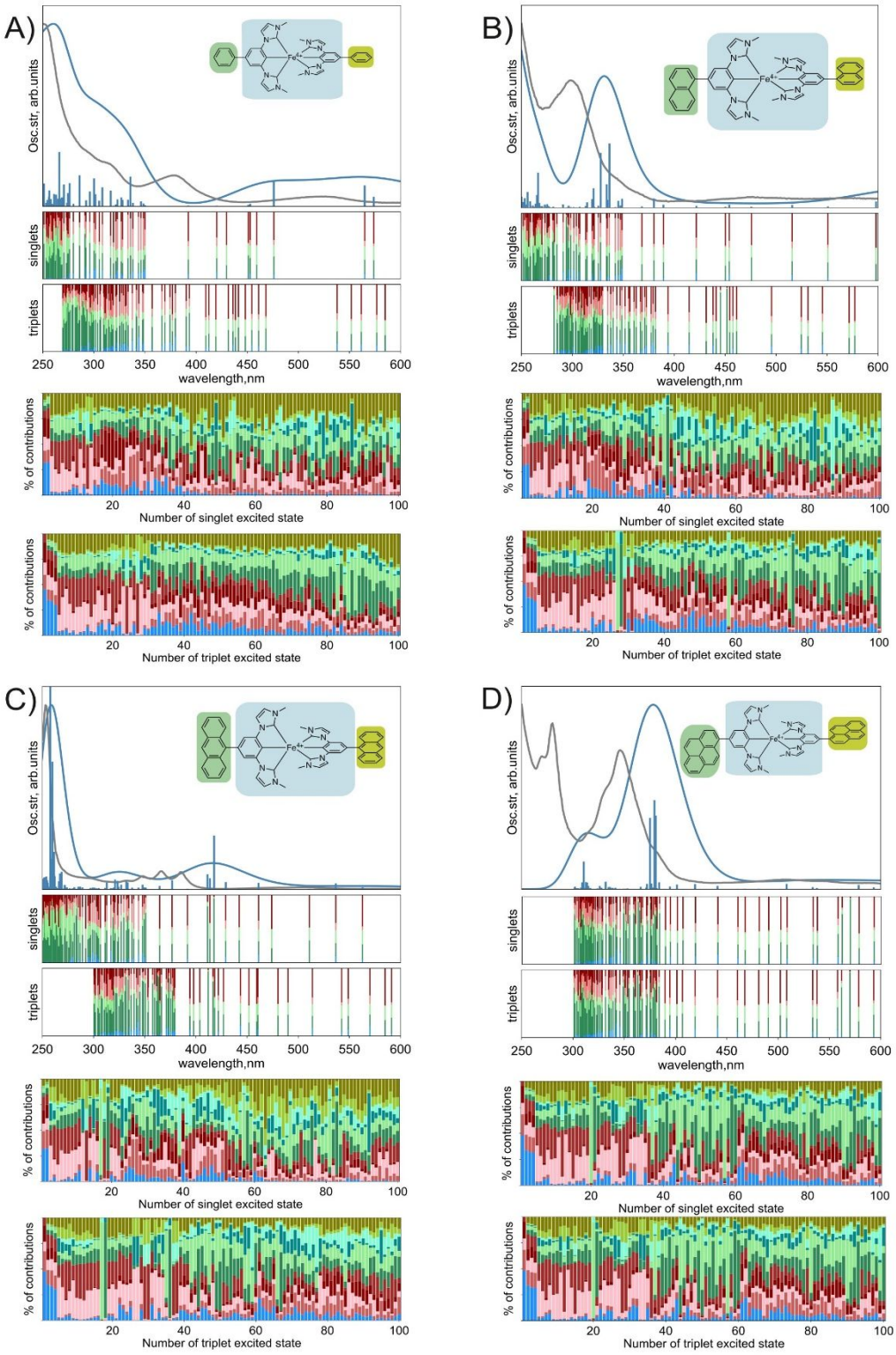

Figure S4: Computed absorption spectrum of oxidized Fe(IV) species ***C2*** $^{2+}$*-****C4*** $^{2+}$ *(Panels A (C1), B (C2), C (C3) and D (C4)) as well as assignment and fragmentation according to the clustering analysis (the color code is the same as in the main text).*

Electrochemistry

The reversibility of the Fe(II)/Fe(III) and Fe(III)/Fe(IV) transitions was investigated by applying the Randles-Sevcik equation and the Nicholson criterion.

Electrochemical data **C1**

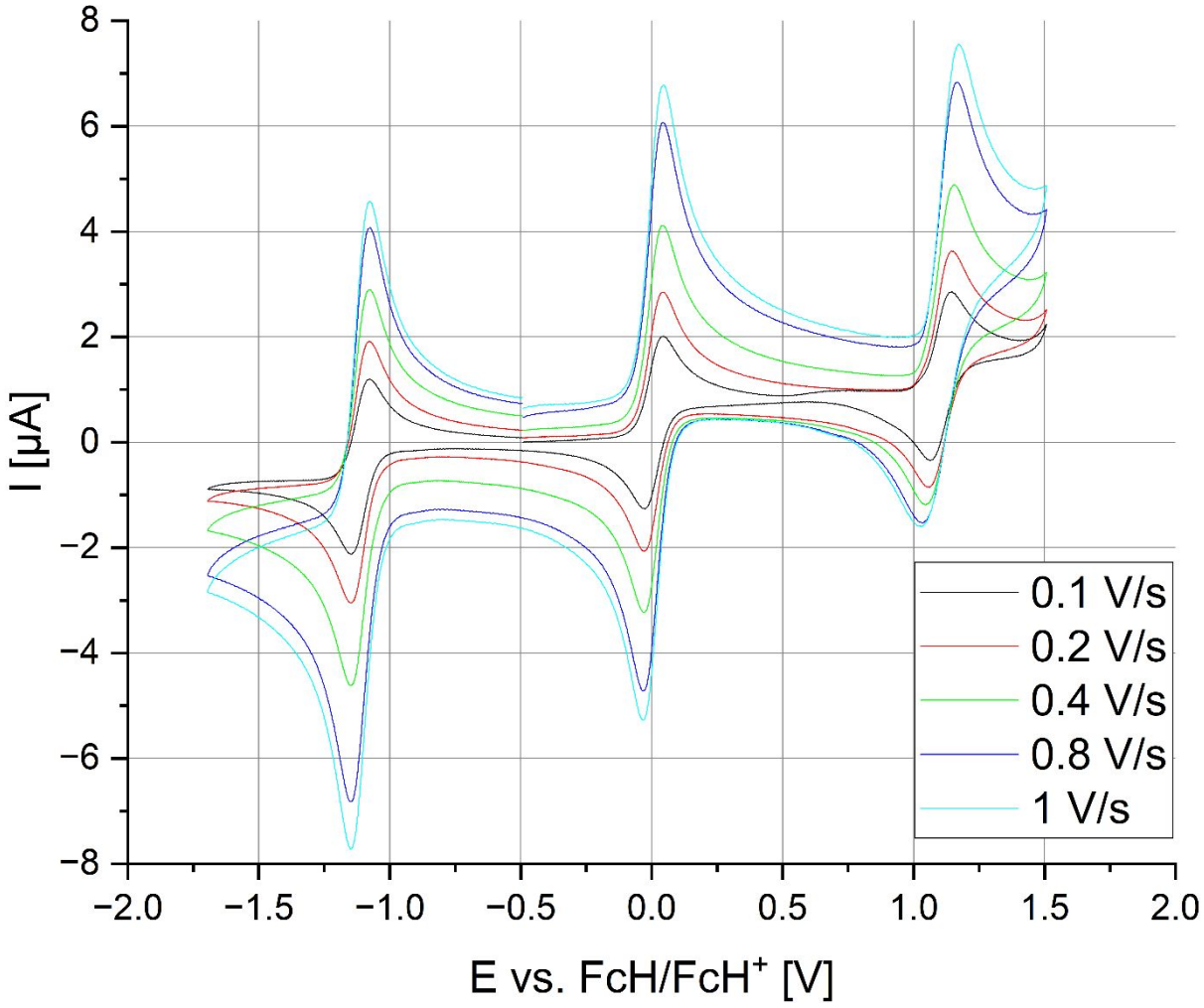

*Figure S5: Cyclic voltammograms of the reversible oxidations/reduciton of **C1** at $E_{1/2}$=-1.11 V, $E_{1/2}$=0.01 V and $E_{1/2}$=1.11 V vs. FcH/FcH$^+$at different scan rates. The diagnostic criterion of Nicholson is confirmed for the first two transitions.*

*Table SS1: Electrochemical data for the reversible oxidation of **C1** at $E_{1/2}$=0.01 V*

Scan rate	[V/s]	0.1	0.2	0.4	0.8	1
E_{cat}	[V]	-0.02	-0.02	-0.02	-0.02	-0.02
E_{An}	[V]	0.05	0.05	0.04	0.05	0.05
$E_{1/2}$	[V]	0.01	0.01	0.01	0.01	0.01
ΔE	[V]	0.07	0.07	0.06	0.07	0.07
I_{cat}	[µA]	1.77	2.44	3.42	4.77	5.29
I_{an}	[µA]	1.72	2.51	3.60	5.12	5.74
I_{an}/I_{cat}	[-]	0.97	1.03	1.05	1.07	1.09

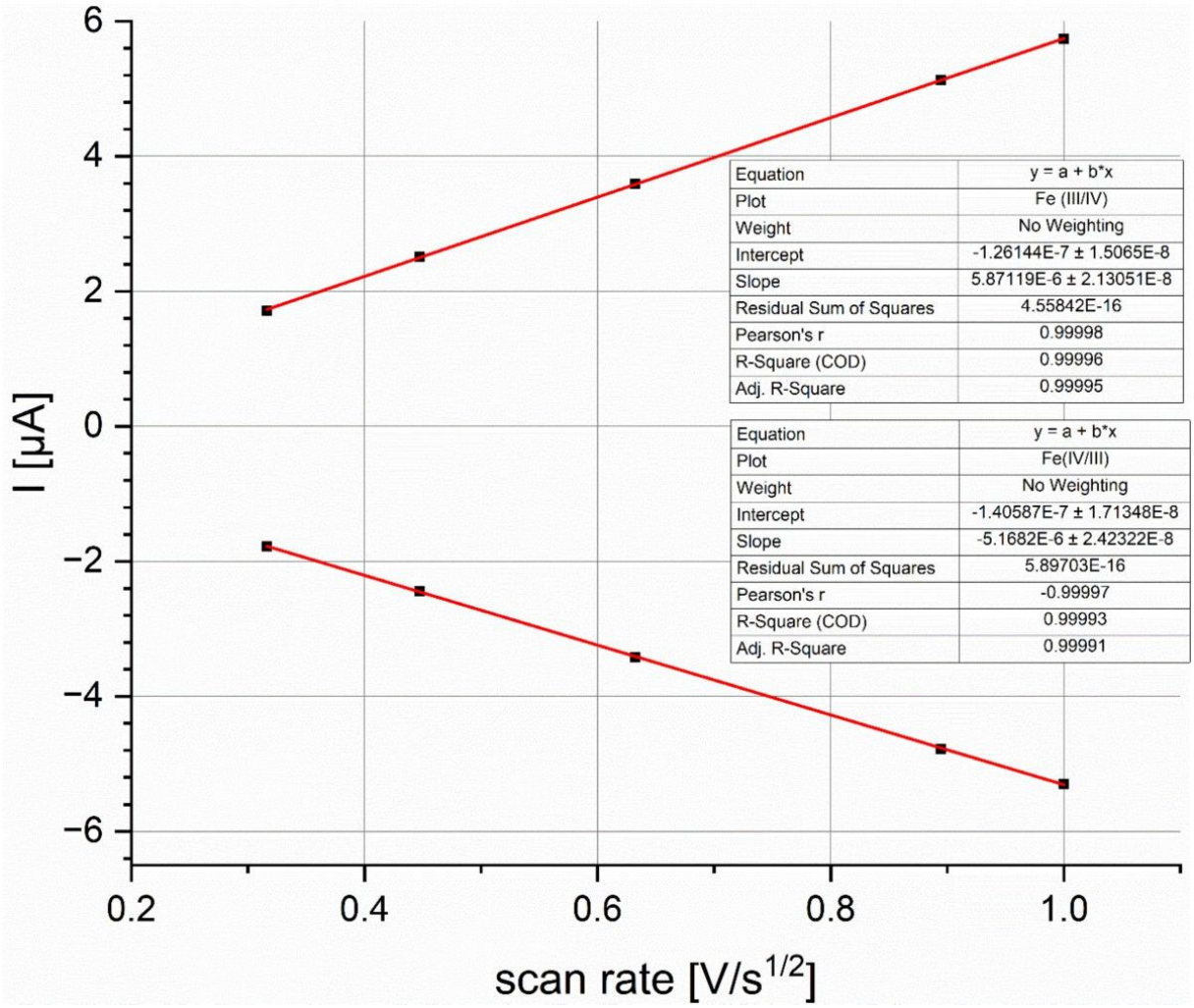

*Figure S6: Linear dependence of forward current peaks I_{an} and I_{cat} vs. the square root of the scan rate for the reversible oxidation of **C1** at $E_{1/2}$=0.01 V vs. FcH/FcH+.*

*Table S2: Electrochemical data for the reversible reductionn of **C1** at $E_{1/2}$=-1.11 V*

Scan rate	[V/s]	0.1	0.2	0.4	0.8	1
E_{cat}	[V]	-1.14	-1.14	-1.14	-1.14	-1.14
E_{An}	[V]	-1.07	-1.07	-1.07	-1.07	-1.07
$E_{1/2}$	[V]	-1.11	-1.11	-1.11	-1.11	-1.11
ΔE	[V]	0.07	0.07	0.07	0.07	0.07
I_{cat}	[µA]	1.74	2.51	3.59	5.13	5.60
I_{an}	[µA]	1.74	2.51	3.60	5.13	5.74
I_{an}/I_{cat}	[-]	1.00	1.00	1.00	1.00	1.03

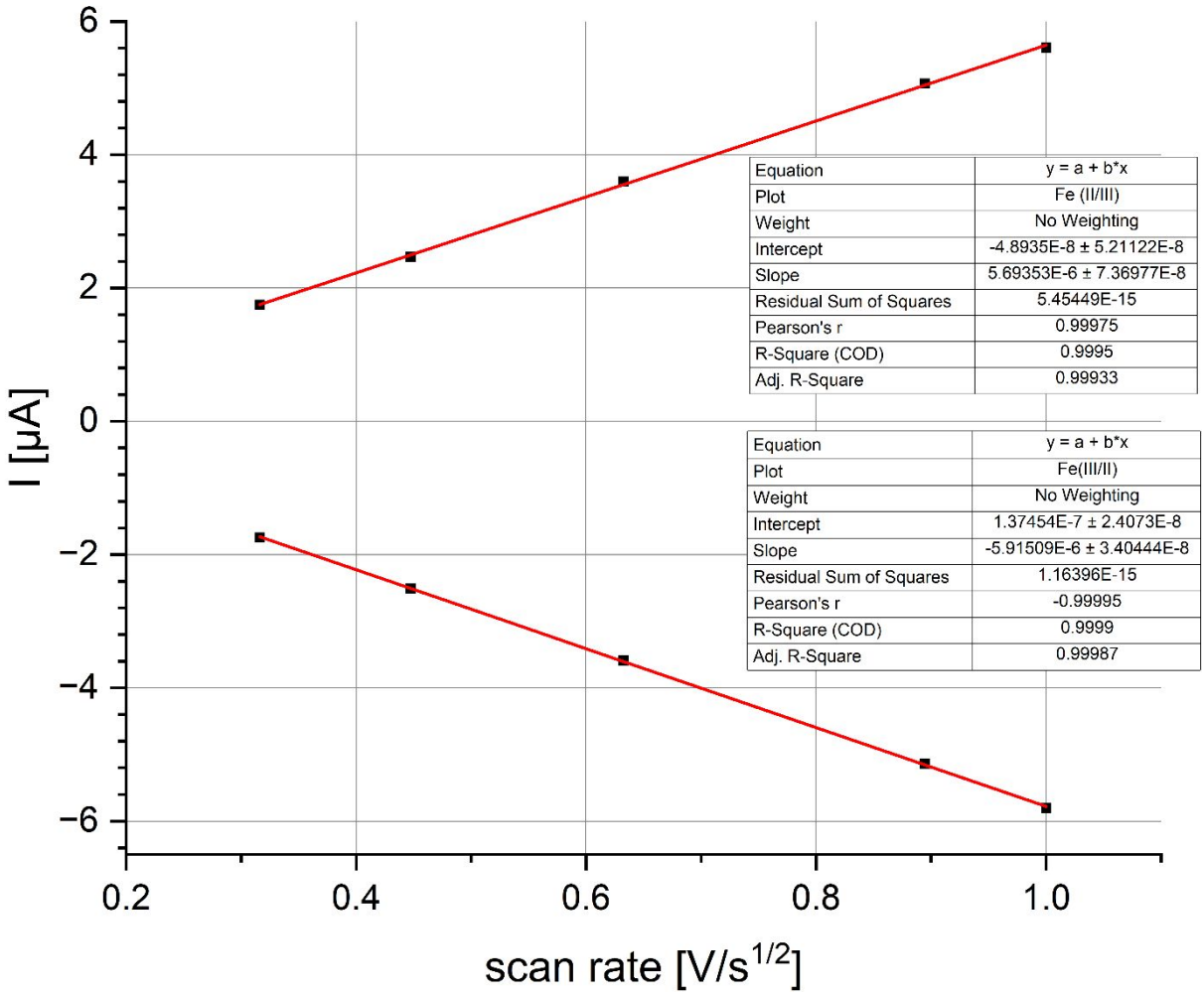

*Figure S7: Linear dependence of forward current peaks I_{an} and I_{cat} vs. the square root of the scan rate for the reversible reduction of **C1** at $E_{1/2}$=-1.11 V vs. FcH/FcH+.*

Electrochemical data **C2**

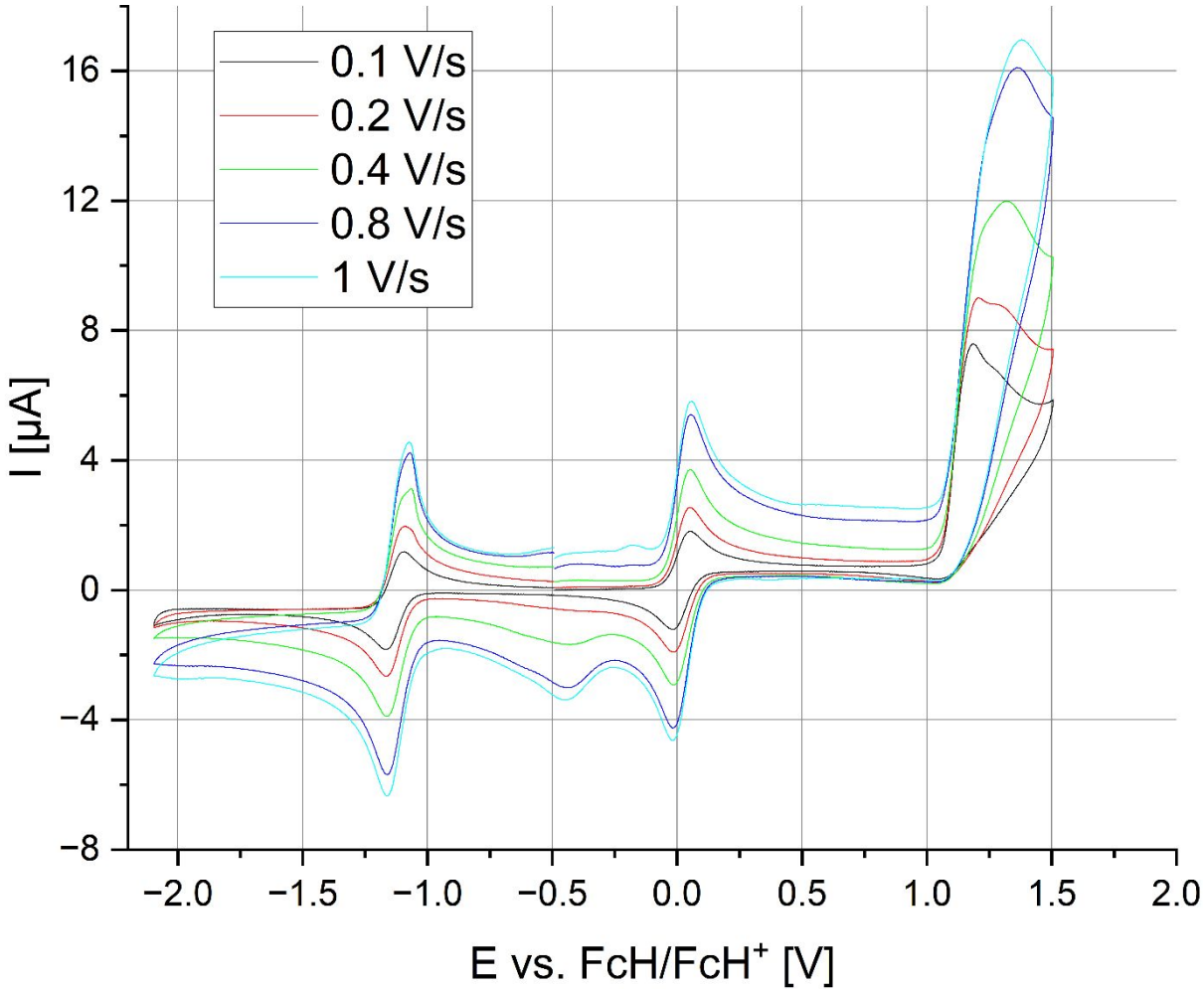

*Figure S8: Cyclic voltammograms of the reversible oxidations/reduciton of **C2** at $E_{1/2}$=-1.11 V, $E_{1/2}$=0.01 V and $E_{1/2}$=1.11 V vs. FcH/FcH⁺ at different scan rates. The diagnostic criterion of Nicholson is confirmed for the first two transitions.*

*Table S3: Electrochemical data for the reversible reduction of **C2** at $E_{1/2}$=-1.11 V*

Scan rate	[V/s]	0.1	0.2	0.4	0.8	1
E_{cat}	[V]	-1.16	-1.16	-1.16	-1.16	-1.14
E_{An}	[V]	-1.09	-1.09	-1.06	-1.06	-1.06
$E_{1/2}$	[V]	-1.13	-1.13	-1.11	-1.11	-1.10
ΔE	[V]	0.07	0.07	0.10	0.10	0.08
I_{cat}	[µA]	1.57	2.26	2.95	3.99	4.32
I_{an}	[µA]	1.62	2.36	3.55	4.59	5.14
I_{an}/I_{cat}	[-]	0.97	0.96	0.83	0.87	0.84

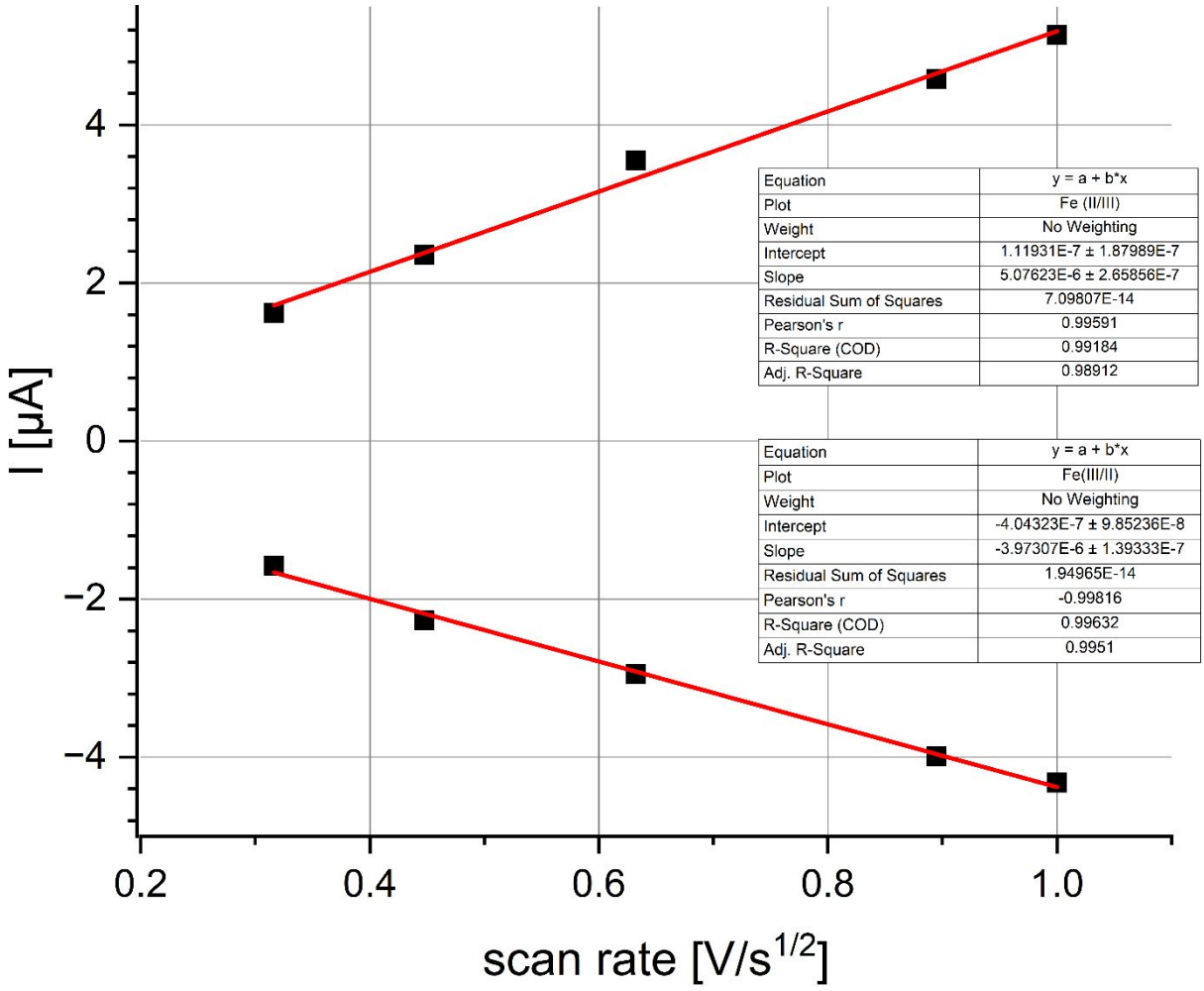

*Figure S9 Linear dependence of forward current peaks I_{an} and I_{cat} vs. the square root of the scan rate for the reversible reduction of **C2** at $E_{1/2}$=-1.11 V vs. FcH/FcH+.*

*Table S4: Electrochemical data for the reversible oxidation of **C2** at $E_{1/2}$= 0.02 V*

Scan rate	[V/s]	0.1	0.2	0.4	0.8	1
E_{cat}	[V]	-0.02	-0.01	0.00	-0.01	-0.01
E_{An}	[V]	0.05	0.05	0.06	0.05	0.06
$E_{1/2}$	[V]	0.01	0.02	0.03	0.02	0.02
ΔE	[V]	0.07	0.06	0.06	0.06	0.07
I_{cat}	[µA]	1.66	2.24	2.61	3.60	3.86
I_{an}	[µA]	1.62	2.29	3.23	4.42	4.24
I_{an}/I_{cat}	[-]	1.02	0.98	0.81	0.81	0.91

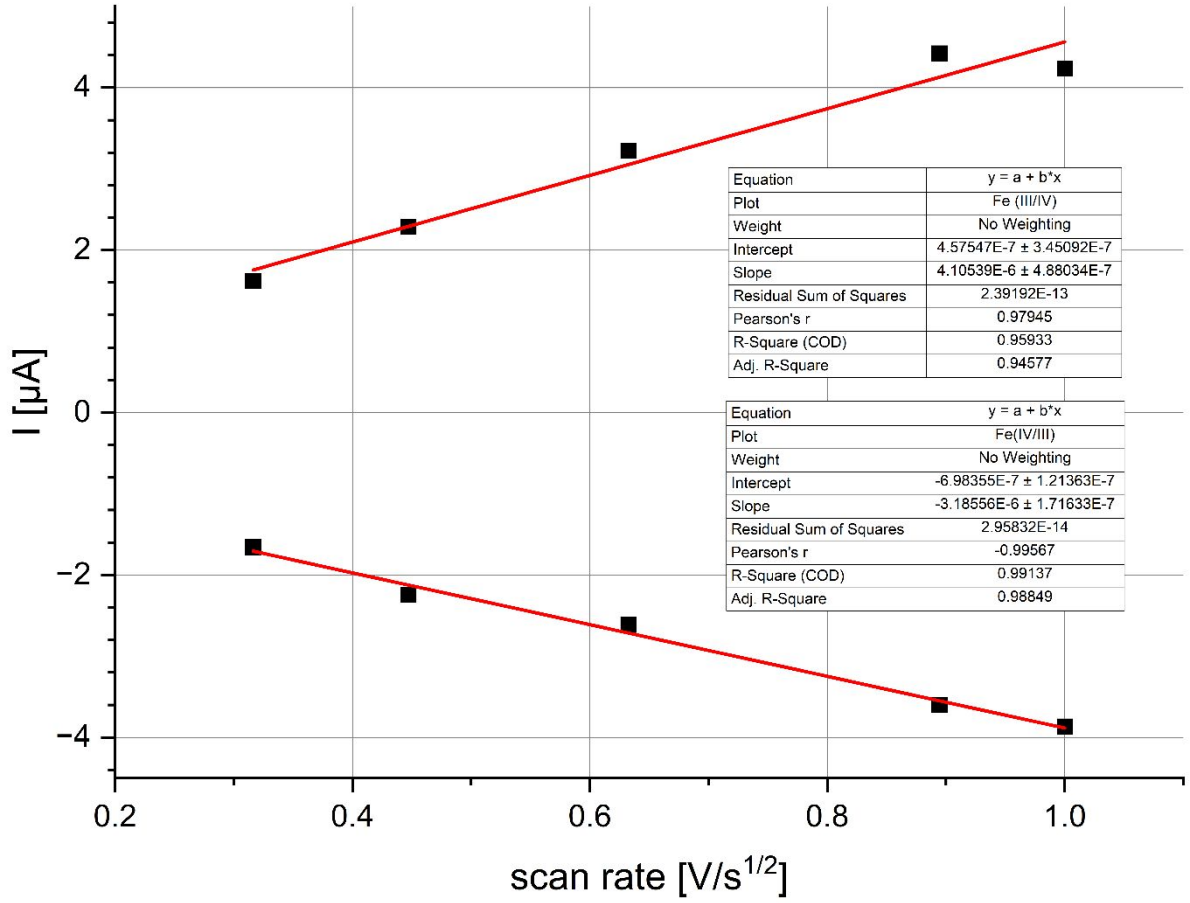

*Figure S10: Linear dependence of forward current peaks I_{an} and I_{cat} vs. the square root of the scan rate for the reversible oxidation of **C2** at $E_{1/2}$= 0.02V vs. FcH/FcH+.*

Electrochemical data **C3**

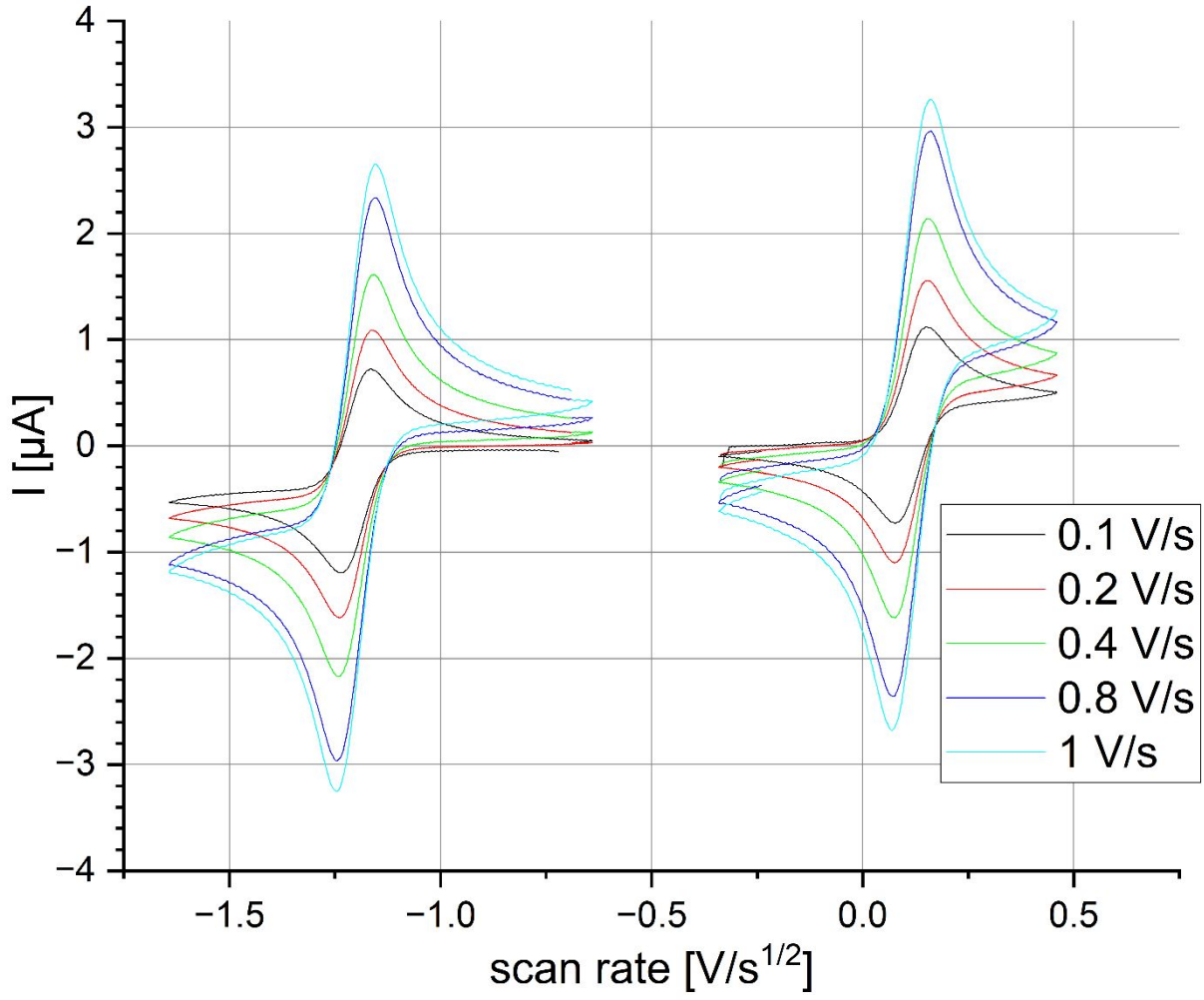

*Figure S11: Cyclic voltammograms of the reversible oxidation/reduction of **C3** at $E_{1/2}$=-1.20V, $E_{1/2}$=0.11V vs. FcH/FcH+ at different scan rates. The diagnostic criterion of Nicholson is confirmed for the first two transitions.*

*Table S5: Electrochemical data for the reversible reduction of **C3** at $E_{1/2}$=-1.20 V*

Scan rate	[V/s]	0.1	0.2	0.4	0.8	1
E_{cat}	[V]	-1.16	-1.16	-1.16	-1.16	-1.15
E_{An}	[V]	-1.23	-1.24	-1.24	-1.24	-1.24
$E_{1/2}$	[V]	-1.20	-1.20	-1.20	-1.20	-1.20
ΔE	[V]	-0.07	-0.08	-0.08	-0.08	-0.09
I_{cat}	[µA]	**0.99**	1.37	1.90	2.67	2.99
I_{an}	[µA]	1.02	1.41	1.94	2.72	3.09
I_{an}/I_{cat}	[-]	0.97	0.97	0.98	0.98	0.97

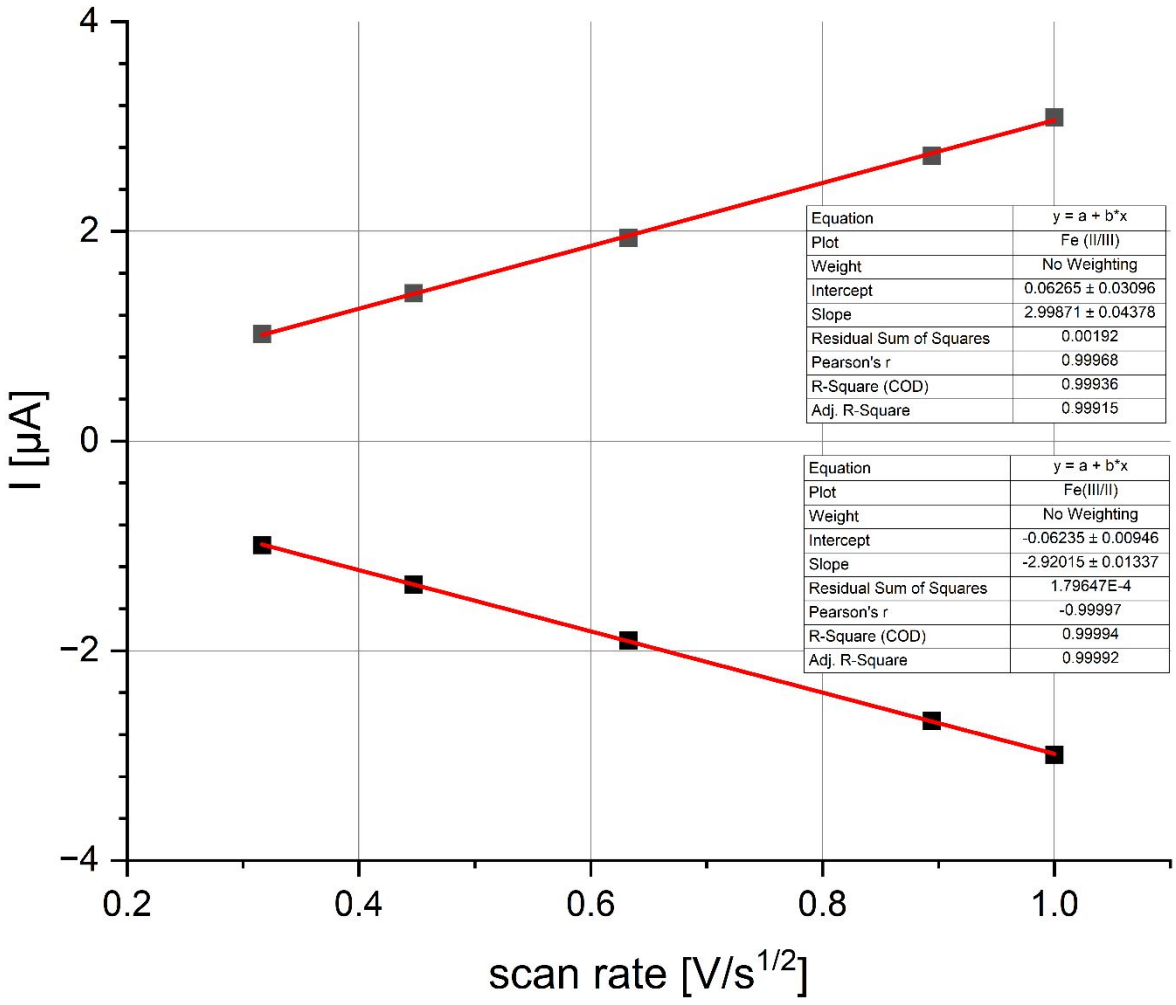

*Figure S12: Linear dependence of forward current peaks I_{an} and I_{cat} vs. the square root of the scan rate for the reversible reduction of **C3** at $E_{1/2}$= -1.20V vs. FcH/FcH+.*

*Table S6: Electrochemical data for the reversible reduction of **C3** at $E_{1/2}$= 0.11 V*

Scan rate	[V/s]	0.1	0.2	0.4	0.8	1
E_{cat}	[V]	0.08	0.08	0.08	0.08	0.07
E_{An}	[V]	0.15	0.15	0.15	0.16	0.16
$E_{1/2}$	[V]	0.11	0.11	0.11	0.12	0.11
ΔE	[V]	0.07	0.07	0.07	0.08	0.09
I_{cat}	[µA]	0.97	1.37	1.96	2.75	3.08
I_{an}	[µA]	0.91	1.3	1.82	2.57	2.88
I_{an}/I_{cat}	[-]	1.07	1.05	1.08	1.07	1.07

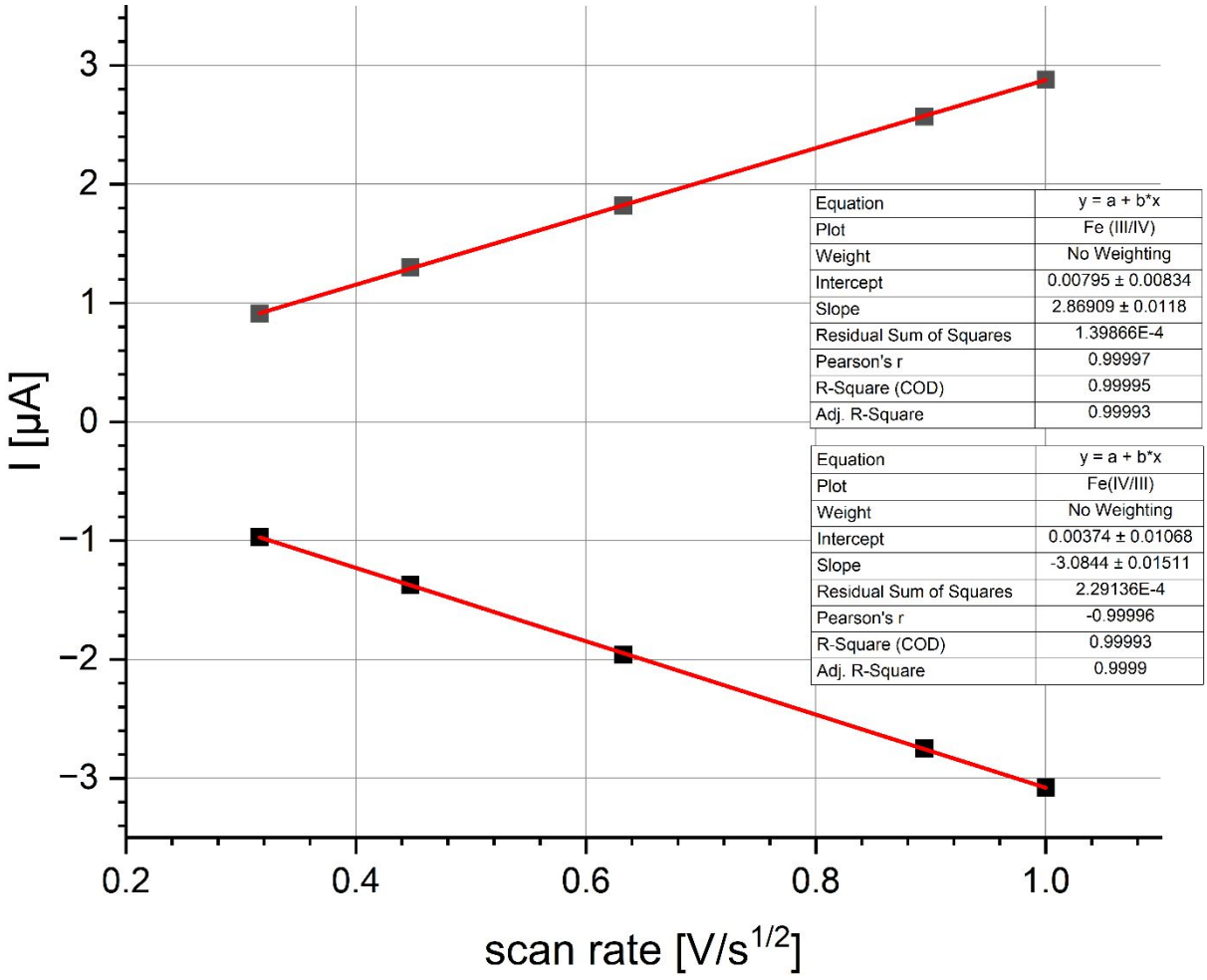

*Figure S13: Linear dependence of forward current peaks I_{an} and I_{cat} vs. the square root of the scan rate for the reversible oxidation of **C3** at $E_{1/2}$= 0.11V vs. FcH/FcH+.*

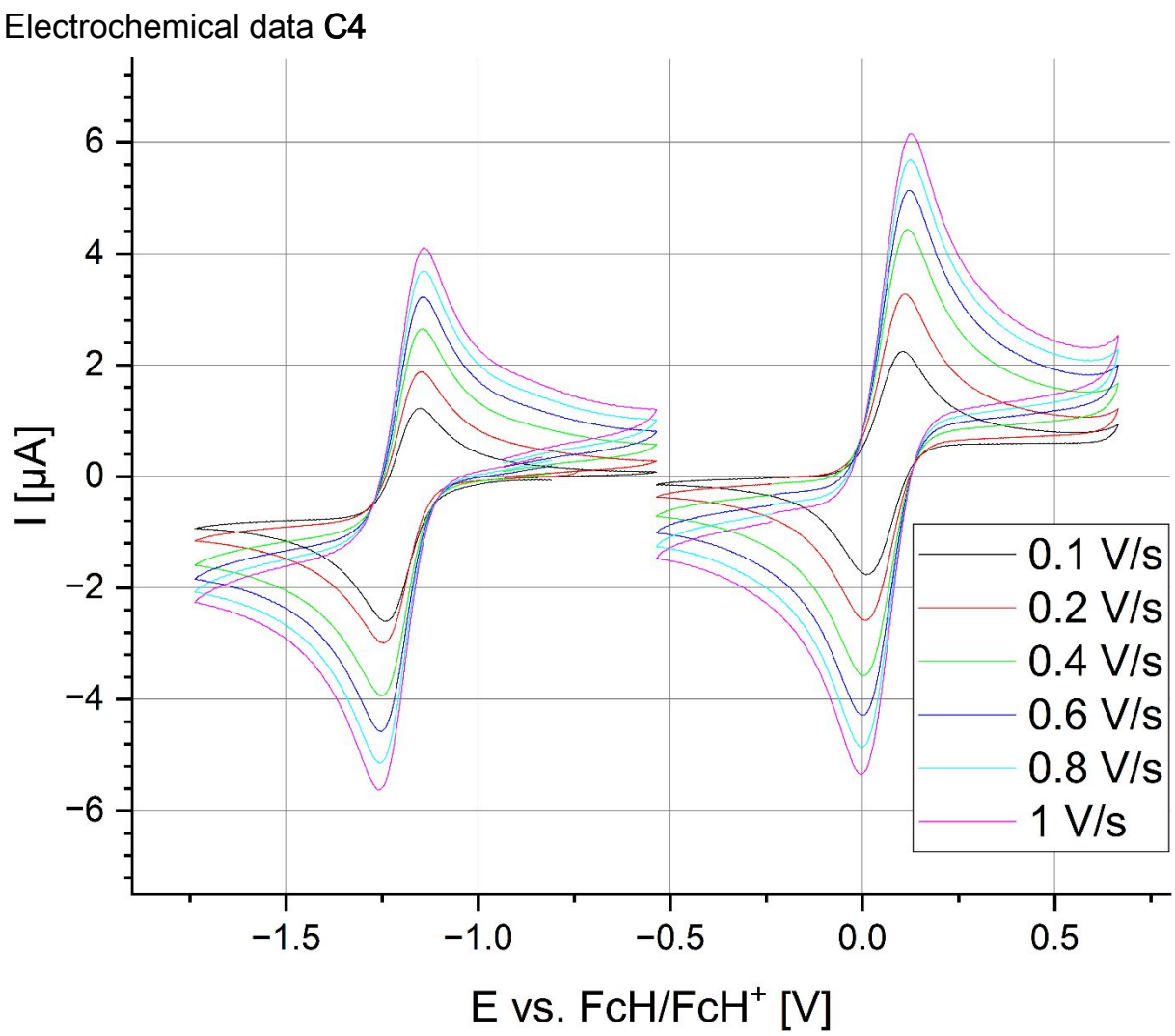

*Figure S14: Cyclic voltammograms of the reversible oxidation/reduciton of **C4** at $E_{1/2}$=-1.20V, $E_{1/2}$=0.06V vs. FcH/FcH+ at different scan rates. The diagnostic criterion of Nicholson is confirmed for the first two transitions.*

*Table S7: Electrochemical data for the reversible reduction of **C4** at $E_{1/2}$= -1.20 V*

Scan rate	[V/s]	0.1	0.2	0.4	0.6	0.8	1
E_{cat}	[V]	-1.24	-1.25	-1.25	-1.25	-1.26	-1.26
E_{An}	[V]	-1.16	-1.16	-1.16	-1.15	-1.15	-1.15
$E_{1/2}$	[V]	-1.20	-1.20	-1.20	-1.20	-1.20	-1.20
ΔE	[V]	0.08	0.09	0.09	0.10	0.11	0.11
I_{cat}	[µA]	2.20	2.55	3.35	3.96	4.49	4.93
I_{an}	[µA]	1.76	2.38	3.24	3.82	4.32	4.75
I_{an}/I_{cat}	[-]	1.25	1.07	1.03	1.04	1.04	1.04

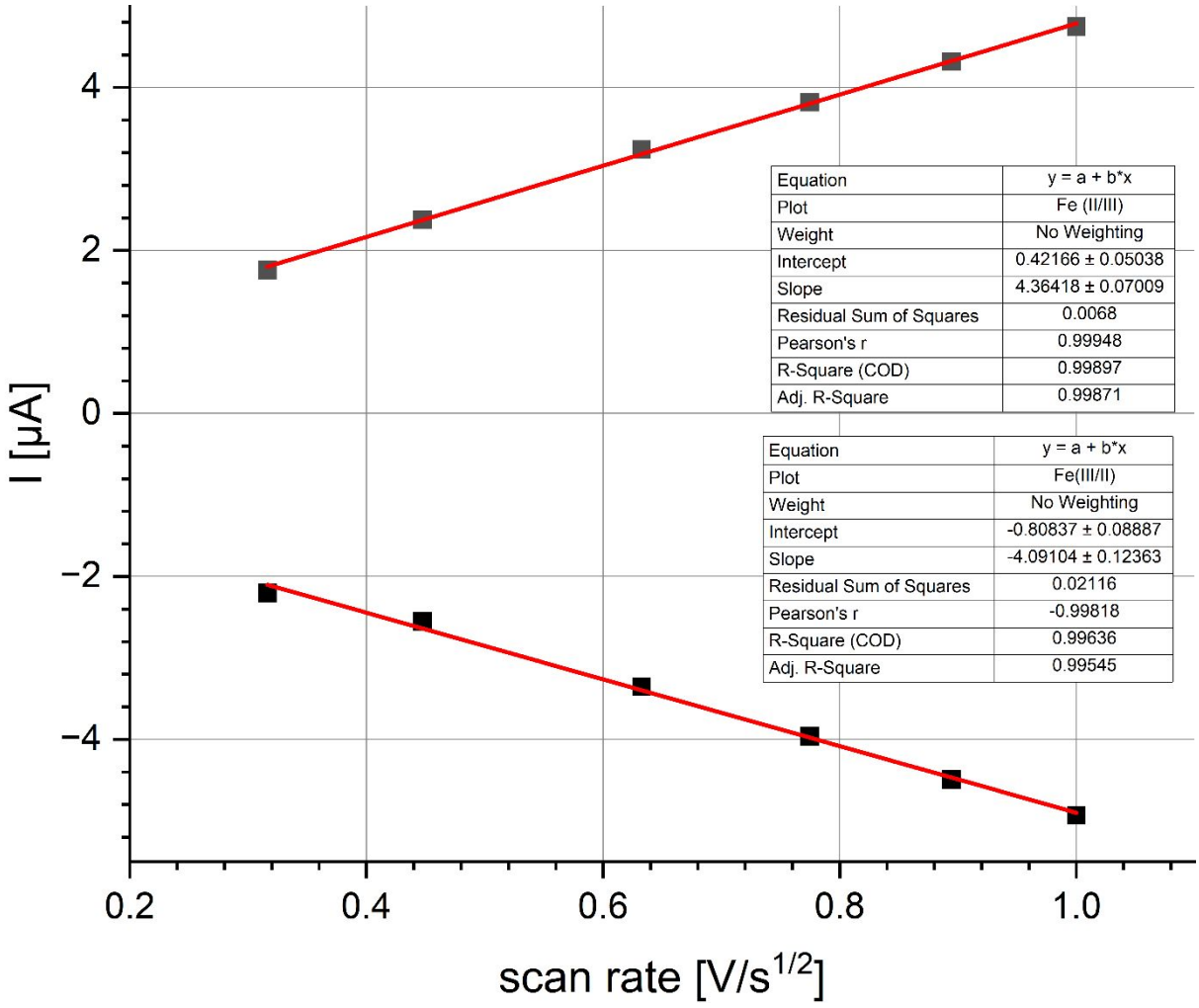

*Figure S15: Linear dependence of forward current peaks Ian and Icat vs. the square root of the scan rate for the reversible reduction of **C4** at $E_{1/2}$= -1.20V vs. FcH/FcH+.*

*Table S8: Electrochemical data for the reversible oxidation of **C4** at $E_{1/2}$= 0.06 V*

Scan rate	[V/s]	0.1	0.2	0.4	0.6	0.8	1
E_{cat}	[V]	0.10	0.10	0.11	0.11	0.12	0.12
E_{An}	[V]	0.01	0.01	0.00	0.00	0.00	-0.01
$E_{1/2}$	[V]	0.06	0.06	0.06	0.06	0.06	0.06
ΔE	[V]	-0.09	-0.09	-0.11	-0.11	-0.12	-0.13
I_{cat}	[µA]	2.11	2.92	3.94	4.65	5.19	5.69
I_{an}	[µA]	1.99	2.90	4.01	4.69	5.27	5.77
I_{an}/I_{cat}	[-]	1.06	1.01	0.98	0.99	0.98	0.99

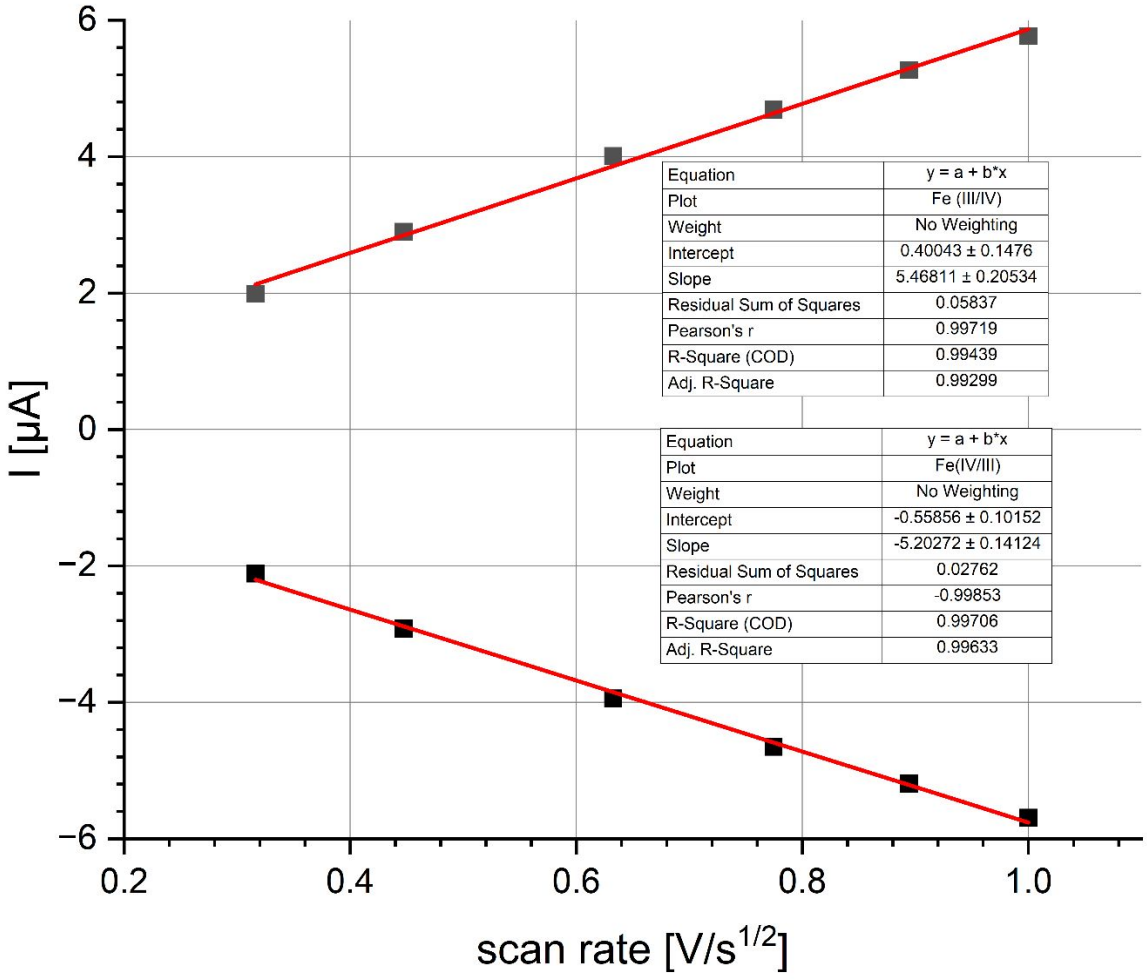

*Figure S16: Linear dependence of forward current peaks Ian and Icat vs. the square root of the scan rate for the reversible reduction of **C4** at $E_{1/2}$= 0.06V vs. FcH/FcH+.*

Cyclic voltammetry of proligands

As expected a clear trend with increasing chromophore size to lower oxidation potentials is observed. This observation follows the same trend as the triplet state energies shown in the manuscript in Scheme 2. This lower oxidation potential, for the larger chromophores anthracene and pyrene supports the postulated theory of a formally oxidized superligand state forming for **C3** and **C4** but not for **C1** and **C2**.

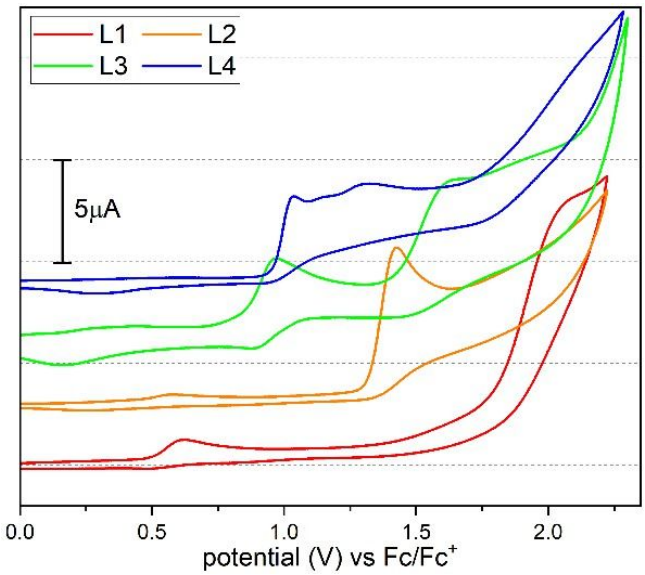

Figure S17: Cyclic voltammograms of the proligands L1 to L4 measured in MeCN at 1 mmol/L. $NBu_4^+PF_6^-$ was added as conducting salt at 10 mmol/l. The X- scale is shifted for each subsequent voltammmogram to improve readability. Some minor impurities leading to weak tra

Ligand absorption

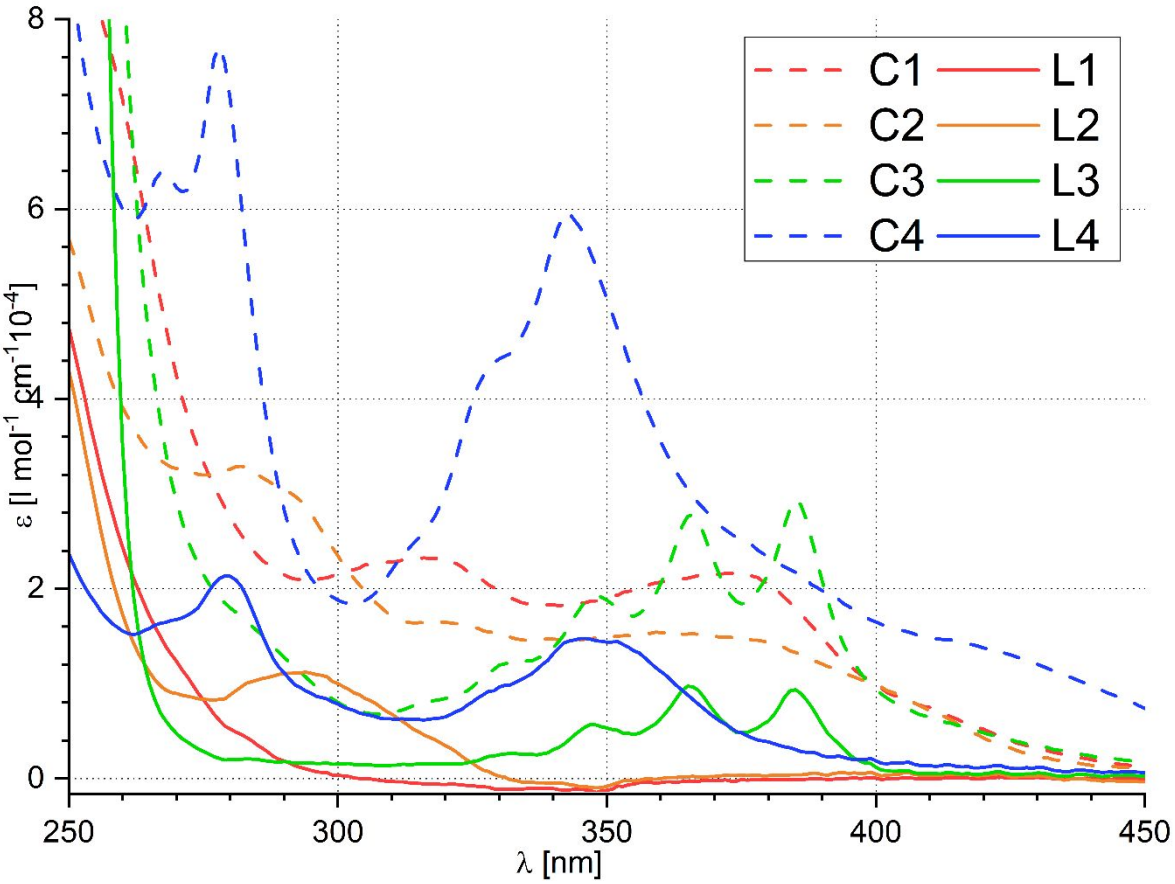

Figure S18: Absorption of all proligands and their corresponding complexes measured in MeCN at $1*10^{-5}$ mol/L.

NMR Spectroscopy

1,1‘-(5-bromo-1,3-phenylene)bis(1H-imidazole)

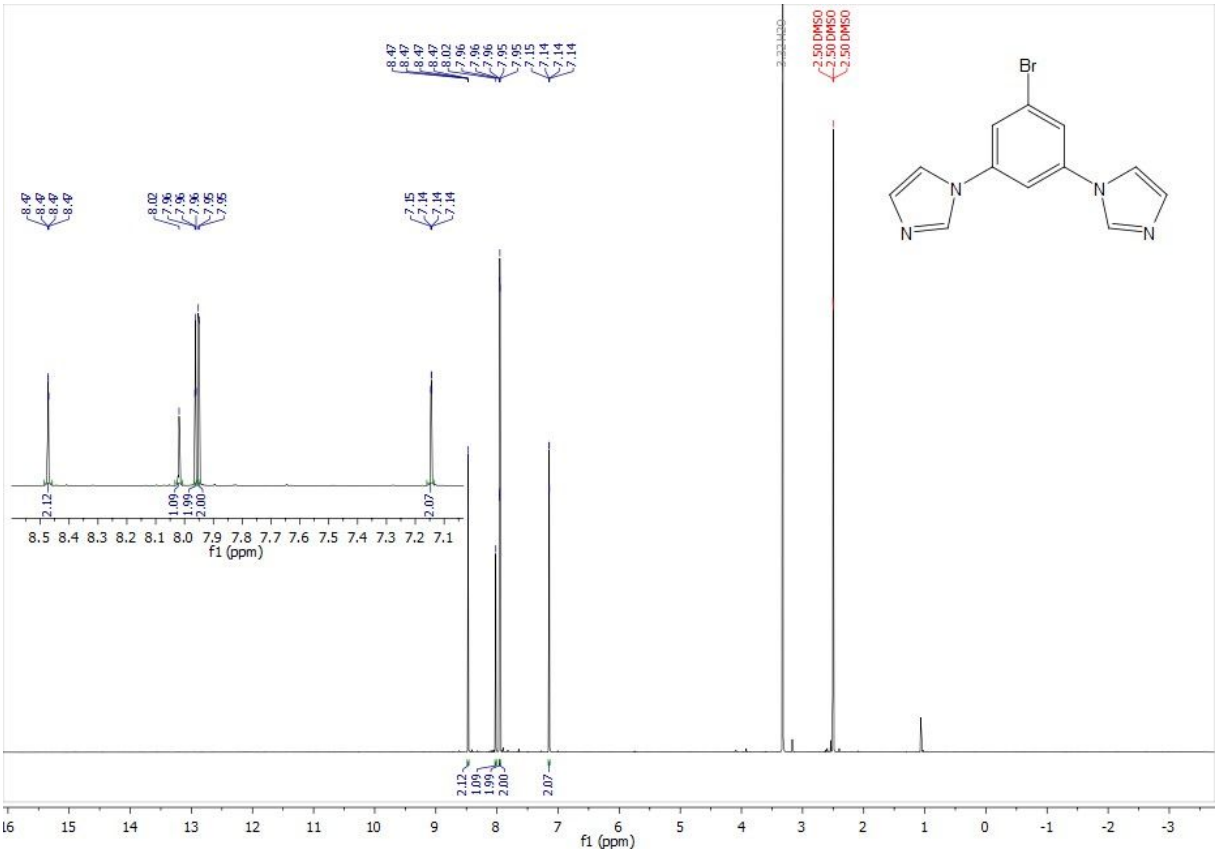

*Figure S19: ^{1}H-NMR-spectrum of 1,1‘-(5-bromo-1,3-phenylene)bis(1*H*-imidazole)*

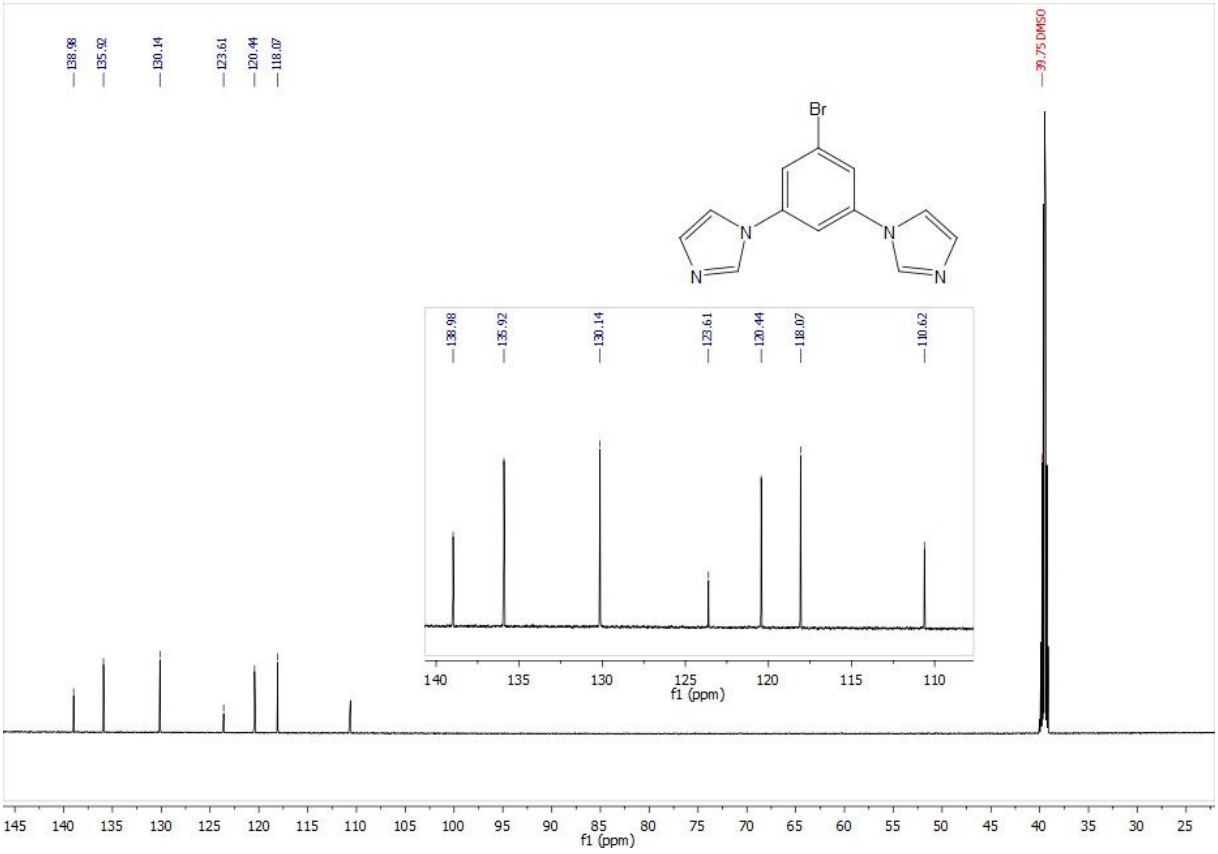

Figure S20: ^{13}C-NMR spectrum of 1,1'-(5-bromo-1,3-phenylene)bis(1H-imidazole)

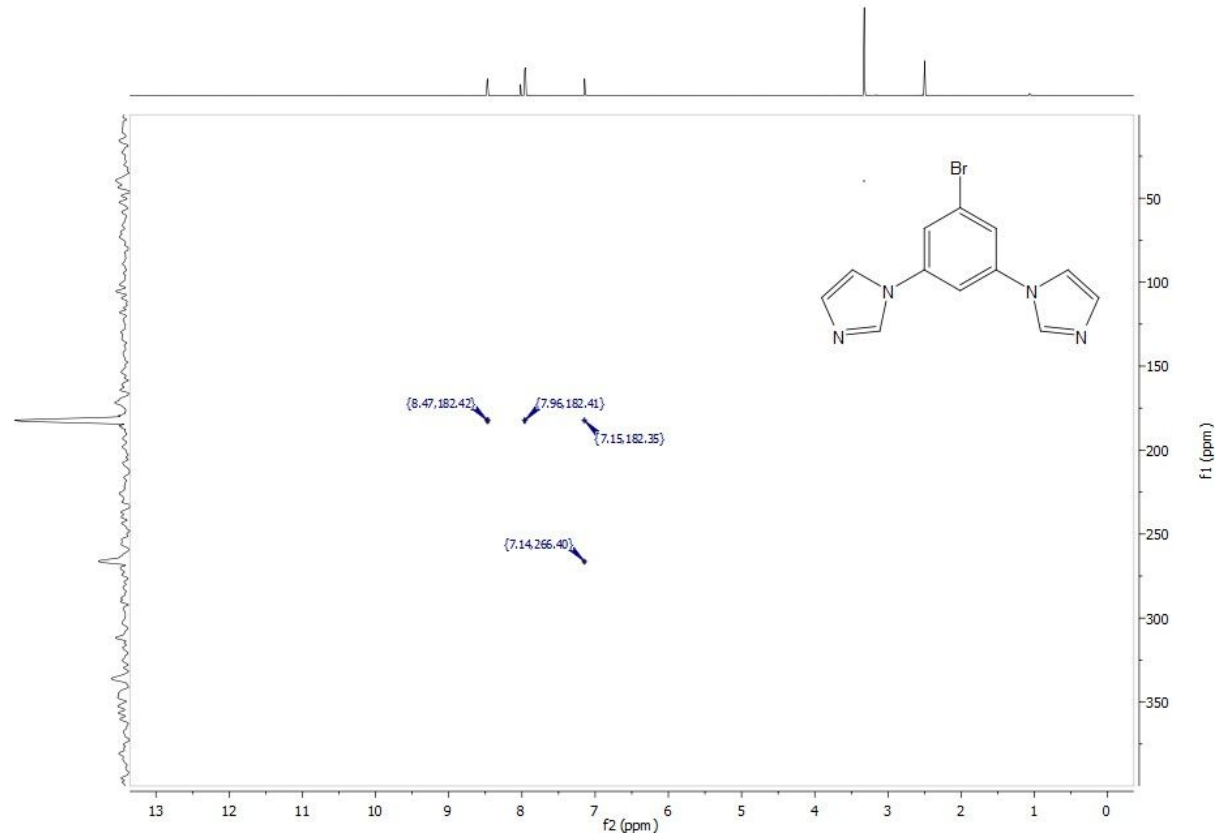

Figure S21: ^{15}N-NMR spectrum of 1,1'-(5-bromo-1,3-phenylene)bis(1H-imidazole)

C1 and precursors

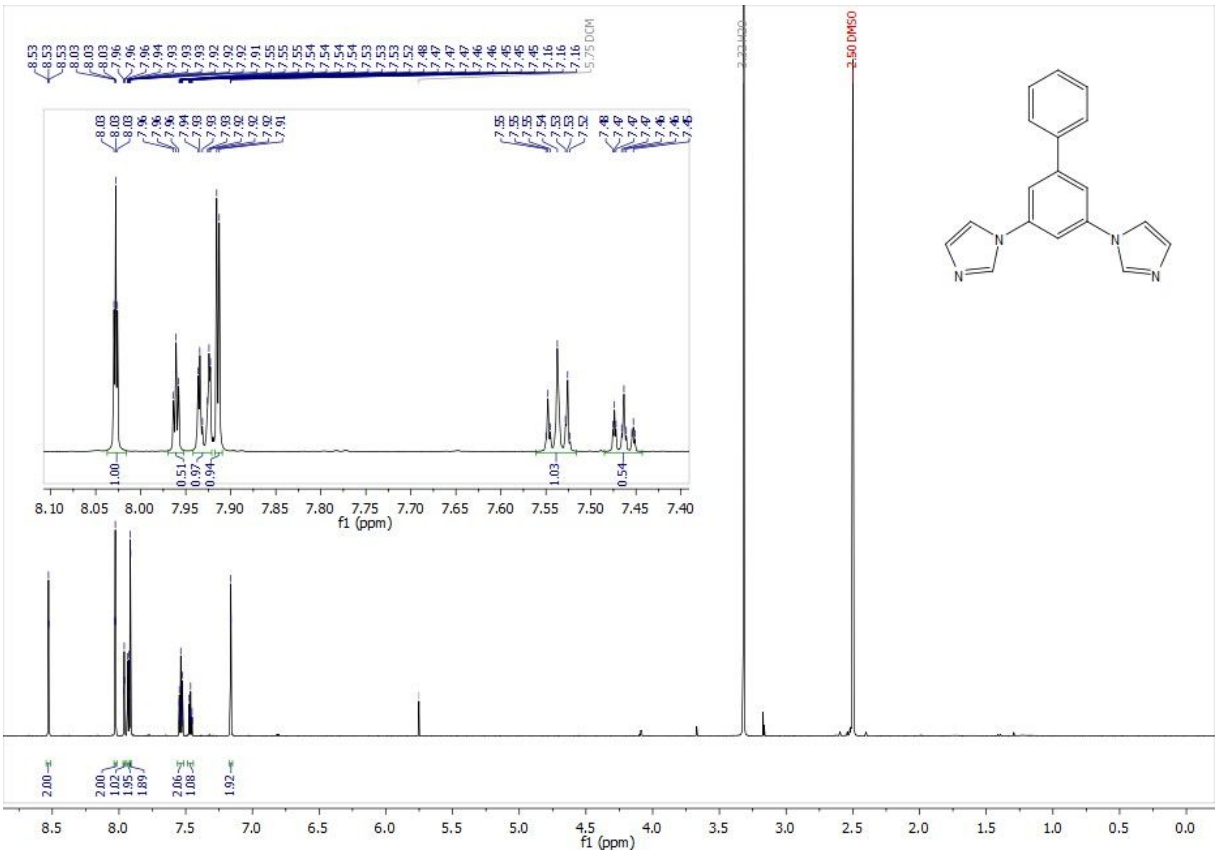

*Figure S22: ^{1}H-NMR spectrum of **1***

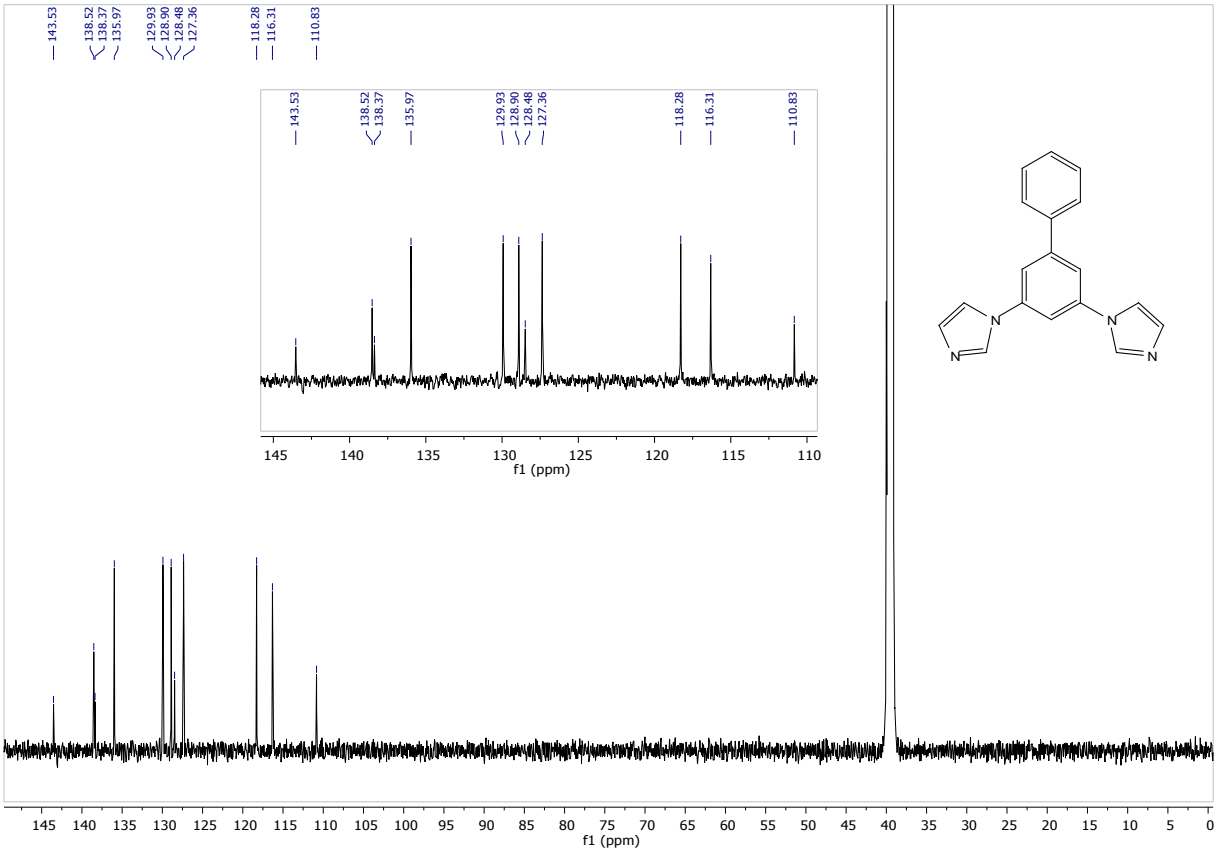

*Figure S23: ^{13}C-NMR spectrum of **1***

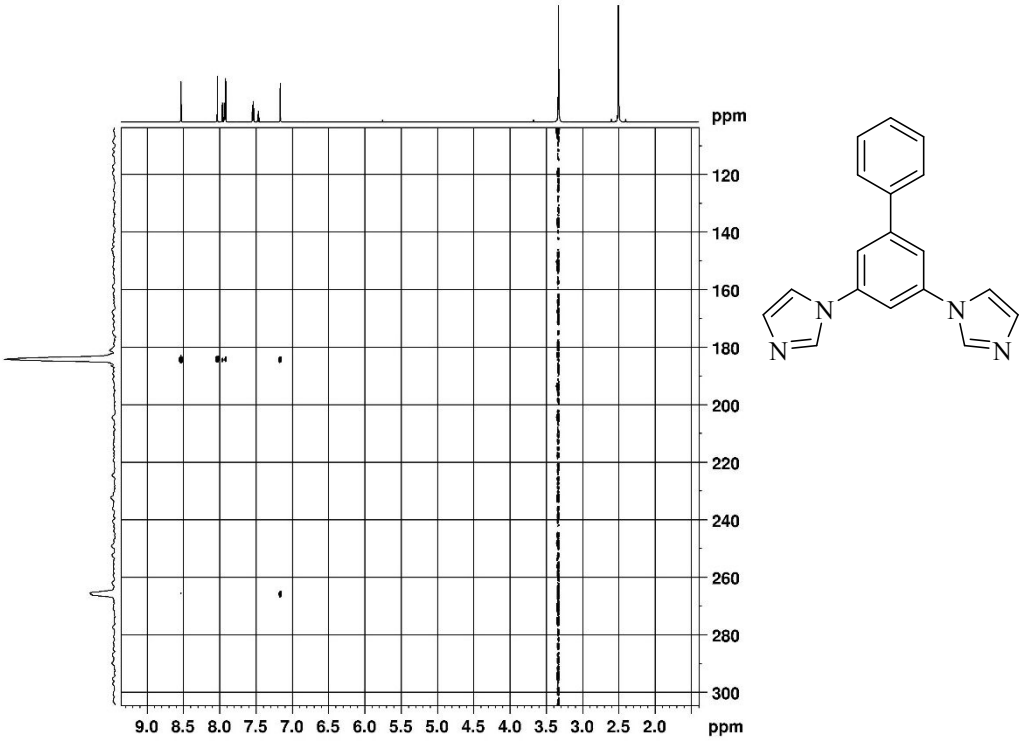

*Figure S24: ^{15}N-HMBC spectrum of **1***

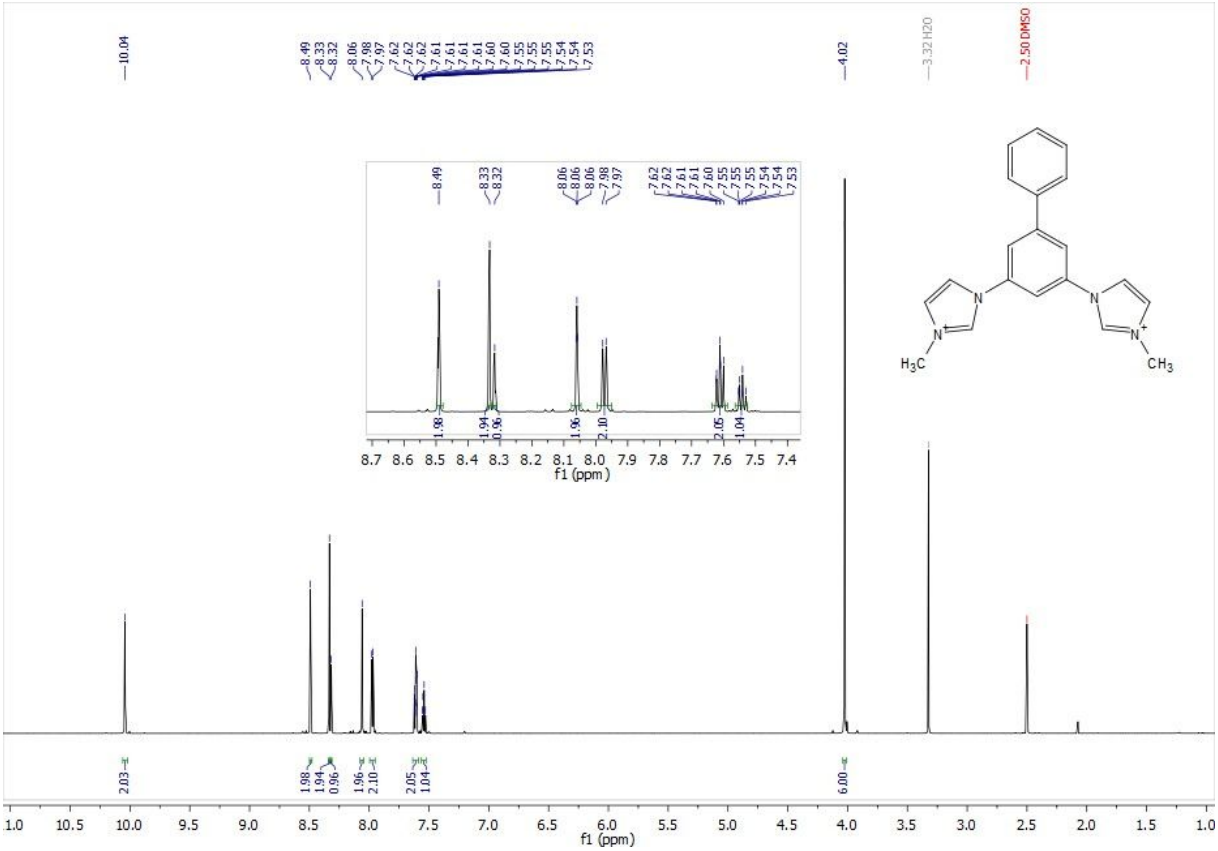

*Figure S25: ^{1}H-NMR spectrum of **L1***

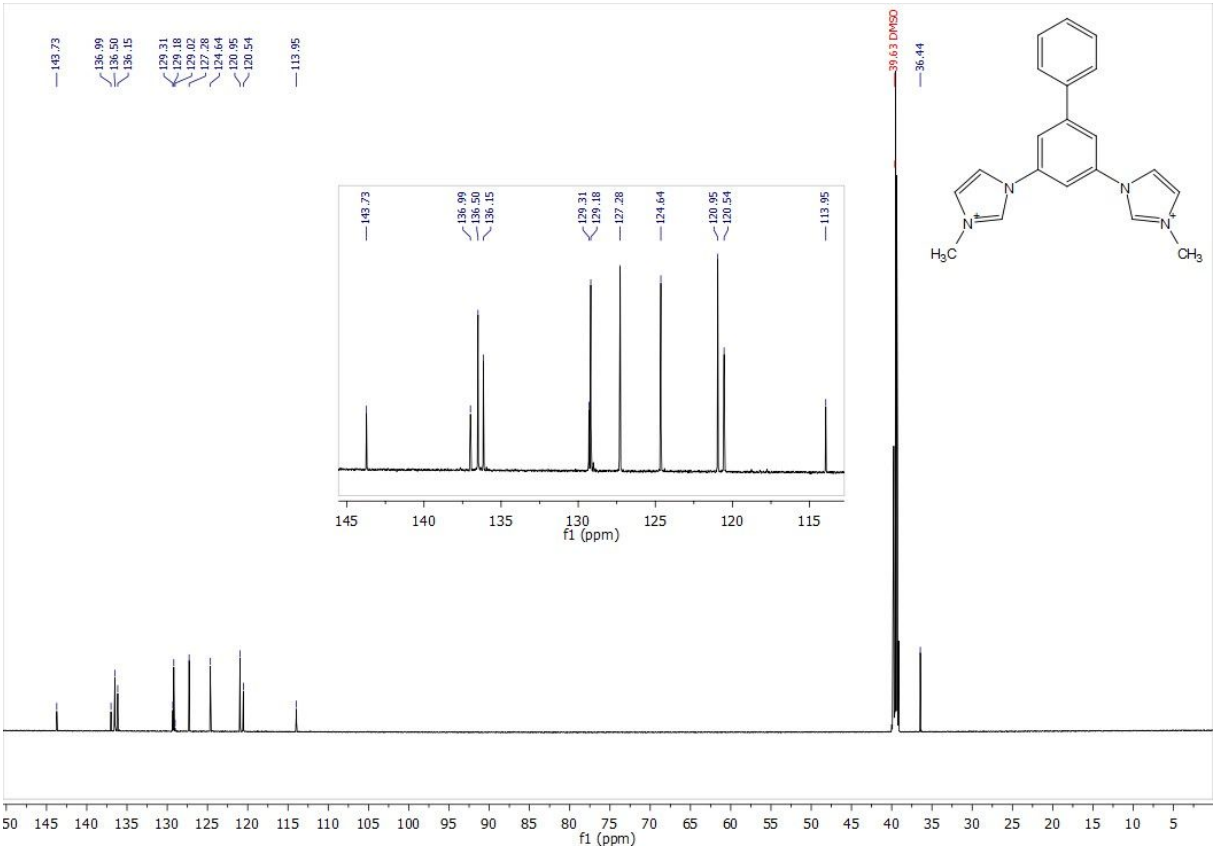

*Figure S26: [13]C-NMR spectrum of **L1***

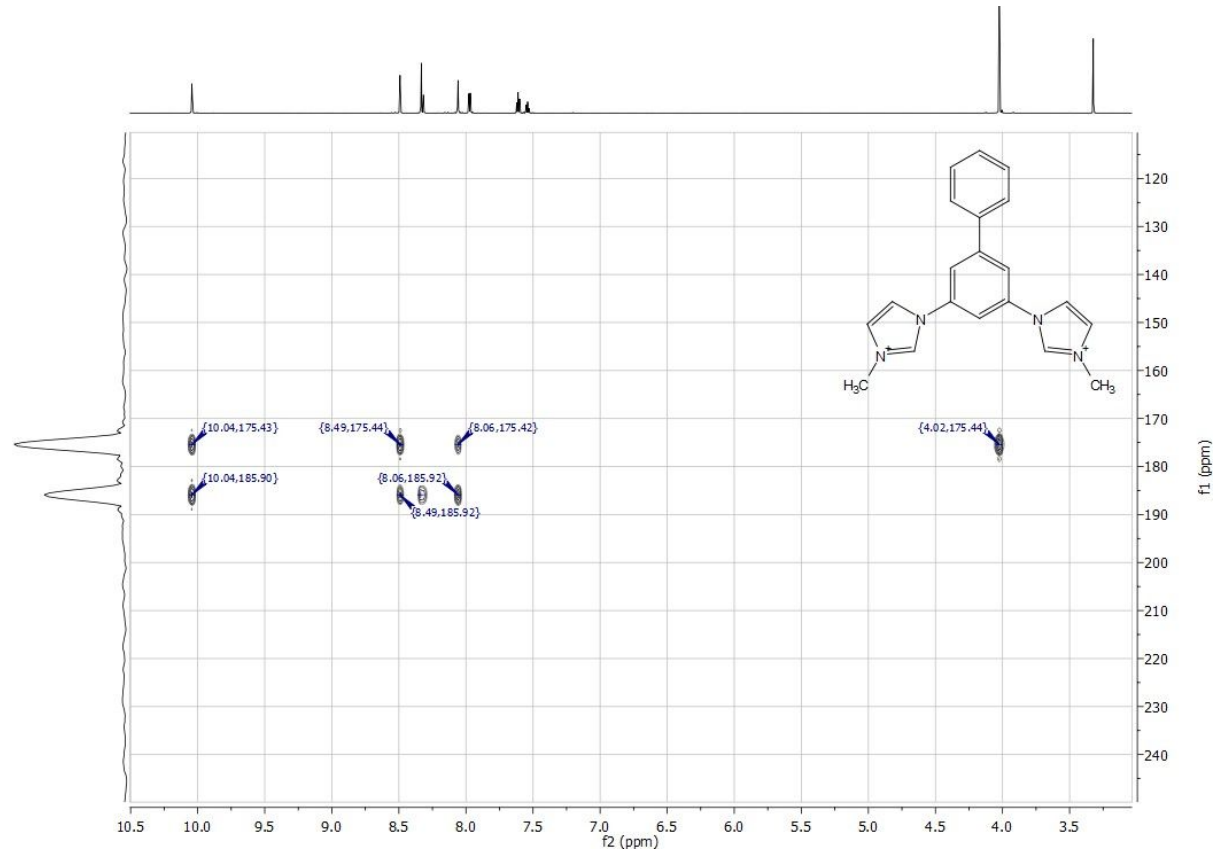

*Figure S27: [15]N-HMBC spectrum of **L1***

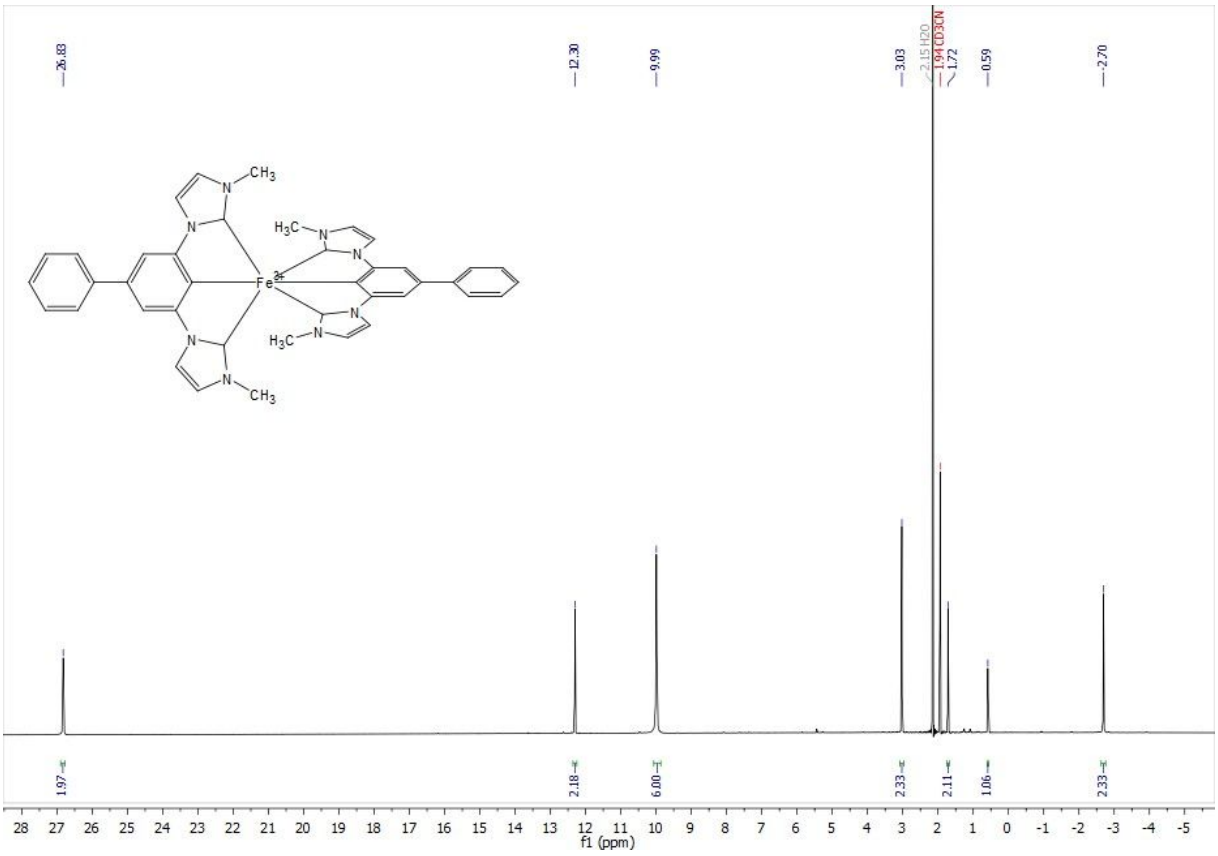

*Figure S28: [1]H-NMR spectrum of **C1***

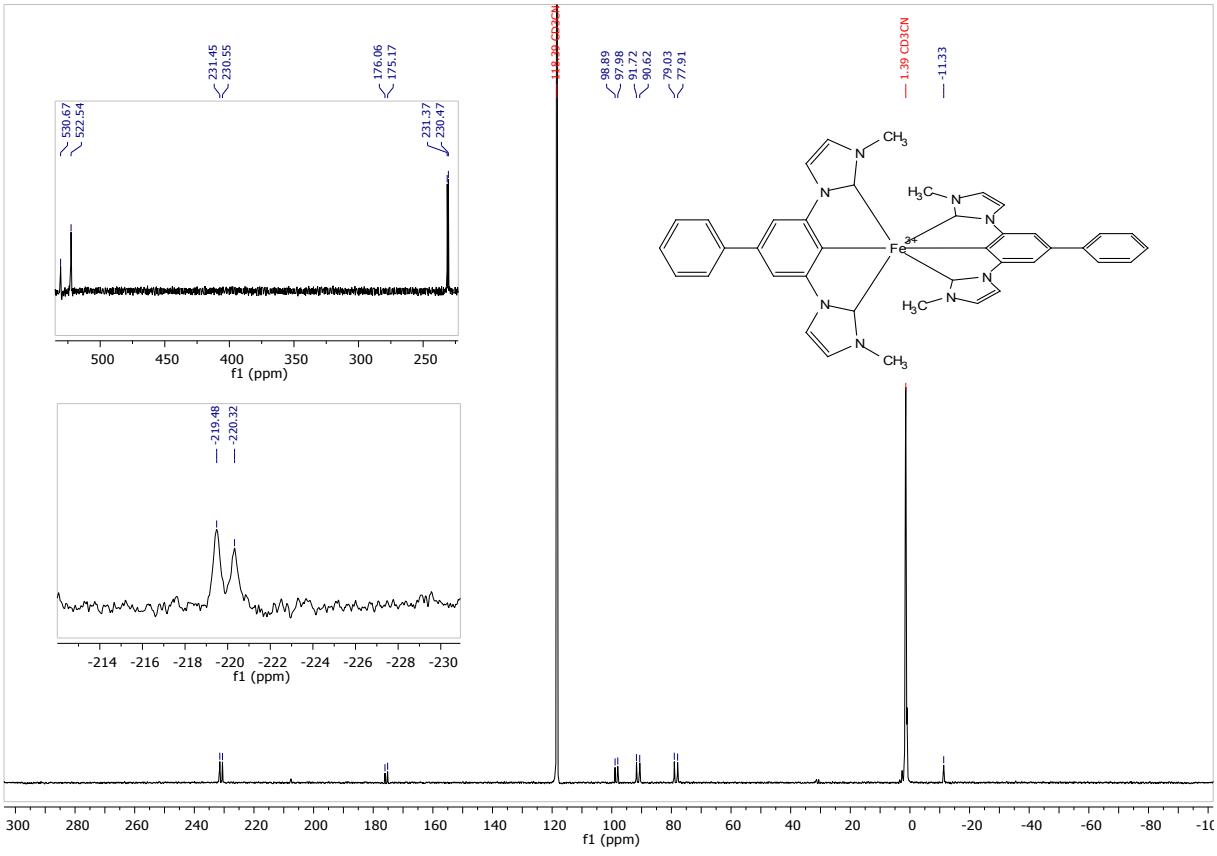

*Figure S29: [13]C-NMR spectrum of **C1***

C2 and precursors

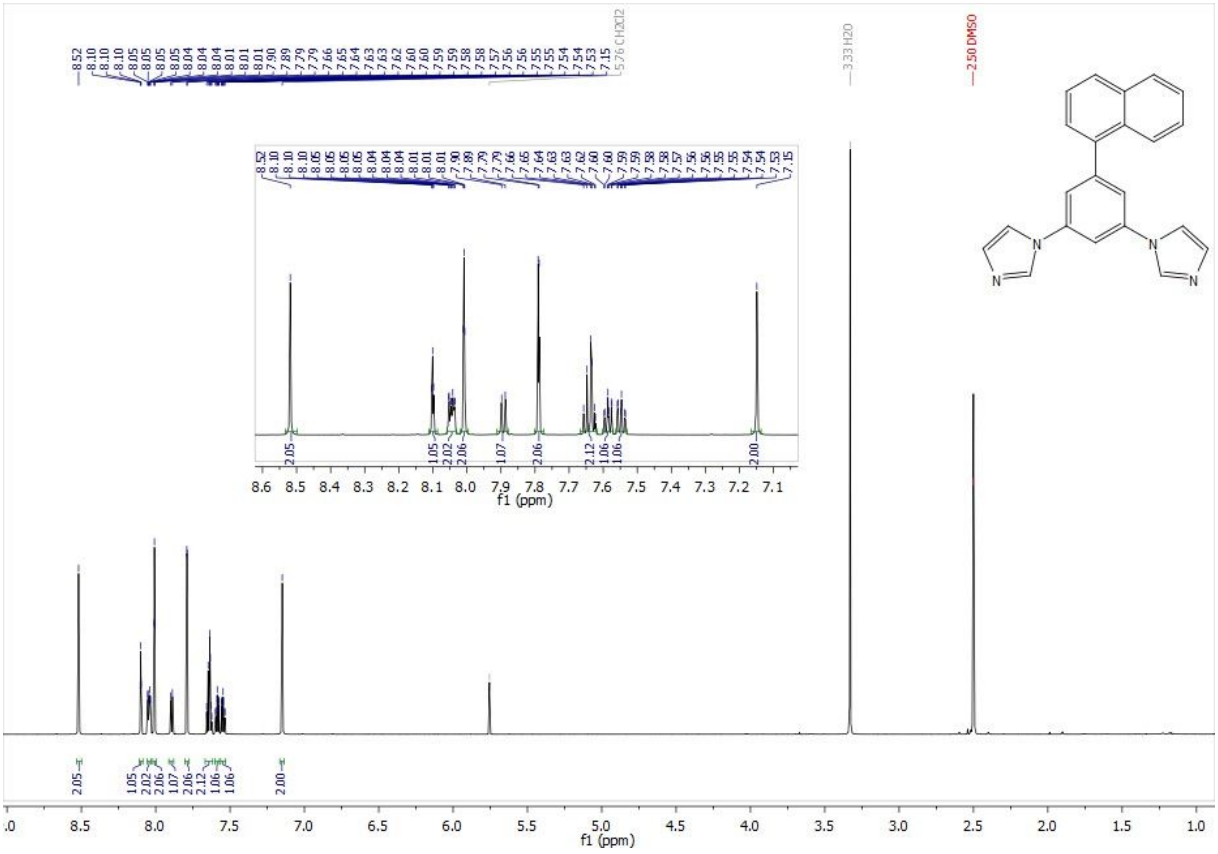

*Figure S30: [1]H-NMR spectrum of **2***

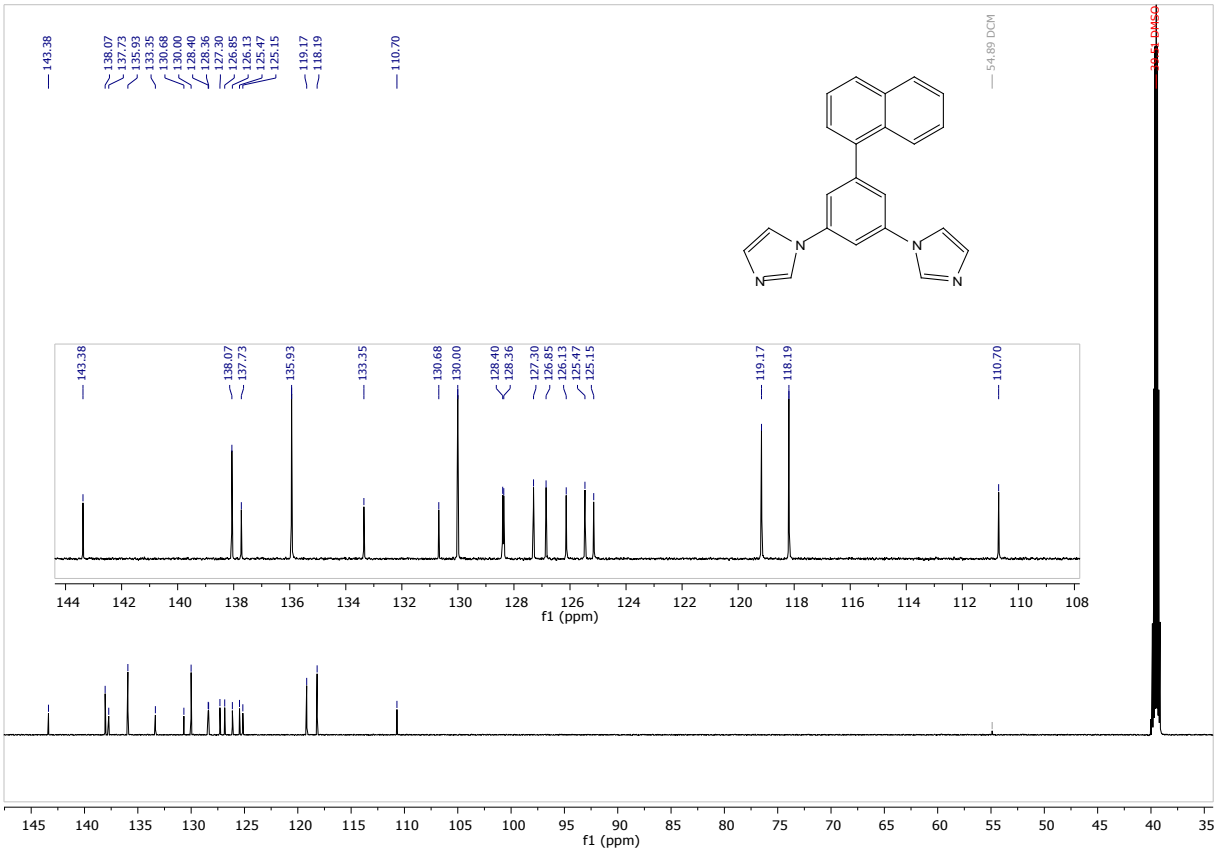

*Figure S31: [13]C-NMR spectrum of **2***

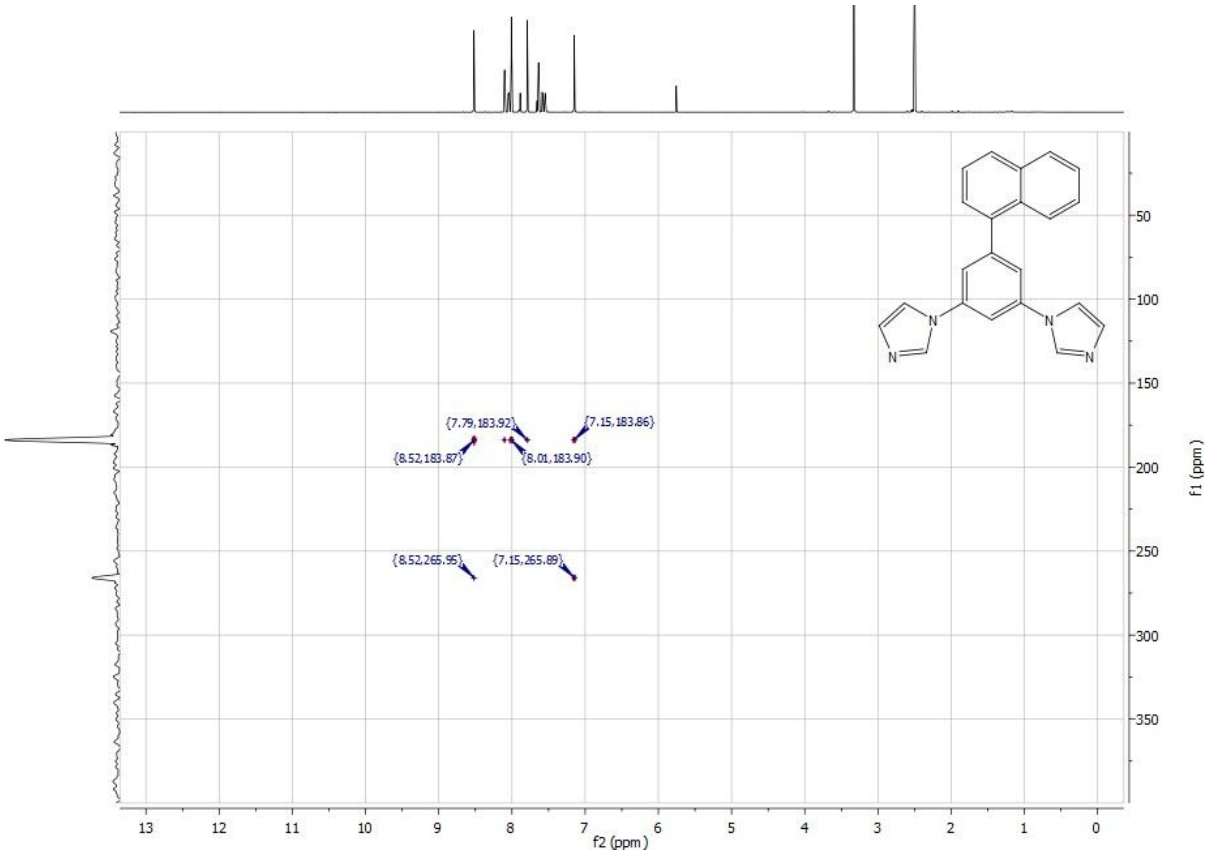

*Figure 32: ^{15}N-HMBC of **2***

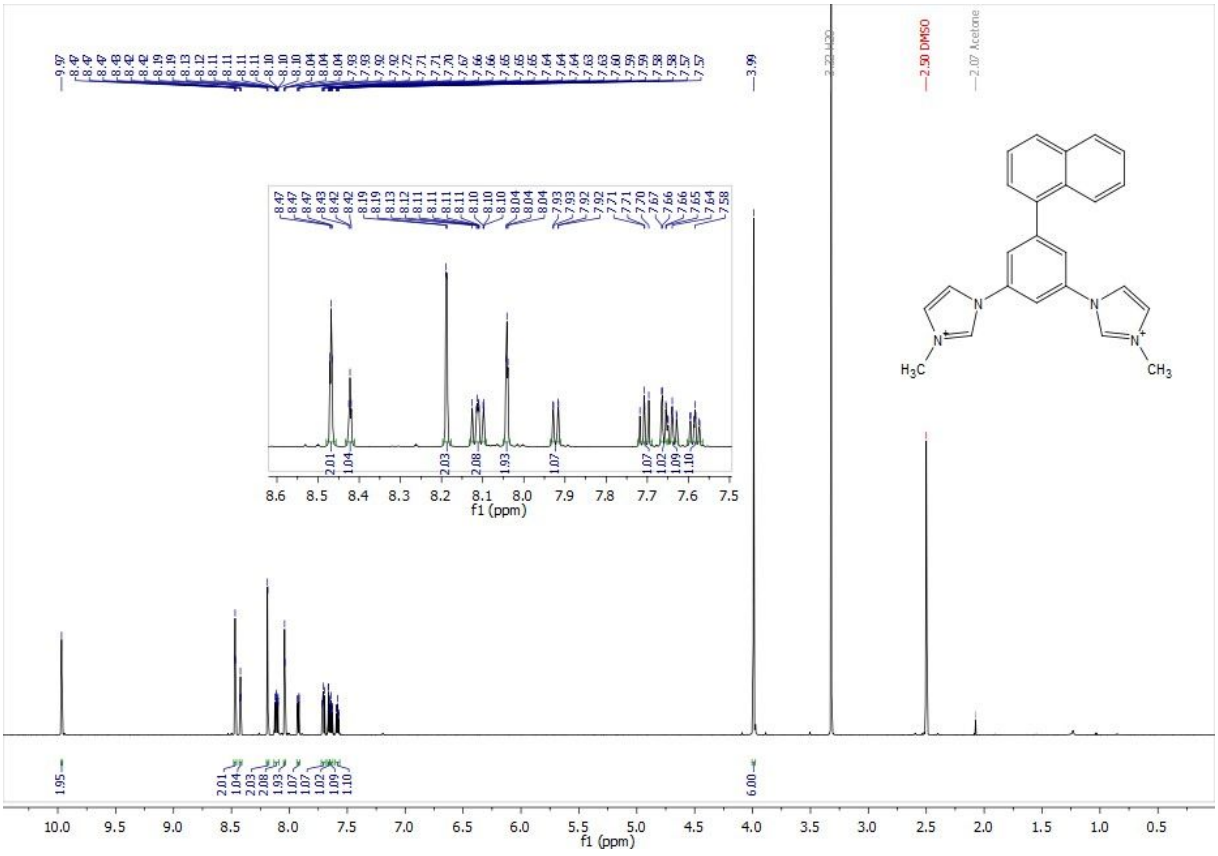

*Figure S33: ^{1}H-NMR spectrum of **L2***

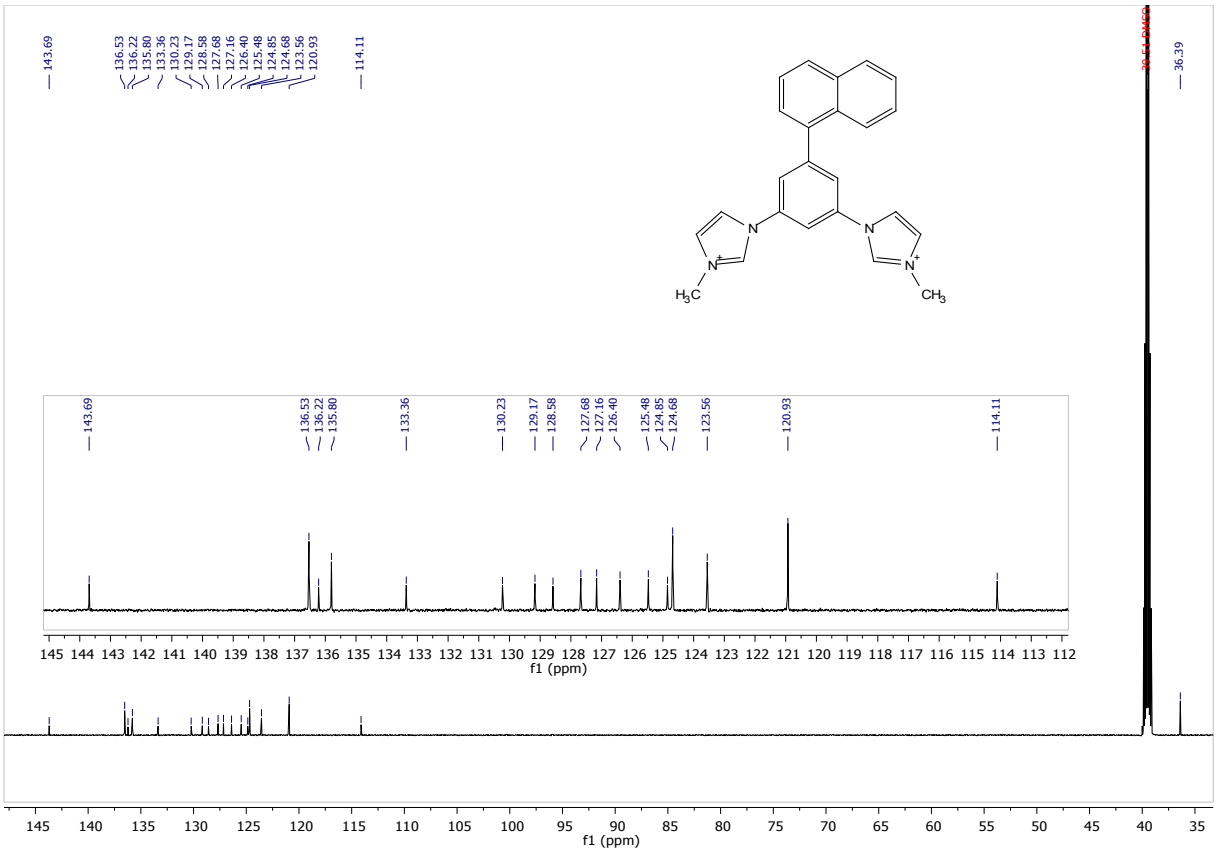

*Figure S34: [13]C-NMR spectrum of **L2***

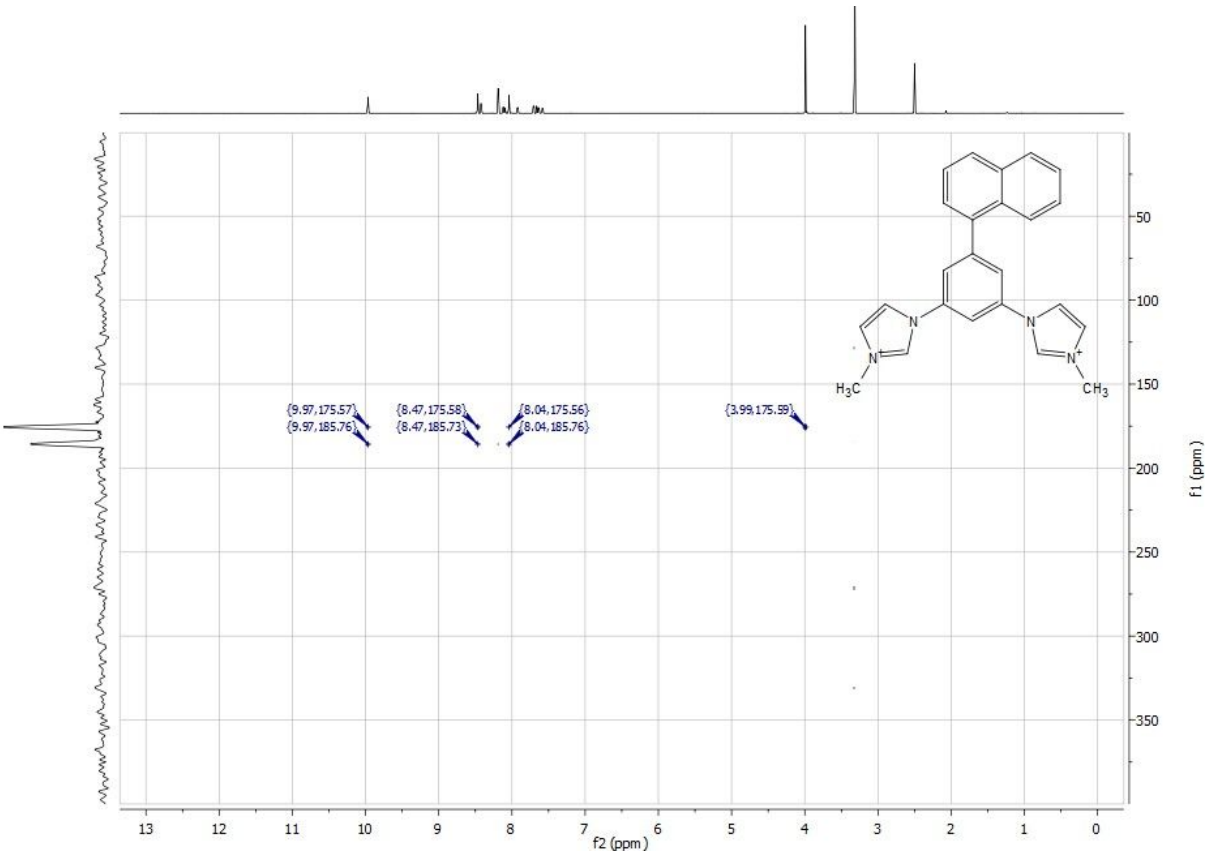

*Figure 35: [15]N-HMBC of **L2***

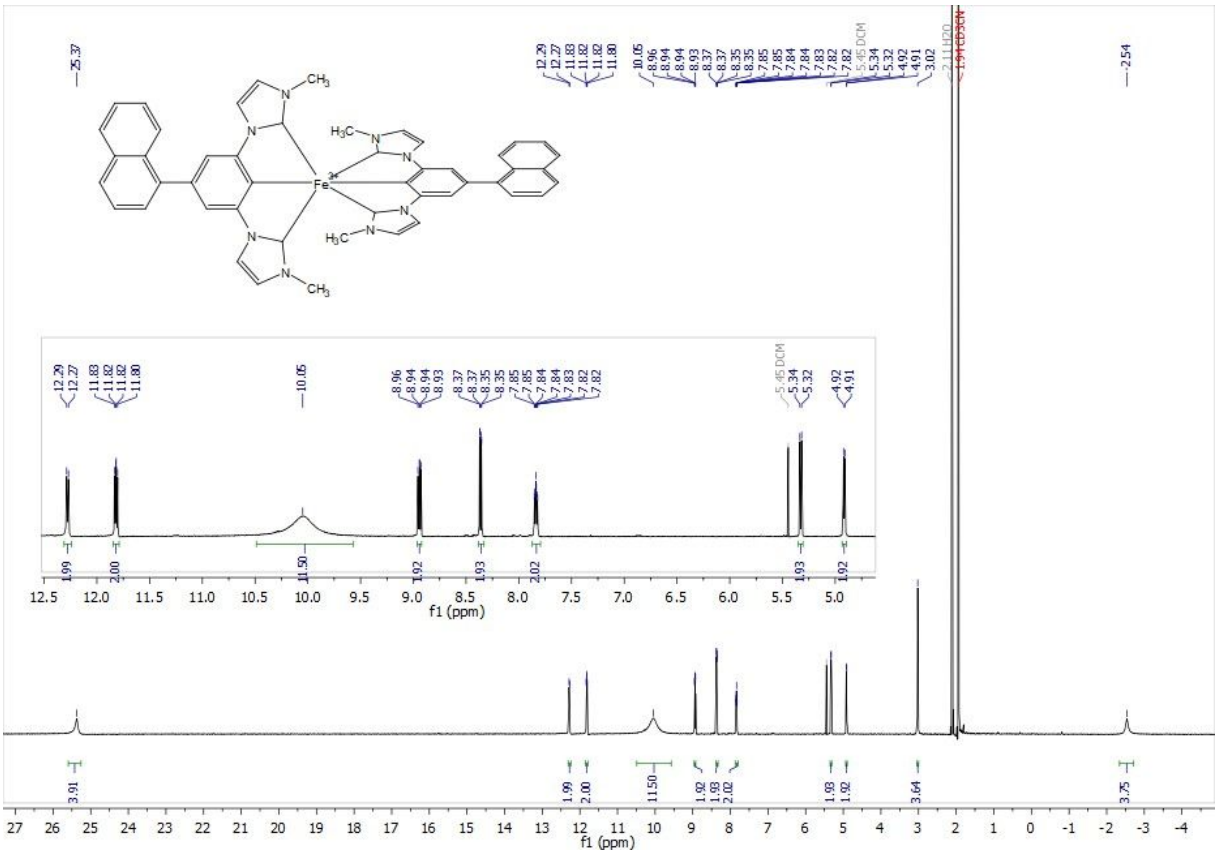

*Figure S36: [1]H-NMR spectrum of **C2***

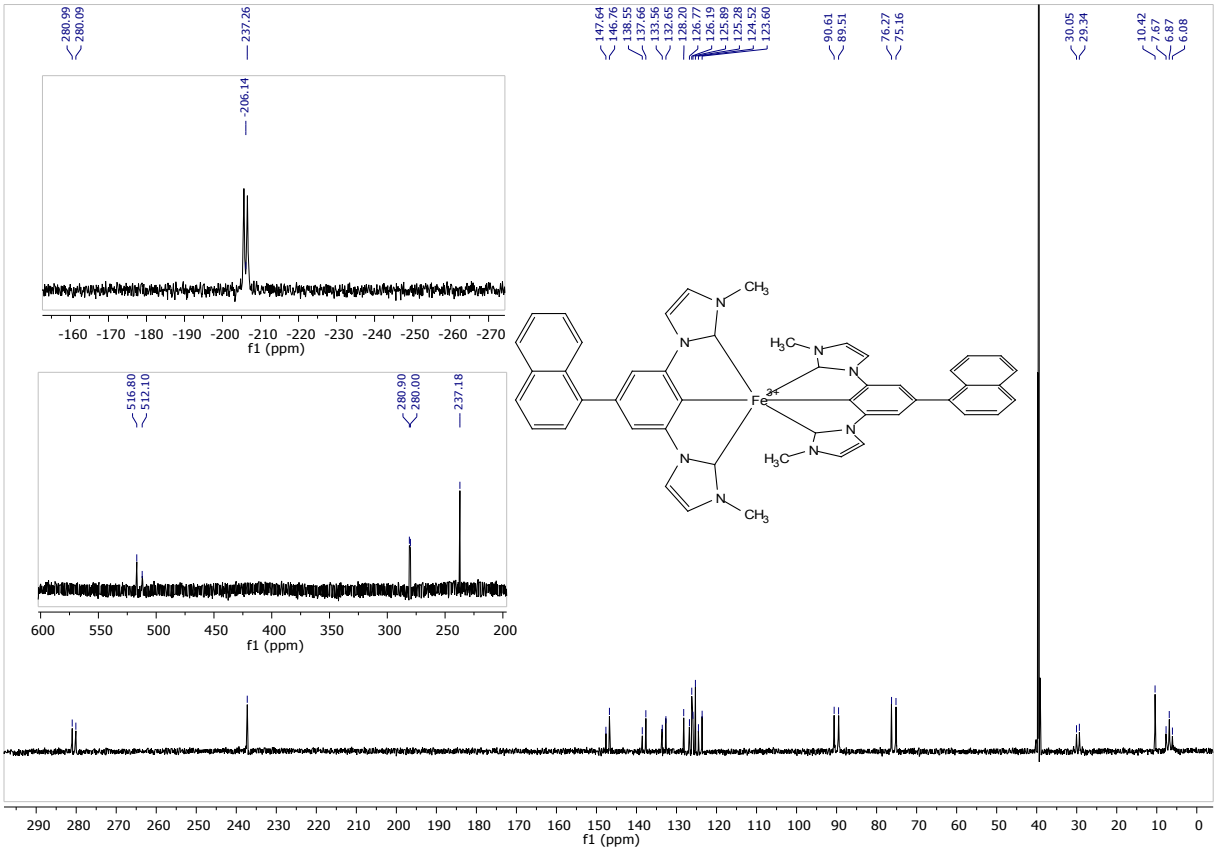

*Figure S37: [13]C-NMR spectrum of **C2***

C3 and precursors

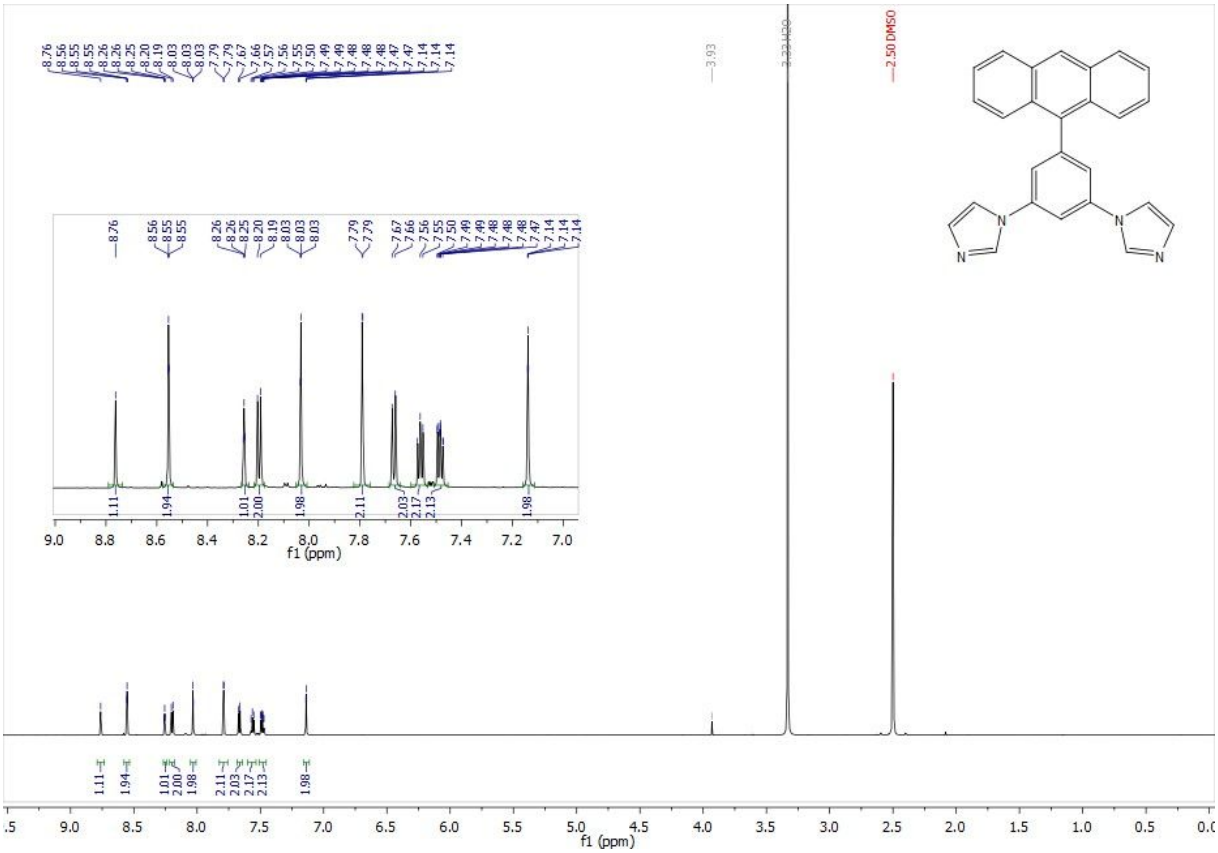

*Figure S38: [1]H-NMR spectrum of **3***

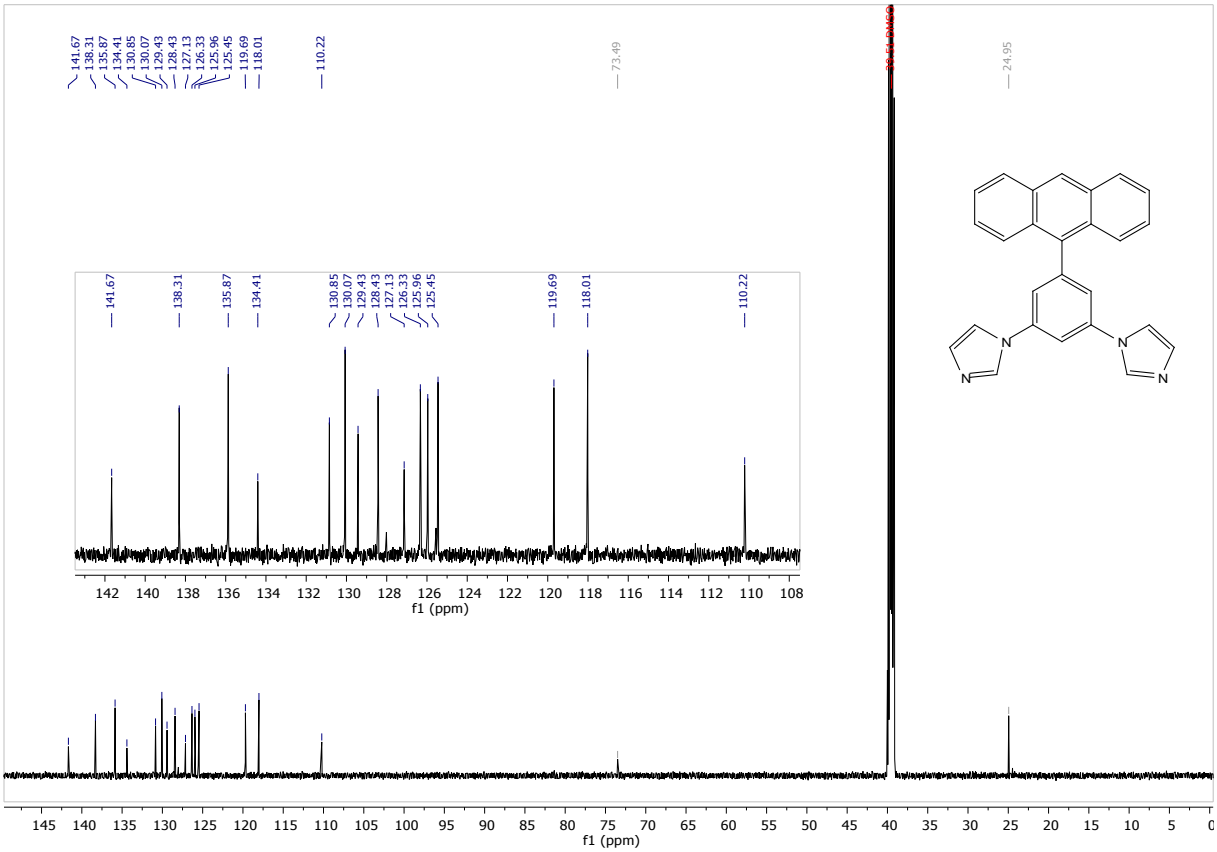

*Figure S39: [13]C-NMR spectrum of **3***

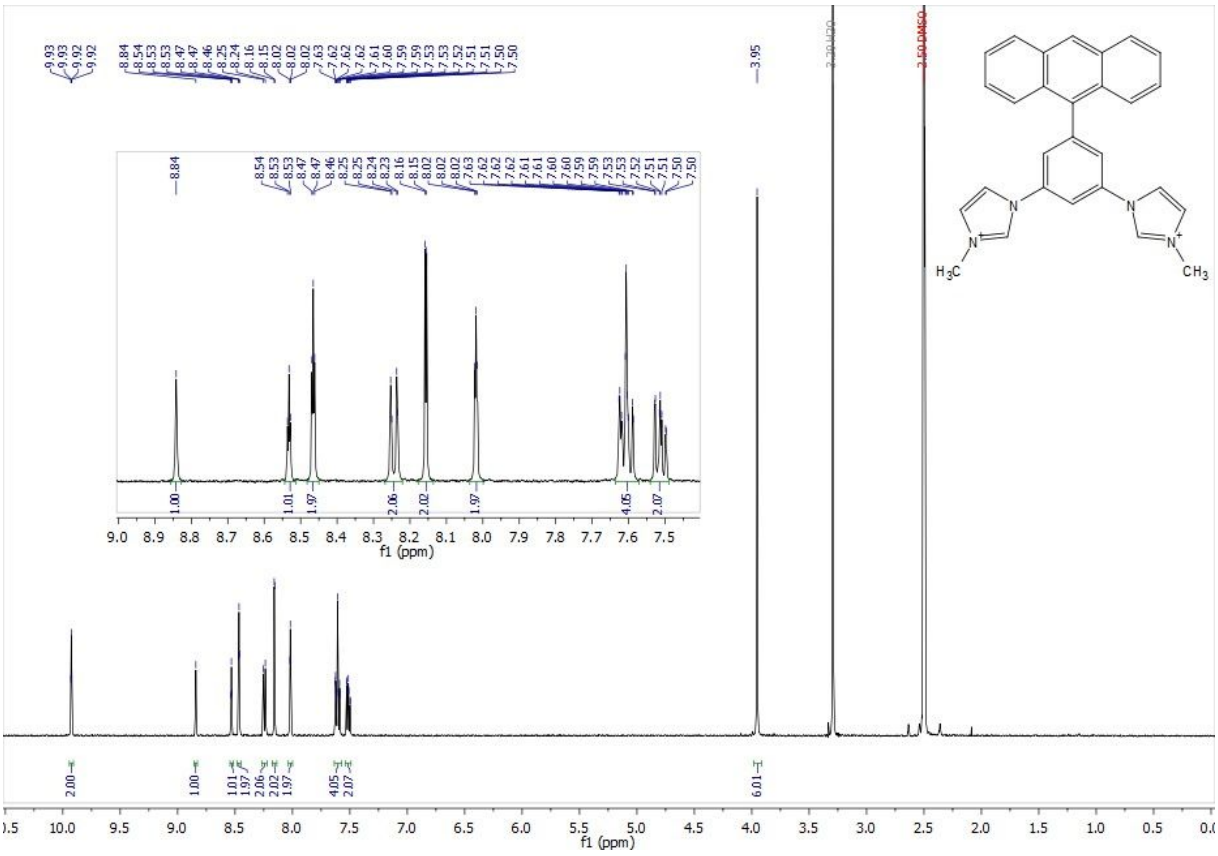

*Figure S40: [1]H-NMR spectrum of **L3***

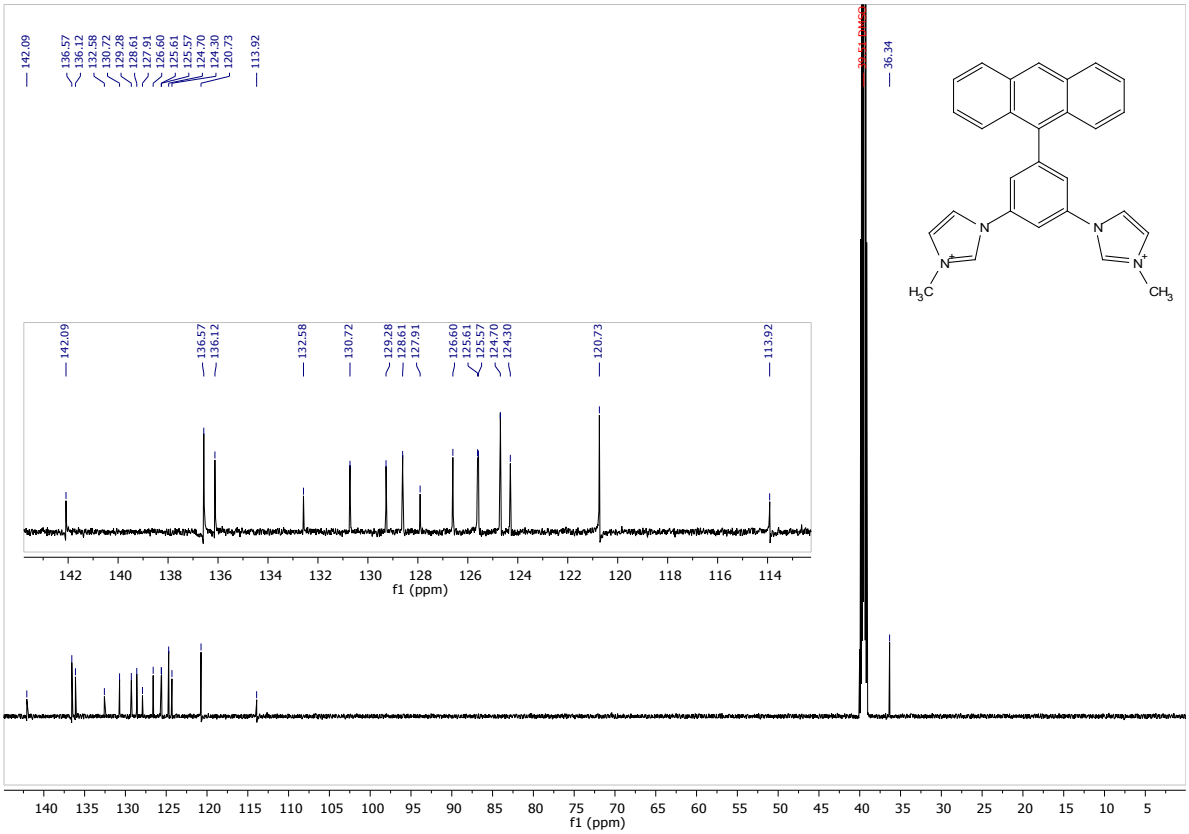

*Figure S41: [13]C-NMR spectrum of **L3***

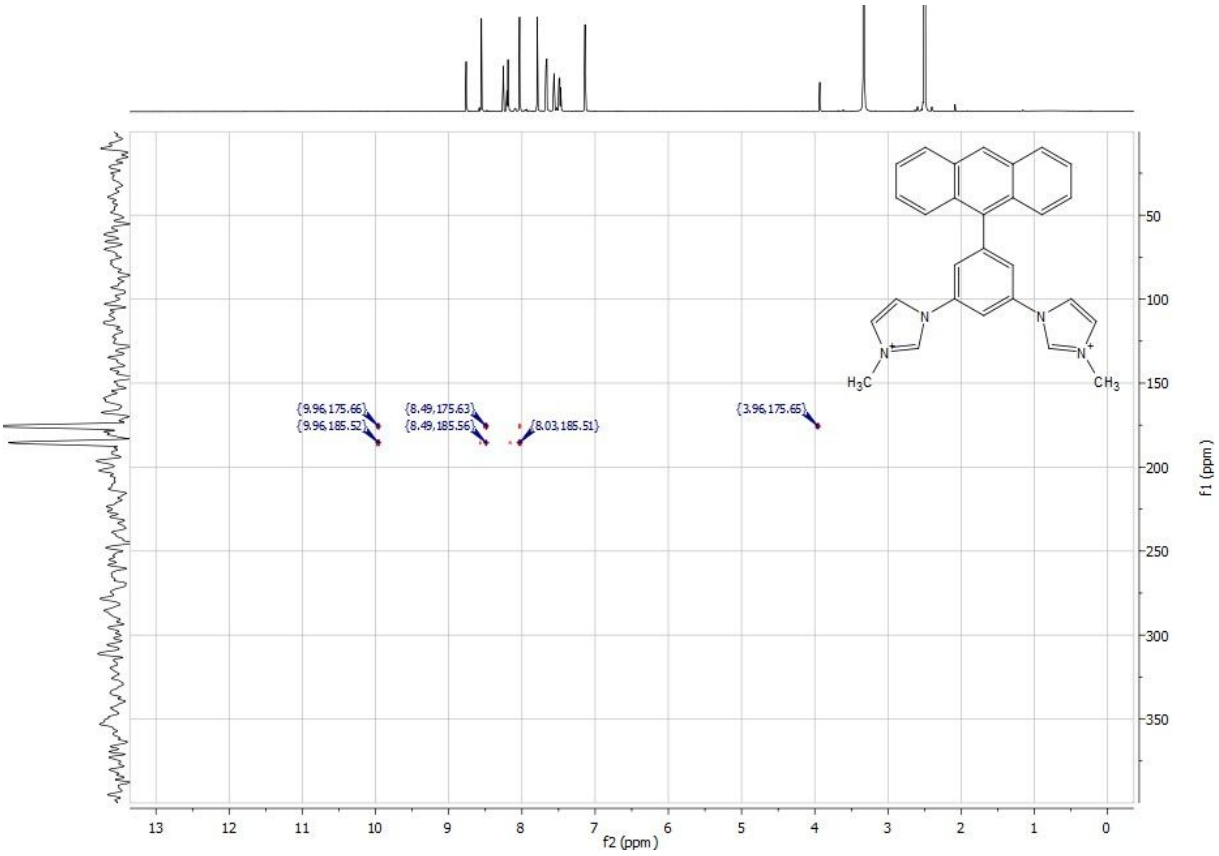

*Figure S42: [15]N-NMR spectrum of **L3***

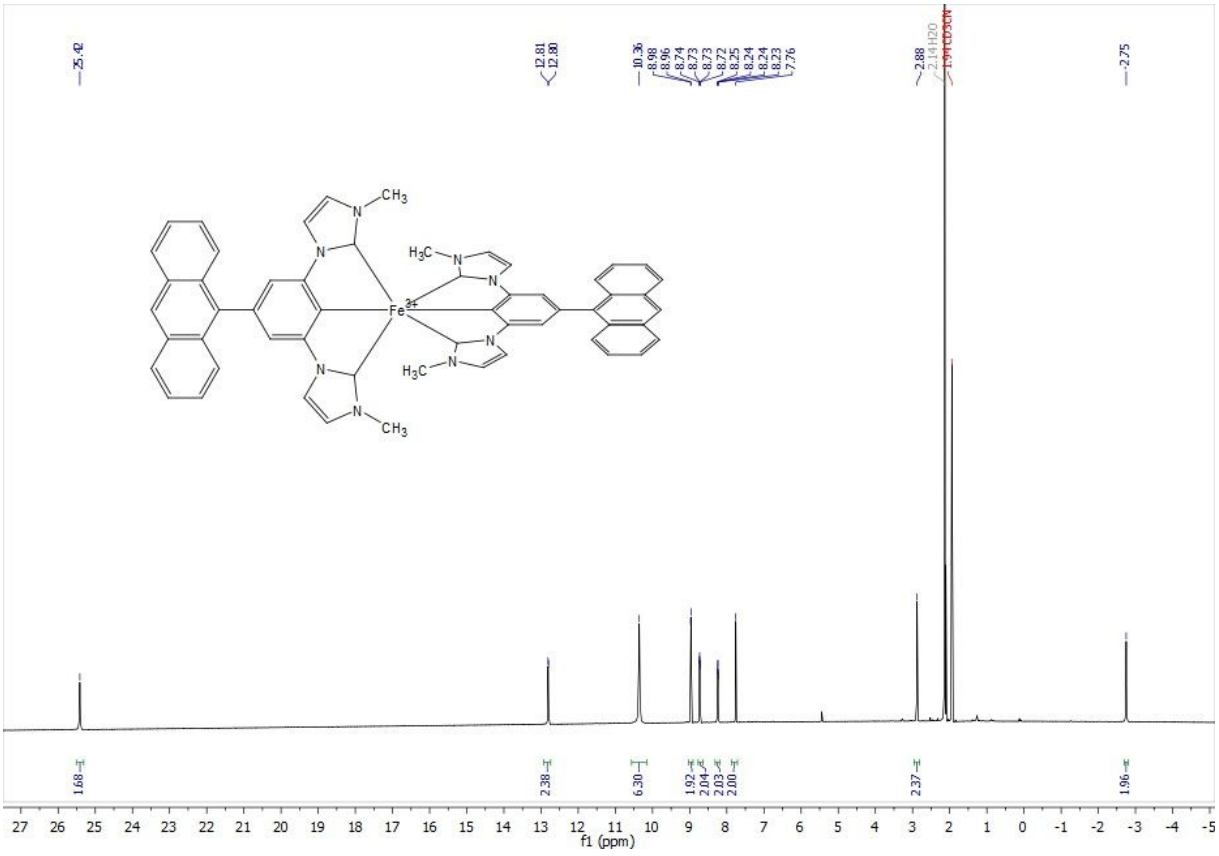

*Figure S43: [1]H-NMR spectrum of **C3***

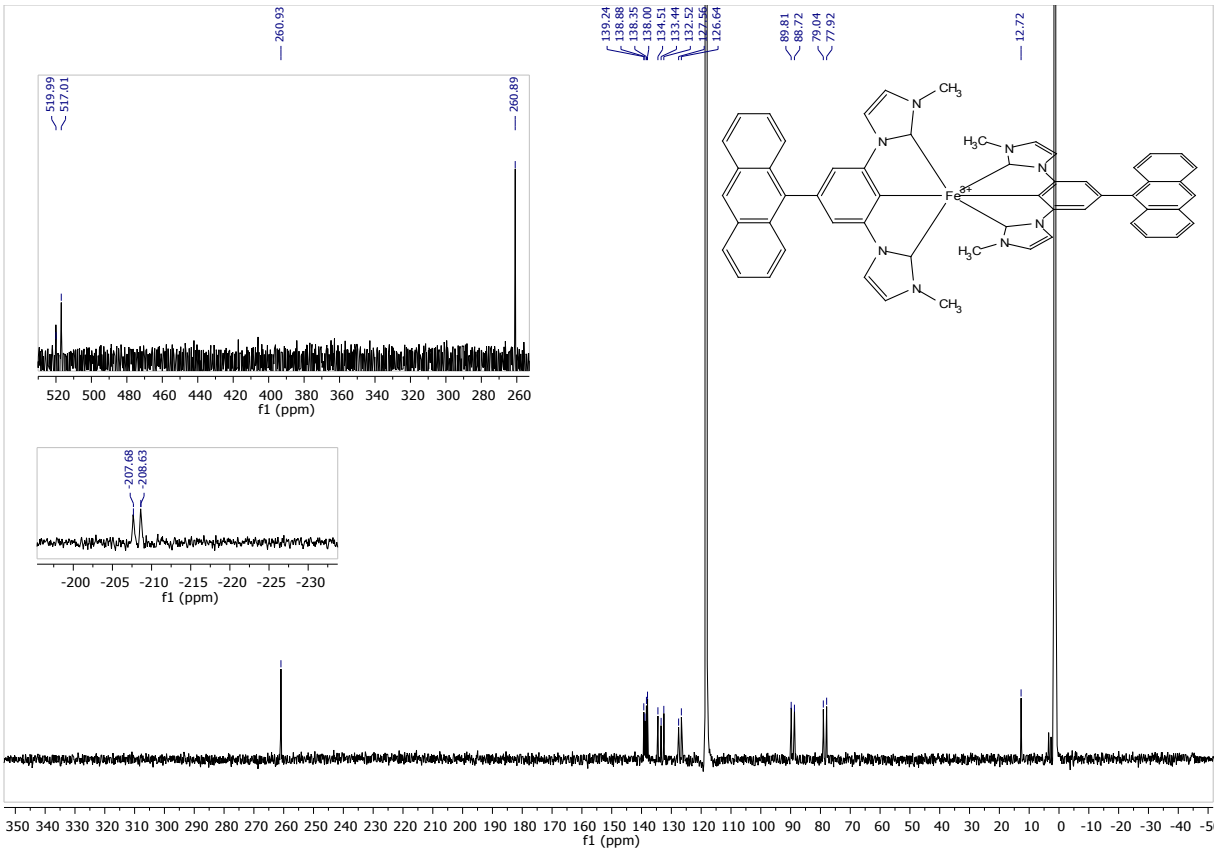

*Figure S44: [13]C-NMR spectrum of **C3***

C4 and precursors

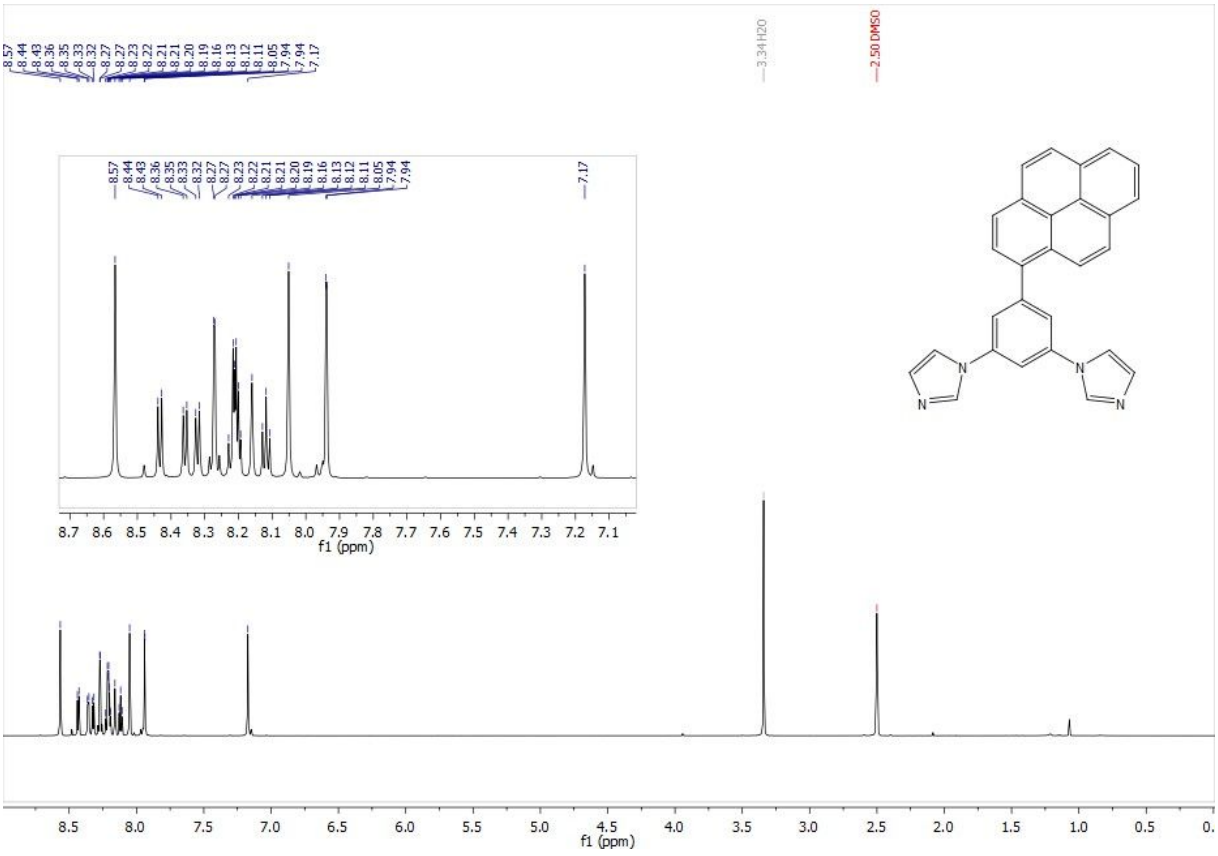

*Figure S45: [1]H-NMR spectrum of **4***

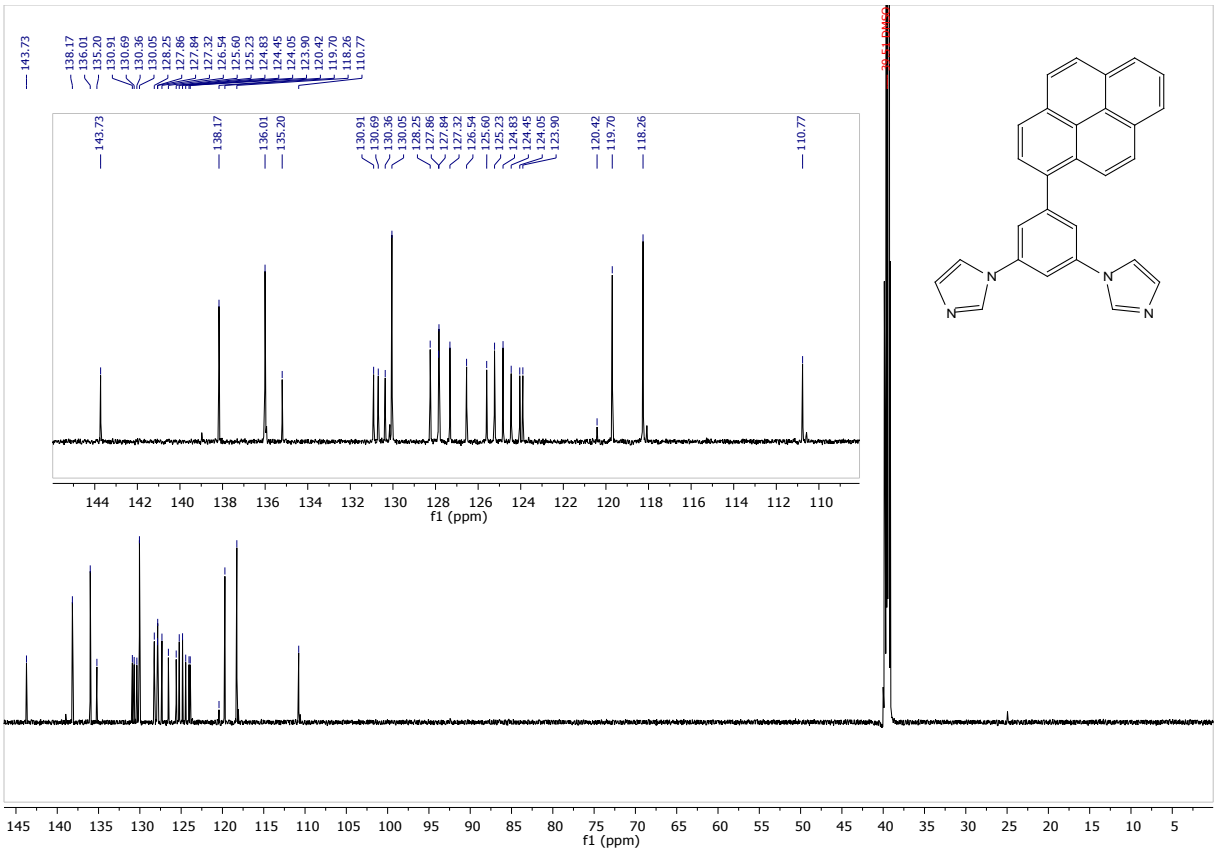

*Figure S46: ^{13}C-NMR spectrum of **4***

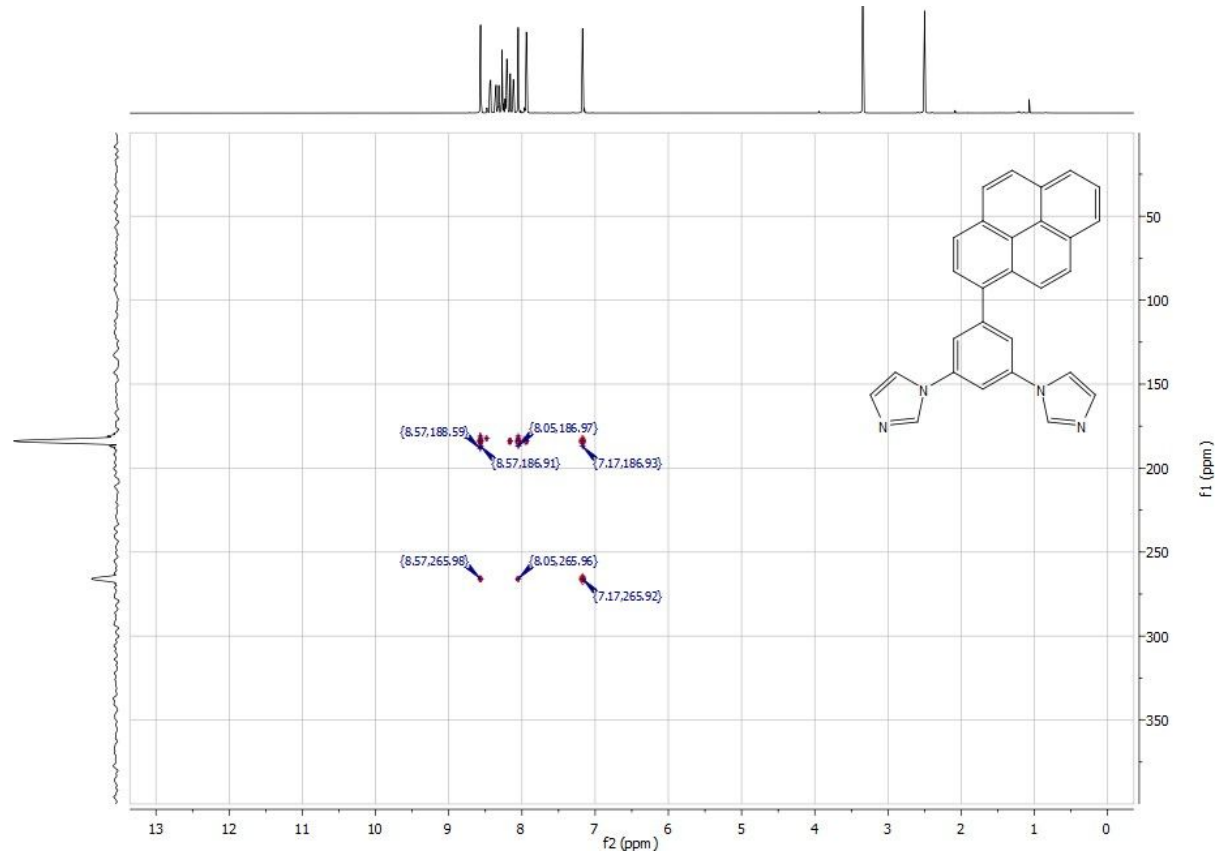

*Figure S47: ^{15}N-HMBC spectrum of **4***

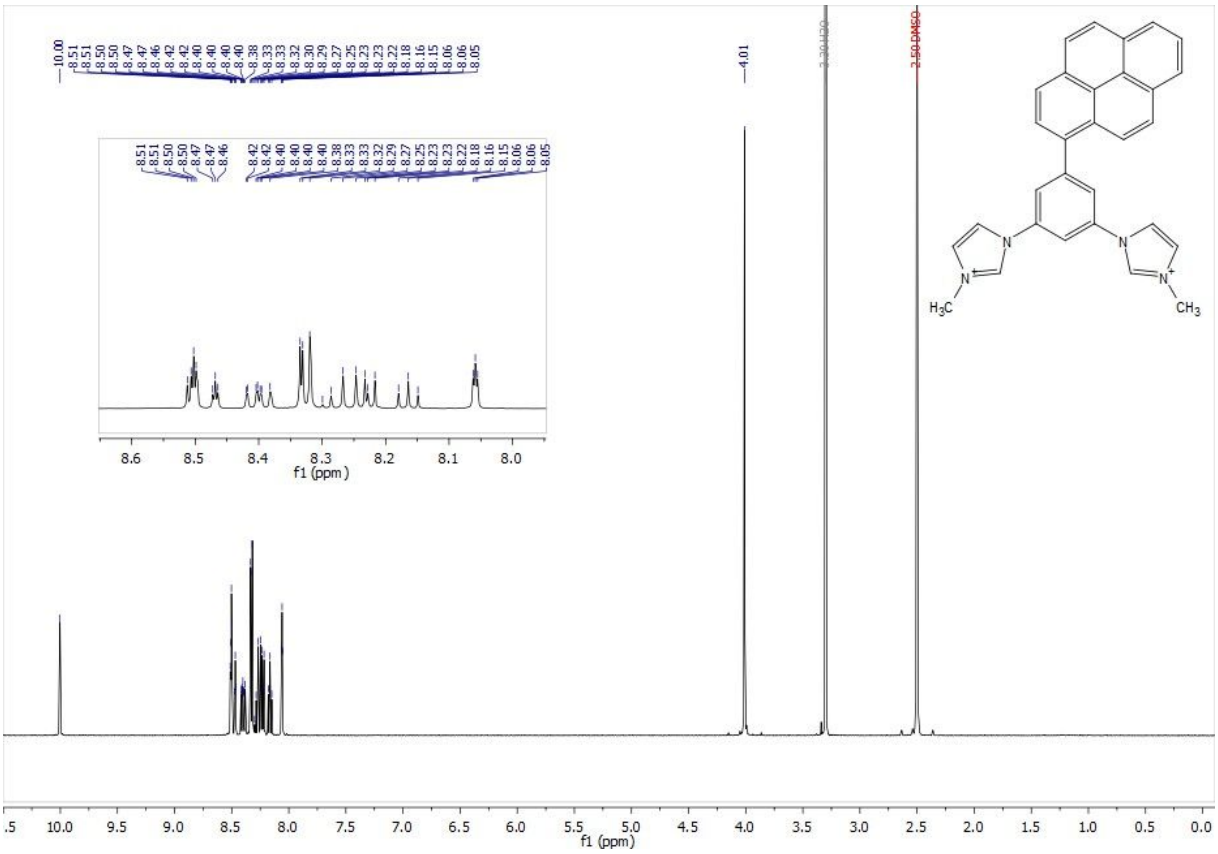

*Figure S48: [1]H-NMR spectrum of **L4***

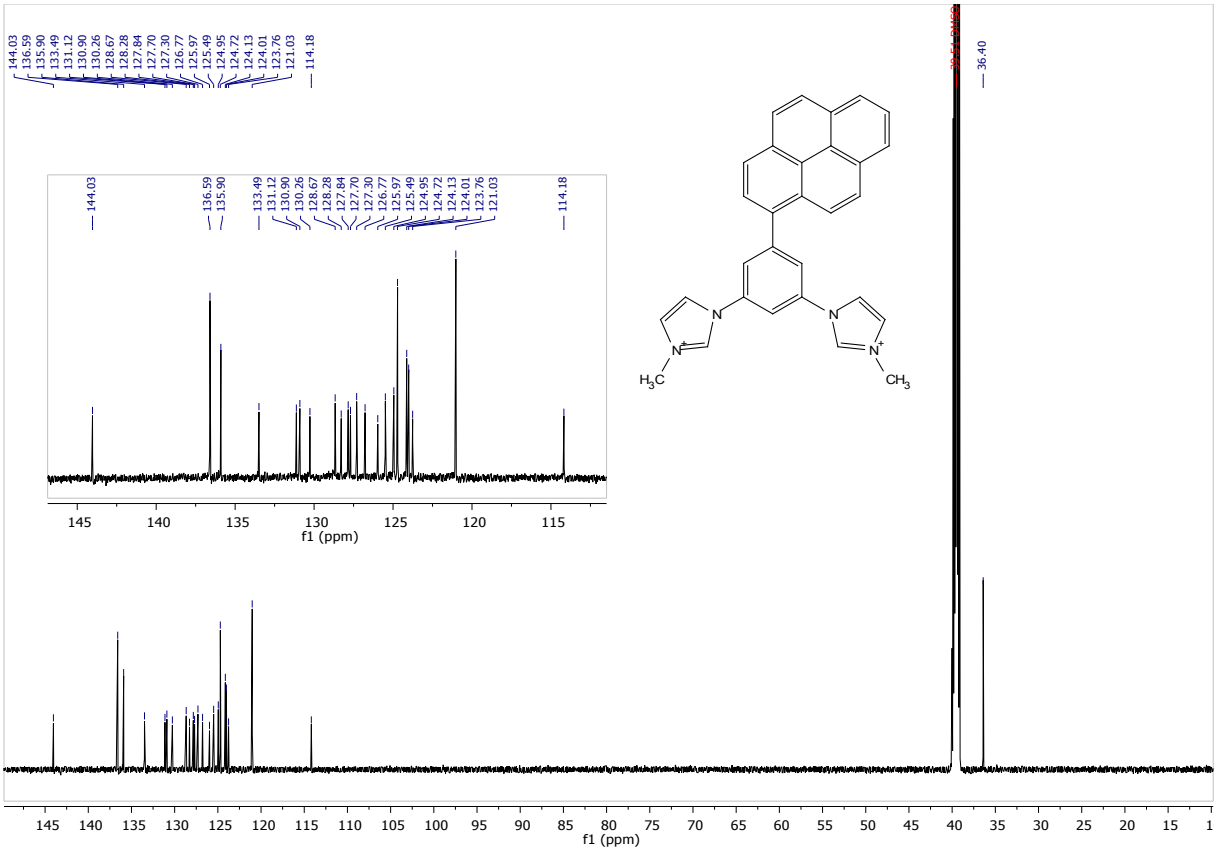

*Figure S49: [13]C-NMR spectrum of **L4***

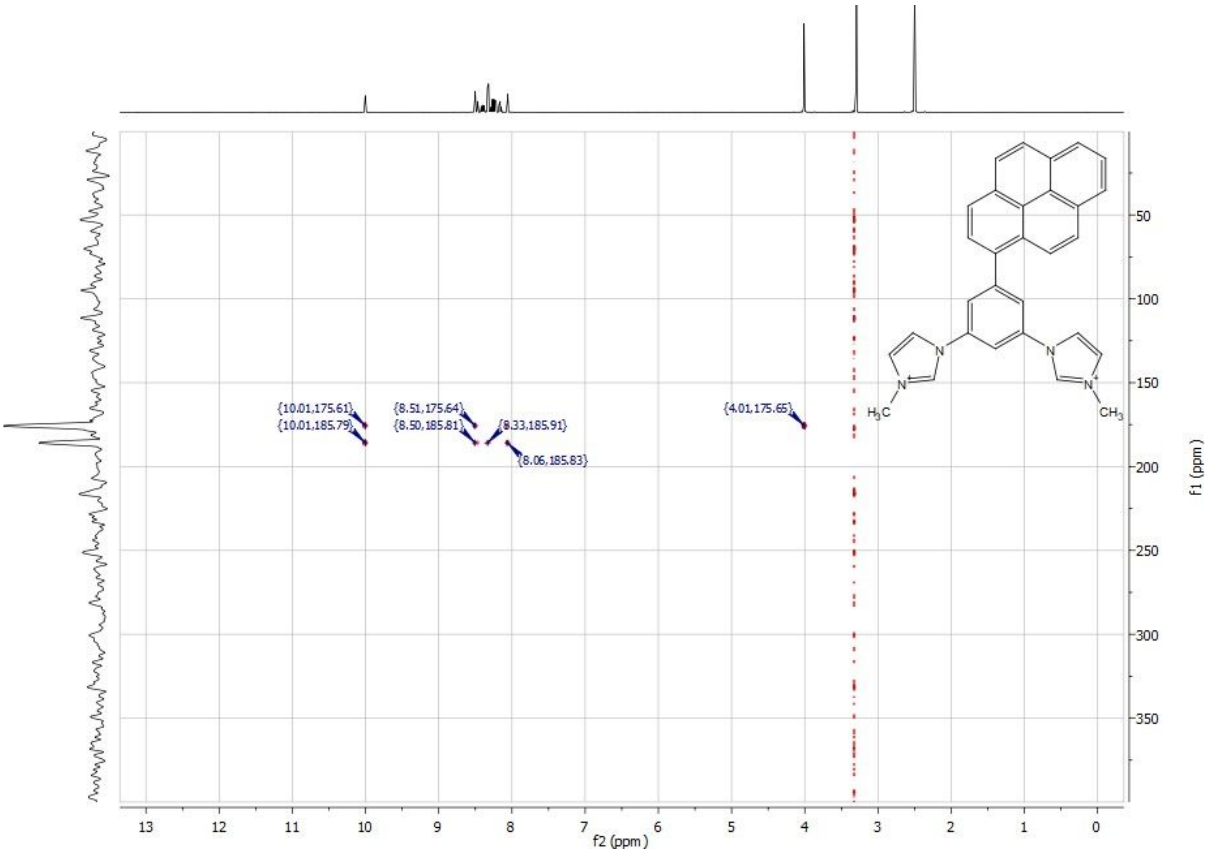

Figure S50: ^{15}N-HMBC spectrum of L4

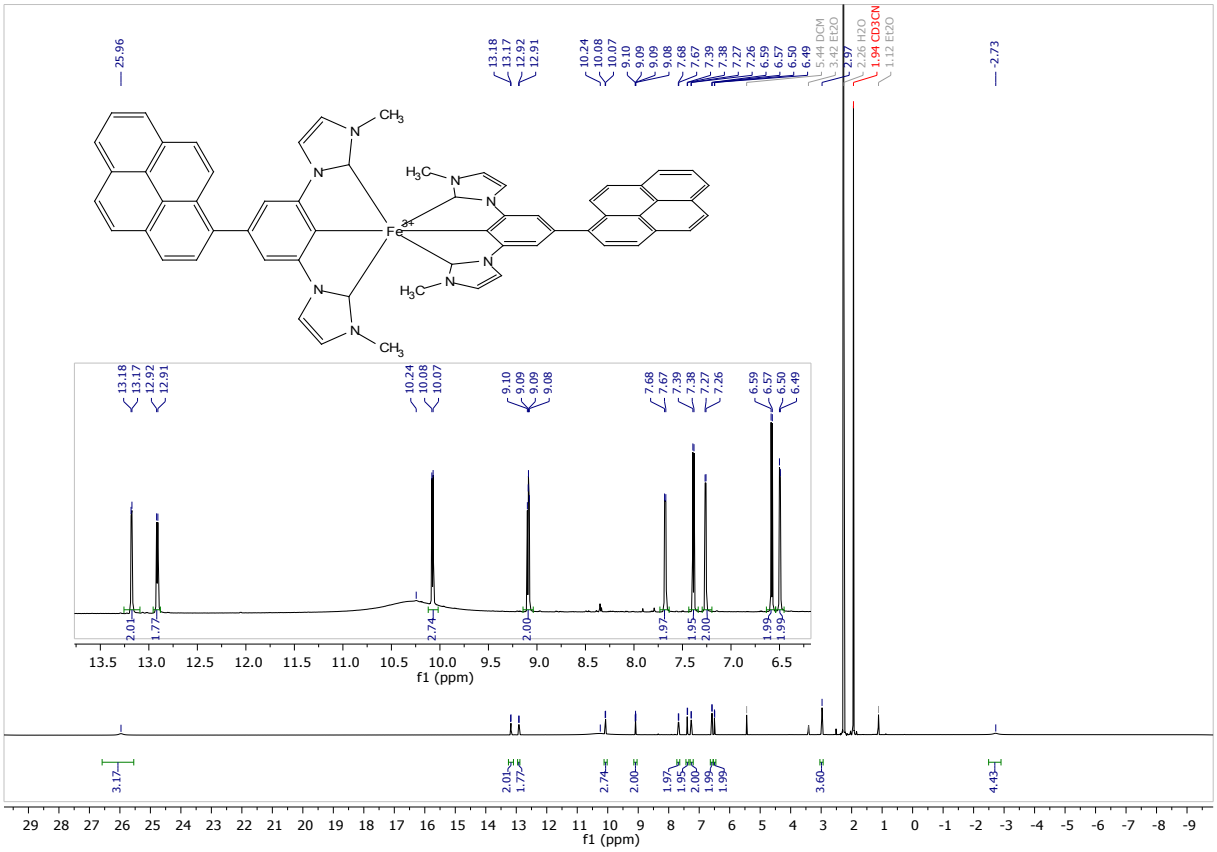

*Figure S51: ^{1}H-NMR spectrum of **C4***

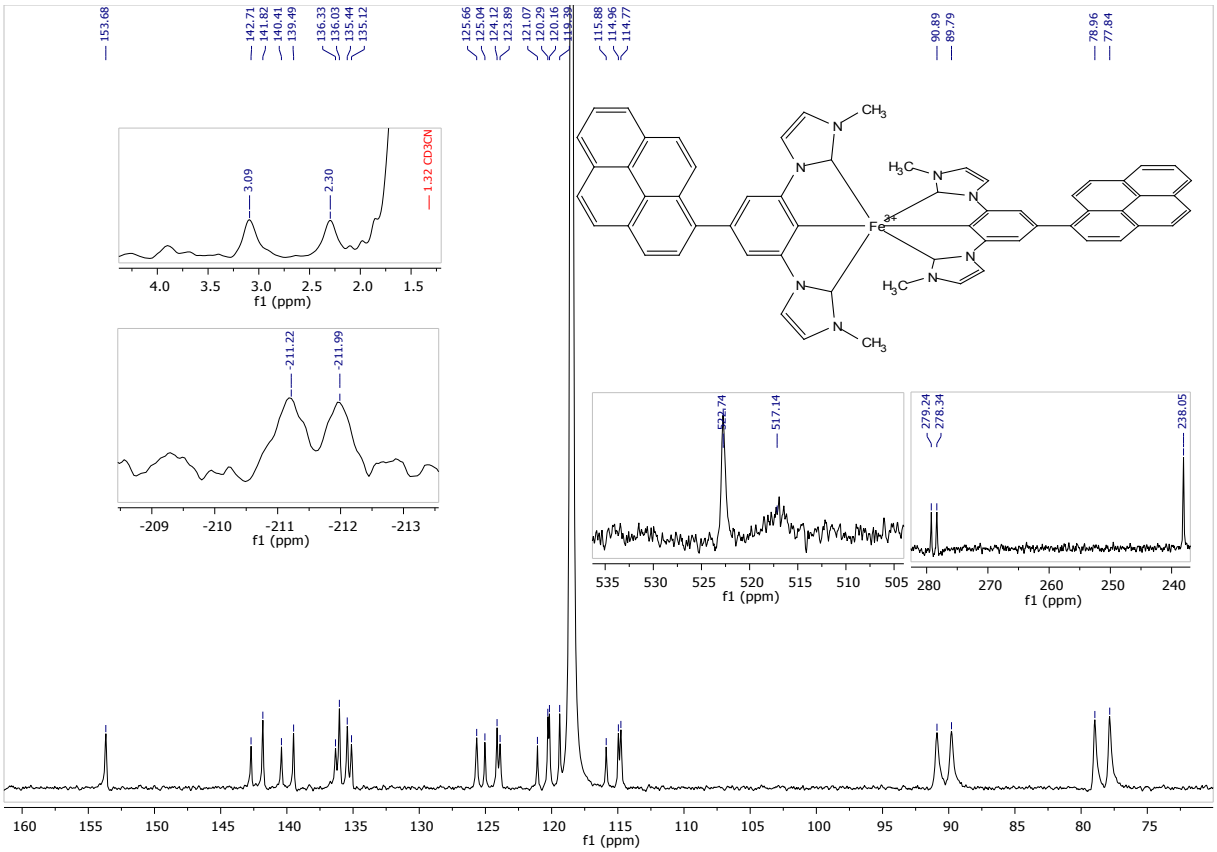

*Figure S52: ^{13}C-NMR spectrum of **C4***

Mass spectroscopy

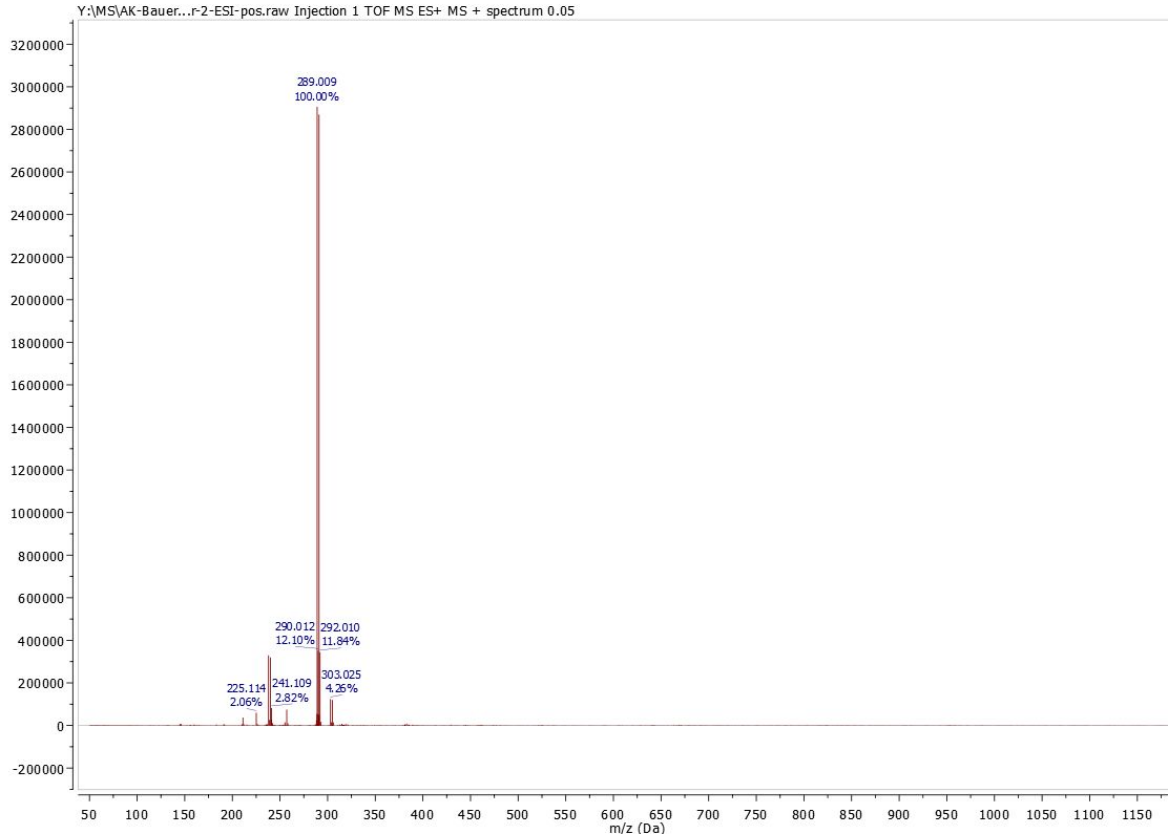

Figure S53: Mass spectrum of 1,1'-(b-bromo-1.3-phenylene)bis(1H-imidazole)

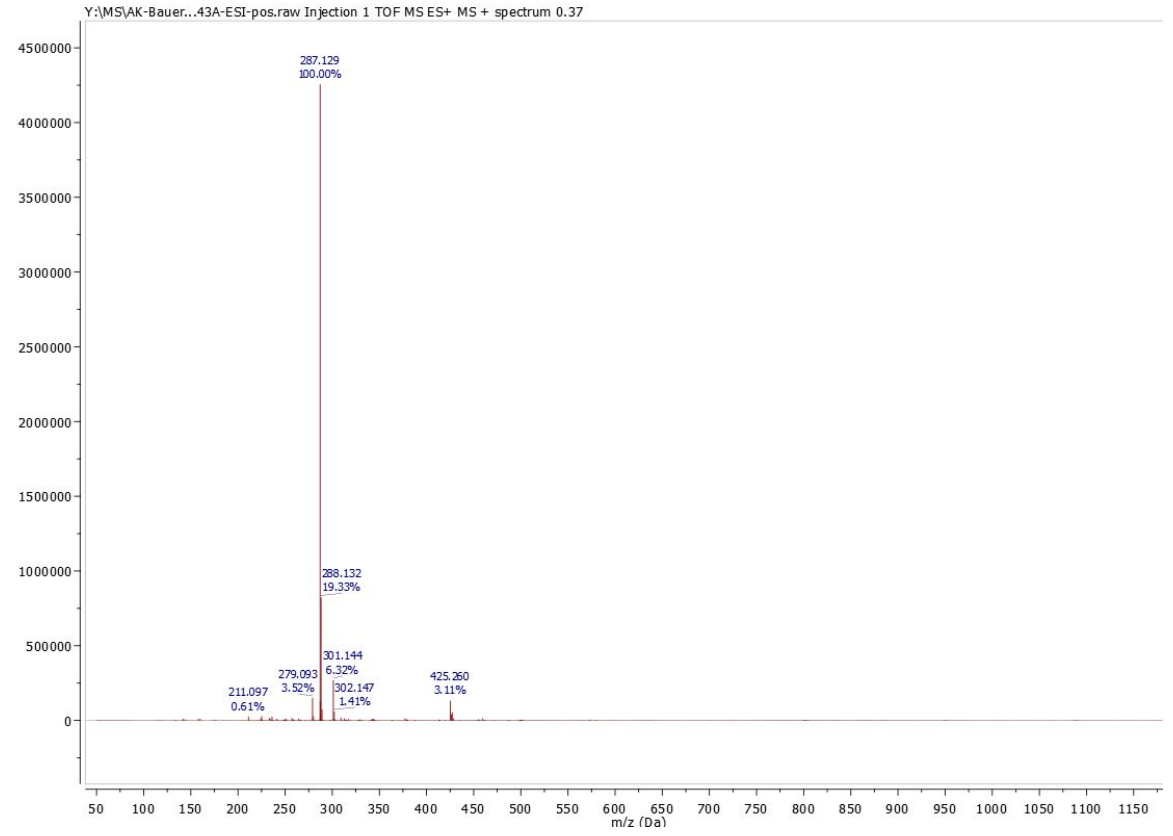

*Figure S54: Mass spectrum of **1***

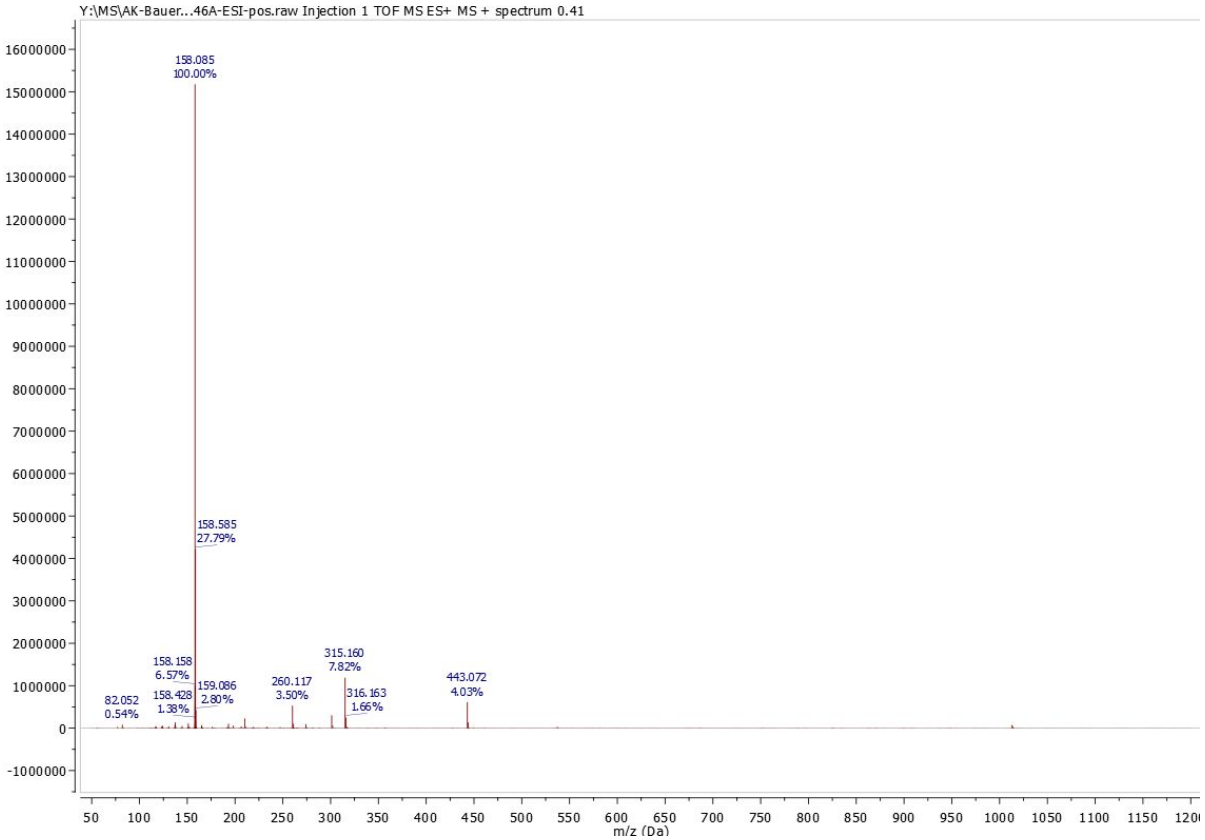

*Figure S55: Mass spectrum of **L1***

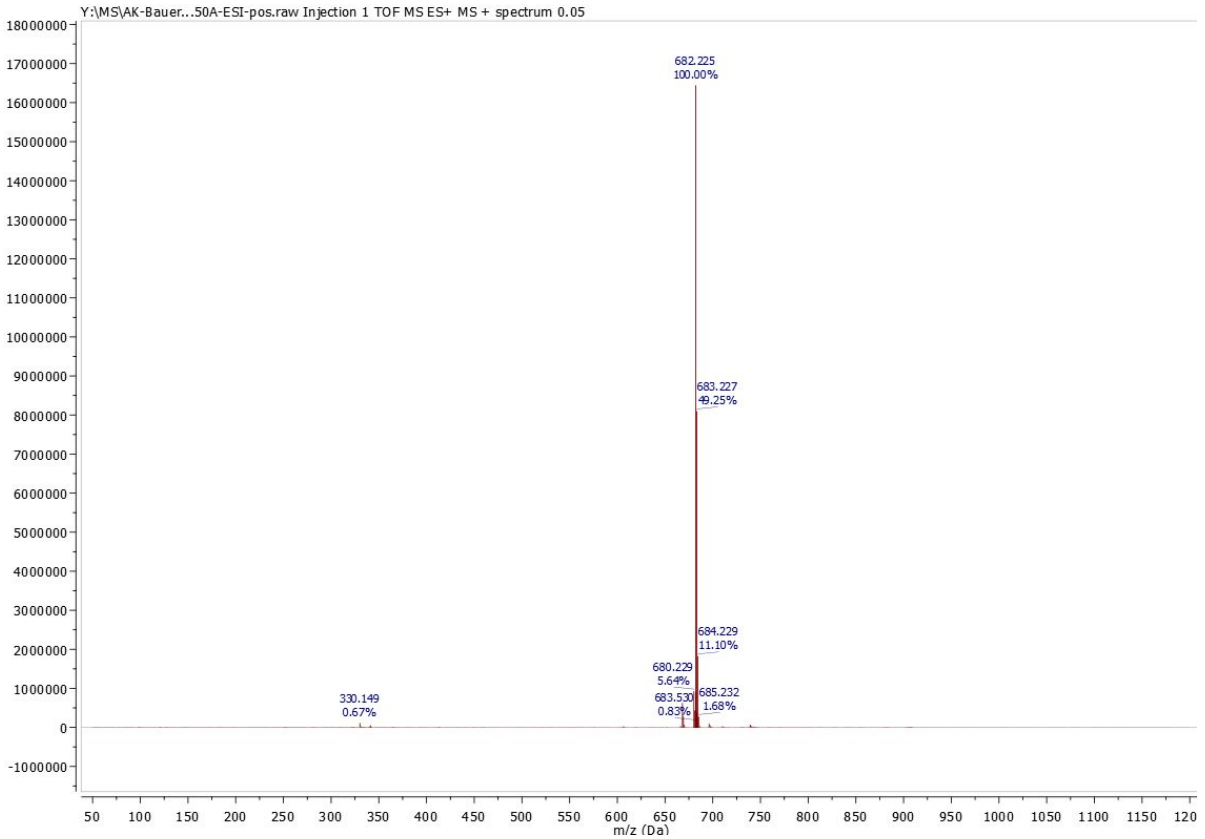

*Figure S56: Mass spectrum of **C1***

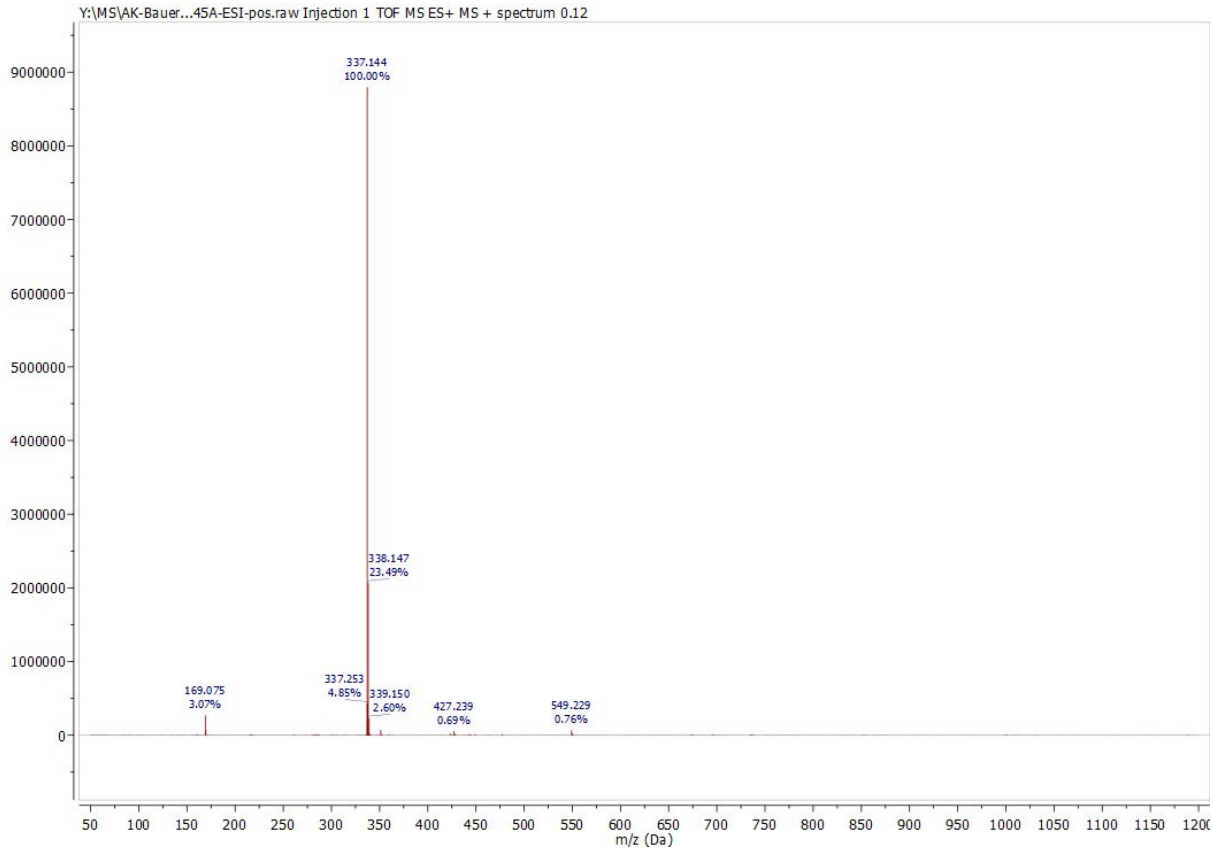

*Figure S57: Mass spectrum of **2***

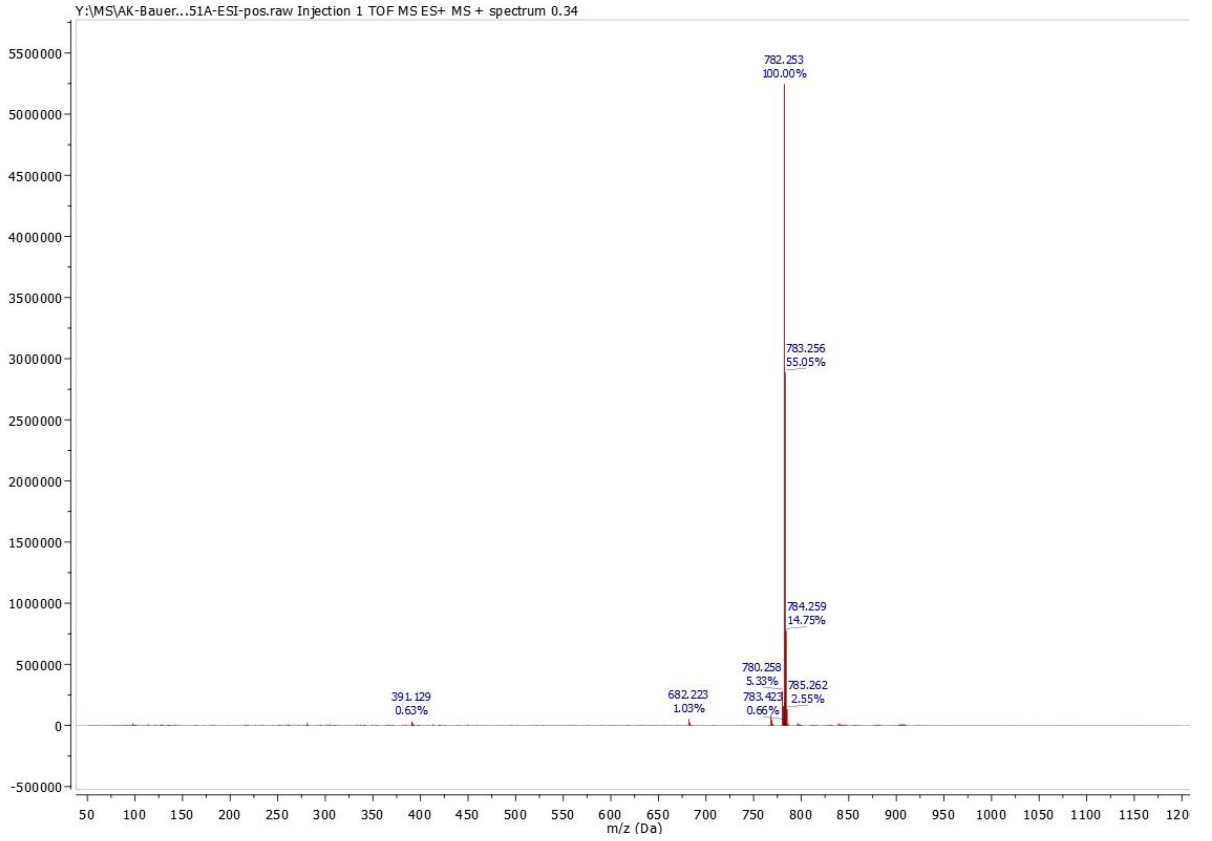

*Figure S58: Mass spectrum of **C2***

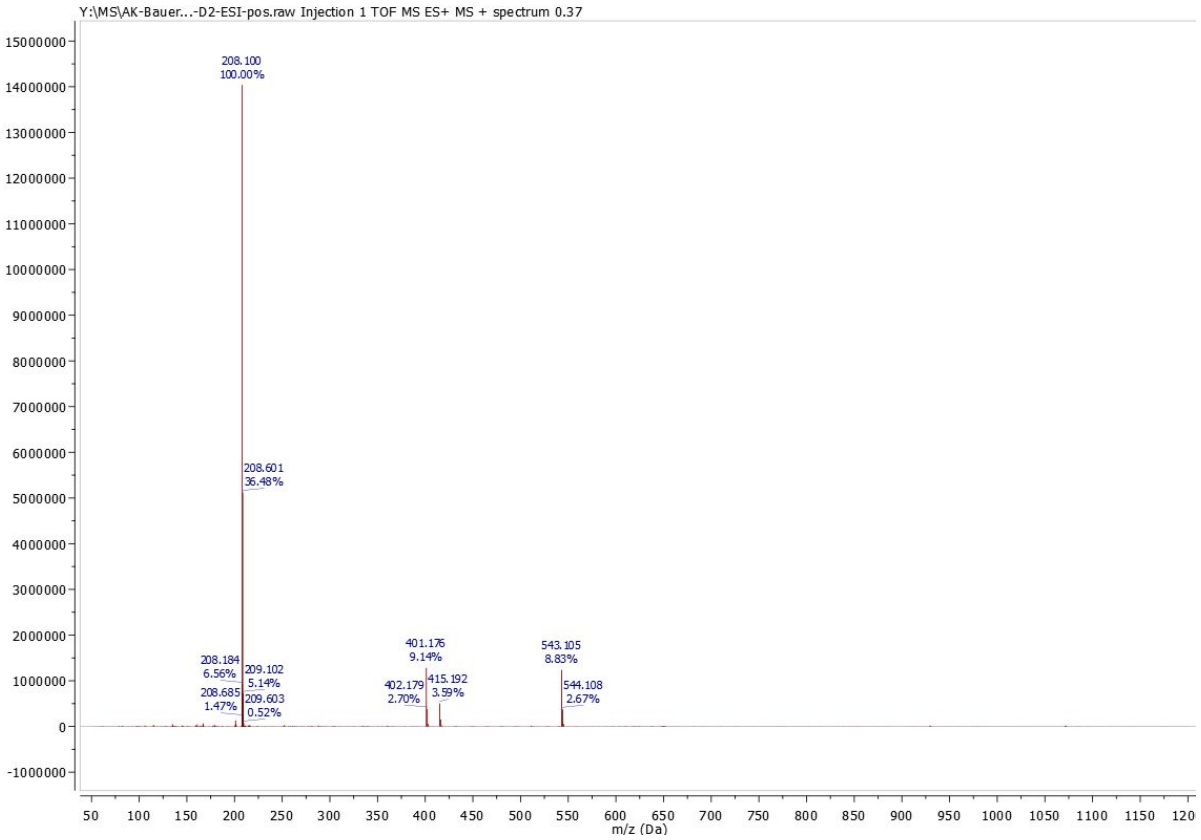

*Figure S59: Mass spectrum of **L3***

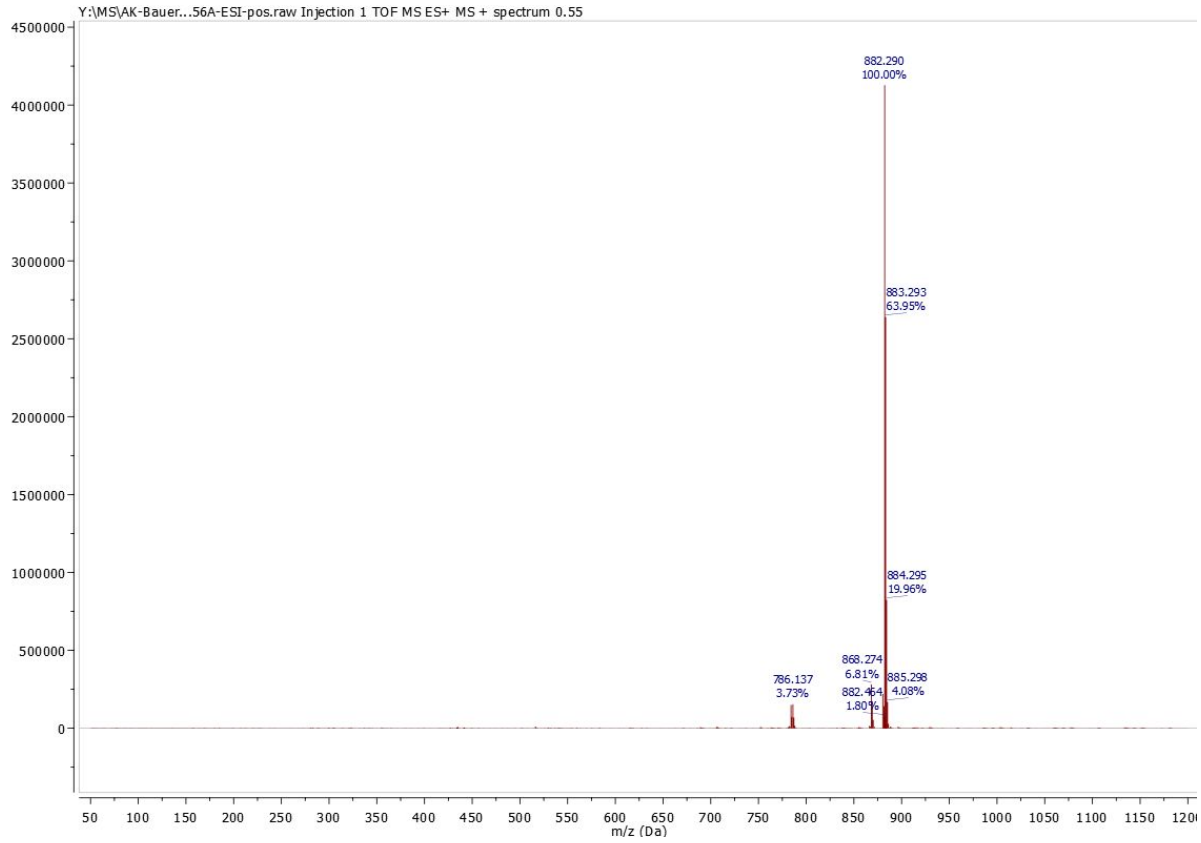

*Figure S60: Mass spectrum of **C3***

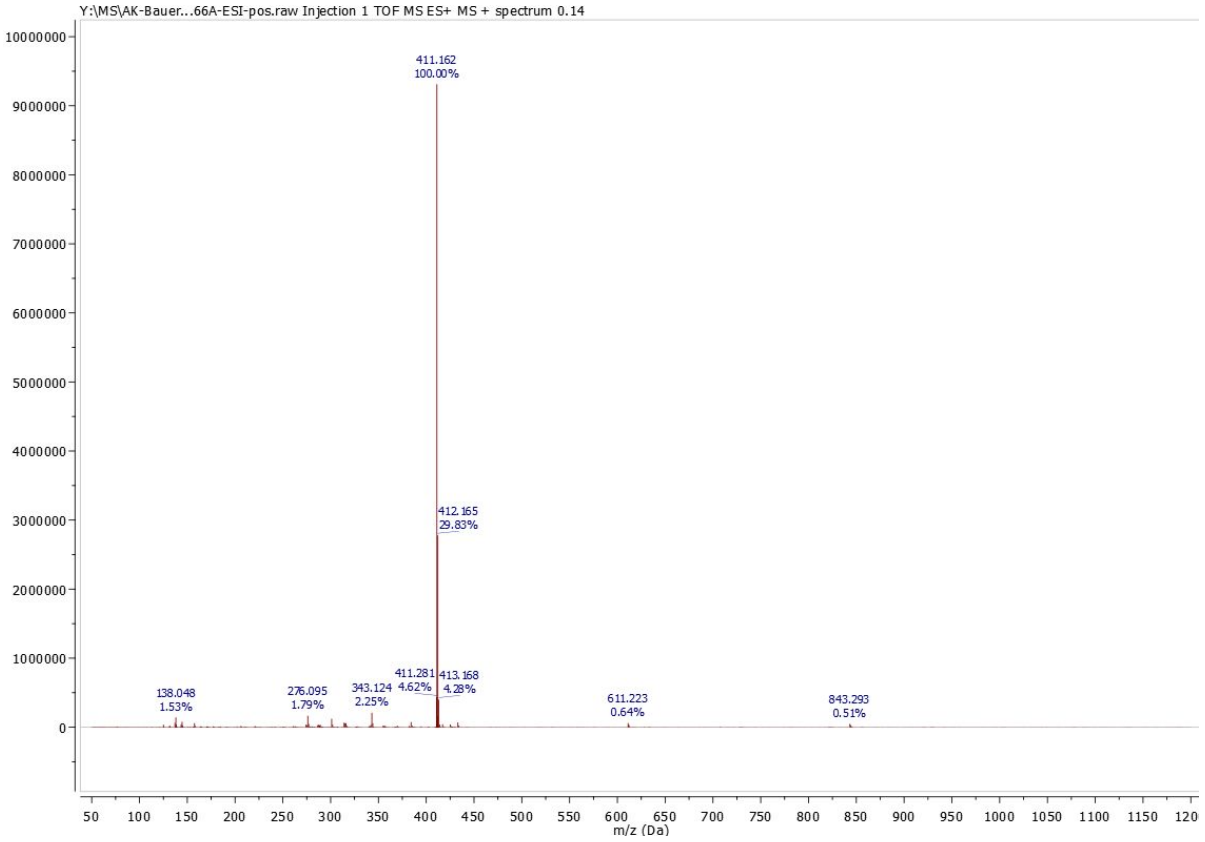

*Figure S61: Mass spectrum of **4***

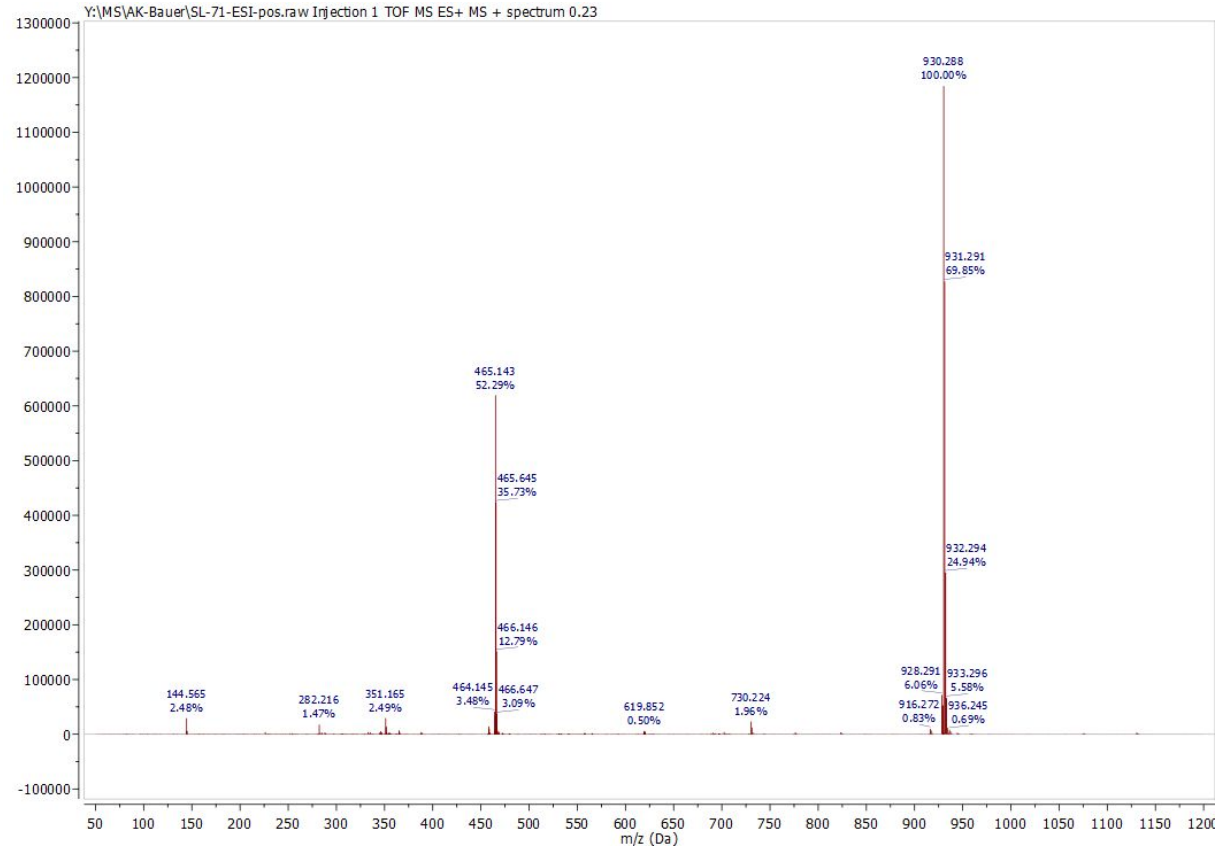

*Figure S62: Mass spectrum of **C4***

Transient Absorption

Excitation of the LMCT-transition

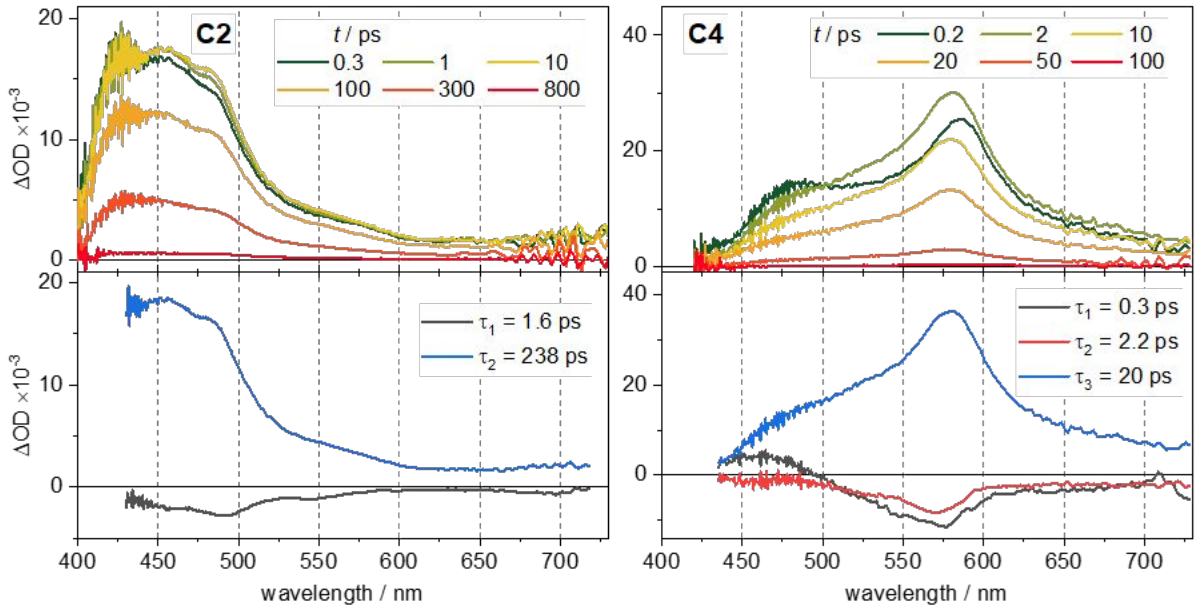

*Figure S63: Ultrafast TA-spectra (top) at the given delay times and DAS (bottom) of **C2** (left) and **C4** (right). The complexes are dissolved in MeCN and optically excited at 650 nm. The polarizations of the pump and probe pulses are set to magic angle.*

Excitation of the MLCT-transition

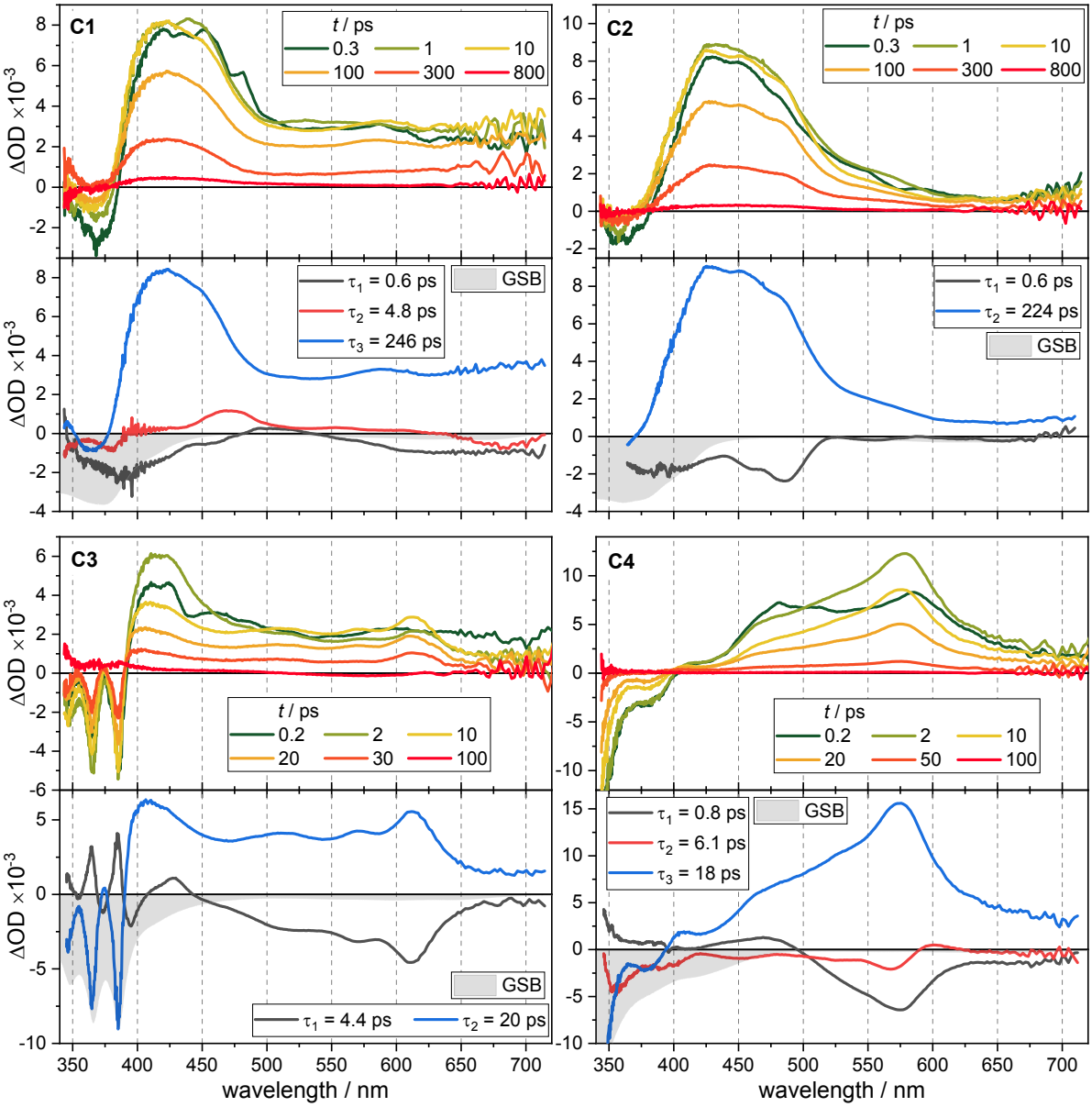

*Figure S64: Ultrafast TA-spectra (top) at the given delay times and DAS (bottom) of **C1**-**C4**. The complexes are dissolved in MeCN and optically excited at 350 nm. The polarizations of the pump and probe pulses are set to magic angle.*

Time- / Kinetic Traces

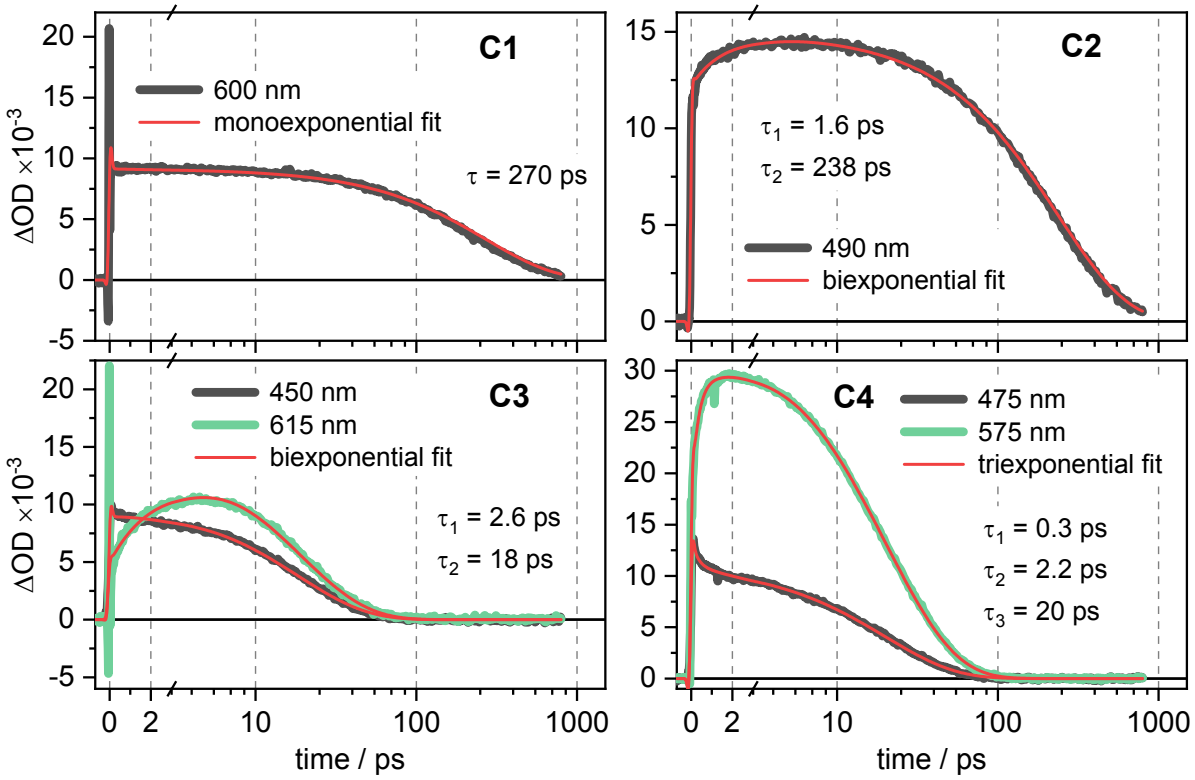

*Figure S65: Ultrafast excited-state kinetics at the given wavelengths of **C1**-**C4**. The complexes are dissolved in MeCN and optically excited at 650 nm. The polarizations of the pump and probe pulses are set to magic angle.*

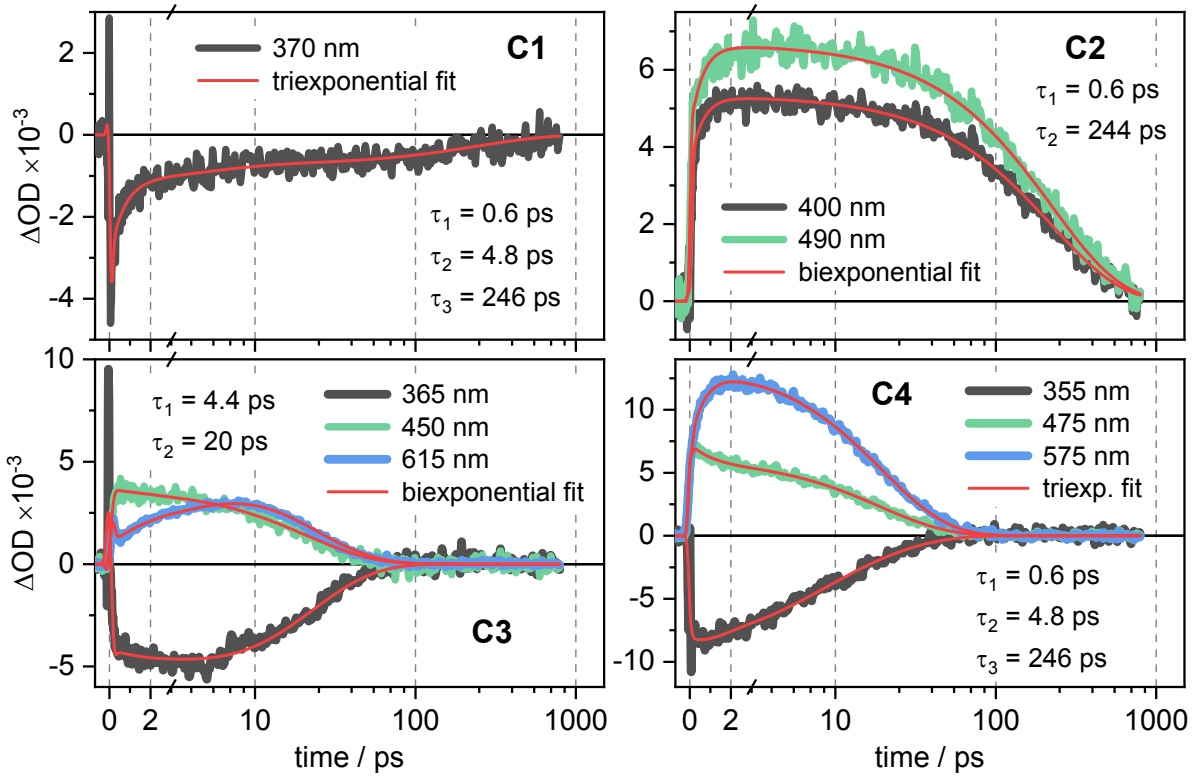

*Figure S66: Ultrafast excited-state kinetics at the given wavelengths of **C1**-**C4**. The complexes are dissolved in MeCN and optically excited at 350 nm. The polarizations of the pump and probe pulses are set to magic angle.*

Spectroelectrochemistry

UV-Vis absorption and electrochemical methods were combined in UV/vis/near-IR spectroelectrochemistry to probe the redox processes of all complexes and the nature of the resulting species. The resulting changes in absorption behaviour can be seen in Figure S67 (theoretical spectra can be found in FigS3 and FigS4). All complexes could be oxidized and reduced reversibly. For **C3** and more so for **C4**, side reactions occurred as expected due to the irreversible ligand oxidation, but the original solution could mostly be reobtained. A full bleach of the LMCT absorption is expected through reduction due to the filled t_2g orbitals. This is observed in **C1** and **C2**. In **C3** and **C4**, however, strong absorption bands arise in this region at 627 nm (**C3**) and 603 nm (**C4**). These could be MLCT bands which are expected to be redshifted compared to Fe(III), so their overlap covers the LMCT bands bleaching. Indeed, two absorption bands appear in the visible range for all complexes in the Fe(II) form. While all four complexes exhibit one of these bands close to 400 nm (**C1** at 361 nm, **C2** at 406 nm, **C3** at 411 nm, and **C4** at 409 nm), the second band shifts to lower energies in correspondence with the excited state energies of the reduced chromophores: **C1** (473 nm) > **C2**(406 nm, 495 nm) > **C4** (409 nm, 603 nm) > **C3** (411 nm, 627 nm). The somewhat lower absorption strength in the range of the chromophore bands of the reduced **C3** and **C4** complex is an additional indication that the Fe(III) forms of **C3** and **C4** exhibit there MLCT bands which are, however, covered by the stronger chromophore bands. A corresponding overlap of the chromophore and MLCT band is desirable for the antenna and the reservoir effect.

Oxidation of all complexes to Fe (IV) leads to two broad bands, one redshifted and one blueshifted with respect to the LMCT band of the Fe(III) complexes. The redshifted bands appear at 526 nm (**C1**), 506 nm (**C3**), and 506 nm (**C4**). For **C2**, a very broad signal with no clear absorption maximum occurs. The redshifted bands appear in the near-IR range at 875 nm (**C1**), 868 nm (**C2**), 860 nm (**C3**) and 945 nm (**C4**).

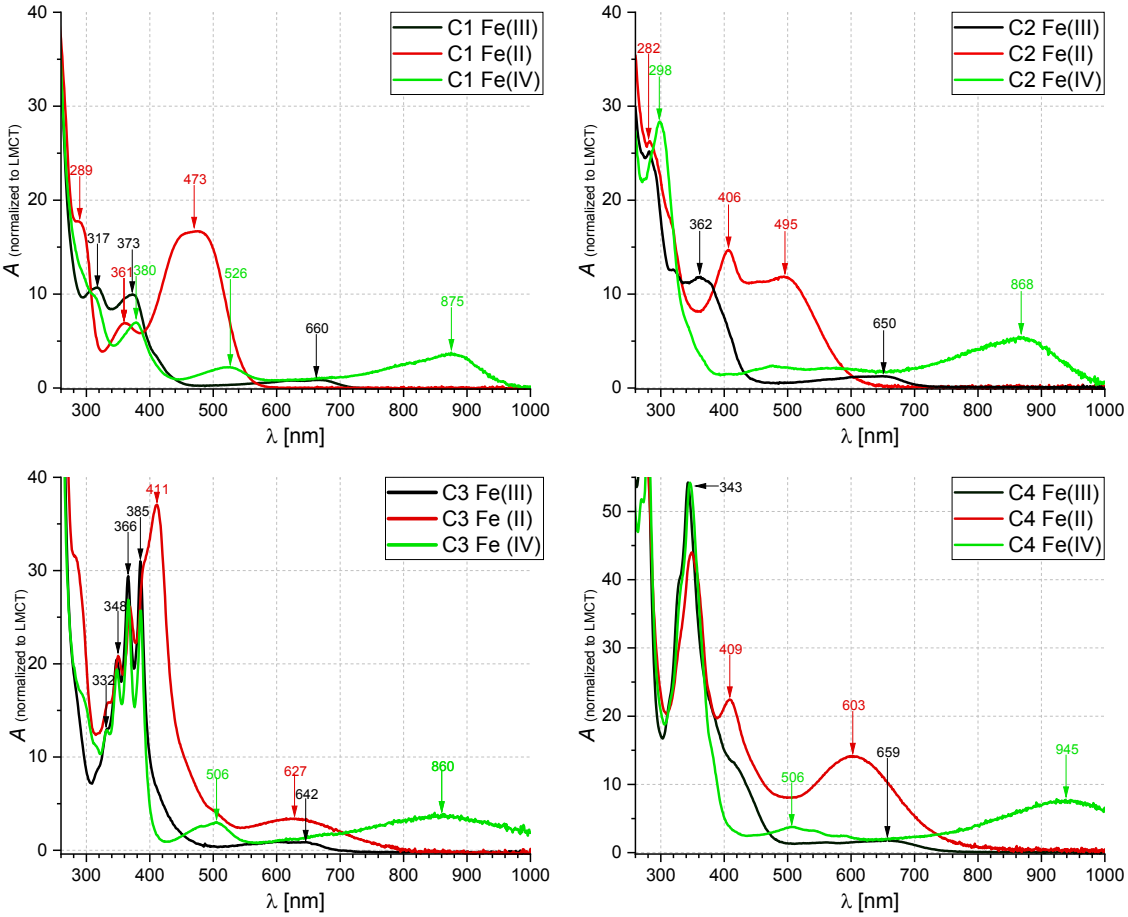

*Figure S67: Changes in the UV/vis/NIR spectra of **C1** to **C4** during oxidation (black -> green) and reduction (black -> red) in MeCN [0.1 M]*

Low-temperature emission of C1 and C2

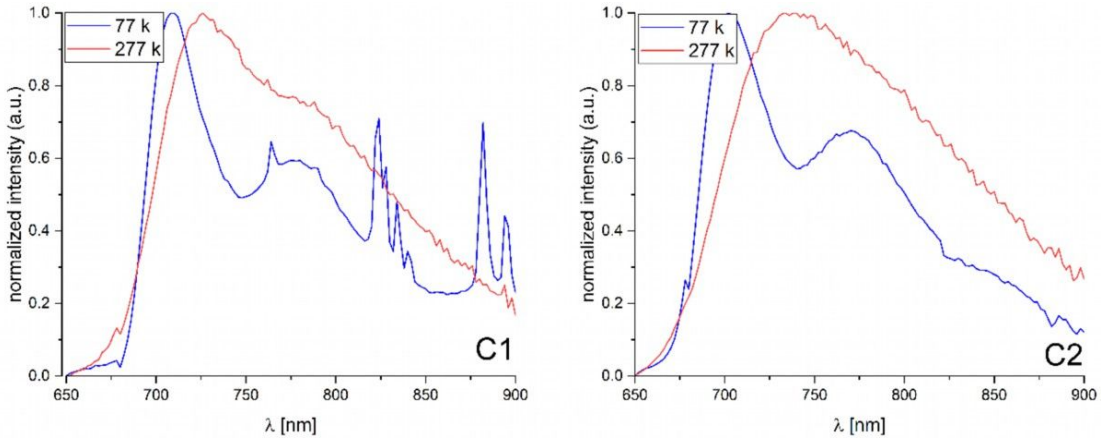

*Figure S68: Emission spectra of **C1** and **C2** in Butyronitrile (10^{-5} mol/l) at 77k and 277k. Solvent spectra of Butyronitrile at the corresponding temperatures were substracted.*

Contrary to the emission of **C3** and **C4**, the band positions of **C1** and **C2** are only slightly influenced by temperature. At lower temperature, the emission is slightly blueshifted, suggesting, that the frozen geometry without planarization also affects these complexes. The second weaker maximum above

750 nm could be explained by a portion of the molecules being frozen in a planar geometry leading to a lower emission energy.

Relative Emission Intensity of C3 and pure Anthracene

The singlet chromophore emission of **C3** was compared with the singlet chromophore emission of pure anthracene at 10^{-5} mol/l in MeCN. For this, the absorptivity of both substances at 365 nm (A_{C3} and A_{ant}) were measured. In addition, the counts of fluorescence spectroscopy between 415 nm and 440 nm were integrated (E_{C3} and E_{ant}). This puts the residual emission from the anthracene moiety of **C3** in contrast to the much higher emission of isolated anthracene following the equation below:

$$\frac{E_{C3}}{A_{C3}} \Big/ \frac{E_{ant}}{A_{ant}} = 1.04\ ‰$$

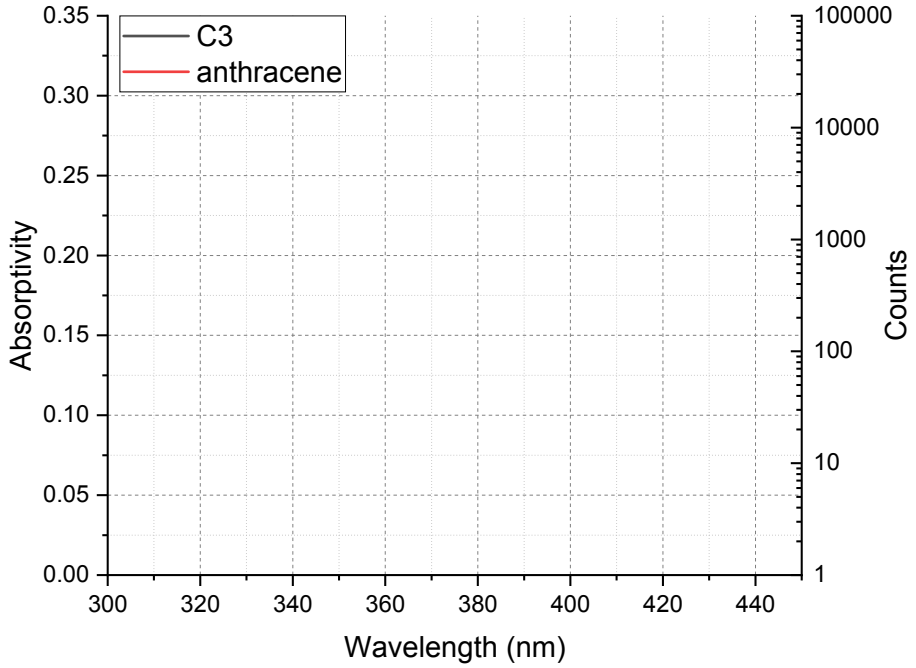

*Figure S69: Absorptivity and emission of **C3** and anthracene in MeCN at 10^{-5} mol/l.*

Comparison of weak C4 emission at room temperature and solvent emission

Due to the weak emission of **C4**, the background emission resulting from the applied solvent would lead to a wrong impression of an additional emission for **C4**. To prevent this the emission spectrum of **C4** in the manuscript was cut off at higher wavelengths than those of the other complexes. The full emission spectrum is shown in Figure S70 and compared to solvent emission.

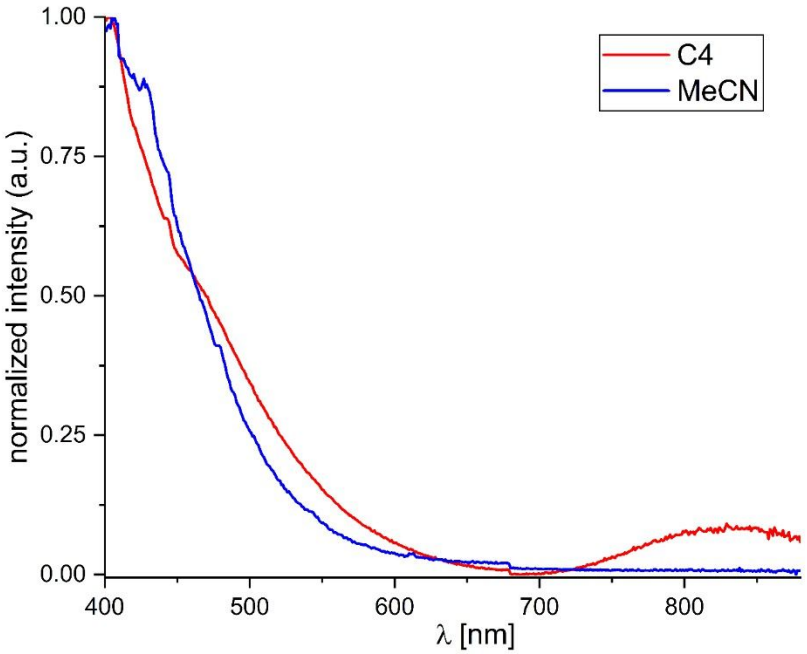

*Figure S70: Comparison of the emission spectrum of **C4** in acetonitrile at 10^{-5} mol/l compared to pure acetonitrile*

Time Correlated Single Photon Counting

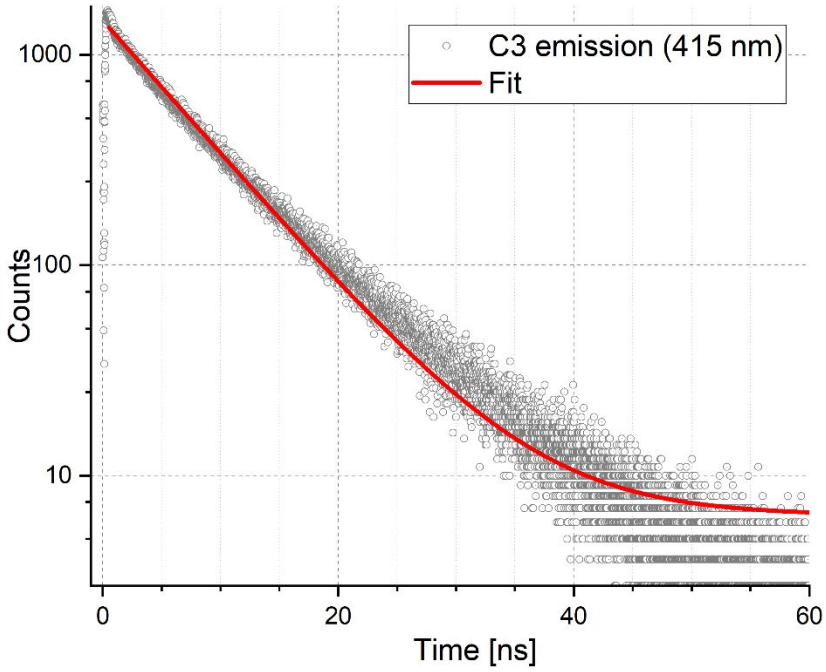

*Figure S71: TCSPC measurement of the **C3** sample in MeCN at $1*10^{-5}$ mol/l*

Single crystal X-ray Analysis

The Cambridge Crystallographic Data Centre provides the presented structures free of charge via www.ccdc.cam.ac.uk assigned to the deposition numbers 2402183-2402186.

C1

$C_{40}H_{34}N_8Fe$, PF_6, M_r = 827.57 Da, green plate, size 0.01 x 0.04 x 0.24 mm³, orthorhombic space group $Pna2_1$ with Z=4, a=24.0126(16), b=10.9981(8) Å, c=14.0018(10) Å, V=3697.8(5) Å³, D_c=1.487 g/cm³, μ=0.524 mm^{-1}, F(000)=1700, ϑ_{max}=29.641°, reflections collected: 82981, independent reflections: 10408, R_{int}=0.0524, refinement converged at $R1$=0.0389 [I>2σ(I)], $wR2$=0.1018 [all data], min./max. ΔF: -0.57 eÅ³ (0.27 Å from P1) / 0.84 eÅ³ (0.96 Å from F13), **CCDC No.: 2402183.**

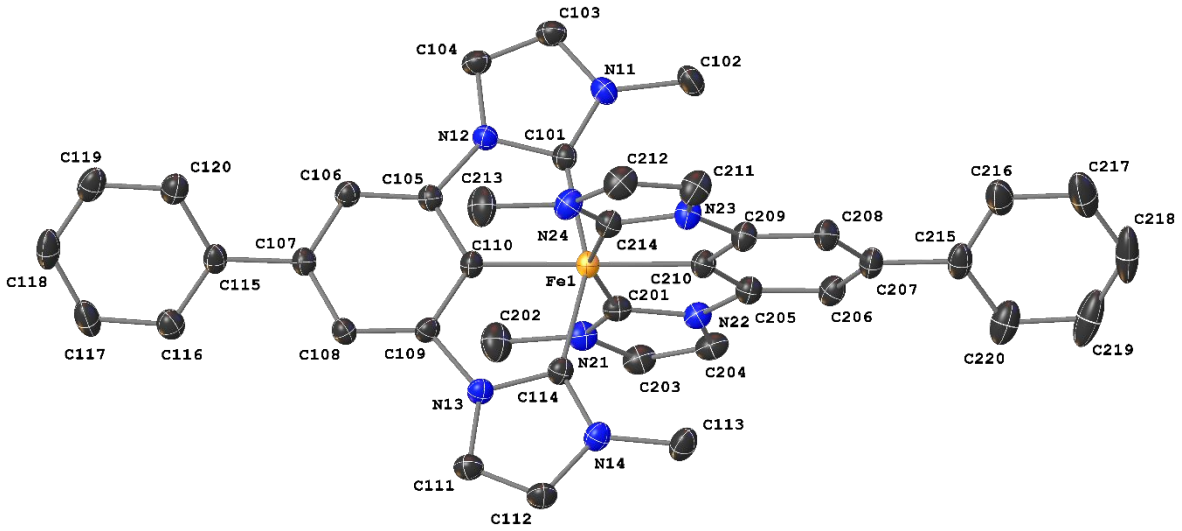

*Figure S72: Crystal structure of **C1** shown with anisotropic displacement ellipsoids drawn at 50% probability level. Hydrogen atoms and one PF_6-anion were omitted for reasons of clarity.*

The structure was refined as a 2-component inversion twin. All non-hydrogen-atoms were refined anisotropically, while the aromatic hydrogen atom positions were refined at idealized positions riding on the carbon atoms with isotropic displacement parameters U_{iso}(H)=1.2 U_{eq}(C) and C-H bond lengths of 0.950 Å (HFIX 43). Methyl groups are idealized with tetrahedral angles in a combined rotating and rigid group refinement with 1.5 fold isotropic displacement parameters of the equivalent U_{ij} of the corresponding carbon atom at a distance of d(C-H)=0.980 Å (HFIX 137).

C2

$C_{48}H_{38}N_8Fe$, PF_6, CH_2Cl_2, M_r = 1012.61 Da, black block, size 0.22 x 0.24 x 0.26 mm³, triclinic space group $P\bar{1}$ with Z=2, a=10.8494(6), b=12.3565(7) Å, c=17.9491(10) Å, α=103.5450(10) °, β=94.5730(10) °, γ=97.0480(10) °, V=2306.9(2) Å³, D_c=1.458 g/cm³, μ=0.547 mm^{-1}, F(000)=1038, ϑ_{max}=33.139°, reflections collected: 354770, independent reflections: 17642, R_{int}=0.0418, refinement converged at $R1$=0.0575 [I>2σ(I)], $wR2$=0.1352 [all data], min./max. ΔF: -1.06 eÅ³ (0.44 Å from Cl2A) / 1.02 eÅ³ (0.64 Å from Cl2D), **CCDC No.: 2402184.**

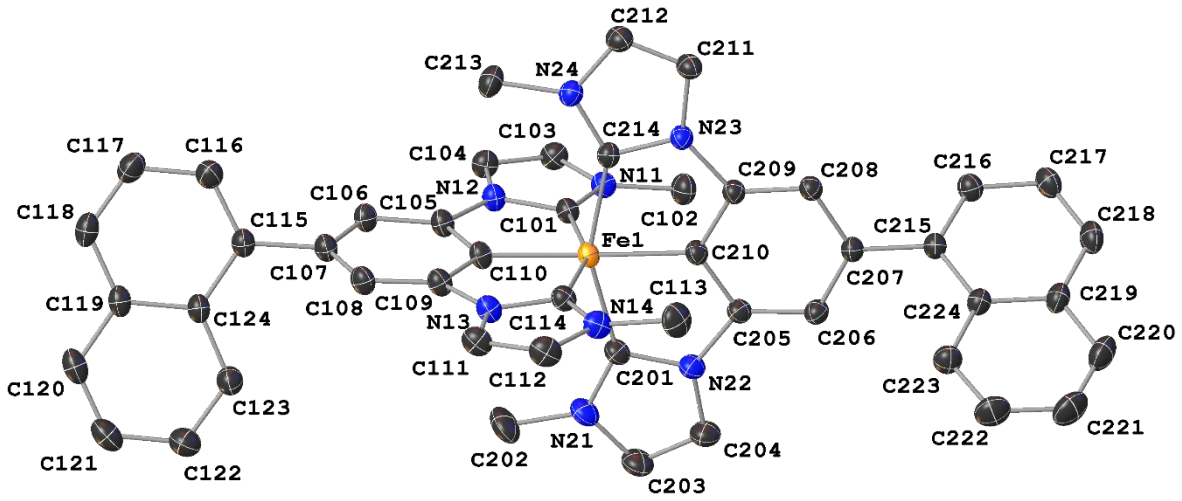

*Figure S73: Crystal structure of **C2** shown with anisotropic displacement ellipsoids drawn at 50% probability level. Hydrogen atoms, one PF_6-anion and one dichloromethane molecule were omitted for reasons of clarity.*

The PF_6 anion is disordered completely over two positions (SOF=79:21), the F atoms of the smaller occupied fraction could only be refined isotropically. One dichloromethane molecule is present in the asym. unit, whereby both Cl atoms are disordered over four positions (SOF=41:22:12:25) and could only be refined isotropically.

All non-hydrogen-atoms were refined anisotropically, while the aromatic hydrogen atom positions were refined at idealized positions riding on the carbon atoms with isotropic displacement parameters $U_{iso}(H)$=1.2 $U_{eq}(C)$ and C-H bond lengths of 0.950 Å (HFIX 43). Methyl groups are idealized with tetrahedral angles in a combined rotating and rigid group refinement with 1.5 fold isotropic displacement parameters of the equivalent U_{ij} of the corresponding carbon atom at a distance of d(C-H)=0.980 Å (HFIX 137).

C3

$C_{56}H_{42}N_8Fe$, PF_6, 2(CH_4O), M_r = 1091.88 Da, grey plate, size 0.02 x 0.14 x 0.30 mm³, monoclinic space group $P2_1/c$ with Z=4, a=21.0442(16), b=14.1359(11) Å, c=18.6099(14) Å, β=110.370(2) °, V=5189.8(7) Å³, D_c=1.397 g/cm³, μ=0.395 mm^{-1}, F(000)=2260, ϑ_{max}=27.422°, reflections collected: 266974, independent reflections: 12477, R_{int}=0.1027, refinement converged at $R1$=0.0764 [I>2σ(I)], $wR2$=0.2059 [all data], min./max. ΔF: -0.90 eÅ³ (0.35 Å from H2BA) / 1.41 eÅ³ (0.45 Å from H1AB), **CCDC No.: 2402185.**

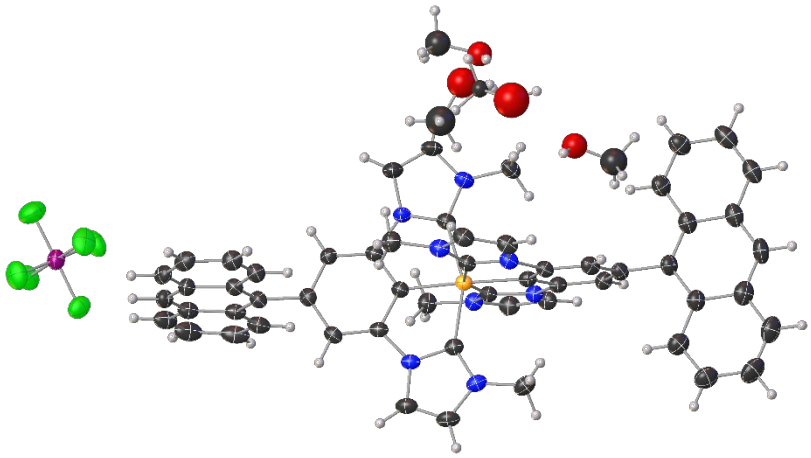

*Figure S74: Asymmetric unit of **C3** including PF_6 anion and two methanol molecules.*

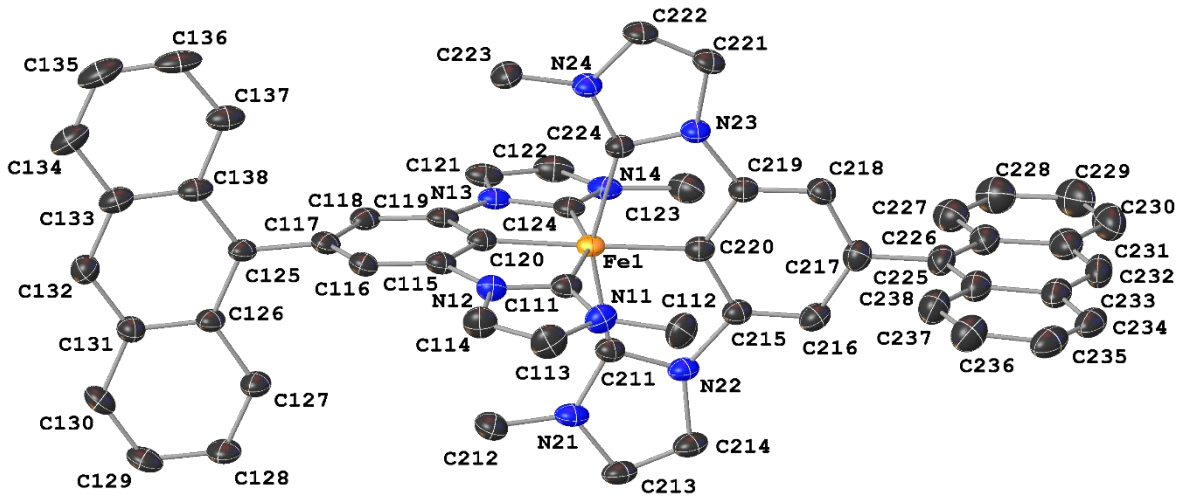

*Figure S75: Crystal structure of **C3** shown with anisotropic displacement ellipsoids drawn at 50% probability level. Hydrogen atoms, one PF_6 anion and two methanol molecules were omitted for reasons of clarity.*

Two methanol molecules are present in the asym. unit, both completely disordered over two positions (SOF=61:39 and 64:36). All non-hydrogen-atoms were refined anisotropically, while the aromatic hydrogen atom positions were refined at idealized positions riding on the carbon atoms with isotropic displacement parameters U_{iso}(H)=1.2 U_{eq}(C) and C-H bond lengths of 0.950 Å (HFIX 43). Methyl groups are idealized with tetrahedral angles in a combined rotating and rigid group refinement with 1.5 fold isotropic displacement parameters of the equivalent U_{ij} of the corresponding carbon atom at a distance of d(C-H)=0.980 Å (HFIX 137). O-H hydrogen atoms were fitted with the 1.5 fold isotropic displacement parameter at a distance of d(O-H)=0.84 \%A (HFIX 147).

C4

$C_{60}H_{42}N_8Fe$, 0.886(PF_6), 0.114I, 4(C_5H_5N), M_r = 1390.20 Da, red block, size 0.12 x 0.18 x 0.22 mm³, monoclinic space group $P2_1/c$ with Z=4, a=17.1442(7), b=14.8488(6) Å, c=26.1465(11) Å, β=97.707(10) °, V=6569.0(5) Å³, D_c=1.400 g/cm³, μ=0.376 mm^{-1}, F(000)=2877, ϑ_{max}=28.332°, reflections collected: 517647, independent reflections: 16408, R_{int}=0.0499, refinement converged at $R1$=0.0472 [I>2σ(I)], $wR2$=0.1374 [all data], min./max. ΔF: -0.55 eÅ³ (0.36 Å from C24) / 0.87 eÅ³ (1.02 Å from C24), **CCDC No.: 2402186.**

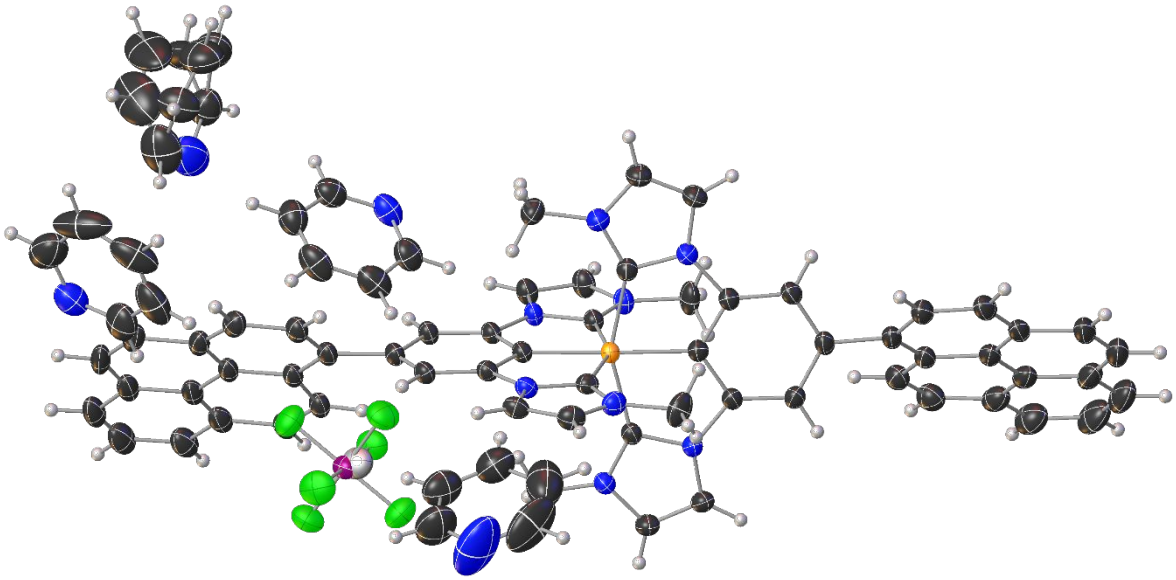

*Figure S76: Asymmetric unit of **C4** including a partially occupied PF_6 anion (SOF=0.886) and Iodide (SOF=0.114). In addition, four pyridine molecules are shown.*

The anion of the complex molecule was not replaced completely before crystallization, therefore a partially occupied PF_6 anion (SOF=0.886) and an Iodide (SOF=0.114) was modelled. In addition to the complex molecule and the anion, four pyridine molecules are present in the asymmetric unit, one with three carbon atoms disordered over two positions.

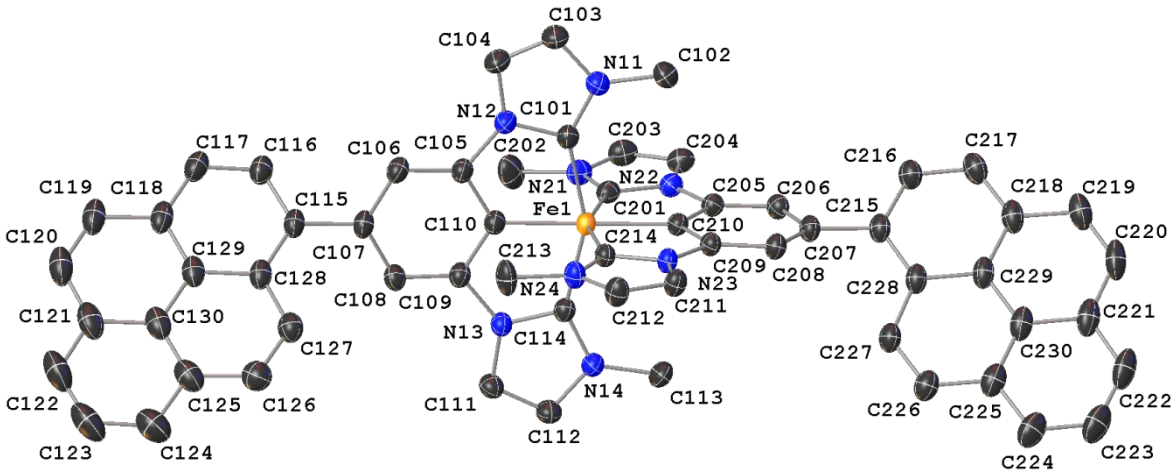

*Figure S77: Crystal structure of **C4** shown with anisotropic displacement ellipsoids drawn at 50% probability level. Hydrogen atoms, one PF_6 anion and two methanol molecules were omitted for reasons of clarity.*

All non-hydrogen-atoms were refined anisotropically, while the aromatic hydrogen atom positions were refined at idealized positions riding on the carbon atoms with isotropic displacement parameters $U_{iso}(H)=1.2\ U_{eq}(C)$ and C-H bond lengths of 0.950 Å (HFIX 43). Methyl groups are idealized with tetrahedral angles in a combined rotating and rigid group refinement with 1.5 fold isotropic displacement parameters of the equivalent U_{ij} of the corresponding carbon atom at a distance of d(C-H)=0.980 Å (HFIX 137).

Reservoir Effect in bichromophoric Fe^{III} Complexes with Methylene Bridge

Supporting Information

Lennart Schmitz, Samira Dabelstein, Miguel Argüello Cordero, Lorena Fritsch, Bastian Bracht, Roland Schoch, Hans Egold, Jakob Steube, Felix Fischer, Stefan Lochbrunner and Matthias Bauer

Table of Contents

1. Experimental Section

Synthesis

The chemicals used were commercially obtained and used without further purification. Column chromatography was conducted on silica gel columns. Reactions under inert conditions were done using Schlenk techniques with argon gas or inside an argon filled glove box. Dry and degassed solvents were obtained utilizing molar sieves in an MBraun SPS solvent purifying system, and subsequent bubbling of argon. For all complexes with chromophores attached via the imidazole groups the same central ligand structure was necessary. A well-established synthetic procedure was applied to obtain 1,3-di(1H-imidazol-1-yl)benzene (1).[1] The used methyl halides for coupling were available commercially. To synthesize 2-Ph, 1 (1 eq, 1 mmol, 210 mg) was dissolved in acetonitrile (5 mL/mmol). Benzylbromide (3 eq., 3mmol, 513 mg) was added, and the solution was stirred for 16 h under reflux. After cooling to room temperature, the resulting suspension was filtered, and the product was washed with acetone.

2-Ph (1,1'-(1,3-phenylene)bis(3-benzyl-1H-imidazol-3-ium)) was obtained as a colorless solid (0.75 mmol, 485 mg, 75%).

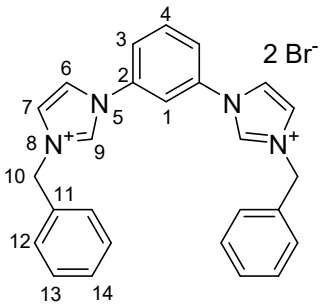

1H NMR (700 MHz, DMSO-d6): δ (ppm) = 10.35 (2H, H9, s), 8.52 (2H, H7, t), 8.46 (1H, H1, t), 8.15 (2H, H6, t), 8.06 (2H, H3, dd), 7.97 (1H, H4, t), 7.57 (4H, H12, d), 7.44-7.48 (4H, H13, m), 7.42 (2H, H14, t), 5.57 (4H, H10, s). 13C NMR (176 MHz, DMSO-d6)): δ (ppm) = 136.0 (2C, C9, CH), 135.6 (2C, C2, Cq), 134.3 (2C, C11, Cq), 131.9 (1C, C4, CH), 129.0 (4C, C13, CH), 128.9 (2C, C14, CH), 128.6 (4C, C12, CH), 123.5 (2C, C6, CH), 122.7 (2C, C3, CH), 121.6 (2C, C7, CH), 115.9 (1C, C1, CH), 52.5 (2C, C10, CH2). 15N NMR (71 MHz, DMSO-d6): δ (ppm) = 188.1 (2N, N8), 186.9 (2N, N5).

ESI-MS ([M-H]+ for C26H24N42+): m/z 391.1906. Found: m/z 391.1923.

Elemental analysis calculated for $C_{42}H_{32}N_4Br_2$: C, 56.54; H, 4.38; N, 10.14. found: C, 56.18; H, 4.66; N, 10.33

For **2-Ant**, an *in-situ* Finkelstein reaction was performed to boost yield of the alkylation:[2] **1** (1 eq., 4 mmol, 841 mg) was suspended in acetone (10mL/mmol). 9-(Chloromethyl)anthracene (3 eq., 12 mmol, 2721 mg) and NaI (4 eq., 16 mmol, 2398 mg) were added and the suspension was refluxed overnight. The hot suspension was filtered, and the product was washed with acetone. Mass spectrometry revealed that some Cl^- salt remained in the product.

2-Ant (1,1'-(1,3-phenylene)bis(9-anthracenyl-1H-imidazol-3-ium))was obtained as a yellow solid (3.4 mmol, 2.9 g, 86%).

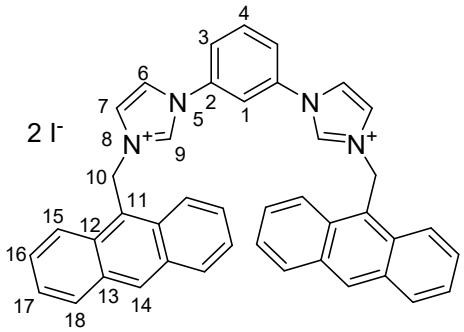

^{1}H NMR (700 MHz, DMSO-d_6): δ (ppm) = 9.90 (2H, H^9, s), 8.87 (2H, H^{14}, s) 8.49 (4H, H^{15}, d), 8.28 (2H, H^6, s), 8.24 (4H, H^{18}, d),

8.16 (1H, H^1, s), 7.93 (2H, H^3, dd), 7.86 (1H, H^4, t), 7.74 (2H, H^7, s), 7.69 (4H, H^{16}, t), 7.63 (4H, H^{17}, t), 6.57 (4H, H^{10}, s). **^{13}C NMR (176 MHz, DMSO-d6)): δ (ppm) =** 135.44 (2C, C^9, CH), 135.38 (2C, C^2, Cq), 131.6 (1C, C^4, CH), 131.1 (4C, C^{13}, Cq), 130.8 (4C, C^{12}, Cq), 130.4 (2C, C^{14}, CH), 129.4 (4C, C^{15}, CH), 127.8 (4C, C^{17}, CH), 125.6 (4C, C^{16}, CH), 123.4 (4C, C^{18}, CH), 123.3 (2C, C^7, CH), 123.2 (2C, C^3, CH), 122.7 (2C, C^{11}, Cq), 121.6 (2C, C^6, CH), 116.5 (1C, C^1, CH), 45.7 (2C, C^{10}, CH_2). **^{15}N NMR (71 MHz, DMSO-d6): δ (ppm) =** 188.2 (2N, N^8), 187.1 (2N, N^5).

ESI-MS ($[M-H]^+$ for $C_{42}H_{32}N_4^{2+}$): m/z 591.2532. Found: m/z 591.2549

Elemental analysis calculated for $C_{42}H_{32}N_4I_2$ + 1 H_2O: C, 58.35; H, 3.96; N, 6.48. found: C, 58.14; H, 4.06; N, 6.48

The complexes **C-R-side** were obtained utilizing a previously published synthetic route.[3] The reactions were carried out in a glovebox with an argon atmosphere in dry solvents. The corresponding proligand (2 eq.) was suspended in THF (20 mL), and Zr(NMe2)$_4$ (2.1 eq.) was added. The resulting suspension was stirred at room temperature for 16 h. $FeBr_2$ (1 eq.) was added to the resulting yellow suspension resulting in a quick color change to red (for **$[Fe((ImPh)_2P)_2]^+$**) or green (for **$[Fe((ImAnt)_2P)_2]^+$**). After stirring for another 24 hours the reaction was exposed to air and quenched with MeOH, resulting in green solutions with solid residue. The residue was filtered off, and the solvent was evaporated. The resulting brownish green solid was dissolved in DCM and filtered off, leaving a yellow residue. After concentrating the solution, it was passed over a silica gel column and thoroughly rinsed with DCM. By switching to MeCN, the green fraction containing the desired product was eluted. KPF_6 was added and the solution volume was reduced by evaporation. Addition of water led to the precipitation of the desired complex. The product was crystallized by diffusion of *n*-pentane into a DCM solution of the respective complex.

$[Fe((ImPh)_2P)_2]^+$ was obtained as green needles (0.08 mmol, 80 mg, 10.9%).

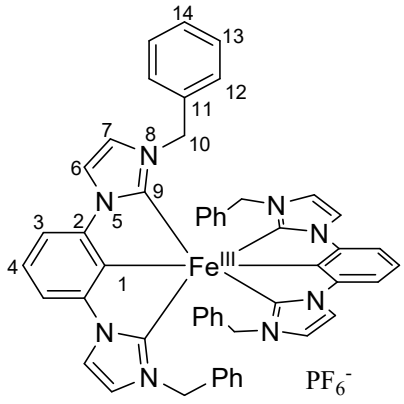

^{1}H NMR (700 MHz, DMSO-d_6): δ (ppm) = 25.17 (4H, H^3, s), 11.03 (8H, H^{10}, s), 6.62 (4H, H^{14}, t), 6.27 (8H, H^{13}, t), 3.73 (8H, H^{12}, d), 2.33 (4H, H^7, s), -2.75 (4H, H^6, s), -35.47 (2H, H^4, s). **^{13}C NMR (176 MHz, DMSO-d6) δ (ppm) =** 515.0 (4C, C^2, C_q), 477.2 (2C, C^4, CH), 149.8 (4C, C^{11}, C_q), 129.9 (8C, C^{13}, CH), 127.6 (4C, C^{14}, CH), 124.3 (8C, C^{12}, CH), 87.3 (4C, C^6, CH), 76.9 (4C, C^7, CH), 16.2 (4C, C^{10}, CH_2), -199.9 (4C, C^3, CH).

ESI-MS ($[M]^+$ for $C_{52}H_{42}FeN_8$): m/z 834.2876. Found: m/z 834.2872.

Elemental analysis calculated for $C_{52}H_{42}FeN_8PF_6$ + 0.5 H_2O: C, 63.17; H, 4.38; N, 11.33. found: C, 63.17; H, 4.62; N, 11.49

$[Fe((ImAnt)_2P)_2]^+$ was obtained as green needles (0.04 mmol, 66 mg, 4.2%).

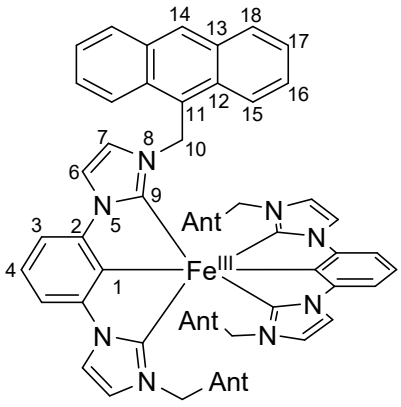

^{1}H NMR (700 MHz, DMSO-d_6): δ (ppm) = 24.77 (4H, H^3, s), 15.70 (8H, H^{10}, s), 8.17 (4H, H^{14}, s), 7.65 (8H, H^{18}, d), 6.78 (8H, H^{17}, t), 5.53 (8H, H^{16}, t), 3.53 (8H, H^{15}, d), 1.74 (4H, H^6, d), -2.85 (4H, H^7, s), -37.4 (2H, H^4, s). **^{13}C NMR (176 MHz, DMSO-d6) δ (ppm) =** 514.8 (4C, C^2, C_q), 483.1 (2C, C^4, CH), 131.2 (8C, C^{13}, C_q), 129.9 (8C, C^{12}, C_q), 129.4 (8C, C^{18}, CH), 127.1 (4C, C^{14}, C_q), 126.9 (8C, C^{16}, CH), 125.1 (8C, C^{17}, CH), 121.1 (8C, C^{15}, CH), 87.5 (4C, C^7,CH), 74.7 (4C, C^6,CH), 9.9 (4C,C^{10},CH_2), -203.3 (4C, C^3,CH).

ESI-MS ($[M]^+$ for $C_{84}H_{58}FeN_8^+$): m/z 1234.4128. Found: m/z 1234.4147.

Elemental analysis calculated for $C_{84}H_{58}FeN_8PF_6$ + 4 H_2O (Due to the inherent photoinstability decomposition products may be the origin of this deviation): C, 69.47; H, 4.58; N, 7.85. found: C, 69.73; H, 4.38; N, 7.77

During our studies we uncovered a photoinstability for **$[Fe((ImAnt)_2P)_2]^+$** as mentioned above. The complex decomposes slightly after excitation in the MLCT/chromophore band, i.e. at wavelengths below 450 nm, resulting in the release of anthracene species. This was first observed during fluorescence measurements, since the normally strongly quenched anthracene emission (compared to free anthracene) was growing with each measurement due to the release of the much more emissive anthracene species, see left panel of Figure S1. This effect is much less pronounced for the more relevant LMCT emission as the decomposed complex is no longer emissive which can be seen in the right panel of Figure S1. Nevertheless, it is difficult to keep the samples of **$[Fe((ImAnt)_2P)_2]^+$** completely clean. Therefore, for measurements on this complex, we always prepared fresh solutions, allowing sensitive analytical methods to remain viable. For the other complexes we didn't observe indications for a photoinstability.

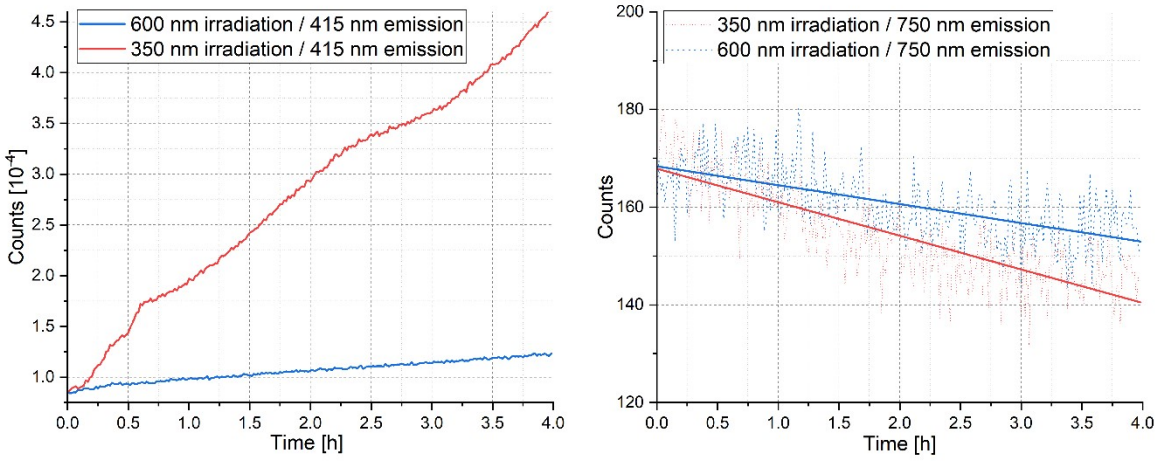

Figure S1: Decomposition study on **[Fe((ImAnt)$_2$P)$_2$]$^+$** with a concentration of 1⋅10-5 mol/l dissolved in MeCN. The samples were irradiated at 350 nm or 600 nm for 1 minute. Then the emission at 415 nm resulting from free antracene species and at 750 nm resulting from the LMCT state is measured after excitation at 350 nm. This sequence was repeated many times to monitor the evolution of the emission over a total irradiation time of four hours. Please note, that the sample irradiated at 600 nm was also irradiated at 350 nm for about 3 seconds per minute to measure the anthracene emission. To show the trend of the weak emission at 750, a linear regression was applied.

The proligand precursors **3-R** were synthesized applying a known synthetic procedure for the phenyl derivative, that was adjusted for the anthracenyl species.[4] 1,3,5-tribromobenzene (1 eq.) was suspended in Et_2O under Argon atmosphere and cooled to -78°C. n-Buthyllithium (n-BuLi) (2.5 mol/L in hexane, 1 eq.) was added slowly and the solution was stirred at this temperature for 45 min. The corresponding chromophore-benzaldehyde (1 eq.) was added, and the solution was stirred while reaching room temperature over 16h. Brine was added, and the mixture was stirred for 10 minutes. The organic phase was separated, and the aqueous phase extracted with Et_2O. After combination of the organic phases, they were dried over $MgSO_4$, and the solvent was reduced by evaporation. The resulting solid was dissolved in DCM under Argon atmosphere and Triethylsilane (4 eq.) was added. After cooling to 0°C BF_3OEt_2 (48 %, 1.5 eq.) was added slowly, and the solution was allowed to reach room temperature overnight under stirring. The mixture was quenched with aqueous $NaHCO_3$ until no bubbling was observed and the organic phase was separated. The aqueous phase was subsequently extracted with DCM, and the organic phases were combined. After drying over $MgSO_4$ and removal of solvent a crude product was obtained. Purification through column chromatography (SiO_2; Hexane/EtOAc 9:1) yielded the desired product.

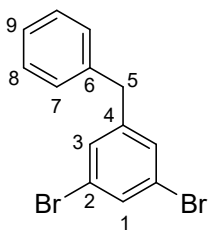

3-Ph (1-benzyl-3,5-dibromobenzene) was obtained as a colorless solid (12.3 mmol, 4.0 g, 61 %)

^{1}H NMR (700 MHz, DMSO-d$_6$): δ (ppm) = 7.63 (1H, H^1, t), 7.47 (2H, H^3, d), 7.30 (2H, H^8, t), 7.26 (2H, H^7, d), 7.20 (1H, H^9, t), 3.94 (2H, H^5, s). **^{13}C NMR (176 MHz, DMSO-**

d6) δ (ppm) = 146.3 (1C, C^4, C_q), 139.9 (1C, C^6, C_q), 131.0 (1C, C^1, CH), 130.6 (2C, C^3, CH), 128.7 (2C, C^7, CH), 128.6 (2C, C^8, CH), 126.4 (1C, C^9, CH), 122.4 (2C, C^2, C_q), 39.9 (1C, C^5,CH_2).

ESI-MS ([M+H]⁺ for $C_{13}H_{10}Br_2$): m/z 326.2902. Found: m/z 326.2936.

3-Ant (9-(3,5-dibromobenzyl)anthracene) was obtained as a pale yellow solid. (2.0 mmol, 830 mg, 9.74 %)

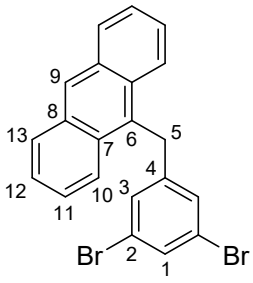

^{1}H NMR (700 MHz, DMSO-d_6): δ (ppm) = 8.63 (1H, H^9, s), 8.31 (2H, H^{13}, d), 8.14 (2H, H^{10}, d), 7.61 (1H, H^1, t), 7.57 (2H, H^{11}, ddd), 7.54 (2H, H^{12}, ddd), 7.28 (2H, H^3, d), 5.07 (2H, H^5, s). **^{13}C NMR (176 MHz, DMSO-d6) δ (ppm) =** 146.1 (1C, C^6, Cq), 131.2 (2C, C^7, Cq), 131.0 (1C, C^1, CH), 130.6 (2C, C^8, Cq), 129.9 (1C, C^4, Cq), 129.8 (2C, C^3, CH), 129.1 (2C, C^{10}, CH), 126.9 (1C, C^9, CH), 126.6 (2C, C^{11}, CH), 125.3 (2C, C^{12}, CH), 124.5 (2C, C^{13}, CH), 122.5 (2C, C^2, Cq), 31.5 (1C, C^5, CH_3)

EI-MS ([M]⁺ for $C_{21}H_{14}Br_2$): m/z 423.9462. Found: m/z 423.9446.

These precursors were then used in an Ullmann adjacent coupling reaction with imidazole to obtain the molecules **4-R**.[5] **3-R** (1 eq.), imidazole (3 eq.), K_2CO_3 (4 eq.) and CuI (0.2 eq.) were suspended in DMSO (2 mL/mmol). The suspension was heated to 150°C for 18 h. Afterwards, the suspension was concentrated under reduced pressure at 150°C until it solidified. The resulting solid was suspended in water and filtered. The residue was repeatedly rinsed with water until no further coloration was visible. The remaining residue was suspended in methanol and filtered. The resulting solution was evaporated under reduced pressure and the remaining solid was purified with column chromatography (SiO_2; CH_2Cl_2/MeOH 9:1).

4-Ph (1,1'-(5-benzyl-1,3-phenylene)bis(1H-imidazole)) was obtained as a colorless solid (0.46 mmol, 140 mg, 46.6%)

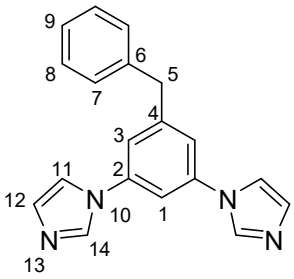

^{1}H NMR (700 MHz, DMSO-d_6): δ (ppm) = 8.38 (2H, H^{12}, s), 7.86 (2H, H^{11}, s), 7.82 (1H, H^1, t), 7.59 (2H, H^3, d), 7.36 (2H, H^7, d), 7.3 (2H, H^8, t), 7.2 (1H, H^9, tt), 7.13 (2H, H^{14}, s), 4.04 (2H, H^5, s). **^{13}C NMR (176 MHz, DMSO-d6) δ (ppm) =** 145.2 (1C, C^4, Cq), 140.4 (1C, C^6, Cq), 138.1 (2C, C^2, Cq), 135.8 (2C, C^{12}, CH), 130.0 (2C, C^{14}, CH), 128.7 (2C, C^7, CH), 128.5 (2C, C^8, CH), 126.2 (2C, C^9, CH), 118.5 (2C, C^3, CH), 118.1 (2C, C^{11}, CH), 109.7 (1C, C^1, CH), 40.9 (1C, C^5, CH_3). **^{15}N NMR (71 MHz, DMSO-d6): δ (ppm) =** 266.0 (2N, N^{13}), 184.4 (2N, N^{10}).

ESI-MS ([M+H]⁺ for $C_{19}H_{16}N_4$): m/z 301.1448. Found: m/z 301.1444.

4-Ant was obtained as a pale yellow solid (4.0 mmol, 1.6 g, 33.3 %)

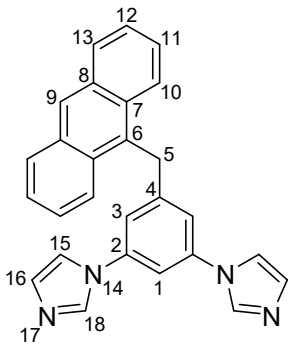

^{1}H NMR (700 MHz, DMSO-d$_6$): δ (ppm) = 8.61 (1H, H^{9}, s), 8.46 (2H, H^{13}, d), 8.17 (2H, H^{16}, s), 8.13 (2H, H^{10}, d), 7.75 (1H, H^{1}, t), 7.59 (4H, H^{12} u H^{15}, m), 7.54 (2H, H^{11}, t), 7.39 (2H, H^{3}, d), 7.06 (2H, H^{18}, d), 5.15 (2H, H^{5}, s). **^{13}C NMR (176 MHz, DMSO-d6) δ (ppm) =** 145.2 (1C, C^{6}, Cq), 138.0 (2C, C^{2}, Cq), 135.6 (2C, C^{16}, CH), 131.2 (2C, C^{7}, Cq), 131.1 (2C, C^{8}, Cq), 130.0 (2C, C^{18}, CH), 129.9 (1C, C^{4}, Cq), 129.1 (2C, C^{10}, CH), 126.9 (1C, C^{9}, CH), 126.5 (2C, C^{12}, CH), 125.2 (2C, C^{11}, CH), 124.6 (2C, C^{13}, CH), 118.04 (2C, C^{3}, CH), 117.99 (2C, C^{15}, CH), 110.6 (1C, C^{1}, CH), 32.3 (1C, C^{5}, CH$_2$). **^{15}N NMR (71 MHz, DMSO-d6): δ (ppm) =** 266.5 (2N, N^{17}), 184.0 (2N, N^{14}).

ESI-MS ([M+H]$^{+}$ for $C_{27}H_{20}N_4$): m/z 401.1761. Found: m/z 401.1768.

The proligands **5-R** were obtained by methylation.[6] The matching **4-R** (1 eq.) is suspended in MeCN (10 mL/mmol). Methyliodide (4 eq.) was added, and the mixture was refluxed overnight. After cooling down the acetonitrile was filtered off, and the remaining crude product was washed with acetone.

5-Ph was obtained as colorless crystalline powder (0.23 mmol, 135 mg, 49.7 %)

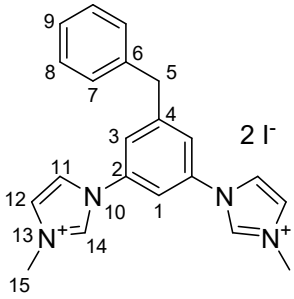

^{1}H NMR (700 MHz, DMSO-d$_6$): δ (ppm) = 9.87 (2H, H^{14}, s), 8.35 (2H, H^{12}, t), 8.16 (1H, H^{1}, t), 8.01 (2H, H^{11}, t), 7.98 (2H, H^{3}, d), 7.37 (2H, H^{7}, d), 7.33 (2H, H^{8}, t), 7.24 (1H, H^{9}, tt), 4.15 (2H, H^{5}, s), 3.98 (6H, H^{15}, s). **^{13}C NMR (176 MHz, DMSO-d6) δ (ppm) =** 145.9 (1C, C^{6}, Cq), 139.5 (1C, C^{4}, Cq), 136.3 (2C, C^{14}, CH), 135.8 (2C, C^{2}, Cq), 128.72 (2C, C^{7}, CH), 128.67 (2C, C^{8}, CH), 126.6 (1C, C^{9}, CH), 124.7 (2C, C^{11}, CH), 122.7 (2C, C^{3}, CH), 120.8 (2C, C^{12}, CH), 113.3 (1C, C^{1}, CH), 40.7 (1C, C^{5}, CH$_2$), 36.4 (2C, C^{15}, CH$_3$). **^{15}N NMR (71 MHz, DMSO-d6): δ (ppm) =** 186.5 (2N, N^{13}), 175.2 (2N, N^{10}).

ESI-MS ([M]$^{2+}$ for $C_{29}H_{26}N_4^{2+}$): m/z 165.0917. Found: m/z 165.095.

Elemental analysis calculated for $C_{21}H_{22}N_4I_2$ + 0.1 H_2O: C, 43.04; H, 3.82; N, 9.56. found: C, 42.67; H, 4.15; N, 9.64

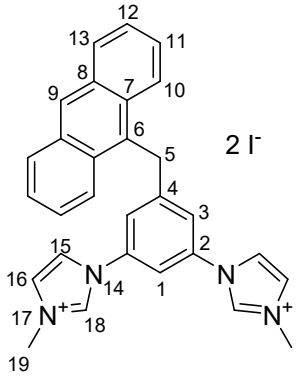

5-Ant was obtained as a faint yellow solid (0.15 mmol, 104 mg, 60.6 %)

^{1}H NMR (700 MHz, DMSO-d$_6$): δ (ppm) = 9.63 (2H, H^{18}, s), 8.67 (1H, H^{9}, s), 8.36 (2H, H^{10}, d, J = 8.6 Hz), 8.19 (2H, H^{16}, t, J = 1.9 Hz), 8.16 (2H, H^{13}, d, J = 8.0 Hz), 8.05 (1H, H^{1}, s), 7.93 (2H, H^{15}, t, J = 18 Hz), 7.73 (2H, H^{3}, d, J = 2.0 Hz), 7.60-7.53 (4H, H$^{1!}$ and H^{12}, m), 5.22 (2H, H^{5}, s), 3.91 (6H, H^{19}, s). **^{13}C NMR (176**

MHz, DMSO-d6) δ (ppm) = 146.4 (1C, C^6, Cq), 136.3 (2C, C^{18}, CH), 135.8 (2C, C^2, Cq), 131.3 (2C, C^8, Cq), 130.1 (2C, C^7, Cq), 129.8 (1C, C^4,Cq), 129.2 (2C, C^{13}, CH), 127.3 (1C, C^9, CH), 126.7 and 125.3 (4C, C^{11} and C^{12}, CH), 124.7 (2C, C^{15}, CH), 124.4 (2C, C^{10}, CH), 122.3 (2C, C^3, CH), 121.1 (2C, C^{16}, CH), 114.5 (1C, C^1, CH), 36.3 (1C, C^5, CH_2), 32.8 (2C, C^{19}, CH_3). **^{15}N NMR (71 MHz, DMSO-d6): δ (ppm) =** 186.5 (2N, N^{14}), 175.2 (2N, N^{17}).

ESI-MS ([M]$^{2+}$ for $C_{29}H_{26}N_4^{2+}$): m/z 215.1073. Found: m/z 215.108.

Elemental analysis calculated for $C_{29}H_{26}N_4I_2$ + 0.5 H_2O: C, 50.24; H, 3.93; N, 8.08. found: C, 49.87; H, 4.20; N, 8.25

The complexes **C-R-backbone** were synthesized based on a modified procedure previously established for heteroleptic complexes of Fe^{II}.[7] In a glove box with Argon atmosphere, the corresponding proligand was dissolved in THF and cooled to -25°C. Lithium-bis-trimethylsilylamide was added and the solution was stirred for 2h at this temperature. Iron-(bis-bis-trimethylsilylamide) was dissolved in THF, added to the prepared ligand solution and the combined solution was allowed to reach room temperature overnight. The resulting suspension was removed from the glove box and additionally quenched with methanol to obtain a green suspension, which was filtered. After removal of the solvent under reduced pressure the remaining solid was dissolved in DCM and filtered off again before it was concentrated and added to a silica column. After elution of impurities with DCM, the product was recovered from the column with MeCN. The obtained green solution again concentrated before adding KPF_6. After addition of water the desired product precipitated as a green PF_6^- salt. The product was filtered off and then dissolved in DCM to obtain crystals by diffusion of pentane. In addition, **[Fe(Im$_2$PAnt)$_2$]$^+$** shows photoinstability to a certain degree, as discussed below.

[Fe(Im$_2$PPh)$_2$]$^+$ was obtained as green plates (0.75 mmol, 80 mg, 10.9%)

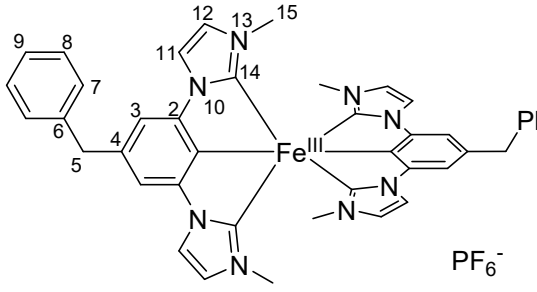

^{1}H NMR (700 MHz, DMSO-d$_6$): δ (ppm) = 49.33 (2H, H^5, s) 25.45 (4H, H^3, s), 9.64 (12H, H^{15}, s), 9.52 (4H, H^7, d, J = 7.8 Hz), 8.89 (4H, H^8, t, J = 7.6 Hz), 7.79 (2H, H^9, t, J = 7.4 Hz), 2.81 (4H, H^{12}, s), -2.64 (2H, H^{11}, s). **^{13}C NMR (176 MHz, DMSO-d6) δ (ppm) =** 528.9 (2C, C^2, Cq), 520.5 (1C, C^4, Cq), 321.9 (2C, C^6, Cq), 132.1 (2C, C^8, CH), 131.0 (1C, C^9, CH), 128.6 (2C, C^7, CH), 89.6 (2C, C^{11}, CH), 77.4 (2C, C^{12}, CH), 1.2 (2C, C^{15}, CH_3), -72.9 (1C, C^5, CH_2), -212.5 (2C, C^3, CH).

ESI-MS ([M]$^+$ for $C_{42}H_{38}FeN_8^+$): m/z 710.2563. Found: m/z 710.2568.

Elemental analysis calculated for $C_{42}H_{38}FeN_8PF_6$ + 1.5 H_2O: C, 57.15; H, 4.68; N, 12.70. found: C, 57.19; H, 4.93; N, 12.61

$[Fe(Im_2PAnt)_2]^+$ was obtained as a green solid (0.5 mmol, 37 mg, 4.7%)

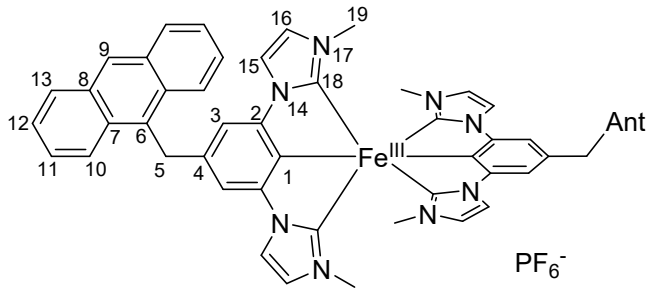

^{1}H NMR (700 MHz, DMSO-d_6): δ (ppm) = 25.23 (4H, H^3, s) 11.71 (4H, H^{10}, d, J = 9.2 Hz), 9.55 (12H, H^{19}, s), 9.26 (2H, H^9, s), 8.78 (4H, H^4, d, J = 8.9 Hz), 8.49 (4H, H^{11}, dd, J = 9.3, 6.5 Hz), 8.00 (4H, H^{12}, dd, J = 8.8, 6.5 Hz), 2.49 (4H, H^{16}, s), -3.08 (4H, H^{15}, s). **^{13}C NMR (176ki MHz, DMSO-d6) δ (ppm) =** 535.0 (4C, C^2, Cq), 517.6 (2C, C^4, Cq), 196.7 (2C, C^6, Cq), 135.7 (4C, C^7, C_q), 130.6 (4C, C^{13}, CH), 130.2 (4C,C^8, Cq), 130.0 (4C, C^{10}, CH),k 128.0 (4C, C^{11}, Cq), 127.7 (2C, C^9, CH), 126.9 (4C, C^{12}, CH), 88.0 (4C, C^{15}, CH), 76.4 (4C, C^{16}, CH), 1.96 (4C, C^{19}, CH_3), -83.9 (2C, C^5, CH_2), -216.1 (4C, C^3, CH).

ESI-MS ($[M]^+$ for $C_{58}H_{46}FeN_8^+$): m/z 910.3189. Found: m/z 910.3182.

Elemental analysis calculated for $C_{58}H_{46}FeN_8PF_6$ + 1.5 H_2O: C, 64.33; H, 4.56; N, 10.35. found: C, 64.23; H, 4.76; N, 10.26

Experimental Methods

Cyclic Voltammetry

Potentiostatic measurements were performed at room temperature using a PGSTAT 101 potentiostat from Metrohm in dry and degassed 0.1 M [*n*-Bu_4N][PF_6] MeCN solution with an analyte concentration of 10^{-3} M. A platinum working electrode (1 mm diameter), an Ag/$AgNO_3$ reference electrode and a platinum pin electrode were utilized in a three-electrode configuration. After measurements, Ferrocene was added as an internal standard to reference against the $FcH^{0/+}$ redox couple. The resulting voltammograms were analyzed using the *NOVA 2.1.3* software. The reversibility of redox couples was investigated with the criteria proposed by Nicholson and Shain, and the Randles-Sevcik equation.[8]

UV/VIS Spectroscopy

Spectroscopic-grade solvents from VWR in quartz cuvettes by Hellma with an optical path length of 10 mm were used. Absorption spectra were recorded at concentrations of 10^{-5} M in 99.9% pure acetonitrile with a PerkinElmer Lambda465 single-beam spectrophotometer.

Luminescence Measurements

The emission and excitation spectra were recorded with an Edinburgh Instruments FLS1000 spectrometer with single monochromators and a red-extended PMT-980 detector. The samples were dissolved in MeCN at a concentration of $1*10^{-5}$ mol/L. and degassed by bubbling argon through.

Time-Correlated Single Photon Counting

Time-Correlated Single Photon Counting (TCSPC) was done using an Ultima 01-DD TCSPC system (HORIBA Jobin Yvon). The degassed sample solution was excited at 374 nm with a HORIBA DD375L laser diode with a maximum repetition rate of 100 MHz. The emission was recorded with an emission monochromator which was set to 415 nm. A histogram of photons was recorded as a function of 16,383 channels on a time range of 100 ns (0.012 ns per channel) until one channel reached 10000 counts. In addition, a scattering solution was measured to characterize the prompt response.

Time-Resolved Emission Measurements

Time-resolved emission measurements were carried out by means of a streak camera system (Streakscope C10627, Hamamatsu Photonics) and applying ultrashort excitation pulses at 350 nm. The latter were generated by frequency doubling the output of a noncollinear optical parametrical amplifier (NOPA) tuned to a center wavelength of 700 nm. The NOPA is pumped by a regenerative Ti:sapphire amplifier system (CPA 2001, CLARK MXR, INC.) operating at a center wavelength of 775 nm and a repetition rate of 1 kHz. MeCN solutions of the compounds were prepared under argon and measured in 1 cm thick fused silica cuvettes. All samples were prepared with an optical density of about 0.1 at the excitation wavelength to avoid signal distortions due to self-absorption. To determine the emission lifetime, the time and wavelength resolved emission was integrated over its spectrum and the resulting decay curve fitted by a monoexponential decay function.

Transient Absorption Spectroscopy

Transient absorption (TA) spectra were recorded with a time resolution of about 100 fs employing a pump-probe setup in which a white light continuum is used for probing and a NOPA for the generation of the excitation pulses.[9] Both, the NOPA and the white light stage are pumped by the regenerative Ti:sapphire laser system (CPA 2001, CLARK MXR, INC.) used also for the measurements with the streak camera. The white light continuum is generated by focusing a small fraction of the near infrared pump light into a moving CaF_2 crystal. To excite the compounds at their lowest absorption band, the NOPA was tuned to a center wavelength of 600 nm. The dispersion of the NOPA output was minimized by a compressor based on fused silica prisms resulting in excitation pulses with a length of about 30 fs. The excitation energy was chosen as low as possible to reduce the probability for photodegradation and was approx. 200 nJ in all measurements. Excitation and probe beam were focused onto the sample to

overlapping spots with diameters of approximately 200 µm and 140 µm, respectively. Behind the sample, the probe was dispersed by a prism and transient absorption changes were spectrally resolved recorded by a photodiode array detector. The chirp of the white light probe was corrected in the evaluated TA spectra. To exclude effects caused by orientational relaxation, the polarizations of the pump and probe pulses were set to magic angle with respect to each other. For the TA measurements, the compounds were dissolved in MeCN and the sample solutions filled into 2 mm thick fused silica cuvettes. The optical density (OD) varied depending on the sample solution and was in the range of 0.13 - 0.2 at the excitation wavelength. The variation was necessary to minimize signal contribution due to scattering of the excitation light.

Quantum-Chemical Calculations of Absorption Spectra

Quantum chemical calculations employing Density Functional Theory (DFT) were carried out using the ORCA quantum chemistry package (version 5.0.3).[10] Geometry optimizations were performed with the PBEh-3c composite method,[11] applying very tight convergence criteria and tight optimization parameters. Frequency calculations confirmed the optimized structures as minima by verifying the absence of imaginary frequencies. The optimized geometries align well with the experimental crystal structures (see Supporting Information, Fig. X) and were used as input for further calculations.)

Absorption spectra were calculated using the linear-response time-dependent density functional theory (TD-DFT) by calculating the vertical electronic singlet-transitions, employing the B3LYP functional[12] in combination with the triple-zeta valence basis set def2-TZVP[13] and the D4 dispersion correction.[14] For comparison with experimental UV/Vis spectra, calculated transitions were shifted by -5000 cm^{-1} for all complexes to account for the well-known systematic overestimations of excitation energies by TD-DFT using hybrid functionals such as B3LYP, particularly for transition-metal complexes.[15] The analysis of the character of the excited states was done using the TheoDORE package.[16] The visualization of spin-density plots was performed with Avogadro version 1.2.0 using an isovalue of 0.0001, while the orbital visualizations were created with IboView v20211019.[17]

NMR-Spectroscopy

NMR spectra were recorded on a Bruker Ascent 700 spectrometer. Chemical shifts are expressed in parts per million (ppm, δ) downfield from tetramethyl silane (TMS). The spectra were referenced to the residual proton signals of the respective deuterated solvent or the solvent carbons respectively. The ^{15}N-HMBC spectra were referenced externally against liquid ammonia. The spectra were analyzed according to first order. Exact assignment of signals was done under consideration of ^{1}H–^{1}H-COSY, ^{1}H–^{13}C-HMQC, ^{1}H^{13}C- HMBC, ^{1}H–^{15}N-HMBC, ^{1}H–^{1}H-NOESY and DEPT135 spectra. For the paramagnetic ^{13}C-NMR spectra no proton decoupling was applied leading to multiplets in ^{13}C-NMR spectra.

2. Single Crystal X-ray diffraction

Despite several attempts, it was not possible to obtain single crystals of the four presented complexes suitable for publication. Due to the high flexibility of the phenyl and anthracene substituents the obtained structures are highly disordered leading to high R_{int} values and could therefore not be modelled precisely. Nevertheless, in case of **[Fe(Im$_2$PPh)$_2$]$^+$** blue crystals and **[Fe(Im$_2$PAnt)$_2$]$^+$** green crystals could be isolated and measured leading to pictures of the complexes demonstrating their connectivities (see Figure S11). In accordance with the calculated structures, **[Fe(Im$_2$PPh)$_2$]$^+$** and **[Fe(Im$_2$PAnt)$_2$]$^+$** both allow the estimation of a distorted octahedral coordination of the iron center and a misalignment of the chromophores with the ligand system due to the methyl bridge.

Figure S2: Connectivities of **[Fe(Im$_2$PPh)$_2$]$^+$** and **[Fe(Im$_2$PAnt)$_2$]$^+$** obtained by single crystal X-ray diffraction. Due to low single crystal quality, it was not possible to obtain more detailed structure.

3. NMR investigation of electronic decoupling

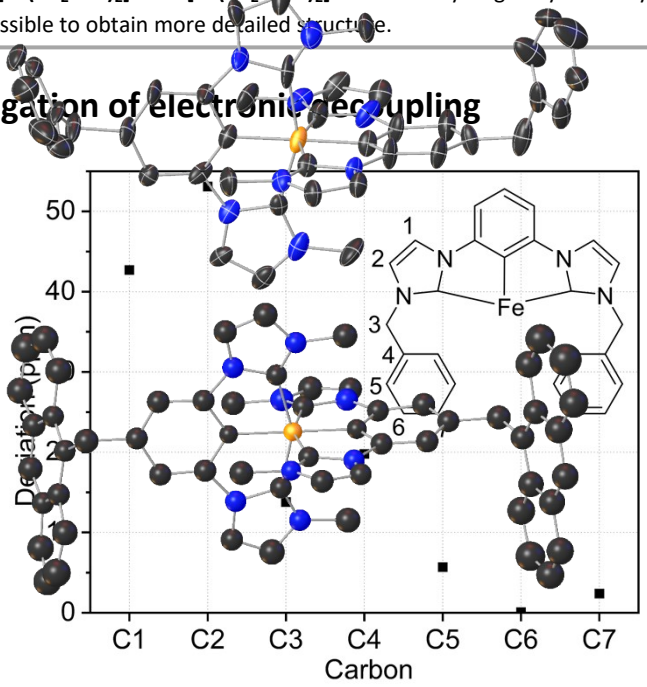

Figure S3: Absolute deviation from the expected chemical shift in ^{13}C-NMR spectroscopy. The imidazole carbons C1 and C2 and sidegroup carbons C4 to C7 for the **[Fe((ImPh)$_2$P)$_2$]$^+$** is referenced against an expected value of 130 ppm.[18] In addition, the aliphatic bridging carbon C3 is referenced against 30 ppm.[18]

4. Linear Combination of absorption spectra

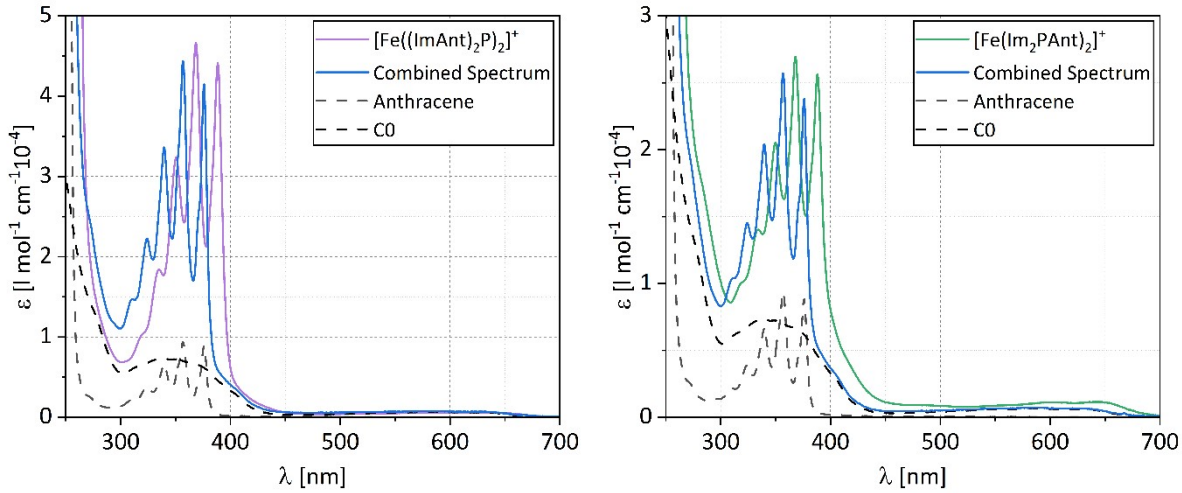

Figure S4: Linear combination of the absorption spectra of base complex C0 and free anthracene compared to the complexes **[Fe((ImAnt$_2$)P)$_2$]$^+$** (left) and **[Fe(Im$_2$PAnt)$_2$]$^+$** (right). The anthracene spectrum was multiplied by 2 or 4 to align with the number of chromophore units in the corresponding complex.

The comparison of the linear combination of the base complex C0 and anthracene with the anthracene substituted complexes (Figure S4) reveals a high similarity, suggesting a decoupling of both moieties. A coupled organic system would lead to excitations delocalized over the entire ligand structure leading to a strong redshift.

5. Steady State Emission

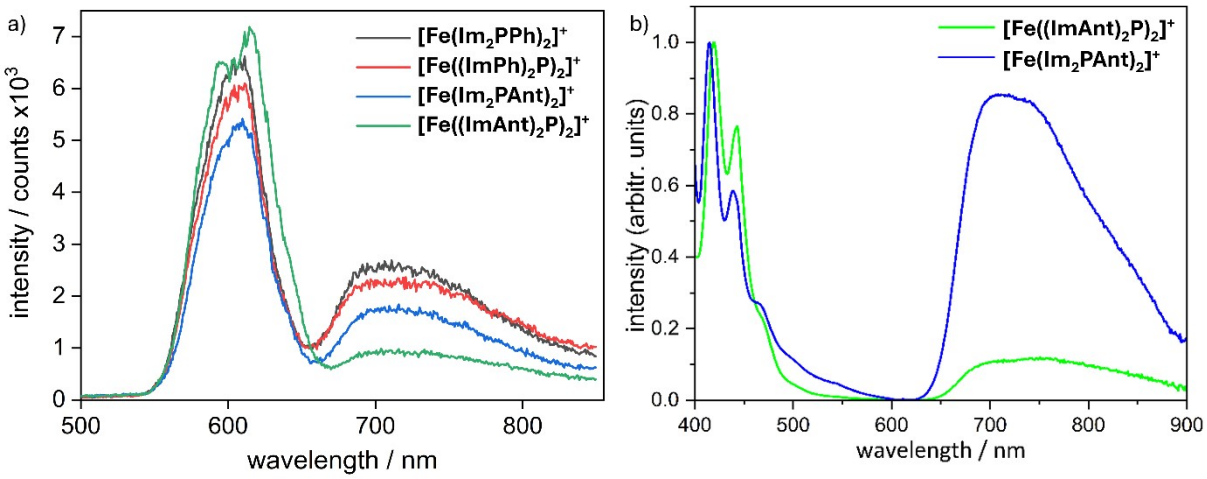

Figure S5: a) Emission spectra of the investigated complexes dissolved in MeCN at an optical density of 0.1 at the excitation wavelength of 600 nm. The emission peak at 600 nm results from scattering of the excitation light source. b) Normalized emission spectra of the investigated anthracene complexes excited at 350 nm. The singlet anthracene emission, most likely originating from an anthracene impurity is clearly stronger in **[Fe((ImAnt)$_2$P)$_2$]$^+$**. Both spectra were measured in MeCN (10^{-5} M).

From the not normalized emission spectra (Figure S5, Panel a) the weaker emission intensity of the anthracene substituted complexes is evident. **[Fe((ImAnt)$_2$P)$_2$]$^+$** exhibits an especially weakened emission, which may be influenced by the increased amount of anthracene moieties. The singlet

emission shown in Panel b) is much stronger in relation to the LMCT emission for **[Fe((ImAnt)$_2$P)$_2$]$^+$**, most likely due to its photo instability, resulting in a higher concentration of dissociated anthracene species.

6. Variable Temperature Emission Spectroscopy

The four chromophore-appended complexes were investigated in the temperature range of 77 K to 297 K in 20 K steps. The results are depicted in Figure S6. All complexes show an increase in general emission intensity at 77 K due to reduced vibrational relaxation, as is expected for lower temperatures. However, an increased solvent background at lower temperatures increases apparent emission intensities additionally. This effect is especially strong for the anthracene substituted complexes due to the weaker emission at 77 K. For the phenyl-substituted complexes, the broad emission bands between 650 and 900 nm are boosted significantly by about one order of magnitude. This behaviour is expected, since there is no low-lying chromophore state to quench the LMCT state and nonradiative decay is reduced at low temperatures. In addition to the general increase, the broadening of the spectra decreases, and two distinct peaks of the vibronic progression become visible for the C-Ph complexes. This was previously observed for the directly conjugated phenyl complex **Fe[(ImP-Ph)2]$^+$**.[19] This behaviour is also observed for **[Fe(Im$_2$PAnt)$_2$]$^+$**, however, the increase in intensity is only half of that in the C-Ph complexes, suggesting an influence of the anthracene substitution. Due to the 3anthracene state being lower in energy than the emissive 2LMCT state it can function as an efficient quenching channel, since no sufficient thermal energy for a back transfer to the 2LMCT state is available. This effect partially compensates for the decreased nonradiative decay, resulting in an overall increase in emission intensity. For **[Fe((ImAnt)$_2$P)$_2$]$^+$**, a faster 2LMCT to 3anthracene transition rate, as is evident in transient absorption spectroscopy, leads to an even stronger quenching, now almost fully offsetting the reduced nonradiative decay, reducing the intensity increase to a factor of 2 , which is almost fully masked by the rising baseline. For the phenyl complexes and **[Fe(Im$_2$PAnt)$_2$]$^+$**, the emission intensity generally rises with decreasing temperature as can be seen in Figure S6. This trend is interrupted around the freezing point of butyronitrile at 161.3 K, with the intensity dropping slightly after freezing. Only for **[Fe((ImAnt)$_2$P)$_2$]$^+$** this trend is not consistent. Here the strongest emission is recorded at 177 K. This may be due to the backtransfer being fully inhibited below this temperature. However, this may also just be an effect of the baseline which is also stronger at these temperatures and/or due to scattering.

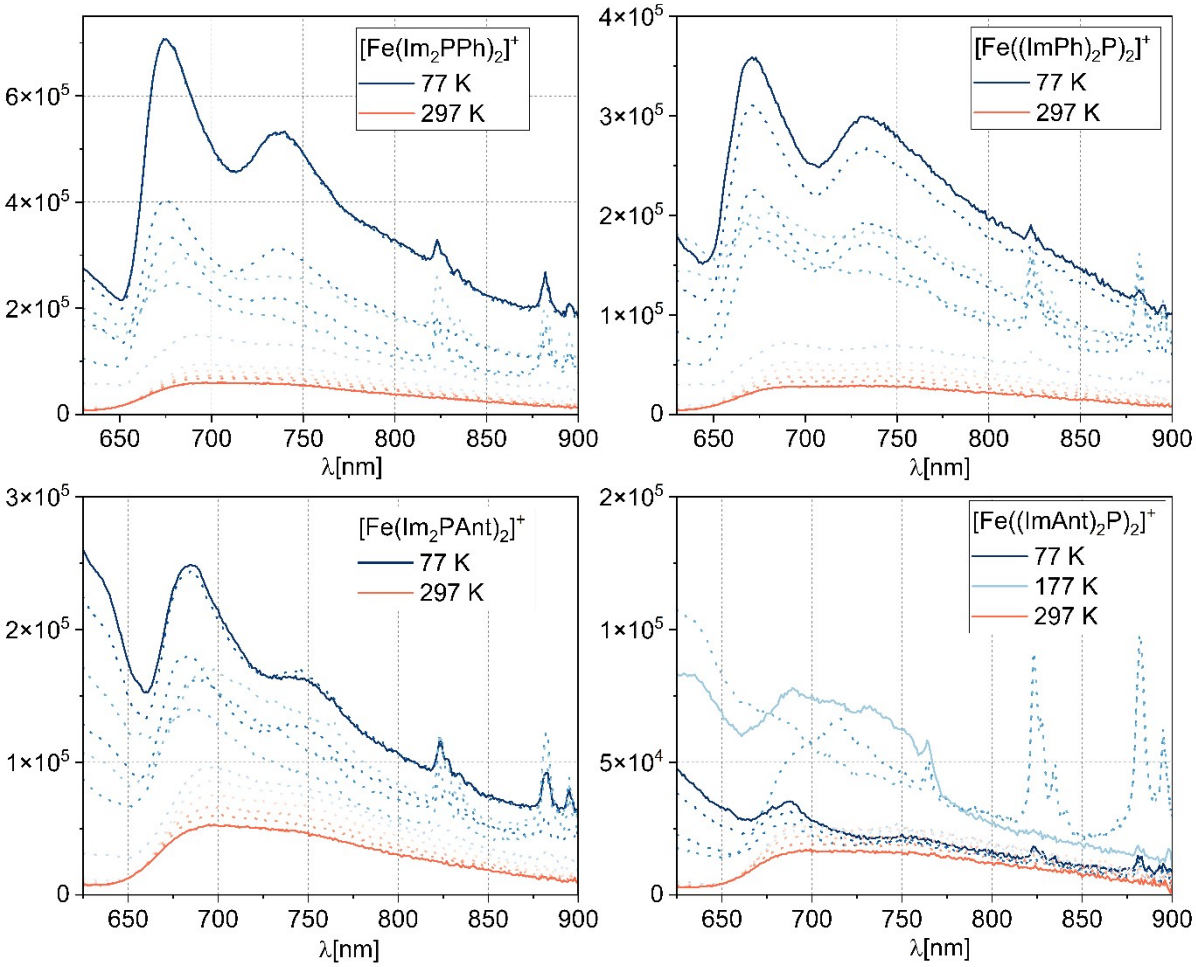

Figure S6: Variable temperature emission spectra in BuCN at 10^{-4} mol/L. Emission intensity in counts is plotted against the wavelength. Measurements were done in 20 K steps. The highest and lowest temperatures are highlighted (77 K and 297 K). For **$[Fe((ImAnt)_2P)_2]^+$** the 197 K spectrum is also highlighted as it is the lowest temperature that still shows a clear fluorescence in the LMCT range. The spectra are further discussed in the manuscript.

7. Time-Resolved Emission Measurements

Streak Camera Measurements

The following figures present the results of time-resolved emission measurements on the complexes dissolved in MeCN which were conducted by means of a streak camera system.

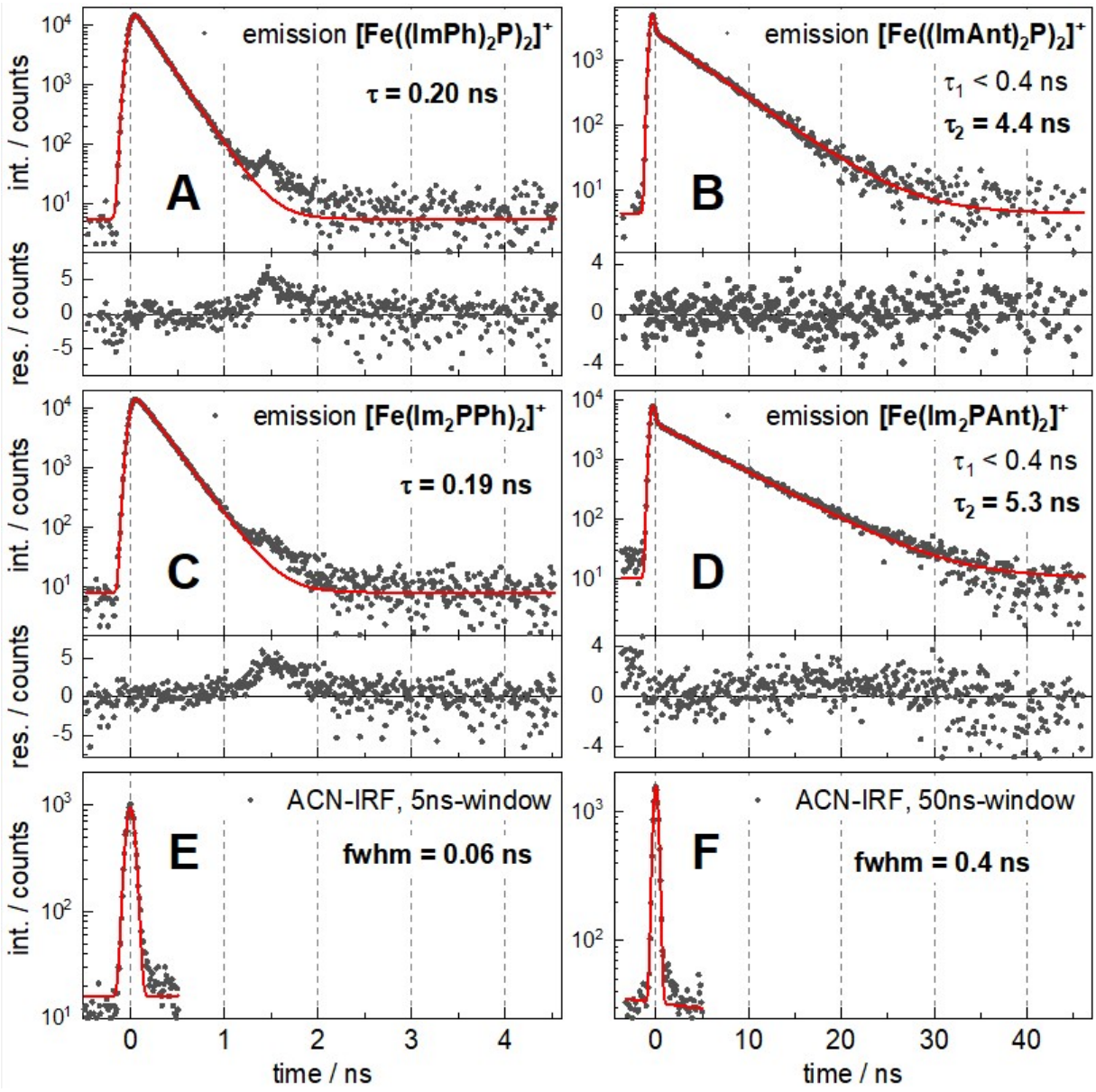

Figure S7: Time traces of the spectrally integrated emission intensity (int., black dots) for the four complexes **[Fe((ImPh)$_2$P)$_2$]$^+$** (A), **[Fe((ImAnt)$_2$P)$_2$]$^+$** (B), **[Fe(Im$_2$PPh)$_2$]$^+$** (C) and **[Fe(Im$_2$PAnt)$_2$]$^+$** (D) dissolved in MeCN as well as the respective exponential fits (red lines) and the corresponding residuals (res., lower graphs). The time constants obtained by the fitting procedure are given in the graphs E and F: Instrument response function (IRF) of the streak camera recorded in pure MeCN and fitted with a Gauss-function. The resulting full width at half maximum (fwhm) represents the time resolution for the time window of the measurement. All samples were excited at 600 nm.

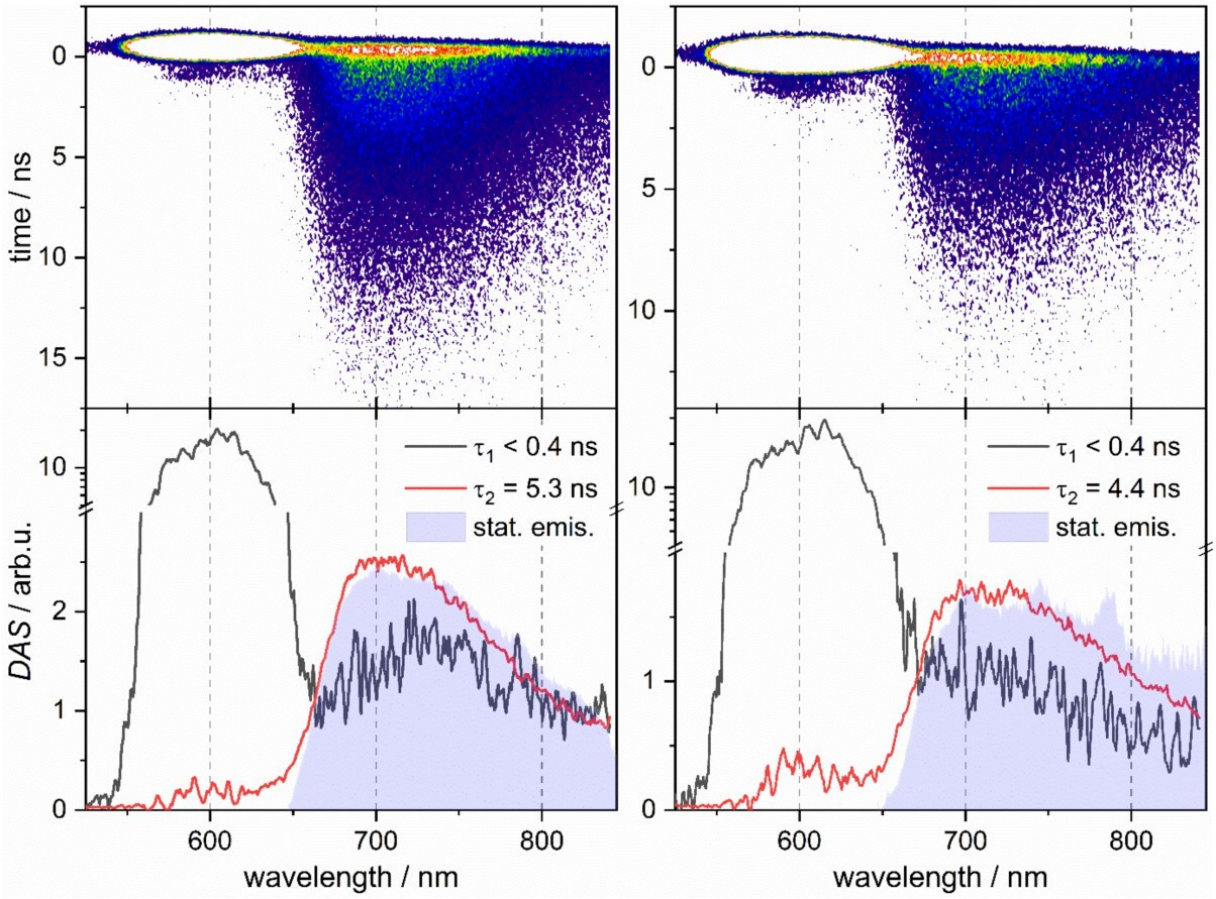

Figure S8: Time-resolved emission of **$[Fe(Im_2PAnt)_2]^+$** (left) and **$[Fe((ImAnt)_2P)_2]^+$** (right) dissolved in MeCN after optical excitation at 600 nm. Top: Two-dimensional plot of the time-resolved emission intensity (color coded). Bottom: Decay associated amplitude spectra (DAS) resulting from a GLA of the datasets with two exponential decay components and labelled by the respective time constants. For comparison also the stationary emission-spectrum is shown (gray area). The y-axis has a logarithmic scale above a break at 3 arb.u. so that the strong scattered light can be shown. The short time constant of the fit is below the time resolution of the measurement, and the corresponding signal contribution can be regarded as practically instantaneous.

TCSPC Measurements

The LMCT emission of **[Fe(Im$_2$PAnt)$_2$]$^+$** was also investigated by time correlated single photon counting (TCSPC). It shows the kinetics of LMCT emission after optical excitation at 374 nm, i.e. in the MLCT/anthracene absorption band, by a pulsed laser diode. A strong signal due to scattering of the excitation light appears at the doubled excitation wavelength because of second order diffraction in the monochromator. The data was fitted with a biexponential function. A fast decay component with a lifetime shorter than the time-resolution of the TCSPC setup is assumed to originate from scattered excitation light. A second decay component exhibits a lifetime of 5.8 ns. It is assigned to the LMCT emission. To support the assignment time-resolved emission spectra were recorded and evaluated by a GLA. The obtained DAS are shown in Figure S9. The DAS of the decay component with a lifetime of about 6 ns fits well to the LMCT emission, whereas the fast decay component appears indeed at the doubled excitation wavelength. Thus, the TCSPC measurements are within the experimental accuracy in perfect agreement with the results obtained by the streak camera.

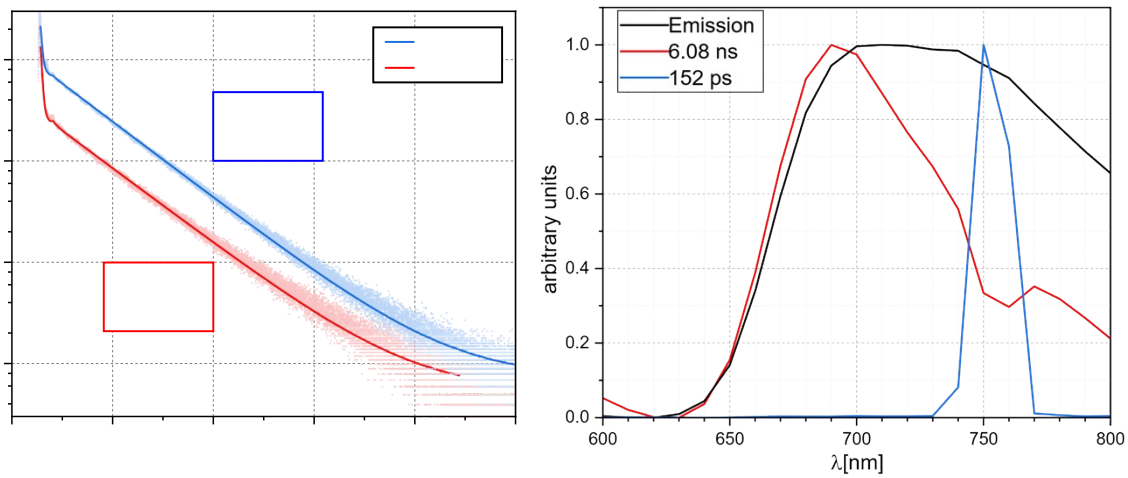

Figure S9: Left panel: Kinetics of the emission of **[Fe(Im$_2$PAnt)$_2$]$^+$** dissolved in MeCN at a concentration of 1*10^{-5} mol/l, measured by TCSPC at two detection wavelengths. The excitation was carried out at 374 nm; Emission up to 30000 counts was measured at 680 nm and 800 nm. The emission maximum at 710 nm was avoided to prevent interference with the second order diffraction of the excitation light (at 750 nm). Right panel: DAS of a GLA applied to spectrally resolved TCSPC data of the same solution recorded in 10 nm steps. The sharp peak at 750 nm and the corresponding lifetime is only due to second order diffraction of scattered excitation light.

Unfortunately, similar experiments with **[Fe((ImAnt)$_2$P)$_2$]$^+$** turned out to be problematic, since no laser diode emitting above 400 nm was in our TCSPC setup and the complex exhibiting photo instability after excitation at wavelengths below 450 nm. However, as the streak camera and the TA experiments show, the photodynamics of both anthracenyl substituted complexes are very similar.

8. Femtosecond Transient-Absorption Spectroscopy

The TA data $\Delta OD(\lambda,t)$ was globally analysed by fitting a sum of exponential decay components to the transient spectra using the following fit function:

$$\Delta OD(\lambda,t) = \sum_i A_i(\lambda) \cdot exp(-\frac{t}{\tau_i})$$

The i-th decay component is characterized by its time constant τ_i and the decay associated amplitude spectrum (DAS) $A_i(\lambda)$.

The following figures present the results of the ultrafast TA measurements on the four complexes **[Fe(Im$_2$PPh)$_2$]$^+$**, **[Fe((ImPh)$_2$P)$_2$]$^+$**, **[Fe(Im$_2$PAnt)$_2$]$^+$** and **[Fe((ImAnt)$_2$P)$_2$]$^+$**.

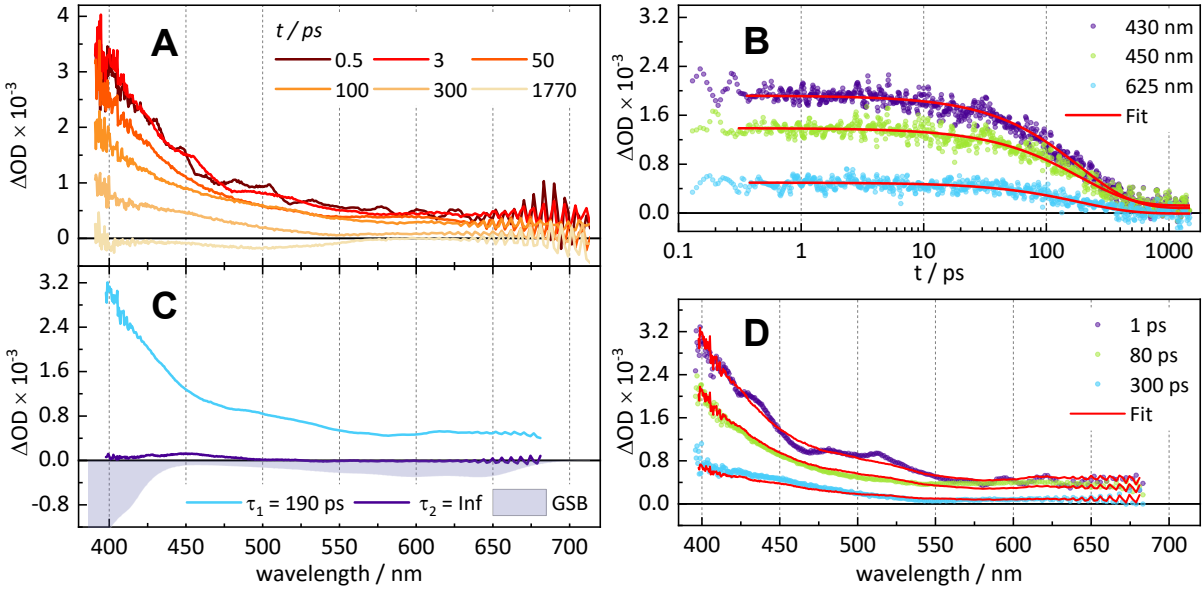

Figure S10, A: TA spectra of **[Fe(Im$_2$PPh)$_2$]$^+$** dissolved in MeCN at different times t after optical excitation at 600 nm. B: Time traces (dots) at the specified probe wavelengths together with respective fit curves resulting from the GLA (red solid lines). C: DAS obtained by the GLA and labelled by the respective time constants. The dynamics is well described by a monoexponential decay with the time constant τ_1 = 190 ps. A further, long-lived component modelled by a decay with an infinite time constant τ_2 = Inf was used to account for tiny offsets at long delay times. The component is at all wavelengths practically zero and within the experimental accuracy insignificant. The negative of the ground state absorption is shown as grey area to indicate where ground state bleach (GSB) might contribute to the TA signal. D: TA spectra (dots) at the given time points together with fitted spectra obtained by the GLA (red solid lines).

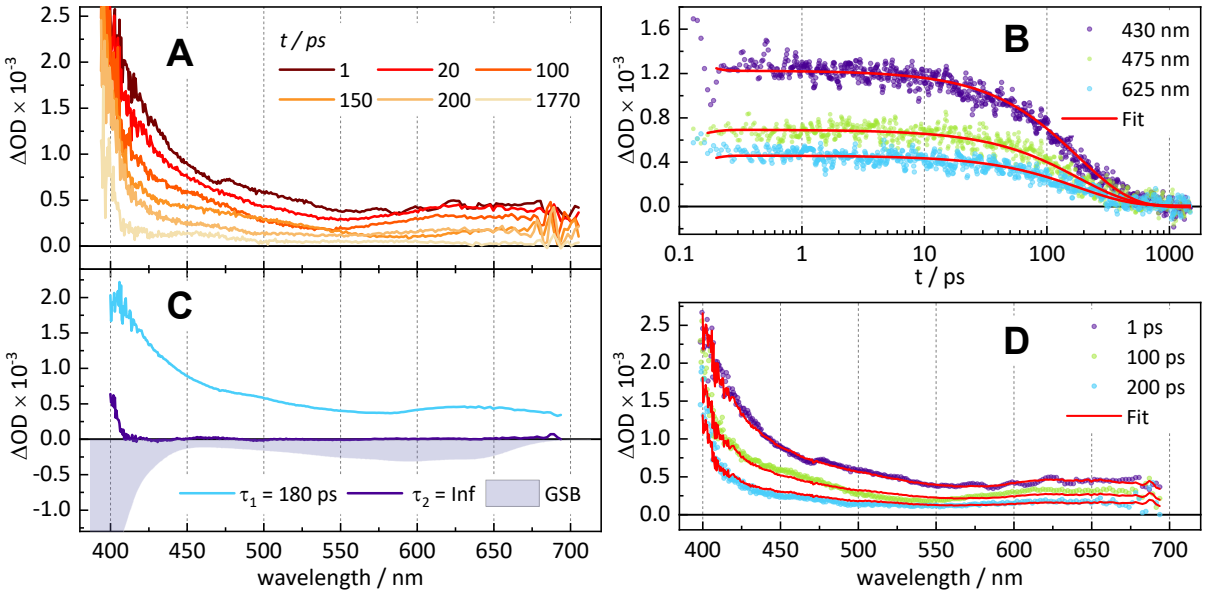

Figure S11, A: TA spectra of **[Fe((ImPh)$_2$P)$_2$]$^+$** dissolved in MeCN at different times t after optical excitation at 600 nm. B: Time traces (dots) at the specified probe wavelengths together with respective fit curves resulting from the GLA (red solid lines). C: DAS obtained by the GLA and labelled by the respective time constants. The dynamics is well described by a monoexponential decay with the time constant τ_1 = 180 ps. A further, long-lived component modelled by a decay with an infinite time constant τ_2 = Inf was used to account for tiny offsets at long delay times. The component is at almost all wavelengths practically zero and within the experimental accuracy insignificant. The negative of the ground state absorption is shown as grey area to indicate where ground state bleach (GSB) might contribute to the TA signal. D: TA spectra (dots) at the given time points together with fitted spectra obtained by the GLA (red solid lines).

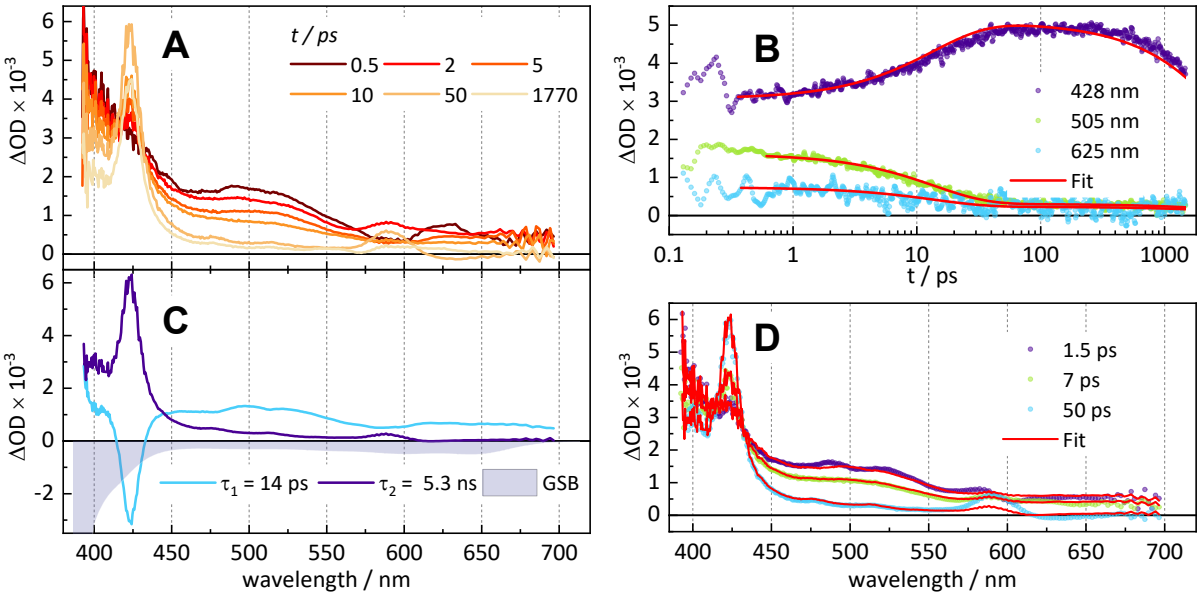

Figure S12, A: TA spectra of **[Fe(Im$_2$PAnt)$_2$]$^+$** dissolved in MeCN at different times t after optical excitation at 600 nm. B: Time traces (dots) at the specified probe wavelengths together with respective fit curves resulting from the GLA (red solid lines). C: DAS obtained by the GLA and labelled by the respective time constants. The dynamics is well described by a double exponential decay with the time constants τ_1 = 14 ps and τ_2 = 5.3 ns. The negative of the ground state absorption is shown as grey area to indicate where ground state bleach (GSB) might contribute to the TA signal. D: TA spectra (dots) at the given time points together with fitted spectra obtained by the GLA (red solid lines).

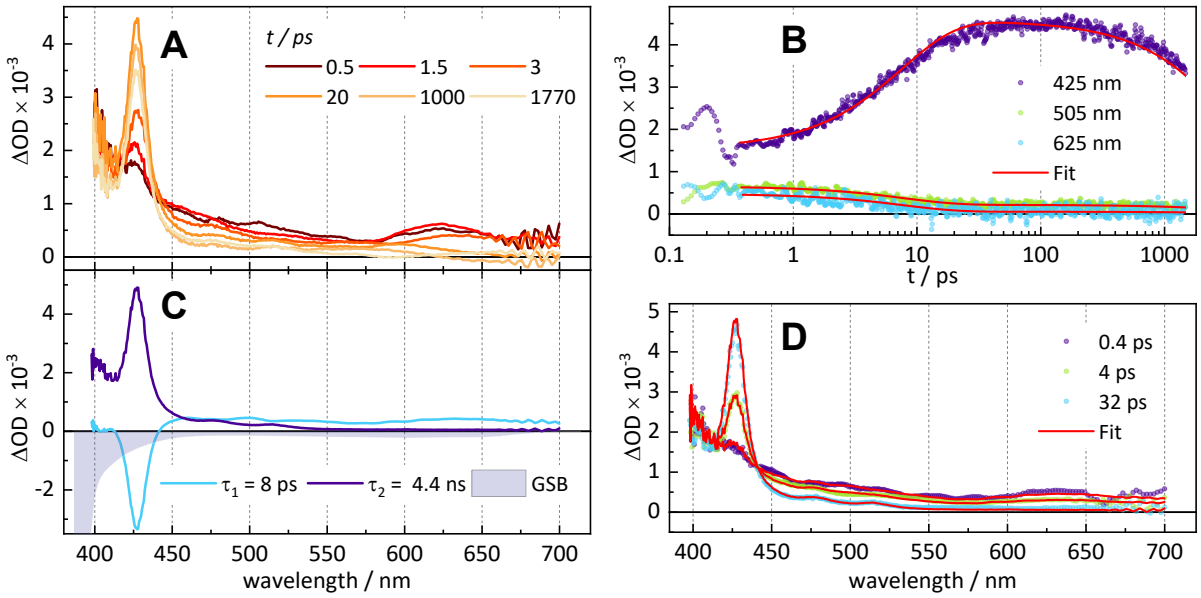

Figure S13, A: TA spectra of **[Fe((ImAnt)$_2$P)$_2$]$^+$** dissolved in MeCN at different times t after optical excitation at 600 nm. B: Time traces (dots) at the specified probe wavelengths together with respective fit curves resulting from the GLA (red solid lines). C: DAS obtained by the GLA and labelled by the respective time constants. The dynamics is well described by a double exponential decay with the time constants τ_1 = 8 ps and τ_2 = 4.4 ns. The negative of the ground state absorption is shown as grey area to indicate where ground state bleach (GSB) might contribute to the TA signal. D: TA spectra (dots) at the given time points together with fitted spectra obtained by the GLA (red solid lines).

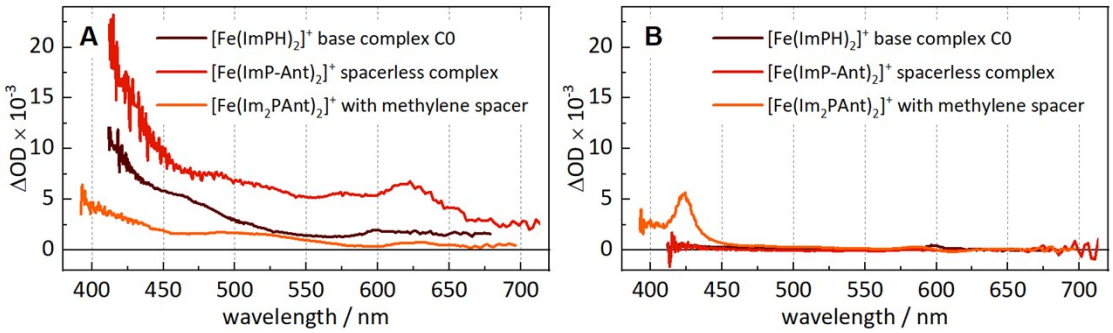

Figure S14: TA spectra of **[Fe(ImPH)$_2$]$^+$**, **[Fe(ImP-Ant)$_2$]$^+$** and **[Fe(Im$_2$PAnt)$_2$]$^+$** at a time delay of 0.5 ps (A) and at a time delay of 600 ps (B). The data from **[Fe(ImPH)$_2$]$^+$** and **[Fe(ImP-Ant)$_2$]$^+$** were adopted from our previous publication.[19] At 0.5 ps the TA signatures of all three compounds are similar indicating that in all cases the LMCT state is initially populated. At 600 ps **[Fe(ImPH)$_2$]$^+$** and **[Fe(ImP-Ant)$_2$]$^+$** show no TA signal any more since the excited state population has already returned to the ground state. In the case of **[Fe(Im$_2$PAnt)$_2$]$^+$** a rather sharp band at about 425 nm remains which is characteristic for the triplet state of anthracene. This demonstrates that at longer delay times the excited state population resides in the local triplet state of the anthracene moiety.

9. TD-DFT calculations

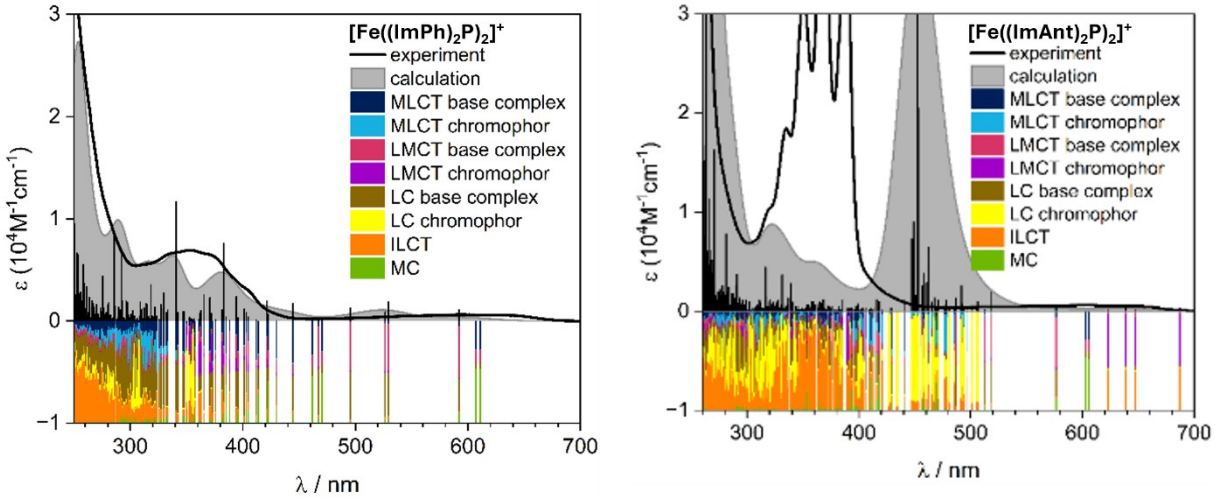

Figure S15: Experimental and TD-DFT-calculated UV-Vis spectra (broadened with a full-width at half maximum (FWHM) of 2000 cm^{-1}) of **$[Fe((ImPh)_2P)_2]^+$** and **$[Fe((ImAnt)_2P)_2]^+$**. LC refers to electronic transitions where the charge remains localized within the same part of the ligand (base complex ligand or chomophore), whereas ILCT describes charge transfer between different regions within the same ligand.

10. NMR-spectroscopy

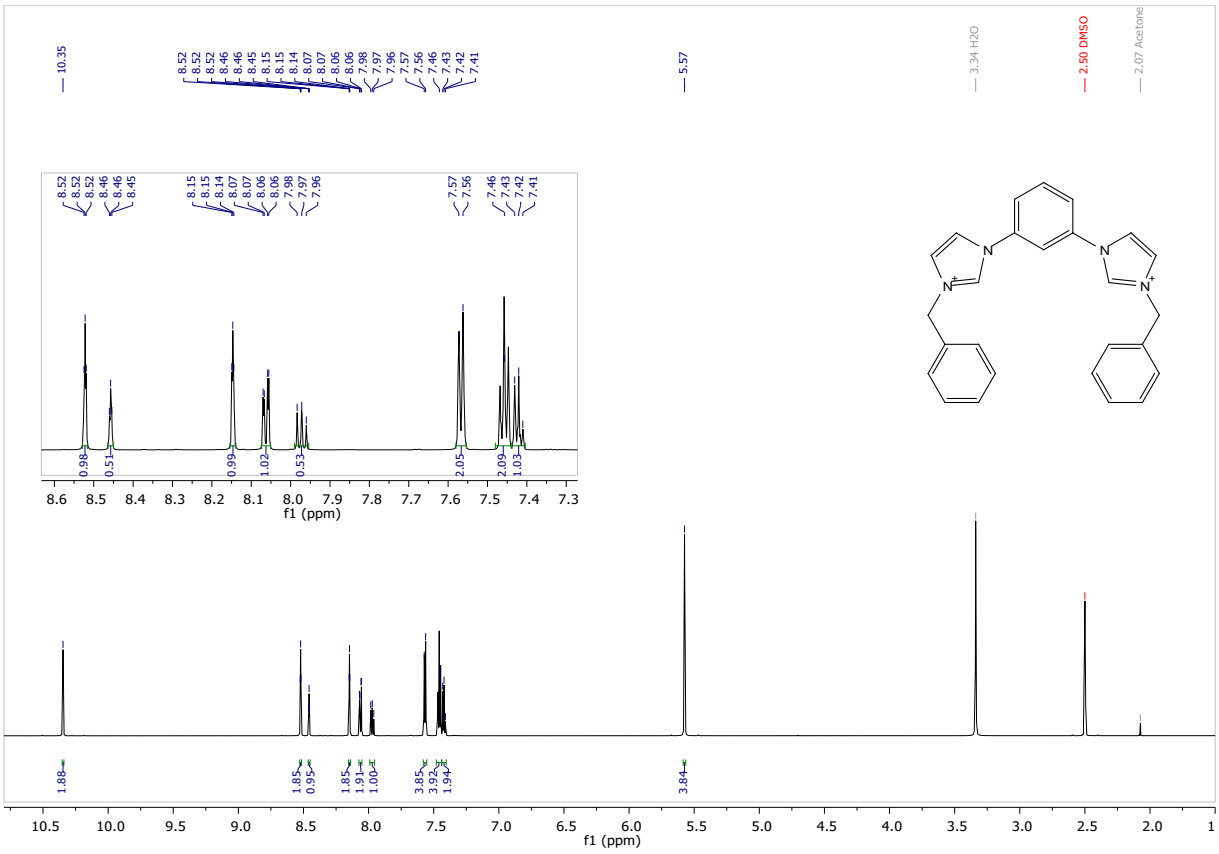

Figure S16: 1H-NMR spectrum of 2-Ph

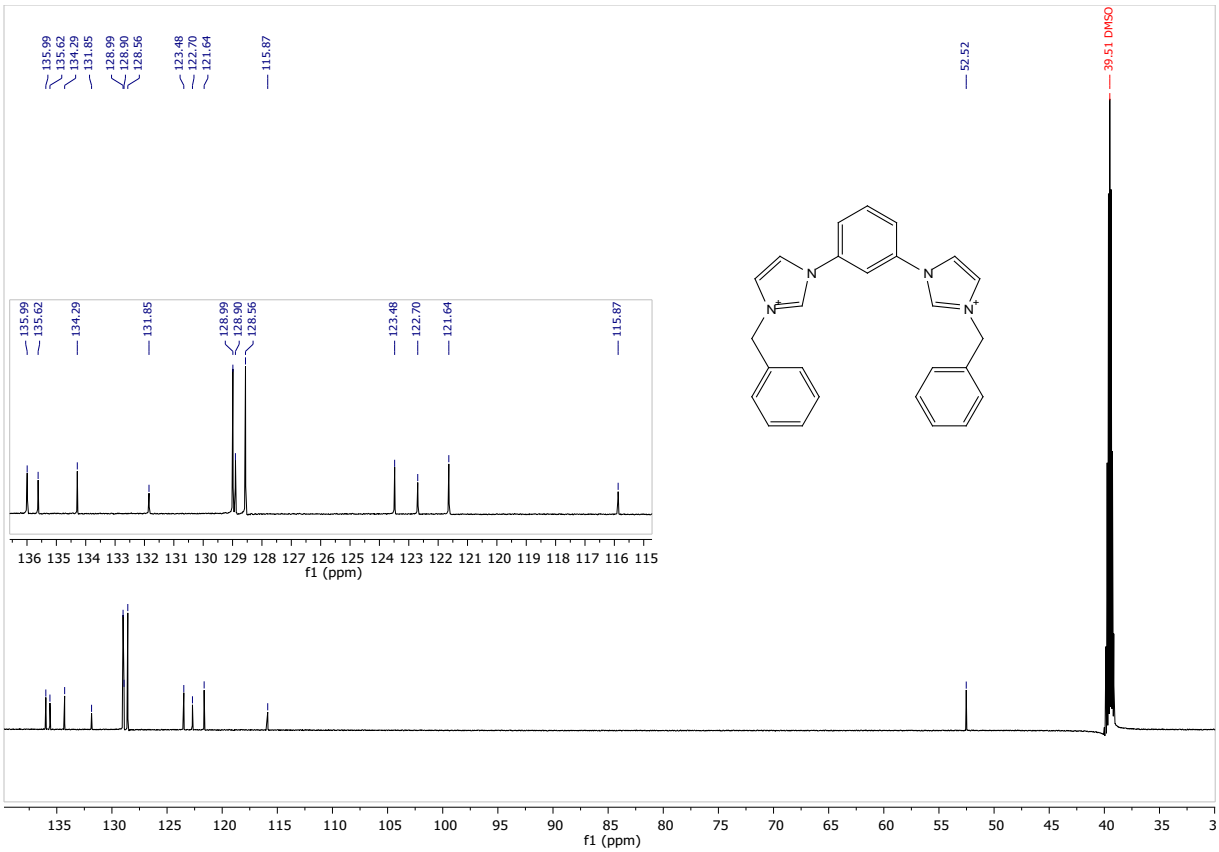

Figure S17: ^{13}C-NMR spectrum of **2-Ph**

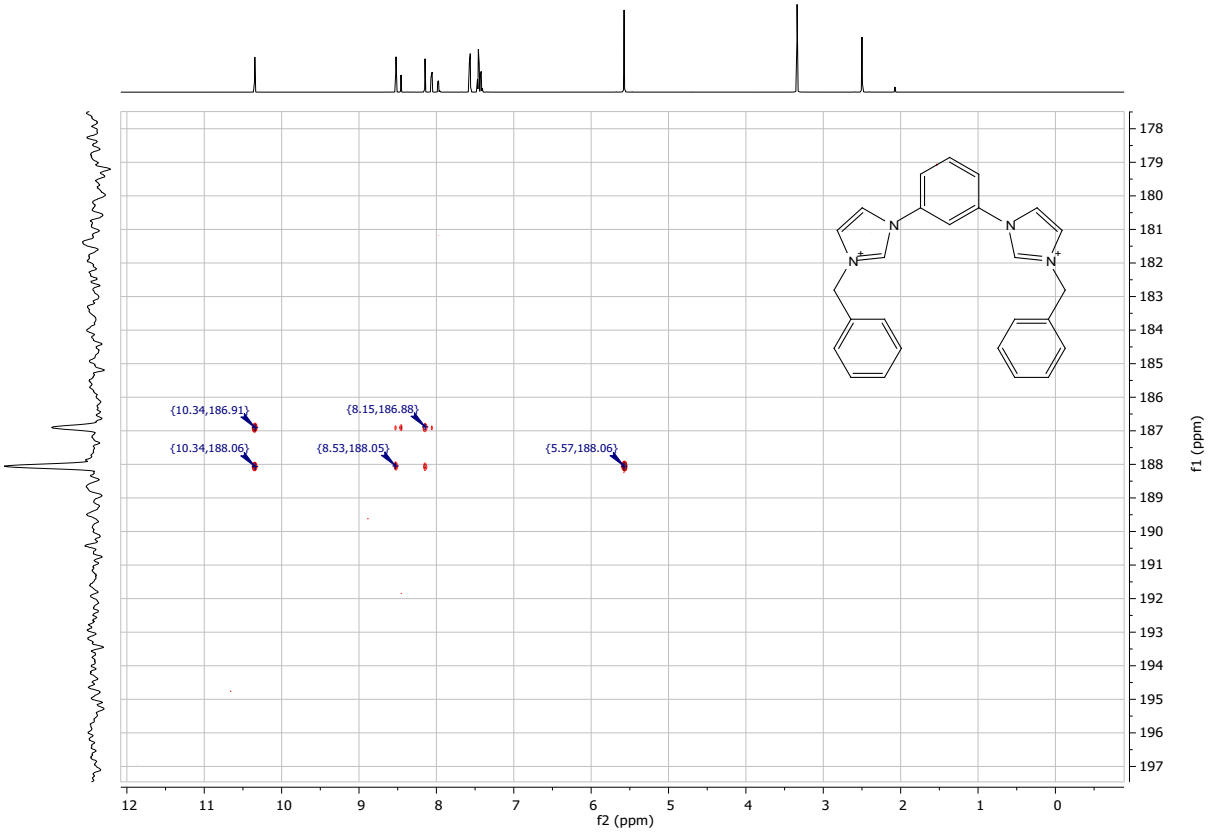

Figure S18: ^{15}N-NMR spectrum of **2-Ph**

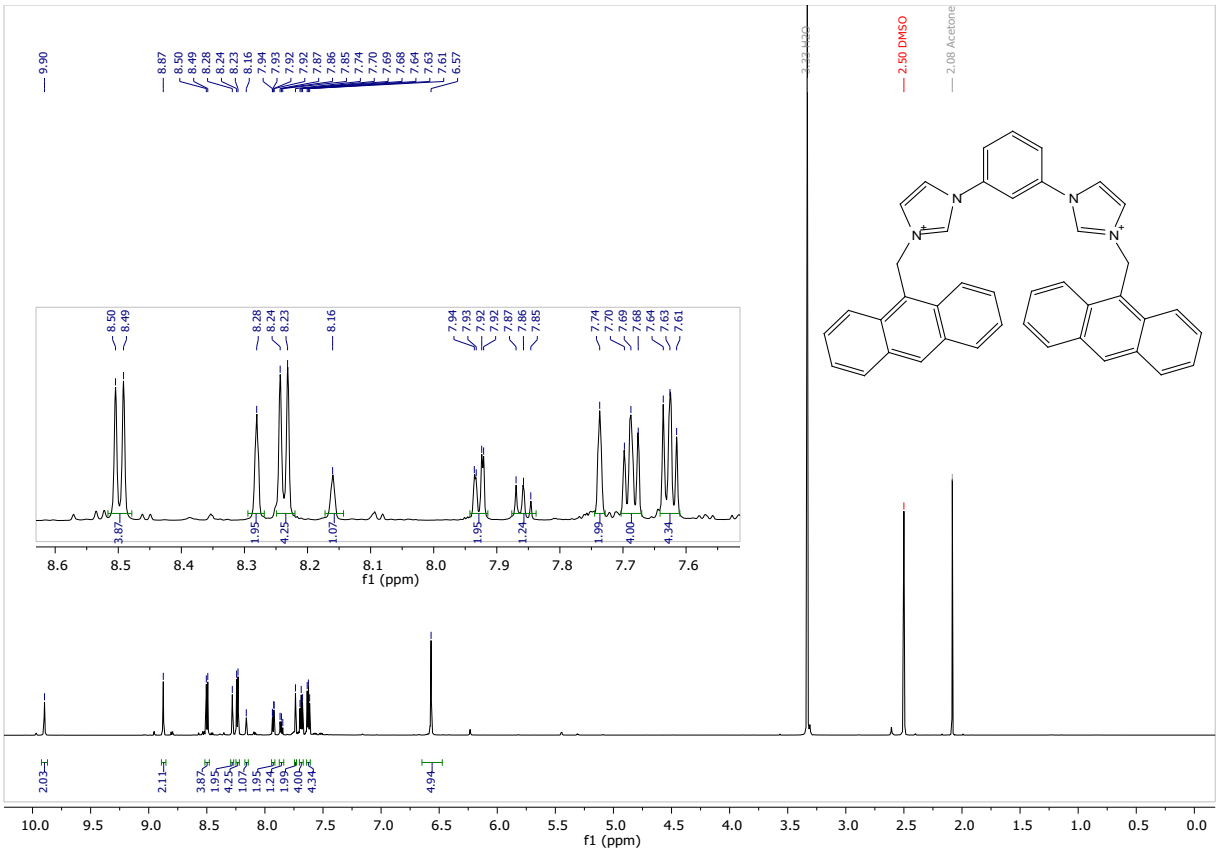

Figure S19: ^{1}H-NMR spectrum of **2-Ant**

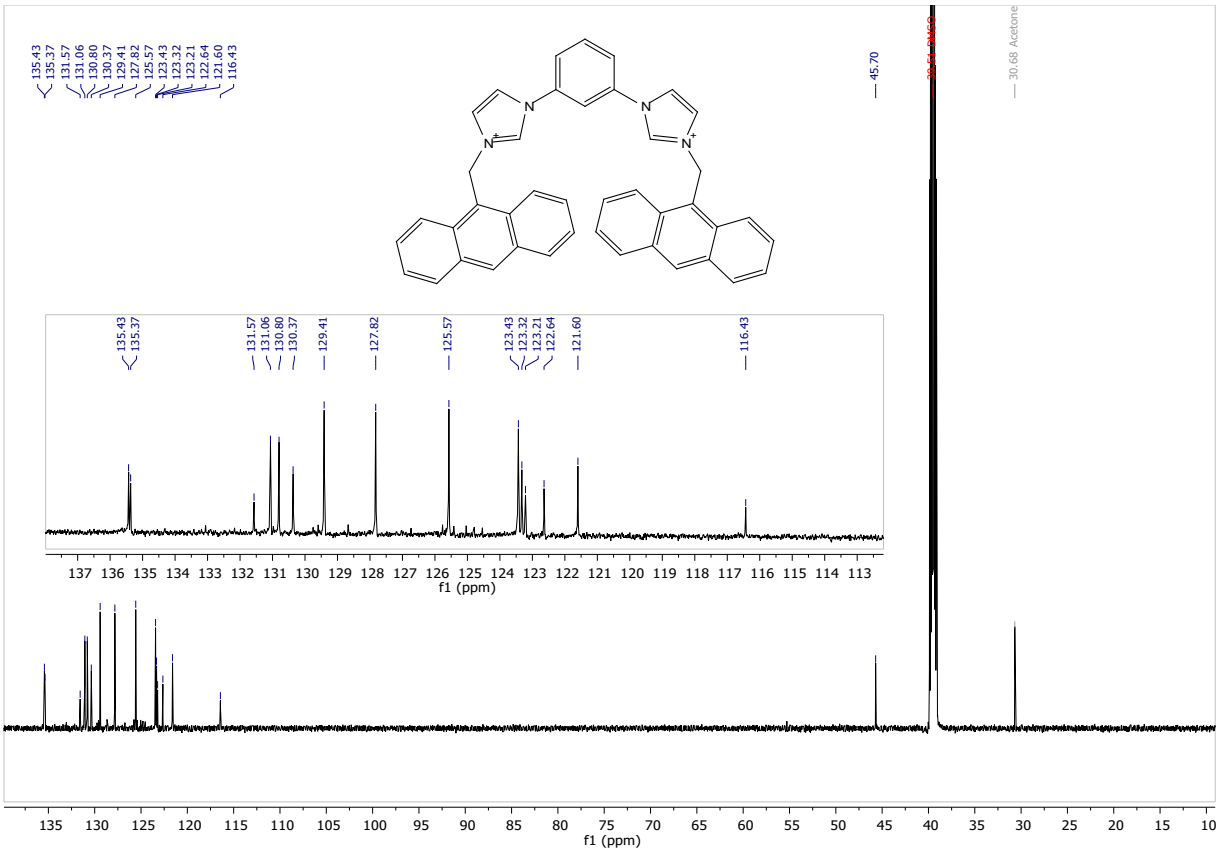

Figure S20: ^{13}C-NMR spectrum of **2-Ant**

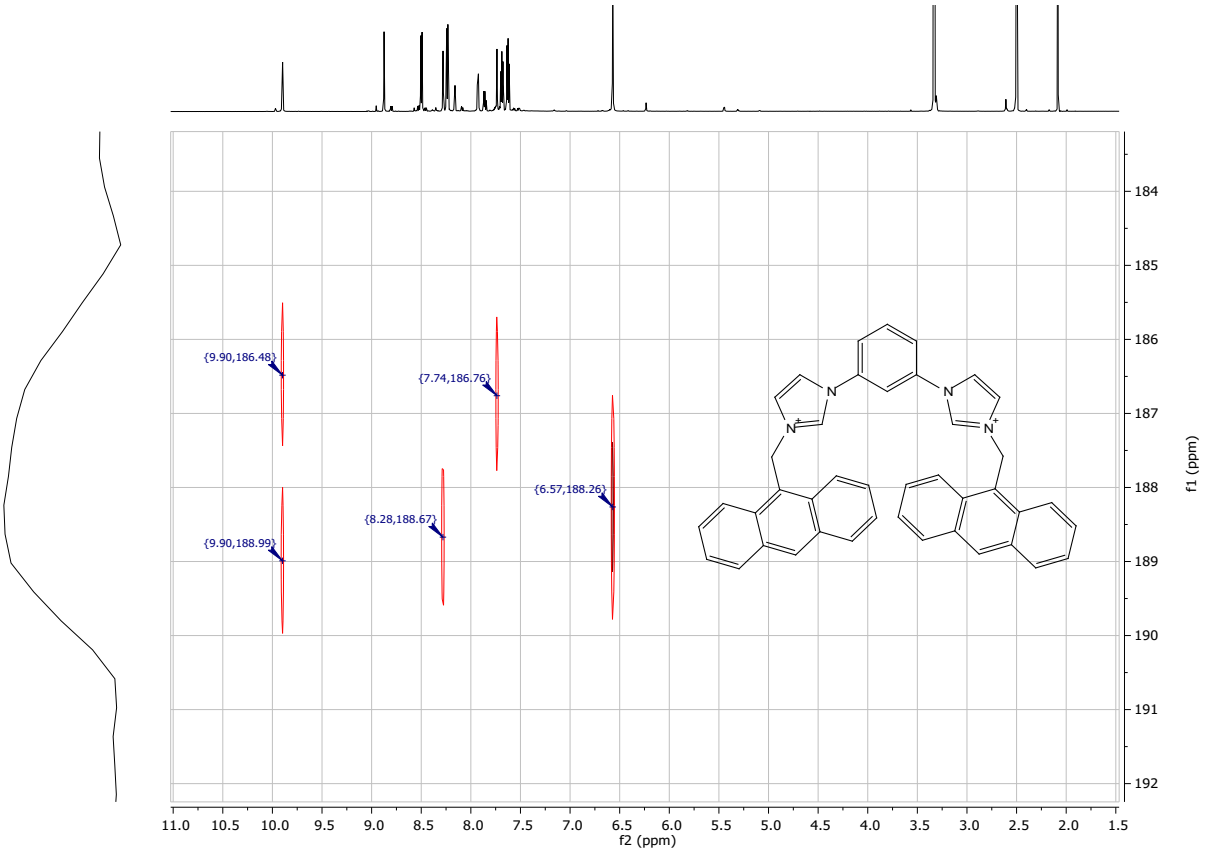

Figure S21: ^{15}N-NMR spectrum of **2-Ant**

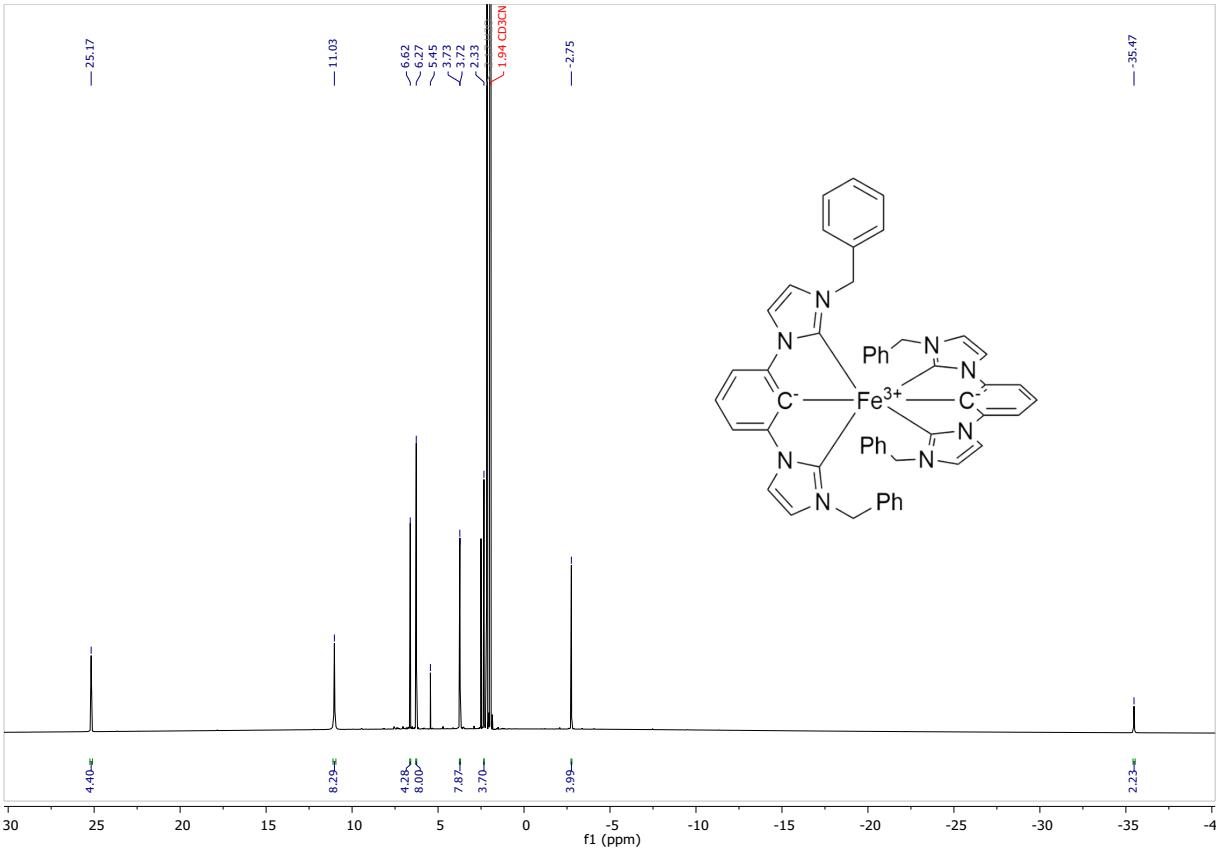

Figure S22: ^{1}H-NMR spectrum of **[Fe((ImPh)$_2$P)$_2$]$^{+}$**

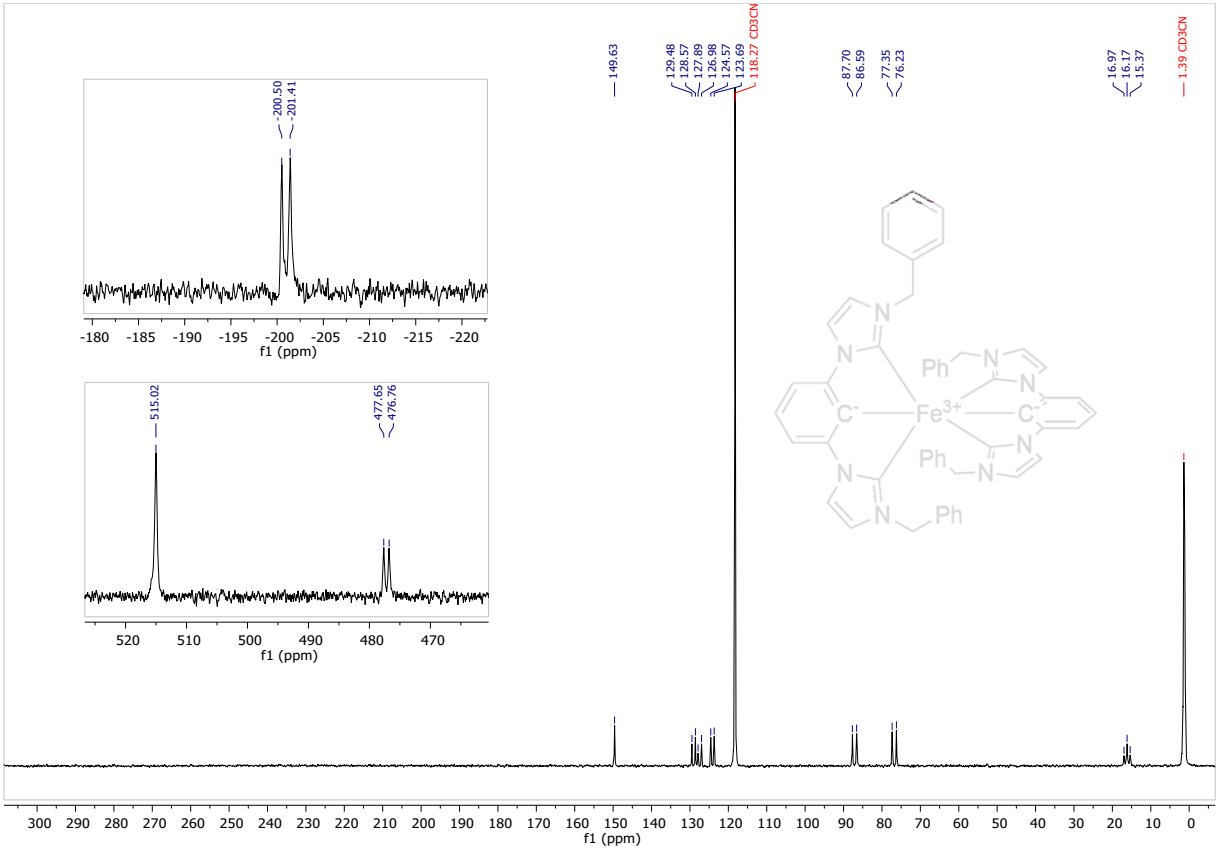

Figure S23: 13C-NMR spectrum of **[Fe((ImPh)$_2$P)$_2$]$^{+}$**

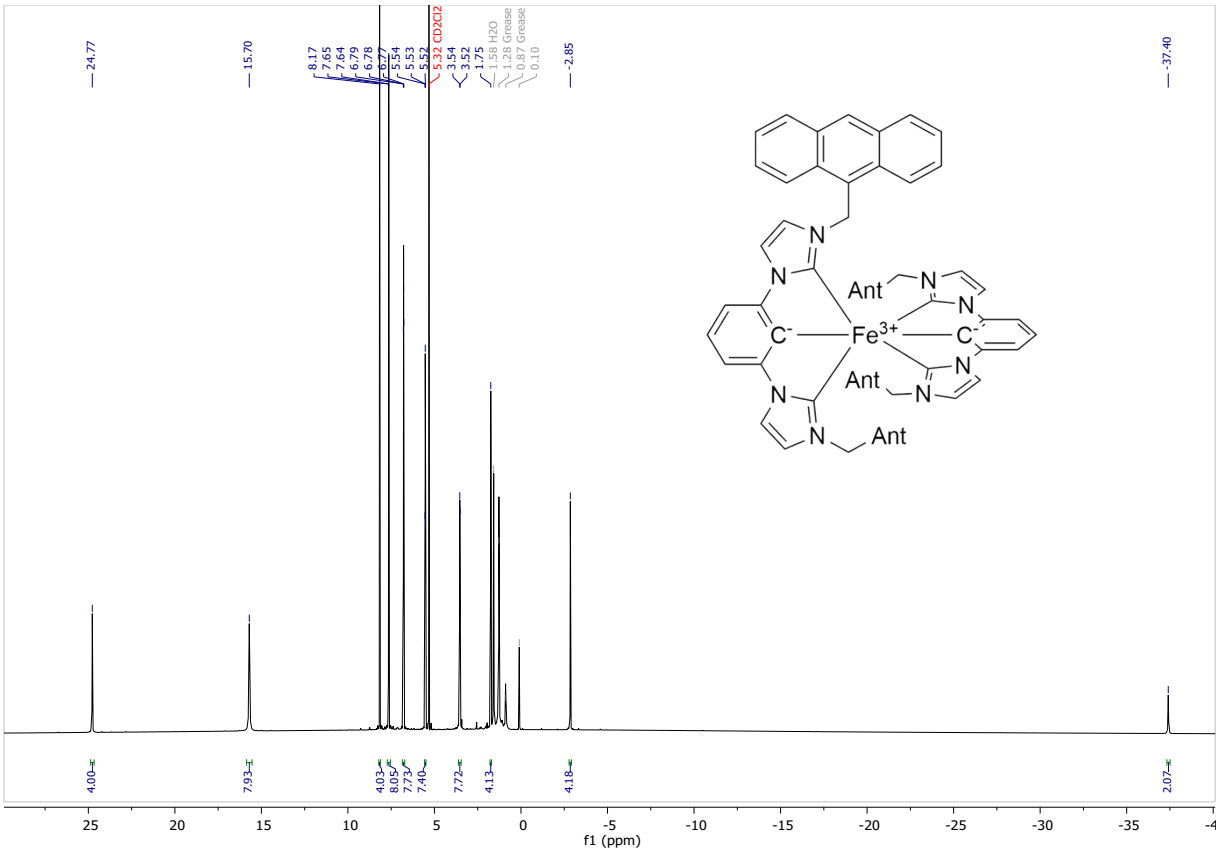

Figure S24: ^{1}H-NMR spectrum of **[Fe((ImAnt)$_2$P)$_2$]$^{+}$**

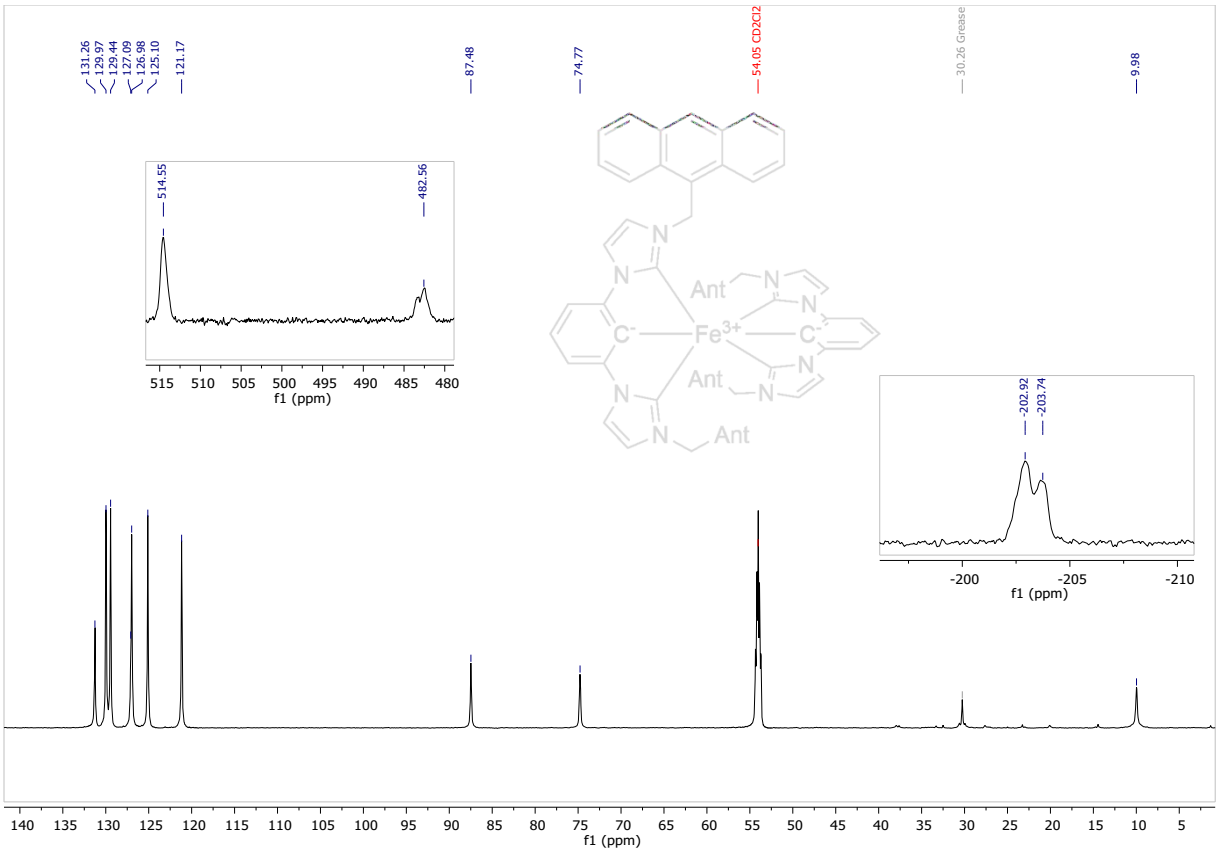

Figure S25: 13C-NMR spectrum of **[Fe((ImAnt)$_2$P)$_2$]$^+$**

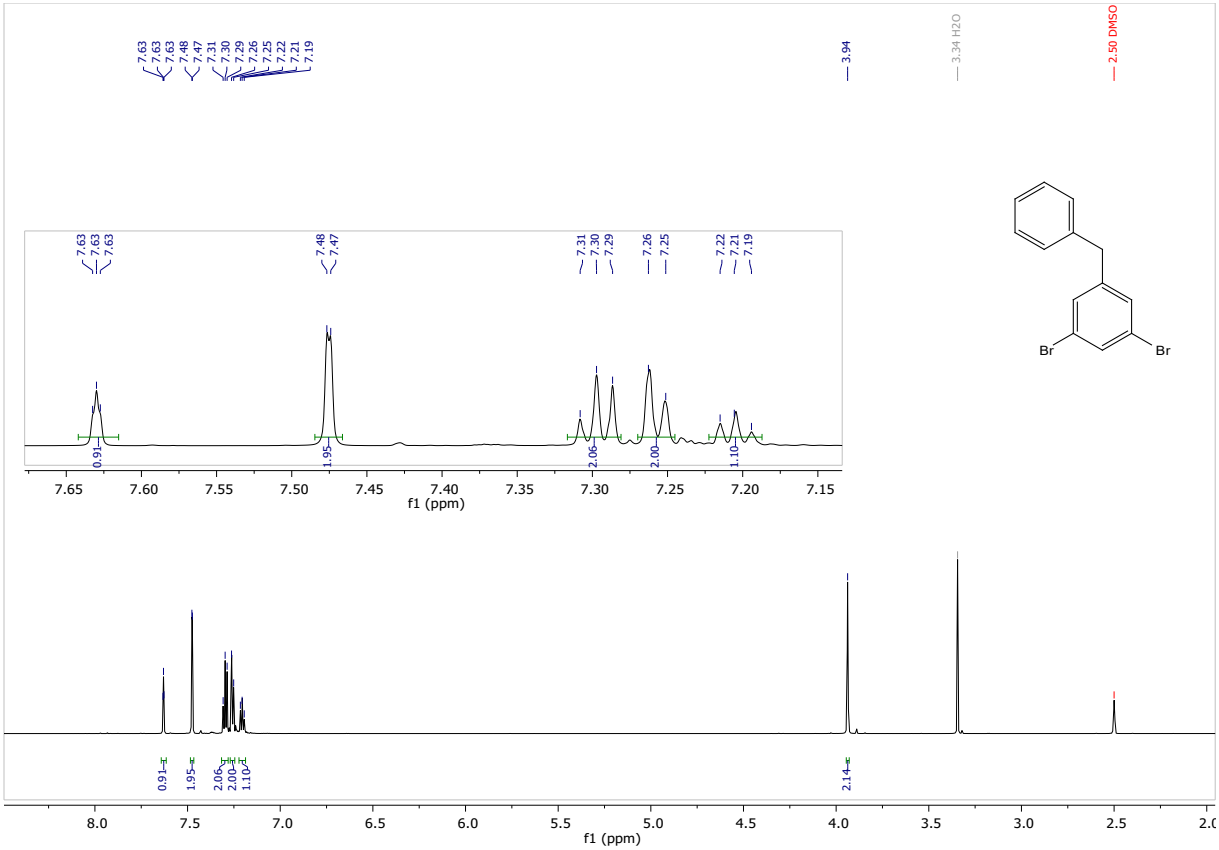

Figure S26: ^{1}H-NMR spectrum of **3-Ph**

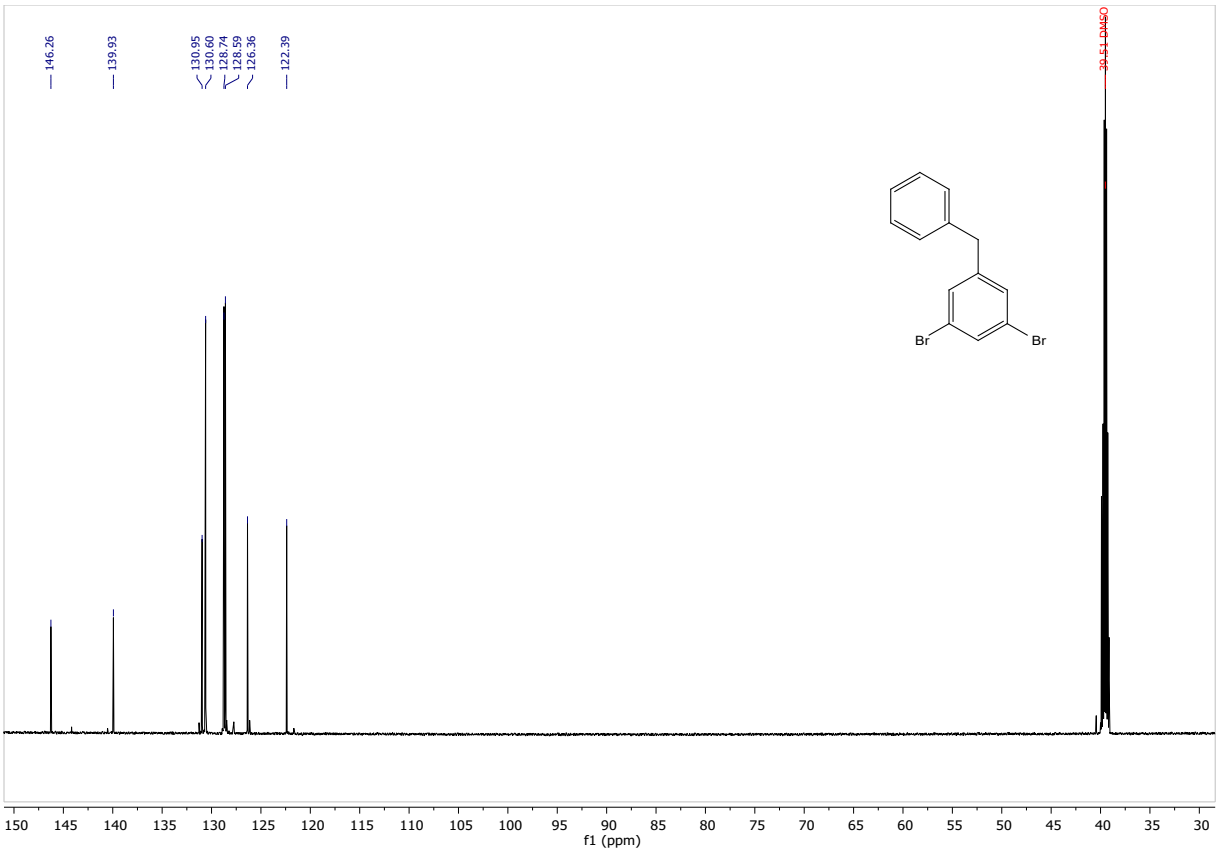

Figure S27: ^{13}C-NMR spectrum of **3-Ph**

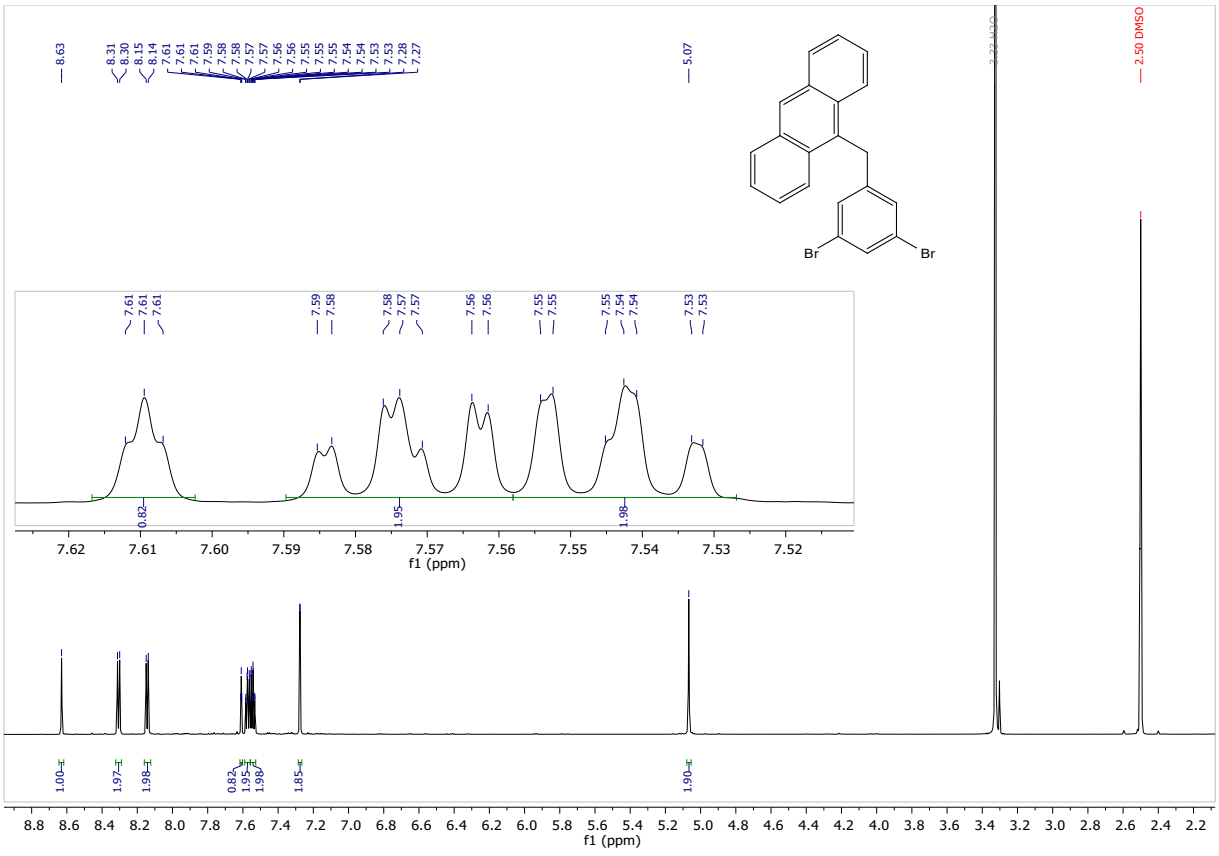

Figure S28: ^{1}H-NMR spectrum of **3-Ant**

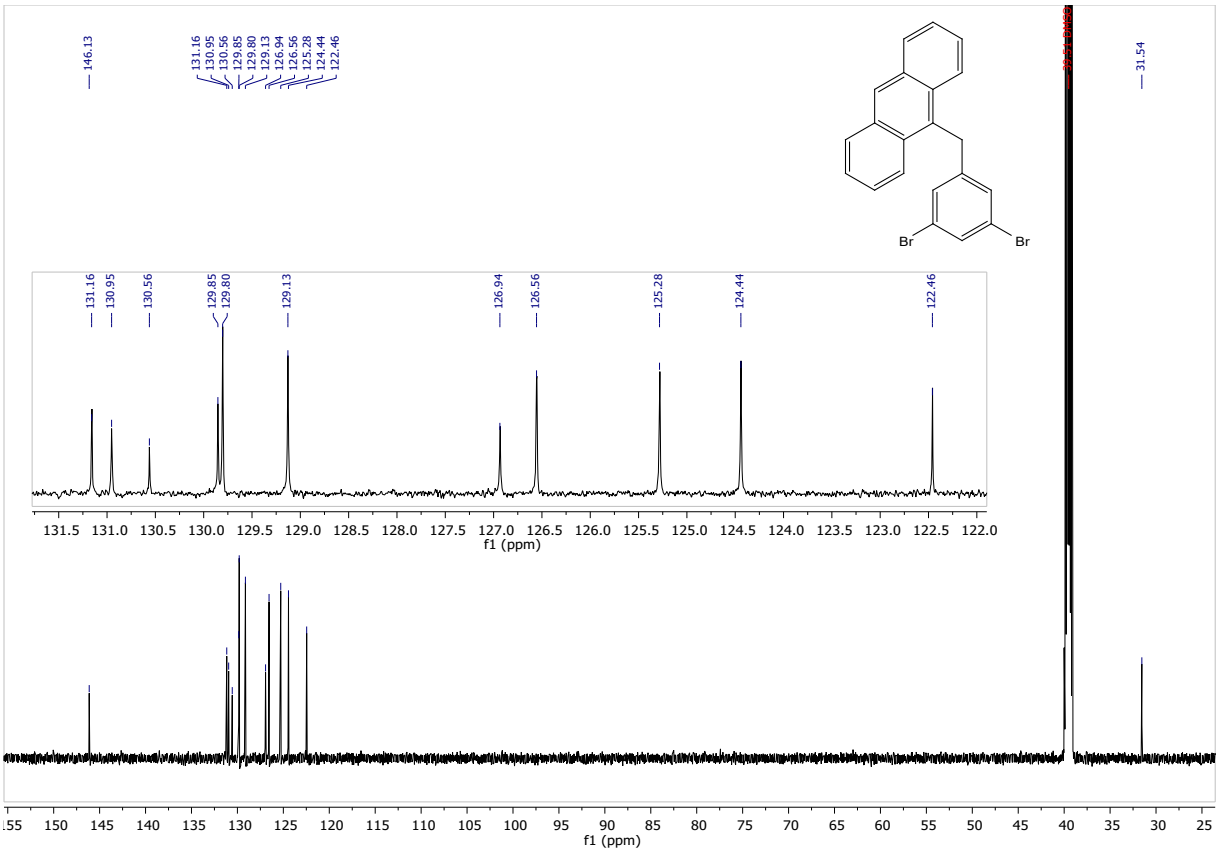

Figure S29: ^{13}C-NMR spectrum of **3-Ant**

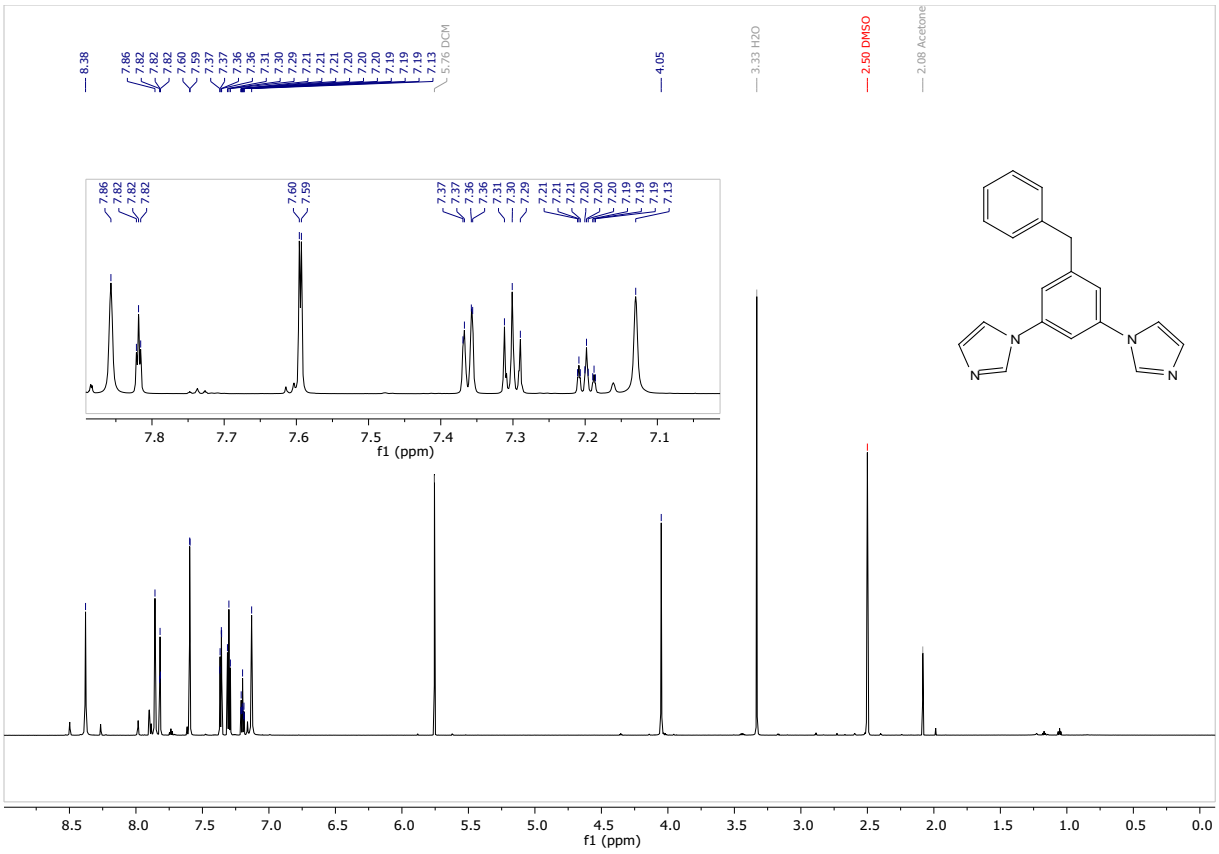

Figure S30: ^{1}H-NMR spectrum of **4-Ph**

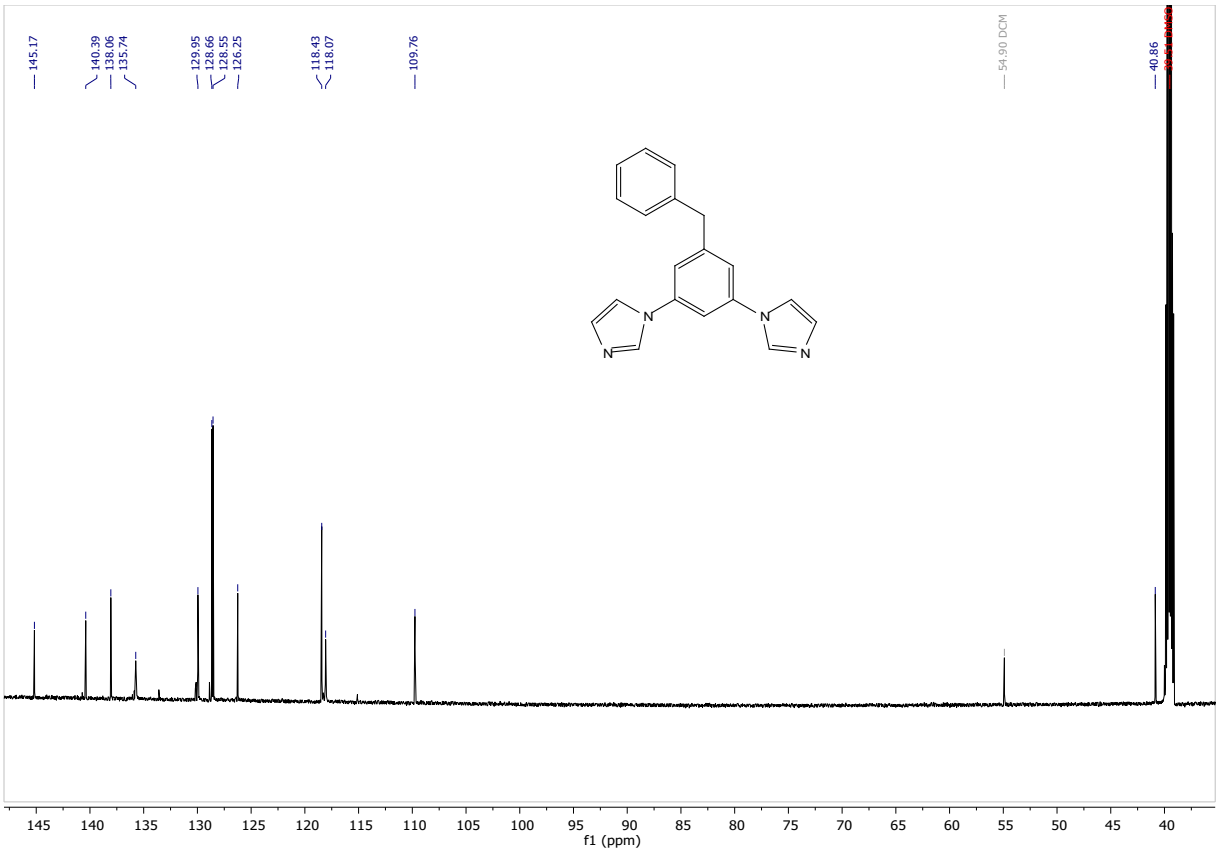

Figure S31: ^{13}C-NMR spectrum of **4-Ph**

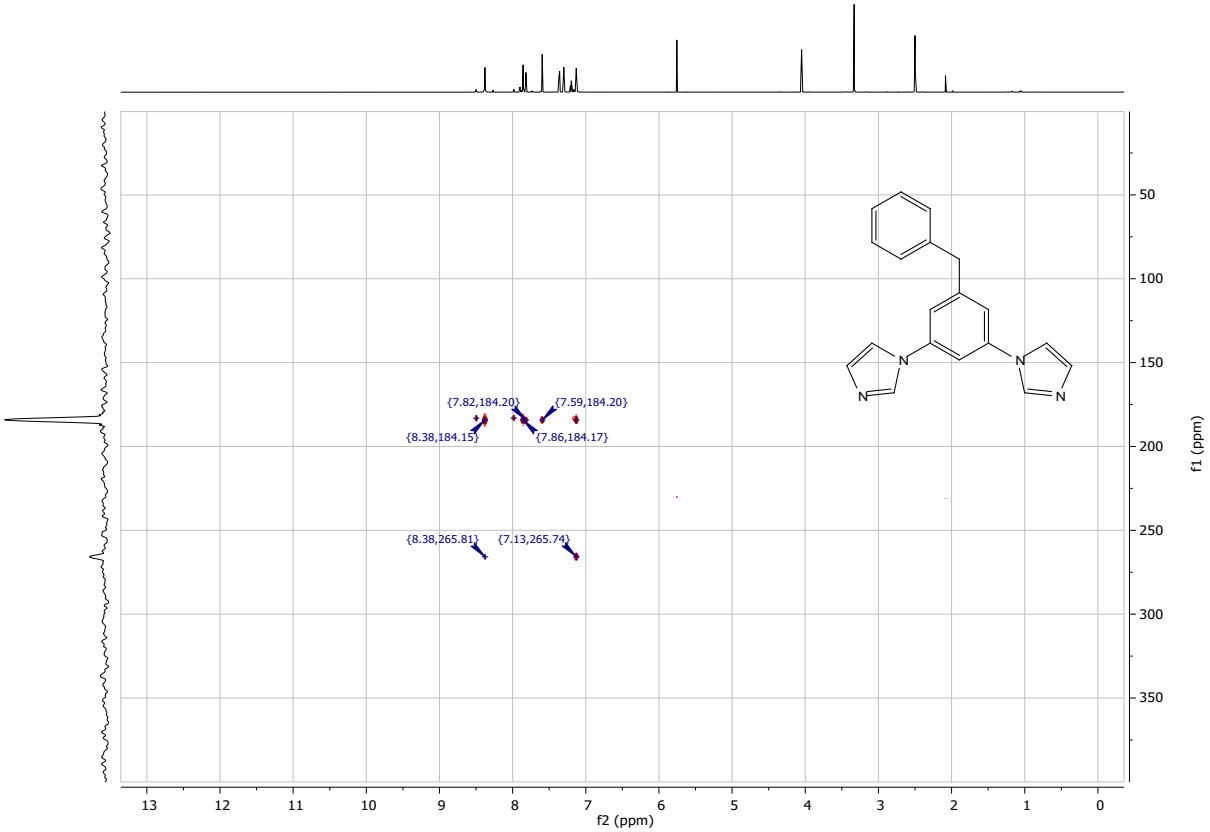

Figure S32: ^{15}N-NMR spectrum of **4-Ph**

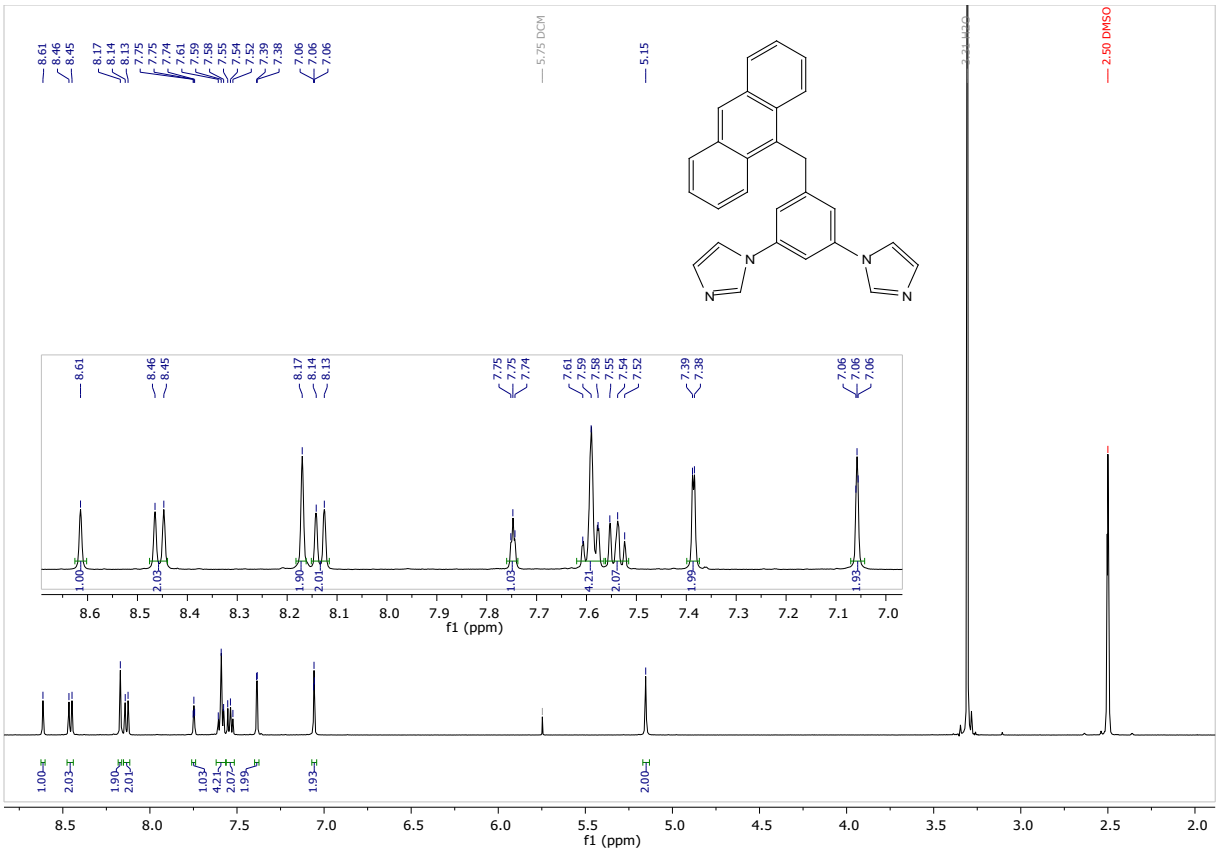

Figure S33: ^{1}H-NMR spectrum of **4-Ant**

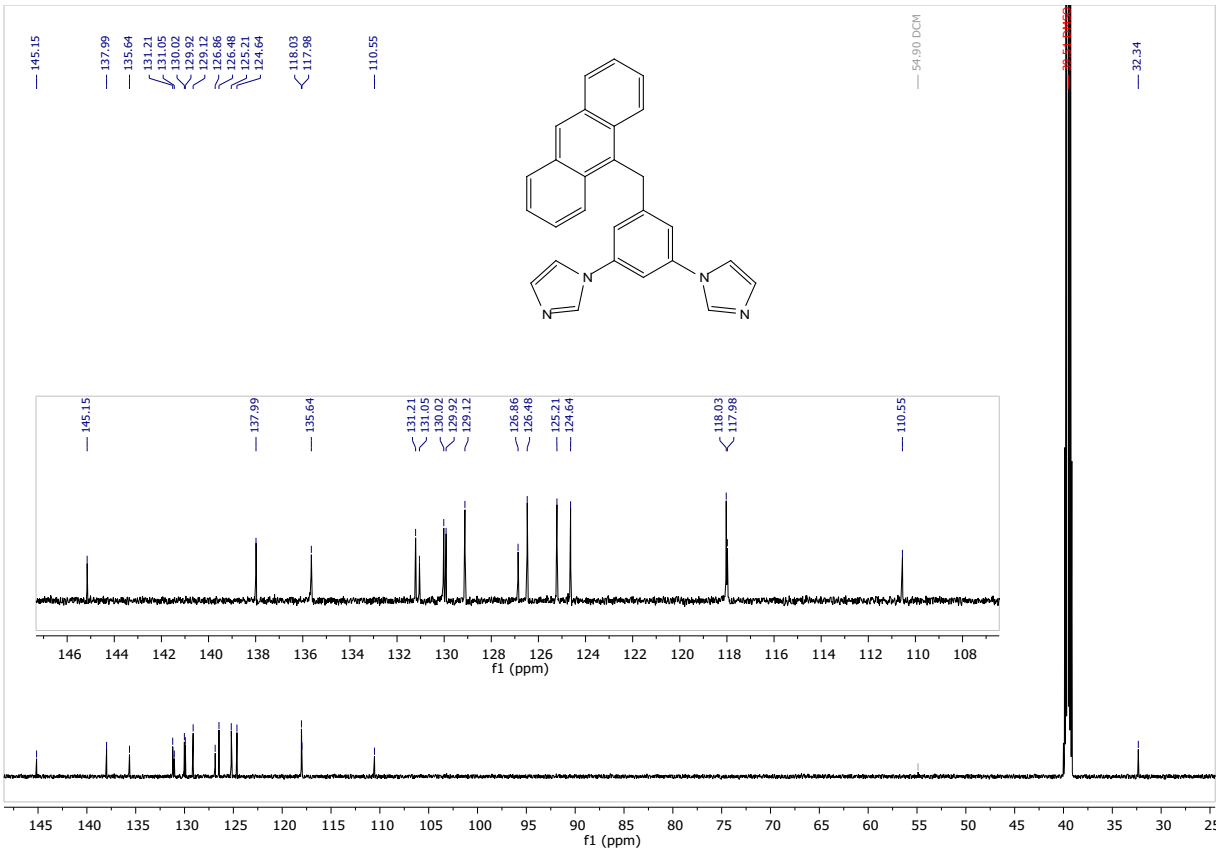

Figure S34: ^{13}C-NMR spectrum of **4-Ant**

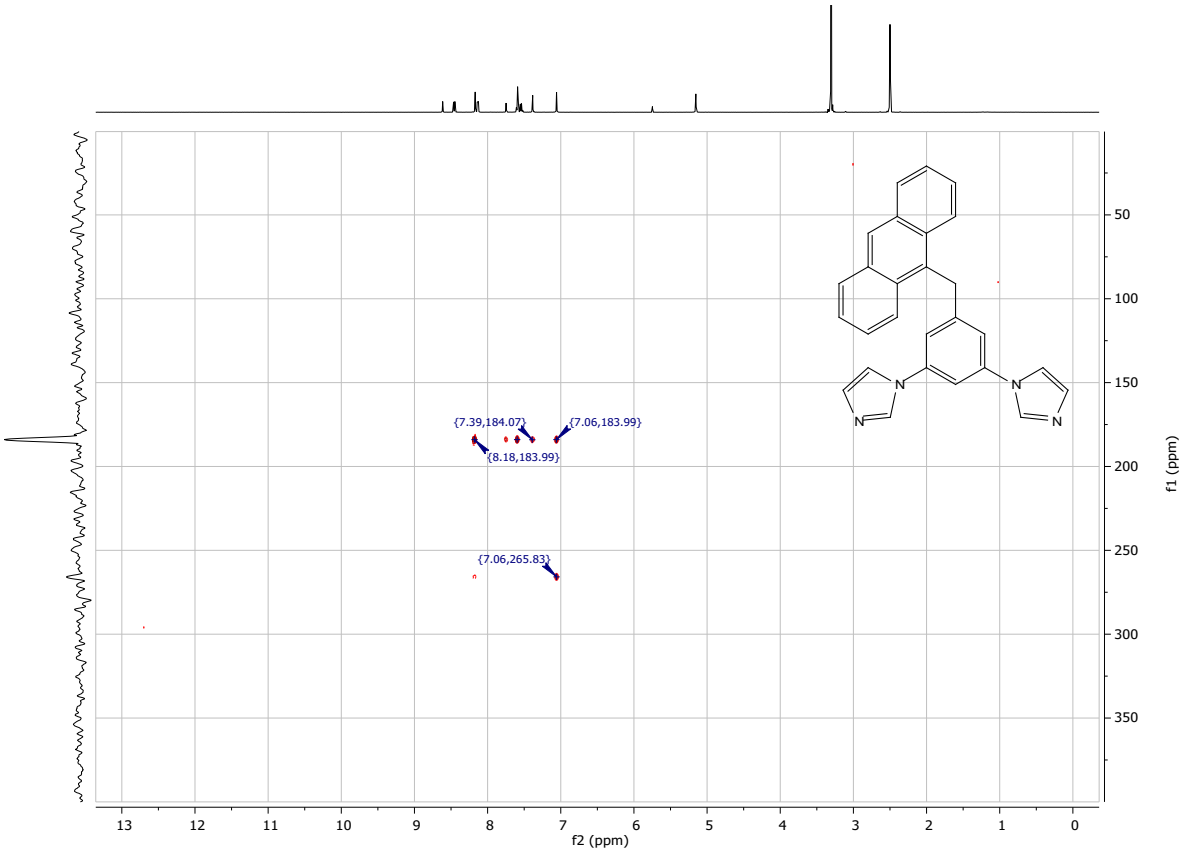

Figure S35: ^{15}N-NMR spectrum of **4-Ant**

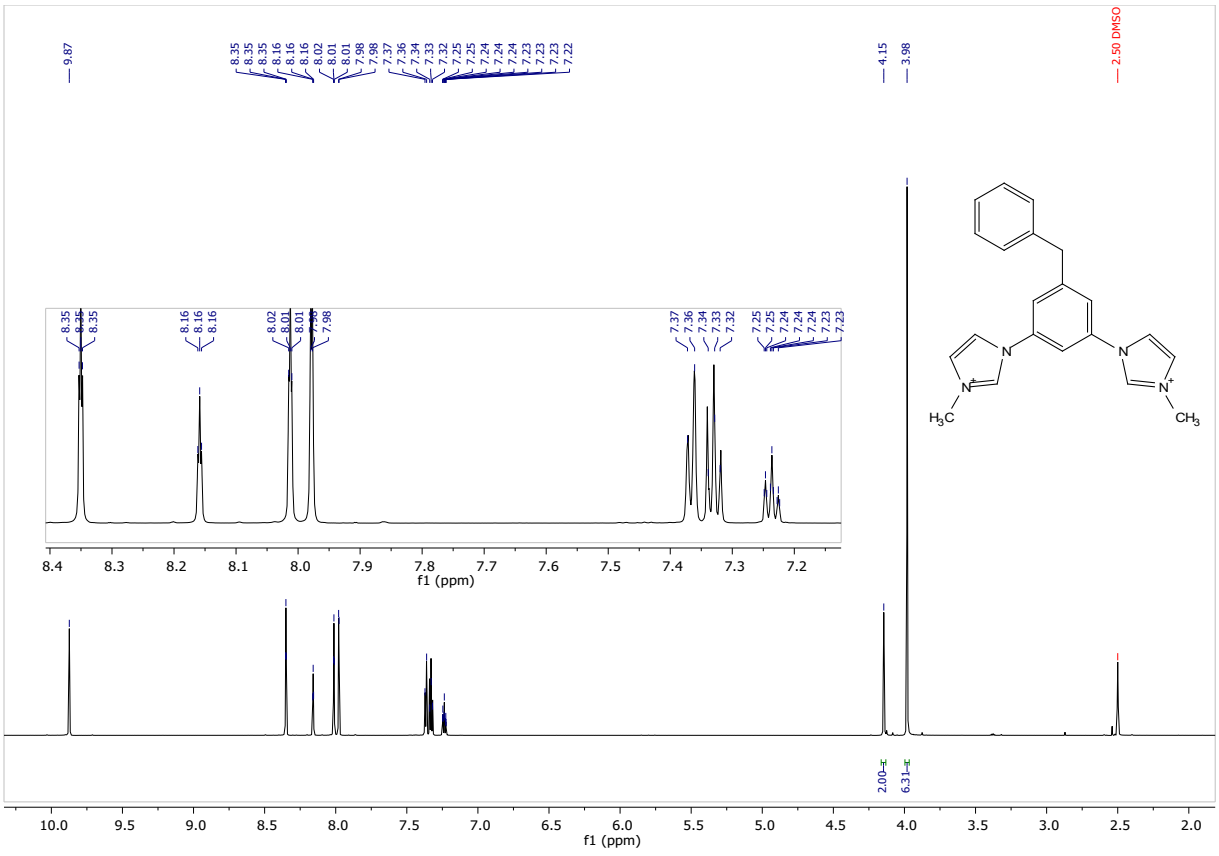

Figure S36: ^{1}H-NMR spectrum of **5-Ph**

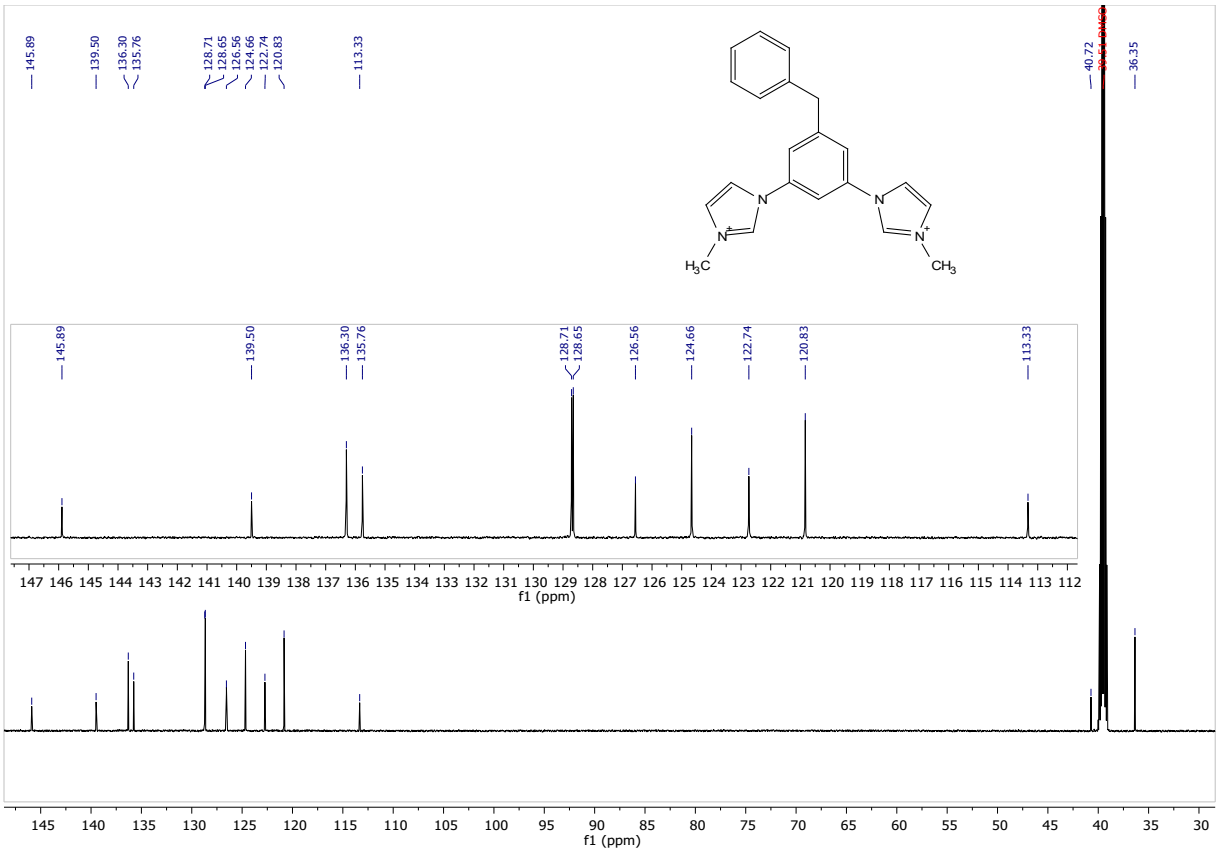

Figure S37: ^{13}C-NMR spectrum of **5-Ph**

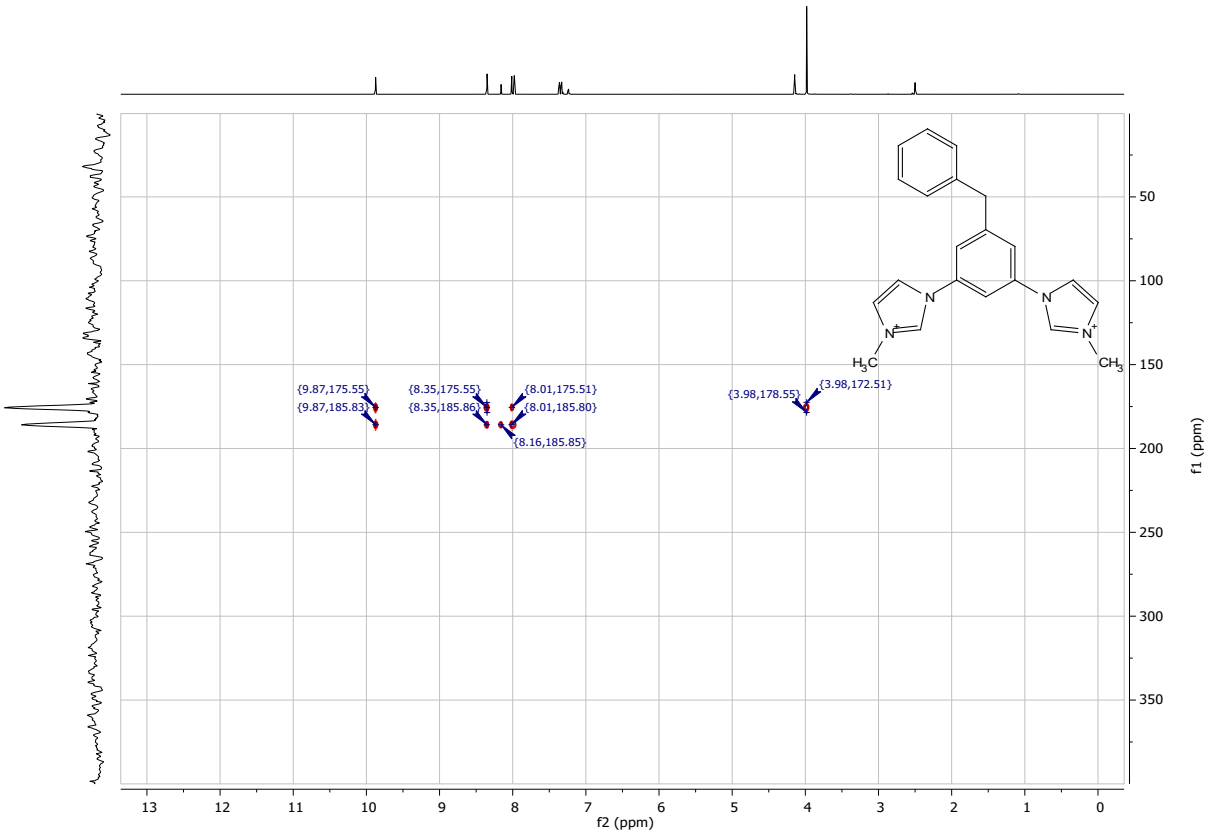

Figure S38: ^{15}N-NMR spectrum of **5-Ph**

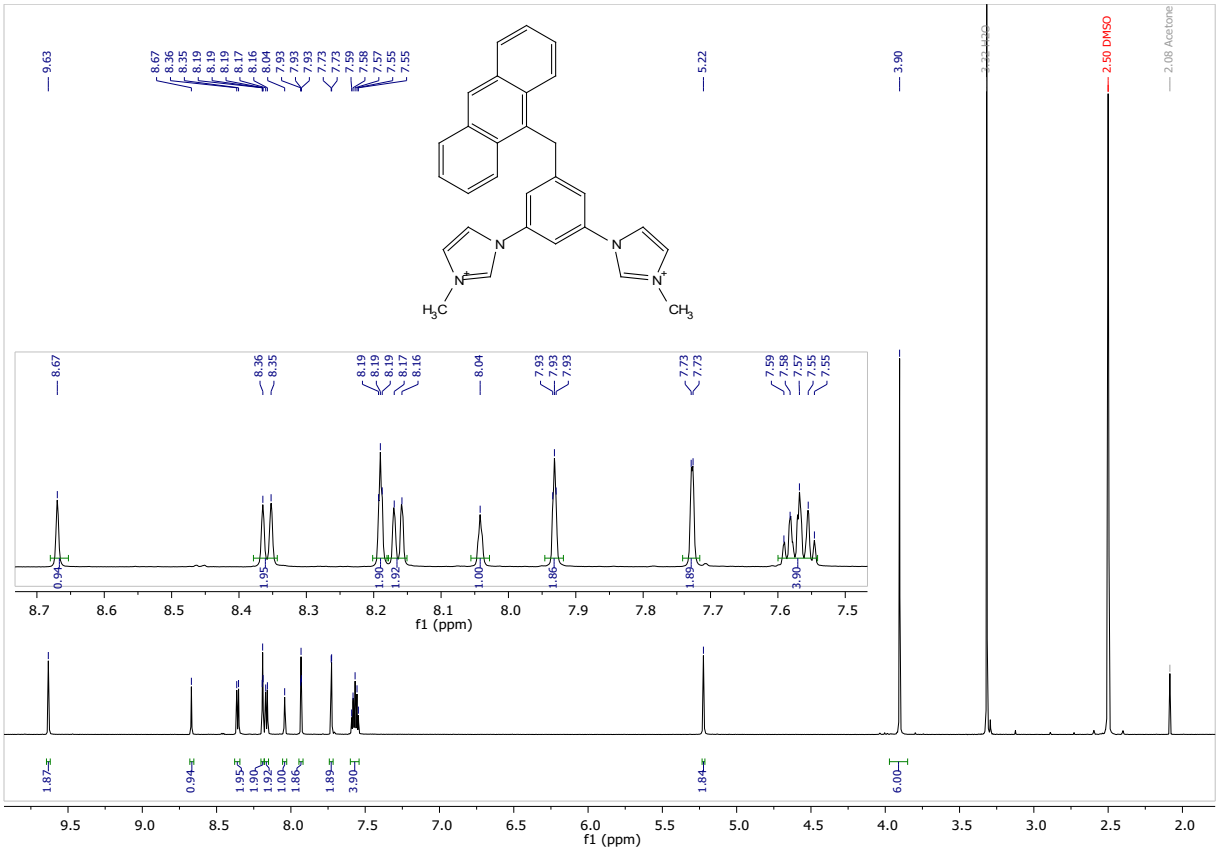

Figure S39: ^{1}H-NMR spectrum of **5-Ant**

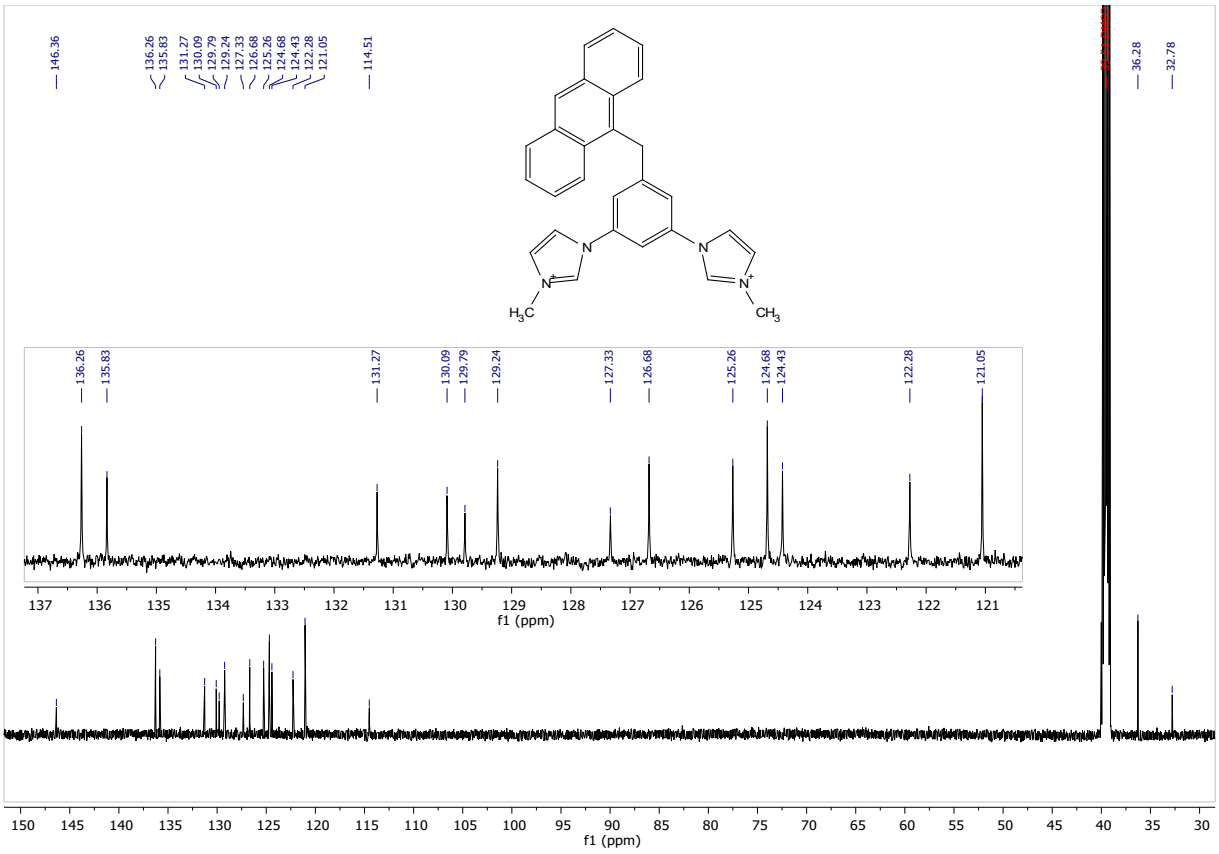

Figure S40: ^{13}C-NMR spectrum of **5-Ant**

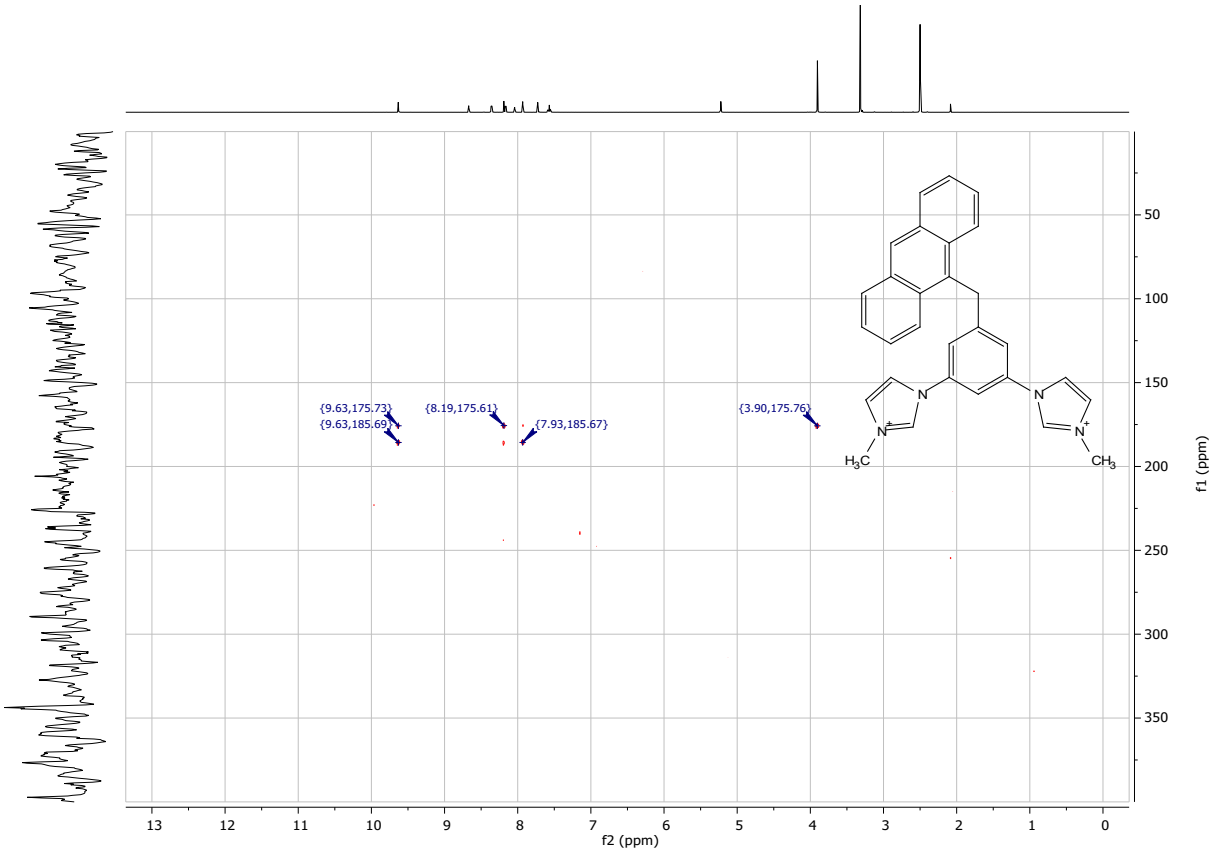

Figure S41: ^{15}N-NMR spectrum of **5-Ant**

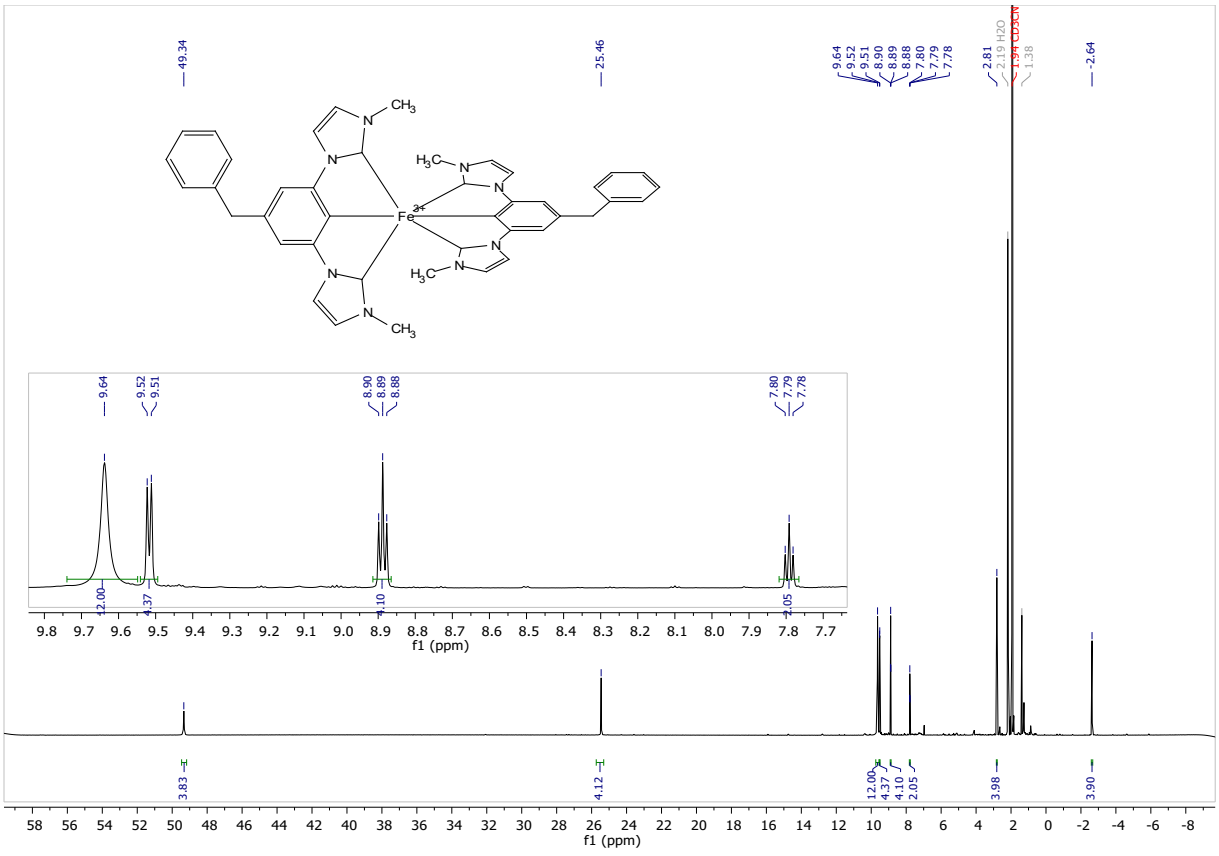

Figure S42: ^{1}H-NMR spectrum of **[Fe(Im$_2$PPh)$_2$]$^{+}$**

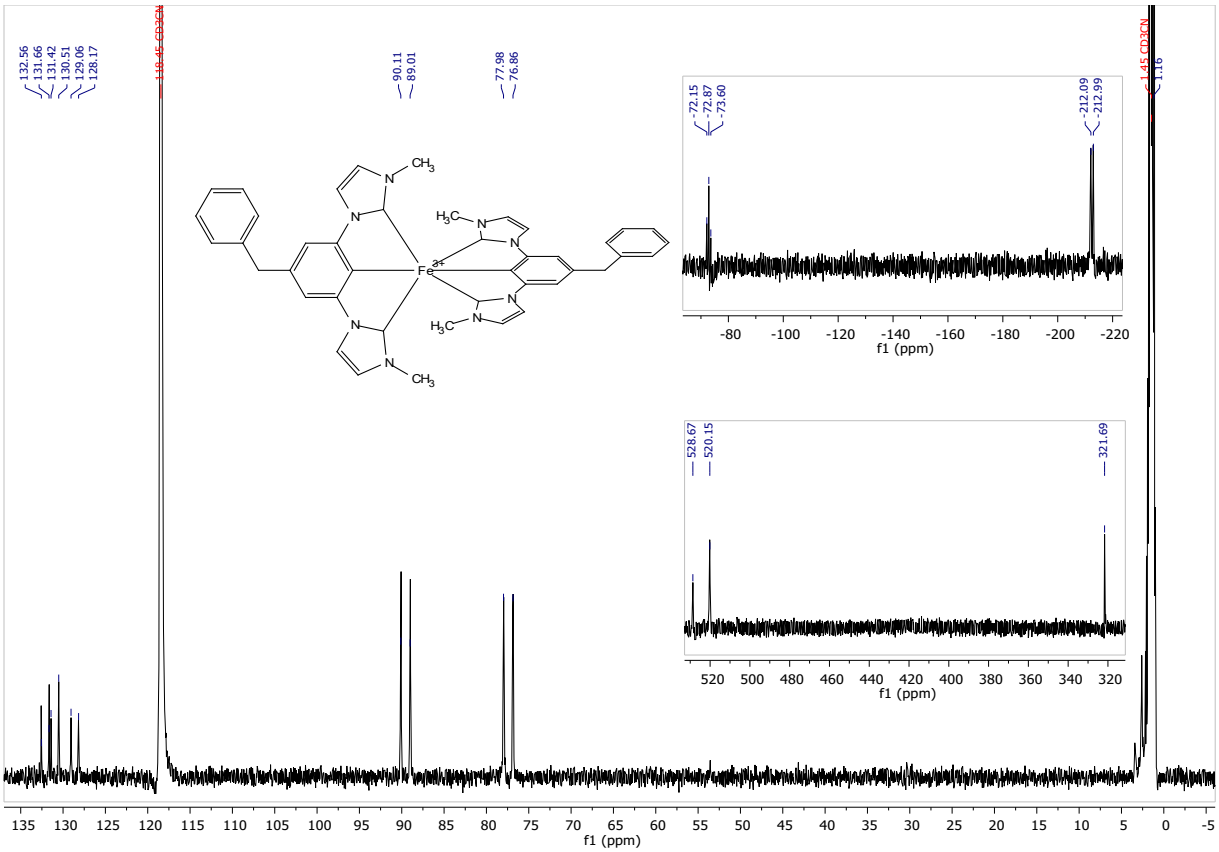

Figure S43: ^{13}C-NMR spectrum of **[Fe(Im$_2$PPh)$_2$]$^+$**

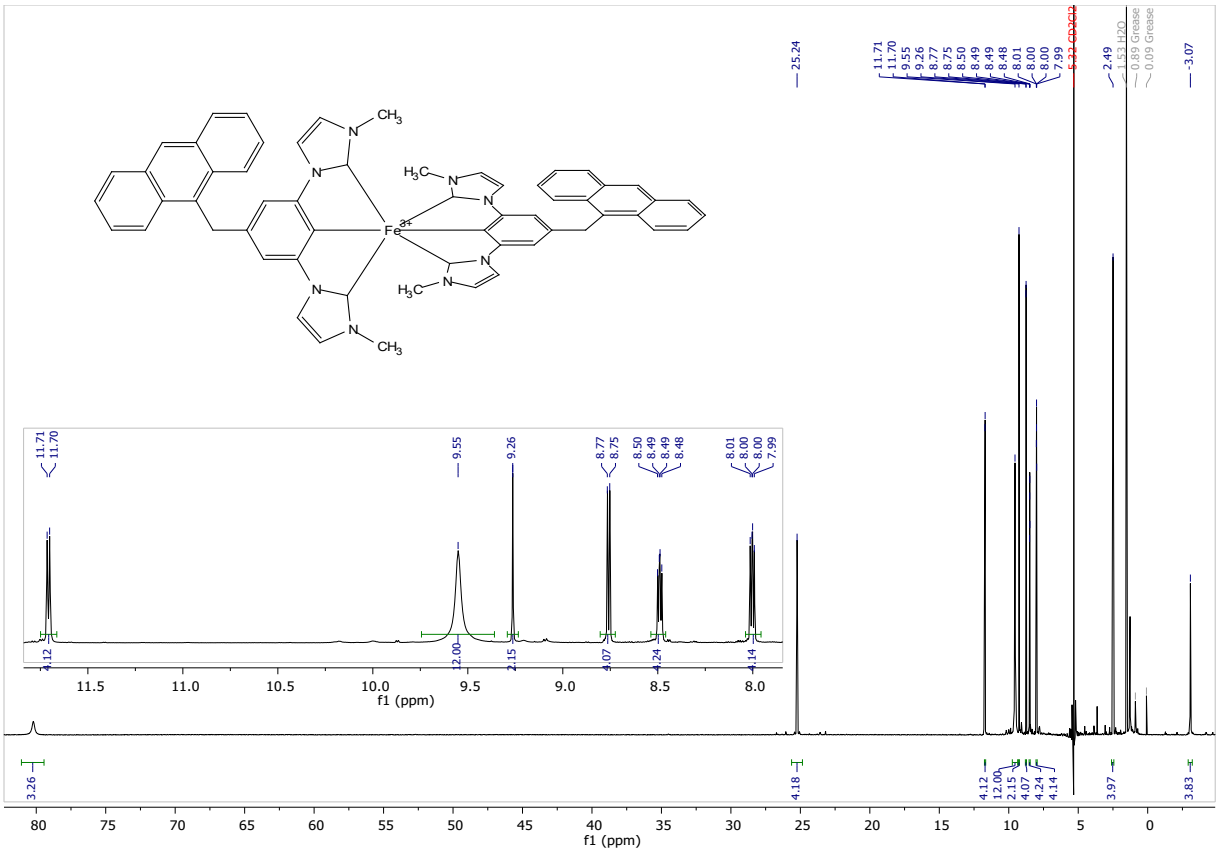

Figure S44: ^{1}H-NMR spectrum **[Fe(Im$_2$PAnt)$_2$]$^{+}$**

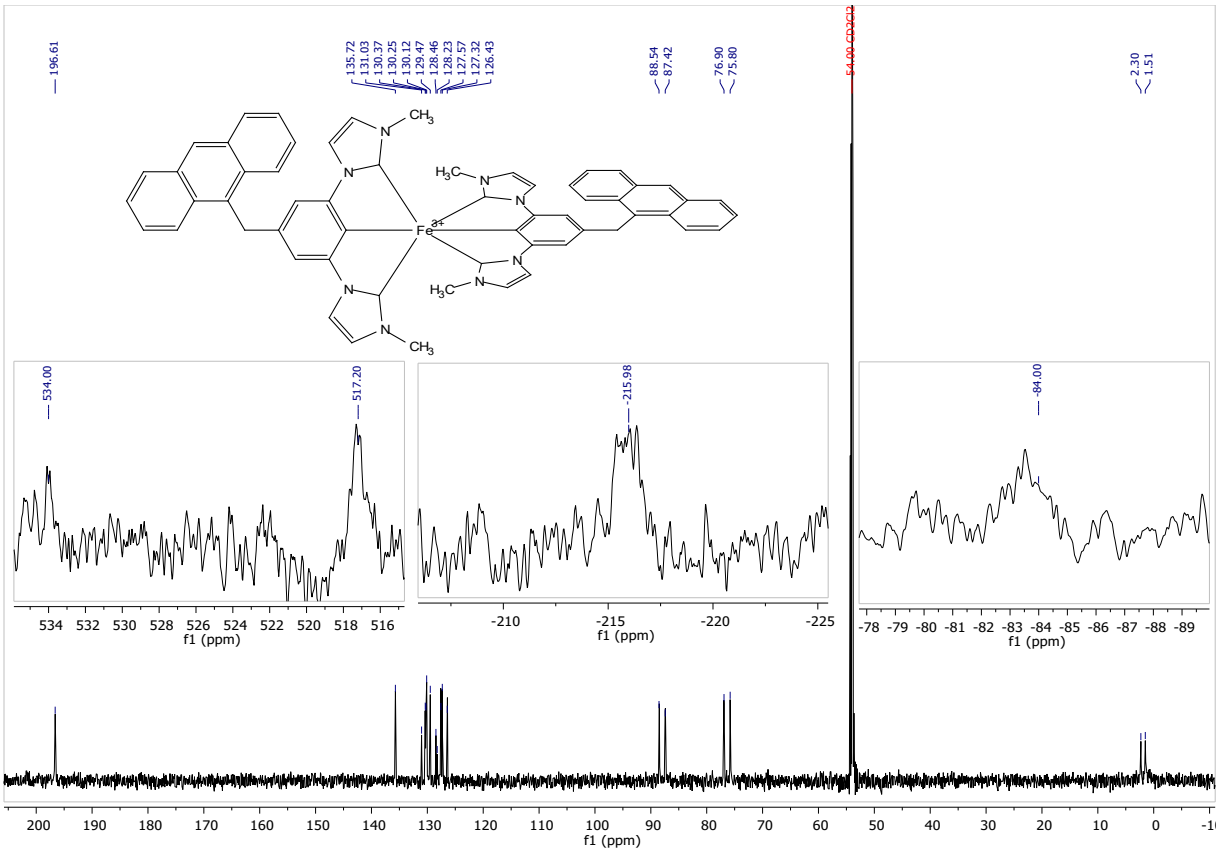

Figure S45: ^{13}C-NMR spectrum of **[Fe(Im$_2$PAnt)$_2$]$^+$**

11. Mass spectroscopy

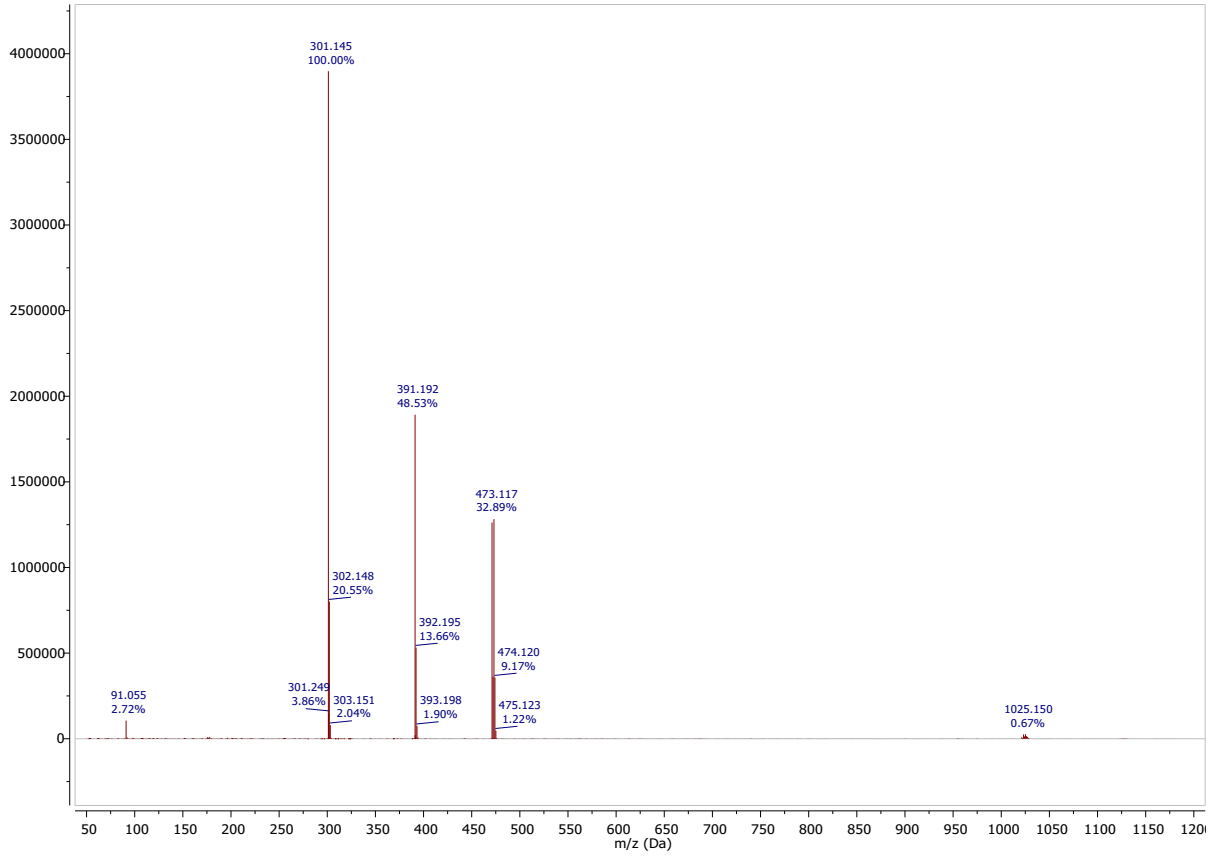

Figure S46: Mass spectrum of **2-Ph**

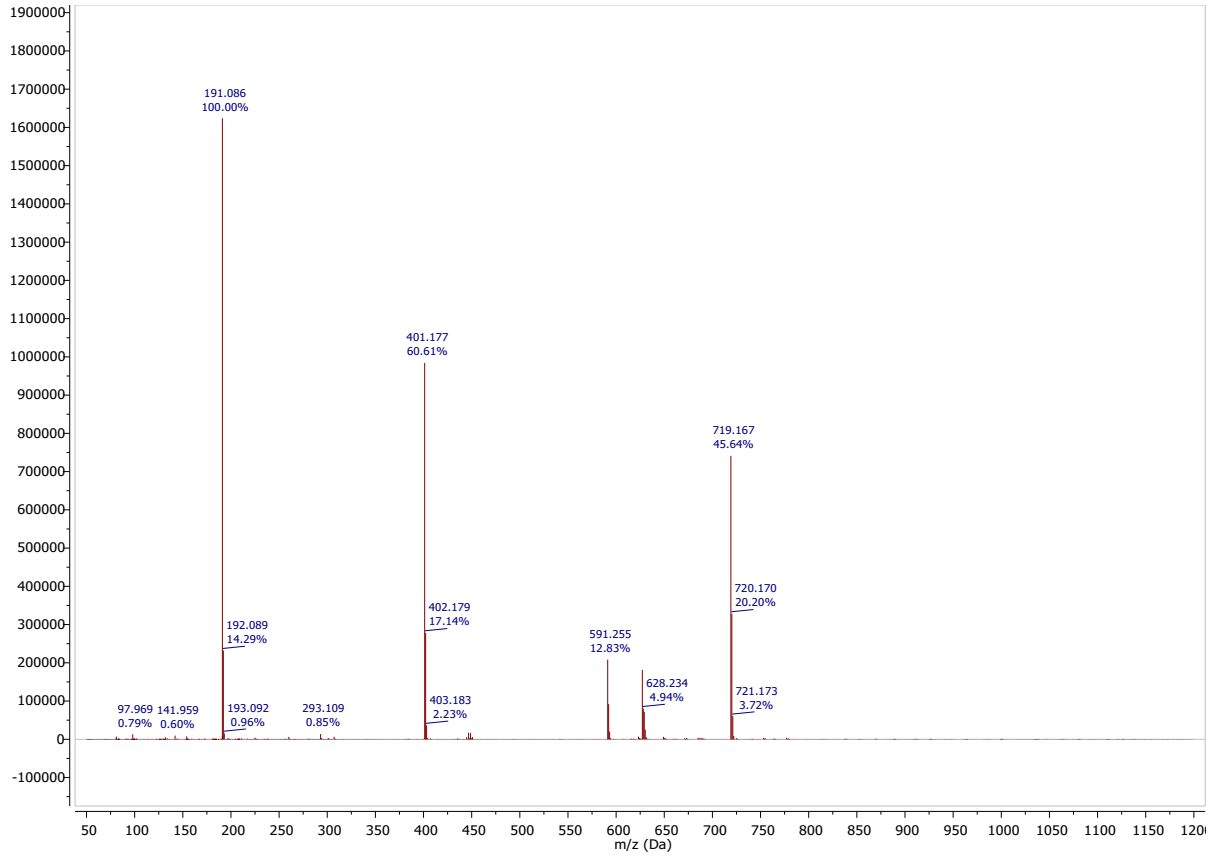

Figure S47: Mass spectrum of **2-Ant**

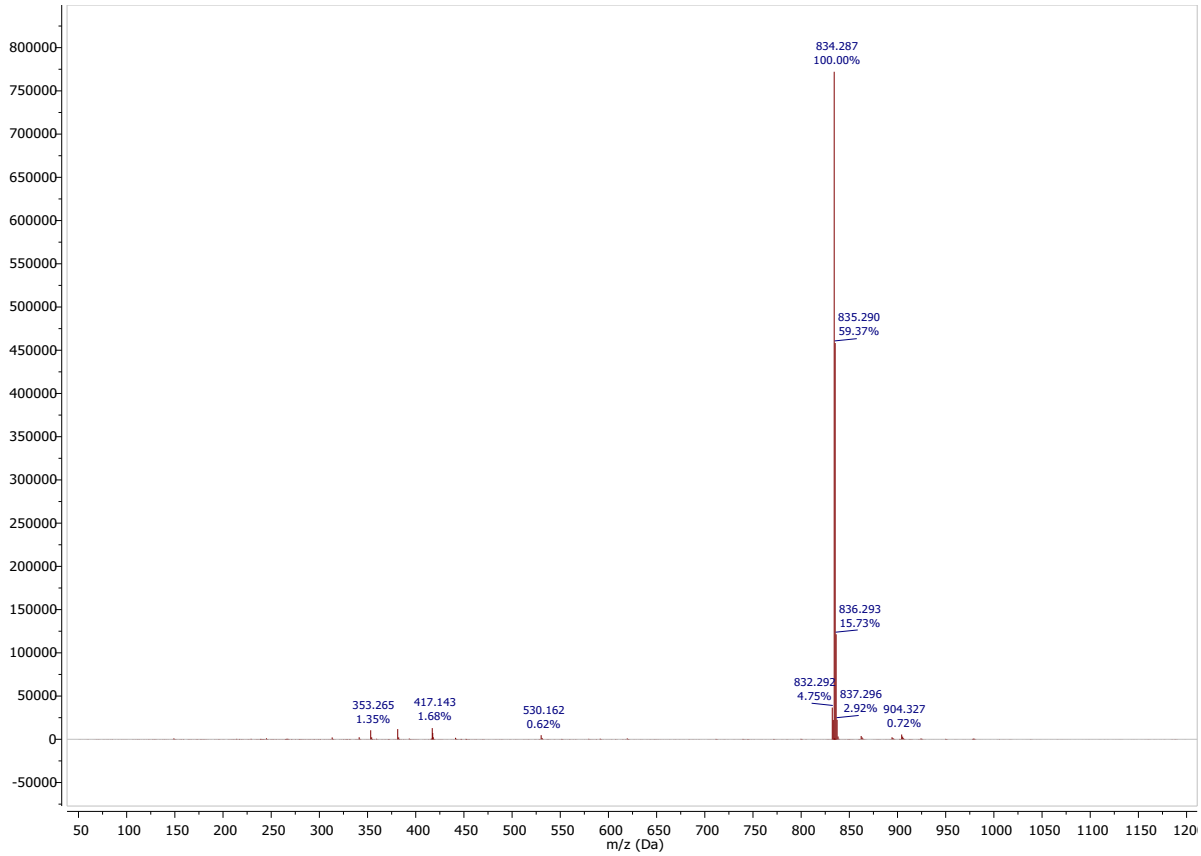

Figure S48: Mass spectrum of **$[Fe((ImPh)_2P)_2]^+$**

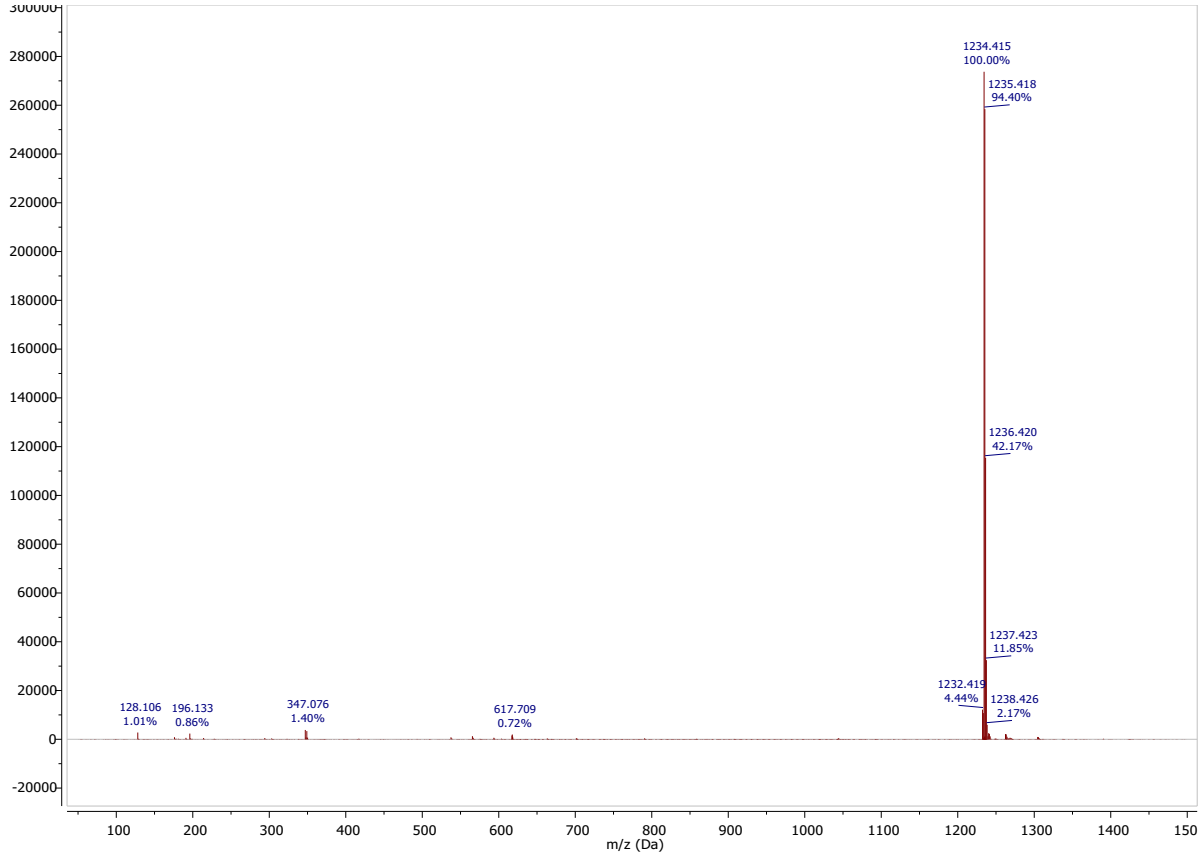

Figure S49: Mass spectrum of **$[Fe((ImAnt)_2P)_2]^+$**

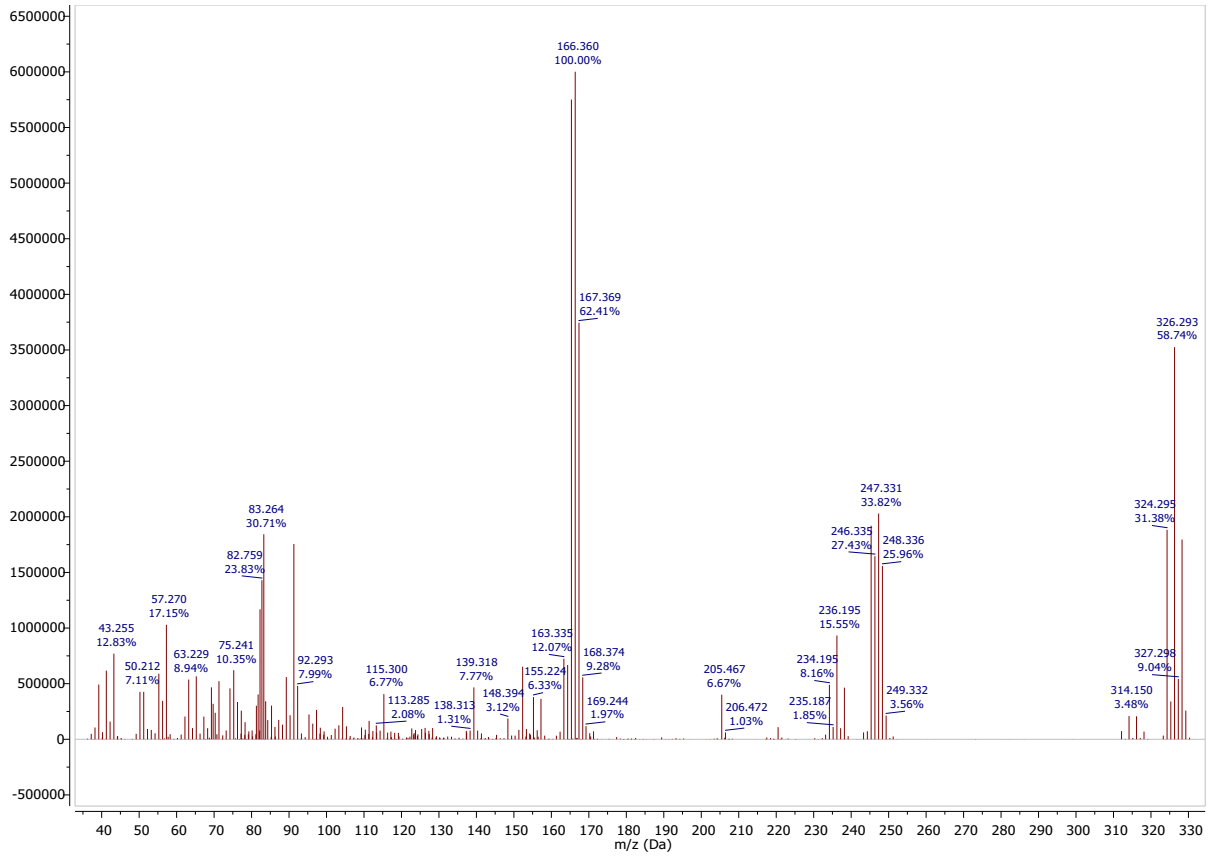

Figure S50: Mass spectrum **3-Ph**

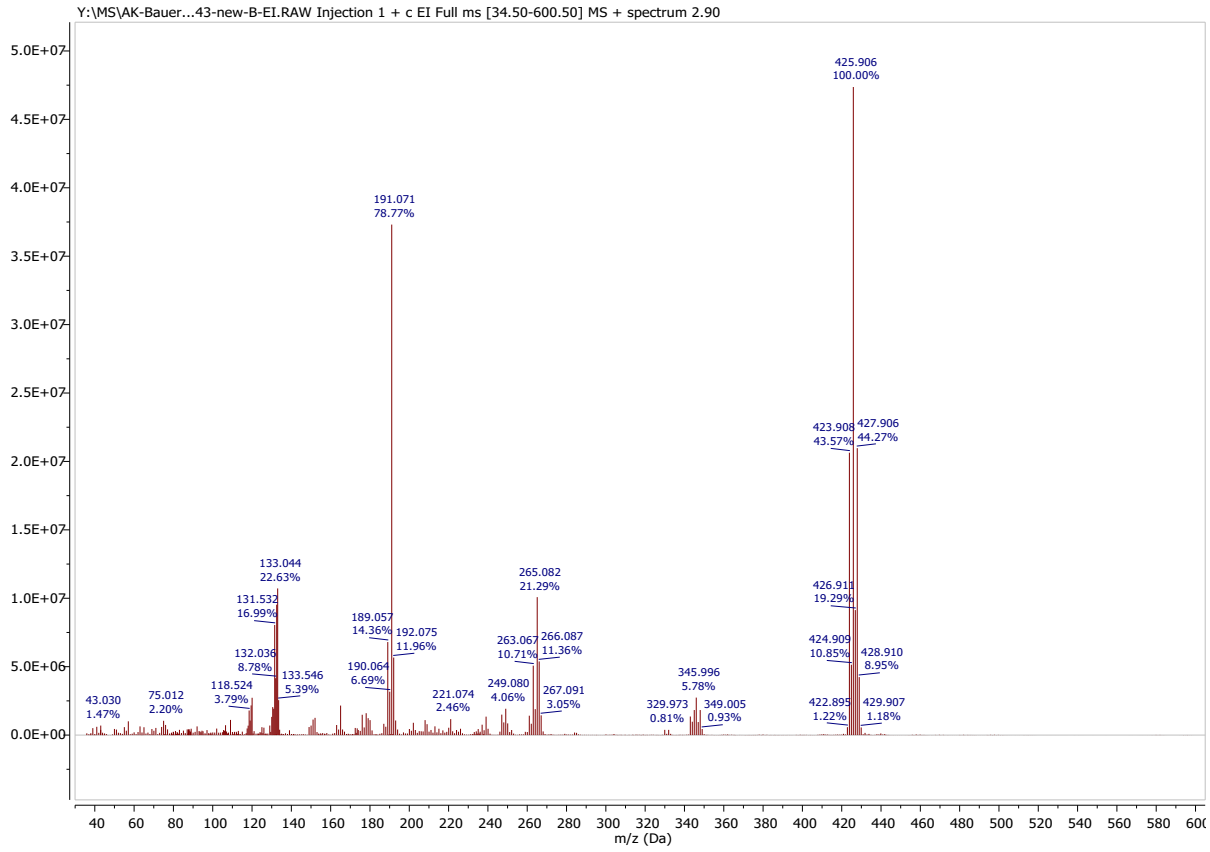

Figure S51: Mass spectrum **3-Ant**

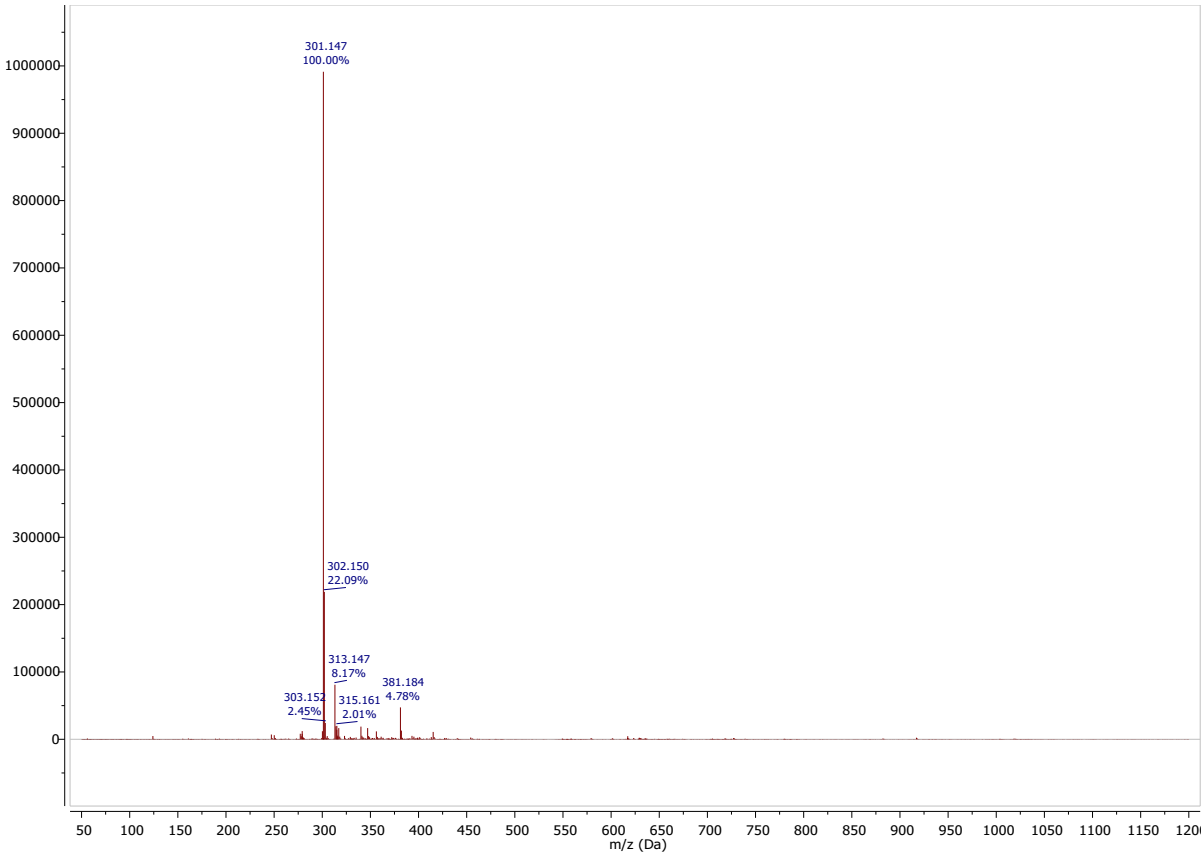

Figure 52: Mass spectrum of **4-Ph**

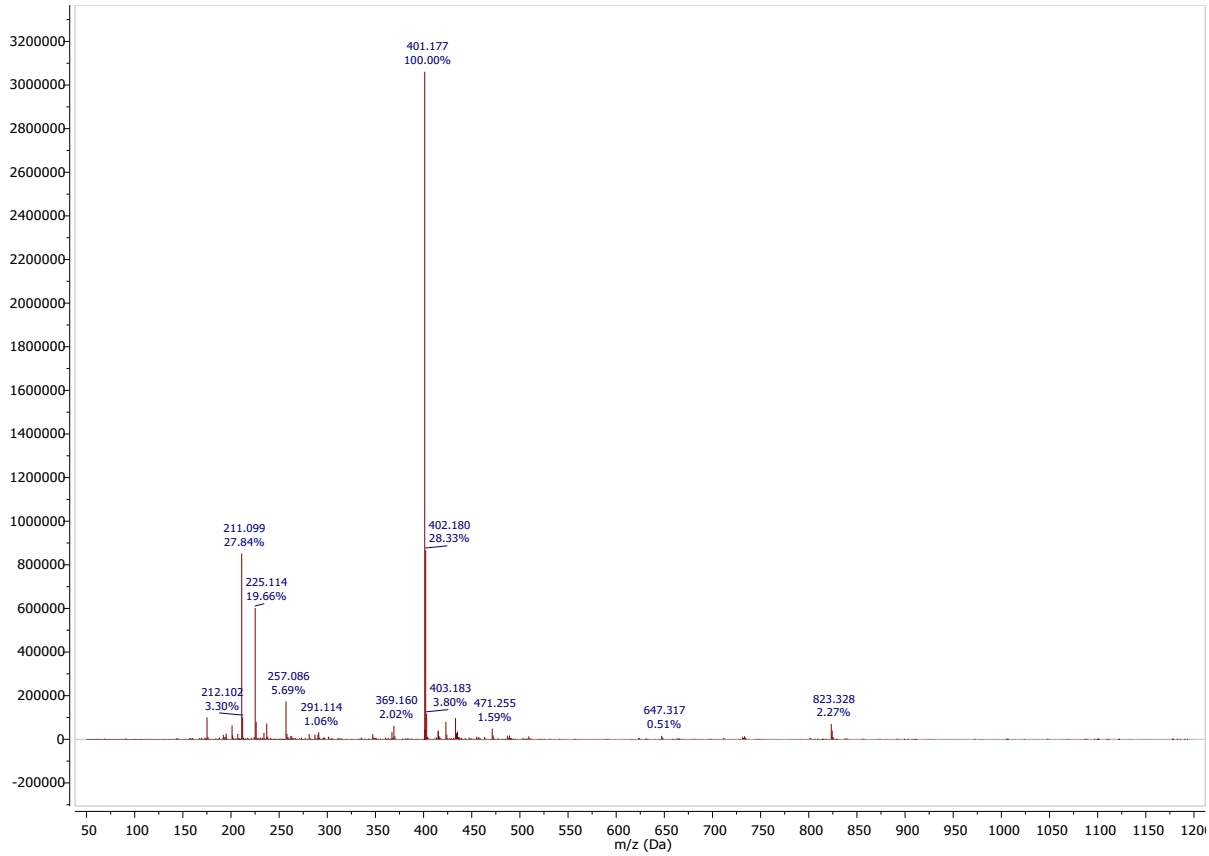

Figure S53: Mass spectrum of **4-Ant**

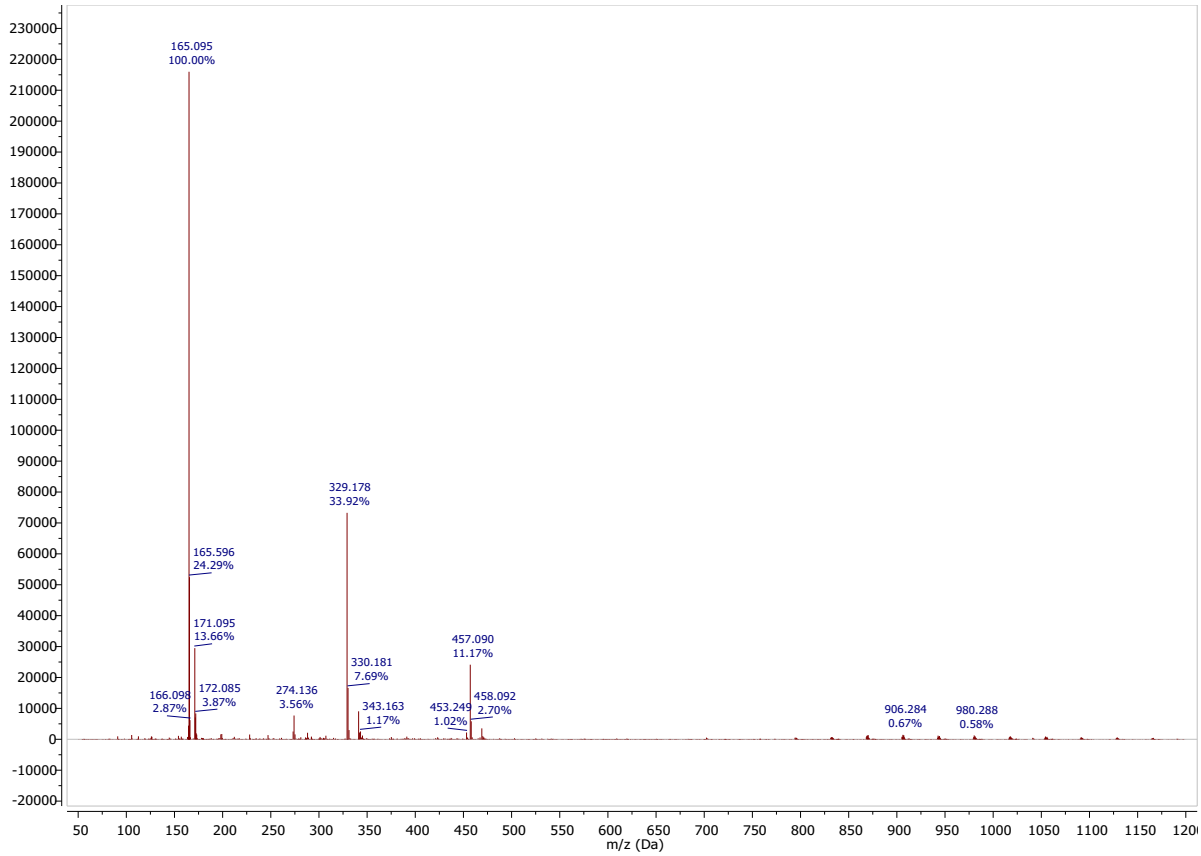

Figure S54: Mass spectrum of **5-Ph**

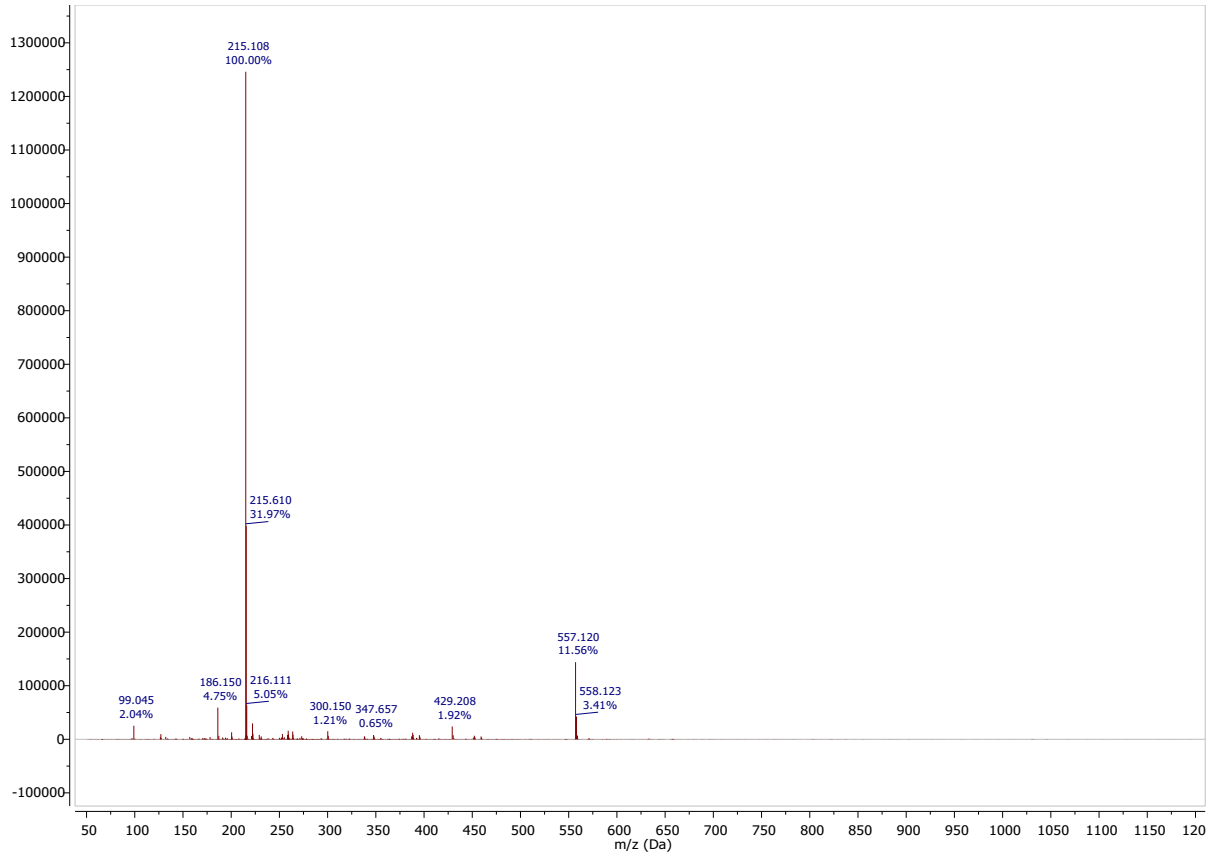

Figure S55: Mass spectrum of **5-Ant**

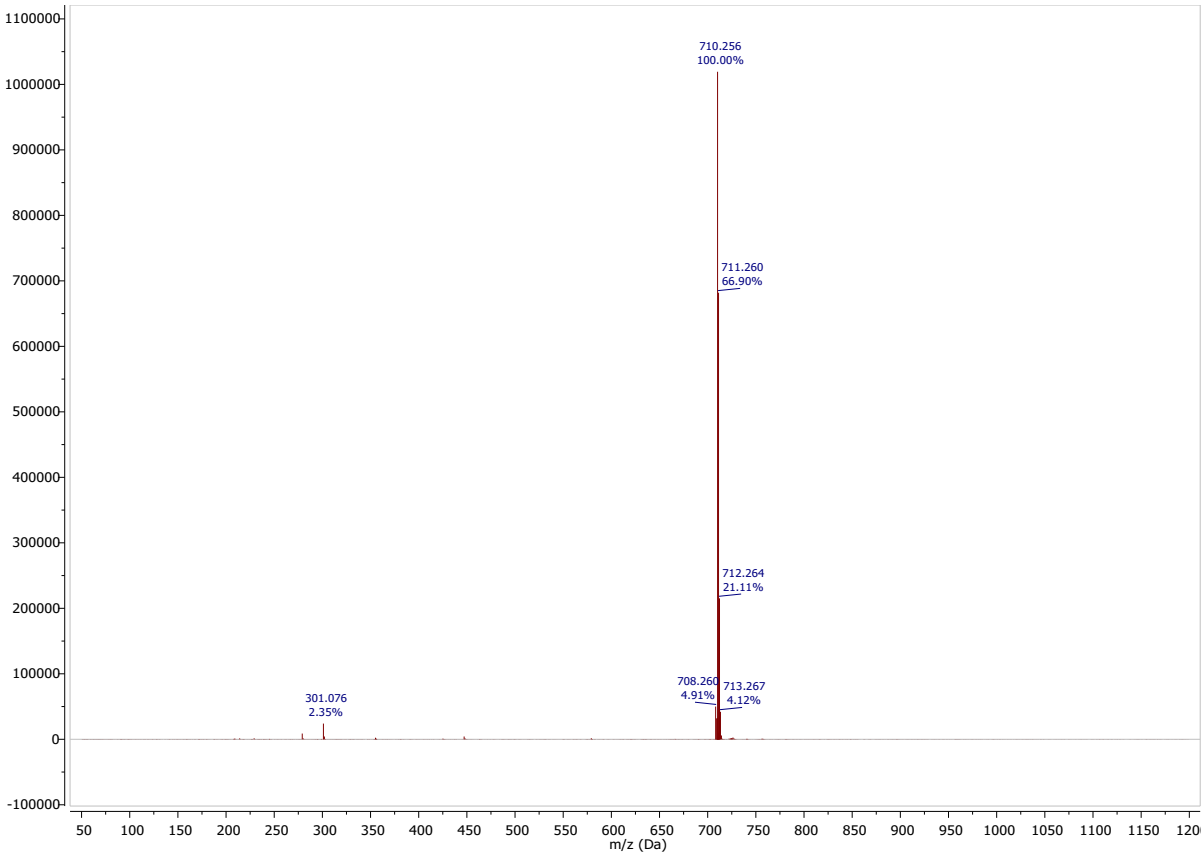

Figure S56: Mass spectrum of **$[Fe(Im_2PPh)_2]^+$**

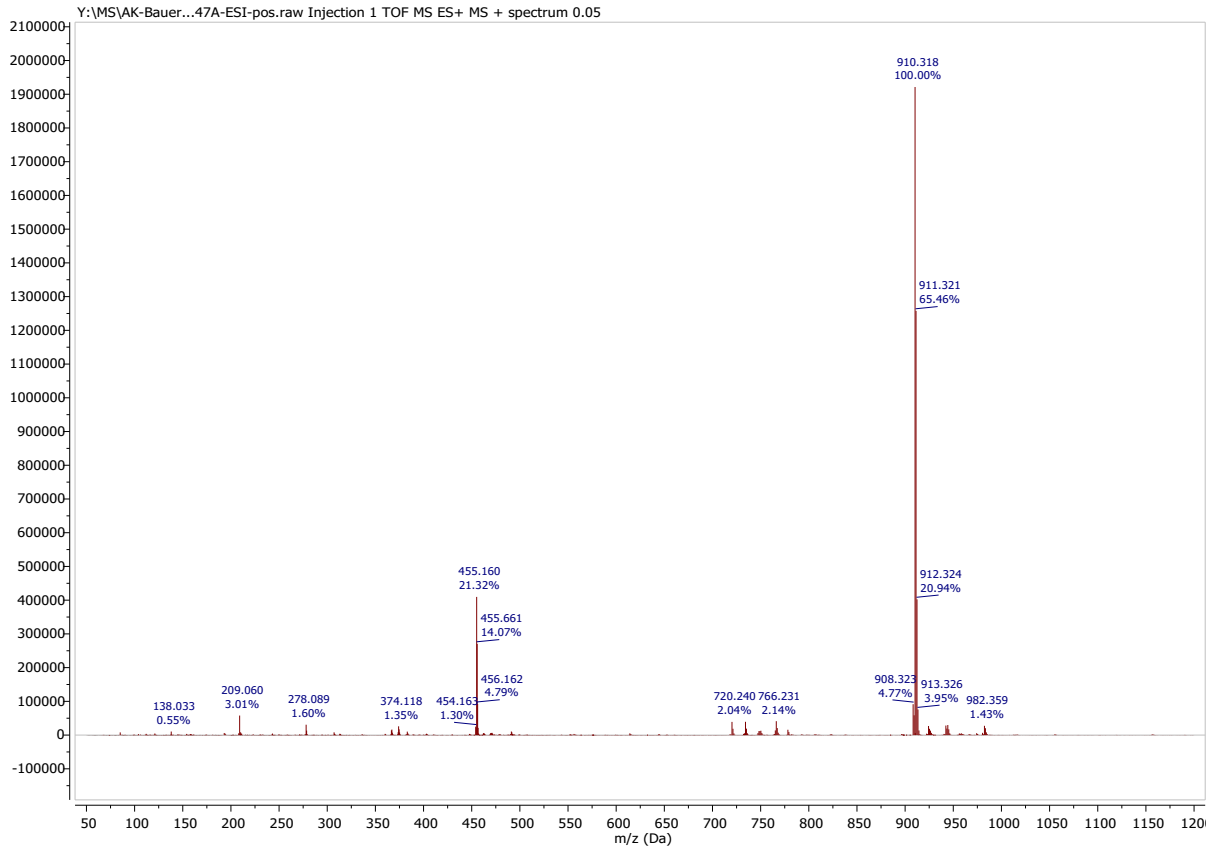

Figure S57: Mass spectrum of **[Fe(Im$_2$PAnt)$_2$]$^+$**

12. References

(1) Cho, J.; Hollis, T. K.; Valente, E. J.; Trate, J. M. CCC–N-heterocyclic carbene pincer complexes: Synthesis, characterization and hydroamination activity of a hafnium complex. *J. Organomet. Chem.* **2011**, *696* (1), 373–377.

(2) Brückner, R. *Reaktionsmechanismen*:*Organische Reaktionen, Stereochemie, moderne Synthesemethoden*, 3. Auflage, Nachdruck 2015; Lehrbuch; Springer Spektrum, **2004**.

(3) Steube, J.; Kruse, A.; Bokareva, O. S.; Reuter, T.; Demeshko, S.; Schoch, R.; Argüello Cordero, M. A.; Krishna, A.; Hohloch, S.; Meyer, F.; Heinze, K.; Kühn, O.; Lochbrunner, S.; Bauer, M. Janus-type emission from a cyclometalated iron(III) complex. *Nat. Chem.* **2023**, *15*, 468–474.

(4) Zhuang, L.; Wai, J. S.; Embrey, M. W.; Fisher, T. E.; Egbertson, M. S.; Payne, L. S.; Guare, J. P.; Vacca, J. P.; Hazuda, D. J.; Felock, P. J.; Wolfe, A. L.; Stillmock, K. A.; Witmer, M. V.; Moyer, G.; Schleif, W. A.; Gabryelski, L. J.; Leonard, Y. M.; Lynch, J. J.; Michelson, S. R.; Young, S. D. Design and synthesis of 8-hydroxy-1,6naphthyridines as novel inhibitors of HIV-1 integrase in vitro and in infected cells. *J. Med. Chem.* **2003**, *46* (4), 453–456.

(5) Li, C.; Gao, C.; Lan, J.; You, J.; Gao, G. An AIE active Y-shaped diimidazolylbenzene: aggregation and disaggregation for Cd(2+) and Fe(3+) sensing in aqueous solution. *Org. Biomol. Chem.* **2014**, *12* (47), 9524–9527.

(6) Rubio, R. J.; Andavan, G. T. S.; Bauer, E. B.; Hollis, T. K.; Cho, J.; Tham, F. S.; Donnadieu, B. Toward a general method for CCC N-heterocyclic carbene pincer synthesis: Metallation and transmetallation strategies for concurrent activation of three C–H bonds. *J. Organomet. Chem.* **2005**, *690* (23), 5353–5364.

(7) Zimmer, P.; Müller, P.; Burkhardt, L.; Schepper, R.; Neuba, A.; Steube, J.; Dietrich, F.; Flörke, U.; Mangold, S.; Gerhards, M.; Bauer, M. N-Heterocyclic Carbene Complexes of Iron as Photosensitizers for Light-Induced Water Reduction. *Eur. J. Inorg. Chem.* **2017**, *2017* (11), 1504–1509.

(8) Randles, J. E. B. A cathode ray polarograph. Part II.—The current-voltage curves. *Trans. Faraday Soc.* **1948**, *44* (0), 327–338.

(9) Päpcke, A.; Friedrich, A.; Lochbrunner, S. Revealing the initial steps in homogeneous photocatalysis by time-resolved spectroscopy. *J. Condens. Matter Phys.* **2020**, *32* (15), 153001.

(10) Neese, F. The ORCA program system. *WIREs Comput. Mol. Sci.* **2012**, *2* (1), 73–78.

(11) Grimme, S.; Brandenburg, J. G.; Bannwarth, C.; Hansen, A. Consistent structures and interactions by density functional theory with small atomic orbital basis sets. *Chem. Phys.* **2015**, *143* (5), 54107.

(12) Becke, A. D. Density-functional thermochemistry. III. The role of exact exchange. *J. Chem. Phys.* **1993**, *98* (7), 5648–5652.

(13) Weigend, F.; Ahlrichs, R. Balanced basis sets of split valence, triple zeta valence and quadruple zeta valence quality for H to Rn: Design and assessment of accuracy. *Phys. Chem. Chem. Phys.* **2005**, *7* (18), 3297–3305.

(14) Caldeweyher, E.; Bannwarth, C.; Grimme, S. Extension of the D3 dispersion coefficient model. *J. Chem. Phys.* **2017**, *147* (3), 34112.

(15) Dreuw, A.; Head-Gordon, M. Single-reference ab initio methods for the calculation of excited states of large molecules. *Chemical reviews* **2005**, *105* (11), 4009–4037.

(16) Plasser, F. TheoDORE: A toolbox for a detailed and automated analysis of electronic excited state computations. *J. Chem. Phys.* **2020**, *152* (8), 84108.

(17) Knizia, G. Intrinsic Atomic Orbitals: An Unbiased Bridge between Quantum Theory and Chemical Concepts. *J. Chem. Theory Comput.* **2013**, *9* (11), 4834–4843.

(18) Günther, H. *NMR Spectroscopy*:*Basic Principles, Concepts, and Applications in Chemistry*, 3. Auflage; Wiley-VCH, **2013**.

(19) Schmitz, L.; Argüello Cordero, M. A.; Al-Marri, M. J.; Schoch, R.; Egold, H.; Neuba, A.; Steube, J.; Bracht, B.; Bokareva, O. S.; Lochbrunner, S.; Bauer, M. Chromophore Induced Effects in Iron(III) Complexes. *Inorg. Chem.* **2025**, *64* (28), 14101–14117.

Supporting Information

Pyridine-substituted Fe(III) complexes – On the way to one-component photo-catalytical systems

Lennart Schmitz[a], J. Luis Pérez Lustres[b], Ronan Viel[c], Jannik Löseke[a], Xiao-Hui Li[b], Roland Schoch[a], Stefan Haacke[c], Karsten Heyne[b], Matthias Bauer[a,*]

[a]*Faculty of Science, Chemistry Department and Centre for Sustainable Systems Design, Paderborn University, 33098 Paderborn, Germany.*

[b]*Department of Physics, Free University of Berlin, 14195 Berlin, Germany.*

[c]*Université de Strasbourg – CNRS, Inst. de Physique et Chimie des Matériaux de Strasbourg (IPCMS), 67100 Strasbourg, France*

Table of contents

Synthesis

The chemicals necessary for synthesis were commercially obtained and used without further purification. For purification with column chromatography, silica gel columns were used. **[Fe(ImPPyMe)$_2$]** was synthesized following a previously published route for the analogous complex with Phenyl backbone.[1] **For [Fe(ImPPy)$_2$]** this synthetic route had to be modified significantly due to the affinity of the pyridine for metal coordination and methylation.

All ligands were synthesized from the same starting molecule 1,3,5-tribromobenzene **(1)**. In a copper-catalyzed *N*-arylation, according to a procedure previously published by our work group[1] based on a similar procedure[2], 1,1‘-(5-bromo-1,3-phenylene)bis(1*H*-imidazole) **(2)** was obtained.

2 was then reacted in Suzuki-Miyaura cross coupling reactions with phenyl-boronic acid (for **3C**) or the pinacol ester of pyridin-4-ylboronic acid (for **3N**) to obtain the products **3C** and **3N**.[1] This procedure is based on a similar synthesis for the corresponding C^N^C complexes.[3] The reactions were carried out under an argon atmosphere. The solvents were deoxygenated before the reaction by sparging them with argon. $PdOAc_2$ (0.05 equiv.) and 2-dicyclohexylphosphino-2’,6’-dimethoxybiphenyl (S-Phos, 0.11 equiv.) were dissolved in toluene (0.1 M). K_2CO_3 (2.4 equiv.), dissolved in water (1 M) was added resulting in a toluene water ratio of 5:1, followed by 1,1‘-(5-bromo-1,3-phenylene)bis(1*H*-imidazole) (1 equiv.) and the corresponding boronic acid/pinacol ester (1.2 equiv.). The mixture was heated to reflux and stirred for 18 h. After cooling, the solvents were removed under reduced pressure. The residue was suspended in methanol and filtered. The solvent was evaporated and the raw product was purified with column chromatography (DCM/MeOH 9:1).

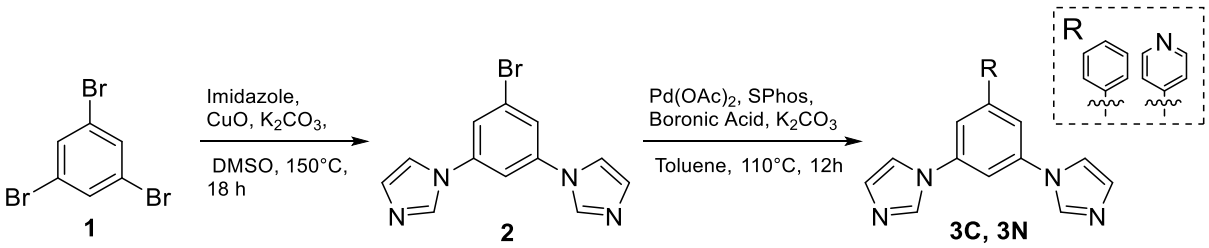

*Figure S1: Synthetic procedure for the ligand precursors **3C** and **3N***

3C. The product was obtained as a colorless solid (2.94 mmol/ 843 mg/ 98% yield).

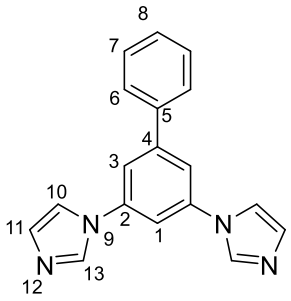

^{1}H NMR (700 MHz, DMSO-d6): δ (ppm) = 8.53 (2H, H^{13}, s), 8.03 (2H, H^{11}, t), 7.96 (1H, H^{1}, t), 7.94-7.92 (2H, H^{7}, m), 7.91 (2H, H^{3}, d), 7.54 (2H, H^{6}, t), 7.46 (1H, H^{8}, tt), 7.16 (2H, H^{6}, t). **^{13}C NMR (176 MHz, DMSO-d6): δ (ppm)** = 143.5 (1C, C^{5}, C_q), 138.5 (2C, C^{2}, C_q), 138.4 (1C, C^{4}, C_q), 136.0 (2C, C^{13}, CH), 129.9 (C2, C^{10}, CH), 128.9 (2C, C^{6}, CH), 128.5 (1C, C^{8}, CH), 127.4 (2C, C^{7}, CH), 118.3 (2C, C^{11}, CH), 116.3 (2C, C^{3}, CH), 110.8 (1C, C^{1}, CH) **^{15}N NMR (71 MHz, DMSO-d6): δ (ppm) =** 266 (2N, N^{12}), 185 (2N, N^{9}).

ESI-MS ([M+H]$^+$ for $C_{18}H_{14}N_4$): m/z 287.1291. Found: m/z 287.1287.

3N. The product was obtained as a colorless solid (12.8 mmol/ 3.7 g/ 64% yield)

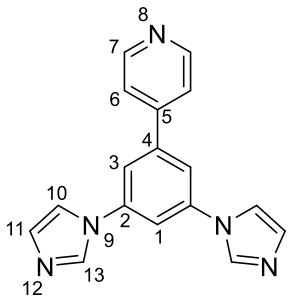

^{1}H NMR (700 MHz, DMSO-d6): δ (ppm) = 8.73 (2H, H^{7},dd), 8.56 (2H, H^{10}, t), 8.08 (1H, H^{1}, t), 8.05 (4H, H^{3}, H^{11}, m), 7.99 (2H, H^{6}, dd), 7.18 (2H, H^{13}, s). **^{13}C NMR (176 MHz, DMSO-d6):** 150.3 (2C, C^{7}, CH), 145.3 (1C, C^{4}, Cq), 140.6 (1C, C^{5}, Cq), 138.8 (2C, C^{2}, Cq), 136.0 (2C, C^{10}, CH), 130.0 (2C, C^{13}, CH), 121.8 (2C, C^{6}, CH), 118.3 (2C, C^{11}, CH), 116.4 (2C, C^{3}, CH), 112.3 (1C, C^{1}, CH). **δ (ppm) ^{15}N NMR (71 MHz, DMSO-d6): δ (ppm) =** 316.1 (1N, N^{8}), 265.9 (2N, N^{12}), 183.9 (2N, N^{9}).

ESI-MS ([M+H]$^+$ for $C_{17}H_{13}N_5$): m/z 288.1244. Found: m/z 288.1249.

The proligands **[ImPPh]I_2** and **[ImPPyMe]I_3** were obtained by meythaltion of **3C** or **3N** in MeCN.[4] After addition of Methyliodide (4 equiv. for **[ImPPh]I_2** and 6 equiv. for **[ImPPyMe]I_3**) the suspension was stirred under reflux for 18h. rubioAfter cooling, the volatiles were removed in vacuo and the residue was washed with acetone.

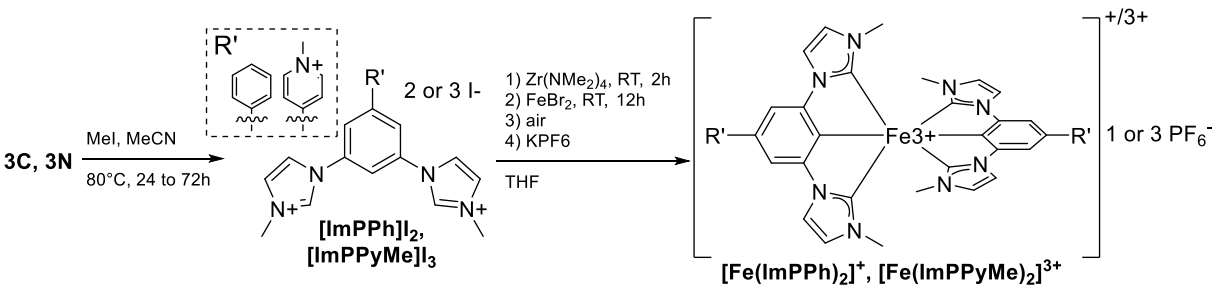

*Figure S2: Synthetic procedure for **[Fe(ImPPh)$_2$]$^+$** and **[Fe(ImPPyMe)$_2$]$^{3+}$***

[ImPPh]I_2. The product was obtained as a colorless solid (0.32 mmol/ 570 mg/ 98% yield)

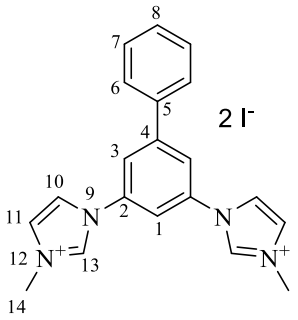

^{1}H NMR (700 MHz, DMSO-d6): δ (ppm) = 10.04 (2H, H^{13}, s), 8.49 (2H, H^6, t), 8.33 (2H, H^1, d), 8.32 (1H, H^1, t), 8.06 (2H, H^{11}, t), 7.97 (2H, H^7, t), 7.61 (2H, H^6, m), 7.54 (1H, H^8, tt), 4.02 (6H, H^{14}, s). **^{13}C NMR (176 MHz, DMSO-d6): δ (ppm)** = 143.7 (1C, C^5, C_q), 137.0 (1C, C^4, C_q), 136.5 (2C, C^{13}, CH), 136.2 (2C, C^2, C_q), 129.3 (1C, C^8, CH), 129.2 (2C, C^6, CH), 127.3 (2C, C^7, CH), 124.7 (2C, C^{11}, CH), 121.0 (2C, C^{10}, CH), 120.6 (2C, C^3, CH), 114.0 (1C, C^1, CH), 36.4 (2C, C^{14}, CH_3) **^{15}N NMR (71 MHz, DMSO-d6): δ (ppm) =** 186 (2N, N^9), 175 (2N, N^{12}).

ESI-MS ([M]$^{2+}$ for $C_{20}H_{20}N_5^{2+}$): m/z 158,5839. Found: m/z 158.5849.

Elemental analysis calculated for $C_{20}H_{20}N_4P_2F_{12}$: C, 39.62; H, 3.32; N, 9.42. found: C, 39.73; H, 3.71; N, 9.55

[ImPPyMe]I_3. The product was obtained as a bright yellow solid (1.38 mmol/ 982 mg/ 46% yield)

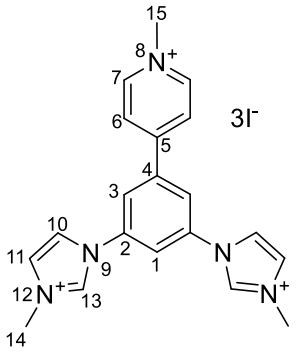

^{1}H NMR (700 MHz, DMSO-d6): δ (ppm) = 10.00 (2H, H^{13}, s), 9.28 (2H, H^6, d), 8.71 (2H, H^7, s), 8.69 (2H, H^3, d), 8.57 (1H, H^1, t), 8.49 (2H, H^{11}, t), 8.09 (2H, H^{10}, t), 4.42 (3H, H^{15}, s), 4.05 (6H, H^{14}, s). **^{13}C NMR (176 MHz, DMSO-d6): δ (ppm)** = 151.1 (1C, C^5, C_q), 146.3 (2C, C^6, CH), 136.7 (1C, C^{13}, CH), 136.7 (1C, C^4, C_q), 136.6 (2C, C^{13}, CH), 136.57 (2C, C^2, C_q), 124.9 (2C, C^{10}, CH), 124.7 (2C, C^7, CH), 122.0 (2C, C^3, CH), 121.1 (2C, C^{11}, CH), 118.0 (1C, C^1, CH), 47.7 (1C, C^{15}, CH_3), 36.6 (2C, C^{14}, CH_3). **^{15}N NMR (71 MHz, DMSO-d6): δ (ppm) =** 202 (1N, N^8), 185 (2N, N^9), 176 (2N, N^{12}).

ESI-MS ([M]$^{2+}$ for $C_{20}H_{20}N_5^{2+}$): m/z 158,5839. Found: m/z 158.5849.

Elemental analysis calculated for $C_{20}H_{22}N_5I_3$: C, 33.68; H, 3.11; N, 9.82. found: C, 33.76; H, 3.34; N, 9.91

The synthesis of **[Fe(ImPPh)$_2$]$^+$**[1] was published previously and **[Fe(ImPPyMe)$_2$]$^{3+}$** was obtained following the same synthetic procedure based on an intermediate Zr-complex.[5] The reaction was carried out in a glovebox. The corresponding proligand (2 equiv.) was suspended in THF (0.1 M) and

$Zr(NMe_2)_4$ (2.1 equiv.) was added. The suspension was stirred for two hours, before $FeBr_2$ (1 equiv.) was added. The resulting suspension was stirred for 18 h. The reaction was quenched under ambient conditions by adding methanol. The resulting suspension was filtered, and the solvent of the filtrate was removed under reduced pressure. The resulting solid was dissolved in DCM, filtered, concentrated and subsequently passed over a silica gel column. Impurities were pushed through the column with DCM and subsequently MeCN. The product was obtained after using a mixture of 90% MeCN and 10% water saturated with KNO_3. KPF_6 was added to the eluent and after removal of MeCN by evaporation the red precipitate was filtered off. A subsequent anion exchange by dissolving in MeCN and dripping into a KPF_6 aqueous solution yielded the desired product. Diffusion of *n*-pentane into a DCM solution yielded red crystals.

$[Fe(ImPPh)_2]^+$. The product was obtained as a dark green PF_6^- salt (0.3 mmol batch size; 0.1 mmol/ 80 mg/ 32 % yield).

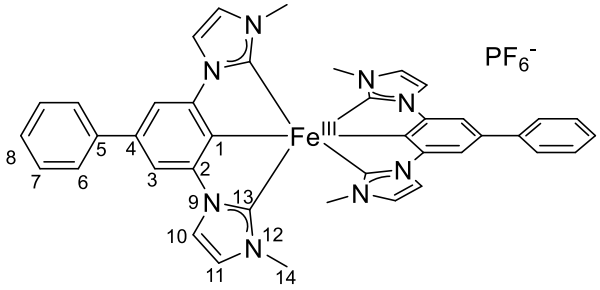

^{1}H NMR (700 MHz, CD_3CN): δ (ppm) = 26.91 (4H, H^3, s), 12.32 (4H, H^7, t), 10.00 (12H, H^{14}, s), 3.00 (4H, H^{11}, s), 1.69 (4H, H^6, d), 0.56 (2H, H^8, t), 2.7 (4H, H^{10}, s). **^{13}C NMR (176 MHz, CD_3CN): δ (ppm)** = 530.8 (4C, C^2, C_q), 522.8 (2C, C^4, C_q), 231.0 (4C, C^6, CH), 175.6 (2C, C^8, CH), 98.4 (4C, C^7, CH), 91.2 (4C, C^{10}, CH), 78.5 (4C, C^{11}, CH), -11.3 (2C, C^5, C_q), -212.4 (4C, C^3, CH).

ESI-MS ($[M]^+$ for $C_{40}H_{34}FeN_8$): m/z 682.2251. Found: m/z 682.2243.

Elemental analysis calculated for $C_{40}H_{34}FeN_8PF_6$ + 0.5 H_2O: C, 57.43; H, 4.22; N, 13.39. found: C, 57.50; H, 4.59; N, 13.65

$[Fe(ImPPyMe)_2]^{3+}$. The product was obtained as a red PF_6^- salt (0.03 mmol/ 40 mg/ 11.6%).

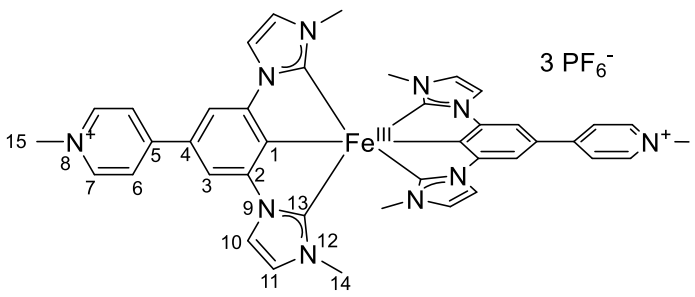

^{1}H NMR (700 MHz, DMSO-d6): δ (ppm) = 23.00 (4H, H^3, s), 12.19 (12H, H^{14}, s), 11.37 (4H, H^7, d), 11.30 (6H, H^{15}, s), 2.78 (4H, H^{11}, s), 2.42 (4H, H^6, d), -4.89 (4H, H^{10}, s). **^{13}C NMR (176 MHz, DMSO-d6): δ (ppm)** = 501.3 (4C, C^2, C_q), 474.5

(2C, C^4, C_q), 196.6 (4C, C^6, CH), 117.2 (4C, C^7, CH), 93.0 (4C, C^{10}, CH), 84.4 (4C, C^{11}, CH), 36.8 (2C, C^2, CH_3), 2.2 (4C, C^{14}, CH_3), -189.0 (4C, C^3, CH_3).

ESI-MS ($[M]^{3+}$ for $C_{40}H_{38}FeN_{10}^{3+}$): m/z 238.0871. Found: m/z 238.0861.

Elemental analysis calculated for $C_{19}H_{19}F_{12}N_5P_2F_{12}$ + 1 H_2O: C, 36.49; H, 3.39; N, 11.20. found: C, 36.48; H, 3.51; N, 11.48

For the proligand **[ImPPy][PF6]$_2$** the pyridine moiety was first protected by introduction of a N-oxide protective group: **3N** (1equiv.) was suspended in DCM (0.04 M) together with 3-chloroperoxybenzoic acid (2.5 equiv.) and NaHCO3 (1 equiv.). The solution was stirred for 18 h at 40°C resulting in a thick slurry. The volatiles were removed and the residue suspended and stirred for several minutes in saturated aqueous NaHCO3 solution. The solids were removed by filtration, washed with water and used without further purification.

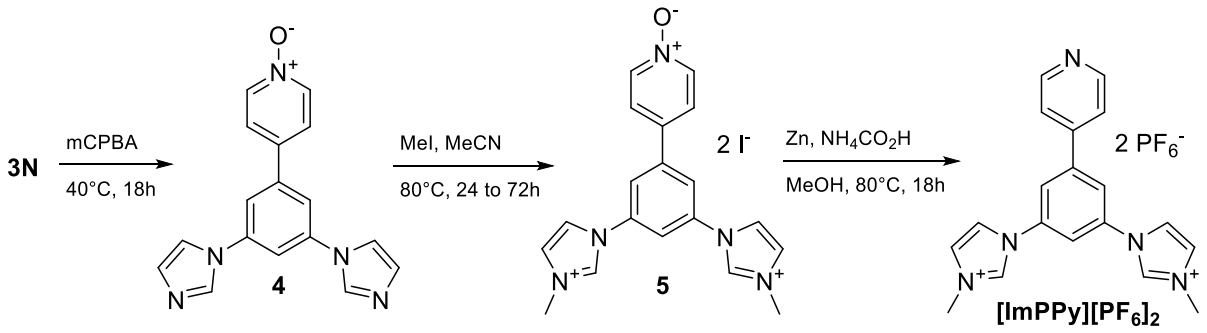

*Figure S3: Synthesis of proligand **[ImPPy][PF$_6$]$_2$***

4. The crude product was obtained as an off white solid (17.8 mmol/ 5.4 g/ 89% yield)

Crude **4** (1 equiv.) was suspended in MeCN (0.1 M). After addition of Methyliodide (4 equiv.) the suspension was stirred under reflux for 18h. After cooling the volatiles were removed in vacuo and the residue was washed with acetone. The product was again used without further purification

5. The crude product was obtained as a beige solid (14.1 mmol/ 8.3 g/ 71%)

To remove the protective group and obtain **[ImPPy][PF$_6$]$_2$**, crude **5** (1 equiv.) was suspended in Methanol (0.1 M). Freshly activated zinc dust (4 equiv.) and NH_4CO_2H (6 equiv.) were added, and the suspension was stirred strongly for 24 h. The zinc dust was filtered off and washed thoroughly with methanol. The combined organic phases were concentrated to a thick solution under vacuo. The solution was added dropwise into an aqueous solution of KPF_6 and the resulting white precipitate was filtered off. The solid was dissolved in Acetone and remaining precipitate was filtered off.

[ImPPy][PF_6]$_2$. The product was obtained as an off white solid (2.4 mmol/ 1.4 g/ 61%)

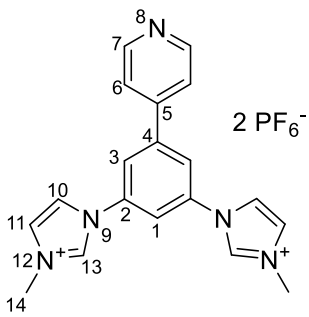

^{1}H NMR (700 MHz, DMSO-d6): δ (ppm) = 9.95 (2H, H^{13}, s), 8.82 (2H, H^7, dd), 8.45 (4H, $H^{3,11}$, m), 8.37 (1H, H^1, t), 8.04 (2H, H^{10}, t), 7.96 (2H, H^6, dd), 4.03 (6H, H^{14}, s). **^{13}C NMR (176 MHz, DMSO-d6): δ (ppm)** = 150.6 (2C, C^7, CH), 144.1 (1C, C^4, C_q), 140.8 (1C, C^5, C_q), 136.4 (2C, C^2, C_q), 136.3 (2C, C^{13}, CH), 124.5 (2C, C^{10}, CH), 121.3 (2C, C^6, CH), 121.0 (2C, C^{11}, CH), 120.97 (2C, C^3, CH) 115.5 (1C, C^1, CH), 36.2 (2C, C^{14}, CH_3). **^{15}N NMR (71 MHz, DMSO-d6): δ (ppm)** = 318 (1N, N^8), 186 (2N, N^9), 176 (2N, N^{12}).

ESI-MS ([M]$^{2+}$ for $C_{19}H_{19}N_5$): m/z 158.5815. Found: m/z 158.5824.

Elemental analysis calculated for $C_{19}H_{19}F_{12}N_5P_2F_{12}$ + 1 H_2O: C, 36.49; H, 3.39; N, 11.20. found: C, 36.48; H, 3.51; N, 11.48

[Fe(ImPPy)2]+ was synthesized using a different route, than the other two complexes, utilizing the iron precursor $Fe(HMDS)_2$ previously used for heteroleptic complexes.[6] The proligand **[ImPPy][PF_6]$_2$** (2 equiv.) was suspended in THF and cooled to -30°C. LiHMDS (6 equiv.) was added, and the solution was stirred for 1h while warming to room temperature. In parallel the iron precursor (1.1 equiv.) was dissolved in THF at -30°C. After cooling the ligand solution down again the precursor solution was added to it and the suspension was allowed to reach room temperature overnight while stirring. The reaction was quenched under ambient conditions with methanol. The suspension was filtered off and the resulting brown solution was evaporated. The residue was suspended in DCM and filtered off again. The green solution was concentrated and purified by column chreomtagophy over silica. Organic impurities were first removed by eluting with DCM and then MeCN. The eluent was then changed to 9/1 MeCN/Water mixture saturated with KNO_3 to eluate the product. The product changed color from green to red due to protonation of the pyridine backbone. Aqueous NaOH (1M) was added until the pH was between 8 and 9 resulting in the original green colour. The acetonitrile was removed from the mixture by evaporation, resulting in a suspension. This suspension was extracted with DCM three times. The resulting organic phases were then combined, and remaining salts were extracted by water. The organic phase was then evaporated. A subsequent anion exchange by dissolving the solid in MeCN and dropping into a KPF_6 aqueous solution yielded the desired product. Crystallization by diffusion of n-pentane into DCM yielded crystals viable for single crystal X-Ray diffraction.

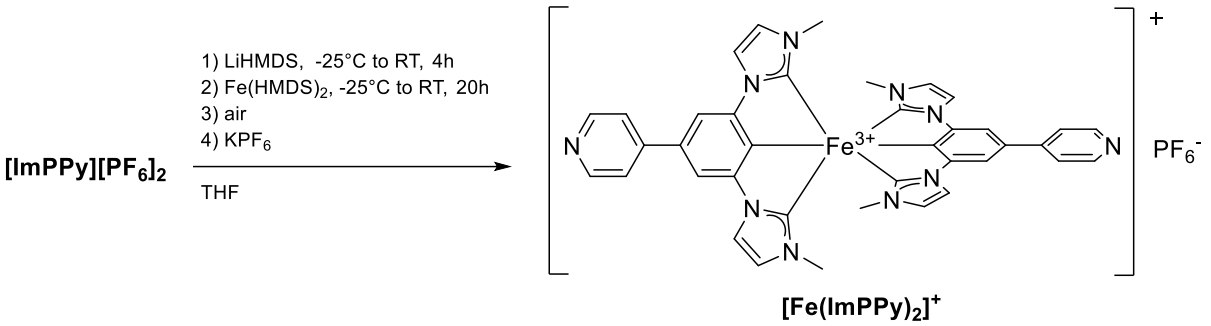

Figure S4: Synthetic procedure for ***[Fe(ImPPy)$_2$]$^+$***

[Fe(ImPPy)$_2$]$^+$. The product was obtained as a green PF_6^- salt (0.05 mmol/ 38 mg/ 15.3%).

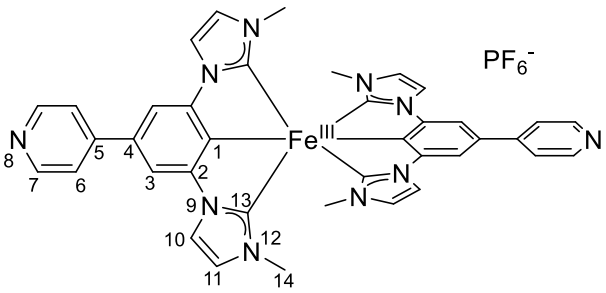

^{1}H NMR (700 MHz, DMSO-d6): δ (ppm) = 26.26 (4H, H^3, s), 12.65 (4H, H^3, s), 10.48 (12H, H^{14}, s), 2.98 (4H, H^{11}, s), 1.78 (4H, H^6, d), -3.13 (4H, H^{10}, s). **^{13}C NMR (176 MHz, DMSO-d6): δ (ppm)** = 516.6 (2C, C^2, C$_q$), 513.5 (1C, C^4, C$_q$), 211.2 (2C, C^6, CH), 120.8 (2C, C^7, CH), 90.2 (2C, C^{10}, CH), 78.8 (2C, C^{11}, CH), 2.2 (2C, C^{14}, CH$_3$), -1.6 (1C, C^5, C$_q$), -212.4 (2C, C^3, CH).

ESI-MS ([M]$^{3+}$ for $C_{40}H_{38}FeN_{10}^{3+}$): m/z 684.2155. Found: m/z 684.2170.

Elemental analysis calculated for $C_{38}H_{32}FeN_8PF_6$ + 1.5 H_2O: C, 53.28; H, 4.12; N, 16.35. found: C, 53.24; H, 4.51; N, 16.73

TD-DFT

Molecular structures

$Fe(ImPPh)_2]^+$	$[Fe(ImPPy)_2]^+$	$[Fe(ImPPyH)_2]^{3+}$	$[Fe(ImPPyMe)_2]^{3+}$
M_S 2, charge 1	M_S 2, charge 1	M_S 2, charge 3	M_S 2, charge 3

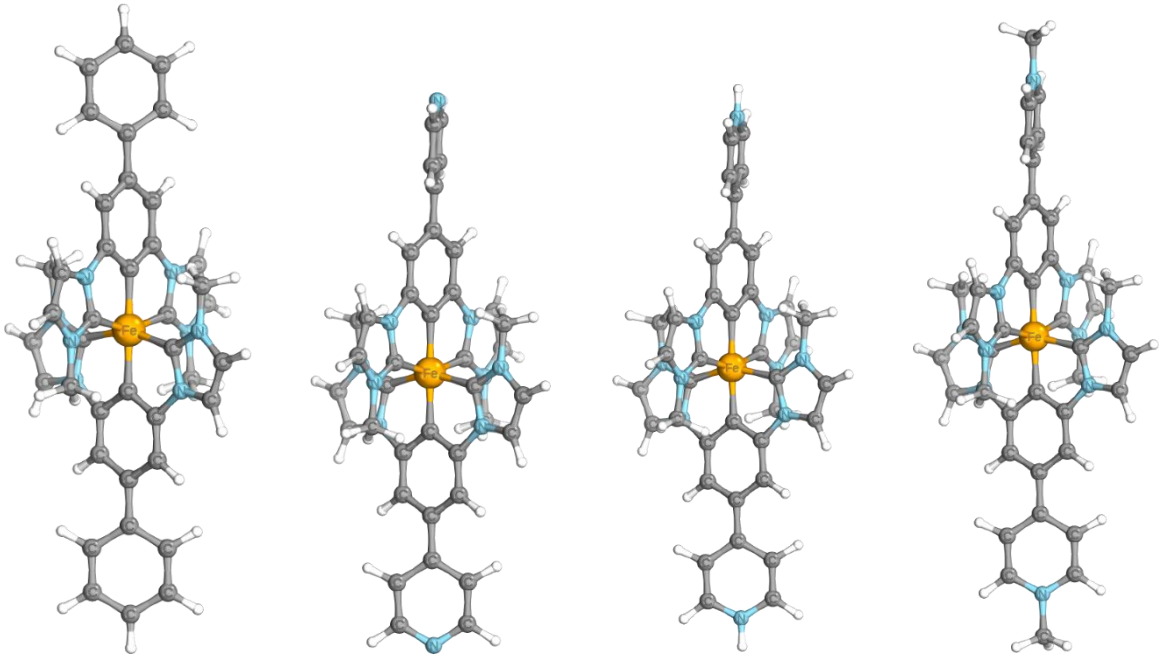

Figure S5: Visualization of DFT optimized molecular structures of the four investigated complexes.

Orbital Structures

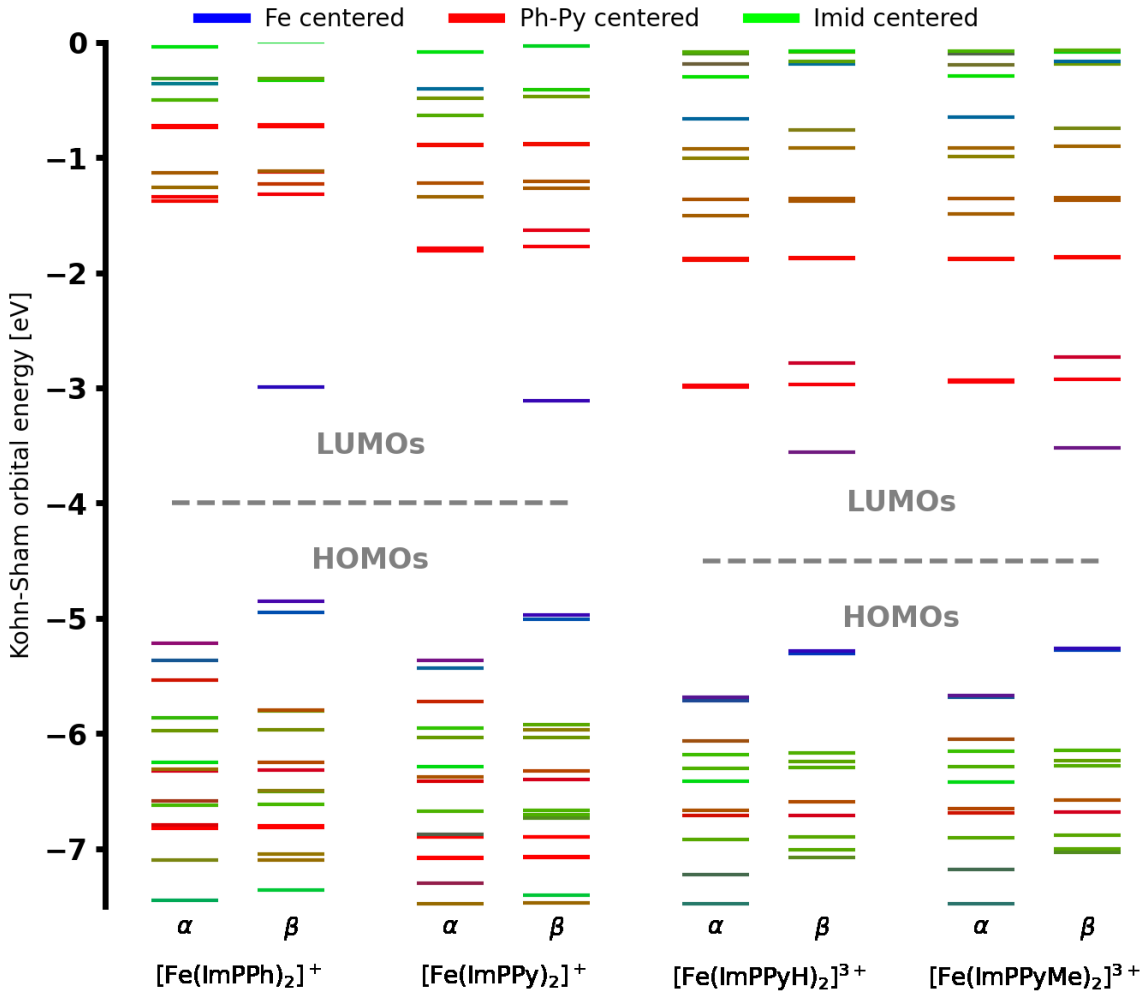

Figure S6: Visualization of the Kohn-Sham orbital energies around the HOMO-LUMO GAP. The colouring of the orbitals is constructed as a mixture of the three colours shown in the legend and indicates the localization of the orbital at the different fragments.

Distribution of added charges

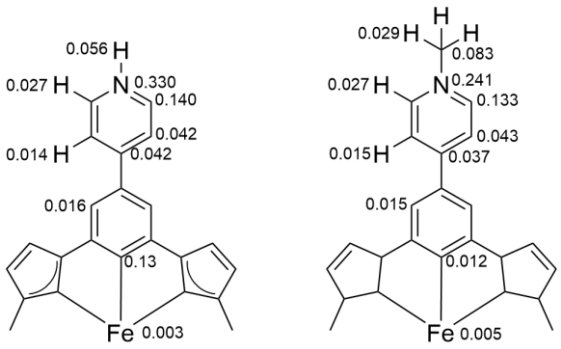

Figure S7: Visualization of the change of the Loewdin atomic charge between the protonated ***[Fe(ImPPyH)2]3+*** *(left) / methylated* ***[Fe(ImPPyMe)2]3+*** *(right) compared to* ***[Fe(ImPPy)2]+****. Note that for atoms only present in the prontonated / methylated complex their total charge is displayed.*

Natural Transition Orbitals $[Fe(ImPPh)_2]^+$

Table S1: Relevant Natural Transition Orbitals of the most significant Transitions in ***$[Fe(ImPPh)_2]^+$*** *for different features of the UV-Vis spectrum. The states considered for each band are noted in brackets. Isosurfaces at +/- 0.035.*

Band	Akzeptor		Donor
650 (3)	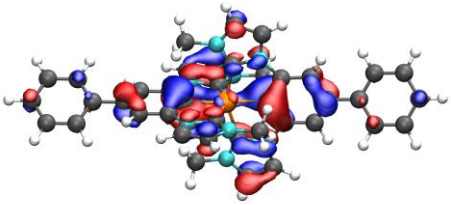	**97% →**	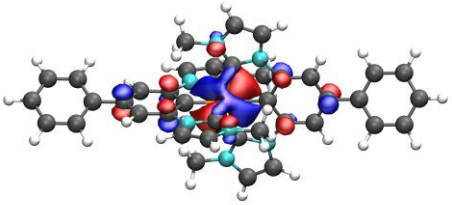
415 (8)	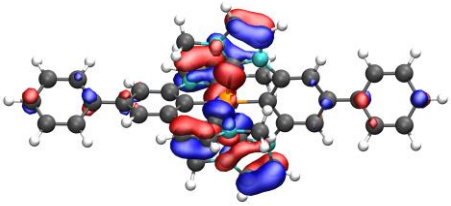	**75% →**	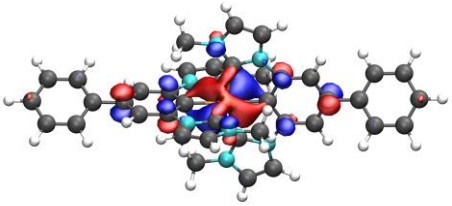
	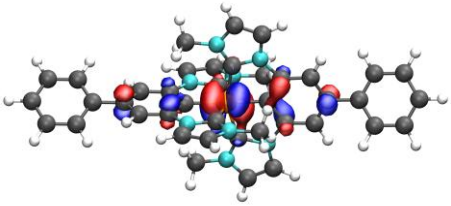	**14% →**	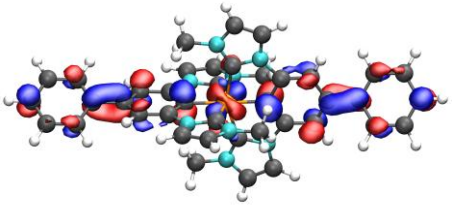
373 (21)	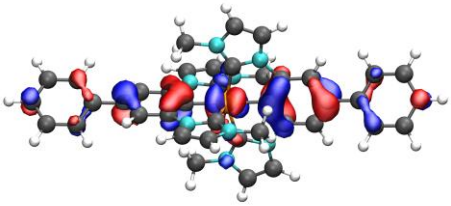	**41% →**	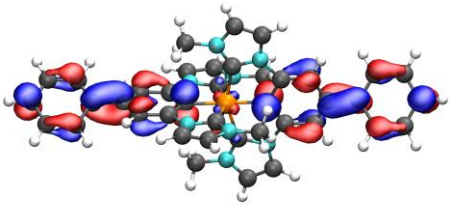
	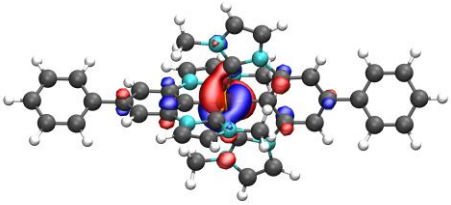	**38% →**	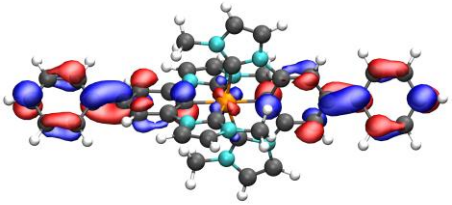

Natural Transition Orbitals $[Fe(ImPPy)_2]^+$

Table S2: Relevant Natural Transition Orbitals of the most significant Transitions in ***$[Fe(ImPPy)_2]^+$*** *for different features of the UV-Vis spectrum. The states considered for each band are noted in brackets. Isosurfaces at +/- 0.035.*

Band	Akzeptor		Donor
650 (3)	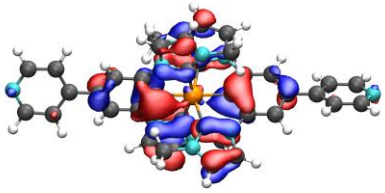	**96% →**	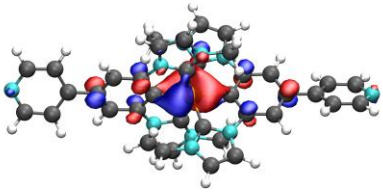
440 (9)	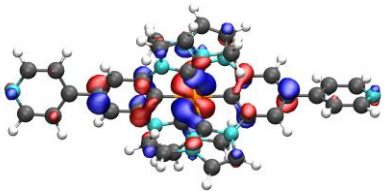	**53% →**	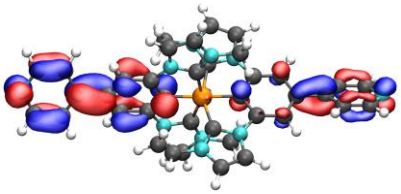
	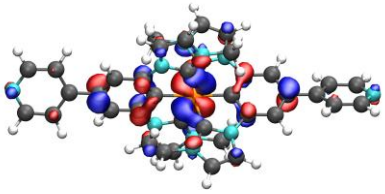	**22% →**	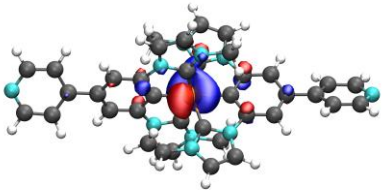
380 (19)	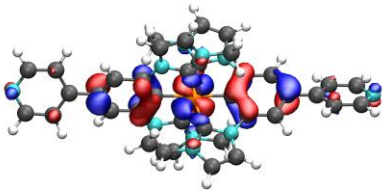	**69% →**	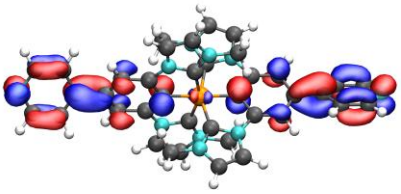
	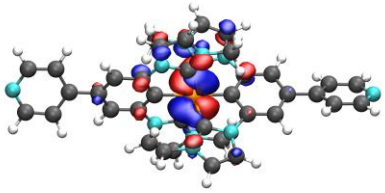	**10% →**	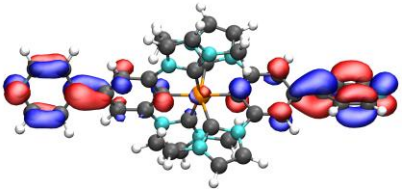

Natural Transition Orbitals $[Fe(ImPPyH)_2]^{3+}$

Table S3: Relevant Natural Transition Orbitals of the most significant Transitions in ***$[Fe(ImPPyH)_2]^{3+}$*** *for different features of the UV-Vis spectrum. The states considered for each band are noted in brackets. Isosurfaces at +/- 0.035.*

Band	Akzeptor		Donor
690 (3)	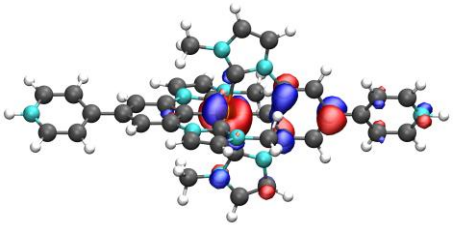	80% →	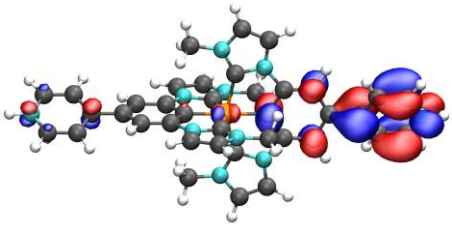
(4)	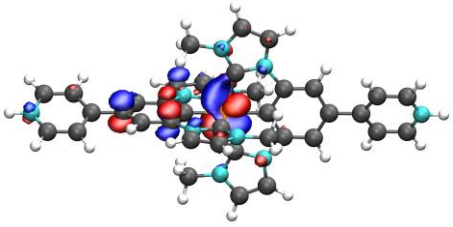	80% →	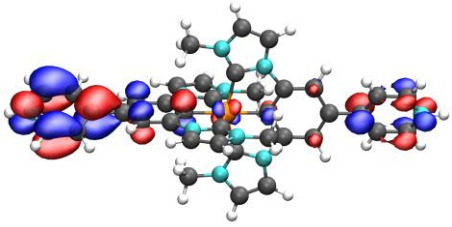
530 (11)	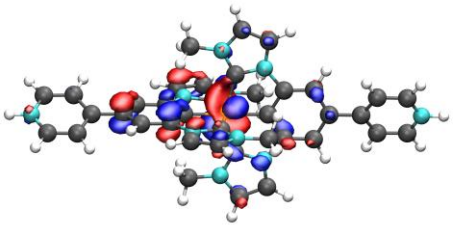	81% →	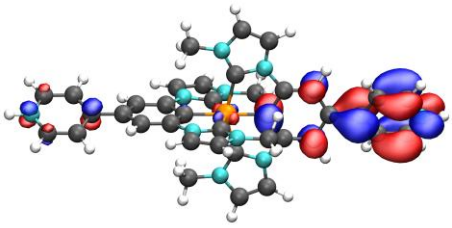
(12)	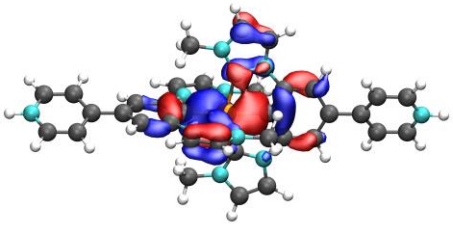	75% →	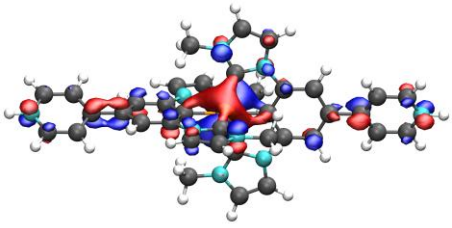
(13)	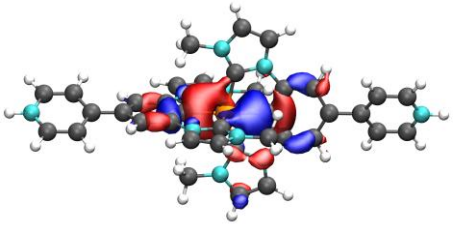	77% →	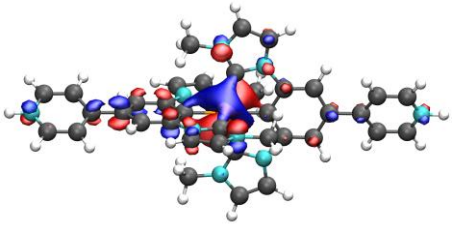
455 (16)	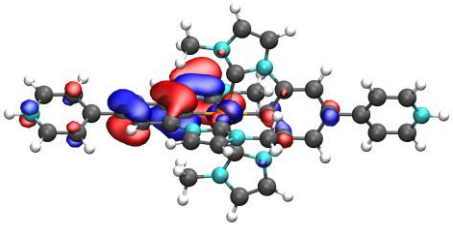	59% →	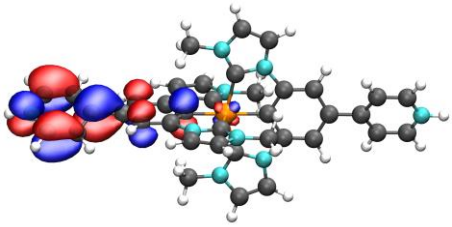
(17)		67% →	

	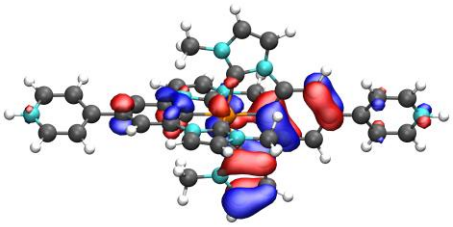		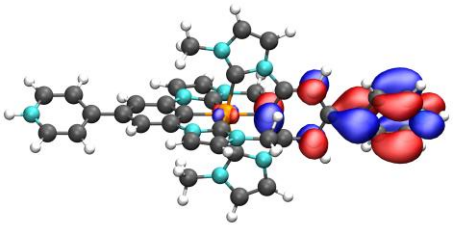
400 **(26)**	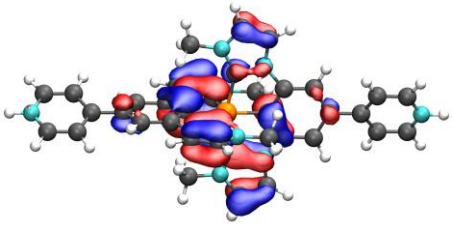	**67%** →	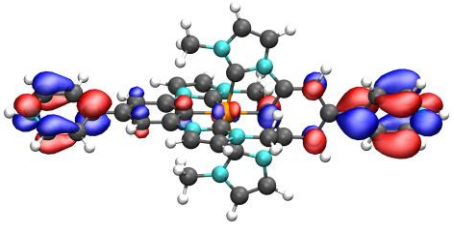
(31)	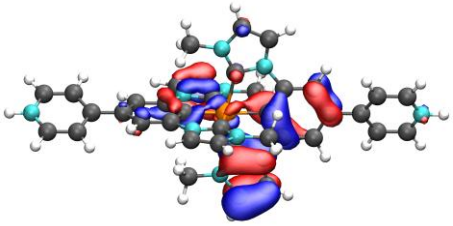	**34%** →	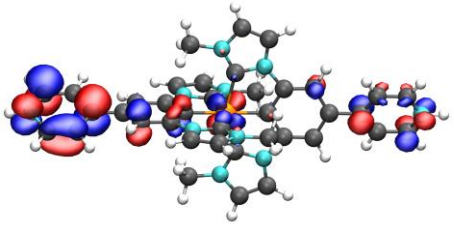
	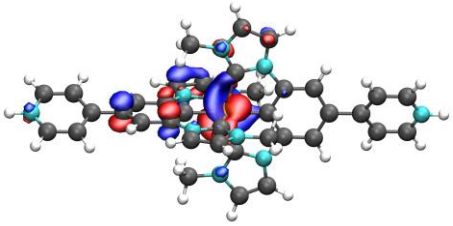	**29%** →	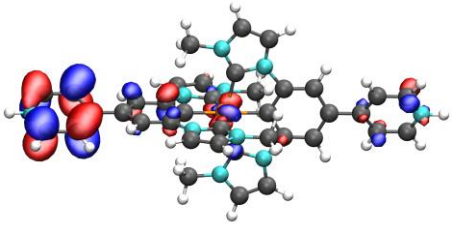

Natural Transition Orbitals $[Fe(ImPPyMe)_2]^{3+}$

Table S4: Relevant Natural Transition Orbitals of the most significant Transitions in ***$[Fe(ImPPyMe)_2]^{3+}$*** *for different features of the UV-Vis spectrum. The states considered for each band are noted in brackets. Isosurfaces at +/- 0.035.*

Band	Akzeptor		Donor
690 (4)	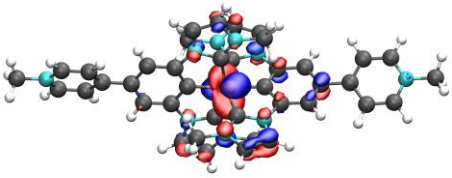	60% →	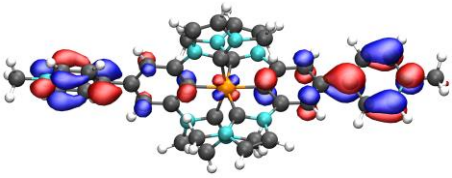
(5)	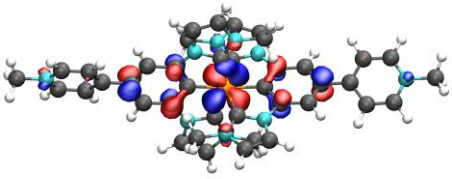	52% →	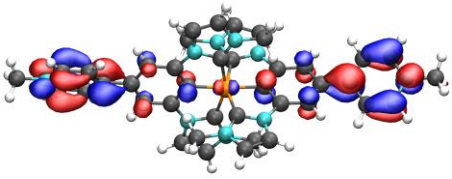
530 (10)	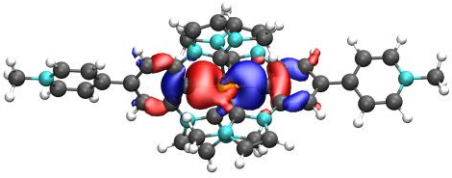	69% →	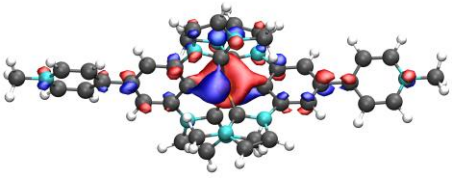
(12)	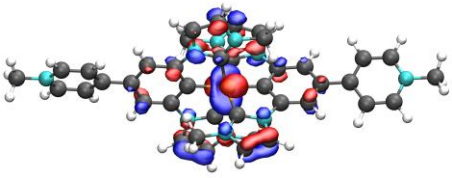	86% →	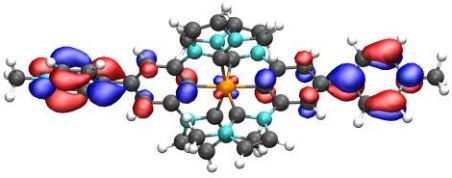
(13)	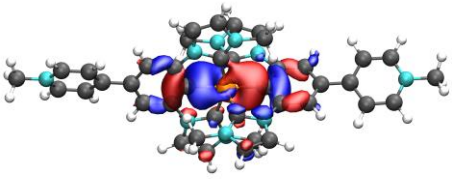	74% →	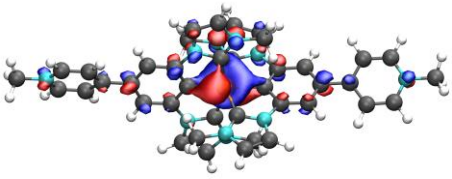
455 (17)	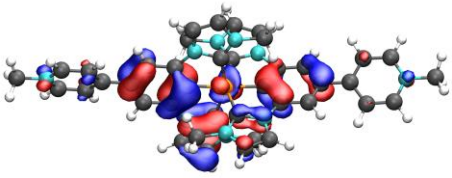	59% →	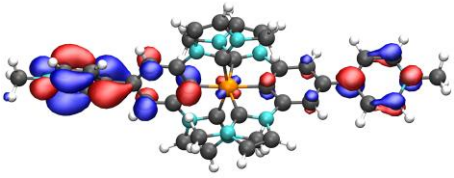

400 **(28)** **(29)** **31**	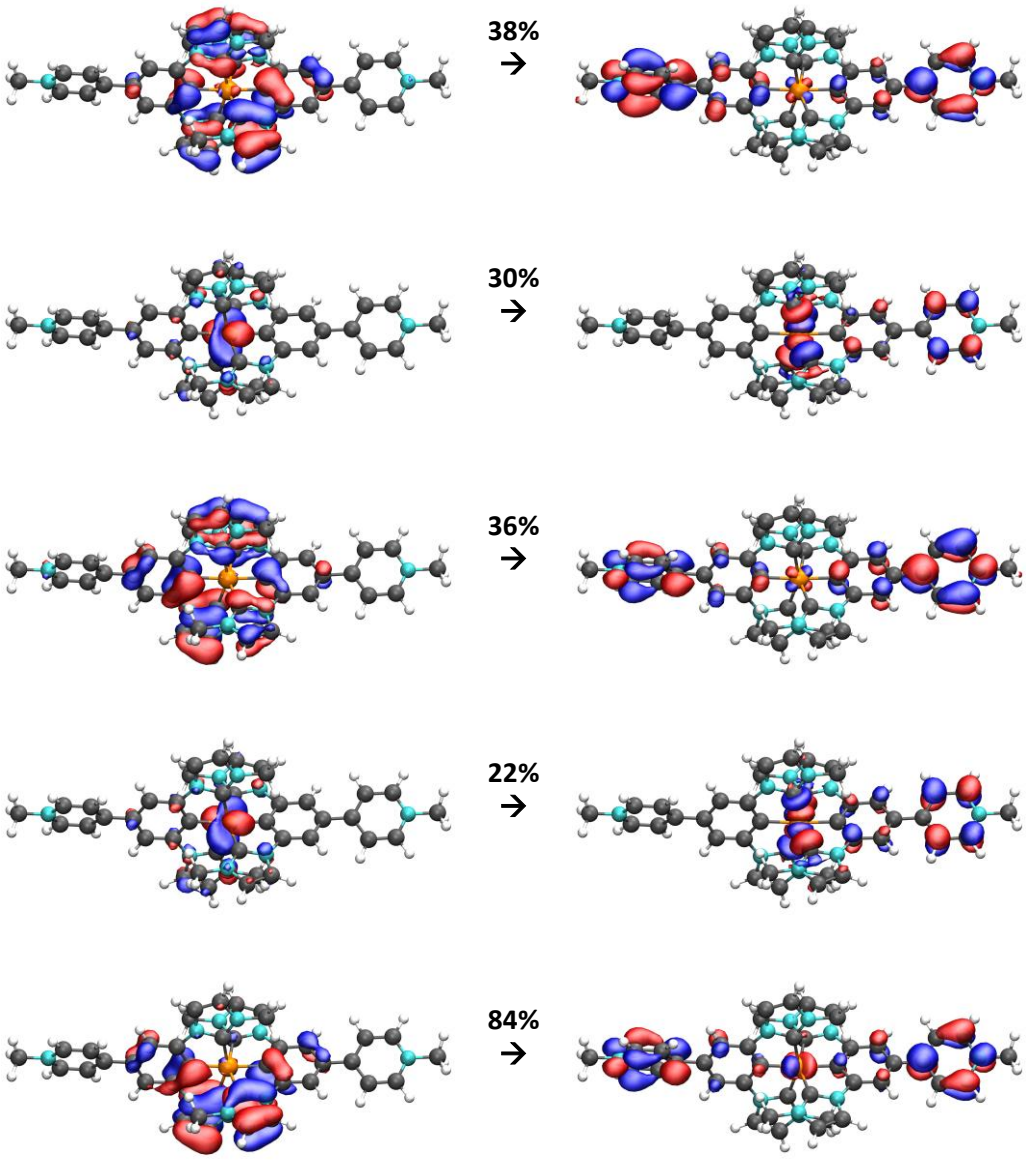

X-ray single crystal structure analysis

$C_{38}H_{32}FeN_{10}$, PF_6, $2(CH_2Cl_2)$, M_r = 999.41 Da, brown block, size 0.16 x 0.20 x 0.22 mm³, triclinic space group $P\bar{1}$ (2) with Z=2, a=11.0261(8), b=11.9069(9) Å, c=16.9707(12) Å, α=80.711(3), β=71.329(2), γ=86.479(2), V=2083.0(3) Å³, D_c=1.593 g/cm³, μ=0.730 mm^{-1}, F(000)=1018, θ_{max}=35.065°, reflections collected: 262885, independent reflections: 18364, R_{int}=0.0557, refinement converged at R1=0.0525 [I>2σ(I)], wR2=0.1552 [all data], min./max. ΔF: -1.69 eÅ³ (0.76 Å from CL11) / 1.60 eÅ³ (0.88 Å from CL11), **CCDC No.: 2488616.**

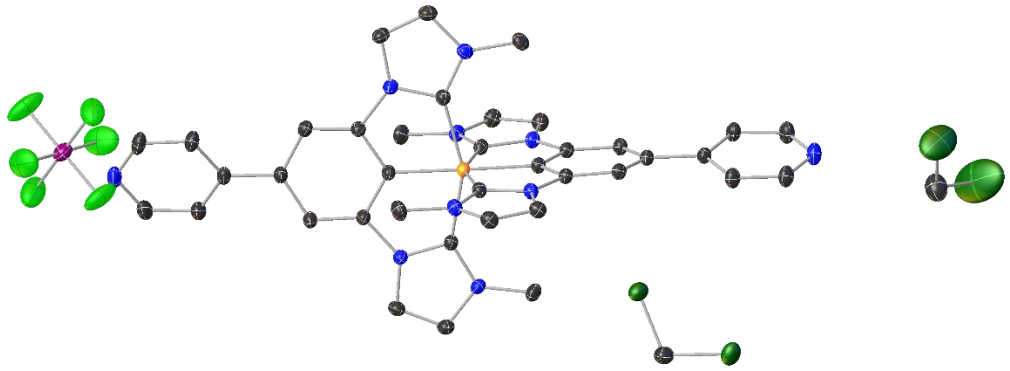

Figure S8: Asymmetric unit of $[Fe(ImPPy)_2]PF_6$ including two dichloromethane molecules. Hydrogen atoms are omitted for clarity.

The brown, block-shaped crystal was obtained from gas-phase diffusion of pentane in dichloromethane solution of $[Fe(ImPPy)_2]PF_6$. All non-hydrogen-atoms were refined anisotropically, while the aromatic hydrogen atom positions were refined at idealized positions riding on the carbon atoms with isotropic displacement parameters $U_{iso}(H)$=1.2 $U_{eq}(C)$ and C-H bond lengths of 0.950 Å. The methyl groups are idealized with tetrahedral angles in a combined rotating and rigid group refinement with the 1.5 fold isotropic displacement parameters of the equivalent Uij of the corresponding carbon atom at a distance of d(C-H)=0.98 Å.

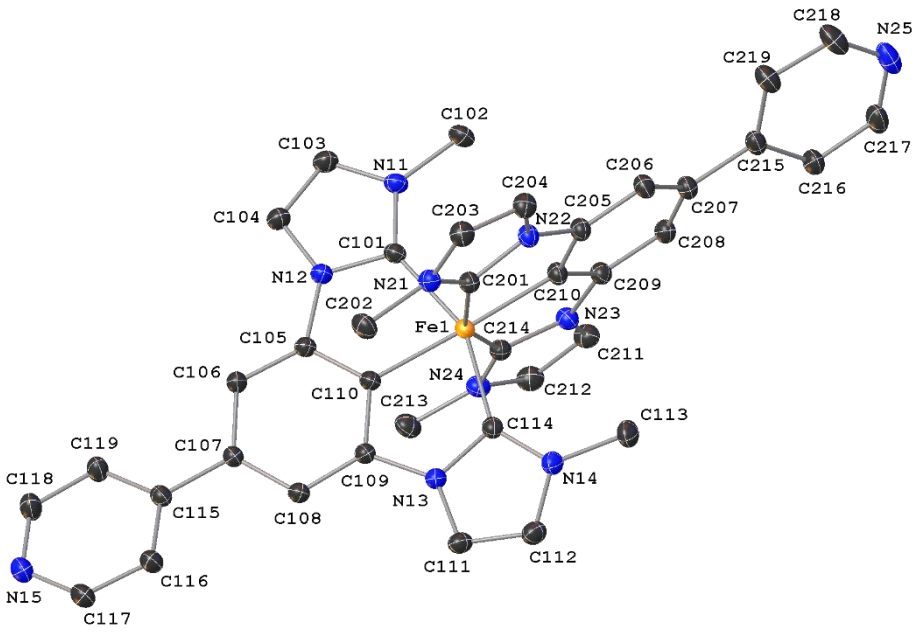

Figure S9: Crystal structure of [Fe(ImPPy)$_2$] with anisotropic displacement ellipsoids drawn on a 50% probability level. Hydrogen atoms are omitted for clarity.

Transient Absorption Spectroscopy

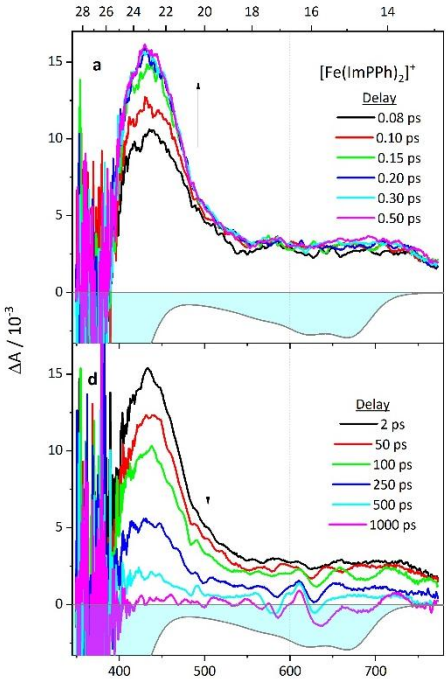

Figure S10: Time evolution of the transient absorption spectra upon 600 nm fs excitation (vertical dotted line). Upper panel focuses early spectral redistribution while the lower one shows overall signal decay on the ps timescale for the three compounds, as indicated in the inset. Signal for magic-angle polarization is shown. Pump-probe time delays are quoted in the legend. Arrows indicate the direction of signal evolution towards longer delays. A horizontal black line marks the zero-signal level. Absorption spectra are shown as negative cyan filled curves as a guide to assign bleach contributions.

Time-Resolved Spectroscopy

Data for $[Fe(ImPPh)_2]^+$

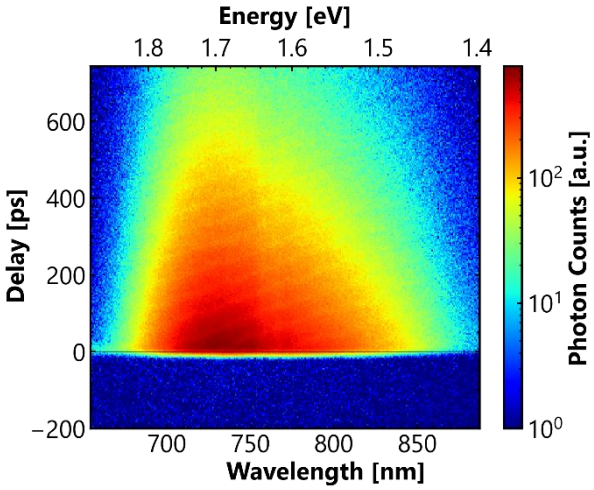

Figure S11: Photon Counting 2D map of complex ***[Fe(ImPPh)$_2$]$^+$****. The complex has been excited by a 630-nm pulsed beam at 100 kHz repetition rate.*

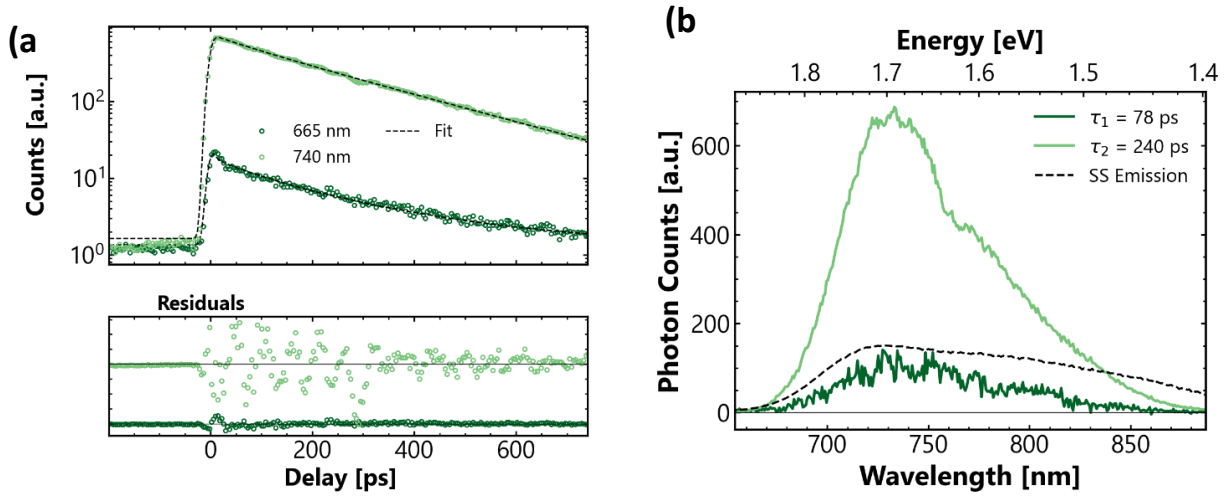

Figure S12: (a) Selection of kinetics with best fitting lines and residuals. (b) Decay Associated Spectra (DAS) obtained from global fitting with two decaying exponentials. The dashed black line represents the steady-state emission spectrum.

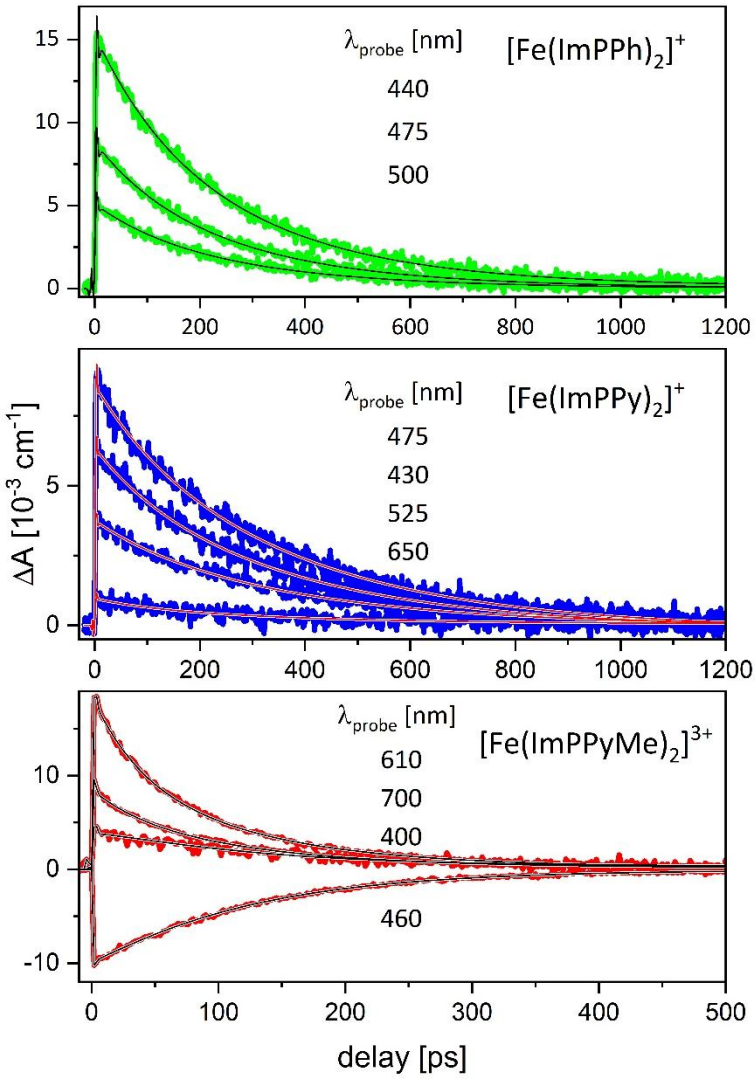

Figure S13: Biexponential fits (see Table 3 of main text) obtained for the global fits of transient absorption spectra of ***[Fe(ImPPh)$_2$]$^+$*** *(green),* ***[Fe(ImPPy)$_2$]$^+$*** *(blue),* ***[Fe(ImPPyMe)$_2$]$^{3+}$*** *(red) compounds in acetonitrile, as indicated in the Figure. Measurements performed under magic angle pump-probe polarization and excitation at 600 nm. 2 ps step sizes were used*

for best comparison with transient fluorescence data. Representative wavelengths are shown and indicated in the legend. Fits are displayed as thin lines over white background, when necessary, for better contrast.

NMR spectroscopy

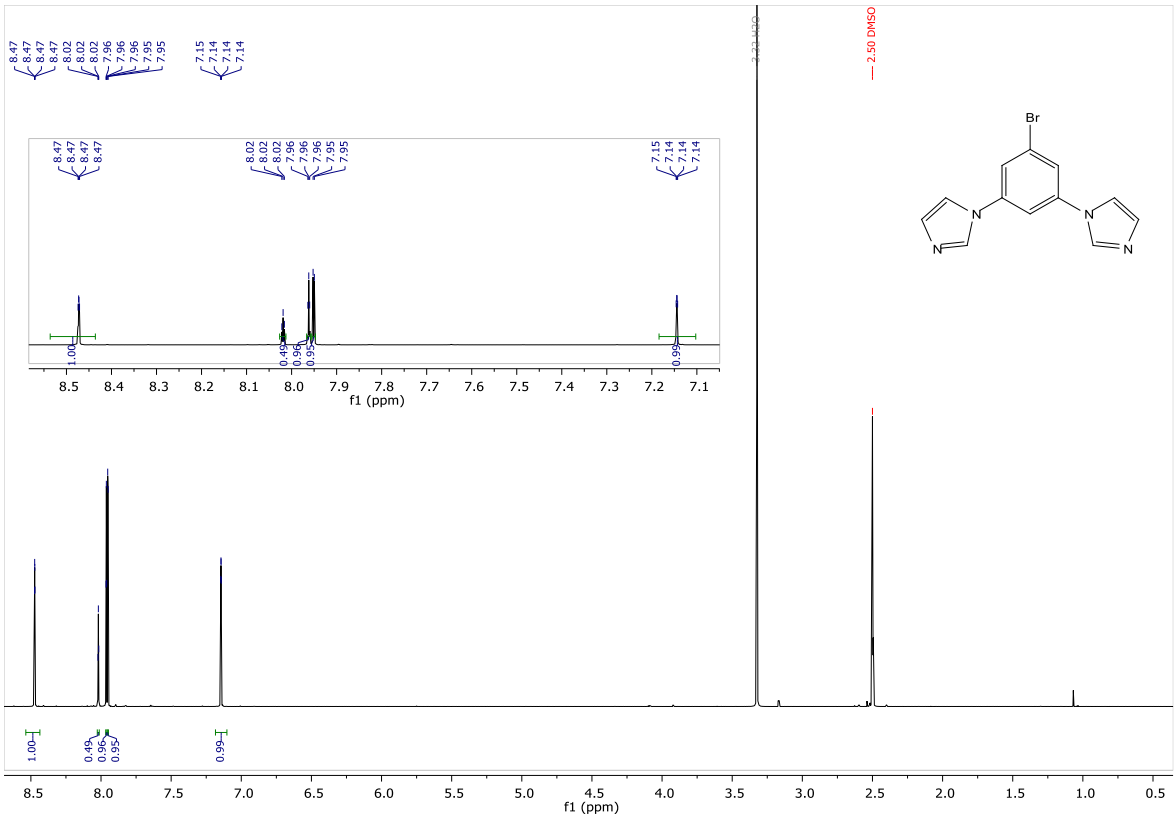

Figure S14: ^{1}H-NMR spectrum of 1'-(5-bromo-1,3-phenylene)bis(1H-imidazole)

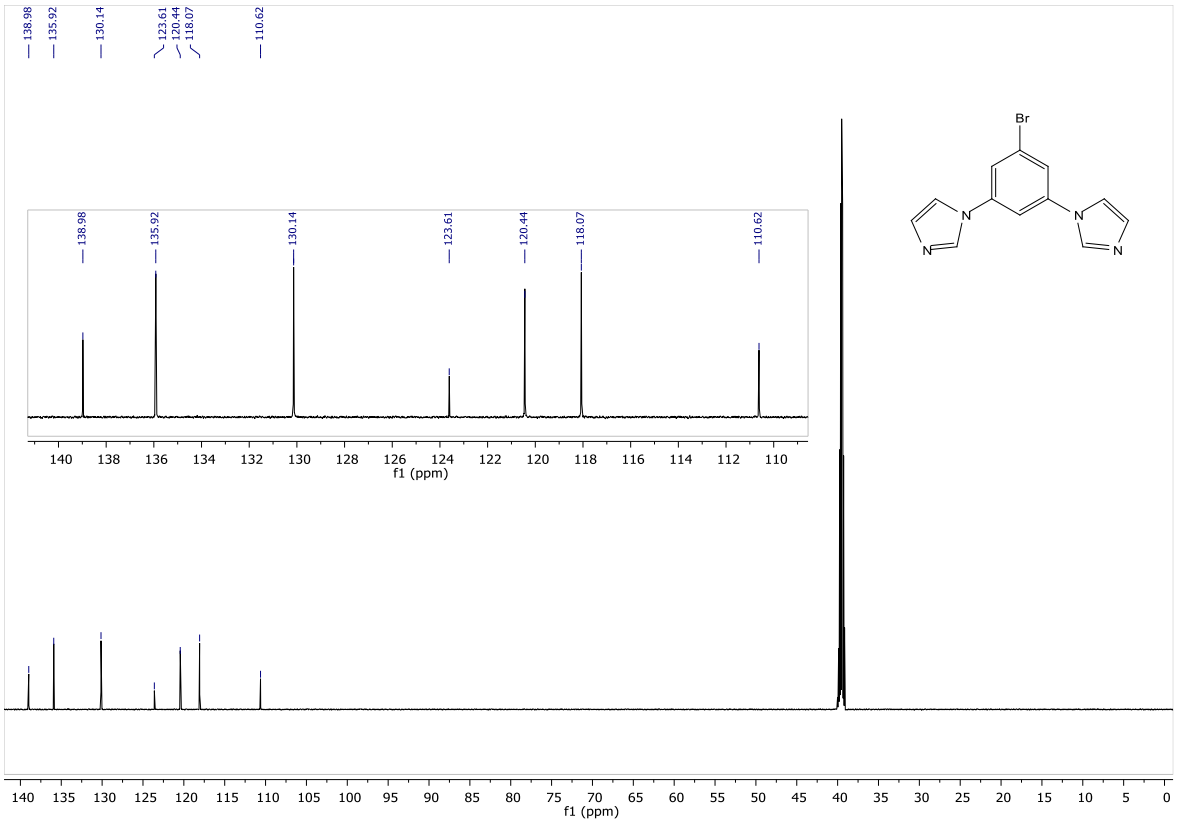

Figure S15: ^{13}C-NMR spectrum of 1'-(5-bromo-1,3-phenylene)bis(1H-imidazole)

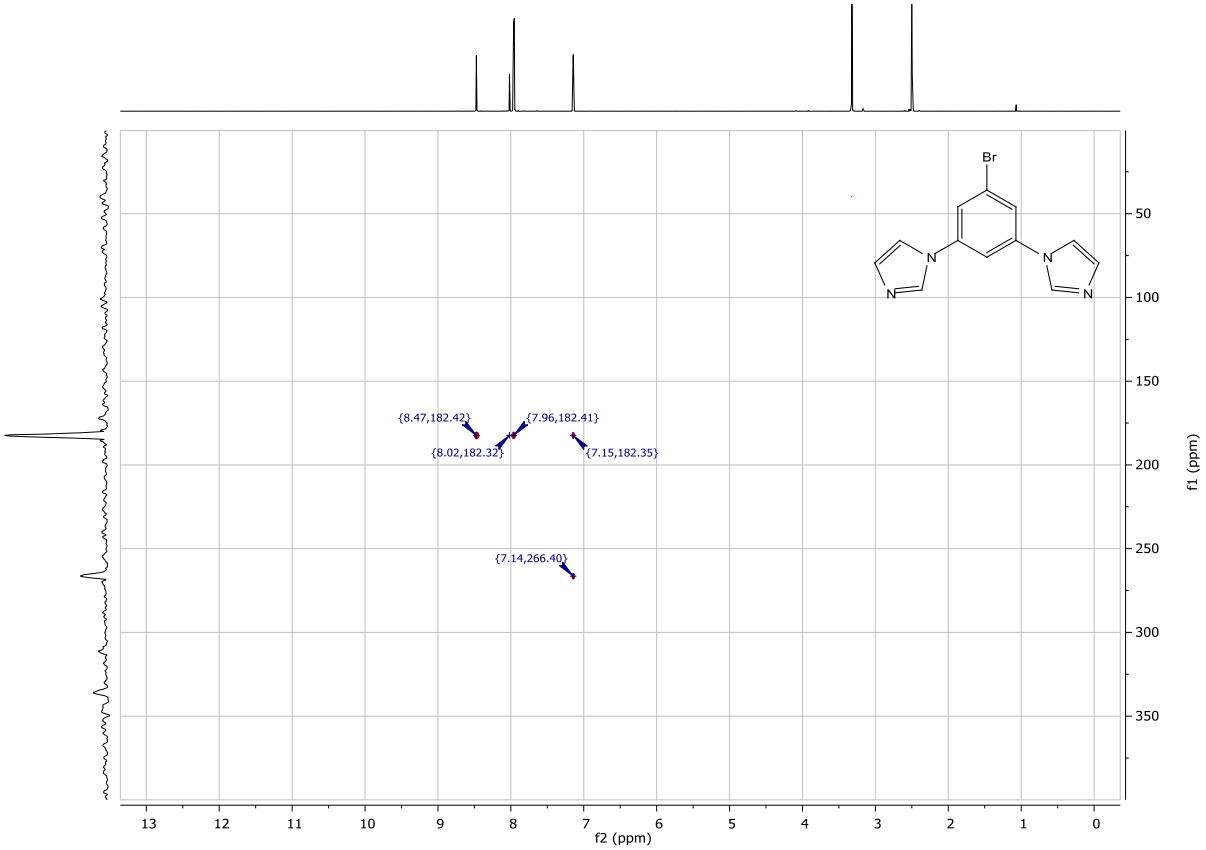

Figure S16: ^{15}N-NMR spectrum of 1'-(5-bromo-1,3-phenylene)bis(1H-imidazole)

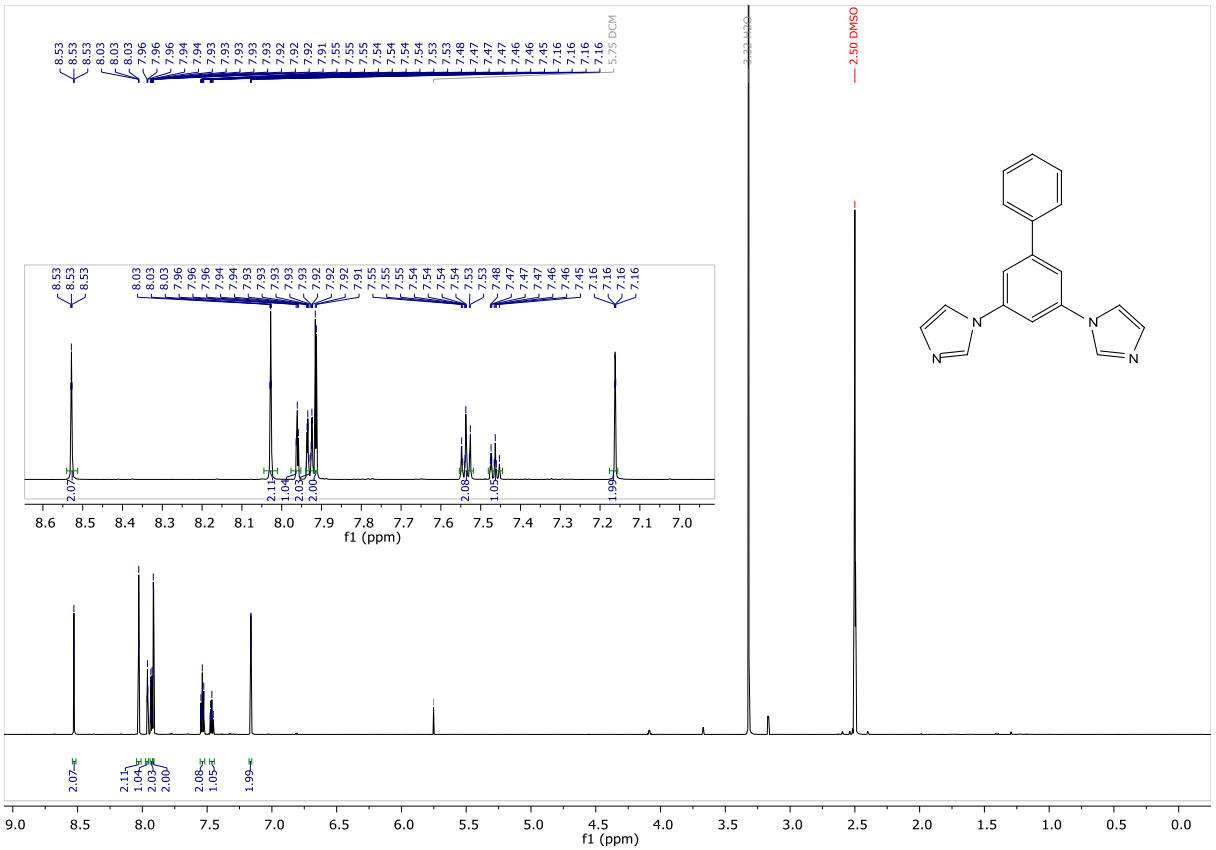

*Figure S17: [1]H-NMR spectrum of **3C***

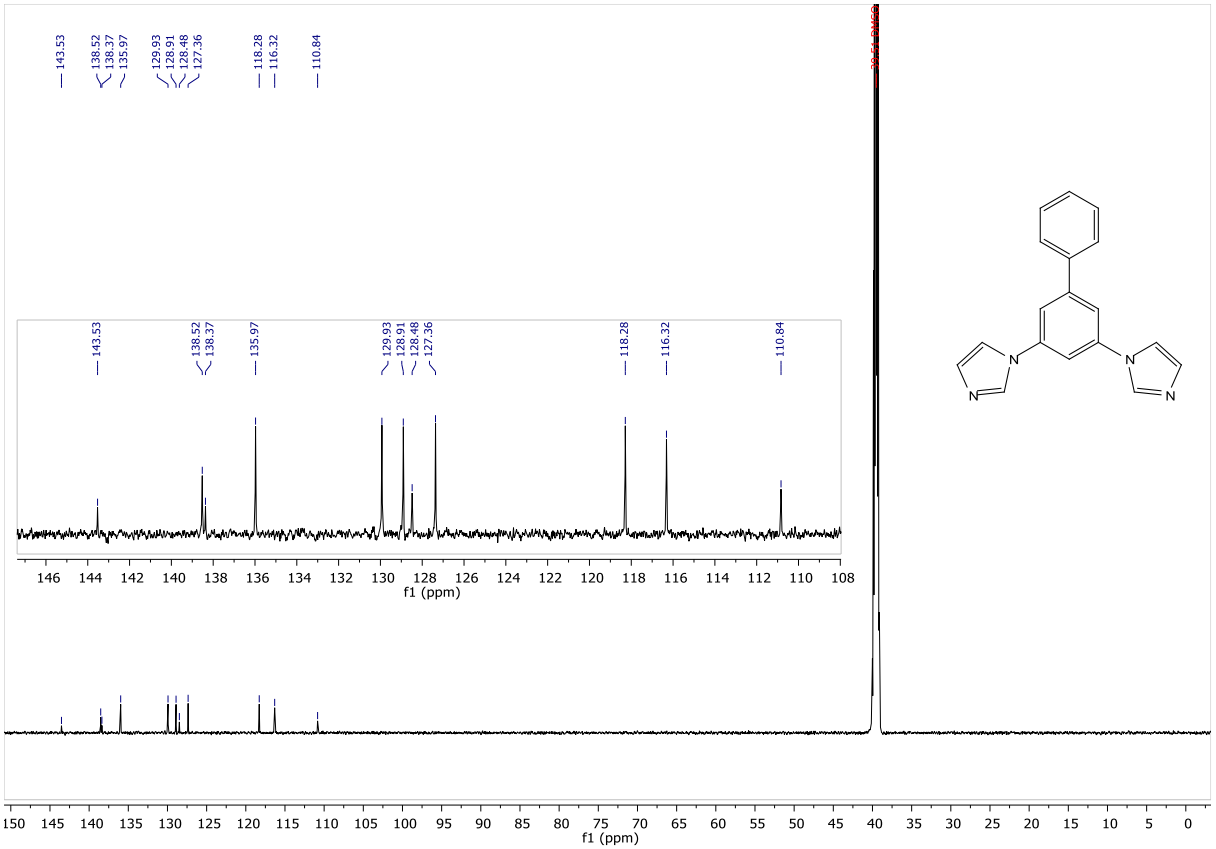

*Figure S18: [13]C-NMR spectrum of **3C***

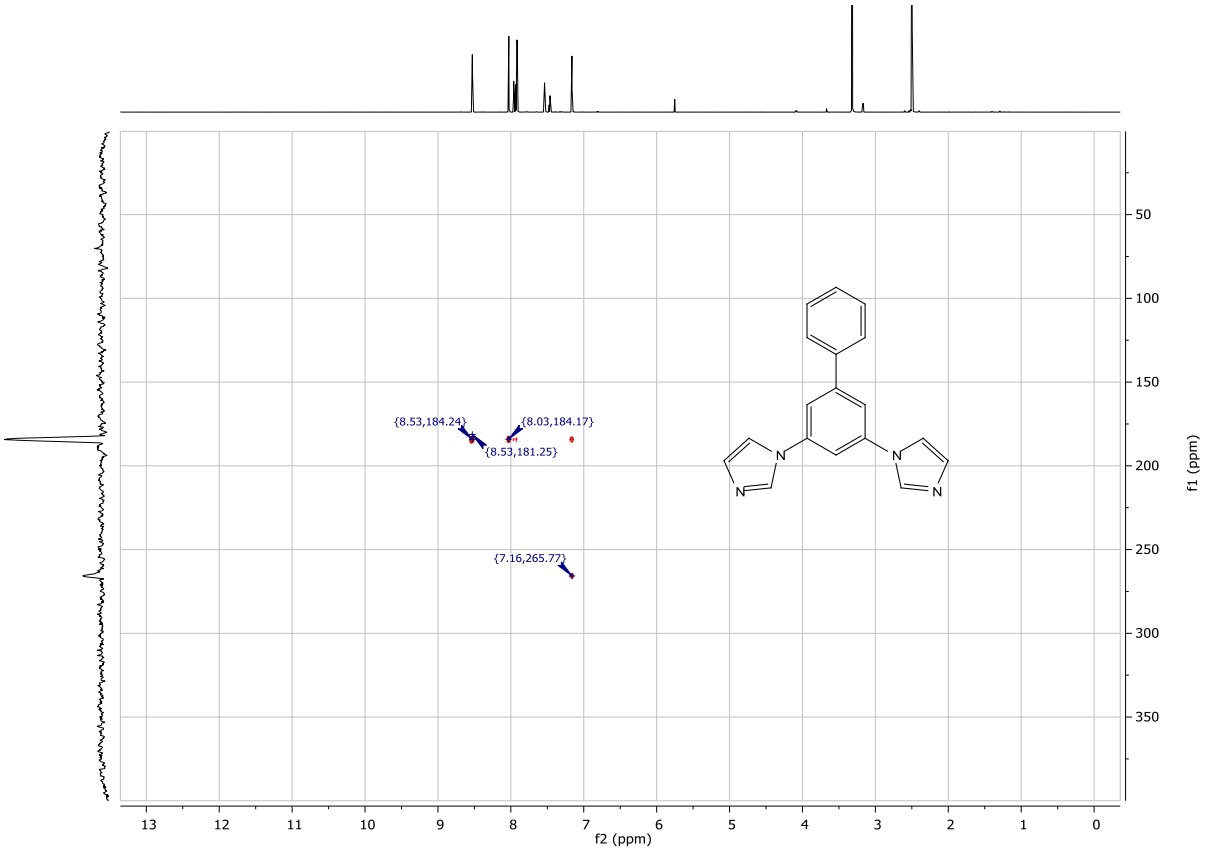

*Figure S19: ^{15}N-HMBC spectrum of **3C***

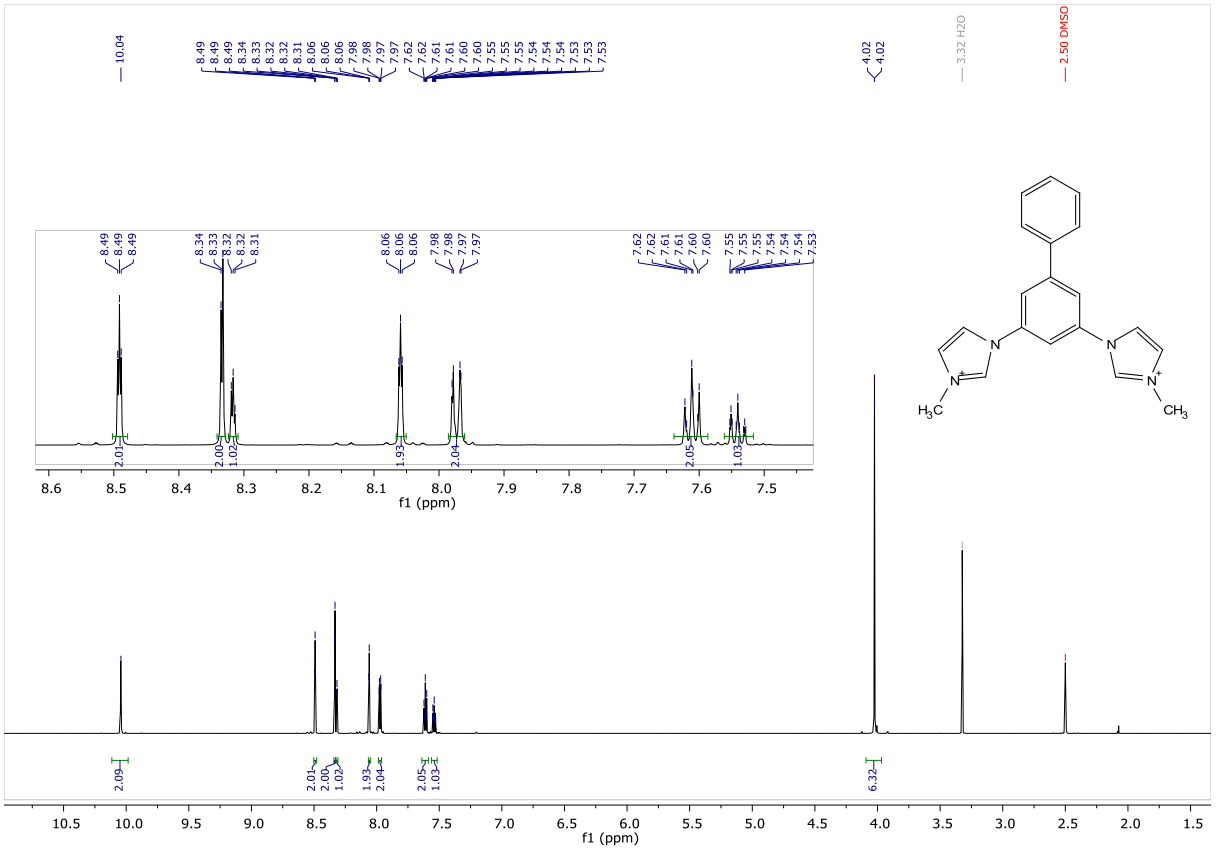

*Figure S20: ^{1}H-NMR spectrum of **[ImPPh]I_2***

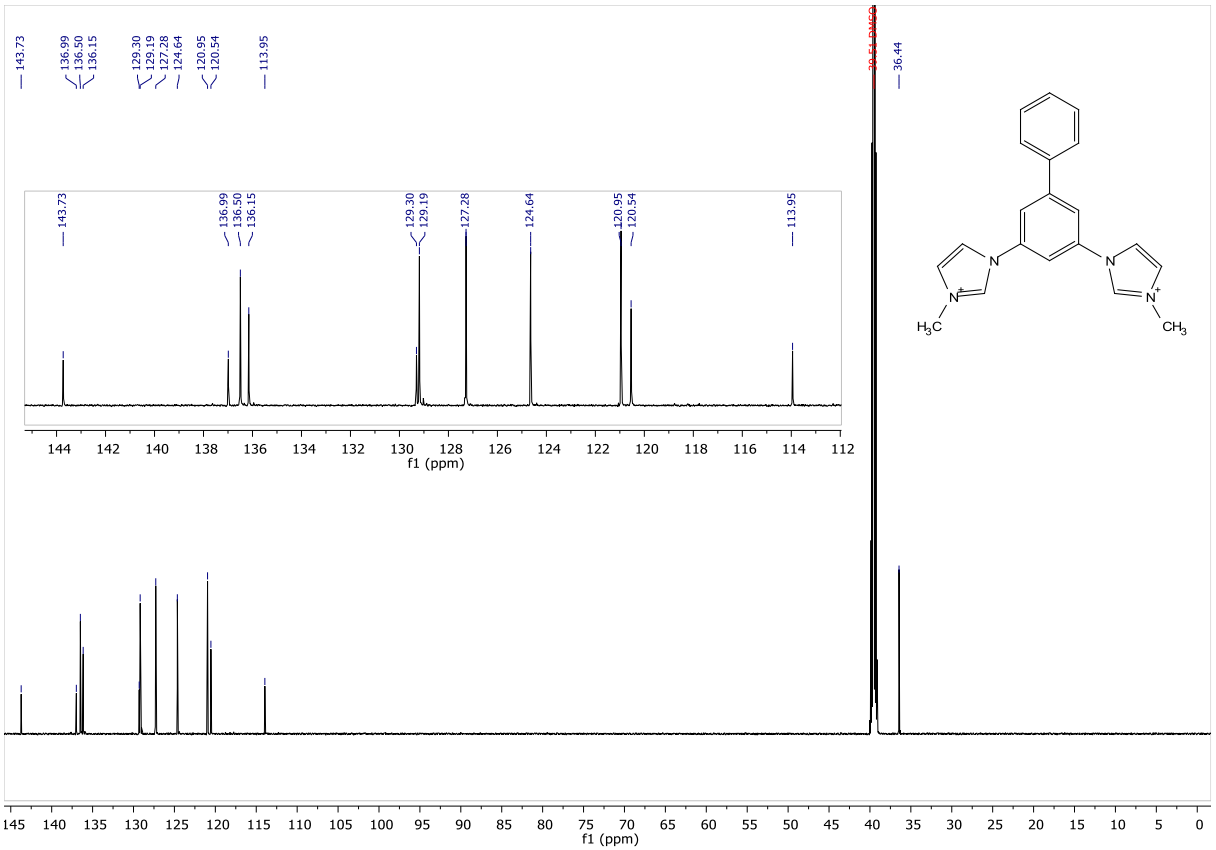

Figure S21: ^{13}C-NMR spectrum of ***[ImPPh]I$_2$***

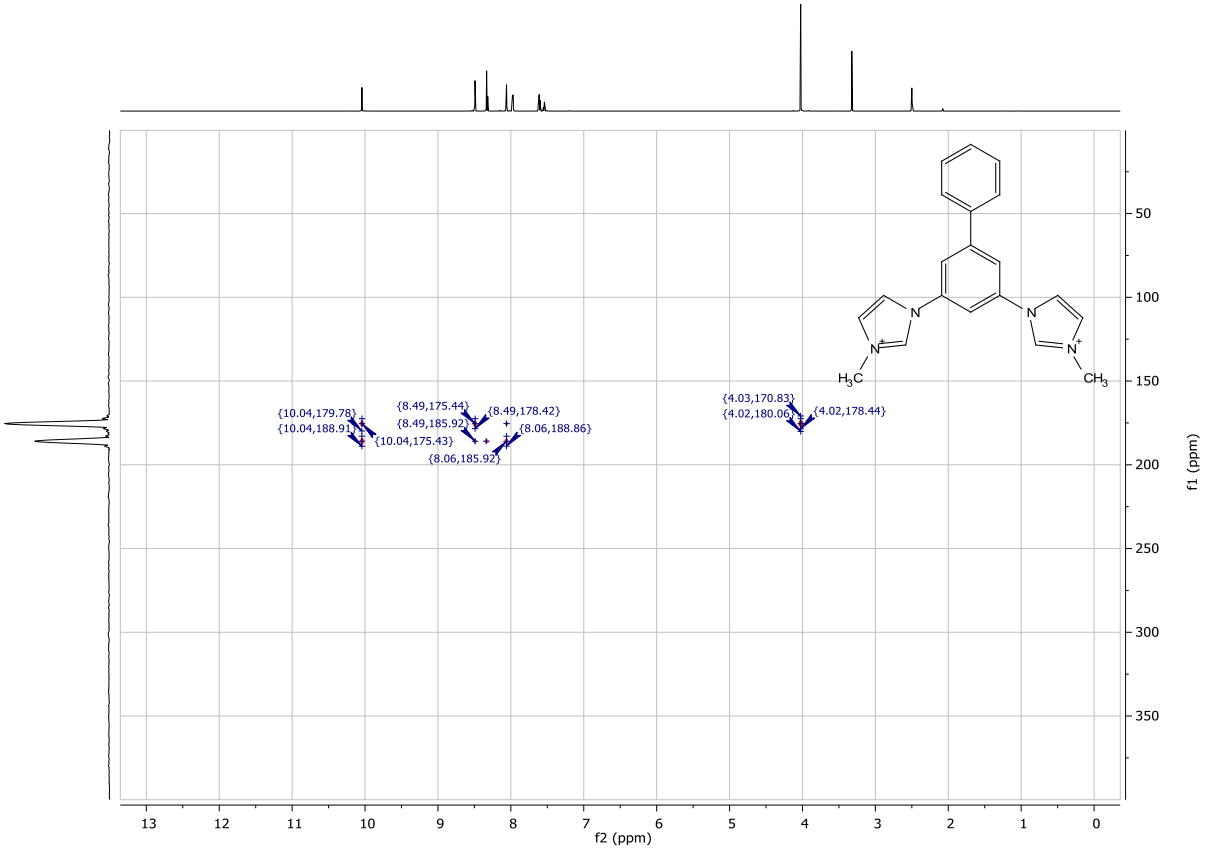

Figure S22: ^{15}N-HMBC spectrum of ***[ImPPh]I$_2$***

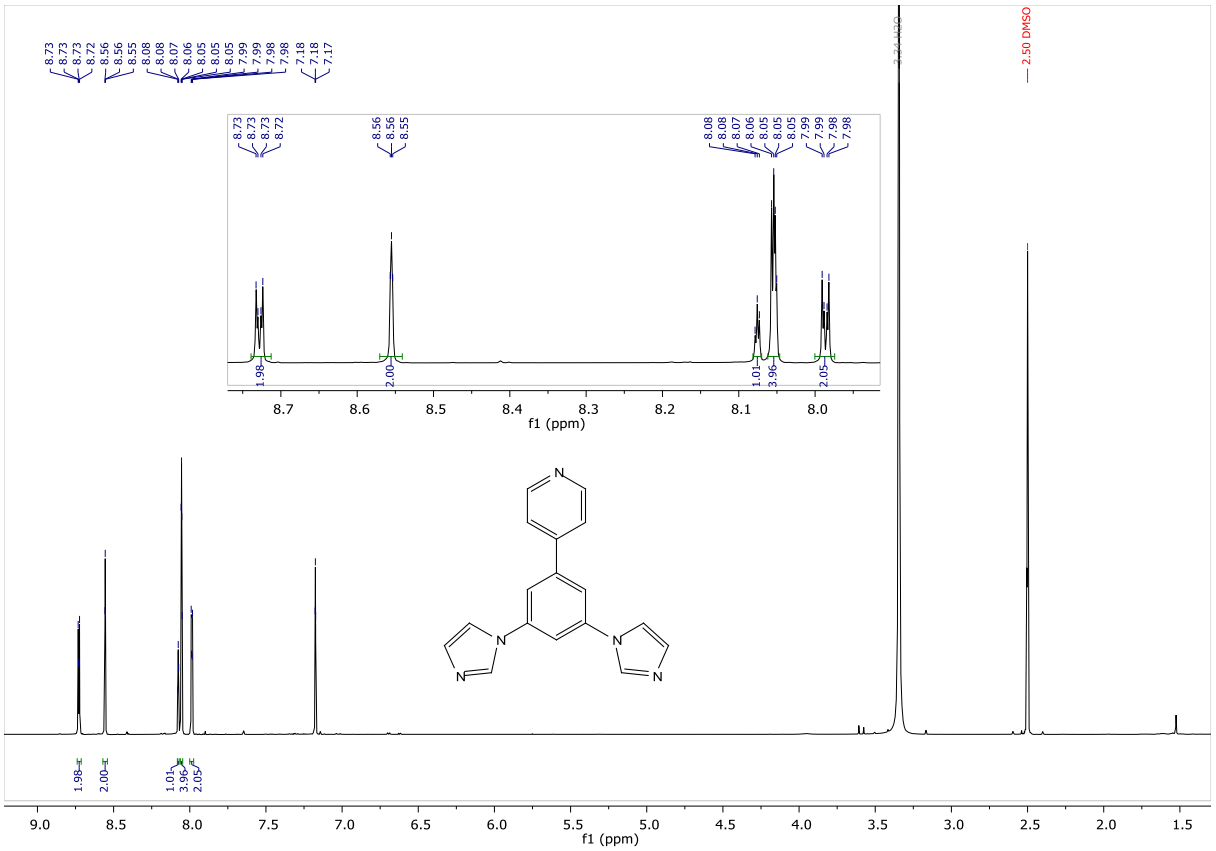

*Figure S23: ^{1}H-NMR spectrum of **3N***

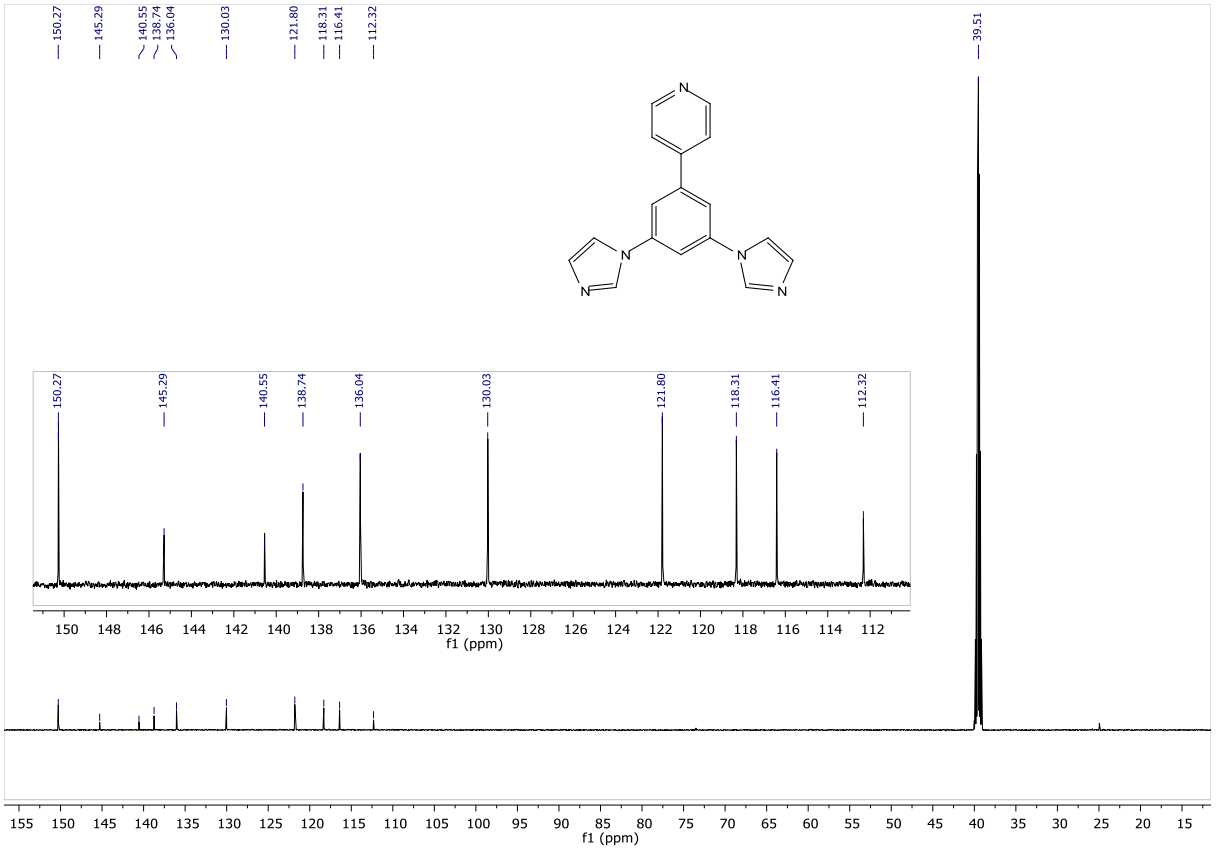

*Figure S24: ^{13}C-NMR spectrum of **3N***

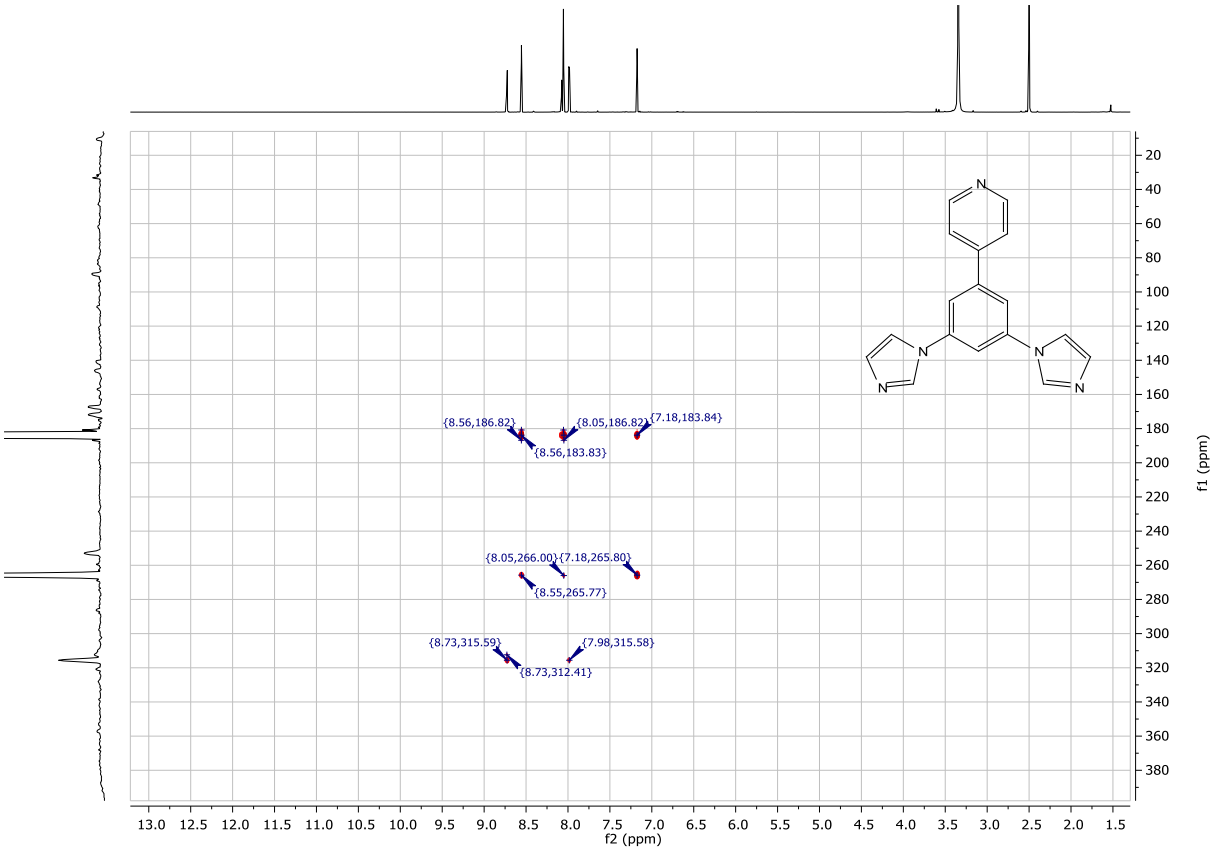

*Figure S25: ^{15}N-HMBC spectrum of **3N***

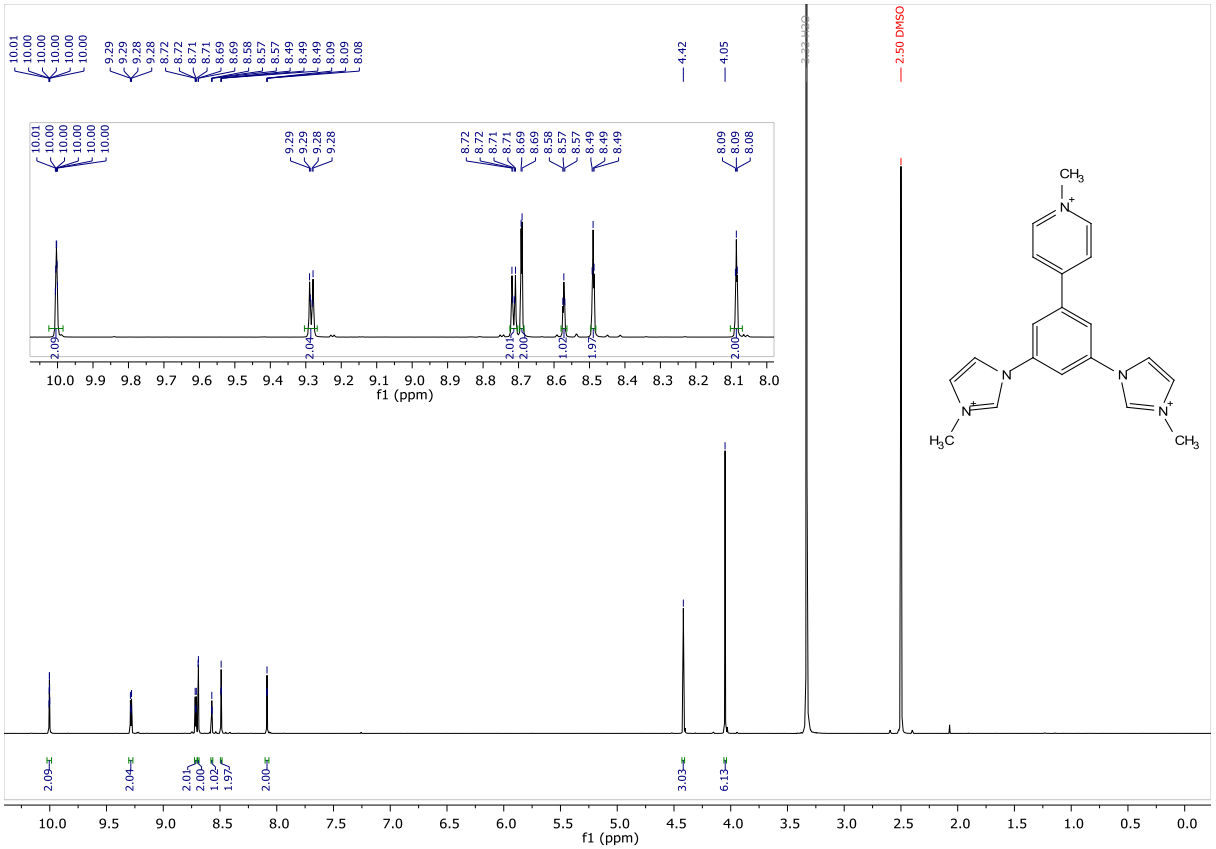

*Figure S26: ^{1}H-NMR spectrum of **[ImPPyMe]I$_3$***

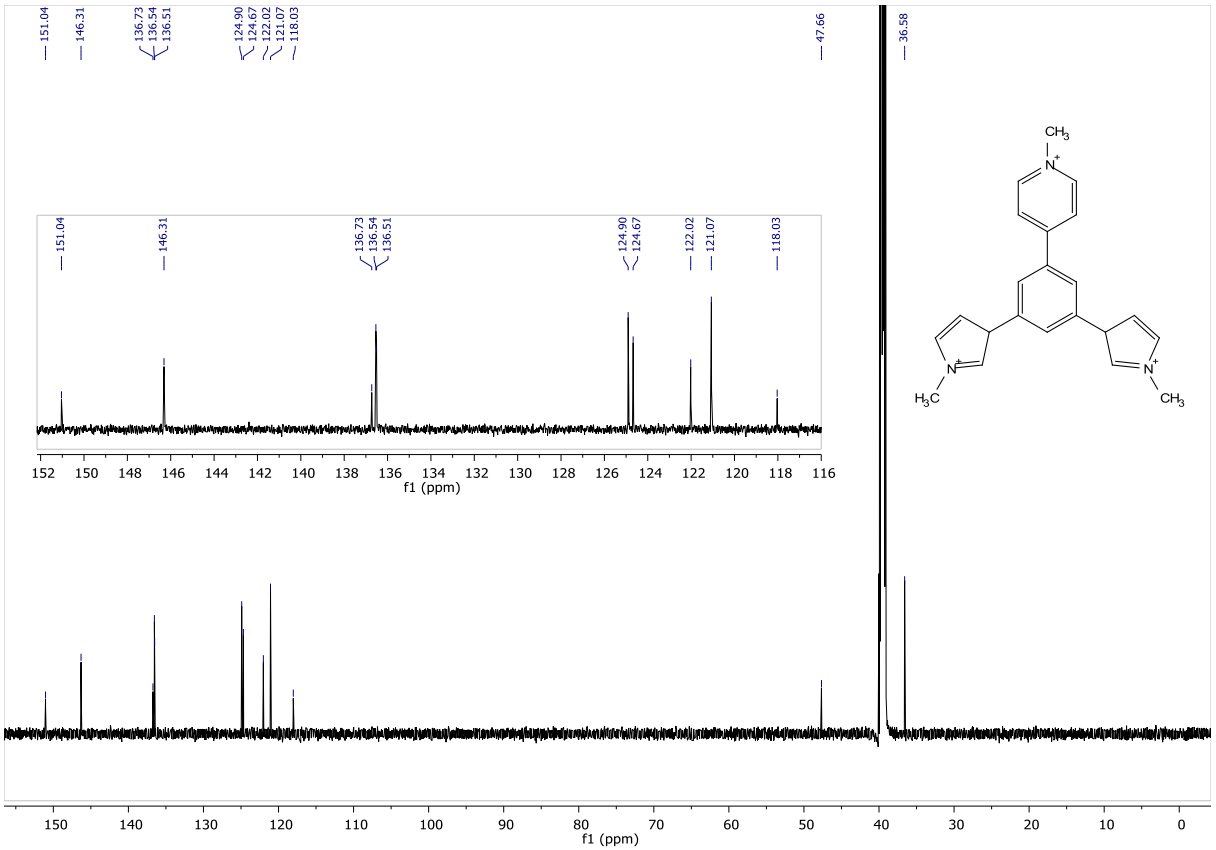

*Figure S27: ^{13}C-NMR spectrum of **[ImPPyMe]I$_3$***

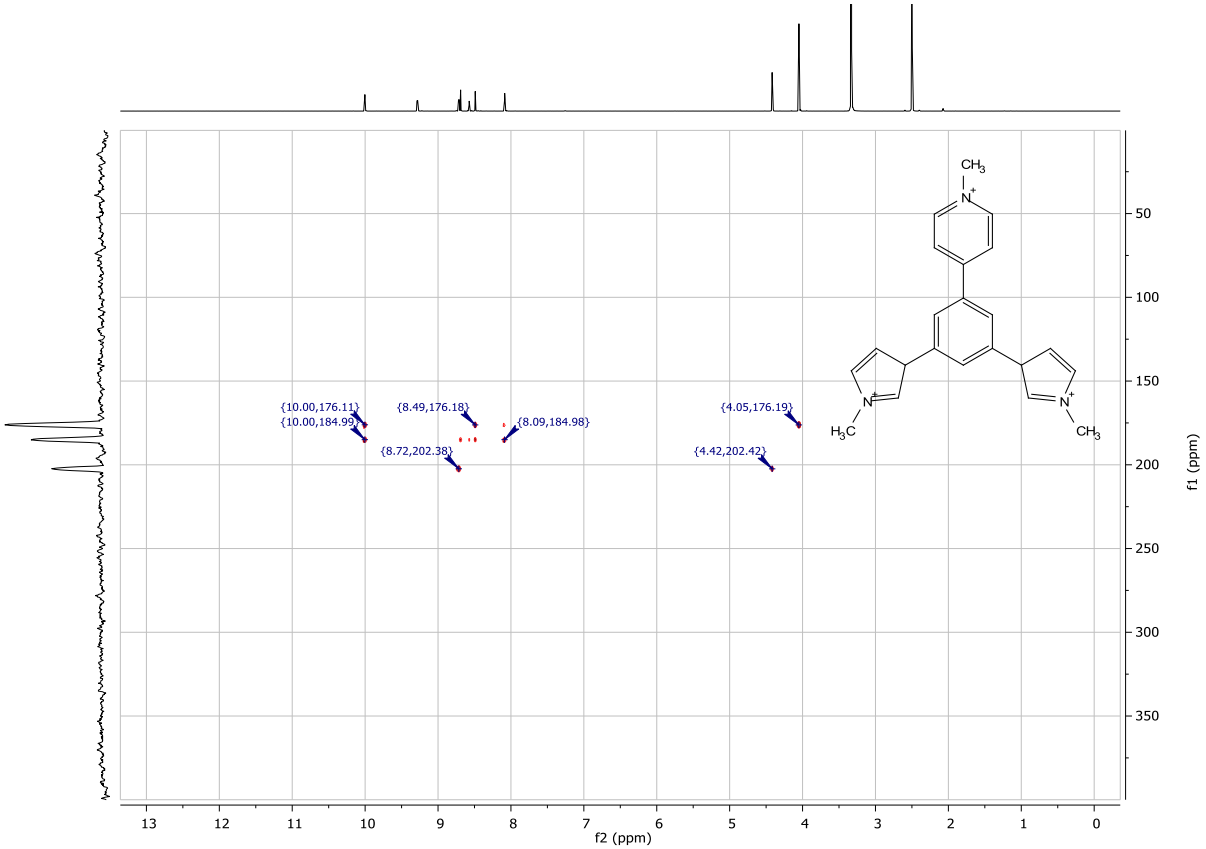

*Figure S28: ^{15}N-HMBC spectrum of **[ImPPyMe]I$_3$***

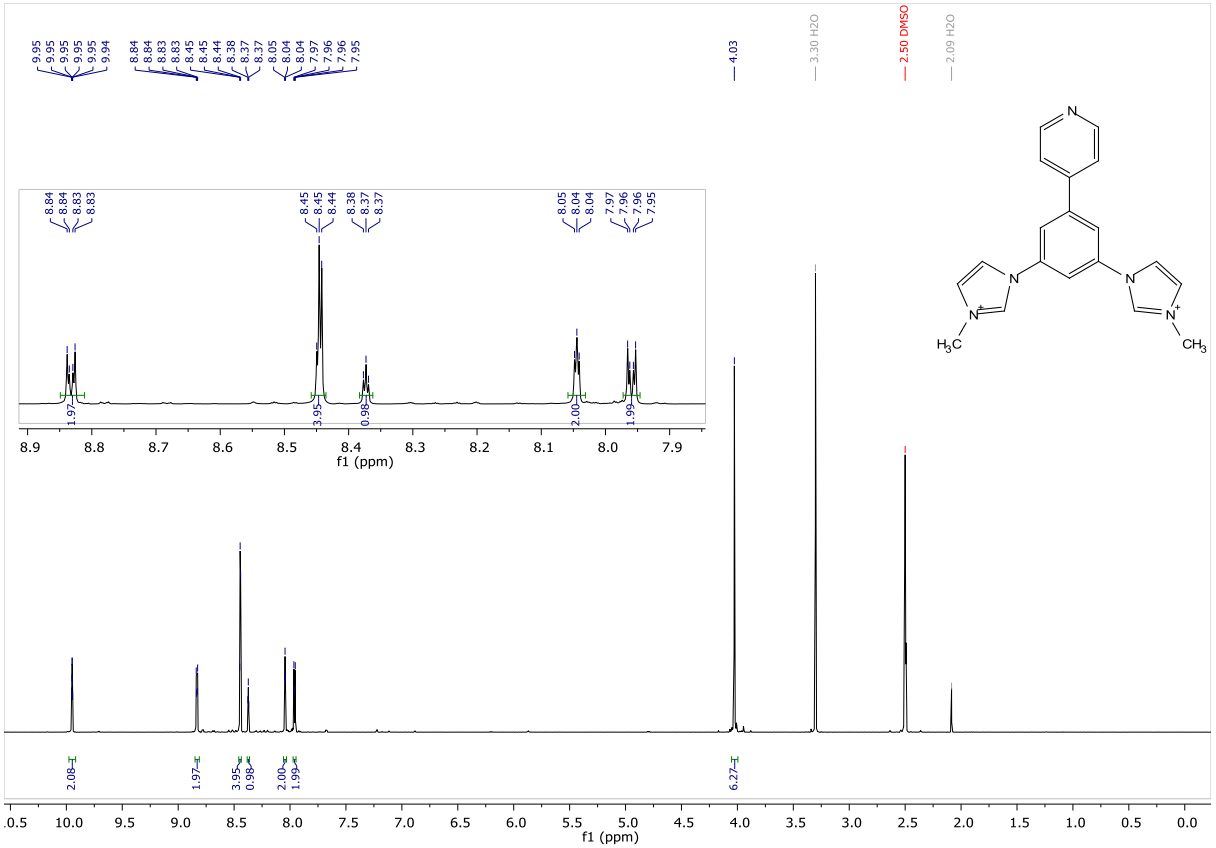

Figure S29: ^{1}H-NMR spectrum of ***[ImPPy]I$_2$***

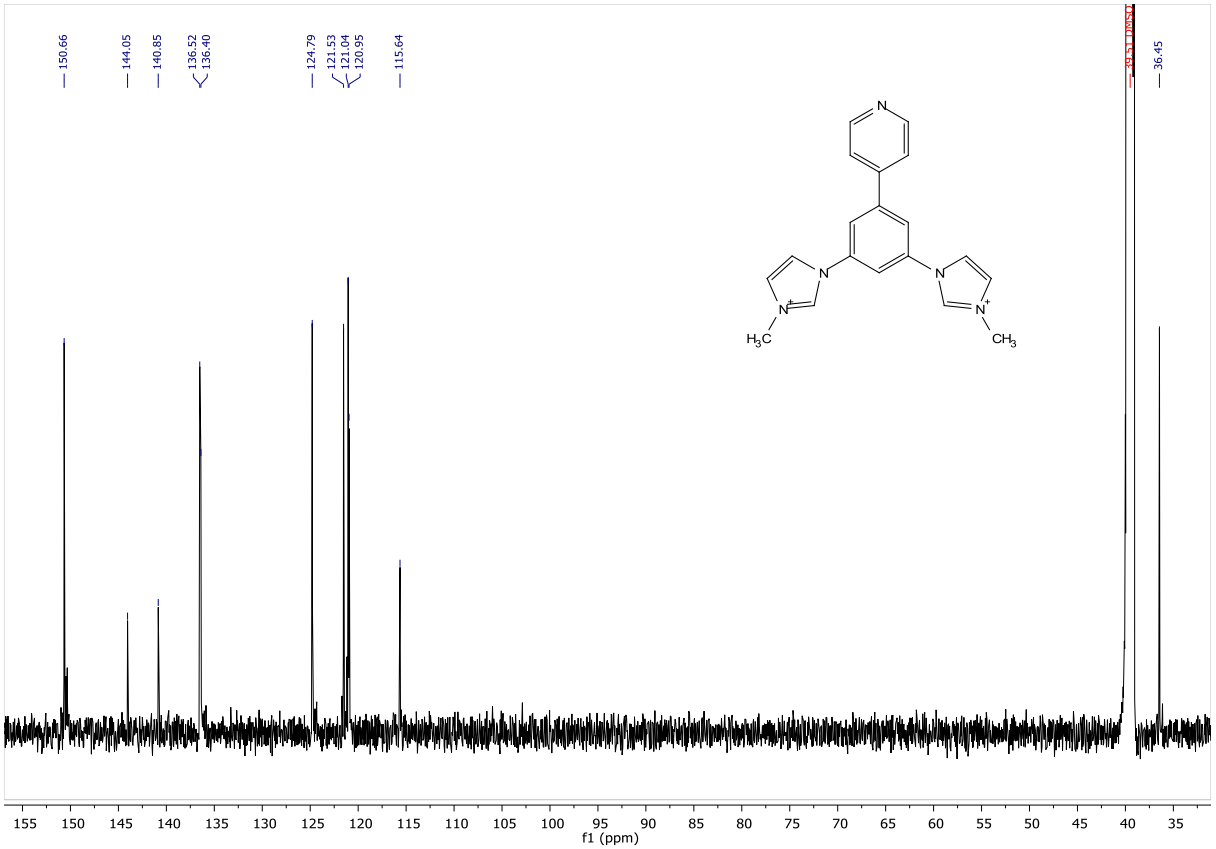

Figure S30: ^{13}C-NMR spectrum of ***[ImPPy]I$_2$***

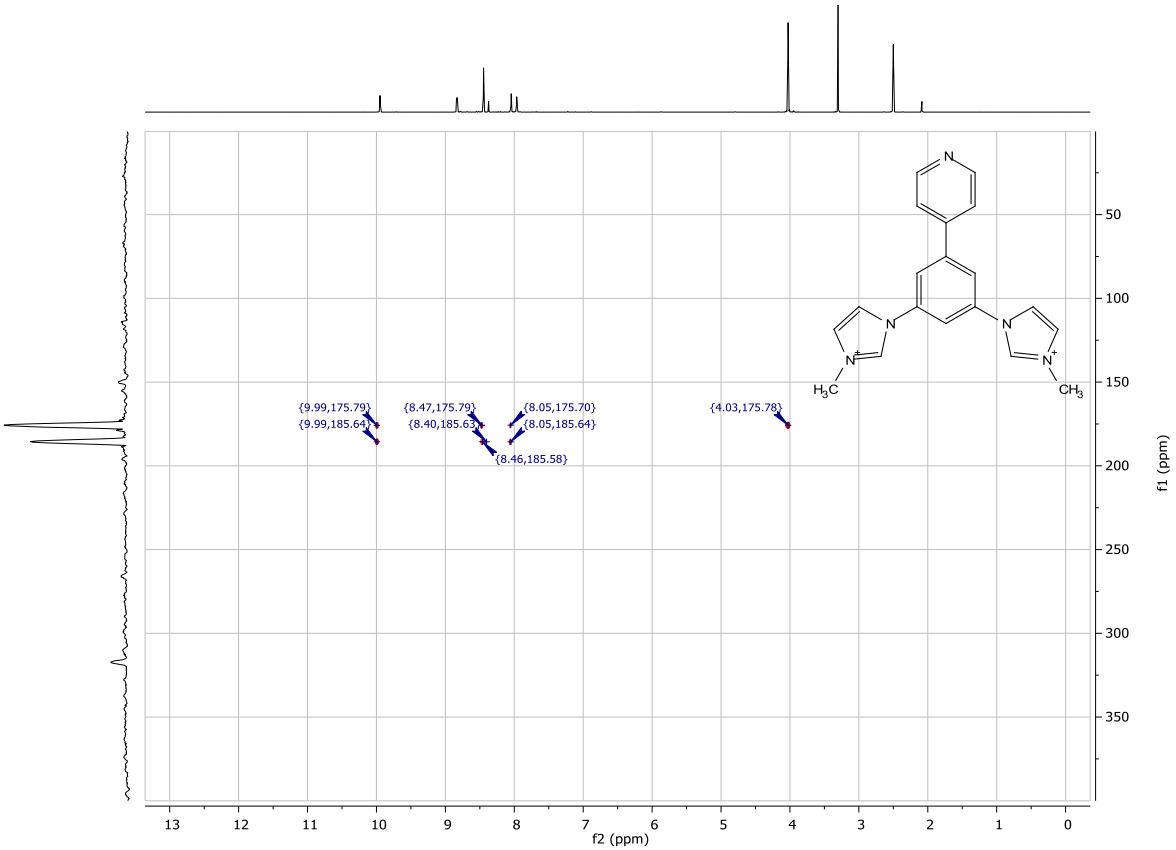

Figure S31: ^{15}N-HMBC spectrum of ***[ImPPy]I$_2$***

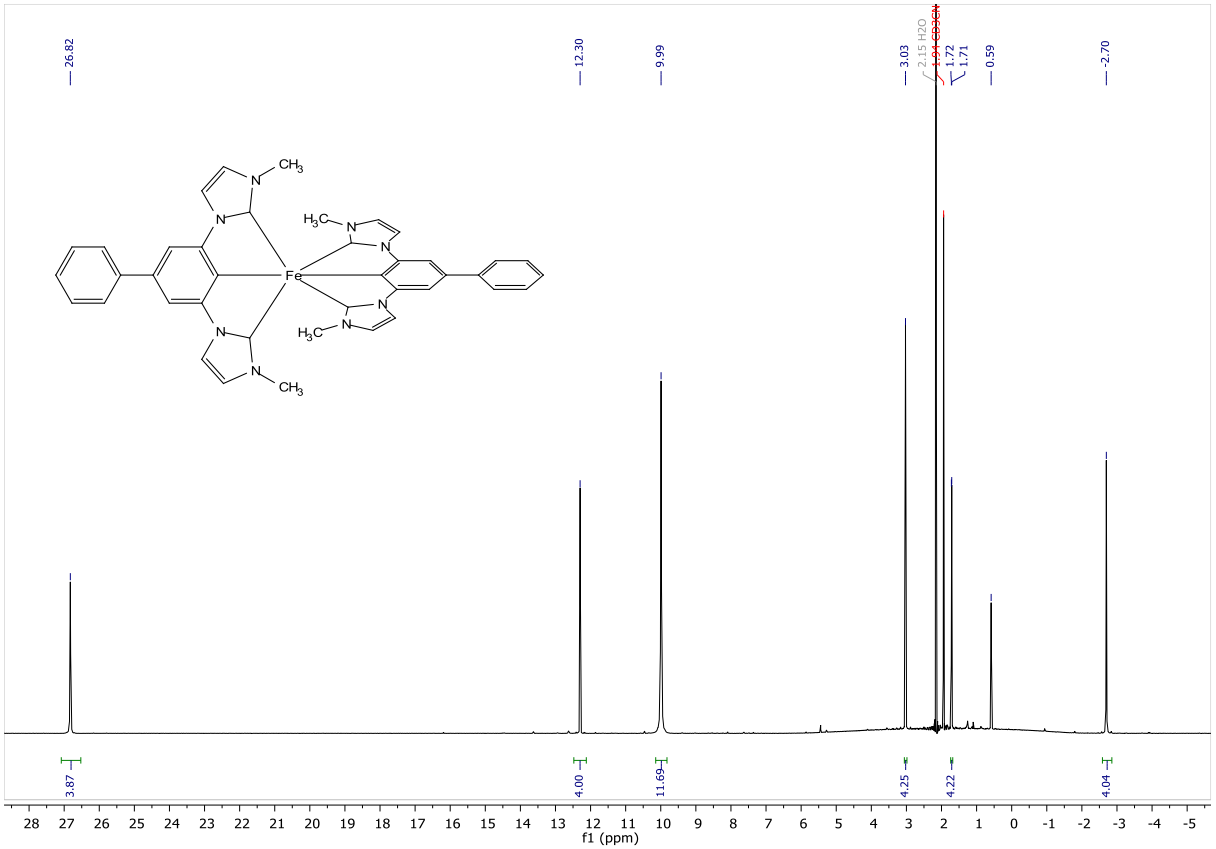

Figure S32: ^{1}H-NMR spectrum of ***[Fe(ImPPh)$_2$]$^+$***

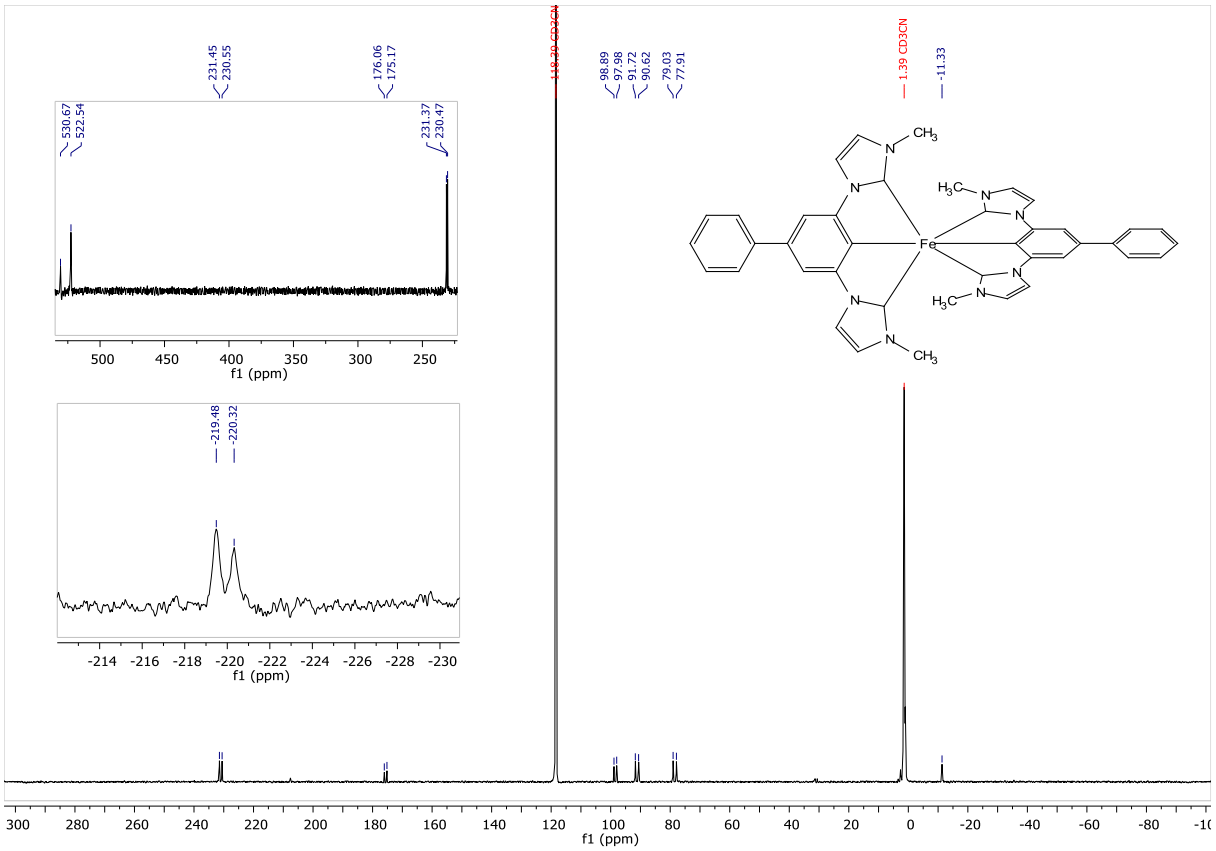

Figure S33: ^{13}C-NMR spectrum of ***[Fe(ImPPh)$_2$]$^+$***

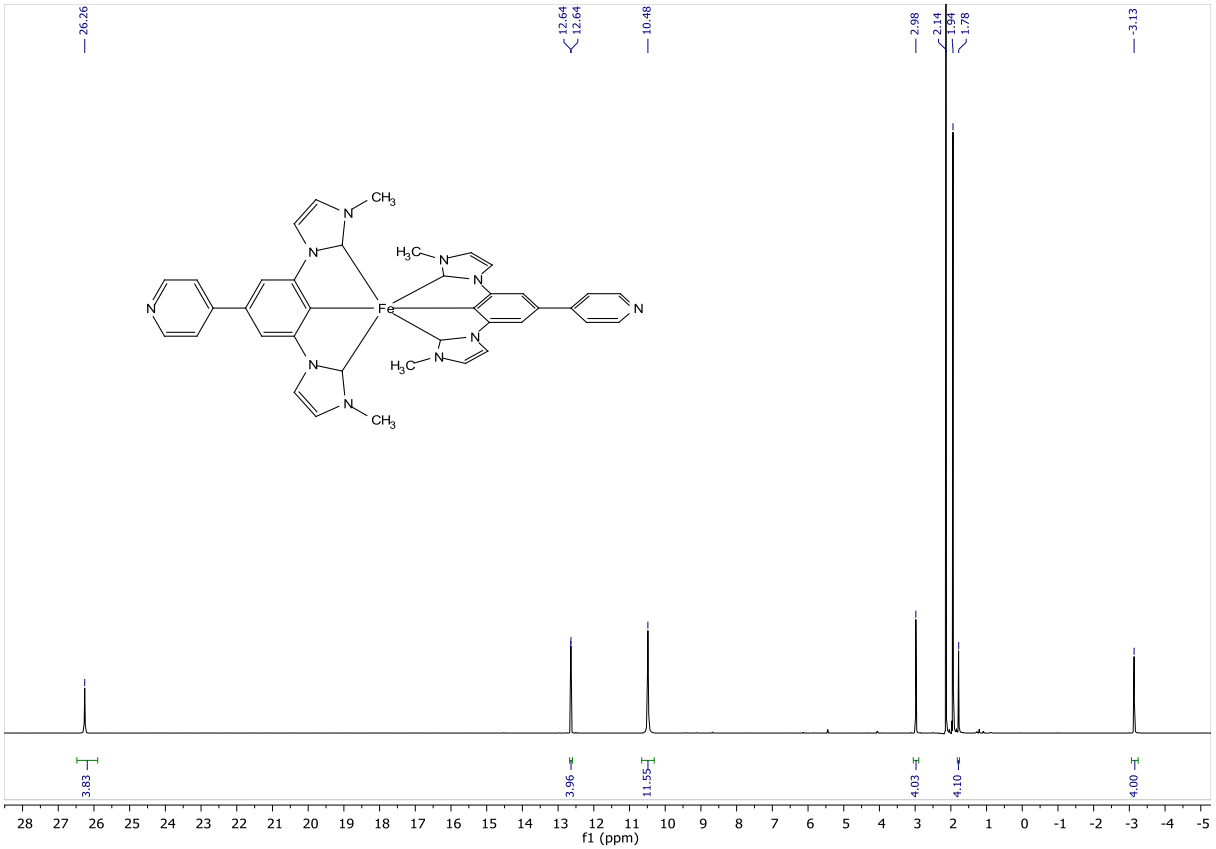

Figure S34: ^{1}H-NMR spectrum of ***[Fe(ImPPy)$_2$]$^+$***

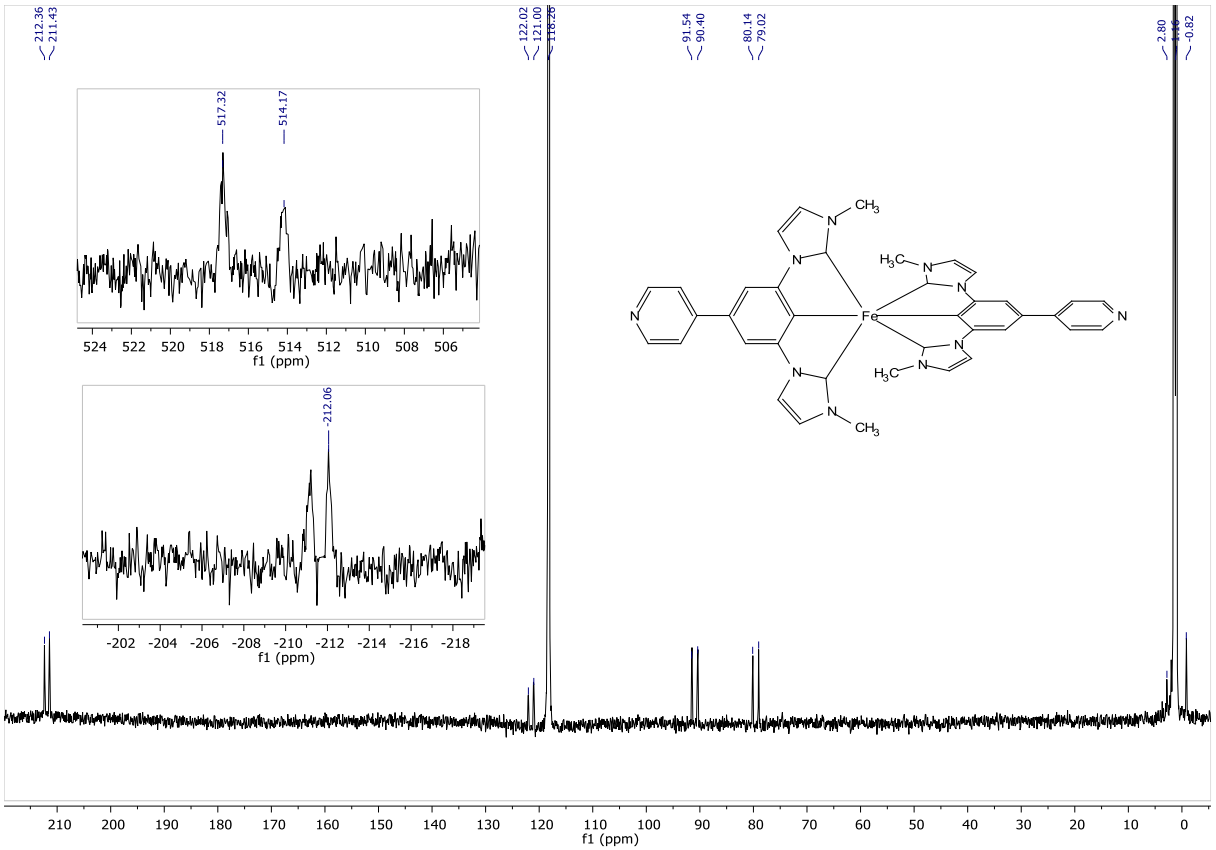

Figure S35: ^{13}C-NMR spectrum of ***[Fe(ImPPy)$_2$]$^+$***

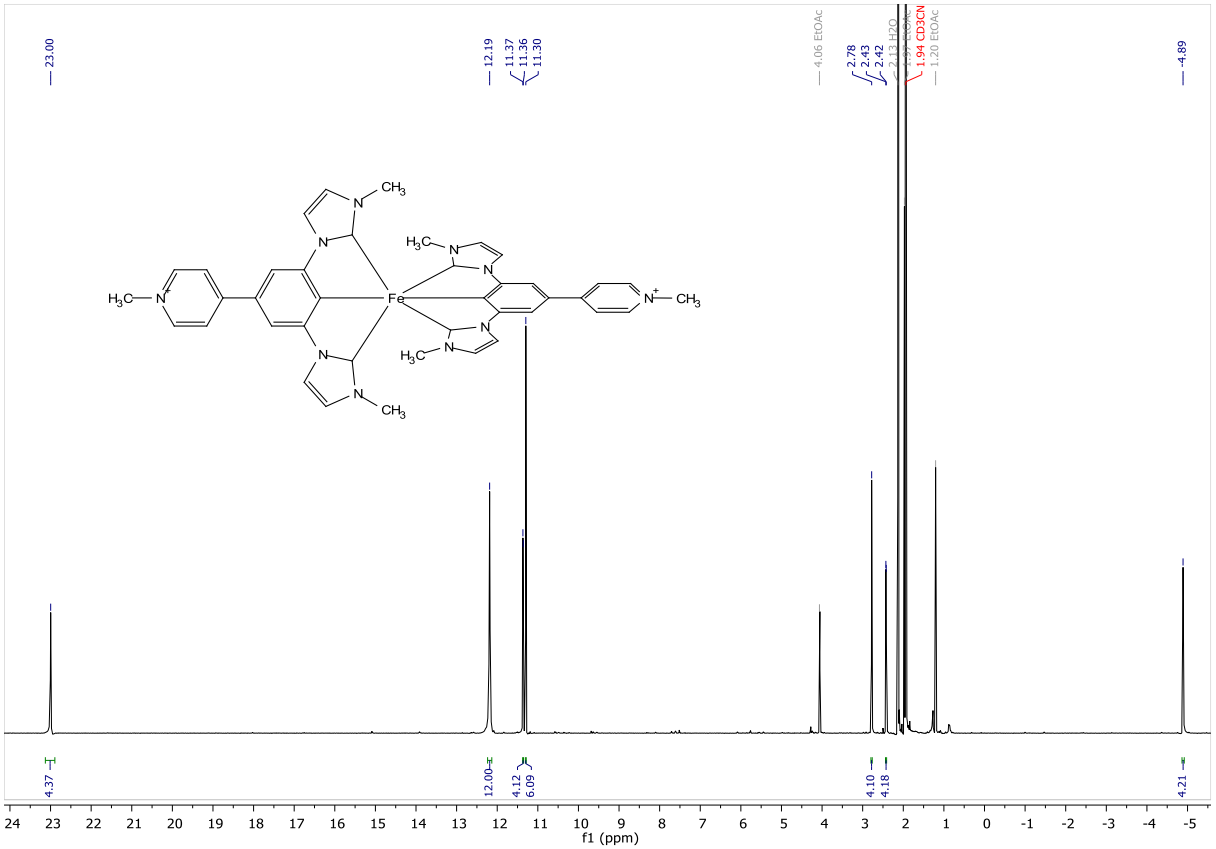

Figure S36: ^{1}H-NMR spectrum of ***[Fe(ImPPyMe)$_2$]$^{3+}$***

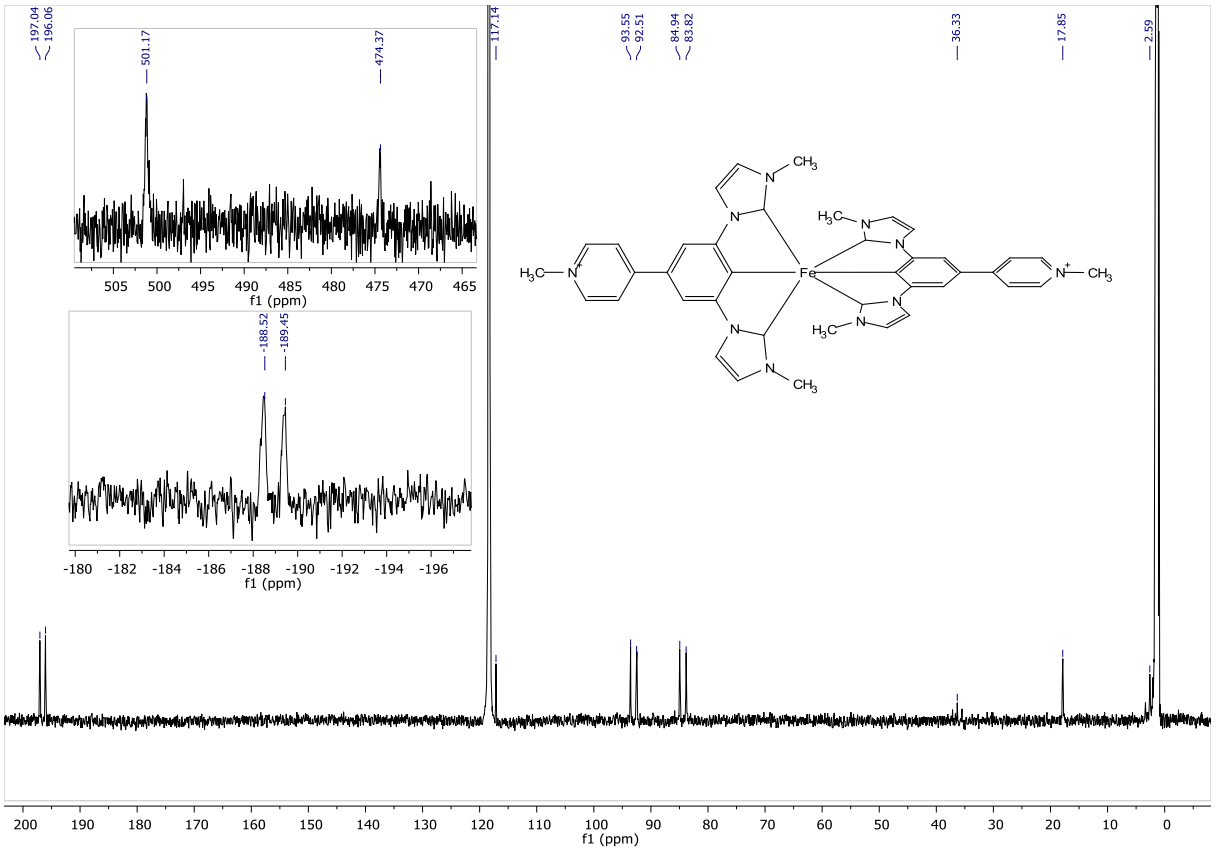

Figure S37: ^{13}C-NMR spectrum of ***[Fe(ImPPyMe)$_2$]$^{3+}$***

Mass spectroscopy

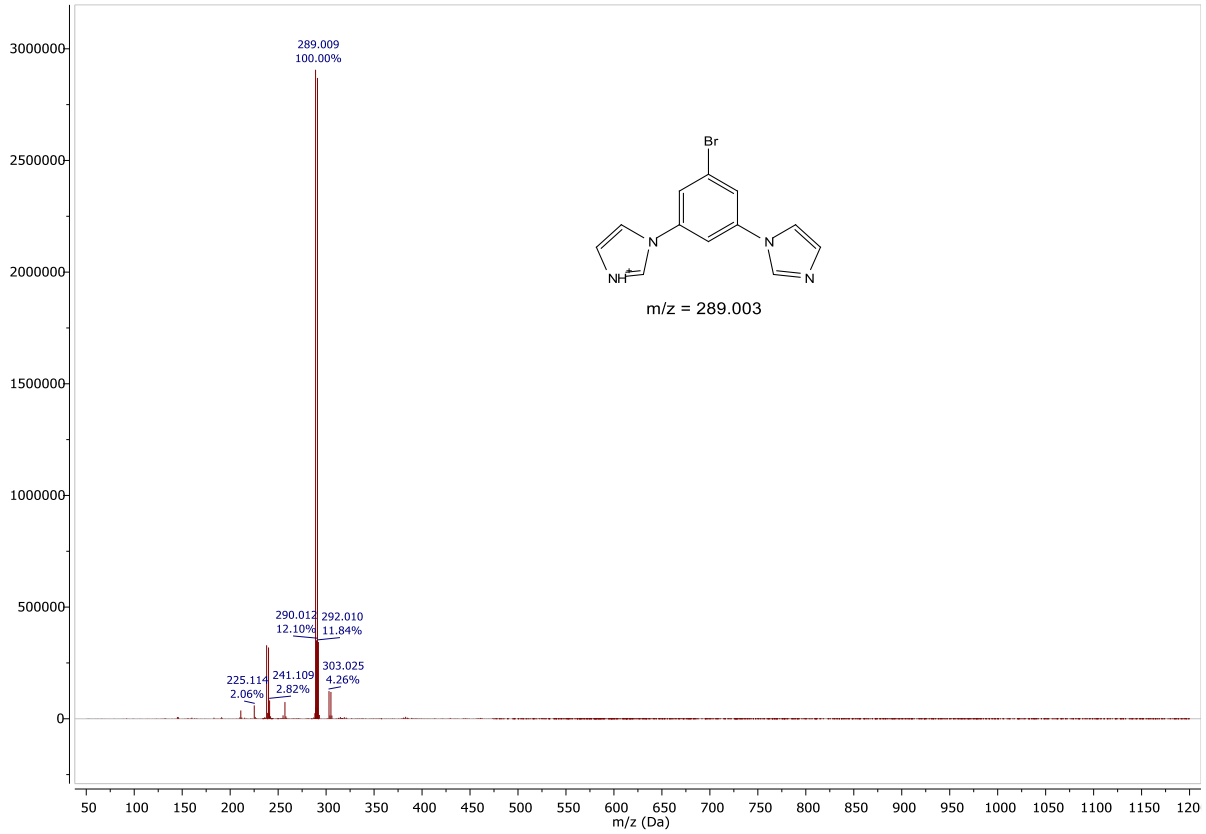

Figure S38: ESI-MS of 1'-(5-bromo-1,3-phenylene)bis(1H-imidazole)

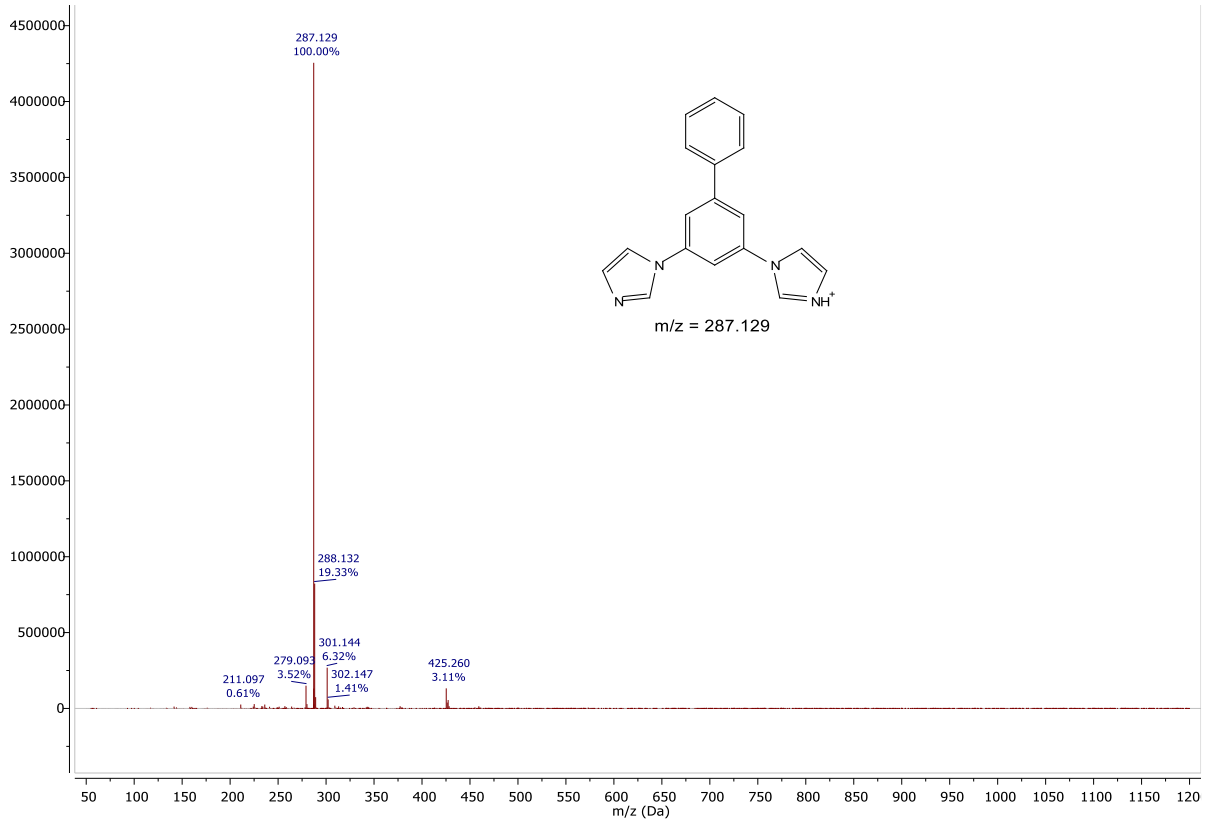

*Figure S39: ESI-MS spectrum of **3C***

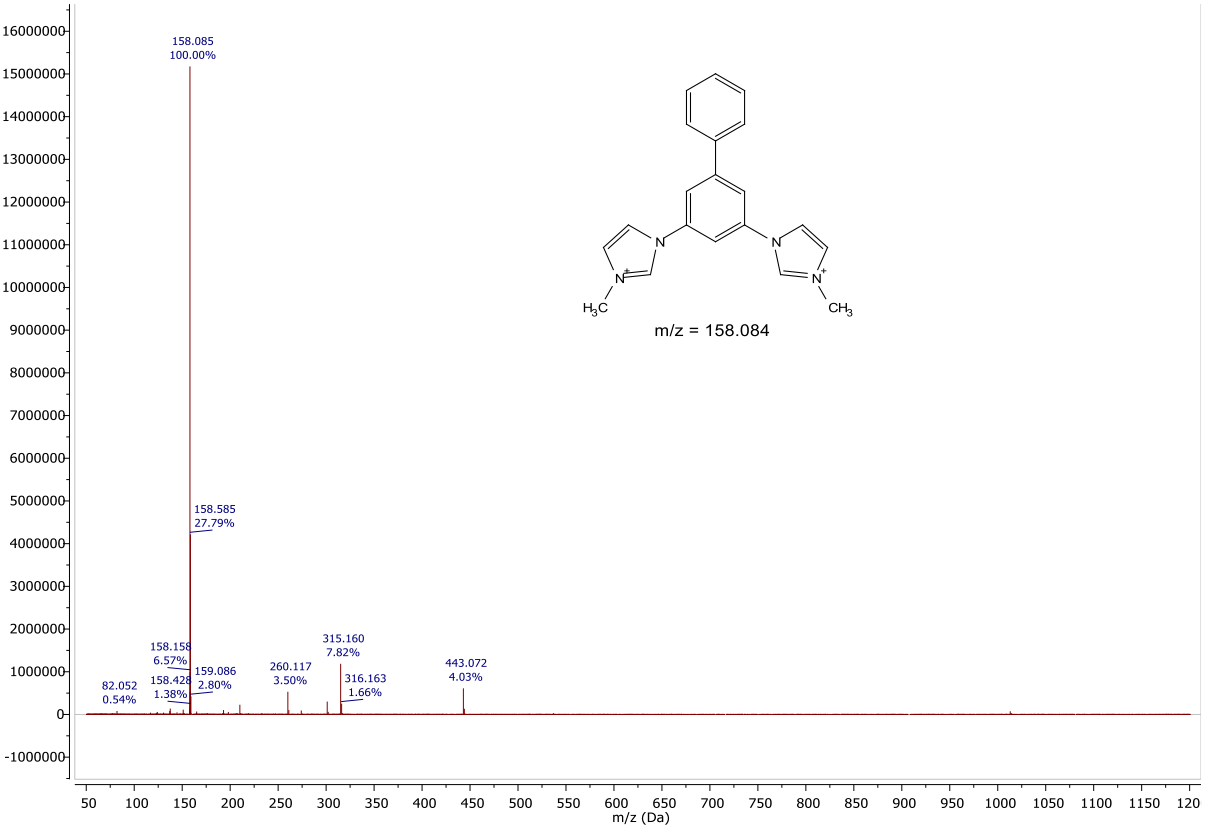

*Figure S40: ESI-MS of **[ImPPh]I₂***

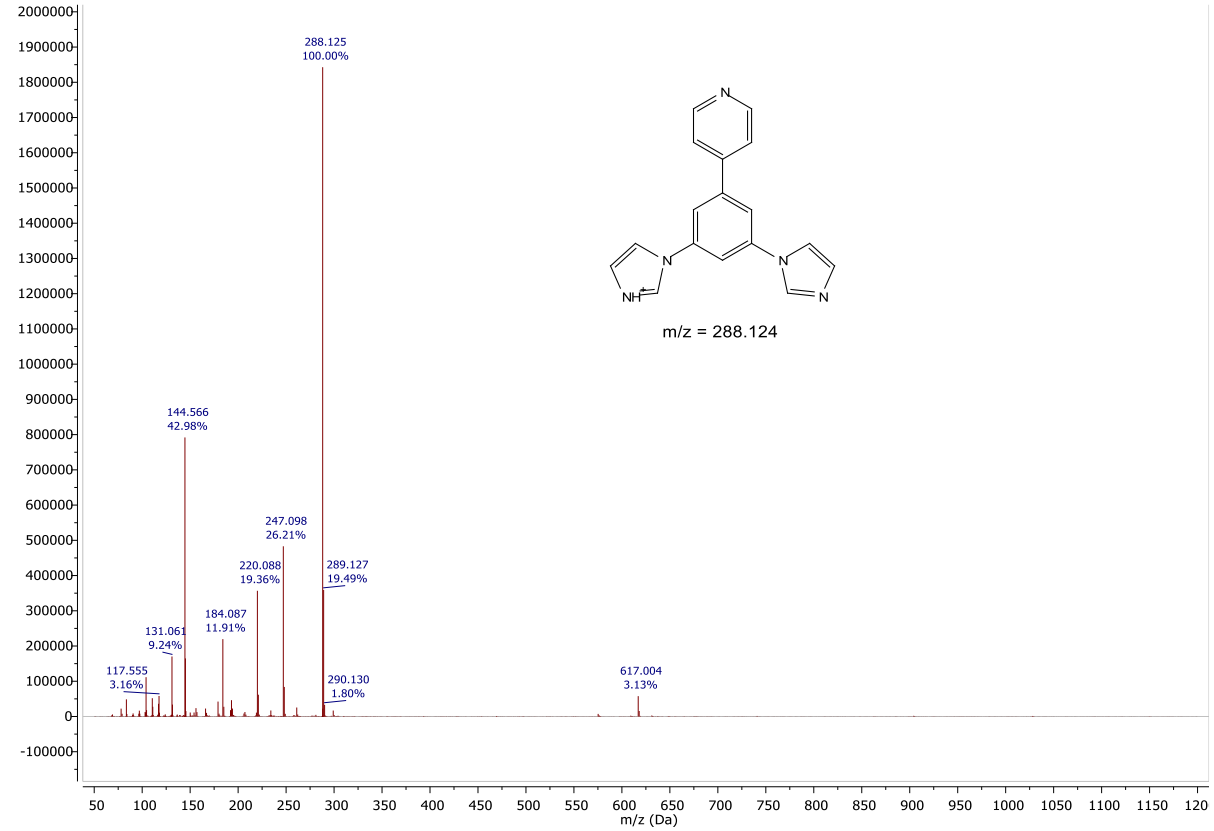

*Figure S41: ESI-MS of **3N***

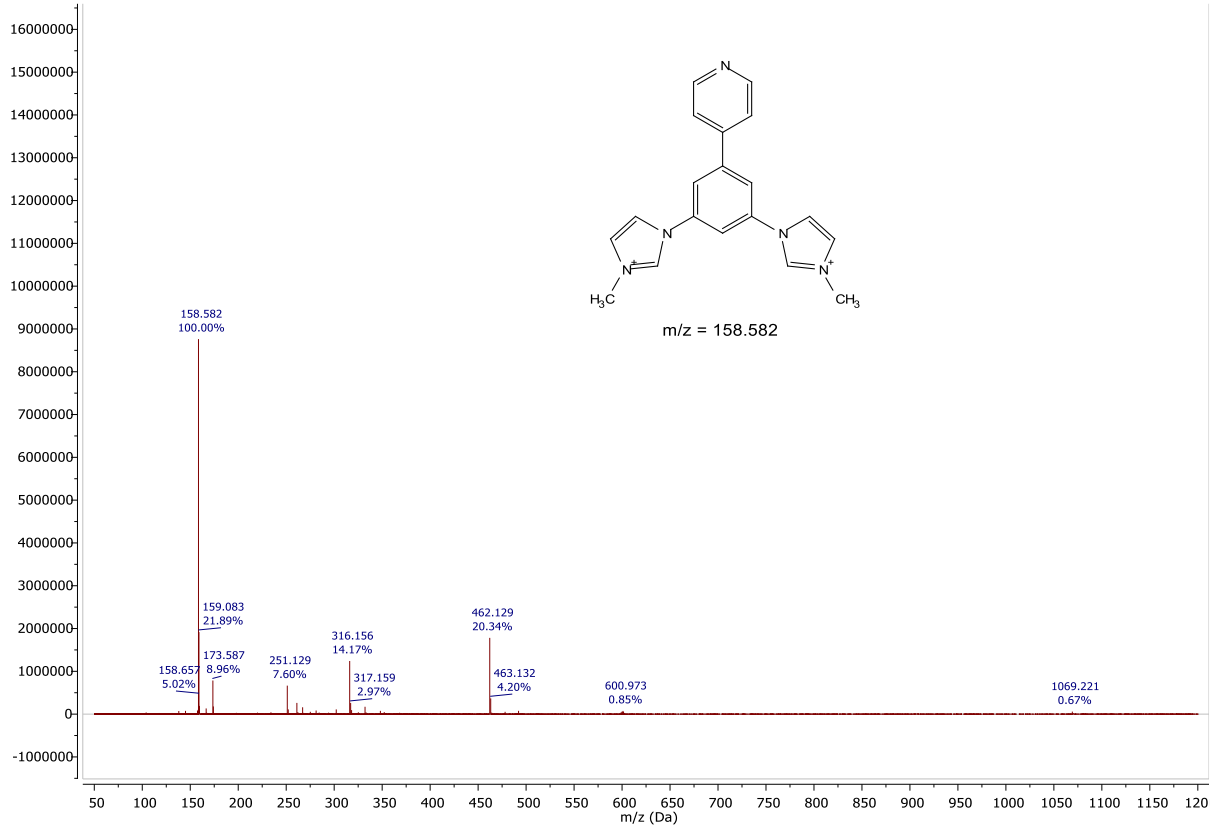

*Figure S42: ESI-MS of **[ImPPy]I$_2$***

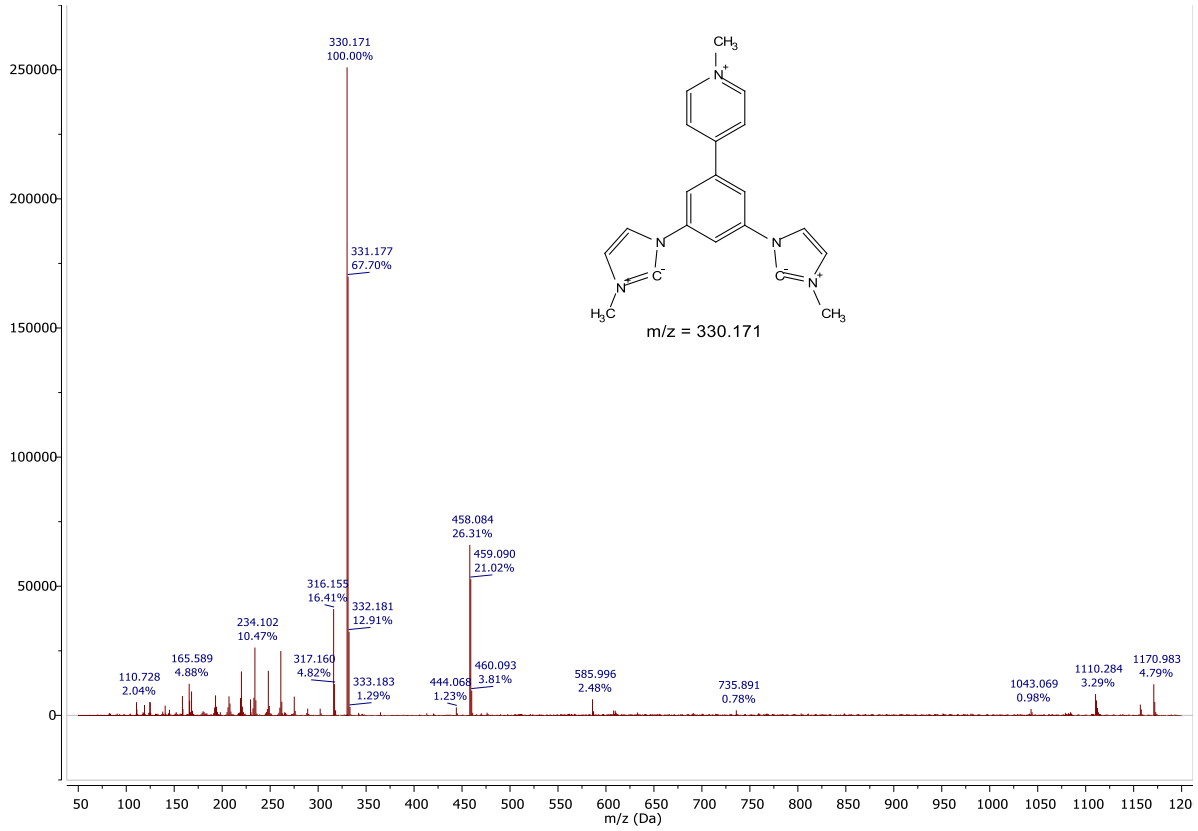

Figure S43: ESI-MS of ***[ImPPyMe]I₃***

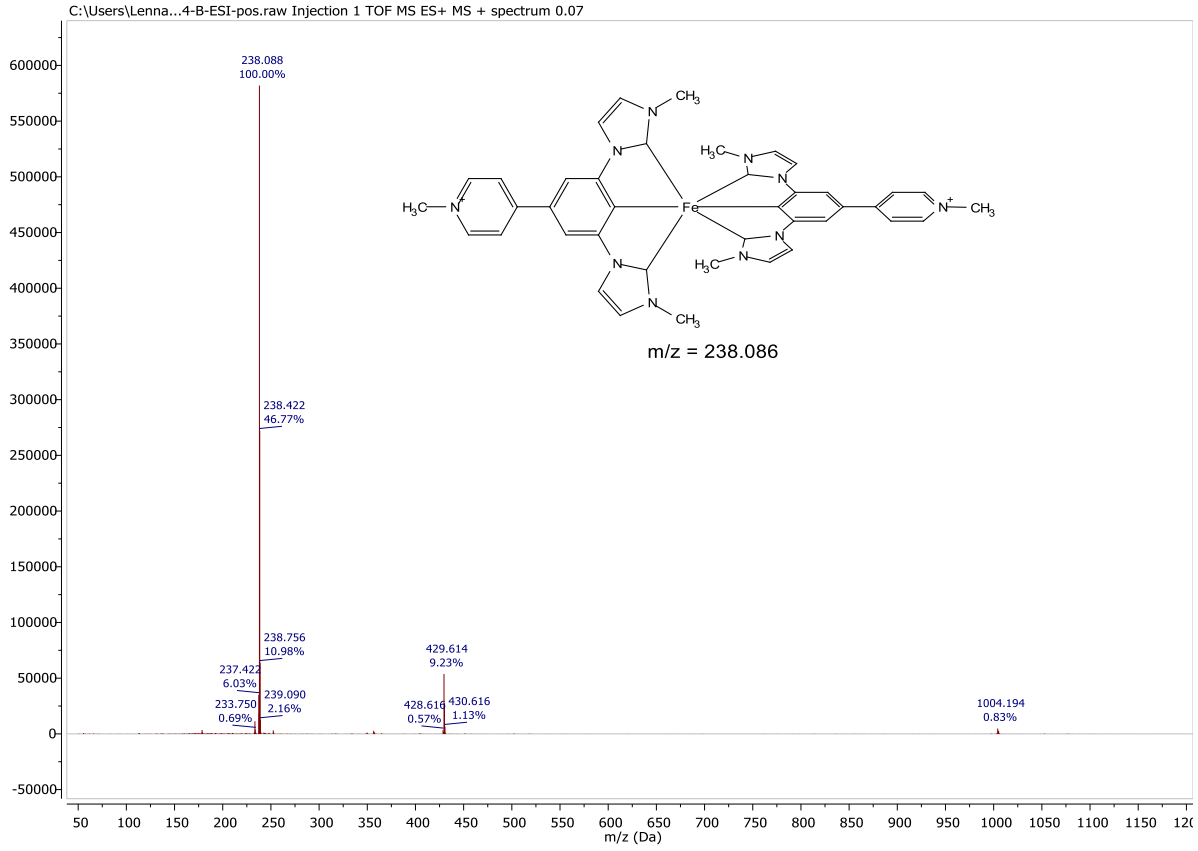

Figure S44: ESI-MS of ***[Fe(ImPPyMe)₂]³⁺***

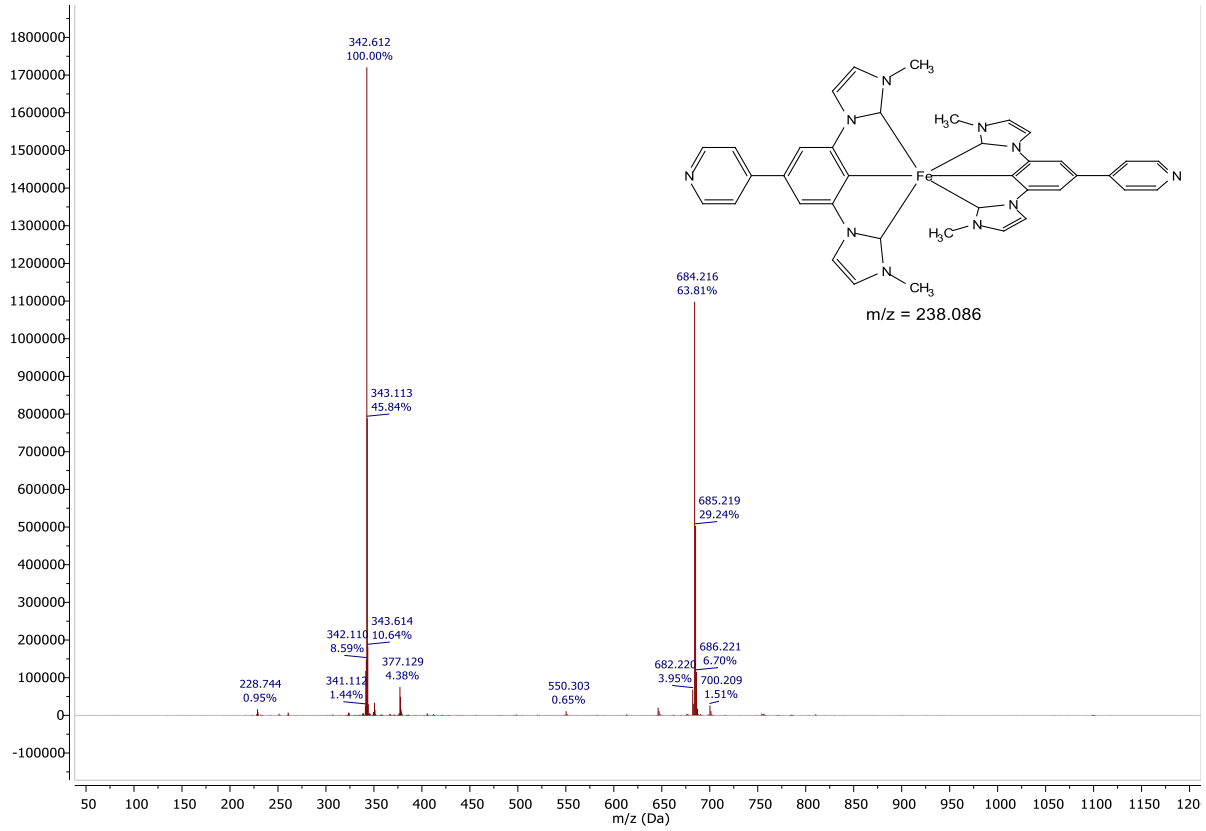

Figure S45: ESI-MS of ***[Fe(ImPPy)$_2$]$^+$***

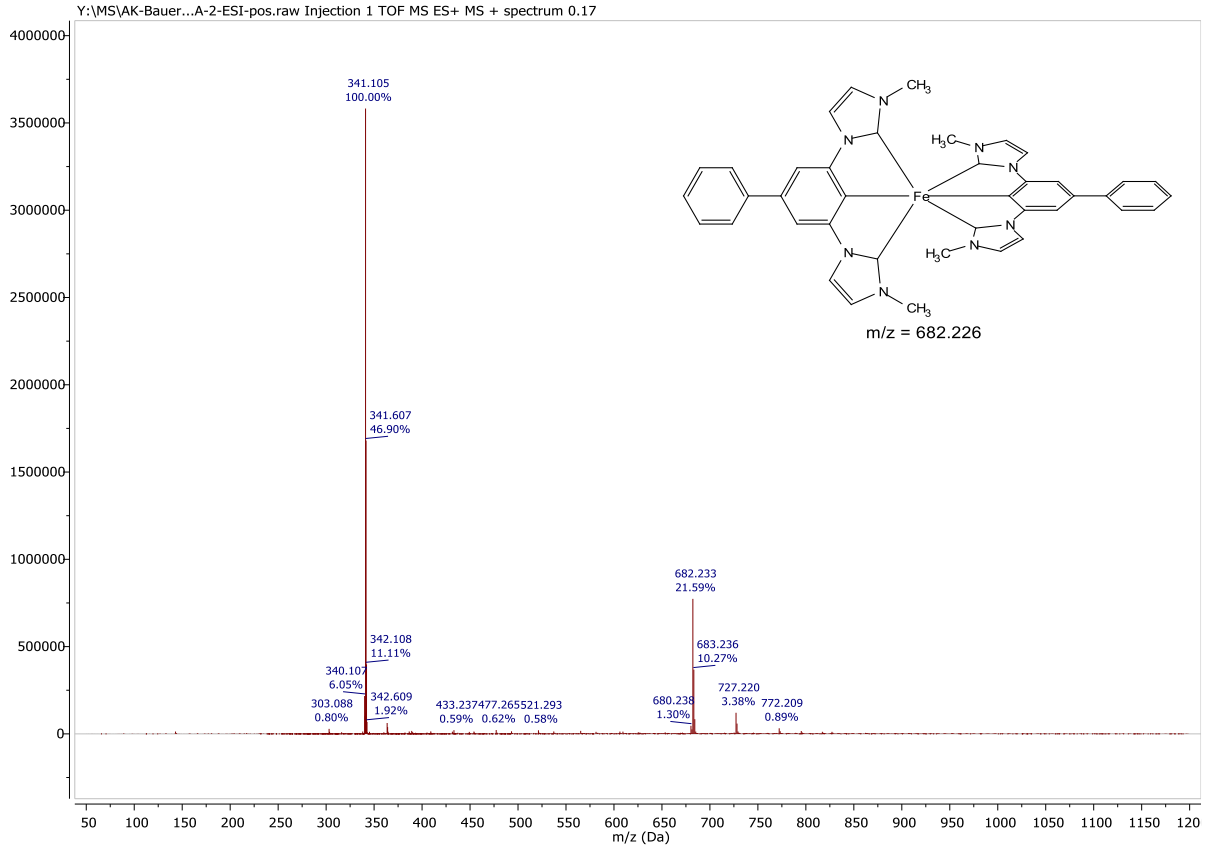

Figure S46: ESI-MS of ***[Fe(ImPPh)$_2$]$^+$***

References

[1] L. Schmitz, M. A. Argüello Cordero, M. J. Al-Marri, R. Schoch, H. Egold, A. Neuba, J. Steube, B. Bracht, O. S. Bokareva, S. Lochbrunner et al., *Inorg. Chem.* **2025**, *64*, 14101.

[2] C. Li, C. Gao, J. Lan, J. You, G. Gao, *Org. Biomol. Chem.* **2014**, *12*, 9524.

[3] Lennart Schmitz **2025**.

[4] P. Dierks, A. Päpcke, O. S. Bokareva, B. Altenburger, T. Reuter, K. Heinze, O. Kühn, S. Lochbrunner, M. Bauer, *Inorg. Chem.* **2020**, *59*, 14746.

[5] R. J. Rubio, G. T. S. Andavan, E. B. Bauer, T. K. Hollis, J. Cho, F. S. Tham, B. Donnadieu **2005**, *690*, 5353.

[6] M. Bauer, J. Steube, A. Päpcke, O. Bokareva, T. Reuter, S. Demeshko, R. Schoch, S. Hohloch, F. Meyer, K. Heinze et al. **2020**.

[7] P. Zimmer, L. Burkhardt, A. Friedrich, J. Steube, A. Neuba, R. Schepper, P. Müller, U. Flörke, M. Huber, S. Lochbrunner et al., *Inorg. Chem.* **2018**, *57*, 360.